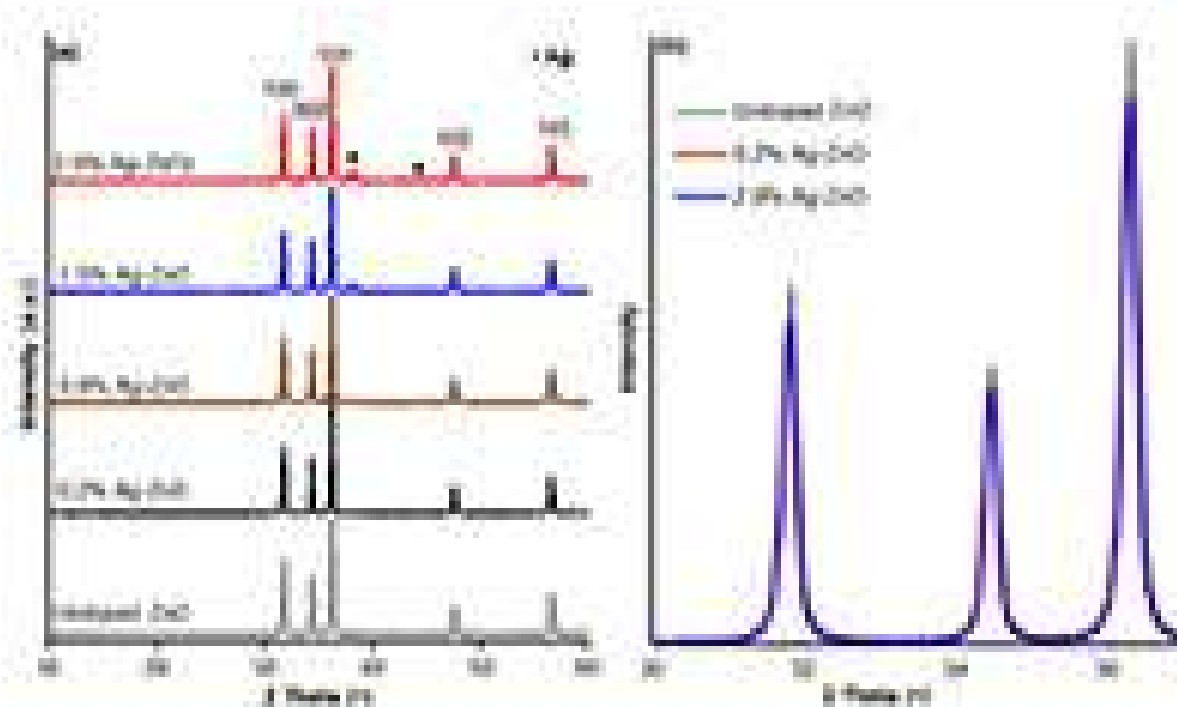


Indonesian Journal of Chemistry

Vol. 22, No. 3, June 2022



Accepted by journal on 04/06/2022
Available online on 06/06/2022

Selection of the Parameters in the Synthesis of Ethylenediamine-Folate Using the Plackett Burman Design

Erianti Siska Purnamasari, Linda Septiana, Ari Hardianto, Ukun Mochammad Syukur Soedjanaatmadja, Anni Anggraeni and Husein Hernadi Bahti*

Department of Chemistry, Faculty of Mathematics and Natural Sciences, Universitas Padjadjaran, Jl. Raya Bandung-Sumedang km 21, Jatinangor 45363, West Java, Indonesia

* Corresponding author:

email: husein.bahti@unpad.ac.id

Received: August 8, 2021

Accepted: February 13, 2022

DOI: 10.22146/ijc.68313

Abstract: This study is concerned with synthesizing ethylenediamine-folate (EDA-Folate), which will then be used as a precursor in synthesizing Gd-PEG-DOTA-Folate, a novel targeted-contrast agent for the diagnosis of cancer, employing the Magnetic Resonance Imaging method. This study aims to determine all the parameters affecting the synthesis of EDA-Folate using the Plackett Burman design. The synthesis method included activation of folic acid using dicyclohexylcarbodiimide and N-Hydroxysuccinimide to result in NHS-Folate, followed by conjugation of ethylenediamine with NHS-Folate to produce EDA-Folate. Analysis of the reaction product confirmed that the reaction product was EDA-Folate. From the resulted data, it can also be concluded that there were four significant parameters (out of the ten parameters studied) in the synthesis of EDA-Folate (with its value presented in the bracket), i.e., time inactivation of NHS-Folate (24 h), stirring rate inactivation of NHS-Folate (300 rpm), the mole of EDA (12 moles), and time of EDA-Folate (12 h). Moreover, the value or desirability of the experimental design was found to be 0.875 (which is < 1.0), meaning that the design will produce optimal conditions and thus the optimal yield of the reaction.

Keywords: ethylenediamine-folate; Plackett-Burman design; yield; contrast agent; Gd-PEG-DOTA-Folate

■ INTRODUCTION

Ethylenediamine-folate (EDA-Folate) is one of the precursors required in the synthesis of a few targeted contrast agents, including Gd-PEG-DOTA-Folate [Gadolinium-(Hexaglycerol Octaaminopropyl Polyoxy ethylene)-(1,4,7,10-Tetraazacyclodecane-1,4,7,10-Tetraacetic acid)-Folate], which is one of the topics of our research program. Contrast agents are, in general, chemical compounds used in the diagnosis of diseases employing the Magnetic Resonance Imaging (MRI) method. And Gd-PEG-DOTA-Folate is a targeted contrast agent and will be used to diagnose cancer. Magnetic Resonance Imaging (MRI) is the most flexible and powerful imaging modality available for clinical use in recent times. For almost five decades, the technology turned into improved, extended, and maintains to evolve, nonetheless no longer accomplishing the physical limits. Technical and

physiological obstacles hamper the advancement and constrain physically feasible developments, making it an increasing number of challenges to innovate [1]. In the MRI method, contrast agents function to increase the difference between the image of sick body tissue and those of healthy one in a human body, so the diagnosis of the disease will be much more accurate [2].

Folic acid is a ligand that has a high affinity to folic receptors ($K_d = 10^{-10}$) found on the surface of various types of cancer. So, folic acid can be used as a carrier to bring about a contrasting compound directly to the target molecule, a folate receptor produced by cancer cells, to result in a clear enough imaging. Folate receptor is a glycosylphosphatidylinositol (GPI), a protein with an MW of 38–40 kDa, found on the surface of cancer cell membranes [3]. While their expression in normal cells is very limited, folate receptors are overexpressed in

epithelial, ovarian, breast, lung, kidney, and brain tumor tissues. When expressed in normal tissues, folate receptors are not located in the lungs, heart, and choroids because, in these tissues, folate receptors are limited to the surface of the apical membrane in epithelial tissue [4]. Folic acid is a type of B vitamin involved in the synthesis of purines. Most cells get folic acid needed through the anion channel or so-called reduced folate carrier, which has a low affinity to folate receptors. So, there is little or almost no expression of folate receptors in normal cells. However, cells that require a lot of folates, such as cancer cells and cells involved in embryonic development, will instead use a high affinity against these folate receptors. Therefore, folate receptors are overexpressed in cancer cells. Due to folate receptor differences between most normal cells and cancer cells, folate receptors are used to selectively target cancer cells for therapy or on compounds for imaging diagnosis [5].

To provide the need for contrast agents in all the hospitals in the country (Indonesia), the number of which is continuously increasing, contrast agents are still being fulfilled through import. In this way, the price is high, the continuity of availability is uncertain, and health service in hospitals is not ensured. Thus, research and development of contrast agents in the country have become a concern.

Synthesis of a targeted contrast agent, i.e., Gd-DTPA-Folate [6] and Gd-DOTA-Poliamidoamine Generation 3-Trastuzumab [7], have recently been done. As a continuation of our research program, its PEG derivative - Gd-PEG-DOTA-Folate - is being studied to get a novel targeted contrast agent by conjugating Gd-DOTA-Folate with branch-structured derivative polyethyleneglycol. Using the novel targeted contrast agent, diagnosis with MRI will theoretically be better than using Gd-DOTA-Folate because the relaxivity and luminance of branch-structured PEG-Gd are higher than those of linear-structured PEG-Gd. Although the terminal Gd conjugation is different, it did not affect the longitudinal relaxivity and luminance in branch-structured PEG-Gds (the eight-arm PEG-Gd). The branch-structured PEG-Gds (eight-arm PEG-Gd) show the highest contrast efficiency and is even higher than that

of commercially available contrast agents [8].

The synthesis of Gd-PEG-DOTA-Folate will be carried out through four reaction steps. The first step is the synthesis of EDA-Folate as a precursor. Synthesis of EDA-Folate can be done using one of the two synthesis methods, namely the direct- and indirect methods [9]. In the direct method, the synthesis is accomplished through two reaction steps: (1) Activation of folic acid using dicyclohexylcarbodiimide (DCC) and *N*-Hydroxysuccinimide (NHS) to produce ethylenediamine-Folate (EDA-Folate) [2-6], and (2) Conjugation of NHS-folate with ethylenediamine (EDA) to form EDA-Folate. Meanwhile, in the indirect method, the synthesis of EDA-Folate is carried out through five reaction steps, i.e., formations of: (1). pyrophoric acid, (2) petrol hydrazide, (3) petrol acid, (4) methyl ester of folic acid, and (5) EDA-Folate, as the final product [10].

In this study, the direct method has been chosen because it is simpler than the indirect method, in that the direct method consists of only two reaction steps. But the problem was that the yield of the reaction synthesis was low, and thus attempts should be made to increase the yield.

To obtain optimal rendement of the EDA-Folate product, a screening design is required to provide information on parameters that have significant effects in the synthesis process. The Plackett-Burman design is the most commonly used screening design because, with the design, estimation of all major effects with the same precision can be done. Another advantage of this fractional factorial design is that it minimizes the experimental process from a large number of variables to a smaller number of most significant factors to save time, cost, and chemicals [11]. The last three mentioned aspects are also important, especially if the experiment will be done later on a bigger scale. The Plackett-Burman design can only be used for experiments that are multiples of 4 with 8 as the starting point ($N = 8, 12, 16, 20, 24, 28, 32, 36$). A minimum of $4n$ experiments is needed for estimating the main effects for $4n-1$ factors. For example, 4, 5, 6, or 7 factors would require 8 experimental runs, 8, 9, 10, or 11 would require 12 runs,

and so on [12]. In this study, the selection parameters of EDA-Folate were carried out, with 10 parameters being selected.

It has been reported that many parameters that affect the synthesis EDA-Folate parameters are lighting intensity, the addition of an organic base, ratio mole of folic acid and DCC, time inactivation of NHS-folate, temperature inactivation of NHS-Folate, stirring rate of NHS-Folate, ratio mole of EDA, and addition of pyridine [13-16]. This study aims to determine parameters that have significant effects in the synthesis of EDA-Folate through the direct method with Plackett Burman's design using the software Design Expert 10.0.1. The parameters studied included lighting intensity (dark/light), the addition of an organic base (DIPEA), the mole of DCC, time inactivation of NHS-Folate, temperature inactivation of NHS-Folate, stirring rate of NHS-Folate, the mole of EDA, the addition of pyridine, time of EDA-Folate, and stirring rate of EDA-Folate. Experiments in this study consisted of activation of folic acid using DCC and NHS, followed by conjugation of EDA with NHS-Folate to produce EDA-Folate. Characterization of the reaction product, i.e., EDA Folate, has been done using the mass spectrometric method, and determination of significant parameters has been done using Plackett Burman's design.

■ EXPERIMENTAL SECTION

Materials

Chemicals used were of analytical grade, purchased from Sigma Aldrich. They included dicyclohexyl carbodiimide (DCC), dimethylsulfoxide (DMSO), ethylenediamine (EDA), *N*-Hydroxysuccinimide (NHS), *N,N*-Diisopropylethylamine (DIPEA), and pyridine.

Instrumentation

The equipment used in this study included glass apparatus, a magnetic stirrer (Heidolph MR 3002), a Mass Spectrometer (Waters Xevo Q-TOF MS), and the software Design Expert 10.0.1. The measurement condition of Mass Spectrometry was Capillary 3 kV, Sampling cone 40, Extraction cone 4.0, Sorce temp 100 °C, Desolvation temp 250 °C, and Desolvation gas 600 L/h.

Inlet system was LC or Direct Probe, Ion Souce was ESI, Mass Analyzer was Quadrupole and Tof, and Detector type was Micro Chanel Plates (MCPs).

Procedure

Synthesis of ethylenediamine-folate

Folic acid (0.0882 g), DCC (0.418 g), and NHS (0.0460 g) were dissolved in 10 mL of DMSO, followed by the addition of DIPEA into the mixture, which was stirred overnight. A white precipitate (dicyclohexyl urea, as a side product) was formed and was removed by filtration. Into the filtrate containing NHS-Folate, ethylenediamine and pyridine were added. The mixture was then stirred using a magnetic stirrer until ethylenediamine-folate (EDA-Folate) as a final product of the reaction was formed. The product was then characterized by Mass Spectrometry. The resulted data were analyzed using the software Design Expert 10.0.1 to determine significant parameters.

Selection parameters of synthesis ethylenediamine-folate using Plackett Burman design

Table 1 shows the parameters (10) and a dummy (one), the upper level (+1), and the lower level (-1), which were determined by the Plackett-Burman design.

■ RESULTS AND DISCUSSION

The synthesis reactions of ethylenediamine-folate are shown in Fig. 1. As is shown in Fig. 1, the synthesis of ethylenediamine-folate was initiated with the activation of folic acid with dicyclohexylcarbodiimide (DCC) and *N*-Hydroxysuccinimide (NHS), followed by the conjugation of ethylenediamine with the activated folic acid (NHS-Folate), to produce ethylenediamine-folate (EDA-Folate). The mass spectrum of EDA-Folate produced is shown in Fig. 2.

Fig. 2. shows the spectrum of EDA-Folate ($C_{21}H_{25}N_9O_5$) theoretically has a molecular mass (m/z) of 483.4760. The molecular mass of the EDA-Folate compound resulting from the HR-TOFMS ES+ spectrum was 484.2191; the peak shows that the EDA-Folate with the addition of a proton. In all these experiments, EDA-Folate were successfully synthesized by using the direct method.

Table 1. Parameters and their levels to be determined using the Plackett Burman's design

No.	Parameter	Code	Unit	Level	
				Lower (-1)	Upper (+1)
1	Lighting intensity	A	-	dark	light
2	Addition of an organic base DIPEA	B	mL	without DIPEA	With DIPEA
3	Mole of DCC	C	mmol	1	2,25
4	Time inactivation of NHS-Folate	D	hours	12	24
5	Temperature inactivation of NHS-Folate	E	(°C)	room temp.	50
6	Stirring rate of NHS-Folate	F	rpm	100	300
7	Mole of EDA	G	mmol	8	12
8	addition of pyridine	H	(μ L)	300	700
9	Stirring rate of EDA-Folate	I	rpm	100	300
10	Time of EDA-Folate	J	hours	6	12
11	Dummy	K	-	-1	+1

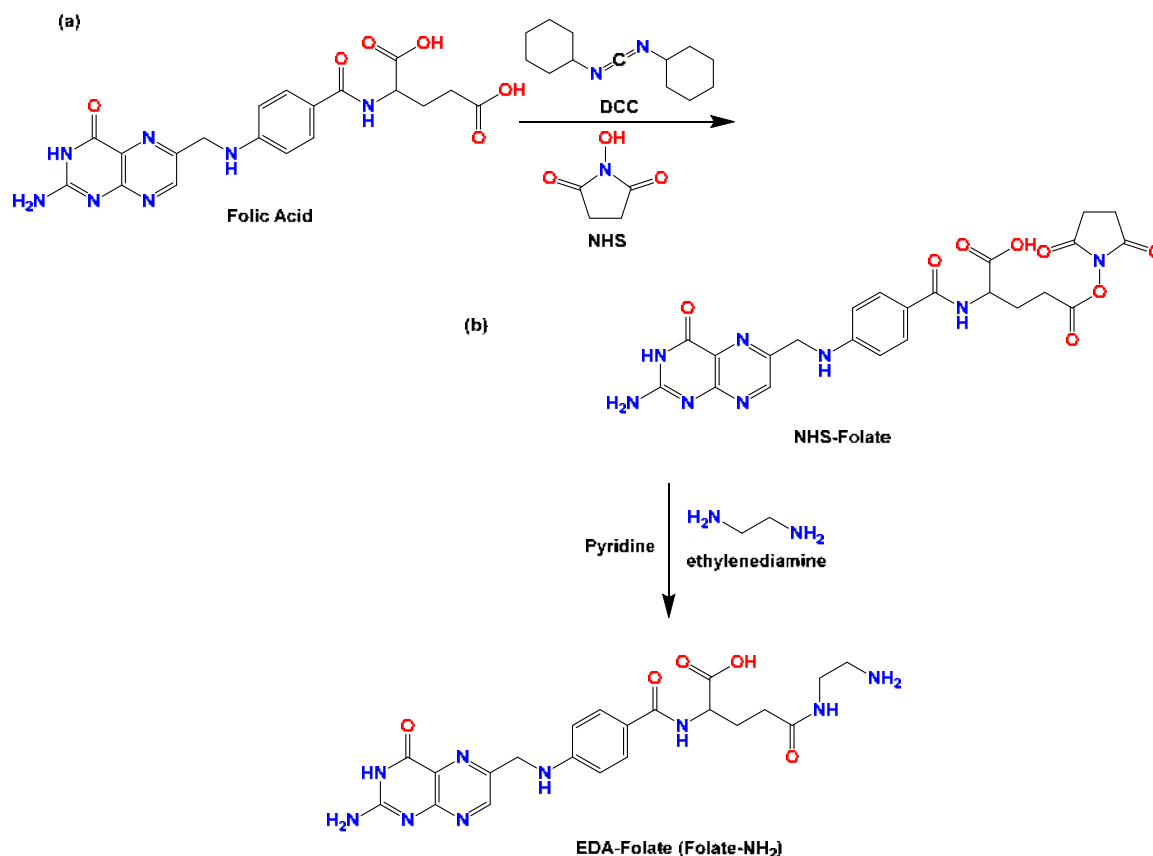
**Fig 1.** (a) Activation reaction of folic acid and (b) Conjugation reaction of NHS-Folate with ethylenediamine

Table 2 shows the resulted data on the responses determined in the synthesis of ethylenediamine-folate. The fractional factorial formula for the Plackett Burman is

$K = N - 1$, where N is a multiplication of 4, so the formula becomes $K = 4n - 1$, where K is the parameter and n is runs. In this study, $n = 3$, and the number of parameters

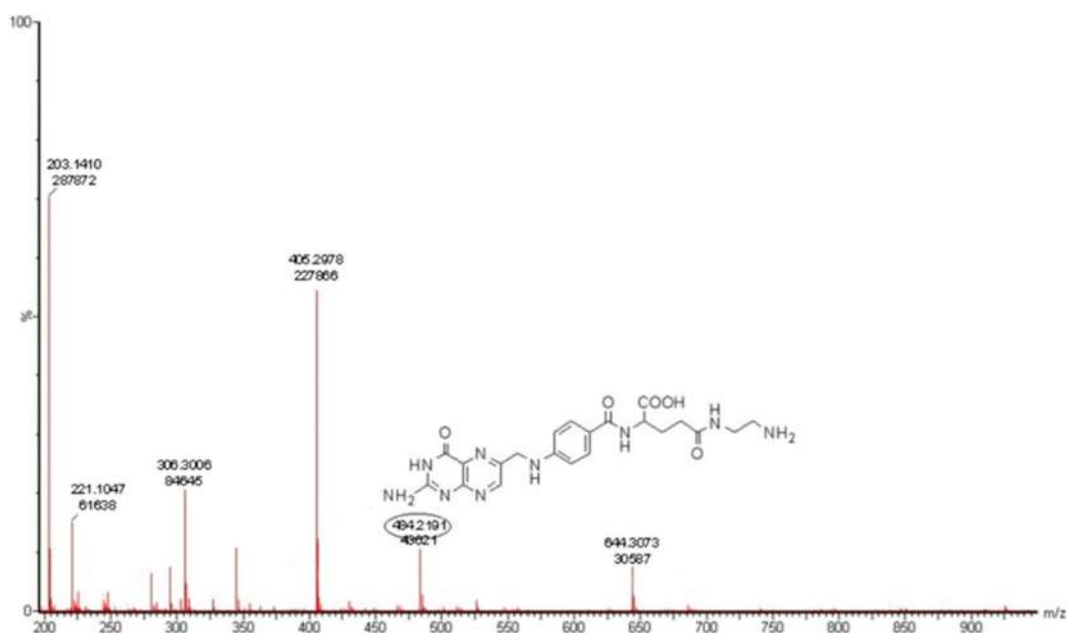


Fig 2. Mass spectrum of EDA-Folate

Table 2. Matrix of the Plackett-Burman design containing resulted data on the responses in the synthesis of ethylenediamine-folate

Std	Run	A Lighting intensity	B DIPEA (addition of 0.1 mL)	C Mole of DCC (mmol)	D Time of NHS- Folate (h)	E Temp. of NHS- Folate (°C)	F Stirring rate of NHS-Folate (rpm)	G Mole of EDA (mmol)	H addition of pyridine (μL)	I Stirring rate EDA- Folate (rpm)	J Time of EDA- Folate (h)	K Dummy	R Peak Intensity
2	1	dark	with	2.25	12	50	300	12	300	100	6	+1	3290
10	2	dark	with	2.25	24	room temp	100	8	700	300	6	+1	4378
7	3	light	without	1	12	50	100	12	700	300	6	+1	775
8	4	light	with	1	12	room temp	300	8	700	100	12	+1	7321
6	5	dark	without	1	24	room temp	300	12	300	300	12	+1	43261
4	6	dark	with	1	24	50	100	12	700	100	12	-1	2973
9	7	light	with	2.25	12	room temp	100	12	300	300	12	-1	2939
12	8	dark	without	1	12	room temp	100	8	300	100	6	-1	1776
11	9	light	without	2.25	24	50	100	8	300	100	12	-1	4292
3	10	light	without	2.25	24	room temp	300	12	700	100	6	-1	27043
1	11	light	with	1	24	50	300	8	300	300	6	-1	3849
5	12	dark	without	2.25	12	50	300	8	700	300	12	-1	14055

to be selected were ten. It was necessary to have the dummy meet the formula, with the number of experiments ($4n$) being 12 (see Table 2).

In the Plackett-Burman design, the upper level (+1) and lower level (-1) were determined to evaluate which parameters significantly impacted the experiment. As can be seen in Table 1, the upper and the lower values for each parameter were selected based on secondary data [13-16]. Furthermore, these parameters were incorporated, and

the Plackett-Burman design matrix with encoding for 12 experiments to be conducted along with the peak intensity mass spectrometry shown in Table 2.

The equation derived from the Plackett-Burman design is presented in Eq. (1)

$$Y = 9662.67 - 1959.50X_1 - 5537.67X_2 - 329.83X_3 + 4636.67X_4 - 4790.33X_5 + 6807.17X_6 + 3717.50X_7 - 238.50X_8 + 1880.17X_9 + 2810.83X_{10} + 890.17X_{11} \quad (1)$$

where: X_1 (lighting intensity); X_2 (addition of an organic base DIPEA); X_3 (mole of DCC); X_4 (time in activation

of NHS-Folate) X_5 (temperature in activation of NHS-Folate); X_6 (stirring rate of NHS-Folate); X_7 (mole of EDA); X_8 (addition of pyridine); X_9 (stirring rate of EDA-Folate); X_{10} (time of EDA-Folate); X_{11} (Dummy).

Calculation of the response or acquisition of intensity (R_1) can statistically be done by using Eq (2).

$$Y = \beta_0 + \beta_1 X_1 + \beta_2 X_2 + \beta_3 X_3 + \beta_4 X_4 + \beta_5 X_5 + \beta_6 X_6 + \beta_7 X_7 + \beta_8 X_8 + \beta_9 X_9 + \beta_{10} X_{10} + \beta_{11} X_{11} \quad (2)$$

where Y is a response, β_0 is a constant, and β_1 and β_n are coefficient of response values.

Using Eq. (1), parameters having positive and negative influences on the response have been determined. The parameters with positive or negative effects were determined using coefficient calculations (β) for each parameter in the experimental data. The eleventh coefficient of parameters ($\beta_1, \beta_2, \beta_3, \dots, \beta_{11}$) can be calculated from the multiplication of each result with the value of each parameter (+1/-1) for each experiment. The results of the coefficient of parameters were then divided by the number of experiments. For example, for parameter 1, which is exposure, the value of the coefficient was:

$$\beta_1 = (+2939 - 2973 - 1776 - 43261 + 775 - 14055 - 4378 + 27043 + 4292 + 7321 + 24.073 + 3849 - 3290)/12 = -1959.5$$

The result of coefficient β_1 was negative, which means that from the average of 12 experiments conducted, the acquisition of EDA-Folate intensity will decrease if this synthesis is made in a bright place. It is because folic acid undergoes decomposition [13,16]. The negative value of a parameter coefficient (β) indicates that increasing the value of the parameter coefficient will decrease the peak intensity of the EDA-Folate. In contrast, a positive value of parameter coefficient (β) indicates that increasing the value will increase the peak intensity of EDA-Folate.

Fig. 3 is a Normal Plot Distribution and Pareto chart of the relevant parameters being studied. As is shown in the figure, six parameters were significant to the normal percent probability and T-value. The six parameters were parameter B (addition of the organic base DIPEA), parameter D (time inactivation of NHS-Folate), parameter E (temperature of NHS-Folate), parameter F (stirring rate of NHS-Folate), parameter G (mole of

EDA), parameter J (time of EDA-Folate). Of the six significant parameters, four parameters, i.e., parameter D (time inactivation of NHS-Folate), parameter F (stirring rate inactivation of folic acid), parameter G (mole of EDA), and parameter J (time of EDA-Folate), showed positive effects. Meanwhile, two parameters, i.e., parameter B (addition of the organic base DIPEA) and parameter E (temperature of NHS-Folate), showed negative effects on normal percent probability and T-values.

From the normal plot distribution (Fig. 3(a)), the stirring rate of NHS-Folate was farthest from the response line. At the same time, the addition of organic base (DIPEA) had the highest negative effect on the intensity of synthesis EDA-Folate because it was at the lowest from the response line. As shown in the Pareto chart (Fig. 3(b)), it can also be seen that the stirring rate of NHS-Folate had the highest positive effect on the intensity of EDA-Folate synthesis.

The graphs shown in Fig. 3 indicate that only four parameters' responses can be used for the next stage of optimization. They are stirring time inactivation of NHS-Folate (24 h.), stirring rate activation of NHS-Folate (300 rpm), a mole of EDA (12 mmol), and stirring time of EDA-Folate (12 h). With these four parameters, a desirability value of 0.875 and a minimum intensity of EDA-Folate of 37962.8 could be obtained.

Desirability value is a function of optimization value that demonstrates the ability of programs to desire based on criteria set on the final product. The range of the value of desirability is from 0.0 to 1.0. A desirability value getting closer to 1.0 indicates that the design or program can produce an optimal product. An optimization goal is not to get a desirability value of 1.0 but to find the best condition that brings all optimal objective functions [17]. Fig 4. Represents the graphs of the parameter of optimum response based on the Plackett-Burman design. The addition of DIPEA and temperature during stirring is zero. It was due to the pH value at the time of addition of DIPEA was not achieved or even exceeding the pH in the process of activation of folic acid (i.e., 4.5-7.5) [18]. It will be noted that activation of folic acid is better to be conducted in a room

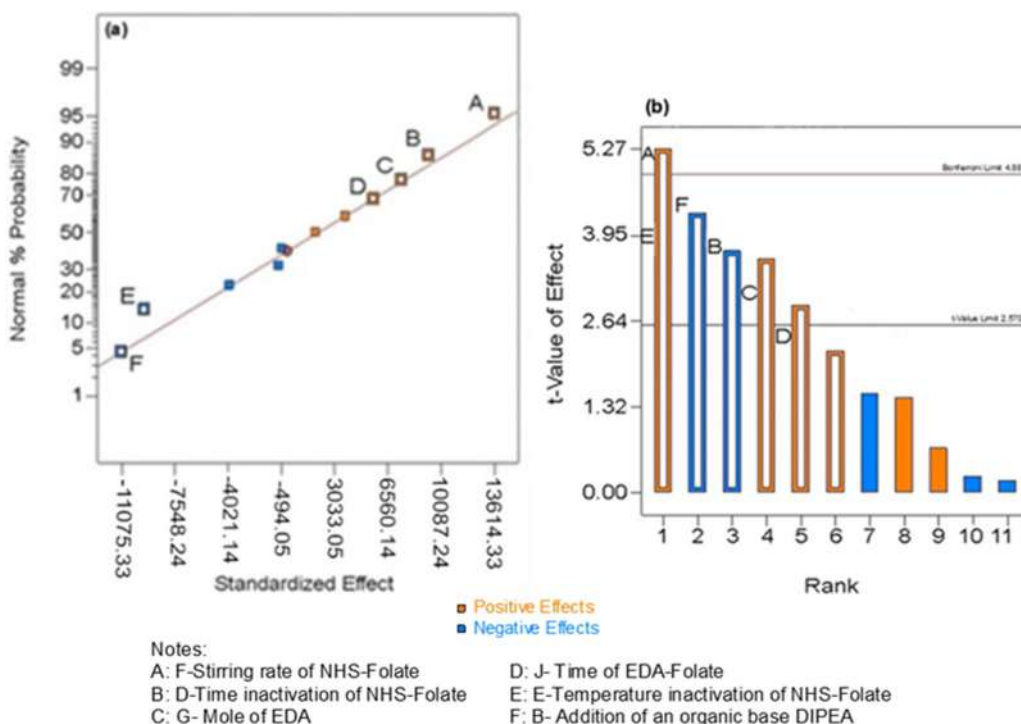


Fig 3. (a) Normal plot distribution and (b) Pareto chart of the eleven parameters

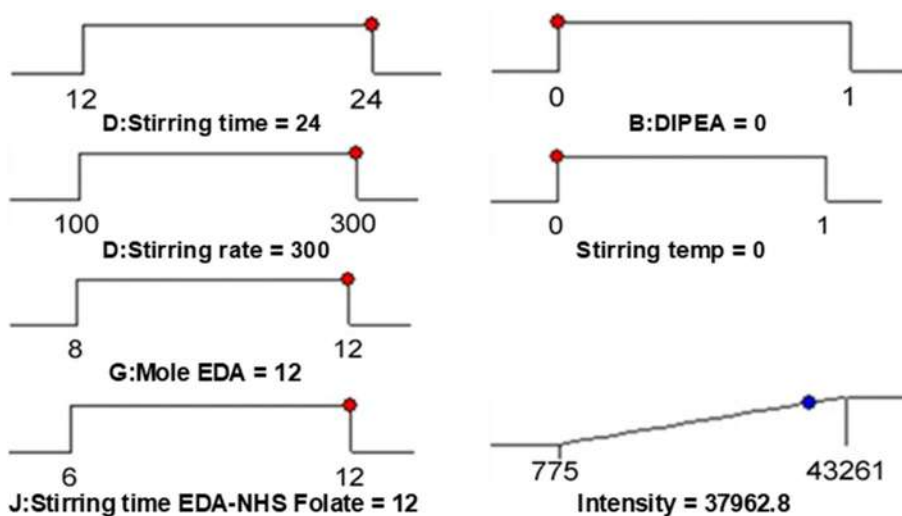


Fig 4. Graphs of the parameter of optimum response based on the Plackett-Burman design

temperature (without heating) because folic acid is undergoing decomposition at high temperatures.

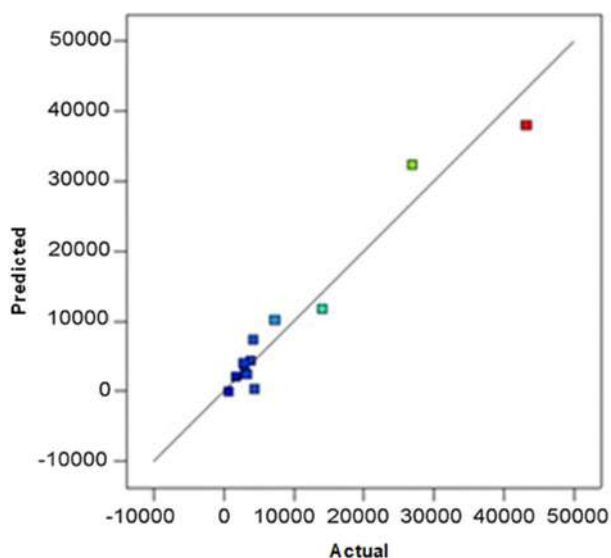
Fig. 5 is the linear regression curve between actual responses and those predicted using the Plackett Burman design. Analysis of this design using ANOVA (Table 3) has resulted in a value of R^2 (coefficient of determination) of 0.9450 that close to one. So, the design was acceptable. This value indicates a match between the predicted value

and the actual value. A slight difference between the measured and calculated values indicates the higher suitability of the model [19-20].

The reliability level of a model is acceptable if the value of P is less than 0.05 (significant). In this experiment, the value of P calculated from the Plackett Burman design was found to be 0.0052. This value of P is therefore acceptable. This design also produces Adeq

Table 3. ANOVA table for the selected factorial model

ANOVA for the Selected Factorial Model						
Analysis of Variance Table [Partial sum of squares-Type III]						
Source	Sum of squares	df	Mean square	F value	p-value Prob > F	
Model	1.718 E + 09	6	2.863 E + 08	14.32	0.0052	(significant)
B-DIPEA	3.680 E + 08	1	3.680 E + 08	18.40	0.0078	
D-Stirring time	2.580 E + 08	1	2.580 E + 08	12.90	0.0157	
E-Stirring temp	2.754 E + 08	1	2.754 E + 08	13.77	0.0138	
F-Stirring rate	5.561 E + 08	1	5.561 E + 08	27.80	0.0033	
G-Mole EDA	1.658 E + 08	1	1.658 E + 08	8.29	0.0346	
J-Stirring time EDA-NHS Folate	9.481 E + 07	1	9.481 E + 07	4.74	0.0814	
Residual	9.999 E + 07	5	2.000 E + 07			
Cor Total	1.818 E + 09	11				
Standard Deviation	4471.98		R-Squared	0.9450		
Mean	9662.67		Adj. R-Squared	0.8790		
C.V. %	46.28		Pred. R-Squared	0.6832		
PRESS	5.76 E+ 08		Adeq Precision	11.1520		
-2 Log Likelihood	225.28		BIC	242.6773		
			AICc	267.2830		

**Fig 5.** Linear regression curve between actual response and prediction of Plackett Burman

Precision which measures the signal-to-noise ratio (S/N). The ratio is expected to be greater than 4. In this study, the resulting S/N was 11.152.

■ CONCLUSION

Based on the mass spectrum of the reaction product, it can be concluded that EDA-Folate has been successfully

synthesized by using the direct method. The method consisted of two reaction steps, i.e., inactivation of folic acid using DCC (dicyclohexylcarbodiimide) and NHS (*N*-Hydroxysuccinimide) to result in NHS-Folate, followed by conjugation of EDA (ethylenediamine) with NHS-Folate to produce EDA-Folate. Based on the Plackett-Burman experimental design, it can also be concluded that there were four significant parameters in the synthesis of EDA-Folate, which were time inactivation of NHS-Folate, stirring rate inactivation of NHS-Folate, a mole of EDA, and time of EDA-Folate. Moreover, the value or desirability of the experimental design was calculated to be 0.875, a value getting closer to 1.0, indicating that the resulting design will be able to produce optimal reaction conditions and, accordingly, optimal reaction products, both qualitatively and quantitatively. EDA-Folate will be used as a precursor in synthesizing the Gd-PEG-DOTA-Folate targeted contrast agent.

■ ACKNOWLEDGMENTS

The authors would like to thank Universitas Padjadjaran for providing financial support to this study through the university's Academic Leadership Grant

(ALG) research program (Contract number: 1427/UN6.3.1/LT2020).

■ REFERENCES

- [1] Stoja, E., Konstandin, S., Philipp, D., Wilke, R.N., Betancourt, D., Bertuch, T., Jenne, J., Umathum, R., and Günther, M., 2021, Improving magnetic resonance imaging with smart and thin metasurface, *Sci. Rep.*, 11, 16179.
- [2] Wald, L.L., McDaniel, P.C., Witzel, T., Stockmann, J.P., and Cooley, C.Z., 2019, Low-cost and portable MRI, *J. Magn. Reson. Imaging*, 52 (3), 686–696.
- [3] Fernandez, M., Javaid, F., and Chudasama, V., 2017, Advances in targeting the folate receptor in the treatment/imaging of cancers, *Chem. Sci.*, 9 (4), 790–810.
- [4] Zwicke, G.L., Mansoori, G.A., and Jeffery, C.J., 2012, Utilizing folate receptor for active targeting of cancer nanotherapeutics, *Nano Rev.*, 3 (1), 18496.
- [5] Arnaud, C.H., 2013, Structure of folic acid bound to folate receptor is solved, *Chem. Eng. News*, 91 (29).
- [6] Fauzia, R.P., Mutalib, A., Soedjanaatmadja, R.U.M.S., Bahti, H.H., Anggraeni, A., Gunawan, A.H., Pujiastuti, H., and Hidayati, Y., 2015, Synthesis and characterization of gadolinium diethylenetriamine pentaacetate-folate, *Procedia Chem.*, 17, 139–146.
- [7] Kusuma, Y.N.W., Mutalib, A., Anggraeni, A., Martalena, R., Fauzia, R.P., and Bahti, H.H., 2018, Analysis and characterization of complex compound gadolinium-(1,4,7,10-Tetraazacyclododecane,1-4-7-10-tetraacetic acid)n-poliamidoamine generation 3-trastuzumab as a novel contrast agent for magnetic resonance imaging, *Res. J. Chem. Environ*, 22, 249–254.
- [8] Hsu, Y.I., Mahara, A., and Yamaoka, T., 2018, Influence of molecular mobility on contrast efficiency of branched polyethylene glycol contrast agent, *Contrast Media Mol. Imaging*, 2018, 1259325.
- [9] Fauzia, R.P., Maolana, I., Mutalib, A., Nafisah, Z., Soedjanaatmadja, R.U.M.S., Anggraeni, A., and Bahti, H.H., 2017, Comparison characteristics of different synthesis methods for production of gadolinium diethylenetriaminepentaacetate-folate, *7th Int'l Conf. on Innovations in Chemical, Biological, Environmental and Food Sciences, (ICBEFS-17)*, Pattaya, Thailand, August 3-4, 2017, 60–63.
- [10] Gunawan, A.H., Yono, S., and Maskur, M., 2012, Sintesis Gd-DTPA-Folat untuk magnetic resonance imaging contrast agent dan karakterisasinya menggunakan perunut radioaktif ¹⁵³Gd-DTPA-Folat, *JUSAMI*, 13 (4), 1–6.
- [11] Ndaliman, M.B., Khan, A.A., Ali, M.Y., and Wahid, Z., 2013, Determination of influential factors on EDMed surface properties using Plackett-Burman design, *World Appl. Sci. J.*, 21, 88–93.
- [12] Fauzia, R.P., Soedjanaatmadja, A.U., Anggraeni, A., Yusuf, M., and Bahti, H., 2017, Aplikasi desain eksperimen Plackett-Burman dan response surface methodology Box-Behnken pada produksi senyawa pengontras magnetic resonance imaging gadolinium dietilentriaminpentaasetat-folat, *JCNA*, 1–8.
- [13] Li, X., McTaggart, M., and Malardier-Jugroot, C., 2016, Synthesis and characterization of pH responsive folic acid functionalized polymeric drug delivery system, *Biophys. Chem.*, 214-215, 17–26.
- [14] Singh, R., Kesharwani, P., Mehra, N.K., Singh, S., Banerjee, S., and Jain, N.K., 2015, Development and characterization of folate anchored Saquinavir entrapped PLGA nanoparticles for anti-tumor activity, *Drug Dev. Ind. Pharm.*, 41 (11), 1888–1901.
- [15] Razjouyan, J., Zolata, H., Khayat, O., Nowshiravan, F., Shadanpour N., and Mohammadnia, M., 2015, Synthesis and evaluation of radiolabeled, folic acid-PEG conjugated, amino silane coated magnetic nanoparticles in tumor-bearing Balb/C mice, *NUCLEONIKA*, 60 (3), 497–502.
- [16] Li, X., Yang, X., Lin, Z., Wang, D., May, D., He, B., Wang, X., Wang, X., Zhang, Q., and Gao, W., 2015, A folate modified pH-sensitive targeted polymeric micelle alleviated systemic toxicity of doxorubicin (DOX) in multi-drug resistant tumor-bearing mice, *Eur. J. Pharm. Sci.*, 76, 95–101.
- [17] Nurmiah, S., Syarief, R., Sukarno, Peranginangin, R., and Nurtama, B., 2013, Aplikasi response

surface methodology pada optimalisasi kondisi proses pengolahan alkali treated cottonii (ATC), *JPBKP*, 8 (1), 9–22.

- [18] Hermanson, G.T., 2013, *Bioconjugate Techniques*, 3rd Ed., Academic Press, Boston, United States.
- [19] Effendi, S., Mutalib, A., Anggraeni, A., and Bahti, H.H., 2020, Penggunaan desain Plackett Burman untuk seleksi parameter pemisahan logam tanah jarang kelompok sedang dari logam tanah jarang kelompok lainnya dengan metode pengendapan, *al-Kimiya*, 7 (1), 1–6.
- [20] Yatim, N.M., Shaaban, A., Dimin, M.F., and Yusof, F., 2015, Statistical evaluation of the production of urea fertilizer-multiwalled carbon nanotubes using Plackett Burman experimental design, *Procedia Soc. Behav. Sci.*, 195, 315–323.

Optimization of High Yield Epoxidation of Malaysian Castor Bean Ricinoleic Acid with Performic Acid

Nadia Salih and Jumat Salimon*

Department of Chemical Sciences, Faculty of Science and Technology, Universiti Kebangsaan Malaysia, 43600 Bangi, Selangor, Malaysia

* Corresponding author:

email: jumstsal@gmail.com

Received: August 21, 2021

Accepted: January 20, 2022

DOI: 10.22146/ijc.68592

Abstract: Epoxidized castor oil (ECO) has shown high potential for industrial applications as value-added products such as polymer coating, plasticizer, and biolubricant. Epoxidized ricinoleic acid recovered from ECO has potential for industrial usage. In this work, epoxidized ricinoleic acid (ERA) was synthesized through in situ generated performic acid epoxidation of ricinoleic acid (RA). The epoxidation process was optimized by several reaction parameters, such as the molar ratio of formic acid to ethylenic unsaturation, the molar ratio of hydrogen peroxide to ethylenic unsaturation, and reaction temperature. The response reaction parameters of oxirane oxygen content (OOC) and iodine value (IV) were then evaluated. The results showed the optimal condition for the epoxidation of RA was obtained at 50 °C, the molar ratio of formic acid and hydrogen peroxide to ethylenic unsaturation of 1:8:1 for 4 h reaction time. A high yield of ERA of 86% with relative conversion into oxirane of 85.3% was achieved at the optimum condition. The optimum ERA showed a high OOC value of 4.00% and a low IV value of 2.24 mg/g. It is plausible that ERA can be used as an intermediate starting material to prepare value-added products such as biosurfactants, biopolymer additives, or biolubricants.

Keywords: in situ epoxidation; oxirane oxygen content; performic acid; ricinoleic acid

■ INTRODUCTION

Plant oils are extensively converted through mild chemical reactions or less extensive oleochemical processing to produce value-added products such as biosurfactants, biopolymer additives, biolubricants, and bio-resin [1-3]. These value-added products are produced based on the reactive headgroup and functional groups present in their fatty acids, and methyl esters of fatty alcohols as intermediates. These compounds are ready for chemical derivatization and modification to create products in industrial applications [4]. Therefore, naturally occurring specialized and functionalized fatty acid groups such as sulfonated fatty acids, oxygenated fatty acids, fatty acids with acetylenic bonds are in high demand due to their importance as industrial feedstocks. These fatty acid groups are also known as unusual fatty acid groups. Some known unusual fatty acid groups are epoxy, hydroxyl (mono- to poly-), keto, oxygenated,

sulfonated, and nitrogen functional groups. Due to the interesting chemical versatility of such functionalized fatty acids [5], researchers worldwide are studying new oilseed species that may be added as oleochemical industry raw materials. However, productions of these natural oils are limited to specific plant and animals species. Oilseed crops that supply hydroxylated fatty acids such as *Ricinus cummunis* (castor bean oil), *Lesquerella* spp. (lesquerella oil) [6], *Dimorphotheca* spp., *Vernonia* spp, *Euphorbia lagascae* (vernonia oil) [7] are of industrial interest. In fact, to date, the only commercially available naturally occurring functionalized fatty acid is ricinoleic acid, which is obtained from castor bean oil. Ricinoleic acid, *cis*-12-hydroxyoctadeca-9-enoic acid (9c, 12OH-18:1), contains monohydroxy monounsaturated fatty acid. The industrial usage of castor bean oil and its derivatives, such as epoxidized castor oil, has long been

reported as biolubricants, plasticizers, bioplastic, and bio coating [2,8-9].

Lesquerolic acid, 14-hydroxy-*cis*-11-eicosenoic (11c, 14OH-20:1), is another hydroxy fatty acid similar to castor oil's ricinoleic acid. Dehydration converts nondrying lesquerella oil into a drying oil with a drying velocity equivalent to that of commercial dehydrogenated castor oil. Vernonia oil has been proposed as precursors for adhesives, varnishes and paints, plasticizers, and industrial coatings [2]. Therefore, researchers began turning to oleochemistry and the potential use of uncommon functionalized fatty acids of vernolic acid (12,13-epoxyoctadecenoic acid or *cis*-12-epoxyoctadeca-*cis*-9-enoic acid or 12-epoxy-*cis*-9-octadecenoic acid) and dimorphecolic acid (9-hydroxyoctadecadienoic acid or 9-hydroxyoctadeca-10,12-dienoic acid) in a variety of high-value products [7,10]. Vernolic acid is a monounsaturated fatty acid that contains an epoxide in its fatty acyl chain. It is produced in abundance by the genera *Vernonia*, and *Euphorbia* spp., natural vernonia oil and is a potentially useful biofeedstock. However, in reality, the revolution of a new oilseed crop from trial plant species to an industrial commodity would be greatly challenging.

However, due to the limited availability of oxygenated, hydroxyl, epoxide functionalized fatty acids in the fatty acyl chain, reactions to modify unsaturated fatty acids become pertinent. For example, the feasibility of a mild chemical modification process such as an epoxidation reaction is worth to be utilized to produce a functionalized epoxide-fatty acid. Plant oils or fatty acids epoxidation can be economically accomplished by reacting the unsaturated double bonds of the fatty acid with a peracid reagent such as peracetic [11] or performic acid [1,12]. Currently, epoxides plant oils [13-16] or fatty acids are prepared on an industrial scale through *in situ* generated peracids [14]. The epoxidations of ricinoleic acid, for example, have been reported elsewhere [8-9,17-22]. Epoxidized ricinoleic acid received great attention due to the wide range of feasible further chemical modification reactions that can be involved. The epoxide oxirane ring's high reactivity makes it easily opened by moderate reaction conditions to produce a variety of value-added intermediates [23]. For instance, different

nucleophiles group attacks on epoxide rings could produce mono-alcohols, diols, alkoxyalcohols, hydroxyesters as intermediates for the production of value-added products such as biolubricants [8-9], bio plasticizer [24], biopolymer additives, or biosurfactants [25-26].

Our work has focused on the production of epoxidized ricinoleic acid (ERA), "vernolic acid-like acid," which contains an epoxy ring in combination with a hydroxy group, as shown in Fig. 1. This uniqueness makes ERA such an interesting building block for unique high-value-added products. The literature survey showed no reports about detailed optimization of the epoxidation of ricinoleic acid and its physicochemical properties. In this paper, the ERA was prepared through the epoxidation process of ricinoleic acid (RA) using *in situ* formed performic acid catalyst, and the epoxidation process was optimized. The parameters of the epoxidation process were optimized for the molar ratio of ricinoleic acid:formic acid:hydrogen peroxide, amount of catalyst, reaction temperature, and reaction time. In addition, the ERA product's reaction responses of oxirane oxygen content (OOC) and iodine value (IV) were evaluated.

■ EXPERIMENTAL SECTION

Materials

Castor bean seeds were collected from various places in Selangor and Kedah, Malaysia. Solvents of *n*-hexane, ethyl alcohol (95%), and chemicals of glacial acetic acid, sodium sulfate anhydrous, sodium chloride, potassium hydroxide, hydrochloric acid, formic acid (Fisher Scientific (USA), aqueous hydrogen peroxide (30 wt.% Merck, Germany), and sodium hydrogen carbonate were purchased from System (UK). Wijs solution (QReC), hydrogen bromide, potassium iodide (Fluka), sodium thiosulphate, sodium chloride, and saturated sodium bicarbonate were purchased from Sigma Aldrich (UK), and crystal violet was from BDH Laboratory Supplies. All the chemicals used in this study were either analytical grade or high-performance liquid chromatography (HPLC) grade and were used without further purification.

Instrumentation

The molecule structure of epoxidized ricinoleic acid was analyzed by using Fourier Transform Infrared spectroscopy (FTIR), Nuclear Magnetic Resonance spectroscopy. FTIR spectra were recorded on a Perkin Elmer Infrared Spectrophotometer in 400–4000 cm^{-1} . In addition, the ^1H (16 scans) and ^{13}C -NMR (3000 scans) spectra were recorded on JEOL-ECP 400 spectrometer (400 MHz ^1H /100.61 MHz ^{13}C) using CDCl_3 as a solvent.

Procedure

Extraction of castor bean oil

Castor bean oil extraction was carried out using a Soxhlet extractor. About 100 g of dry ground seeds were first oven-dried at 105 °C for 1 h. Next, the oil was extracted by refluxing (55–60 °C) the samples in *n*-hexane for 6 h in a Soxhlet extractor. The solvent was then evaporated using a rotary evaporator. The extracted castor bean oil was kept in an oven at 60 °C for 30 min before being accurately weighed. Finally, the extracted castor bean oil was kept in a closed container and stored in a desiccator.

Hydrolysis of castor bean oil

The castor bean oil (50 g) was hydrolyzed using 200 mL 1 M ethanolic KOH solution (95% v/v) in a reflux apparatus for 2 h. The hydrolysis product and fatty acid mixture were then neutralized with 200 mL 1 M HCl and washed with 200 mL distilled water before extracting with 100 mL ethyl acetate. The organic layer was dried with anhydrous sodium sulfate overnight. Finally, the solvent was evaporated to yield a light-yellow liquid containing a mixture of fatty acids mixture.

Oxirane oxygen content (OOC%) determination

Around 0.3 g of sample was weighed in a 50 mL Erlenmeyer flask and dissolved in 10 mL benzene. Five drops of 0.1 g of the crystal violet indicator in 100 mL glacial acetic acid were gradually added into the sample solution [27]. A rubber stopper was placed to cover the titration flask and magnetically stirred at room temperature for 5 min. The sample solution was gradually stirred and titrated rapidly with 0.1 M HBr solution (prepared in acetic acid) to a bluish-green endpoint that persisted for 30 s. The experiments were done in triplicate.

The Equations 1, 2 and 3 were used to calculate the experimental oxirane oxygen content (OOC_{exp}) value, theoretical OOC (OOC_{theo}), and the relative percentage of conversion to oxirane (RCO), respectively.

$$\text{OOC}_{\text{exp}} = \frac{V \times M \times 1.60}{W} \quad (1)$$

where: V = volume (mL) of the HBr titrant solution, M = molarity of the titrant, W = weight (g) of the sample, 1.6 = Atomic weight of oxygen divided by ten.

$$\text{OOC}_{\text{theo}} = \frac{IV_o / 2A_i}{100 + (IV_o / 2A_i)A_o} A_o \times 100 \quad (2)$$

where: IV_o = initial iodine value, A_i = atomic weight of iodine (g mol^{-1}), A_o = atomic weight of oxygen (g mol^{-1}).

$$\text{RCO} = \frac{\text{OOC}_{\text{exp}}}{\text{OOC}_{\text{theo}}} \times 100 \quad (3)$$

where: OOC_{exp} = experimental OOC, OOC_{theo} = theoretical OOC (max).

Iodine value (IV) determination

The sample's iodine value (IV) was calculated according to the AOCS Official Method Cd 1-25. About 0.4 g of sample was placed in a 500 mL flask. The sample was dissolved in an aliquot of 15 mL carbon tetrachloride (CCl_4). A Wijs solution (25 mL) was added to the flask and covered with a rubber cork stopper. The mixture in the flask was vigorously shaken and then left in the dark for 60 min. After 1 h incubation, 150 mL of distilled water and 20 mL of 10% KI solution were added to the mixture. The titrant 0.1 N sodium thiosulphate solution was used to titrate the mixture until the liquid turned yellow and reached the endpoint. Then, 1 mL of 1% starch indicator solution was added. The titration was continued while the solution mixture was vigorously shaken until the blue color completely vanished at the titration endpoint. According to Yildiz et al. [28], the experiments were done in triplicate. The blank solution was treated under the same conditions. The IV value was calculated using Eq. (4):

$$IV = \frac{12.69 \times N (V_b - V_s)}{W} \quad (4)$$

where: N = exact normality of $\text{Na}_2\text{S}_2\text{O}_3$ solution (eq/L), V_b = volume (mL) of $\text{Na}_2\text{S}_2\text{O}_3$ solution used for blank titration, V_s = volume (mL) of $\text{Na}_2\text{S}_2\text{O}_3$ solution used for sample titration, W = weight (gram) of sample, 12.69 =

equivalent thiosulphate weight to gram iodine (relative molecular mass of iodine = 126.9).

Synthesis of epoxidized ricinoleic acid

The epoxidation reaction of ricinoleic acid (RA) was carried out according to Salimon et al. [9]. The optimization of the epoxidation process was set at a molar ratio of RA:HCOOH:H₂O₂ (1:1:X), reaction temperature range of 30–70 °C, and reaction time range of 1–5 h. At first, variable X was set to 1–10 mol of H₂O₂. After variable X was obtained, the following optimization process was then set at a molar ratio of RA:HCOOH:H₂O₂ (1:Y:X). Next, variable Y was set at 0.4–1.2 mol of HCOOH. The important reaction response parameters involved to produce a high yield with significant reaction responses of high OOC and low IV values were examined. The epoxidation process was carried out in a round bottom flask equipped with a reflux condenser, thermometer, and magnetic stirrer. At selected parameters for the optimization, a solution of 1-mol hydrogen peroxide solution was slowly added to a stirred mixture solution of ricinoleic acid:formic acid in 1:1 mol ratio at 4 °C (ice bath). Then the reaction proceeded at a selected temperature (30–70 °C) with vigorous stirring (900 rpm) until a powdery solid formed in the reaction vessel at the selected reaction time (1–5 h). After the reaction complete, the catalyst and remaining unreacted RA were neutralized by adding saturated sodium chloride, saturated sodium bicarbonate, and 1 M NaOH solutions. The solid was collected via vacuum filtration, washed with H₂O (chilled, 3×10 mL), and dried for 12 h under high vacuum to provide epoxidized ricinoleic acid (ERA) as a white, powdery solid. Every experiment was repeated in triplicate. The same procedure was repeated for different optimization reaction parameters, and the results were presented as mean ± standard deviation.

RESULTS AND DISCUSSION

Synthesis of Epoxidized Ricinoleic Acid

In this study, the results showed that Malaysia's castor bean seeds contain a relatively high percentage, 45% of oil content, well in agreement with the previous report. The hydrolysis of extracted castor oil produced a dominant ricinoleic acid (RA) content at 86% and was

used as a representative of the mixture of castor oil fatty acids. RA was converted into epoxidized ricinoleic acid (ERA) through the *in situ* generated performic acid as the epoxidation catalyst. Hydrogen peroxide solution was slowly added to a reaction solution containing RA and formic acid to avoid the sudden exothermic conditions where it could lead to the reopening of the epoxide ring at a high temperature of the acidic reaction medium. Fig. 1 shows the epoxidation reaction of RA producing ERA.

The Optimization of the Epoxidation Process

The optimization process for the epoxidation of RA was performed to produce the optimum values or higher yields and OOC reaction responses. The interaction between all variable parameters and criteria chosen for all the reaction responses affected the optimum reaction conditions. The effect of the reaction temperature, reaction time, substrate molar ratio (molar ratio of hydrogen peroxide and formic acid for the double bond in RA), and the amount of *in situ* catalysts (performic acid) were selected as parameters to determine the most optimum reaction condition. The optimization process was first set at a molar ratio of RA:HCOOH:H₂O₂ (1:1:X), the reaction temperature in the range of 30–70 °C, and the reaction time range of 1–5 h. The important reaction response parameters involved to produce high reaction yield with significant-high reaction responses of OOC and significant low IV values were examined.

The Effect of Hydrogen Peroxide Molar Ratio

The optimization process was first set at the molar

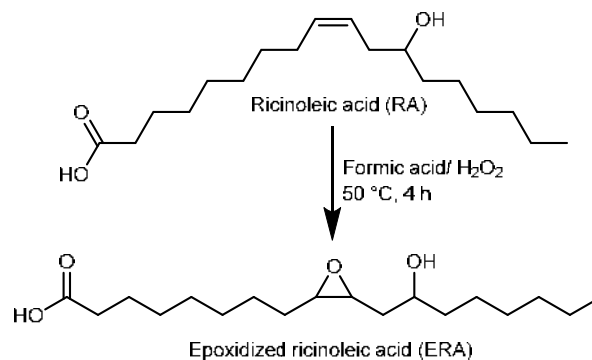


Fig 1. The chemical reaction synthesis of ERA

ratio for RA: HCOOH:H₂O₂ at 1:1:X and fixed reaction temperature of 40 °C and reaction time of 5 h. Variable X was set from 1 to 10 mol of H₂O₂. Hydrogen peroxide acts as an oxygen donor in the epoxidation process. The influence of the H₂O₂ amount at selected reaction conditions on the ERA yield, IV, and OOC values is shown in Fig. 2. The results have shown that increasing the moles of H₂O₂ increased the ERA yield and OOC. Higher values of yield and OOC were obtained at 8 mol of H₂O₂. Increasing H₂O₂ moles up to 8 increased the OOC value to 4% with 85.3% RCO and 85% ERA yield due to effective performic acid catalyst formation. However, a high amount of H₂O₂ must be avoided because it raised the additional agitation problem and decreased the mass transfer rate, thereby decreasing the OOC [18]. A high concentration of H₂O₂ also causes the epoxy-functional group to become unstable [29]. Higher H₂O₂ causes the stability of the oxirane ring to reduce and leads to an accelerated rate of oxirane ring decomposition or degradation [18], which is in agreement with the report for the stability of epoxide sunflower and soybean oil degraded at 30 wt.% H₂O₂ [30]. Others reported that the cleavage of oxirane rings of epoxide oleic acid-based palm oil was affected the most by hydrogen peroxide, followed by formic acid, which leads to the formation of diol and α -glycol as side products [31].

The Effect of the Formic Acid Molar Ratio

Formic acid, HCOOH, can act as an oxygen carrier and be regenerated once the epoxidation reaction occurs [32]. HCOOH also takes part in the overall reaction as a catalyst (performic acid) in the formation of the oxirane ring. At the same time in an acidic medium, HCOOH serves as a reactant in the hydrolysis or degradation of the oxirane ring and should be avoided. The next optimization process was set at the molar ratio for RA:HCOOH:H₂O₂ at 1:X:8, fixed reaction temperature of 40 °C and reaction time of 5 h. Variable X was set at 0.4 to 1.2 mol of HCOOH. The results showed that an increasing amount of HCOOH increased the ERA yield and OOC value, as reflected by its RCO percentage (Fig. 3). High yield percentage and OOC were observed at high HCOOH amount range of 0.8–1.2 mol. Increasing the

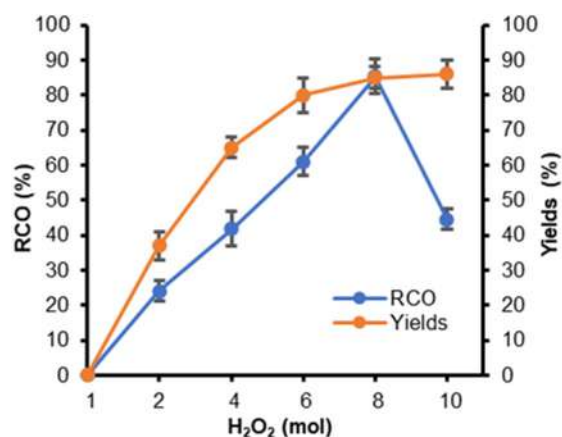


Fig 2. Effect of H₂O₂ molar ratio on RCO and yields

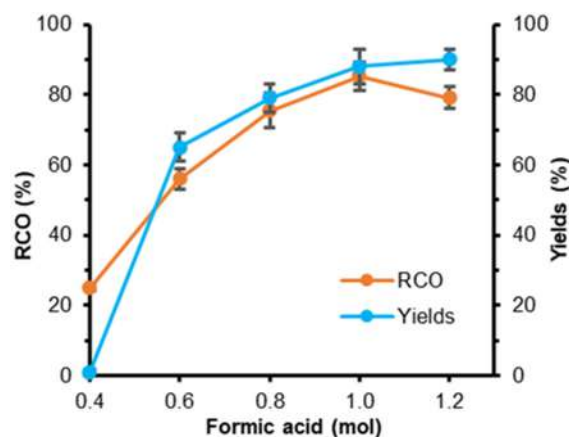


Fig 3. Effect of formic acid molar ratio on RCO and yields

mole of HCOOH up to 1.0 mol had increased OOC value to 4.0%. However, further increment of HCOOH amount led to a decline in the OOC. When the HCOOH mole was higher than 1.0 there was a decrease in ERA yield (90%) and OOC (reduced to 3.71%). The maximum OOC value was attained using the optimum level of formic acid where it acts as an oxygen carrier for the formation of the required peracid catalyst and the epoxy ring hydrolysis are equilibrated [33]. High concentrations of HCOOH may cause the epoxy ring to degrade, thus this condition needs to be avoided [29]. Increasing the HCOOH concentration had a detrimental effect on the epoxide ring due to the epoxide ring being unstable in an acidic medium and hence easier to be degraded [30]. Therefore, the epoxide ring's hydrolysis was promoted and reduced the final OOC value [31], which agrees with the report that stated that

the epoxide ring degraded faster at the molar ratio of epoxidized oleic acid-based palm oil to HCOOH of 1:1 [31].

The Effect of Reaction Temperature

The next optimization process was set at a molar ratio of RA:HCOOH:H₂O₂ at 1:1:8, a reaction time of 5 h, and a reaction temperature in the range of 30–70 °C. The results showed that high values of yield and OOC were achieved at reaction temperatures between 40–60 °C (Fig. 4). Increasing the reaction temperature increased the ERA OOC value (shown by its RCO) as the peroxy acid catalyst (performic acid) increased. However, further increment of reaction temperature led to a decline in OOC value. Reaction temperatures of higher than 50 °C decreased ERA yields to less than 78.3% and OOC down to 1.18%. The higher concentration of performic acid must be controlled to avoid extreme exothermic epoxidation conditions, leading to low oxirane ring stability [30].

The Effect of Reaction Time

The final optimization process was set at a molar ratio of RA: HCOOH: H₂O₂ (1:1:8), reaction temperature of 50 °C, and reaction time range of 1–5 h. As mentioned earlier, a high concentration of performic acid (as the reaction time is prolonged) must be avoided due to the exothermic epoxidation process, which leads to the low stability of the oxirane ring formed [29]. The reaction time increment up to 4 h increased the ERA yield up to 91.1% and RCO to 85.3 % (Fig. 5). Further increase in reaction time caused a decrease in the epoxide yield. Due to the degradation of the oxirane ring, more by-products are formed, and the undesirable oxirane ring-opening reaction occurs [34]. The results have shown that the optimal RA epoxidation reaction conditions were achieved at a molar ratio of RA:HCOOH:H₂O₂ at 1:1:8, reaction temperature of 50 °C, and reaction time of 4 h.

The final triplicate confirmation experiments have shown that at the optimal RA epoxidation reaction condition, the white powdery solid of ERA was produced at 86% yield with an OOC value of 4.0 (85.3% RCO) and IV value of 2.33 mg/g. In this study, OOC for the ERA was 4.69%, equivalent to 0.29 mol of oxygen/100 g of

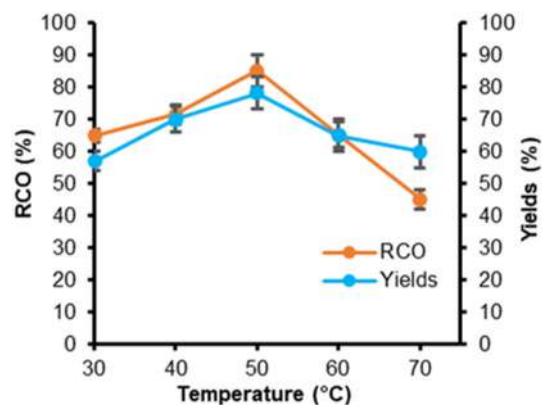


Fig 4. Effect of reaction temperature on RCO and yields

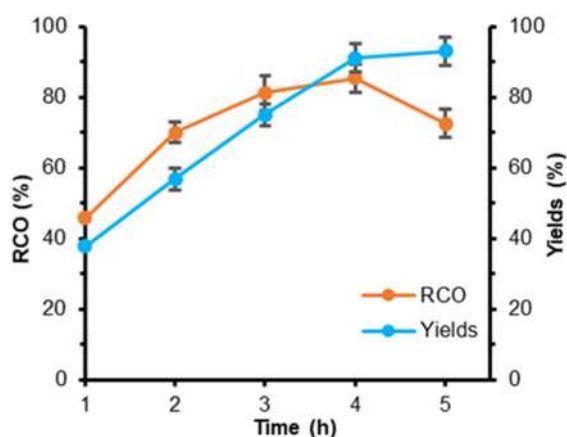


Fig 5. Effect of reaction time on RCO and yields

epoxidized RA or ERA. This value is lower than 0.34 mol of oxygen/100 g of epoxidized sunflower oil [30]. The theoretical IV value of ERA is 77.63 mg/g RA. Therefore, the theoretical relative conversion to oxirane ring oxygen (RCO_{the}) is 97%. Thus, it indicates that about 11.7% of the oxirane ring in ERA had been degraded or hydrolyzed during the epoxidation process at the optimal condition. Nevertheless, this is an acceptable value in an adequate reaction control condition because the epoxidation process requires an acidic medium.

Product Characterization

FTIR peaks of RA indicate an unsaturation functional group at 3010 cm⁻¹ (Csp²-H) 3010 cm⁻¹ (C=C). After the epoxidation of RA, the unsaturation peak disappeared, and an additional new peak appeared in the 823–843 cm⁻¹ range. The appearance of an epoxy peak at 825 cm⁻¹ provided evidence that epoxidation

reaction took place using *in situ* performic acids as a catalyst. The change of functionality in this range indicates that all the unsaturation content was transformed into epoxide products (Fig. 6). Salimon et al. [9] described that the characteristic signals in the FTIR spectrum of RA at 823–843 cm^{-1} represent the tertiary carbons of the oxirane ring. The complete disappearance of C=C bonds in the ERA epoxide spectra further indicates the almost complete conversion of double bonds to oxirane (i.e., 85.3%). In this study, FTIR spectra exhibited the –OH absorption peak at approximately 3400–3500 cm^{-1} , representing the hydroxyl groups belonging to the RA.

The epoxidized compound was synthesized to produce an intermediate compound such as ERA to produce a value-added product such as bio lubricant base stock. The $^1\text{H-NMR}$ spectra of RA and its epoxide, ERA, are shown in Fig. 7. During the epoxidation of RA, the unsaturation group was converted into an oxirane ring. The chemical shift, δ of the unsaturation in RA, was shown at 5.3 to 5.6 ppm (Fig. 7). The epoxidized product, ERA, was confirmed by the disappearance of the double bonds of the unsaturation and the appearance of a new chemical shift of the epoxy group (oxirane ring) at δ 1.45 and 2.47 ppm (Fig. 7). Similar observations were observed by Salimon et al. [9] during their study on ricinoleic acid epoxidation and Borugadda and Goud [18] for the

epoxidation of castor oil.

Furthermore, the presence of unsaturated acyl carbon groups in RA was determined by identifying the alkene group (C=C). The alkene group (C=C) in RA was detected at the chemical shift of 132.30 ppm [35] as shown in Fig. 8. The disappearance of this unsaturation peak of RA was replaced by the appearance of a new carbon epoxy group of ERA that proved the success of the epoxidation process. Significant signals of new chemical shifts were observed at 56.82 and 56.86 ppm for a doublet corresponding to the oxirane ring's carbons and a chemical shift at 32.84 ppm for carbon adjacent to the oxirane ring (Fig. 8). The same observation was reported by Salimon et al. [9].

NMR spectra multiplet reports for RA and ERA are as follows:

RA - $^1\text{H-NMR}$ (400 MHz, CDCl_3): δ ppm 0.76–0.86 (m, 3 H), 1.30–1.32 (d, $J = 13.73$ Hz, 22H), 1.40–1.43 (m, 2H), 1.59–1.60 (m, 2H), 2.00–2.02 (m, 2H), 2.22–2.26 (m, 2H), 2.29–2.30 (m, 2H), 3.62–4.05 (s, 1H), 5.40–5.50 (m, 1H), 5.51–5.55 (m, 1H), 6.50–6.52 (br. s., 1H); $^{13}\text{C-NMR}$ (101 MHz, CDCl_3): δ ppm 14.12 (s, 1C), 22.71 (s, 1C), 24.71 (s, 1C), 25.19 (s, 1C), 27.24 (s, 1C), 29.15 (s, 1C), 29.20 (s, 1C), 29.37 (s, 1C), 29.57 (s, 1C), 29.73 (s, 1C), 31.40 (s, 1C), 34.17 (s, 1C), 35.50 (s, 1C), 37.12 (s, 1C), 71.30 (s, 1C), 123.21 (s, 1C), 132.30 (s, 1C), 179.50 (s, 1C).

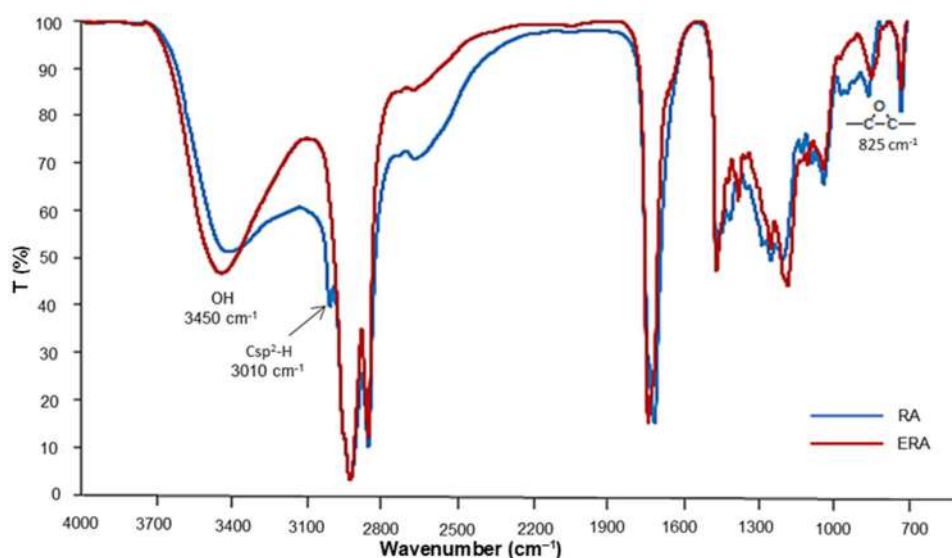


Fig 6. FTIR spectra of RA and ERA

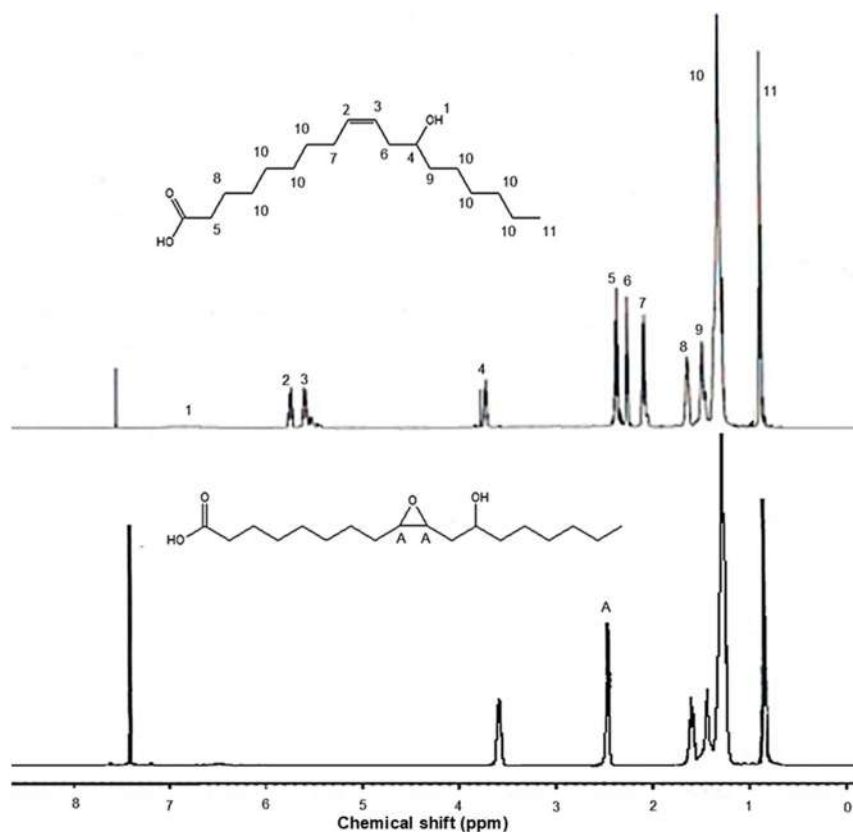
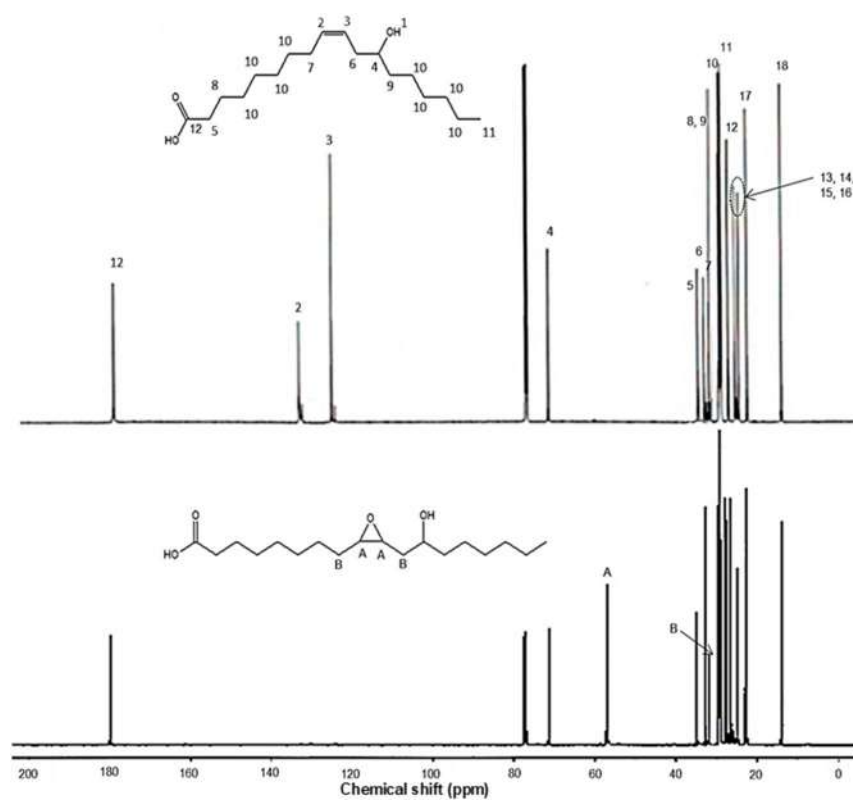
Fig 7. ¹H-NMR spectrum of RA and ERAFig 8. ¹³C-NMR spectrum of RA and ERA

Table 1. Physicochemical properties of epoxidized plants oil and epoxidized ricinoleic acid

Property	ESO ^a	ECO ^b	ERA
Refractive index (@ 25 °C)	1.470	1.412	1.274
Epoxy/Oxirane Oxygen Content value, (%)	6.6 min	4.84	4.0
Acid value, (KOH mg/g)	0.5 max	1.32	128
Iodine value, (g I ₂ /100 g)	2.8 max	6.34	2.24
Flash point, (°C)	280 min	285	250
Pour point (°C)	10	-11	30

Note: ESO = Epoxidized soybean oil [34], ECO = Epoxidized castor bean oil [22], ERA = Epoxidized ricinoleic acid (this study)

ERA - ¹H-NMR (400 MHz, CDCl₃): δ ppm 0.76–0.86 (m, 3H), 1.30–1.32 (d, *J* = 13.73 Hz, 22H), 1.40–1.43 (m, 2H), 1.45–1.47 (m, 2H), 1.59–1.60 (d, *J* = 7.48 Hz, 2H), 2.29–2.30 (m, 2H), 2.47–2.49 (m, 2H), 3.62–4.05 (s, 1H), 6.50–6.52 (br. s., 1H); ¹³C-NMR (101 MHz, CDCl₃): δ ppm 14.12 (s, 1C), 22.71 (s, 1C), 29.15 (s, 1C), 29.20 (s, 1C), 29.37 (s, 1C), 31.11 (s, 1C), 31.11 (s, 1C), 31.11 (s, 1C), 31.11 (s, 1C), 31.11 (s, 1C), 31.40 (s, 1C), 31.41 (s, 1C), 32.84 (s, 1C), 34.17 (s, 1C), 56.82 (s, 1C), 56.90 (s, 1C), 71.50 (s, 1C), 179.6 (s, 1C).

Physicochemical Properties

In this study, the resulting ERA showed relatively high epoxy value or OOC content compared to epoxidized castor bean oil (ECO) and commercial epoxidized soya bean oil (ESO). Table 1 shows the comparative physicochemical properties of ESO, ECO, and ERA. Most of the epoxidized plant oils showed relatively high OOC and low IV values. ESO has been commercialized and shown to enhance soft PVC's softness and shine due to it being a good plasticizer and stabilizer for PVC. The enhancement of the modified PVC includes good sunlight-resistance, heat-resistance, and low volatility. Soy-based polyurethane (PU) made from soybean oil through preliminary epoxidation, followed by methanolysis of the ESO resulting in soy-methanol polyol with suitable resultant soy-methanol polyol diisocyanates has been reported [36]. Most epoxidized plant oils are used as components of polyurethane compositions [35], plasticizers, and stabilizers of polymers [36]. The same range of industrial application has been shown by ECO [4,18,21-22]. This study showed that the obtained ERA had similar

properties to ESO and ECO. This indicates that it is plausible for ERA to be used in the same industrial application as ESO and ECO, particularly for biolubricants application [8-9].

CONCLUSION

The epoxidation process of RA was successfully optimized. The optimum reaction conditions were obtained at a molar ratio of RA:HCOOH:H₂O₂ of 1:1:8, reaction temperature of 50 °C, and reaction time of 4 h. At this optimum condition, the yields of RCO and ERA were 85.3% and 86%, respectively. The resulting ERA showed a high OOC value of 4.0 % and a low IV value of 2.24 mg/g. The results showed that all reaction variables significantly affected the reaction responses and strong interactions between reaction variables on the epoxidation process. The optimized conditions had successfully produced a high epoxide product (ERA) with high OOC value and are plausible to be used as an intermediate compound for further production of high-end and value-added products such as biolubricants.

ACKNOWLEDGMENTS

We would like to thank Universiti Kebangsaan Malaysia for the grand numbers (UKM-GUP-NBT-2016-058) and the Ministry of Science, Technology, and Innovation for funding the project (MOSTI 05-01-02-SF0199, FRGS/2/2016/ST01/UKM/02/1).

REFERENCES

- [1] Nor, N.M., Salih, N., and Salimon, J., 2021, Chemically modified *Jatropha curcas* oil for biolubricant applications, *Hem. Ind.*, 75 (2), 117–128.

- [2] Samidin, S., Salih, N., and Salimon J., 2021, Synthesis and characterization of trimethylolpropane based esters as green biolubricant basestock, *Biointerface Res. Appl. Chem.*, 11 (5), 13638–13651.
- [3] Salih, N., and Salimon, J., 2022, A review on new trends, challenges and prospects of ecofriendly friendly green food-grade biolubricants, *Biointerface Res. Appl. Chem.*, 12 (1), 1185–1207.
- [4] Bahadi, M., Salih, N., and Salimon, J., 2021, Synthesis and characterization of green biodegradable palm oleic acid based polyester, *Biointerface Res. Appl. Chem.*, 11 (6), 14359–14371.
- [5] Armylisas, A.H.N., Hazirah, M.F.S., Yeong, S.K., and Hazimah, A.H., 2017, Modification of olefinic double bonds of unsaturated fatty acids and other vegetable oil derivatives via epoxidation: A review, *Grasas y Aceites*, 68 (1), e174.
- [6] Lin, J.T., and Chen, G.Q., 2017, Structural characteristics of the molecular species of tetraacylglycerols in lesquerella (*Physaria fendleri*) oil elucidated by mass spectrometry, *Biocatal. Agric. Biotechnol.*, 10, 167–173.
- [7] Zeleke, T.D., and Ayana, Y.M., 2017, Epoxidation of vernonia oil in acidic ion exchange resin, *Am. J. Appl. Chem.*, 5 (1), 1–6.
- [8] Salimon, J., and Salih N., 2010, Modification of epoxidized ricinoleic acid for biolubricant base oil with improved flash and pour points, *Asian J. Chem.*, 22 (7), 5468–5476.
- [9] Salimon, J., Salih, N., and Yousif, E., 2012, Synthesis and characterization of esters derived from ricinoleic acid and evaluation of their low temperature properties, *Sains Malays.*, 41 (10), 1239–1244.
- [10] Cahoon, E.B., and Kinney, A.J., 2004, Dimorphelic acid is synthesized by the coordinate activities of two divergent Δ^{12} -oleic acid desaturases, *J. Biol. Chem.*, 279 (13), 12495–12502.
- [11] Silviana, S., Anggoro, D.D., and Kumoro, A.C., 2019, Kinetics study of waste cooking oil epoxidation with peroxyacetic acid using acid catalysts, *Rasayan J. Chem.*, 12 (3), 1369–1374.
- [12] Jumaah, M.A., Salih, N., and Salimon, J., 2021, Optimization for esterification of saturated palm fatty acid distillate by D-optimal design response surface methodology for biolubricant production, *Turk. J. Chem.*, 45, 1391–1407.
- [13] Jalil, M.J., Md Zaini, M.S., Mohd Yamin, A.F., Azmi, I.S., Chang, S.H., Morad, N., and Hadi, A., 2019, Synthesis and physicochemical properties of epoxidized oleic acid-based palm oil, *IOP Conf. Ser.: Earth Environ. Sci.*, 291, 012046.
- [14] Janković, M.R., Govedarica, O.M., and Sinadinović-Fišer, S.V., 2020, The epoxidation of linseed oil with *in situ* formed peracetic acid: A model with included influence of the oil fatty acid composition, *Ind. Crops Prod.*, 143, 111881.
- [15] Gamage, P.K., O'Brien, M., and Karunanayake, L., 2019, Epoxidation of some vegetable oils and their hydrolysed products with peroxyformic acid - Optimised to industrial scale, *J. Natl. Sci. Found. Sri Lanka*, 37 (4), 229–240.
- [16] Lewandowski, G., Musik, M., Malarczyk-Matusiak, K., Sałaciński, Ł., and Milchert, E., 2020, Epoxidation of vegetable oils, unsaturated fatty acids and fatty acid esters: A review, *Mini-Rev. Org. Chem.*, 17 (4), 412–422.
- [17] Yeboah, A., Ying, S., Lu, J., Xie, Y., Amoanimaa-Dede, H., Boateng, K.G.A., Chen, M., and Yin, X., 2020, Castor oil (*Ricinus communis*): A review on the chemical composition and physicochemical properties, *Food Sci. Technol.*, 41, 399–413.
- [18] Borugadda, V.B., and Goud, V.V., 2015, *In-situ* epoxidation of castor oil using heterogeneous acidic ion-exchange resin catalyst (IR-120) for biolubricant application, *Tribol. Online*, 10 (5), 354–359.
- [19] Aranda, C., Olmedo, A., Kiebist, J., Scheibner, K., del Río, Martínez, A.T., and Gutiérrez, A., 2018, Selective epoxidation of fatty acids and fatty acid methyl esters by fungal peroxygenases, *ChemCatChem.*, 10 (18), 3964–3968.
- [20] Chauke, N.P., Mukaya, H.E., and Nkazi, D.B., 2019, Chemical modifications of castor oil: A review, *Sci. Prog.*, 102 (3), 199–217.
- [21] Thirupathiah, G., Satapathy, S., and Palanisamy, A., 2019, Studies on epoxidised castor oil as co-

- plasticizer with epoxidised soyabean oil for PVC processing, *J. Renewable Mater.*, 7 (8), 775–785.
- [22] Fu, Q., Long, Y., Gao, Y., Ling, Y., Qian, H., Wang, F., and Zhu, X., 2019, Synthesis and properties of castor oil-based plasticizers, *RSC Adv.*, 9 (18), 10049–10057.
- [23] Chen, J., de Liedekerke Beaufort, M., Gyurik, L., Dorresteyn, J., Otte, M., and Klein Gebbink, R.J.M., 2019, Highly efficient epoxidation of vegetable oils catalyzed by a manganese complex with hydrogen peroxide and acetic acid, *Green Chem.*, 21 (9), 2436–2447.
- [24] Silviana, S., Anggoro, D.D., and Kumoro, A.C., 2017, Waste cooking oil utilisation as bio-plasticiser through epoxidation using inorganic acids as homogeneous catalysts, *Chem. Eng. Trans.*, 56, 1861–1866.
- [25] Di Mauro, C., Malburet, S., Genua, A., Graillot, A., and Mija, A., 2020, Sustainable series of new epoxidized vegetable oil-based thermosets with chemical recycling properties, *Biomacromolecules*, 21 (9), 3923–3935.
- [26] Aguilera, A.F., Tolvanen, P., Heredia, S., Muñoz, M.G., Samson, T., Oger, A., Verove, A., Eränen, K., Leveneur, S., Mikkola, J.P., and Salmi, T., 2018, Epoxidation of fatty acids and vegetable oils assisted by microwaves catalyzed by a cation exchange resin, *Ind. Eng. Chem. Res.*, 57 (11), 3876–3886.
- [27] Campanella, A., Fontanini, C., and Baltanás, M.A., 2008, High yield epoxidation of fatty acid methyl esters with performic acid generated *in situ*, *Chem. Eng. J.*, 144 (3), 466–475.
- [28] Yildiz, Y., Karadag, R., Jackson, S., and Gensinger, B., 2020, Iodine value in partially hydrogenated castor oil (Ricinus oil) as determined by AOCS official method Cd 1-25 (Wijs' Method), *Adv. Clin. Toxicol.*, 5 (3), 000190.
- [29] Trinh, T.K.H., and Kim, I., 2015, Epoxidation and ring-opening of palm oil to produce high functionality polyols, *Aust. J. Basic Appl. Sci.*, 9 (8), 89–93.
- [30] Arbain, N.H., Salimon, J., Salih, N., and Ahmed W.A., 2022, Optimization for epoxidation of Malaysian *Jatropha curcas* oil based trimethylolpropane ester biolubricant, *Appl. Sci. Eng. Prog.*, 15 (3), 5552.
- [31] Jalil, M.J., Zaini, M.S.M., Yamin, A.F.M., Morad, N., and Hadi A., 2019, Degradation of catalytic epoxidation of oleic acid palm oil by in situ performic acid, *J. Phys.: Conf. Ser.*, 1349, 012001.
- [32] Salih, N., and Salimon, J., 2021, A review on eco-friendly green biolubricants from renewable and sustainable plant oil sources, *Biointerface Res. Appl. Chem.*, 11 (5), 13303–13327.
- [33] Japir, A.A.W., Salih, N., and Salimon, J., 2021, Synthesis and characterization of biodegradable palm palmitic acid based bioplastic, *Turk. J. Chem.*, 45 (3), 585–599.
- [34] Rafiee-Moghaddam, R., Salimon, J., Jelas-Haron, M.D., Jahangirian, H., Shah Ismail, M.H., Hosseini, S., and Rezayi, M., 2014, Lipase epoxidation optimizing of *Jatropha curcas* oil using perlauric acid, *Dig. J. Nanomater. Biostruct.*, 9 (3), 1159–1169.
- [35] Pavia, D.L., Lampman, G.M., Kriz, G.S., and Vyvyan, J.R., 2015, *Introduction to Spectroscopy*, 5th Ed., Cengage Learning, Inc., Stamford, CT, USA.
- [36] Pantone, V., Annese, C., Fusco, C., Fini, P., Nacci, A., Russo, A., and D'Accolti, L., 2017, One-pot conversion of epoxidized soybean oil (ESO) into soy-based polyurethanes by MoCl₂O₂ catalysis, *Molecules*, 22 (2), 333.

Natural Magnetic Particles/Chitosan Impregnated with Silver Nanoparticles for Antibacterial Agents

Annisa Afra Martha, Defia Indah Permatasari, Elma Retna Dewi, Nikho Asyoka Wijaya, Eko Sri Kunarti, Bambang Rusdianso, and Nuryono Nuryono*

Department of Chemistry, Faculty of Mathematics and Natural Sciences, Universitas Gadjah Mada, Sekip Utara, Yogyakarta 55281, Indonesia

* **Corresponding author:**

email: nuryono_mipa@ugm.ac.id

Received: August 26, 2021

Accepted: February 23, 2022

DOI: 10.22146/ijc.68691

Abstract: In this research, silver nanoparticles (AgNP) impregnated on natural magnetic material/chitosan composite (NMP/Chi) have been conducted with different AgNP concentrations (0.5, 1.0, 1.5 mM). Their antibacterial activity was examined against *Escherichia coli* (*E. coli*) and *Staphylococcus aureus* (*S. aureus*). The AgNP samples were characterized with UV-Vis spectrophotometer and TEM. The NMP/Chi/AgNP samples were identified with FTIR and XRD, while NMP/Chi/AgNP1.0 (with the highest antibacterial activity) were analyzed with TEM and SEM-EDX. The antibacterial test with a well-diffusion method showed that NMP/Chi/AgNP was categorized as a strong antibacterial agent. The composite showing the largest inhibition zone diameters was NMP/Chi/AgNP prepared using 1.0 M AgNO₃, namely 14.39 and 16.8 mm against *E. coli* and *S. aureus*, respectively. Characterization of AgNP1.0 showed a spherical shape with an average particle diameter of 17.9 nm in suspension and 32.4 nm in NMP/Chi. The presence of 1000 mg/kg NMP/Chi/AgNP1.0 composite in water was able to reduce the growth of *E. coli* and *S. aureus* bacteria by 60.4% (from 5.3 to 2.1 CFU/mL) and 71.6% (from 6.34 to 1.86 CFU/mL), respectively, within 5 h. The NMP/Chi/AgNP1.0 showed an effective antibacterial agent against both bacteria (*E. coli* and *S. aureus*) and could be applied potentially in aquatic environments.

Keywords: silver nanoparticle; antibacterial; composite; natural magnet; chitosan

■ INTRODUCTION

Chlorination, ozonation, UV irradiation, photocatalytic degradation, and silver (Ag) metal have been widely used to deactivate wastewater's bacteria. Chlorination is a disinfection method using chlorine, acid, and hypochlorite ions. This process is effective but generates Cl₂ gas, which is mutagenic and carcinogenic to human health [1]. Ag metal has been known as an excellent antibacterial agent that inhibits growth and even kills bacteria, but its usage is required in large quantities and fancy. So, this can be overcome by producing Ag metal on a nanometer scale (ranging 1–10 nm) or embedded on the surface of the matrix materials [2]. In this way, only a small amount of Ag metal is used but more beneficial because Ag nanoparticles (AgNP) are more toxic for bacteria, especially *Escherichia coli* (*E. coli*)

and *Staphylococcus aureus* (*S. aureus*) [3]. In addition, there is no evidence that the microbes are resistant when exposed to silver nanoparticles.

The application of AgNP as antibacterial agents for aquatic environments possesses weakness. Namely, it cannot be re-usable since the agent is not easily separated from the media. Therefore, the impregnation of the AgNP on matrix materials is currently being developed. A natural matrix, like chitosan, revealed that antibacterial property is considerably capable of forming composites to produce a better antibacterial property. Chitosan, a polysaccharide obtained from the deacetylation of chitin, is used as an antibacterial agent due to its ability to interact with a negatively charged surface of a bacterial cell, disrupting the growth of bacterial growth colonies [4]. It can inhibit the pathogenic bacteria and spoilage

microorganisms, fungi, and gram-positive and -negative bacteria. Previous reports of the isolation and the excellent antibacterial property of chitosan from natural sources have been carried out [5]. In acidic conditions ($\text{pH} < 6.5$), a free amine group ($-\text{NH}_2$) of chitosan is protonated into a cationic amine group ($-\text{NH}_3^+$) and can combine with various negatively charged materials, such as the surface of bacterial cells [6]. Chitosan attached to the magnetic materials causes to quickly separate it from the liquid medium after application using an external magnetic field. Chitosan coated on Fe_3O_4 surfaces aims to keep Fe_3O_4 stable, not readily oxidized, and not form aggregates. Chitosan is also known as toxic chelating metal. In addition, magnetite with nanometer size tends to aggregate to form bulk materials or form agglomerations caused by a decrease in surface energy. Aggregation can be prevented by coating the magnetite surface with a surfactant [7].

Besides synthetic, magnetic materials isolated from natural materials such as iron sand are currently applied [8], since material contains magnetic minerals such as magnetite (Fe_3O_4), hematite ($\alpha\text{-Fe}_2\text{O}_3$), and maghemite ($\gamma\text{-Fe}_2\text{O}_3$) [9]. Iron sand is used as a source of Fe cation in the cobalt ferrite synthesis, which is less than 30 nm and is superparamagnetic. These sizes and properties make the resulting nanoparticles very good to be applied as an antibacterial agent. The magnetic property of iron sand can create a reused effect on the composite. Further, Fe_3O_4 magnetic material tends to be unstable and easily oxidized, so the composite formation is needed to overcome it. One of the composites used is chitosan. Chitosan is a natural polymer with charged sites due to electrolyte groups [10]. The synthesis of hybrid nanoparticles consisting of several components with a fine structure and excellent antibacterial properties has a high potential to be developed [11].

Magnetite nanoparticles mixed with polyaniline can be used as metal adsorbents, dyestuffs, or microwave absorbers [12]. Materials can be used as microwave absorbers due to their electrical and magnetic properties [13]. Several previous studies have shown that the antibacterial effectiveness of silver is higher when bound with Fe_3O_4 . The $\text{Ag}/\text{Fe}_3\text{O}_4$ core-type nanoparticles showed antibacterial properties against bacterial strains such as *E.*

coli, *Staphylococcus epidermis*, and *Bacillus subtilis*. Their paramagnetic properties cause nanoparticles to be easily separated from liquids, recycled and reused, and possibly widely applied as a disinfectant in the water [13]. However, due to the chemically unstable property of Fe_3O_4 , the nanoparticles are easily broken down in aquatic media, particularly in acidic conditions. Coating Fe_3O_4 with polymers such as silica and chitosan is an alternative technique to prevent the dissolution of the Fe_3O_4 in the media. Substitution of synthetic magnetite with natural magnetic particles is expected to produce more stable magnetic material and is prospective for the future due to low cost.

This study reports the application of impregnated AgNP on natural magnetic particles/chitosan (NMP/Chi) composites as antibacterial agents. The antibacterial activity tests of *E. coli* and *S. aureus* were performed with a well-diffusion method and in aqueous media. The magnetic particles provide easy separation of the agent from the aqueous media.

■ EXPERIMENTAL SECTION

Materials

The materials used were natural magnetic particles (NMP) isolated from iron sand collected from Glagah Kulon Progo beach, Yogyakarta, using a procedure reported by Nuryono et al. [14]. The chemicals used included hydrochloric acid (HCl 37%), sodium citrate ($\text{Na}_3\text{C}_6\text{H}_5\text{O}_7$, p.a), acetic acid (CH_3COOH 96%), silver nitrate (AgNO_3 99.98%), and ammonia (NH_3 25%) purchased from Merck, technical chitosan from CV. Chi Multiguna. Other materials such as distilled water were obtained from CV. Progo. The antibacterial test using bacterial cultures, *E. coli*, *S. Aureus*, nutrient agar, and nutrient broth (NB) were conducted at the Faculty of Biology, Universitas Gadjah Mada.

Instrumentation

The non-analytical instruments used included laboratory glassware (Pyrex, Iwaki), a hotplate completed with a magnetic stirrer, mortar, oven (Memmert UN 55 53L), 200 mesh sieve. Analytical instruments used were an analytical balance (Mettler

Toledo; Shimadzu AUW120), and universal pH (Merck). Characterization of all composite samples was performed with Fourier Transform Infrared spectrophotometer (FTIR; Shimadzu Prestige-21) and X-ray diffractometer (XRD; PANalytical X'Pert Pro series 2318 using Cu source). The AgNP in suspension was measured their absorbance with UV-Visible spectrophotometer (Shimadzu UV-1700) and Transmission Electron Microscope (TEM; JEOL series JEM-1400). The Scanning Electron Microscope-Energy Dispersive X-ray (SEM-EDX; Hitachi SU 3500) was used to identify the morphology and elemental composition of NMP/Chi/AgNP1.0.

Procedure

Synthesis of silver nanoparticles

AgNP samples were synthesized by reducing Ag(I) using sodium citrate, referring to the procedure reported by Fosso-Kankeu et al. [15]. A total of 50 mL of (0.5; 1.0; and 1.5 mM) AgNO₃ in an Erlenmeyer flask was heated at 100 °C for 1 h, then 5 mL of 1% sodium citrate was added dropwise. The mixture was stirred with a magnetic stirrer during heating until it turned pale yellow, indicating AgNP in suspension had been formed. AgNP samples were characterized with a UV-Visible spectrophotometer. The analysis with a UV-Visible spectrophotometer was carried out by measuring the absorbance at a 300–800 nm wavelength. The suspensions of AgNP obtained from 0.5, 1.0, and 1.5 mM AgNO₃ were called AgNP0.5, AgNP1.0, and AgNP1.5, respectively.

Preparation of HCl-activated NMP

Ten grams of iron sand was washed repeatedly and dried under sunlight for 48 h. Then, iron sand was separated using an external magnet. The separated iron sand was mashed and sieved with 200-mesh size. Iron sand (lower than 200 mesh) was rewashed using distilled water and dried in an oven for 18 h at 95 °C. Subsequently, 0.5 g of the sample was added with 1 mL of HCl 1 M, soaked for 15 min, and dried in an oven for 24 h at 95 °C.

Synthesis of composite NMP/Chi/AgNP

Typically, 0.15 g of chitosan was dissolved in a beaker glass in 30 mL of 1% acetic acid solution. Chitosan solution (30 mL) was added with 0.5 g of HCl-activated

NMP then stirred for 5 h at room temperature (25 °C). The mixture was added with 0.5 M NH₄OH until pH of 7 (neutral) has achieved. Then the mixture was poured with 52 mL of AgNP suspensions which were prepared from all concentrations of AgNO₃ solution. The mixture was dried in an oven at a temperature of 60 °C for 24 h.

All NMP/Chi/AgNP prepared were characterized with FTIR and XRD. SEM-EDX and TEM were used to characterize NMP/Chi/AgNP1.0. For TEM analyses, the sample was prepared by dipping the copper grid into colloidal AgNP, then dried at room temperature. AgNP images were obtained at an accelerated voltage of 120 kV. FTIR characterization was performed to determine the functional groups of composites, and XRD was used to identify the electro-oxidation product of the sample phase according to the standard peak patterns of the ICDD card. SEM-EDX data was collected to identify the morphology and elemental composition.

Antibacterial activity test with well-diffusion method

After the equipment and material sterilizations, 1 mL of *E. coli* bacteria was taken using a micropipette and put in a liquid medium. Then, the bacteria were incubated for 24 h at 37 °C. The base media was poured into a petri dish, cooled, and stored until hardened for 1 h. Subsequently, the bacteria were evenly spread on the base media using a cotton swab. For the antibacterial test of NMP, NMP/Chi, and all prepared NMP/Chi/AgNP samples, one well was made in the agar medium with a diameter of ± 6 mm, which was put in the tested samples. After adding the tested samples, the petri dish was then incubated at 37 °C for 24 h. Antibacterial activity was calculated by their inhibition zone (in mm diameter). Similar work was also performed for *S. aureus*.

Antibacterial activity test in water

Antibacterial activity test in water was performed for NMP/Chi/AgNP1.0 composite with a shake flask turbidimetry method. The absorbance (turbidity/optical density) in aqueous media was measured with a UV-Vis spectrophotometer. Absorbance (turbidity/optical density) shows the number of bacteria contained in the media. Liquid media (150 mL) containing nutrient broth (1.3 g/100 mL) was mixed with 150 mg of

NMP/Chi/AgNP1.0 composite and was stirred for 1 min. At each particular interval time, the absorbance of the mixture was measured with a UV-vis spectrophotometer.

■ RESULTS AND DISCUSSION

Silver Nanoparticles (AgNP)

The concentration of silver nitrate (AgNO_3) as a precursor affects the number of AgNP formed. The investigation was conducted over the varied AgNO_3 concentrations (0.5, 1.0, and 1.5 mM). At the same condition, with a higher concentration of precursors, the reduction of silver nanoparticles occurs faster. In addition, the color change to darker at higher AgNO_3 concentration. AgNO_3 solution with the highest concentration (1.5 mM) produced the most concentrated color of AgNP suspension.

As shown in Fig. 1, the resulted AgNP could be identified by the wavelength profile of surface plasmon resonance (SPR). The maximum wavelength of SPR ranges from 400 up to 450 nm [16]. The absorbance at a wavelength of 416, 424, and 425 nm can be observed at the samples of 0.5, 1.0, and 1.5 mM, respectively. It means that the AgNP in suspension has been formed.

Based on Fig. 1, the increase in AgNO_3 concentration enhances the sample's absorbance gradually. The highest

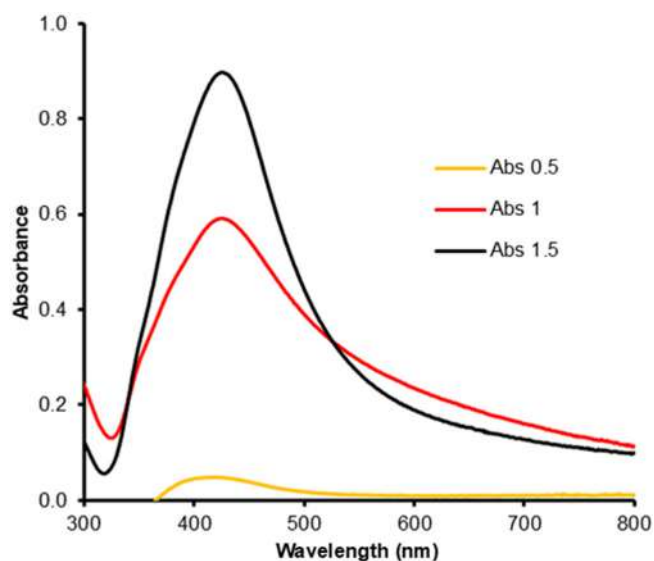


Fig 1. Absorbance at UV-Vis region of AgNP suspensions prepared from various concentrations of AgNO_3 solutions

absorbance was observed in the sample of 1.5 mM. However, the sample of 0.5 mM showed the lowest absorbance profile, which appeared at the wavelengths of 300 to 500 nm. It might be caused by a low concentration of AgNO_3 addition, thus producing a small AgNP quantity. Mulfinger et al. [17] stated that the low and high profile of the sample's absorbance reveals the amount of AgNP produced and the increase of the reaction rate. Herein, the resulted AgNP (sample 0.5 mM) could not be easily detected by using the spectrophotometer instrument.

Characteristics of NMP/Chi/AgNP

Functional groups

Composites of NMP/Chi/AgNP, including NMP and NMP/Chi, were characterized with FTIR to identify their functional groups in the samples and displayed in Fig. 2.

The O-H stretching vibrations of chitosan are observed at around $3000\text{--}3500\text{ cm}^{-1}$, and C-H stretching appears at 2924 cm^{-1} , whereas O-H bending is at 1620 cm^{-1} . The N-H angular deformation on the CO-NH plane is observed at a wavenumber of 1543 cm^{-1} , and the C-O stretching at 1080 cm^{-1} . These results were similar to the previous data reported [18]. The sharp characteristic absorption peaks at wavenumbers 574 and 455 cm^{-1} correspond to the Fe-O bond of Fe_3O_4 in the NMP/Chi composite impregnated with AgNP (Fig. 2(c-e)), revealing that the composite is formed via in situ pathway [16].

Samples with the addition of various concentrations show the changes in their intensity, peak width, and wavenumber of some specific peaks of chitosan (Fig. 2(c-e)). The peak of -OH stretching moves to the small wavenumbers. Bonds between O-Ag and N-Ag are probably weakening the O-H and N-H hydrogen bonds. In contrast, at a wavenumber of 1080 cm^{-1} , the intensity of C-O stretching of C-OH chitosan increases. The large quantity of the acetyl group of chitin substituted by hydrogen atom into amine ($-\text{NH}_2$) leads to lower vibration energy and thus causes significant changes; a shift to the lower wavenumber of the amine group ($-\text{NH}_2$) is observed.

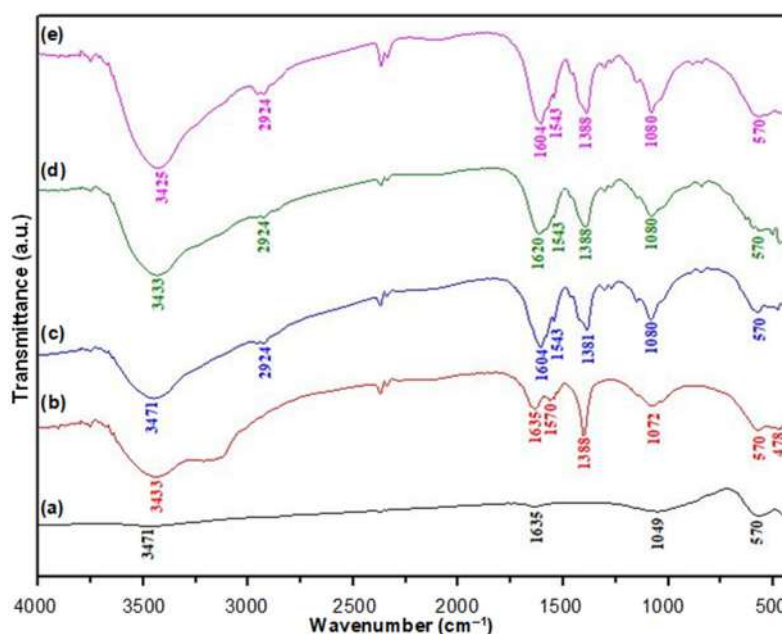


Fig 2. FTIR spectra of (a) NMP, (b) NMP/Chi, (c) NMP/Chi/AgNP0.5, (d) NMP/Chi/AgNP1.0, and (e) NMP/Chi/AgNP1.5, respectively

The absorption around 2924 cm^{-1} corresponds to the doubled C–H stretching, yet the presence of AgNP reduced single C–H stretching. It may be caused by the interaction between Ag nanoparticles with the groups of –OH and –NH₂ and then creating a stiffer chitosan structure, and the absorption intensity at 2924 cm^{-1} become much lower.

Structure of NMP/Chi/AgNP

The second characterization of the NMP/Chi/AgNP composite was carried out with X-ray diffraction. It is generally performed to identify the crystallinity and the present minerals. Additionally, it is performed to identify the phase of an electro-oxidation product by comparing it to the XRD pattern of NMP. The results obtained are presented in Fig. 3. As can be seen in Fig. 3, there are seven typical peaks of magnetite in NMP as the main content, which corresponds to an angle of 25° to 65° between the experimental XRD pattern of Fe₃O₄ in NMP and the standard XRD pattern of Fe₃O₄ (ICDD card no. 01-073-2273), namely at the angles 30° , 35° , 43° , 56° , and 62° . It indicates that Fe₃O₄ dominates the NMP component. The XRD pattern of NMP/Chi shows that the decreased peaks are observed at 30° , 35° , and 56° . In addition, new peaks at 27° , 29° , 31° appear and a peak at 35° decreases.

According to the Miller ICDD card no. 00-039-1894, those peaks belong to chitosan. The intensity of the prominent peak of chitosan is proportional to the quantity or amount and degree of crystallinity. Chitosan crystallinity is strongly influenced by the strength of chitosan polymer's intramolecular and intermolecular hydrogen bonds [19-20]. The chitosan crystallinity increases after being modified into NMP, probably due to the increased number of intramolecular and intermolecular hydrogen bonds.

The XRD patterns of NMP/Chi/AgNP with different AgNO₃ concentrations affect the composite crystallinity. It can be seen that the characteristic peak and intensity are broader and lower, respectively, with the increase in AgNP concentration. The broader peak indicates the heterogeneity of the polymer chains [21]. In addition, the increase in the AgNP concentration also causes an increase in the primary peak intensity of chitosan. Chitosan is a polymer with low crystallinity due to the loss of existing intramolecular and intermolecular hydrogen bonds. The AgNP at low concentrations can be involved in intramolecular and intermolecular hydrogen bonds, causing an increase in the crystallinity of NMP/Chi/AgNP composites. The

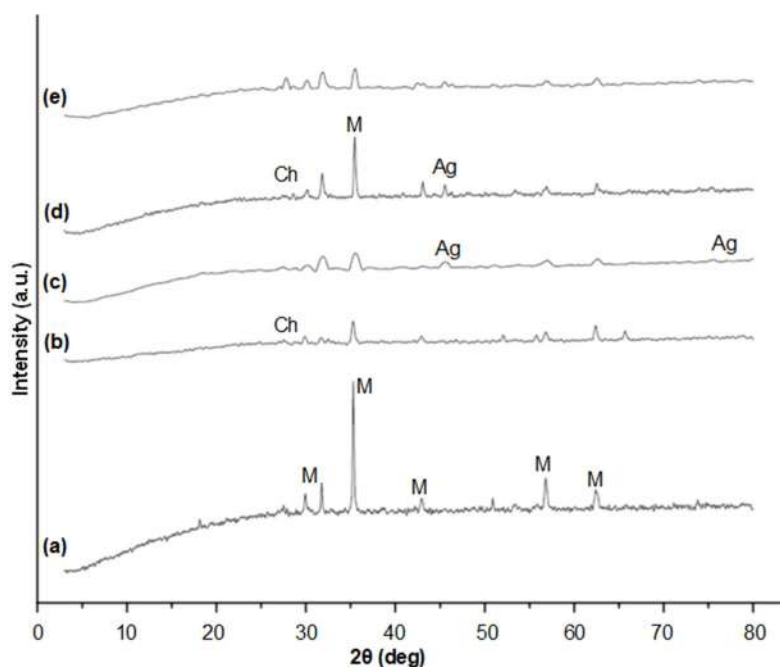


Fig 3. XRD patterns of (a) NMP, (b) NMP/Chi, (c) NMP/Chi/AgNP0.5, (d) NMP/Chi/AgNP1.0, (e) NMP/Chi/AgNP1.5, respectively

linking model of hydrogen bonding of chitosan and AgNP can be illustrated in Fig. 4.

Intermolecular interactions lead to regularity between polymer units, while intramolecular interactions lead to plane order of chitosan polymer units [18]. The AgNP impregnation causes to increase in the regularity of the chitosan crystal plane. The amount of AgNP used to replace intramolecular hydrogen bonds is more significant than that of intermolecular hydrogen bonds. The XRD pattern of NMP/Chi/AgNP shows that a peak intensity of 2θ about 31° is lower than NMP/Chi (before AgNP impregnation). The peak at 2θ 31° may be influenced more by intramolecular hydrogen bond interactions. Meanwhile, the peak intensity increase of 2θ around 27° , 30° , and 35° is probably due to the intermolecular interaction of hydrogen bonds of chitosan and NMP. The appearance of new peaks around 44° and 64° indicates AgNP peaks. As mentioned in the Miller ICDD card No. 01-089-3722, Ag metal has the hkl value of (111), (200), (220), (311) and (222) with 2θ of 38° , 44° , 64° , and 77° , respectively. It is reported that with the increasing number of metal ions bound by chitosan in the composite, the crystallinity index of chitosan decreased [22]. It is caused by the breakdown of intramolecular and

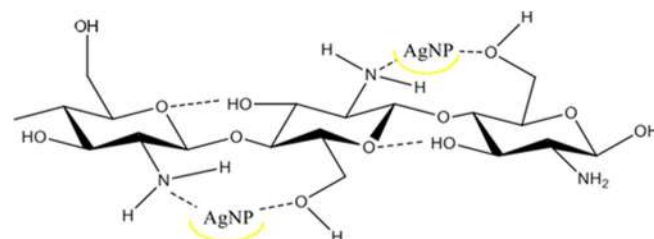


Fig 4. Substitution Model of intramolecular hydrogen bonds with AgNP

intermolecular hydrogen bonds, chitosan tends to form complexes, and Ag metal is not involved in intramolecular and intermolecular bonds.

Morphology of NMP/Chi/AgNP1.0

The morphology of NMP/Chi/AgNP1.0 characterized by Transmission Electron Microscope (TEM) is presented by AgNP1.0 and NMP/Chi/AgNP1.0, and the images can be seen in Fig. 5. From the image, the size distribution of each particle has been measured with ImageJ, and the average size is calculated. The result shows that the average size of AgNP in suspension and in the composite is 17.9 and 32.44 nm, respectively. The particle size of NMP is 47.02 nm, and the chitosan layering the NMP reaches 81.06 nm.

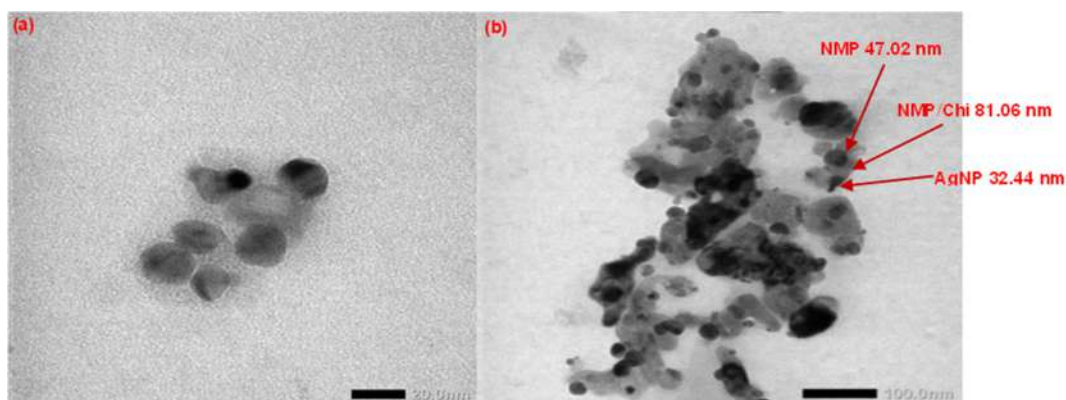


Fig 5. TEM images of (a) AgNP1.0 and (b) NMP/Chi/AgNP1.0

Scanning Electron Microscope (SEM) is used to observe the morphology of the NMP/Chi/AgNP composites. The SEM images of samples are presented in Fig. 6. The morphology of NMP/Chi/AgNP1.0 shows an uneven surface; there are rough bumps on the surface, whereas NMP/Chi (before AgNP impregnation) appears to have a smooth surface even when viewed up to 5000 times magnification. Additionally, there are no spots on the NMP/Chi surface, while NMP/Chi/AgNP shows white spots. The spots indicate AgNP in the sample.

The elemental composition in the samples investigated was analyzed with SEM-EDX, and the result is summarized in Table 1. This analysis may provide semi-quantitative data on elements in samples [23]. It can be seen that NMP/Chi/AgNP1.0 contains silver with an atomic percentage of 0.1%. The SEM-EDX data also show the presence of carbon, nitrogen, oxygen, and iron. The carbon and nitrogen contents come from chitosan, while the iron appears from iron oxide magnetite (Fe_3O_4) or hematite ($\alpha\text{-Fe}_2\text{O}_3$). The percentage of C and N elements is higher in NMP/Chi/AgNP than in NMP.

Antibacterial Activity

The antibacterial activity of NMP/Chi/AgNP was carried out referring to the well-diffusion method. When the inhibition zone diameter of 5 mm or less, the activity can be categorized as weak, an inhibition zone of 5–10 mm as moderate, 10–20 mm is categorized as strong, and an inhibition zone of 20 mm or more is categorized as very strong [24]. The qualitative test results of the antibacterial activity of the samples can be seen in Fig. 7, and the activity based on the inhibition

Table 1. The results of EDX analysis on the composite of NMP/Chi/AgNP1.0

Element	NMP	NMP/Chi	NMP/Chi/AgNP1.0
C	4.54	15.99	22.14
N	0.41	6.42	8.43
O	51.73	30.30	32.42
Fe	15.44	3.99	3.28
Al	4.84	1.29	0.97
Si	14.65	5.36	4.52
Ag			0.10

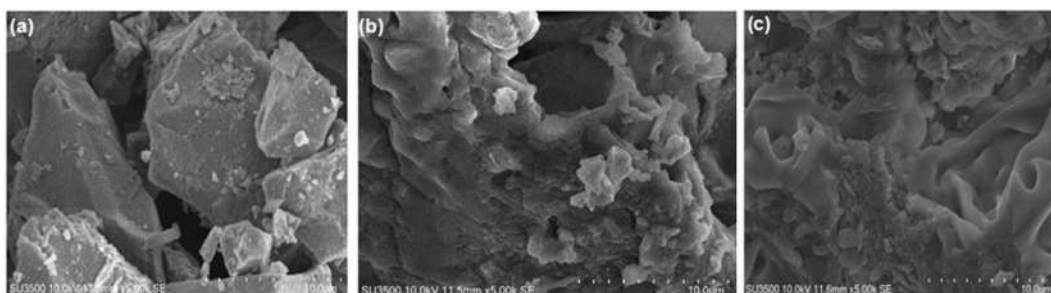


Fig 6. SEM images of composite (a) NMP, (b) NMP/Chi, and (c) NMP/Chi/AgNP1.0, with a magnification of 5000×

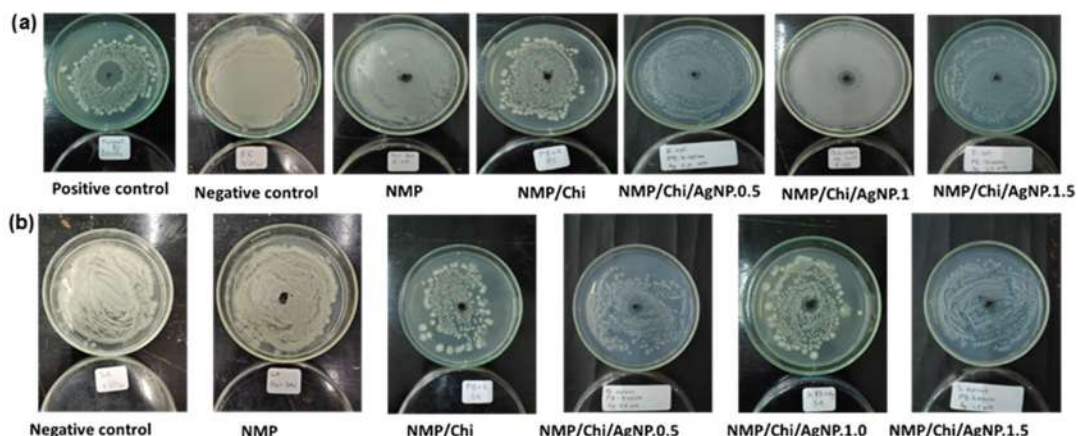


Fig 7. Images of antibacterial testing results for (a) *E. coli* and (b) *S. aureus* by measuring the diameter of the inhibition zone

Table 2. Measurements result of the inhibition zone diameter of bacteria

Antibacterial sample	Inhibition zone diameter (mm)		Category
	<i>E. Coli</i>	<i>S. Aureus</i>	
Negative control	0	0	Weak
NMP	0	0	Weak
NMP/Chi	7.56	9.62	Moderate
NMP/Chi/AgNP0.5	11.49	14.00	Strong
NMP/Chi/AgNP1.0	14.39	16.18	Strong
NMP/Chi/AgNP1.5	12.66	16.79	Strong
Positive control (betadine)	24.51	28.41	Very strong

zone measurement is summarized in Table 2. In Fig. 7, the colloidal AgNP indicates inhibitory activity against *E. coli* and *S. aureus* bacteria. The results showed that NMP/Chi/AgNP gives an antibacterial activity stronger than other tested samples. The highest inhibition zone diameter occurs in NMP/Chi/AgNP1.0, from AgNO₃ 1.0 mM, (14.39 mm) for *E. coli* and NMP/Chi/AgNP1.5, from AgNO₃ 1.5 mM for *S. aureus* (16.79 mm). NMP/Chi/AgNP composites tested are less active than the positive control (betadine), giving the zone diameter of 24.51 mm and 29.41 mm for *E. Coli* and *S. aureus*, respectively. The antibacterial activity of NMP/Chi/AgNP1.0 and NMP/Chi/AgNP1.5 is not significantly different for *S. aureus*; hence, the characterization is conducted only for NMP/Chi/AgNP1.0.

The lower activity of the AgNP impregnated is probably caused by the low distribution of the particles in the media. AgNP bound to chitosan resulted in the breakdown of intermolecular and intramolecular hydrogen

bonds so that chitosan tends to form chelates with AgNP. The intermolecular and intramolecular hydrogen bonds that are no longer formed can reduce the interaction of the entry of the composite surface, namely the AgNP active site, with the bacterial cell surface, thereby reducing antibacterial activity. From Table 2, it can be seen that chitosan alone gives inhibitory activity even though it is lower than AgNP. The factor responsible for the lowest activity of NMP/Chi/AgNP1.5 is unclear. However, the higher concentration leads to the aggregation of the particles and reduces the activity. It agrees with previous research that silver with nanoparticle size has a higher bacterial inhibitory power [25]. Silver nanoparticles are chemically more reactive and more easily ionized than silver particles in large materials. Therefore, nanoparticles are indicated to have high antibacterial abilities. Silver ions interact with cells to prevent protein synthesis, decrease surface permeability, and ultimately cause cell death.

Table 3. The bacterial growth in water without and with antibacterial agent NMP/Chi/AgNP1.0

Time (h)	Number of <i>E. coli</i> produced (CFU/mL)		Number of <i>S. aureus</i> produced (CFU/mL)	
	Without composite	With composite	Without composite	With composite
0	2.4	2.1	0.8	0.8
1	2.4	2.0	0.8	0.7
2	2.3	2.3	1.9	1.9
3	2.3	2.3	1.9	2.1
4	3.8	2.1	3.2	2.1
5	5.3	2.1	6.3	1.8
50	4.9	2.4	21.3	4.5

Antibacterial Activity of NMP/Chi/AgNP1.0 in Water

The antibacterial activity of NMP/Chi/AgNP in aqueous media was tested by comparing the growth of bacteria in water with and without the addition of composites. The bacteria's presence resulted in the media's turbidity, which could be measured by the turbidimetric method and presented in CFU/mL. The results of the calculation of the number of bacteria expressed in CFU/mL are shown in Table 3.

From Table 3, it appears that the bacteria grew after incubation lasted for 3 h. The effect of the composite as antibacterial inhibition was only visible starting at 4 h. For *E. coli* bacteria, growth is prolonged, and the addition of composites practically prevents bacteria from growing. Up to 50 h, the inhibition rate reaches 51%. In contrast to *E. coli*, *S. aureus* can grow well up to 50 h. The addition of NMP/Chi/AgNP in the media inhibited growth significantly, namely 80%.

CONCLUSION

It can be concluded that the NMP/Chi composite powder has been successfully made with black color and an irregular shape on the surface. AgNP1.0 impregnation on the NMP/Chi increased the average particle diameter from 17.88 to 32.44 nm. Antibacterial test with the well-diffusion method showed that NMP/Chi/AgNP1.0 effectively inhibits the growth of bacteria for both *E. coli* and *S. aureus*. In water media, the composite indicated similar antibacterial properties, and *S. aureus* growth revealed more significance to be inhibited than *E. Coli*. Therefore, a separable and effective antibacterial composite, NMP/Chi/AgNP is prospective to be applied in aquatic environments.

ACKNOWLEDGMENTS

The authors would like to thank the Universitas Gadjah Mada for the financial support through the Research Grant *Rekognisi Tugas Akhir* (RTA) with No. Contact: 3143/UN1.P.III/DIT-LIT/PT/2021.

REFERENCES

- [1] Mohamadshafiee, M.R., and Taghavi, L., 2012, Health effects of trihalomethanes as chlorinated disinfection by products: A review article, *Int. J. Environ. Ecol. Eng.*, 6 (8), 545–551.
- [2] Ghasemi, N., Jamali-Sheini, F., and Zekavati, R., 2017, CuO and Ag/CuO nanoparticles: biosynthesis and antibacterial properties, *Mater. Lett.*, 196, 78–82.
- [3] Susanty, D., Santosa, S.J., and Kunarti, E.S., 2020, Antibacterial activity of silver nanoparticles capped by *p*-aminobenzoic acid on *Escherichia coli* and *Staphylococcus aureus*, *Indones. J. Chem.*, 20 (1), 182–189.
- [4] Ke, C.L., Deng, F.S., Chuang, C.Y., and Lin, C.H., 2021, Antimicrobial actions and applications of chitosan, *Polymers*, 13 (6), 904.
- [5] Kumar, U., Mishra, M., and Prakash, V., 2012, Assessment of antioxidant enzymes and free radical scavenging activity of selected medicinal plants, *Free Radicals Antioxid.*, 2 (3), 58–63.
- [6] Setiyani, R., and Maharani, D.K., 2015, Pemanfaatan komposit kitosan ZnO-SiO₂ sebagai agen antibakteri terhadap bakteri *Staphylococcus aureus* pada kain katun, *Unesa J. Chem.*, 4 (2), 88–93.
- [7] Ayad, M., Salahuddin, N., Fayed, A., Bastakoti, B.P., Suzuki, N., and Yamauchi, Y., 2014, Chemical design of a smart chitosan-polypyrrole magnetite

- nanocomposite toward efficient water treatment, *Phys. Chem. Chem. Phys.*, 16 (39), 21812–21819.
- [8] Sukamto, Kamiya, Y., Rusdiarso, B., and Nuryono, 2021, “Highly effective magnetic silica-chitosan hybrid for sulfate ion adsorption” in *Sustainable Development of Water and Environment*, Eds. Jeon, H.Y., Springer International Publishing, New York, 203–216.
- [9] Fahmiati, F., Nuryono, N., and Suyanta, S., 2017, Characteristics of iron sand magnetic material from Bugel Beach, Kulon Progo, Yogyakarta, *IOP Conf. Ser.: Mater. Sci. Eng.*, 172, 012020.
- [10] Victor, S., Andhika, B., and Syaunqiah, I., 2016, Pemanfaatan kitosan dari limbah cangkang bekicot (*Achatina fulica*) sebagai adsorben logam berat seng (Zn), *Konversi*, 5 (1), 22–26.
- [11] Wang, L., Hu, C., and Shao, L., 2017, The antimicrobial activity of nanoparticles: Present situation and prospects for the future, *Int. J. Nanomed.*, 12, 1227–1249.
- [12] Xu, F., Ma, L., Huo, Q., Gan, M., and Tang, J., 2015, Microwave absorbing properties and structural design of microwave absorbers based on polyaniline and polyaniline/magnetite nanocomposite, *J. Magn. Magn. Mater.*, 374, 311–316.
- [13] Pachla, A., Lendzion-Bieluń, Z., Moszyński, D., Markowska-Szczupak, A., Narkiewicz, U., Wróbel, R.J., Guskos, N., and Żołnierkiewicz, G., 2016, Synthesis and antibacterial properties of Fe₃O₄-Ag nanostructures, *Pol. J. Chem. Technol.*, 18 (4), 110–116.
- [14] Nuryono, N., Miswanda, D., Sakti, S.C.W., Rusdiarso, B., Krisbiantoro, P.A., Utami, N., Otomo, R., and Kamiya, Y., 2020, Chitosan-functionalized natural magnetic particle@silica modified with (3-chloropropyl)trimethoxysilane as a highly stable magnetic adsorbent for gold(III) ion, *Mater. Chem. Phys.*, 255, 123507.
- [15] Fosso-Kankeu, E., De Klerk, C.M., van Aarde, C., Waanders, F., Phoku, J., and Pandey, S., 2016, Antibacterial activity of a synthesized chitosan-silver composite with different molecular weights chitosan against Gram-positive and Gram-negative bacteria, *International Conference on Advances in Science, Engineering, Technology & Natural Resources (ICASETNR-16)*, November 24–25, 2016, Parys, South Africa, 142–146.
- [16] Cao, X., Shen, F., Zhang, M., and Sun, C., 2014, Rapid and highly-sensitive melamine sensing based on the efficient inner filter effect of Ag nanoparticles on the fluorescence of eco-friendly ZnSe quantum dots, *Sens. Actuators, B*, 202, 1175–1182.
- [17] Mulfinger, L., Solomon, S.D., Bahadory, M., Jeyarajasingam, A.V., Rutkowsky, S.A., and Boritz, C., 2007, Synthesis and study of silver nanoparticles, *J. Chem. Educ.*, 84 (2), 322–325.
- [18] Lin, Y.F., Chen, H.W., Chien, P.S., Chiou, C.S., and Liu, C.C., 2011, Application of bifunctional magnetic adsorbent to adsorb metal cations and anionic dyes in aqueous solution, *J. Hazard. Mater.*, 185 (2-3), 1124–1130.
- [19] Caro, C., Castillo, P.M., Klippstein, R., Pozo, D., and Zaderenko, A.P., 2010, “Silver nanoparticles: Sensing and imaging application” in *Silver Nanoparticles*, Eds. Perez, D.P., IntechOpen, Rijeka, 201–223.
- [20] Ioelovich, M., 2014, Crystallinity and hydrophilicity of chitin and chitosan, *J. Chem.*, 3 (3), 7–14.
- [21] Sibilia, J.P., 1996, *A Guide to Materials Characterization and Chemical Analysis*, 2nd Ed., Wiley-VCH, New York.
- [22] Modrzejewska, Z., and Kaminski, W., 1999, Separation of Cr(VI) on chitosan membranes, *Ind. Eng. Chem. Res.*, 38 (12), 4946–4950.
- [23] Bindhu, M.R., and Umadevi, M., 2013, Synthesis of monodispersed silver nanoparticles using *Hibiscus cannabinus* leaf extract and its antimicrobial activity, *Spectrochim. Acta, Part A*, 101, 184–190.
- [24] Davis, W.W., and Stout, T.R., 1971, Disc plate methods of microbiological antibiotic assay, *Appl. Microbiol.*, 22 (4), 659–665.
- [25] Avicenna, S., Nurhasanah, I., and Kumaeni, A., 2021, Synthesis of colloidal silver nanoparticles in various liquid media using pulse laser ablation method and its antibacterial properties, *Indones. J. Chem.*, 21 (3), 761–768.

Development of Arduino Uno-Based TCS3200 Color Sensor and Its Application on the Determination of Rhodamine B Level in Syrup

Muhammad Syukri Surbakti¹, Muhammad Farhan², Zakaria Zakaria¹, Muhammad Isa¹, Elly Sufriadi², Sagir Alva³, Elin Yusibani¹, Leni Heliawati⁴, Muhammad Iqhrammullah⁵, and Khairi Suhud^{2*}

¹Department of Physics, Faculty of Mathematics and Natural Sciences, Universitas Syiah Kuala, Banda Aceh 23111, Indonesia

²Department of Chemistry, Faculty of Mathematics and Natural Sciences, Universitas Syiah Kuala, Banda Aceh 23111, Indonesia

³Department of Mechanical Engineering, Faculty of Engineering, Mercubuana University, Jakarta 11650, Indonesia

⁴Department of Chemistry, Faculty of Mathematics and Natural Sciences, Ibnu Khaldun University, Bogor 16162, Indonesia

⁵Graduate School of Mathematics and Applied Science, Universitas Syiah Kuala, Banda Aceh 23111, Indonesia

* **Corresponding author:**

tel: +62-85297492376

email: khairi@unsyiah.ac.id

Received: September 18, 2021

Accepted: February 1, 2022

DOI: 10.22146/ijc.69214

Abstract: The use of the notorious synthetic dye, rhodamine B, in food and beverage products has been widely reported. This application urges the need to develop an analytical method that can provide reliable rhodamine B data with an easy operational technique. Therefore, this research is aimed to develop an Arduino Uno-based TCS3200 color sensor and study its application to determine rhodamine B levels in syrup. The design of the analytical instrument included TCS3200, an Arduino Uno microcomputer, an Integrated Development Environment (IDE) software, a black box container, and a 24 × 2 matrix display screen, where samples were prepared via absorption using wool thread. With a linear range of 1–20 mg/L, our proposed colorimetric sensor had recoveries of 96.25–110.3%, which was better compared to that was obtained from the UV-vis (81.8–100.6%) method. The detection and quantification limits of the sensor were 2.766 and 8.383 mg/L, respectively. The syrup samples used in this study were purchased from the local stores in Banda Aceh. Based on the proposed TCS3200 color sensor, the highest rhodamine B concentration from the syrup sample was 16.74 mg/L. The t-test analysis in this study revealed that the Rhodamine B levels quantified using the newly developed TCS3200 color sensor were not statistically or significantly different from the UV-Vis spectrophotometer method.

Keywords: color sensor; TCS3200; rhodamine B; Arduino Uno; Zn(CNS)₂; IDE software

■ INTRODUCTION

As a form of consumer protection efforts, sensor technology for food or beverage products has been developed intensely [1-3]. For example, Fourier Transform Infrared (FTIR) spectroscopy has been employed to separate halal and non-halal meatballs [4]. The color spectroscopy method has also reported the detection and analysis of synthetic dye rhodamine B in chili powder [5]. Dyes used in food products are derived from natural and artificial chemicals. Synthetic dyes are widely used because it is more cost-efficient and available.

Additionally, the synthetic dye may give a brighter color to the food or beverage product [6].

As one of 30 synthetic dyes available, Rhodamine B is considered as a dangerous dye, where its use in food or beverage products has been prohibited. Nevertheless, Rhodamine B is often used in processing industries, papers, and fabrics [7-8]. Moreover, it could be employed as a ligand to bind metal ions [9]. However, in Indonesia, rhodamine B is still very popular as a food coloring agent, including in iced syrup. The syrup is intentionally added with rhodamine B, so the products obtain a more attractive appearance [10].

Methods that have been previously developed to identify rhodamine B in food ingredients include thin-layer chromatography (TLC) [11], voltammetry [12], and the standard method using UV-Vis spectrophotometer (the best option for identifying compounds with color). However, UV-Vis spectrophotometry has several drawbacks; not portable, complicated, and expensive [13]. Hence, this study tried to overcome the stated drawbacks by developing a simple measurement method using a portable sensor.

The sensor system developed in the present work was based on the TCS3200 color sensor constructed by the console to overcome external noise and program library modification [14]. The TCS3200 color sensor has been widely reported for different applications, including measuring levels of cyanide [14], nitrogen [15], and heavy metals [16]. In the case of colorimetric sensors, analytes should first be reacted with a complexing agent to cause a color change [17-18]. In this study, the sensor detects color degradation from tissue paper that has been spiked with reagents, so its sensitivity is specifically improved for rhodamine B analysis. The reagent used was $Zn(CNS)_2$, which can cause a color change from red to purple due to the formation of the rhodamine B-Zn-thiocyanate ((RhB) complex $2Zn(CNS)_4$) [19].

The color intensity contributed by the presence of rhodamine B was converted through the sensor output pin in the form of a square signal in which its frequency depends on the concentration. The box's signal with varied frequency was then processed using a microcontroller on Arduino Uno. In this processing, four filters were used, namely green, blue, red, and *no filter*. In this case, *no filter* was excluded because the three parameters were sufficient to represent the color degradation of rhodamine B in the sample [20]. Filter settings were performed by providing low and high logic in the Arduino IDE program, following the reported study [21].

The distance between the sample and the 8×8 diode array was set at 3 cm, following the sensor system's geometry. The console's color was made black so the color could be absorbed fully, and influence from the degradation of colors that enter the diode array could be

avoided. After obtaining the concentration of rhodamine B using the Arduino Uno-based TCS3200 color sensor, the results were compared with the standard UV-Vis spectrophotometric method. Finally, the analysis results were compared to obtain the data on sensitivity and accuracy of the newly developed sensor [22].

■ EXPERIMENTAL SECTION

Materials

The materials used were a UV-Vis spectrophotometer (Thermo Fisher Scientific, Selangor Malaysia), a color sensor TCS3200 (ICTAOS/AMS), a console, and an Arduino Uno (wavgat). Syrup samples tested for rhodamine B levels were procured from local stores in Banda Aceh. The standard rhodamine B was purchased from The National Agency of Drug and Food Control of Indonesia (BPOM RI). All other chemicals used, i.e. NH_4OH , $NaOH$, HCl , C_2H_5OH , CH_3CO_2Na , $ZnCl_2$, CH_3CO_2H , and $KCNS$, were obtained from Merck (Selangor, Malaysia) in analytical grade.

Hardware Design

The hardware design was initiated by developing a console for the TCS3200 color sensor, then connecting the output port of the color sensor via a jumper cable to the Arduino Uno microcomputer to process frequency data and convert it into 8-bit RGB digital data. There were 256 color digit variations for each RGB color component that was sortable and distinguishable by the processing. These color digit variations were displayed on the computer screen and converted to reduce color variations. These color variations were also recorded in .xls format (MS Excel) (Fig. 1).

Development of the TCS3200 Sensor Console

The TCS3200 console sensor was designed in black to absorb all color wavelengths. The distance between the diode array and the color object was 3 cm. The console was arranged in such a way that light from outside could not enter. The TCS3200 sensor was positioned opposite the color sample, which was absorbed into a filter paper. Four LED units with white

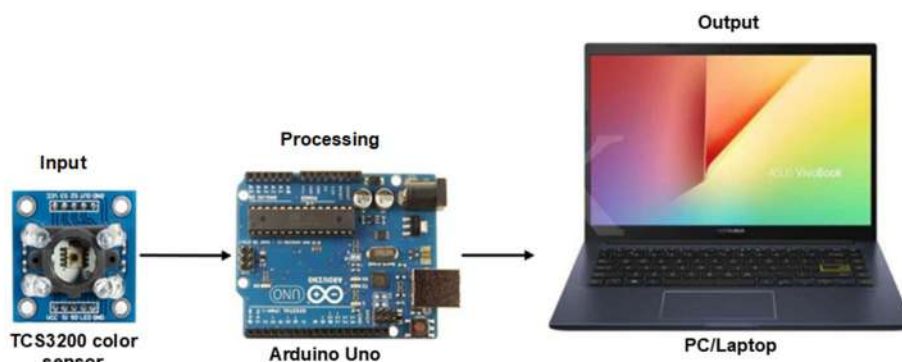


Fig 1. Schematic diagram of hardware design

wavelengths would hit the filter paper, and the intensity light reflected the diode array following the color intensity of the sample.

Software Design

Construction of the software design was initiated with a blink test on the Arduino Uno system to determine the response and performance of the microcomputer. The software used was Arduino IDE with available open-source libraries – C programming language. The program library was modified to enable the required color filters, Arduino Uno pins, the required display format, and data storage mode (Fig. 2).

Rhodamine Analysis Using TCS3200 Color Sensor

Construction of the calibration curve for rhodamine B

Briefly, the rhodamine B solution was added with 3.0 mL of Zn-thiocyanate. Then, the standard solution $(\text{RhB})_2\text{-Zn}(\text{CNS})_4$ with different concentrations measured the RGB value with the TCS3200 color sensor and absorbance with UV-Vis at the maximum wavelength obtained. The solution was prepared with 100 mg/L rhodamine B as the stock solution, which was then diluted using distilled water into standard solutions with varying concentrations ranging from 1 to 20 mg/L. These solutions were prepared to determine the maximum wavelength of rhodamine B and as a database for the TCS3200 color sensor. Following that, a solution of 1 mL ZnCl_2 2 M and 2 mL KCNS 2 M as a reagent was made to detect the presence of rhodamine B, as suggested by a previous report [23].

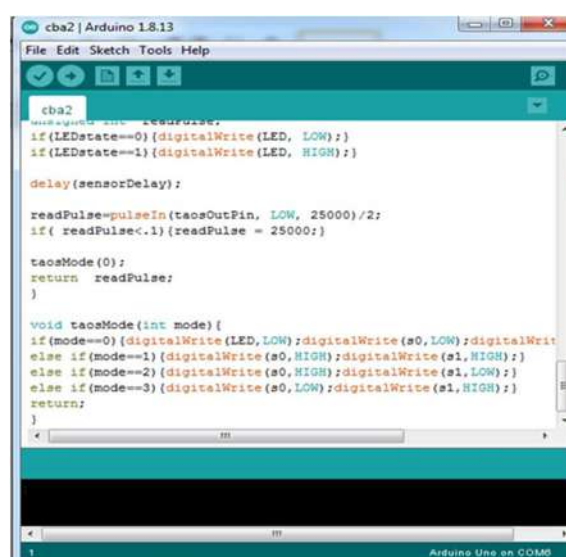


Fig 2. Display of the Arduino IDE Software main menu

Determination of rhodamine B level using the TCS3200 color sensor

The standard curve of $(\text{RhB})_2\text{-Zn}(\text{CNS})_4$ was obtained by measuring the RGB values of the standard solution $(\text{RhB})_2\text{-Zn}(\text{CNS})_4$ using the TCS3200 sensor. The concentration of rhodamine B used was 1 to 20 mg/L, which were priorly reacted with reagents. Measurements were carried out three times, and the concentration was averaged. Thereafter, RGB values were converted into a color index, namely Hue, Intensity, and Saturation (HIS). Conversion of RGB values to HIS values was carried out using the following Equations.

$$\text{Red color index } (I_R) = \frac{R}{R + G + B} \quad (1)$$

$$\text{Green color index } (I_G) = \frac{G}{R+G+B} \quad (2)$$

$$\text{Blue color index } (I_B) = \frac{B}{R+G+B} \quad (3)$$

The HIS color model was designed to resemble the perception of human vision, while the RGB values resembled the image of the display system [20]. The results of the calculation of the HIS value were then plotted as the dependent variable (y -axis) to the variation of concentration $(\text{RhB})_2\text{-Zn}(\text{CNS})_4$ (x -axis).

TCS3200 color sensor method validation

Method validation included accuracy, precision, sensitivity, and linearity, which were conducted based on the suggestion from a previous report [22].

Syrup sample preparation

Samples of commercial red syrup were purchased from local stores in Banda Aceh. Each sample (10 mL) was taken and put into an Erlenmeyer which was subsequently mixed in 20 mL of 25% ammonia solution (dissolved in 70% ethanol) for 24 h and evaporated on a hot plate. The evaporation residue was dissolved in 10 mL distilled water containing acid (10 mL distilled water and 5 mL acetic acid 10%). Wool thread (15 cm) was dipped into the acid solution and simmered for 10 min until the dye colors appeared on the wool thread, then lifted. The wool thread was then washed with distilled water, and the wool thread was dissolved in ethanol 70% and heated to a boil (Fig. 3). This solution was used as the sample, per suggestion by a published work [24]. The wool thread was used to extract

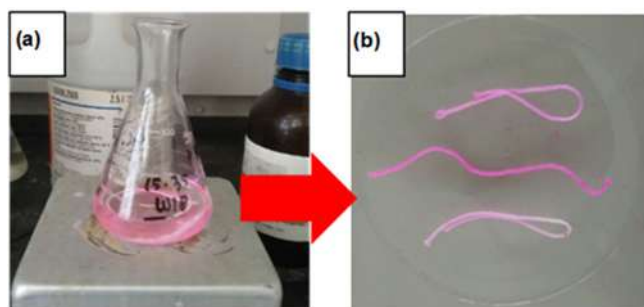


Fig 3. The extraction of rhodamine B from commercial red syrups using wool thread. Wool thread was dipped into the dissolved syrup residue for 10 min (a). Rhodamine B-containing wool thread before re-immersed to ethanol 70% and boiled (b)

rhodamine B-containing samples in an acidic environment. A comparative study has reported that wool thread has the highest dye adsorption as compared with silk and nylon [25]. Adsorption of dye analyte in wool thread is determined by its O- and N-containing functional groups, which has been reported in many published papers [26-28]. The dyed wool was then immersed in ethanol 70% and boiled until its original color returned. The obtained solution was analyzed for its rhodamine B levels using the TCS3200 color sensor and a reference method – UV-Vis spectrophotometry.

Quantitative Analysis

The prepared sample was added with Zn-thiocyanate and then dipped in filter paper. Rhodamine B levels were measured using the TCS3200 color sensor [29]. The concentration was obtained based on the linear equation obtained from the calibration curve.

Method Comparison using Two-Way t-Test

Results of the samples between the TCS3200 color sensor and the UV-Vis spectrophotometry method were compared [30]. In addition, a two-way t -test was carried out to see the significance between the newly studied TCS3200 color sensor method and the reference method using UV-Vis spectroscopy by calculating the t value for each method and then comparing it with the $t_{\text{theoretical}}$.

RESULTS AND DISCUSSION

Maximum λ of Rhodamine B Complex

The complex $(\text{RhB})_2\text{-Zn}(\text{CNS})_4$ was produced to give rhodamine B a specific color, allowing easier analysis. The solution of rhodamine B, which was initially red, turned to purple and was then measured using a UV-Vis spectrophotometer at a wavelength ranging from 574 to 600 nm. The UV-vis absorbance corresponding to the $(\text{RhB})_2\text{-Zn}(\text{CNS})_4$ complex scanned from 574 to 600 nm is presented in Fig. 4.

Based on the measurement results, the UV-Vis spectrometer spectrum of $(\text{RhB})_2\text{-Zn}(\text{CNS})_4$ showed a maximum absorption (0.442 au) at a wavelength of 590 nm. The difference in wavelength between rhodamine B and $(\text{RhB})_2\text{-Zn}(\text{CNS})_4$ is due to a shift in

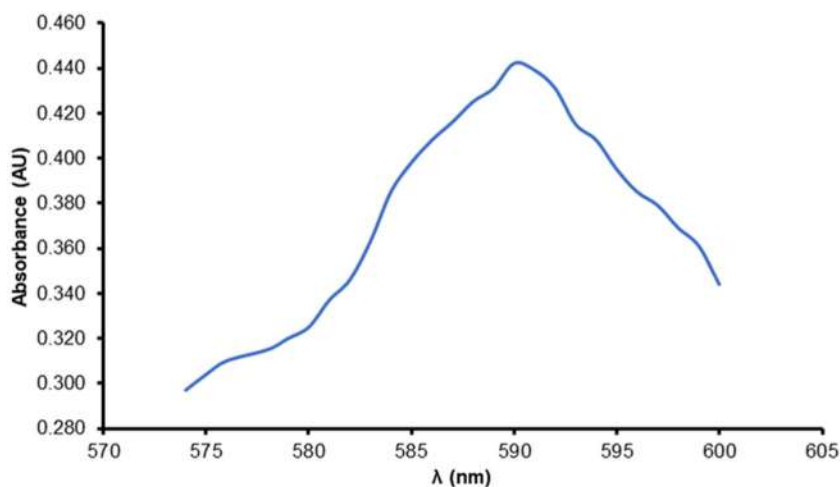


Fig 4. UV-Vis spectrometer spectrum of $(\text{RhB})_2\text{-Zn}(\text{CNS})_4$ showing a maximum wavelength at 590 nm

wavelength towards the bathochromic direction caused by substitution, solvent effects, and the influence of the chromophore group [31]. The successful formation of the $(\text{RhB})_2\text{-Zn}(\text{CNS})_4$ complex was indicated by a color change from red to purple and a shift in wavelength. The equation for the reaction between rhodamine B and $\text{Zn}(\text{CNS})_2$ can be seen in Fig. 5.

Based on the graph, we can see three regression equations obtained from each RGB index value, namely I_R $y = 0.0028x + 0.3411$; I_G $y = 0.0032x + 0.3513$ and I_B $y = -0.0058x + 0.3059$. The values of the determination coefficient (R^2) were 0.9792, 0.9700, and 0.9729 respectively. The R index had the best determination coefficient (R^2) of 0.9792. Therefore, the regression

equation for the R index was used to determine the concentration of rhodamine B in the sample.

Measurement using UV-Vis Spectrophotometer

The standard curve of $(\text{RhB})_2\text{-Zn}(\text{CNS})_4$ was measured at a wavelength of 590 nm by a UV-Vis spectrophotometer. The concentration of rhodamine B that was used ranged from 1 to 20 mg/L, which was priorly reacted with reagents. Measurements were carried out three times and averaged for each concentration. The absorbance measurements can be seen in Fig. 6. The regression equation $y = 0.0023x + 0.0773$ had a determination coefficient (R^2) of 0.9927. Hence, it can be concluded that the concentration was

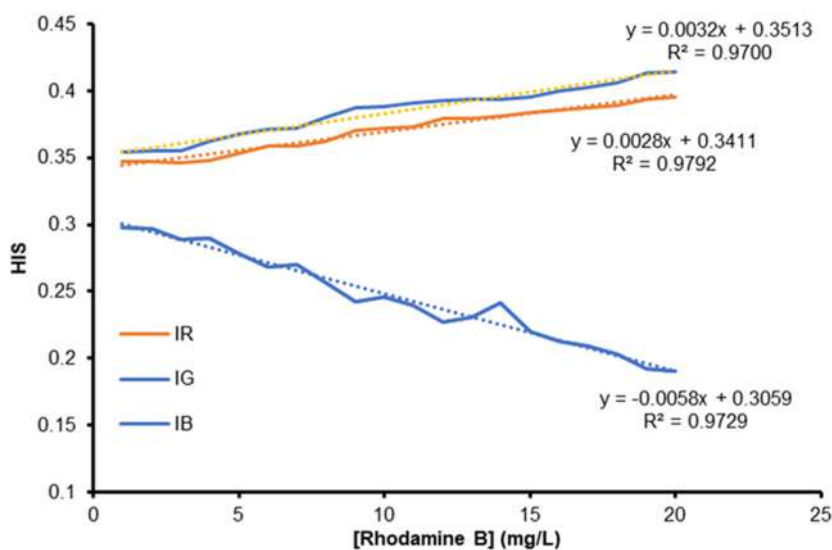


Fig 5. Calibration curve for $(\text{RhB})_2\text{-Zn}(\text{CNS})_4$

directly proportional to the absorbance, meaning that the absorbance for the complex $(\text{RhB})_2\text{-Zn}(\text{CNS})_4$ was dependent on rhodamine B concentration.

Method Validation

Accuracy

The accuracy of the proposed sensor method was based on the recovery (%), representing the value proximity of the standard concentration solution to the actual concentration. The concentrations of $(\text{RhB})_2\text{-Zn}(\text{CNS})_4$ used were 1, 10, and 20 mg/L for the analysis with TCS3200 and UV-Vis color sensors. The actual concentration values and the percent recovery values from each method can be seen in Table 1. The recovery % calculation for the TCS3200 color sensor was still within the allowable error range of 90–110% [32]. However, at a concentration of 1 mg/L, UV-Vis had a recovery value below the permissible range (81.8%). Therefore, our proposed method was suggested to have better accuracy for determining rhodamine B levels at a low concentration (1 mg/L).

Precision

The precision was determined to see the proximity of the value changes in the repetition process. The precision value was derived from the standard curve with a respective concentration of $(\text{RhB})_2\text{-Zn}(\text{CNS})_4$ (1, 10, and 20 mg/L), expressed by the variation coefficient (VC). The precision values for both methods based on intra-day and inter-day repetition are presented in Table 2. The variation coefficient value obtained by the two measurements increased with the decrement in the concentration of the standard solution. The method is accurate if it provides a variation coefficient value of less than 2% [32]. Nonetheless, inter-day repetition yielded higher variation coefficient, especially when rhodamine B concentration was 1 mg/L.

Linearity

Linearity is the functional area of sample measurement. The linearity of measurements using the TCS3200 color sensor and UV-Vis spectrophotometer for a concentration range of 1–20 mg/L is depicted in Fig. 5 and 6, respectively. Several studies used a

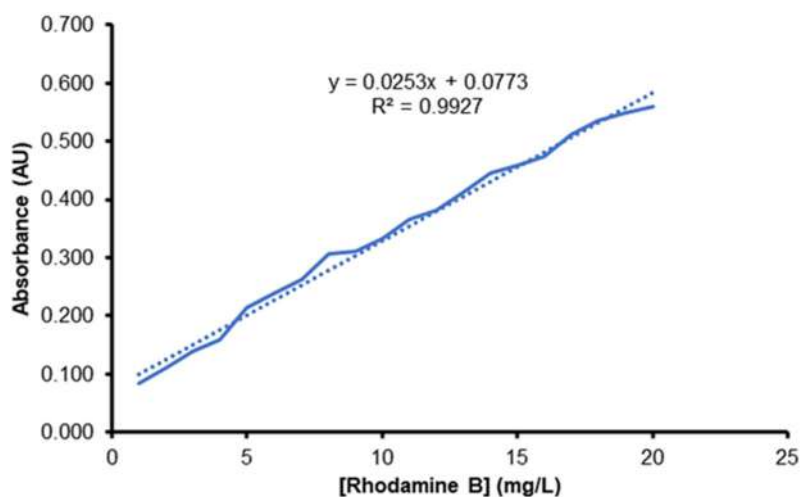


Fig 6. Calibration curve for $(\text{RhB})_2\text{-Zn}(\text{CNS})_4$

Table 1. Recovery percentages of TCS3200 sensor and UV-vis spectrophotometer

Concentration (mg/L)	Actual concentration (mg/L)		Recovery (%)	
	TCS3200	UV-Vis	TCS3200	UV-Vis
1	1.030	0.818	103.5	81.80
10	11.03	10.06	110.3	100.6
20	19.25	19.03	96.25	95.15

Table 2. VC values of TCS3200 sensor and UV-vis spectrophotometer obtained from intra-day and inter-day repetition

[Rhodamine B] (mg/L)	Intra-day variation coefficient (%)		Inter-day variation coefficient (%)	
	TCS3200	UV-Vis	TCS3200	UV-Vis
1	0.291	0.721	7.966	8.563
10	0.268	0.521	1.294	1.664
20	0.253	0.357	0.509	0.851

non-linear calibration curve because the sensor system formed an exponential response [33]. However, in the present study, the quantitative analysis was conducted based on linear regression.

Sensitivity

The sensitivity value is shown from the slope of the complex standard curve of $(\text{RhB})_2\text{-Zn}(\text{CNS})_4$ for each method. Based on the linear regression standard curve equation, the slope value for the TCS3200 color sensor measurement method was obtained from the regression equation $y = 0.0028x + 0.3411$, which was 0.0028. While the slope value for the UV-Vis spectrophotometer measurement method was obtained from the regression equation $y = 0.0253x + 0.0773$ is 0.0253. Based on the constructed standard curve, we calculated the limit of detection (LOD) by multiplying the standard deviation of response by 3.3 and dividing with the slope. Meanwhile, the limit of quantification (LOQ) could be obtained by multiplying the standard deviation of response by 10 and dividing it with the slope. The LOD obtained for the TCS3200 color sensor and UV-Vis spectrophotometer was 2.766 and 1.715 mg/L, respectively. These values explain why the inter-day precision for the 1 mg/L rhodamine B sample obtained for both methods exceeded the acceptable maximum variation coefficient ($< 2\%$). As for the LOQ, the values reached 8.383 and 5.196 mg/L for the TCS3200 sensor and UV-Vis spectrophotometer, respectively. Lower LOD and LOQ in UV-Vis spectrophotometer suggest its superiority in comparison to the TCS3200 color sensor, in terms of sensitivity.

Quantitative Analysis Using the TCS3200 Color Sensor

Samples were measured using a series of tools that had been readily connected to the TCS3200 color sensor. The measurement was carried out by dipping the filter paper

into the sample solution to which 3 mL of $\text{Zn}(\text{CNS})_2$ reagent had been added, then dried and measured using the TCS3200 color sensor in dark conditions. Measurements were carried out three times on each sample with 3 cm-long distance between the sensor and the sample. Such distance was given to allow even distribution of the emitted light from four Light Emitting Diodes (LEDs) to the sample and the photodiode, in which the sample could emit a current proportional to the basic color of received light.

Table 3 shows that the RGB value obtained from each sample is a code to indicate a specific color. The HIS value in the table was obtained using Eq. (1-3). The I_R value was used to determine the concentration of rhodamine B in the sample because it had the best R^2 (0.9792) among the others (Fig. 6). The total concentration of rhodamine B obtained from the measurement using the TCS3200 color sensor based on the I_R value can be observed in Table 4, showing the concentration of each sample with five repetitions. The red index value obtained from Eq. (1) has the same function as the absorbance value, the dependent variable in determining the concentration. Therefore, the concentration of rhodamine B in the sample was calculated by substituting the red color index value of the sample into the standard curve regression equation $(\text{RhB})_2\text{-Zn}(\text{CNS})_4$ R index.

Following the analysis, we found that samples A, B, and C contained rhodamine B with an average of 1.74, 16.74, and 5.10 mg/L, respectively. However, sample A had a rhodamine B concentration lower than the LOD of both the TCS3200 and UV-Vis spectrophotometer (2.766 and 1.715 mg/L, respectively). In this case, the response generated from sample A could not be differentiated from that of the blank standard. Hence, the presence of rhodamine B in sample A could not be

Table 3. RGB value samples

Repetition	RGB Measurement			HIS Value Measurement			Color	
	R	G	B	I _R	I _G	I _B		
Sample A	1	232	213	224	0.346	0.317	0.334	
	2	233	213	224	0.347	0.317	0.334	
	3	233	212	224	0.348	0.317	0.334	
	4	231	211	222	0.343	0.312	0.330	
	5	230	210	223	0.346	0.316	0.336	
	\bar{A}	231.8	211.8	223.4	0.345	0.316	0.334	
Sample B	1	206	108	215	0.389	0.203	0.406	
	2	206	107	216	0.388	0.202	0.407	
	3	206	108	216	0.386	0.203	0.407	
	4	205	106	215	0.389	0.201	0.408	
	5	206	107	215	0.388	0.203	0.407	
	\bar{B}	205.2	107.2	215.4	0.388	0.203	0.407	
Sample C	1	222	173	228	0.356	0.278	0.366	
	2	221	173	227	0.355	0.278	0.365	
	3	221	172	226	0.357	0.276	0.366	
	4	220	171	227	0.355	0.276	0.367	
	5	220	172	228	0.354	0.277	0.367	
	\bar{C}	220.8	172.2	227.2	0.355	0.276	0.366	

Table 4. Sample concentration value of TCS3200 color sensor

Sample (X)	Repetition (mg/L)					\bar{X} (mg/L)
	1	2	3	4	5	
A	1.75	2.10	2.46	0.67	1.75	1.74
B	17.10	16.75	16.03	17.10	16.75	16.74
C	5.32	4.96	5.67	4.96	4.61	5.10

confirmed by either method. As for sample C, the calculated concentration was lower than the LOQ of the TCS3200. Although its presence was confirmed, its quantitative concentration value was not reliable. Therefore, for the following analysis of comparing TCS3200 with UV-Vis spectrophotometer, samples A and C were excluded.

Comparing Methods Between the TCS3200 Color Sensor with UV-Vis Spectrophotometry Using the Two-Way t-Test

Method comparisons were carried out to see whether the TCS3200 color sensor had similar results to a UV-Vis spectrophotometer. The prepared samples were measured for five repetitions with UV-Vis at a wavelength of 590 nm and TCS 3200. Concentrations of rhodamine B in sample B were 16.74 and 17.26 mg/L for measurements using

TCS3200 and UV-Vis spectrophotometer, respectively. *T*-test ($\alpha = 8.95\%$) performed on the obtained data revealed that the $t_{\text{experimental}}$ and $t_{\text{theoretical}}$ values were 1.21 and 2.31, respectively. Therefore, H_0 is accepted because the value of $t_{\text{experimental}} < t_{\text{theoretical}}$. H_0 states that differences of data obtained from TCS3200 and the UV-Vis spectrophotometer are not meaningful or significant. This analysis validates the high concentration of rhodamine B in sample B, calculated using TCS3200. It is worth mentioning that high concentrations of rhodamine B exposed to the human body could cause adverse health effects [34].

CONCLUSION

The analytical performance of the newly developed TCS3200 color sensor was satisfactory, considering that

the analysis could be run *in situ* and available at an affordable cost, and the components were free to access. The results showed that the color gradation only occurred in the R (Red) component, while the other components, G (Green) and B (Blue), were not concentration-dependent. The *t*-test results showed that $t_{\text{experimental}} < t_{\text{theoretical}}$ suggesting the absence of statistical significance between the results obtained from the TCS3200 color sensor and the UV-Vis spectrophotometric method. The syrup samples procured from the local stores in Banda Aceh were tested qualitatively and quantitatively and was found to contain rhodamine B with high concentrations.

■ REFERENCES

- [1] Nazaruddin, N., Afifah, N., Bahi, M., Susilawati, S., MD Sani, N.D., Esmaeili, C., Iqhrammullah, M., Murniana, M., Hasanah, U., and Safitri, E., 2021, A simple optical pH sensor based on pectin and *Ruellia tuberosa* L-derived anthocyanin for fish freshness monitoring, *F1000Research*, 10, 422.
- [2] Hasanah, U., Setyowati, M., Efendi, R., Muslem, M., Md Sani, N.D., Safitri, E., Yook Heng, L., and Idroes, R., 2019, Preparation and characterization of a pectin membrane-based optical pH sensor for fish freshness monitoring, *Biosensors*, 9 (2), 60.
- [3] Safitri, E., Humaira, H., Murniana, M., Nazaruddin, N., Iqhrammullah, M., Md Sani, N.D., Esmaeili, C., Susilawati, S.L., Mahathir, M., and Nazaruddin, S.L., 2021, Optical pH Sensor based on immobilization anthocyanin from *Dioscorea alata* L. onto polyelectrolyte complex pectin–chitosan membrane for a determination method of salivary pH, *Polymers*, 13 (8), 1276.
- [4] Rahayu, W.S., Rohman, A., Martono, S., and Sudjadi, S., 2018, Application of FTIR spectroscopy and chemometrics for halal authentication of beef meatball adulterated with dog meat, *Indones. J. Chem.*, 18 (2), 376–381.
- [5] Rohaeti, E., Muzayanah, K., Septaningsih, D.A., and Rafi, M., 2019, Fast analytical method for authentication of chili powder from synthetic dyes using UV-Vis spectroscopy in combination with chemometrics, *Indones. J. Chem.*, 19 (3), 668–674.
- [6] Olas, B., Białeccki, J., Urbańska, K., and Bryś, M., 2021, The effects of natural and synthetic blue dyes on human health: A review of current knowledge and therapeutic perspectives, *Adv. Nutr.*, 12 (6), 2301–2311.
- [7] Jannah, O.Z., Suwita, K., and Jayadi, L., 2021, Analisis pewarna rhodamin b dan pengawet natrium benzoat pada saus tomat yang diperdagangkan di pasar besar tradisional kota Malang, *Jurnal Riset Kefarmasian Indonesia*, 3 (1), 10–17.
- [8] Morsi, R.E., Elsaywy, M., Manet, I., and Ventura, B., 2020, Cellulose acetate fabrics loaded with rhodamine B hydrazide for optical detection of Cu(II), *Molecules*, 25 (16), 3751.
- [9] Patil, A., and Salunke-Gawali, S., 2018, Overview of the chemosensor ligands used for selective detection of anions and metal ions (Zn^{2+} , Cu^{2+} , Ni^{2+} , Co^{2+} , Fe^{2+} , Hg^{2+}), *Inorg. Chim. Acta*, 482, 99–112.
- [10] Setiyanto, H., Ferizal, F., Saraswaty, V., Rahayu, R.S., and Zulfikar, M.A., 2021, Carbon paste electrode modified Poly-Glutamic Acid (PGA) with molecularly imprinted for detection of Rhodamine B, *IOP Conf. Ser.: Mater. Sci. Eng.*, 1088, 012113.
- [11] Tonica, W.W., Hardianti, M.F., Prasetya, S.A., and Rachmaniah, O., 2018, Determination of Rhodamine-B and Amaranth in snacks at primary school Sukolilo district of Surabaya-Indonesia by thin layer chromatography, *AIP Conf. Proc.*, 2049, 020043.
- [12] He, Q., Liu, J., Xia, Y., Tuo, D., Deng, P., Tian, Y., Wu, Y., Li, G., and Chen, D., 2019, Rapid and sensitive voltammetric detection of Rhodamine B in chili-containing foodstuffs using MnO_2 nanorods/electro-reduced graphene oxide composite, *J. Electrochem. Soc.*, 166, B805.
- [13] Muzdhalifah, B., Sudewi, S., and Citraningtyas, G., 2019, Analisis pewarna Rhodamin B pada saos bakso tusuk yang beredar di beberapa sekolah dasar di kota Manado, *Pharmacon*, 8 (1), 120–126.
- [14] Singh, H., Singh, G., Mahajan, D.K., Kaur, N., and Singh, N., 2020, A low-cost device for rapid 'color to concentration' quantification of cyanide in real

- samples using paper-based sensing chip, *Sens. Actuators, B*, 322, 128622.
- [15] Riskiawan, H.Y., Rizaldi, T., Setyohadi, D.P.S., and Leksono, T., 2017, Nitrogen (N) fertilizer measuring instrument on maize-based plant microcontroller, *Proceedings of the 2017 4th International Conference on Electrical Engineering, Computer Science and Informatics (EECSI)*, Yogyakarta, Indonesia 19-21 September 2017, 1–4.
- [16] Fitri, Z., Adlim, M., Surbakti, M.S., Omar, A.F., Sijabat, F.A., and Syahreza, S., 2019, Mercury (II) ions assessment as a toxic waste hazard in solution based on imagery data for a part of environmental disaster management, *IOP Conf. Ser.: Earth Environ.*, 273, 012052.
- [17] Amirjani, A., and Fatmehsari, D.H., 2018, Colorimetric detection of ammonia using smartphones based on localized surface plasmon resonance of silver nanoparticles, *Talanta*, 176, 242–246.
- [18] Amirjani, A., and Rahbarimehr, E., 2021, Recent advances in functionalization of plasmonic nanostructures for optical sensing, *Microchim. Acta*, 188 (2), 57.
- [19] Kesuma, S., 2020, Pengembangan metode penentuan kandungan Rhodamine B dalam kerupuk berwarna merah menggunakan reagen Zn(CNS)₂ dan pencitraan digital, *MEDFARM: Jurnal Farmasi dan Kesehatan*, 9 (2), 63–72.
- [20] Brambilla, M., Romano, E., Buccheri, M., Cutini, M., Toscano, P., Cacini, S., Massa, D., Ferri, S., Monarca, D., Fedrizzi, M., Burchi, G., and Bisaglia, C., 2021, Application of a low-cost RGB sensor to detect basil (*Ocimum basilicum* L.) nutritional status at pilot scale level, *Precis. Agric.*, 22 (3), 734–753.
- [21] Rusman, J., Michael, A., and Pasae, N., 2021, Deteksi tingkat kematangan buah kopi arabika menggunakan sensor TCS3200 berbasis Arduino Uno, *Dynamicsaint*, 6, 60–66.
- [22] Singh, A.K., and Jha, S.K., 2019, Fabrication and validation of a handheld non-invasive, optical biosensor for self-monitoring of glucose using saliva, *IEEE Sens. J.*, 19 (18), 8332–8339.
- [23] Gupta, S.K., Tapadia, K., and Sharma, A., 2020, Selective fluorometric analysis of Hg(II) in industrial waste water samples, *J. Fluoresc.*, 30 (6), 1375–1381.
- [24] Kumalasari, E., 2015, Identifikasi Rhodamin B dalam kerupuk berwarna merah yang beredar di pasar Antasari kota Banjarmasin, *Jurnal Ilmiah Manuntung*, 1 (1), 85–89.
- [25] Wei, B., Chen, Q.Y., Chen, G., Tang, R.C., and Zhang, J., 2013, Adsorption properties of lac dyes on wool, silk, and nylon, *J. Chem.*, 2013, 546839.
- [26] Rahmi, R., Lubis, S., Az-Zahra, N., Puspita, K., and Iqhrammullah, M., 2021, Synergetic photocatalytic and adsorptive removals of metanil yellow using TiO₂/grass-derived cellulose/chitosan (TiO₂/GC/CH) film composite, *Int. J. Eng.*, 34 (8), 1827–1836.
- [27] Fathana, H., Iqhrammullah, M., Rahmi, R., Adlim, M., and Lubis, S., 2021, Tofu wastewater-derived amino acids identification using LC-MS/MS and their uses in the modification of chitosan/TiO₂ film composite, *Chem. Data Collect.*, 35, 100754.
- [28] Rahmi, R., Iqhrammullah, M., Audina, U., Husin, H., and Fathana, H., 2021, Adsorptive removal of Cd (II) using oil palm empty fruit bunch-based charcoal/chitosan-EDTA film composite, *Sustainable Chem. Pharm.*, 21, 100449.
- [29] Iwanto, I., Suryadi, D., and Priyatman, H., 2018, Rancang bangun alat pendeteksi kadar boraks pada makanan menggunakan sensor warna TCS3200 berbasis Arduino, *Jurnal Teknik Elektro Universitas Tanjungpura*, 2 (1), 1–9.
- [30] Potash, A.D., Greene, D.U., Foursa, G.A., Mathis, V.L., Conner, L.M., and McCleery, R.A., 2020, A comparison of animal color measurements using a commercially available digital color sensor and photograph analysis, *Curr. Zool.*, 66 (6), 601–606.
- [31] Zhang, Y.S., Balamurugan, R., Lin, J.C., Fitriyani, S., Liu, J.H., and Emelyanenko, A., 2017, Pd²⁺ fluorescent sensors based on amino and imino derivatives of rhodamine and improvement of water solubility by the formation of inclusion complexes with β-cyclodextrin, *Analyst*, 142 (9), 1536–1544.

- [32] Harmita, H., 2004, Petunjuk pelaksanaan validasi metodean cara perhitungan, *Majalah Ilmu Kefarmasian*, 1 (3), 117–135.
- [33] Iqhrammullah, M., Suyanto, H., Rahmi, R., Pardede, M., Karnadi, I., Kurniawan, K.H., Chiari, W., and Abdulmadjid, S.N., 2021, Cellulose acetate-polyurethane film adsorbent with analyte enrichment for *in-situ* detection and analysis of aqueous Pb using Laser-Induced Breakdown Spectroscopy (LIBS), *Environ. Nanotechnol. Monit. Manage.*, 16, 100516.
- [34] Gičević, A., Hindija, L., and Karačić, A., 2020, "Toxicity of Azo Dyes in Pharmaceutical Industry" in *CMBEBIH 2019*, IFMBE Proceedings, vol. 73, Badnjevic, A., Škrbić, R., and Gurbeta Pokvić, L., Eds., Springer, Cham, 581–587.

Adsorption of Bemacid Red by Poly Tetra (Ethylene Glycol) Dimethacrylate Crosslinked with 2-Hydroxypropyl Methacrylate Hydrogels: Equilibrium and Kinetic Studies

Asmahane Fasla^{1,2*}, Zoubida Seghier¹, Abdelkader Iddou³, and Laura Caserta⁴

¹Laboratory of Macromolecular Physical Chemistry, Faculty of Exact and Applied Sciences, Oran 1 Ahmed Benbella El Mnaouer University, Oran, Algeria

²Department of Chemistry, Faculty of Science, of Science and Technology University, Oran, El Mnaouer, Oran, Algeria

³Laboratory of Materials Recovery and Nuisance Treatment, Mostaganem University, Mostaganem, Algeria

⁴Catalysis-Master Park Company, Marseille, France

* **Corresponding author:**

tel: +213-771820794

email: afasla2005@yahoo.fr

Received: October 4, 2021

Accepted: March 8, 2022

DOI: 10.22146/ijc.69548

Abstract: Besides others, textile industries are the primary sources of discharging a massive amount of highly colored wastewater. Adsorption can be considered the most economically favorable technology method for removing dyes from wastewater. This paper reports the synthesis of Poly tetra (ethyleneglycol) dimethacrylate crosslinked with 2-hydroxypropyl methacrylate (Poly (TtEGDMA-cross-2-HPMA)) hydrogels and its application as a novel sorbent to remove bemacid red (ET₂) dye from aqueous solution under various operating conditions. The equilibrium adsorption capacity was found 142.82–883.60 mg ET₂ g⁻¹ of 1% TtEGDMA. The adsorbent was characterized using Fourier transform infrared radiation (FTIR) and ¹³carbon solid-state nuclear magnetic resonance spectra (¹³C-NMR). The effects of the experimental parameters include dye concentration and crosslinked agent concentration. The kinetic sorption uptake for ET₂ by Poly (TtEGDMA-cross-2-HPMA) at various initial dye concentrations was analyzed by pseudo-first and pseudo-second models. Two sorption isotherms, namely the Langmuir and Freundlich isotherms, were applied to the sorption equilibrium data. The sorption kinetics of ET₂ onto the hydrogels followed the pseudo-second-order kinetics model (R² = 0.999) and the adsorption equilibrium data obeyed the Langmuir isotherm model (R² = 0.999). It can be concluded that Poly (TtEGDMA-cross-2-HPMA) is an alternative economic sorbent to more costly adsorbents used for dye removal in wastewater treatment processes.

Keywords: tetra (ethylene glycol) dimethacrylate; 2-hydroxypropyl methacrylate; bemacid red; pseudo-second model; Langmuir isotherm

■ INTRODUCTION

More than 10,000 dyes have been widely used in textile, paper, rubber, plastics, leather, cosmetics, pharmaceutical, and food industries to color their products, which generates a huge volume of wastewater every year [1-2]. The disposal of dye wastewater without proper treatment is a big challenge and has caused harm to the aquatic environment, such as reducing light penetration and photosynthesis [1]. Some of the dyes contained in wastewater are decomposed into

carcinogenic aromatic amines under anaerobic conditions, which could cause serious health problems to humans and animals [1]. Dyes prevent light from penetrating water masses and suppress the photosynthesis process. Thus, the biological energy flow in the water environment is affected. Due to the carcinogenic and mutagenic properties of the dyes, they also affect microbial and other living organisms in water [3].

Due to the low biodegradability, conventional biological wastewater treatment processes are not

efficient in treating dyes wastewater [1]. Therefore, dye wastewater is usually treated by physical, chemical, and biological processes [3-4]. Due to its cost-effectiveness, simple design, and ease of use, adsorption is the most preferred method for physical-chemical wastewater treatment [3,5-7]. Several adsorbents have been reported in the literature, such as clay such as smectites [8-10], zeolite [11-13], fly ash [10,14-15], silica gel [16-18], chitosan [9,19], and algae [20-21] regarding the adsorption of basic dyes from aqueous solution. Several methods were developed for wastewater treatment [21-24].

Adsorption is the best process, the most comprehensive technique [25], the most effective process of advanced wastewater treatment employed to reduce hazardous pollutants present in the effluent [21,26-27], the most economical and effective way to eliminate many types of contaminants [21].

The major advantages of adsorption over conventional treatment methods include; low operating cost [21,28-32], simplicity of implementation [21,28-31], affordability [28-31], ease of operation [32], high efficiency [21,28-32], minimization of chemical or biological sludge [32], no additional nutrient requirement [32], regeneration of biosorbent [32], possibility of sorbate recovery [32], and reusability of the adsorbent [28-31].

Hydrogels with three-dimensional crosslinking networks can be used to treat printing and dyeing wastewater with simple operations efficiently. Most hydrogels are intelligently responsive to external stimuli, such as light, electric field, temperature, pH, magnetism, and so on [33]. These unique properties of hydrogel endow it with broad application prospects and great application values in printing and dyeing wastewater treatments. Due to the excellent properties of carbohydrate polymers, they have been used as the main materials to construct hydrogel skeletons [33].

In this study, we prepared Poly (TtEGDMA-cross-2-HPMA) hydrogels as a novel sorbent to remove ET₂ from aqueous solutions. Adsorption isotherm, the effect of initial dye concentration, and crosslinked agent were studied. The adsorption isotherms were fitted by

Langmuir and Freundlich models. The adsorption was examined by using pseudo-first-order and pseudo-second-order kinetic models.

■ EXPERIMENTAL SECTION

Materials

Sorbent

The crosslinked agent, tetraethylene glycol dimethacrylate (TtEGDMA) (C₁₆H₂₆O₇) (MW = 330.38 g mol⁻¹) was supplied by Fluka, the monomer, 2-hydroxypropylmethacrylate (2-HPMA) (MW = 144.17 g mol⁻¹) was supplied by Merck-Schuchardt and the initiator, 1-azobisisobutyronitrile (AIBN) was supplied by Merck, Darmstadt, Germany. All chemicals were used as received. The mole number of 2-HPMA is 7 × 10⁻² mol, and the concentration of 1, 5, and 10% of TtEGDMA are 7.1 × 10⁻⁴, 3.55 × 10⁻³, and 7.1 × 10⁻³ mol, respectively.

Sorbate

The basic cationic dye, bemacid red (C₁₄H₁₇NSO₃Cl) [34], was obtained from the silk production (SOITEX) Tlemcen industry (Algeria). The structure of this dye is displayed in Fig. 1. A 500 mg L⁻¹ stock solution was prepared by dissolving the required amount of dye in distilled water. Working solutions of desired concentrations were obtained with successive dilutions.

Instrumentation

The samples were analyzed using FTIR spectroscopy IFS66 in 4000–400 cm⁻¹. Before the measurement, the samples were dried under a vacuum until reaching a constant weight. The dried samples were pressed into the powder, mixed with 10 times as much KBr powder, and then compressed to make a pellet for FTIR characterization.

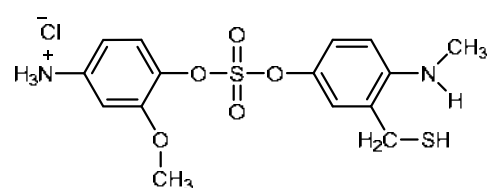


Fig 1. Chemical structure of bemacid red

The ^{13}C solid-state nuclear magnetic resonance spectra of Poly (TtEGDMA-cross-2-HPMA) were measured at 400 MHz on a Bruker MSL 300 spectrometer, using the cross-polarization/magic angle spinning (CP/MAS) probe with 4 mm O.D. rotors, under high power proton decoupling. The sample spinning was performed at 7.5 kHz, to easily recognize the sidebands. For each spectrum, 1000 scans were averaged using a recycling time of 4 s. The ^{13}C chemical shifts were calibrated in ppm relative to TMS by taking the ^{13}C chemical shift of the methine carbon of solid adamantane (29.5 ppm) as an external reference standard. All the measurements were performed at room temperature.

Procedure

Preparation of analytical method TtEGDMA-cross-2-HPMA

Poly (tetra (ethylene glycol) dimethacrylate-cross-2-hydroxypropyl methacrylate) materials, henceforth designated as Poly (TtEGDMA-cross-2-HPMA), were prepared by solution polymerization with a total concentration 10 wt.% (10.3 g of 2-HPMA). The concentration of 0.1 wt.% (0.1 g) was the initiator shown in Fig. 2. The free radical copolymerization was carried out under a nitrogen atmosphere in a three-necked flask equipped with a nitrogen inlet and a reflux condenser immersed in a constant temperature oil bath (yellow, $\pm 1^\circ\text{C}$). The reaction mixture was stirred using a magnetic stirrer. A continuous supply of nitrogen was maintained

throughout the reaction period. The solution polymerization proceeded for 24 h at 60°C . Three various crosslinked Poly (TtEGDMA-cross-2-HPMA) samples were prepared with nominal crosslinking ratios, X, of 1, 5 and 10% mol TtEGDMA/mol 2-HPMA. Then, the copolymers obtained were washed by CH_2Cl_2 several times to extract unreacted monomers. The solid copolymer slab was cut into circular disks using punches.

Adsorption kinetics

Batch adsorption experiments were carried out at 25°C by adding adsorbent (2.0 g) into several 300 mL glass Erlenmeyer flasks containing 200 mL solution of different initial concentrations (5, 10, 20, 30, 40, and 50 mg L^{-1}) of dye. The flasks were placed on a rotary shaker (120 rpm) in a thermostat. Agitation was provided for 240 min, which was more than sufficient to reach equilibrium. The samples (5 mL aliquot) were taken at suitable time intervals and centrifuged for 10 min at 3000 rpm. The ET_2 concentration in the supernatant solution was analyzed by measuring the optical density at 505 nm, using a spectrophotometer (Spectronic Genesys 5).

To investigate the kinetic mechanism, which controls the adsorption process of ET_2 on the hydrogel, the pseudo-first-order (PFO) [9,35] and pseudo-second-order (PSO) models were used to test the experiment data [9,35-37]. The pseudo-first-order kinetic model can

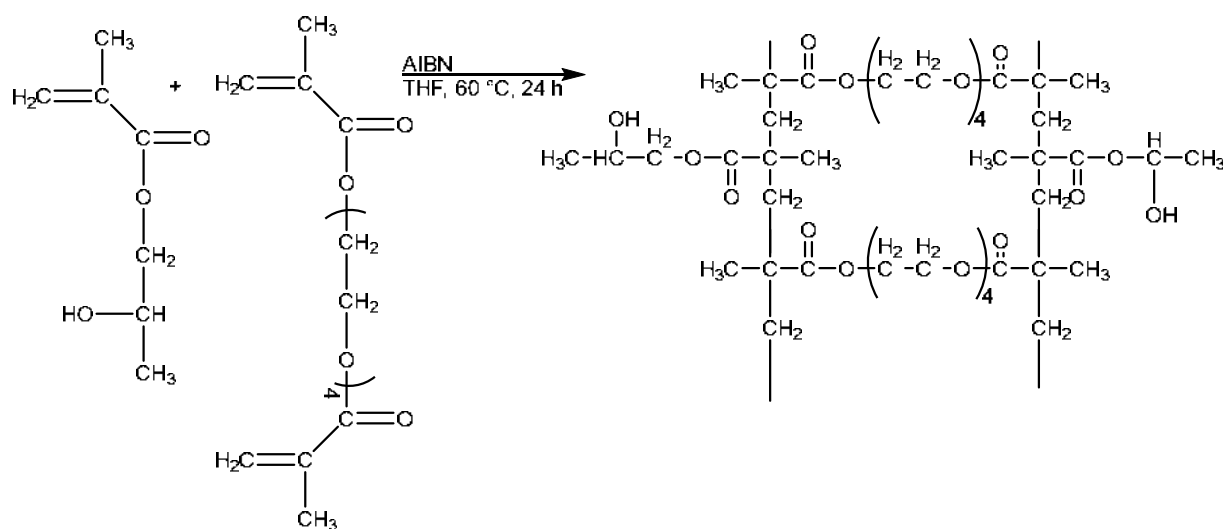


Fig 2. Chemical structure of Poly (TtEGDMA-cross-2-HPMA) hydrogel

be as Eq. (1). The pseudo-second-order model is based on the assumption of chemisorption of the adsorbate on the adsorbents. This model is given as Eq. (2):

$$\ln(q_e - q) = \ln q_e - \frac{k_{1,s}}{2.303} t \quad (1)$$

$$\frac{t}{q} = \frac{1}{k_{2,s} q_e^2} + \frac{1}{q_e} t \quad (2)$$

where, q_e is equilibrium adsorption capacity (mg g^{-1}), and $k_{1,s}$ is the pseudo-first-order rate constant (min^{-1}). The q_t parameter is the amount of adsorption dye (mg g^{-1}) at a time (min) while $k_{2,s}$ is the pseudo-second-order rate constant (min g mg^{-1}).

■ RESULTS AND DISCUSSION

Characterization of Copolymer

The FTIR spectra of poly (TtEGDMA-cross-2-HPMA) (a) 1% (b) 5% and (c) 10% TtEGDMA are shown in Fig. 3(a-c). It is observed that poly (TtEGDMA-cross-2-HPMA) spectra showed an absorption band typical at 1060 cm^{-1} , which is attributed to C-O [38-40], and the O-H bending vibrations 1006 cm^{-1} correspond to the HPMA comonomer of the copolymer. The ester stretching vibration (-C=O) of -COOR band at 1738 cm^{-1} , the C-O stretching at 1255 cm^{-1} . The other strong bands at 1450 correspond to the C-H bending (alkane, -CH_3 , alkane, $\text{-CH}_2\text{-}$) of the alkane [41]. The FTIR shows C-O-C stretching peaks of the ester group of 1108 cm^{-1} [2,42], 1385 cm^{-1} due to the symmetrical deformation of its

methyl (CH_3) [39] and deformation of the group CH-OH [43]. The absorption peak at 976 cm^{-1} corresponds to its $\text{-CH}_2\text{-CH}_2\text{-O}$ group vibration [2].

The ^{13}C -NMR spectrum of Poly (TtEGDMA-cross-2-HPMA) and its assignment are shown in Fig. 4. The α -methyl of TtEGDMA and 2-HPMA appeared at 18.8 ppm , the methylene of TtEGDMA and 2-HPMA appeared at 55.5 ppm . The signal due to the backbone methylene carbon of TtEGDMA is observed at 65.1 and 75 ppm , while the ester carbonyl of TtEGDMA and 2-HPMA appeared at 167 and 178.2 ppm , respectively.

Adsorption Studies

Fig. 5-6 shows experimental data, and the predicted curves for the sorption of ET_2 by Poly (TtEGDMA-cross-2-HPMA) using a linear method for the three hydrogels used models pseudo-second-order. Table 1 shows the pseudo-first and pseudo-second-order kinetic parameters for different initial concentrations of ET_2 obtained by utilizing the linear regression analysis method.

According to experimental data, a straight-line plot with a correlation coefficient of 0.995 suggests the applicability of the pseudo-first-order kinetics model to fit the experimental data (Table 1). The calculated value of adsorption capacity for 1% TtEGDMA for 50 mg g^{-1} , $q_{e,\text{cal}}$ (9.33 mg g^{-1}) is higher than the value of experimental adsorption capacity, $q_{e,\text{exp}}$ (9.25 mg g^{-1}). Therefore, the theoretical q_e values estimated from the

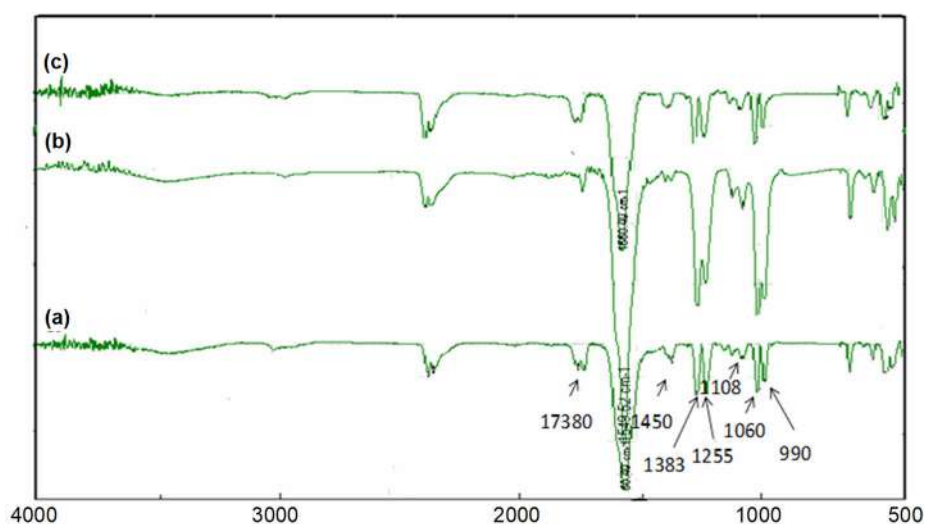


Fig 3. FTIR spectrum of Poly (TtEGDMA-cross-2-HPMA) hydrogels: (a) 1%, (b) 5% and (c) 10% of TtEGDMA

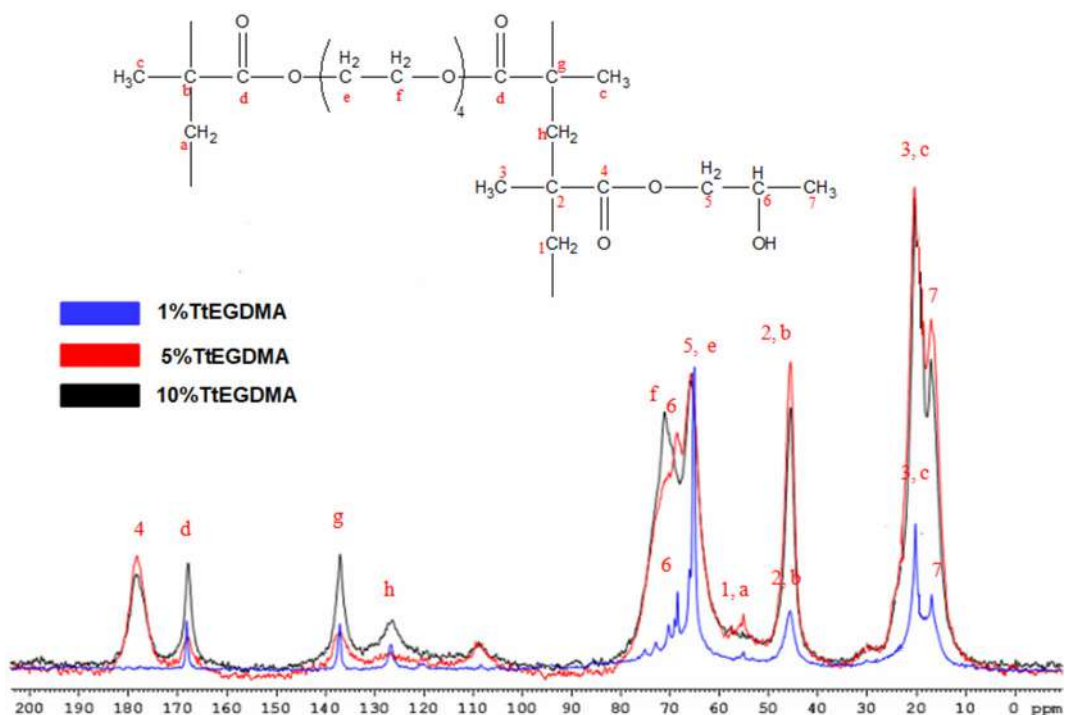


Fig 4. ¹³C-NMR spectrum of Poly (TtEGDMA-cross-2-HPMA) hydrogels

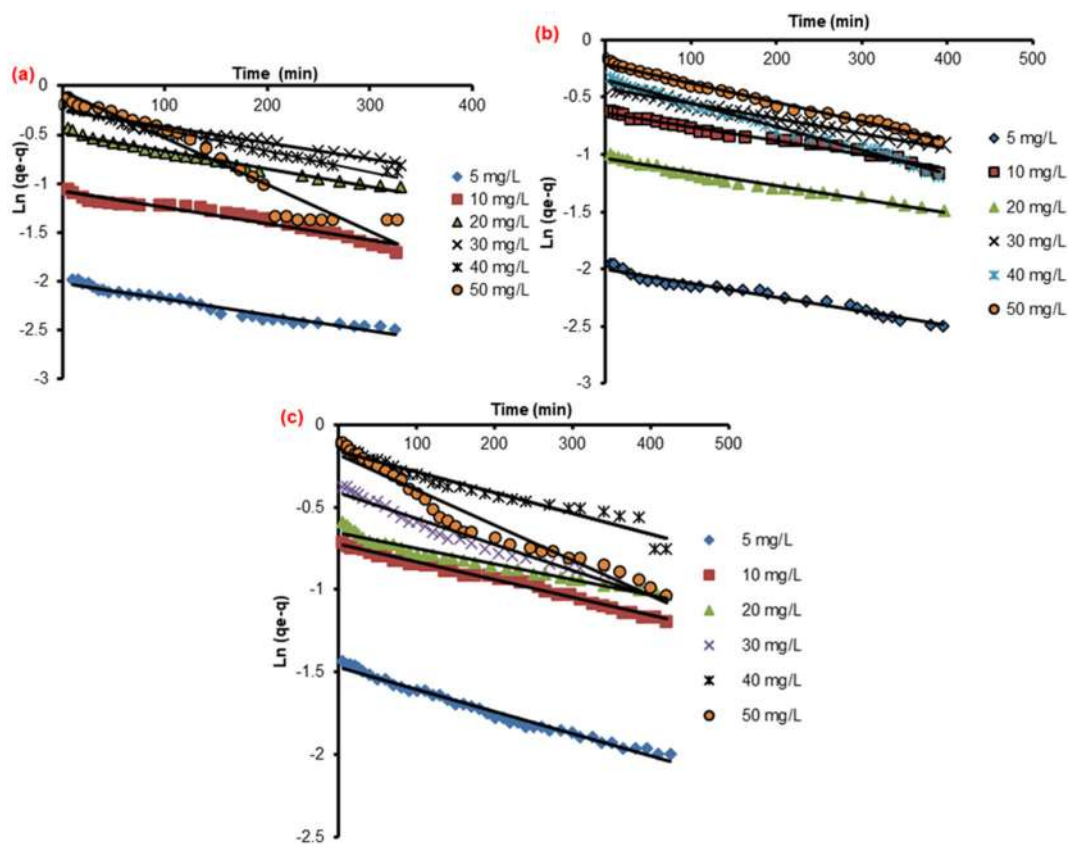


Fig 5. Pseudo-first order adsorption kinetics dyes of ET₂ by Poly (TtEGDMA-cross-2-HPMA) with (a) 1, (b) 5, and (c) 10% of TtEGDMA for various initial dye concentrations

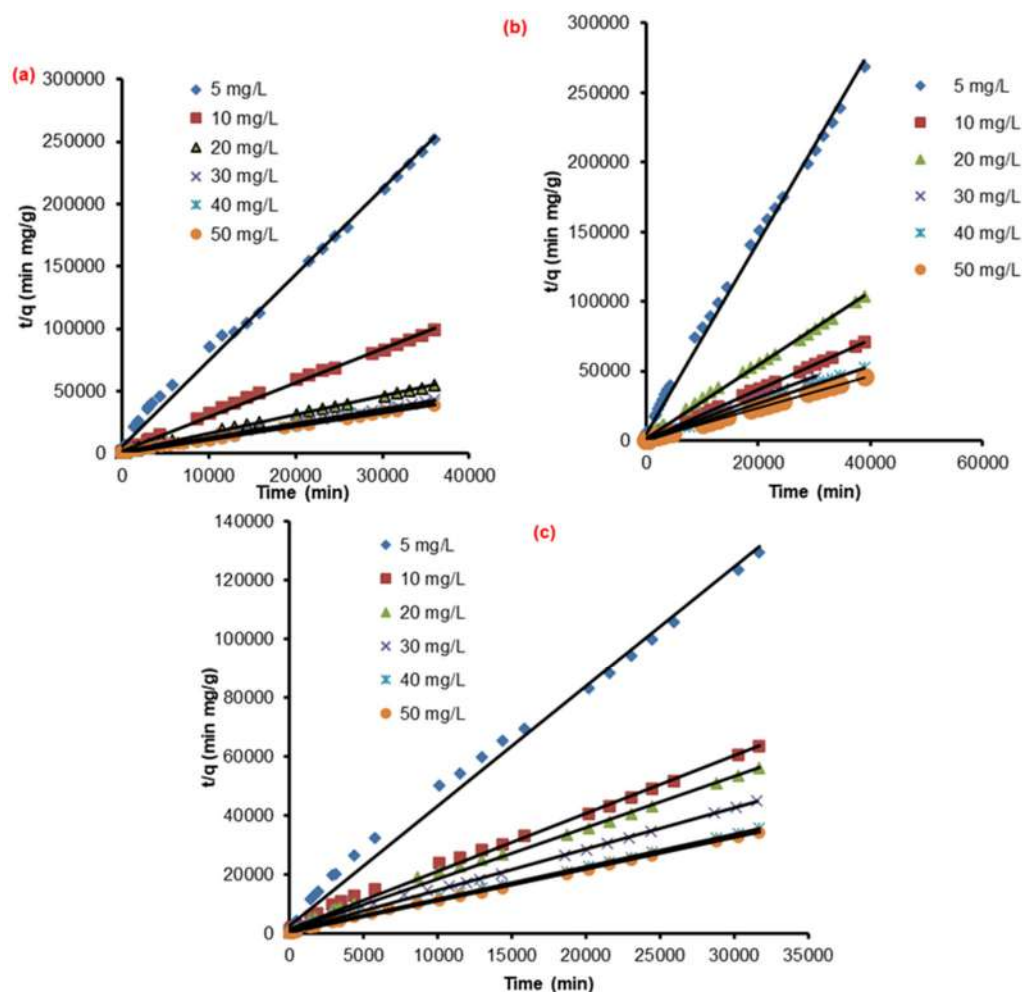


Fig 6. Pseudo-second order adsorption kinetics dyes of ET_2 by Poly (TtEGDMA-cross-2-HPMA) with (a) 1, (b) 5, and (c) 10% of TtEGDMA for various initial dye

Table 1. Calculated model parameters and regression coefficients for the pseudo-first-order and pseudo-second order for all studied concentration

TtEGDMA (% mol)	Concentration ($mg L^{-1}$)	Pseudo first order			Pseudo second order			
		$k_{1,s} 10^2$ (min^{-1})	$q_{e,cal}$ ($mg g^{-1}$)	R^2	$k_{2,s} 10^4$ ($g mg^{-1} min^{-1}$)	$q_{e,cal}$ ($mg g^{-1}$)	$q_{e,exp}$ ($mg g^{-1}$)	R^2
1	5	3.76	1.81×10^{-9}	0.958	9.00	1.45	1.42	0.966
	10	3.86	2.20×10^{-5}	0.950	4.97	3.62	3.65	0.998
	20	4.23	8.00×10^{-3}	0.982	2.26	6.65	6.58	0.998
	30	3.81	8.30×10^{-2}	0.965	1.89	8.51	8.44	0.997
	40	4.97	9.60×10^{-2}	0.978	2.72	8.94	8.84	0.999
	50	1.99	5.59×10^{-1}	0.931	3.97	9.33	9.25	0.999
5	5	1.27	1.21×10^{-4}	0.963	2.03	0.65	0.65	0.997
	10	1.24	5.72×10^{-2}	0.975	8.02	1.71	1.69	0.998
	20	1.23	9.51×10^{-3}	0.980	5.06	2.52	2.48	0.999
	30	1.35	1.48×10^{-1}	0.992	4.01	3.05	3.02	0.998
	40	2.14	2.12×10^{-1}	0.994	8.20	3.37	3.33	0.999
	50	1.74	3.90×10^{-1}	0.993	5.92	3.87	3.82	0.999

Table 1. Calculated model parameters and regression coefficients for the pseudo-first-order and pseudo-second order for all studied concentration (*Continued*)

TtEGDMA (% mol)	Concentration (mg L ⁻¹)	Pseudo first order			Pseudo second order			
		k _{1,s} 10 ² (min ⁻¹)	q _{e,cal} (mg g ⁻¹)	R ²	k _{2,s} 10 ⁴ (g mg ⁻¹ min ⁻¹)	q _{e,cal} (mg g ⁻¹)	q _{e,exp} (mg g ⁻¹)	R ²
10	5	0.70	3.67 × 10 ⁻²	0.981	26.6	0.55	0.55	0.995
	10	0.56	19.5 × 10 ⁻²	0.990	10.3	1.14	1.12	0.996
	20	0.48	22.4 × 10 ⁻²	0.980	10.4	1.29	1.27	0.996
	30	0.38	39.3 × 10 ⁻²	0.961	9.50	1.60	1.58	0.997
	40	0.65	69.8 × 10 ⁻²	0.952	6.30	2.04	1.99	0.997
	50	0.19	66.4 × 10 ⁻²	0.949	13.2	2.09	2.07	0.999

first-order kinetic model gave significantly different values compared to experimental values comparing pseudo-second-order kinetic model, the correlation coefficient (R²) of PSO model (0.996) is higher than that of PFO kinetic model (0.949) for ET₂, indicating that chemisorptions dominate the removal mechanism and due to the sharing or exchange of electrons of ET₂ [36,44-45]. These results showed that the first-order kinetic model did not describe these sorption systems. Thus, it could be suggested that the adsorption of ET₂ on hydrogel follows the pseudo-second-order better than the pseudo-first-order model. The pseudo-second-order kinetic model assumes that the rate-limiting step may be chemical adsorption. The rate-determining step may be chemical sorption involving valence forces through sharing or exchange of electrons between adsorbent and adsorbate. It may lead to the inference of a greater affinity and rapid bonding of ET₂ molecules to the surface of poly (TtEGDMA-cross-2-HPMA) [35,46].

Adsorption Isotherms

In this work, the most commonly used equilibrium isothermal models, Langmuir and Freundlich models, were adopted to simulate the adsorption isotherm of the prepared foams. Langmuir model is based on the assumption of a homogeneous adsorbent surface with

identical adsorption sites, which can be expressed in Eq. (3) [36,47]:

$$q_e = \frac{q_0 \times b \times c_e}{1 + b \times c_e} \quad (3)$$

where, b is an equilibrium adsorption constant (L mg⁻¹), and q₀ is the saturated monolayer adsorption capacity (mg g⁻¹). A linearized plot of 1/q_e against 1/c_e gives a q₀ and b.

Freundlich adsorption isotherm describes the adsorption of adsorbates onto heterogeneous surfaces with different functional groups or adsorbent-adsorbate interactions as shown in Eq. (4) [36,48].

$$q_e = k_f \times c_e^{1/n} \quad (4)$$

This expression can be linearized to give:

$$\text{Ln}q_e = \text{Ln}k_f + \frac{1}{n}\text{Ln}c_e \quad (5)$$

where, k_f and n are Freundlich constants, which represent adsorption capacity and adsorption intensity, respectively. K_f and n can be calculated from a linear plot of Lnq_e against Lnc_e.

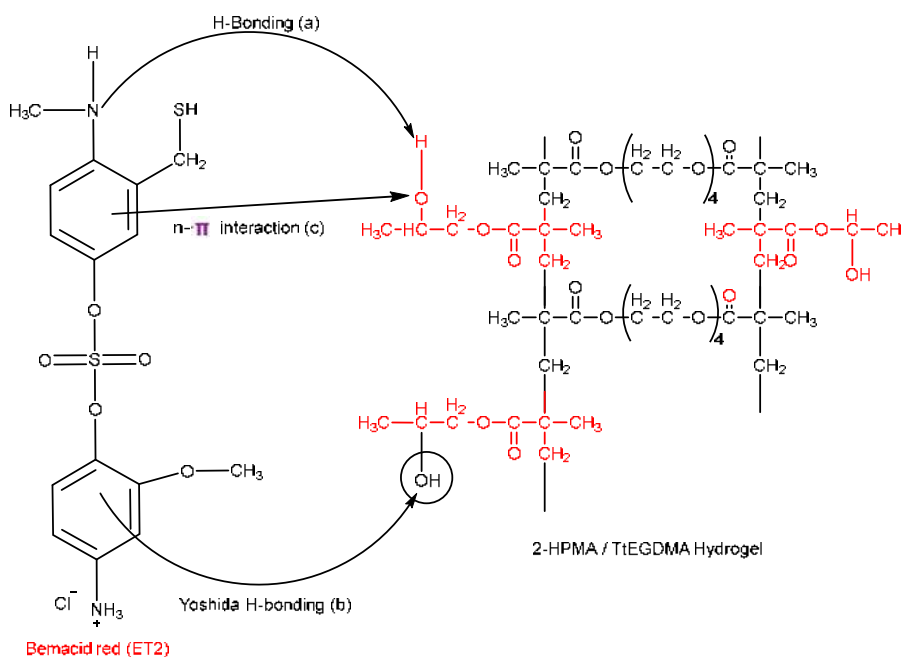
The calculated results of the Langmuir and Freundlich isotherm constants are given in Table 2. The R² of the Langmuir isothermal model for the ET₂ is 0.999, higher than those of the Freundlich isotherm model 0.959, demonstrating that the cationic dyes are

Table 2. Langmuir and Freundlich isotherm model constants and correlation coefficients

Hydrogel	TtEGDMA (% mol)	Langmuir model			Freundlich model		
		b	q ₀	R ²	K _f 10 ⁶	n	R ²
Poly (TtEGDMA-Cross-2-HPMA)	1	953.16	0.13	0.999	9.26	0.18	0.959
	5	329.31	0.25	0.999	25.33	0.39	0.981
	10	48.39	0.85	0.999	208.88	1.03	0.959

Table 3. Comparing the adsorption capacities of the various hydrogels adsorbents towards ET₂ dye adsorption

Q _{max} (mg g ⁻¹)	Hydrogel adsorbent	Ref.
0.7	Poly (methacrylic acid-cross-dodecylacrylate ammonium bromide)	[34]
0.159	Poly (acrylamide-cross-hydroxyethylmethacrylate)	[41]
0.85	Poly (TtEGDMA-cross-2-HPMA)	

**Fig 7.** Proposed adsorption mechanisms of ET₂ on poly (TtEGDMA-cross-2-HPMA)

adsorbed in poly (TtEGDMA-cross-2-HPMA) a monolayer mode [36].

The adsorption capacity of Poly (TtEGDMA-cross-2-HPMA) towards ET₂ was compared with various types of hydrogel adsorbents reported in the literature, as recorded in Table 3. The results indicate a higher adsorption capacity than those used by other researchers.

Adsorption Mechanism

The proposed mechanisms for the adsorption of ET₂ dye onto poly (TtEGDMA-cross-2-HPMA) are illustrated in Fig. 7. Poly (TtEGDMA-cross-2-HPMA) contains a large number of hydroxyl functional groups, making it an ideal adsorbent for removing basic pollutants from the aqueous systems. Two types of hydrogen bonding interactions can occur in the 2-H system: (1) between hydroxyl groups (H-donor) on the poly (TtEGDMA-cross-2-HPMA) surface and H-acceptor atoms (i.e., nitrogen) in ET₂, and (2) between hydroxyl groups on the

poly (TtEGDMA-cross-2-HPMA) surface and the aromatic rings in ET₂. The former is known as dipole-dipole H-bonding (Fig. 7(a)) and the latter is known as Yoshida H-bonding (Fig. 7(b)). The n-π interactions (also known as n-π electron donor-acceptor interactions) between oxygen groups on the poly (TtEGDMA-cross-2-HPMA) surface act as electron donors, while the aromatic rings of ET₂ act as electron acceptors (Fig. 7(c)) [35,49-50].

CONCLUSION

The potential of poly tetra (ethylene glycol) dimethacrylate-crosslinked-2-hydroxypropyl methacrylate) for the sorption of ET₂ from an aqueous solution was investigated. FTIR and ¹³C-NMR confirmed the chemical structures. The effects of experimental parameters such as initial dye and crosslinked agent concentrations were studied. Initial dye concentration

and crosslinked agent concentration were found to have an influence on the sorption efficiency. Kinetic studies showed that the adsorption followed a pseudo-second-order kinetic model, indicating that chemical adsorption was the rate-limiting step. According to the best correlation results, the adsorption data of both hydrogels are found to fit well with the Langmuir isotherm. The dye adsorption mechanism onto hydrogels was electrostatic attraction, dipole-dipole hydrogen bonding, and Yoshida H-bonding. It can be concluded that Poly (TtEGDMA-cross-2-HPMA) is an alternative economic sorbent to more costly adsorbents used for dye removal in wastewater treatment processes.

■ ACKNOWLEDGMENTS

The authors acknowledge the research grant provided by The General Directorate for Scientific Research and Technological Development (PNR project) and the Ministry of Higher Education and Scientific Research of Algeria (Project No. E0182100066).

■ REFERENCES

- [1] Santhi, T., Manonmani, S., Vasantha, S.V., and Chang, T.Y., 2016, A new alternative adsorbent for the removal of cationic dyes from aqueous solution, *Arabian J. Chem.*, 9, S466–S474.
- [2] Bhattacharyya, R., and Ray, S.K., 2015, Removal of Congo red and methyl violet from water using nano clay filled composite hydrogels of poly acrylic acid and polyethylene glycol, *Chem. Eng. J.*, 260, 269–283.
- [3] Ilgin, P., Ozay, H., and Ozay, O., 2019, Selective adsorption of cationic dyes from colored noxious effluent using a novel N-tert-butylmaleamic acid based hydrogels, *React. Funct. Polym.*, 142, 189–198.
- [4] Yaseen, D.A., and Scholz, M., 2019, Textile dye wastewater characteristics and constituents of synthetic effluents: A critical review, *Int. J. Environ. Sci. Technol.*, 16 (2), 1193–1226.
- [5] Khan, M., and Lo, I.M.C., 2016, A holistic review of hydrogel applications in the adsorptive removal of aqueous pollutants: Recent progress, challenges, and perspectives, *Water Res.*, 106, 259–271.
- [6] Tran, V.V., Park, D., and Lee, Y.C., 2018, Hydrogel applications for adsorption of contaminants in water and wastewater treatment, *Environ. Sci. Pollut. Res.*, 25, 24569–24599.
- [7] Pakdel, P.M., and Peighambaroust, S.J., 2018, A review on acrylic based hydrogels and their applications in wastewater treatment, *J. Environ. Manage.*, 217, 123–143.
- [8] Titchou, F.E., Ait Akbour, R., Assabane, A., and Hamdani, M., 2020, Removal of cationic dye from aqueous solution using Moroccan pozzolana as adsorbent: Isotherms, kinetic studies, and application on real textile wastewater treatment, *Groundwater Sustainable Dev.*, 11, 100405.
- [9] Wang, F., Li, L., Iqbal, J., Yang, Z., and Du, Y., 2022, Preparation of magnetic chitosan corn straw biochar and its application in adsorption of amaranth dye in aqueous solution, *Int. J. Biol. Macromol.*, 199, 234–242.
- [10] Jawad, A.H., and Abdulhameed, A.S., 2020, Mesoporous Iraqi red kaolin clay as an efficient adsorbent for methylene blue dye: Adsorption kinetic, isotherm and mechanism study, *Surf. Interfaces*, 18, 100422.
- [11] Munthalia, M.W., Johan, E., Aono, H., and Matsue, N., 2015, Cs⁺ and Sr²⁺ adsorption selectivity of zeolites in relation to radioactive decontamination, *J. Asian Ceram. Soc.*, 3 (3), 245–250.
- [12] Niaei, H.A., and Rostamizadeh, M., 2020, Adsorption of metformin from an aqueous solution by Fe-ZSM-5 nano-adsorbent: Isotherm, kinetic and thermodynamic studies, *J. Chem. Thermodyn.*, 142, 106003.
- [13] Brião, G.V., Jahn, S.L., Foletto, E.L., and Dotto, G.L., 2017, Adsorption of crystal violet dye onto a mesoporous ZSM-5 zeolite synthesized using chitin as template, *J. Colloid Interface Sci.*, 508, 313–322.
- [14] Zhao, X., Zhao, H., Huang, X., Wang, L., Liu, F., Hu, X., Li, J., Zhang, G., and Ji, P., 2021, Effect and mechanisms of synthesis conditions on the cadmium adsorption capacity of modified fly ash, *Ecotoxicol. Environ. Saf.*, 223, 112550.

- [15] Benvenuti, J., Fisch, A., dos Santos, J.H.Z., and Gutterres, M., 2019, Silica-based adsorbent material with grape bagasse encapsulated by the solgel method for the adsorption of Basic Blue 41 dye, *J. Environ. Chem. Eng.*, 7 (5), 103342.
- [16] Raghav, S., Jain, P., and Kumar, D., 2022, Assembly of cerium impregnated pectin/silica-gel biopolymeric material for effective utilization for fluoride adsorption studies, *Mater. Today: Proc.*, 50, 273–281.
- [17] Wang, D., Zhang, J., Yang, Q., Li, N., and Sumathy, K., 2014, Study of adsorption characteristics in silica gel-water adsorption refrigeration, *Appl. Energy*, 113, 734–741.
- [18] Zhang, Y., Xia, K., Liu, X., Chen, Z., Du, H., and Zhang, X., 2019, Synthesis of cationic-modified silica gel and its adsorption properties for anionic dyes, *J. Taiwan Inst. Chem. Eng.*, 102, 1–8.
- [19] Sadiq, A.C., Olasupo, A., Wan Ngah, W.S., Rahim, N.Y., and Mohd Suah, F.B., 2021, A decade development in the application of chitosan-based materials for dye adsorption: A short review, *Int. J. Biol. Macromol.*, 191, 1151–1163.
- [20] Singh, A., Pal, D.B., Kumar, S., Srivastva, N., Syed, A., Elgorban, A.M., Singh, R., and Gupta, V.K., 2021, Studies on Zero-cost algae based phytoremediation of dye and heavy metal from simulated wastewater, *Bioresour. Technol.*, 342, 125971.
- [21] Benafqir, M., Hsini, A Laabd, M., Laktif, T., Ait Addi, A., Albourine, A., and El Alem, N., 2020, Application of Density Functional Theory computation (DFT) and Process Capability Study for performance evaluation of orthophosphate removal process using Polyaniline@Hematite-titaniferous sand composite (PANI@HTS) as a substrate, *Sep. Purif. Technol.*, 236, 116286.
- [22] Liu, C., Chen, X.X., Zhang, J., Zhou, H.Z., Zhang, L., and Guo, Y.K., 2018, Advanced treatment of bio-treated coal chemical wastewater by a novel combination of microbubble catalytic ozonation and biological process, *Sep. Purif. Technol.*, 197, 295–301.
- [23] Zhou, L., Zhou, H., and Yang, X., 2019, Preparation and performance of a novel starch-based inorganic/organic composite coagulant for textile wastewater treatment, *Sep. Purif. Technol.*, 210, 93–99.
- [24] Gupta, V.K., Tyagi, I., Agarwal, S., Singh, R., Chaudhary, M., Harit, A., and Kushwaha, S., 2016, Column operation studies for the removal of dyes and phenols using a low cost adsorbent, *Global J. Environ. Sci. Manage.*, 2, 1–10.
- [25] Darwish, A.A.A., Rashad, M., and AL-Aoh, H.A., 2019, Methyl orange adsorption comparison on nanoparticles: Isotherm, kinetics, and thermodynamic studies, *Dyes Pigm.*, 160, 563–571.
- [26] Mahmoud, G.A., Abdel-Aal, S.E., Badway, N.A., Elbayaa, A.A., and Ahmed, D.F., 2017, A novel hydrogel based on agricultural waste for removal of hazardous dyes from aqueous solution and reuse process in a secondary adsorption, *Polym. Bull.*, 74 (2), 337–358.
- [27] Nasef, M.M., and Güven, O., 2012, Radiation-grafted copolymers for separation and purification purposes: Status, challenges and future directions, *Prog. Polym. Sci.*, 37 (12), 1597–1656.
- [28] El Haouti, R., Ouachtak, H., El Guerdaoui, A., Amedlous, A., Amaterz, E., Haounati, R., Ait Addi, A., Akbal, F., El Alem, N., and Taha, M.L., 2019, Cationic dyes adsorption by Na-montmorillonite nano clay: Experimental study combined with a theoretical investigation using DFT based descriptors and molecular dynamics simulations, *J. Mol. Liq.*, 290, 111139.
- [29] El-Zahhar, A.A., Awwad, N.S., and El-Katori, E.E., 2014, Removal of bromophenol blue dye from industrial waste water by synthesizing polymer-clay composite, *J. Mol. Liq.*, 199, 454–461.
- [30] Fayazi, M., Afzali, D., Taher, M.A., Mostafavi, A., and Gupta, V.K., 2015, Removal of Safranin dye from aqueous solution using magnetic mesoporous clay: Optimization study, *J. Mol. Liq.*, 212, 675–685.
- [31] Zhang, Z., Wang, W., Kang, Y., Zong, L., and Wang, A., 2016, Tailoring the properties of palygorskite by various organic acids via a one-pot hydrothermal process: A comparative study for removal of toxic dyes, *Appl. Clay Sci.*, 120, 28–39.

- [32] Subbaiah, M.V., and Kim, D.S., 2016, Adsorption of methyl orange from aqueous solution by aminated pumpkin seed powder: Kinetics, isotherms, and thermodynamic studies, *Ecotoxicol. Environ. Saf.*, 128, 109–117.
- [33] Chang, Z., Chen, Y., Tang, S., Yang, J., Chen, Y., Chen, S., Li, P., and Yang, Z., 2020, Construction of chitosan/polyacrylate/graphene oxide composite physical hydrogel by semi-dissolution/acidification/sol-gel transition method and its simultaneous cationic and anionic dye adsorption properties, *Carbohydr. Polym.*, 229, 115431.
- [34] Sebti, H., Fasla, A., and Ould Kada, S., 2015, Swelling properties of hydrogel networks of poly (methacrylic acid-cross-Nacrylate-N,N-dimethyl-N-dodecyl ammonium bromide). Application in the sorption of an industrial dye, *Pharma Chem.*, 7 (11), 17–25.
- [35] Abd Malek, N.N., Jawad, A.H., Ismail, K., Razuan, R., and AlOthman, Z.A., 2021, Fly ash modified magnetic chitosan-polyvinyl alcohol blend for reactive orange 16 dye removal: Adsorption parametric optimization, *Int. J. Biol. Macromol.*, 189, 464–476.
- [36] Ilgin, P., Ozay, H., and Ozay, O., 2019, Selective adsorption of cationic dyes from colored noxious effluent using a novel N-tert-butylmaleamic acid based hydrogels, *React. Funct. Polym.*, 142, 189–198.
- [37] Tiwari, J.N., Mahesh, K., Le, N.H., Kemp, K.C., Timilsina, R., Tiwari, R.N., and Kim, K.S., 2013, Reduced graphene oxide-based hydrogels for the efficient capture of dye pollutants from aqueous solutions, *Carbon*, 56, 173–182.
- [38] Bello, K., Sarojini, B.K., Narayana, B., Rao, A., and Byrappa, K., 2018, A study on adsorption behavior of newly synthesized banana pseudo-stem derived superabsorbent hydrogels for cationic and anionic dye removal from effluents, *Carbohydr. Polym.*, 181, 605–615.
- [39] Bhattacharyya, R., and Ray, S.K., 2014, Micro- and nano-sized bentonite filled composite superabsorbents of chitosan and acrylic copolymer for removal of synthetic dyes from water, *Appl. Clay Sci.*, 101, 510–520.
- [40] Maity, J., and Ray, S.K., 2014, Enhanced adsorption of methyl violet and Congo red by using semi and full IPN of polymethacrylic acid and chitosan, *Carbohydr. Polym.*, 104, 8–16.
- [41] Bhattacharyya, R., Ray, S.K., and Mandal, B., 2013, A systematic method of synthesizing composite superabsorbent hydrogels from crosslink copolymer for removal of textile dyes from water, *J. Ind. Eng. Chem.*, 19 (4), 1191–1203.
- [42] Bhattacharyya, R., and Ray, S.K., 2014, Enhanced adsorption of synthetic dyes from aqueous solution by a semi-interpenetrating network hydrogel based on starch, *J. Ind. Eng. Chem.*, 20 (5), 3714–3725.
- [43] Pandey, S., Do, J.Y., Kim, J., and Kang, M., 2020, Fast and highly efficient removal of dye from aqueous solution using natural locust bean gum based hydrogels as adsorbent, *Int. J. Biol. Macromol.*, 143, 60–75.
- [44] Bai, X., Gao, S., and Chen, W., 2014, The effect of anion $\text{NO}_3^-/\text{SO}_4^{2-}/\text{F}^-$ on the optical performance and chroma index of glass coloured by cobalt, *Int. J. Microstruct. Mater. Prop.*, 9 (6), 525–531.
- [45] Li, Y., Li, L., Chen, T., Duan, T., Yao, W., Zheng, K., Dai, L., and Zhu, W., 2018, Bioassembly of fungal hypha/graphene oxide aerogel as high performance adsorbents for U(VI) removal, *Chem. Eng. J.*, 347, 407–414.
- [46] Baig, U., Uddin, M.K., and Gondal, M., 2020, Removal of hazardous azo dye from water using synthetic nano adsorbent: Facile synthesis, characterization, adsorption, regeneration and design of experiments, *Colloids Surf., A*, 584, 124031–124046.
- [47] Li, R., An, Q.D., Xiao, Z.Y., Zhai, B., Zhai, S.R., and Shi, Z., 2017, Preparation of PEI/CS aerogel beads with a high density of reactive sites for efficient Cr(vi) sorption: Batch and column studies, *RSC Adv.*, 7 (64), 40227–40236.
- [48] Cao, Q., Huang, F., Zhuang, Z., and Lin, Z., 2012, A study of the potential application of nano-Mg(OH)₂ in adsorbing low concentrations of uranyl tricarbonate from water, *Nanoscale*, 4 (7), 2423–2430.

- [49] Jawad, A.H., Abd Malek, N.N., Abdulhameed, A.S., and Razuan, R., 2020, Synthesis of magnetic chitosan-fly ash/Fe₃O₄ composite for adsorption of reactive orange 16 dye: Optimization by Box- Behnken design, *J. Polym. Environ.*, 28 (3), 1068–1082.
- [50] Abd Malek, N.N., Jawad, A.H., Abdulhameed, A.S., Ismail, K., and Hameed, B., 2020, New magnetic Schiff's base-chitosan-glyoxal/fly ash/Fe₃O₄ biocomposite for the removal of anionic azo dye: An optimized process, *Int. J. Biol. Macromol.*, 146, 530–539.

A Potential Approach for Converting Rubber Waste into a Low-Cost Polymeric Adsorbent for Removing Methylene Blue from Aqueous Solutions

Muhammad Aliyu^{1,2}, Abdul Halim Abdullah^{1,3*}, and Mohamed Ibrahim bin Mohamed Tahir¹

¹Department of Chemistry, Faculty of Science, Universiti Putra Malaysia, 43400 UPM Serdang, Selangor, Malaysia

²Department of Chemistry, Faculty of Natural and Applied Science, Sule Lamido University, Kafin Hausa, Jigawa State, Nigeria

³Institute of advanced Technology, Universiti Putra Malaysia, 43400 Serdang, Selangor Darul Ehsan Malaysia

* **Corresponding author:**

email: halim@upm.edu.my

Received: October 9, 2021

Accepted: February 18, 2022

DOI: 10.22146/ijc.69674

Abstract: Exploiting waste materials to make cost-effective adsorbents and waste management methods are gaining more attention. In the current study, rubber wastes derived from dipping tank coagulum (DTC) in the glove manufacturing industry were converted into a novel polymeric-adsorbent via a simple sulfonation reaction with concentrated sulphuric acid and was used for the adsorption of methylene blue (MB) dye from aqueous solutions commonly found in contaminated waters. FT-IR, EDX, FESEM, and BET techniques were used to characterize the rubber waste before and after modification. The highest MB removal efficiency of 99.03% was achieved in the condition of initial concentration, adsorbent dosage, pH, contact time, and temperature were 15 mg/L, 30 mg, pH 7, 300 min, and 25 °C, respectively. The adsorption of MB was analyzed using experimental data fitted in a monolayer isotherms model with a maximum adsorption capacity of 119 mg/g. The kinetic model was revealed to agree with the pseudo-second-order kinetic model. Furthermore, SRW retained 90.45% of the removal percentage after four cycles of the repeated adsorption-desorption process. Conclusively, these findings suggest that rubber waste could be a suitable low-cost adsorbent to remove organic dyes from polluted water.

Keywords: methylene blue; adsorption; rubber waste; polymeric materials; environmental remediation

■ INTRODUCTION

Malaysia is amongst the world's largest manufacturers and suppliers of rubber products such as examination and surgical gloves, which account for more than 70% of total rubber product exports and almost 60% of global consumption [1]. The rubber products market has expanded significantly in recent years to meet worldwide demand. The global rubber market was worth \$29.8 billion in 2018 and is predicted to grow by 5.2% between 2019 and 2026 [2]. Despite having a substantial market share in global rubber products exports, the rubber glove manufacturing industry currently faces the difficulty of regulating massive volumes of waste generated throughout the rubber glove manufacturing process [3]. In addition, rubber latex manufacturing

plants generate large amounts of formulated rubber latex waste, known as dipping tank coagulum (DTC), mostly created by rubber glove dipping tanks. It is classified as scheduled waste and must be disposed of via incineration as scheduled waste under the Environmental Quality Act [4]. However, incineration of these solid rubber wastes has a severe environmental impact since they pollute land and air [5]. Therefore, an important topic addressed in this research is a new method of converting rubber waste into usable and sustainable materials for the benefit of the environment.

Methylene blue (MB) is a cationic dye whose component is a crystalline dark green powder with a bronze luster [6]. Although MB is not regarded as acutely toxic, it does have negative effects. Inhaling MB dye directly may induce breathing difficulties, while

ingestion may cause nausea, vomiting, and diarrhea [7]. In addition, a substantial amount of MB inhalation may potentially result in methemoglobinemia, jaundice, quadriplegia, cyanosis, and mental disorientation [8-10]. Furthermore, MB is a high-demand material in the textile industry, which is utilized in silk and cotton painting [11]. Therefore, the removal of MB from wastewater using cost-effective adsorbents is a key environmental concern. For the removal of dyes, several techniques such as membrane filtration [12], biosorption [13], adsorption [14], and photocatalytic processes [15] are frequently used. Among the techniques mentioned, the adsorption method is considered as the most outstanding technique since it is the simplest, cheapest, and most successful technique for generating high-quality dye effluents. Agricultural bio-sorbents such as [16], weeping willow [17], and mango leaf powder [18], as well as industrial wastes such as red mud [19] and fly ash [20], have recently been used as non-conventional adsorbents.

There is yet to be any research on the use of rubber waste obtained from DTC in the rubber industry as a polymeric adsorbent for adsorption and reusability. Therefore, the focus of this research paper was on the MB dye adsorption experiments and the reusability of rubber waste as polymeric adsorbents. The rubber waste was functionalized via a sulfonation process with concentrated sulfuric acid. All available characterizations were employed to analyze the functionality, morphology, elemental composition, and textual properties of the polymeric material before and after modification. In addition, the influence of adsorbent dose, solution pH, initial MB concentration, and contact time on MB adsorption were investigated. Furthermore, to analyze the adsorption equilibrium and evaluate the adsorption mechanism, adsorption data were fitted with different isotherms (Langmuir and Freundlich isotherm models) as well as kinetic models (pseudo-first and pseudo-second-order kinetic models). Afterwards, the reusability of the adsorbent was investigated using several types of desorbing solutions (0.1 M NaOH, 0.1 M HCl, and distilled water).

■ EXPERIMENTAL SECTION

Materials

The rubber waste (RW) used in this study was obtained from the dipping tank coagulum (DTC), collected from a glove manufacturing factory in Selangor, Malaysia. The chemicals used in this study include H₂SO₄ (98% purity Merck, Germany), NaOH (99% purity Merck, Germany), C₁₆H₁₈N₃SCl (95% purity Sigma Aldrich, China), and CH₃OH (99% purity Sigma Aldrich, China). All reagents were of analytical grade and applied without any further purification. Deionized and distilled water were produced from the Millipore Alpha Q system and distiller, respectively. Aqueous solutions were prepared with distilled water.

Instrumentation

Field Emission Scanning Electron Microscopy (FESEM) was used to analyze the microstructure and morphology of materials (FEI NOVA SEM 230). Energy-dispersive X-ray spectroscopy was used to determine the elemental composition of the samples (EDX). Fourier transform infrared (FTIR) spectroscopy was performed (IRTracer-100) with a Shimadzu model spectrophotometer to identify the functional groups of the polymeric materials. The spectra were examined in the 4000–400 cm⁻¹ wavenumber region. Polymeric materials' surface area and pore characteristics were investigated using the Brunauer-Emmett-Teller (BET) methodology for N₂ adsorption/desorption (Micromeritics ASAP2020).

Procedure

Modification of rubber waste

The collected rubber waste (RW) was masticated into fine particles with a mortar and pestle and sieved through a 150-mesh sieve and washed three times with distilled water to dissolve the water-soluble impurities and surface adhered particles. The solid particles were then dried in an oven at 50 °C for 5 h to remove moisture and volatile undesirable substances and later cooled to room temperature. The RW was then suspended in 50 mL

of methanol to eliminate any organic residue on the solid material's surface and oven-dried at 50 °C overnight to ensure there was no moisture on the sample. Next, 15 g of the RW was modified by suspending it in 30 mL of 75% sulfuric acid for 20 min. Then, the sulfonated rubber waste (SRW) was filtered, rinsed with excess distilled water, and neutralized with 40 mL of 5 M sodium hydroxide solution. Finally, the SRW was rinsed with deionized water until the wash water reached neutral pH before being oven-dried at 75 °C for 10 h. The modification of rubber waste via sulfonation reaction is depicted in Fig. 1.

Point of zero charges (pH_{PZC})

The pH_{PZC} of polymeric materials was determined using the pH drift method [21]. For this experiment, 40 mL of 0.1 M NaCl salt solution was placed in ten separate 50 mL beakers. The pH of the solution was adjusted to pH 2–12 using 0.1 M HCl and 0.1 M NaOH solutions. 0.1 g of polymeric materials were then added into the solution and the mixtures were stirred for 24 h. A calibrated pH meter was used to measure both the initial (pH_i) and the final pH values (pH_f). The difference in pH between the initial and final values ($pH_i - pH_f$) was plotted as a function of pH_i . pH_{PZC} is the intersection of the drawn curve with the horizontal axis.

Preparation of methylene blue stock solution and construction of calibration curve

The preparation of the methylene blue (MB) stock solution and construction of the calibration curve were conducted using the dilution series method and UV-visible spectroscopy measurements described by Temel et al. at a maximum wavelength (λ_{max}) of 664 nm, respectively [7]. In summary, the stock solution was made by dissolving 100 mg of MB in 1000 mL of distilled water. The solution for the adsorption studies was made by diluting the MB with distilled water to the desired

concentration. The chemical calibration standard is constructed to determine the accuracy and precision of the UV-visible spectroscopy measurements based on the measurement of an unknown sample. In order to make a calibration curve for the instrument, a blank and five standards diluted from the stock solution were prepared. The MB standard solutions were prepared with different concentrations of 5, 10, 15, 20, and 25 mg/L. The absorbance value was recorded at their respective λ_{max} and was plotted against the concentration which gave a linear calibration curve with correlation coefficients (R^2) ranging from 0.999 to 1.0000.

Adsorption experiment

Adsorption studies were carried out in a batch experiment to determine the best conditions for removal processes; contact time, adsorbent dose, solution pH, and initial concentration of MB. In order to determine the adsorption equilibrium time, adsorption experiments were performed on exactly 120 mL of methylene blue solution (15 mg/L) with the dose of 30 mg in a 250 mL conical flask under 25 °C for 300 min. The conical flask was shaken by a shaker (PROTECH, Malaysia) at 150 rpm. To investigate the influence of pH on adsorption, the pH of 120 mL of MB solution (15 mg/L) was adjusted with 0.1 M HCl or 0.1 M NaOH solution to obtain solutions with pH ranging from 3 to 11, and then a 30 mg adsorbent dosage was added into the solution. To determine the effect of adsorbent dose on the MB adsorption rate, various experiments were run at optimum pH (pH 7) and adsorption equilibrium of 300 min with varied doses of adsorbent (10–50 mg). An experiment to determine the influence of initial MB concentrations solutions (5–25 mg/L) was performed using 30 mg adsorbent at pH 7 and adsorption equilibrium time of 300 min.

The final solution was filtered with Whatman filter



Fig 1. The sulfonation reaction of the rubber waste

paper and the residual concentration of the MB was measured using a UV-vis Spectrophotometer (PerkinElmer Lambda 35) at $\lambda_{\max} = 664$ nm. All experiments were carried out in triplicate, and the mean and standard deviation of the results were used to make further calculations.

The adsorption capacity (Q_e) was estimated using Eq. (1), and the removal percentage was computed using Eq. (2), as shown below.

$$Q_e = \frac{(C_o - C_e) \times V}{m} \quad (1)$$

$$\text{Removal (\%)} = \frac{C_o - C_e}{C_o} \times 100 \quad (2)$$

where, C_e (mg/L) is the MB concentration in an aqueous solution at equilibrium and C_o (mg/L) is the initial MB concentration in an aqueous solution. Q_e (mg/g) is the actual amount of MB adsorbed per gram SRW at equilibrium, V (L) is the volume of MB solution, and m (g) is the weight of SRW.

Regeneration and reusability experiment

Adsorption of MB on 30 mg of SRW was performed

in 120 mL of 15 mg/L of MB dye solution fixed at pH 7 at a temperature of 25 °C for reusability analysis. After the adsorption process, the used adsorbent was dried overnight at a temperature of 25 °C. After that, the adsorbent was immersed in various solutions (0.1 M NaOH, 0.1 M HCl, and distilled water) and shaken for 2 h. The SRW was then dried at room temperature (25 °C) overnight. The adsorption and washing processes were conducted four times. The experiments were carried out in triplicate, and the mean and standard deviations were reported.

RESULTS AND DISCUSSION

Characterization of Polymeric Adsorbent

The FTIR spectrum was used to validate the existence of various functional groups in the polymeric materials with a distinct adsorption band. Fig. 2(a-c) show the IR spectrum of RW, SRW, and SRW after MB adsorption, respectively. The IR spectrum of RW (Fig. 2(a)) show a strong spectral band detected at 3314.14 cm^{-1} which was due to O-H stretching vibration.

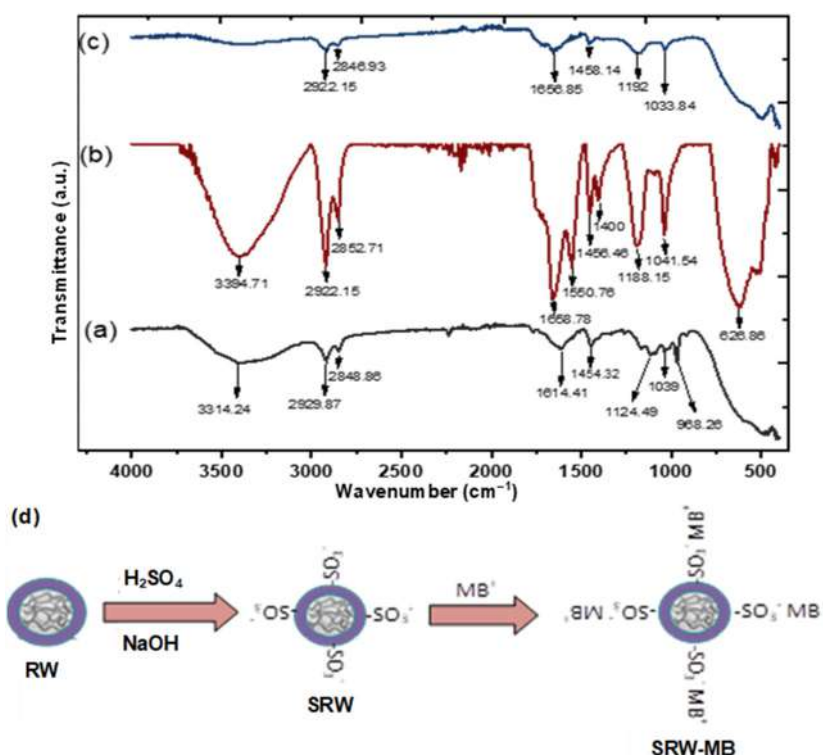


Fig 2. (a) FTIR of RW (b) SRW (c) SRW-after adsorption and (d) the mechanism of the sulfonate group during the adsorption process

Intense spectral bands observed at 2929.87 and 2848.87 cm^{-1} were attributed to C–H stretching vibration, while peaks at 1614.41 and 1454.22 cm^{-1} were assigned to the C=C stretching vibration for alkene and aromatic, respectively. The peak at 1124.49 cm^{-1} was caused by C–O stretching vibration. The intense spectra band observed at 1039.63 cm^{-1} corresponded to the stretching vibration of sulfoxide S=O, while the spectra band observed at 966.26 cm^{-1} corresponded to the bending vibration of C=C alkene (disubstituted trans). The FTIR spectrum of SRW, depicted in Fig. 2(b), showed multiple intense peaks with several new peaks and a minor transition compared to the FTIR spectrum of RW. The presence of sulfonate groups ($-\text{SO}_3^-$) in the recent spectrum peak at 1400 cm^{-1} indicates that the sulfonate group was added during the sulfonation reaction. The FTIR spectrum of SRW after MB adsorption (Fig. 2(c)) did not show the peak of 1400 cm^{-1} . The results imply that the $-\text{SO}_3^-$ functional group plays an important role in the adsorption process. Fig. 2(d) depicts the mechanism of the sulfonate group during the adsorption process.

The point of zero charge pH (pH_{PZC}) of polymeric adsorbents was used to determine the variation in the magnitude of the surface charge caused by various functional groups present on the surface of the polymeric adsorbents [21]. As revealed in Fig. 3, the pH_{PZC} values for RW and SRW were 8.78 and 2.62, respectively. The pH_{PZC}

of SRW was higher than the neutral pH point, indicating that the SRW surface was negatively charged due to the presence of a sulfonate group, resulting in preferred cation adsorption [22]. On the other hand, the surface of RW was positively charged due to $\text{pH}_{\text{PZC}} < \text{pH}$ and protonated by abundant H^+ ions.

The surface morphology and particle size distribution of polymeric materials were characterized by field emission scanning electron microscopy (FESEM). The FESEM images revealed in Fig. 4(a) and (b), show that the RW and SRW materials were comprised from particles of spherical and irregular shapes. Fig. 4(a) depicts the average size distribution of

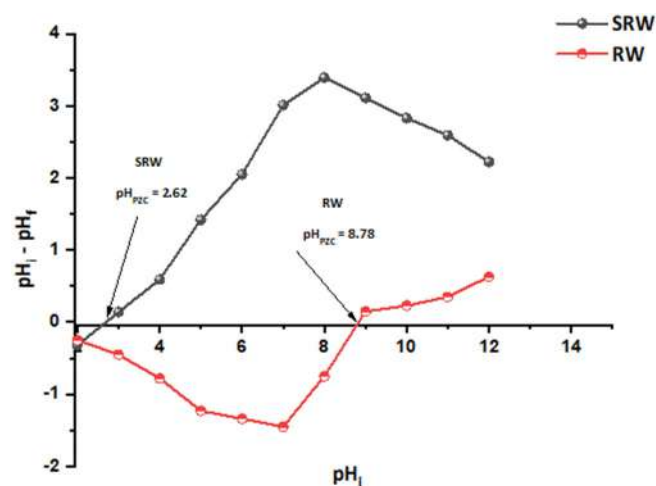


Fig 3. pH of point of zero charges of RW and SRW

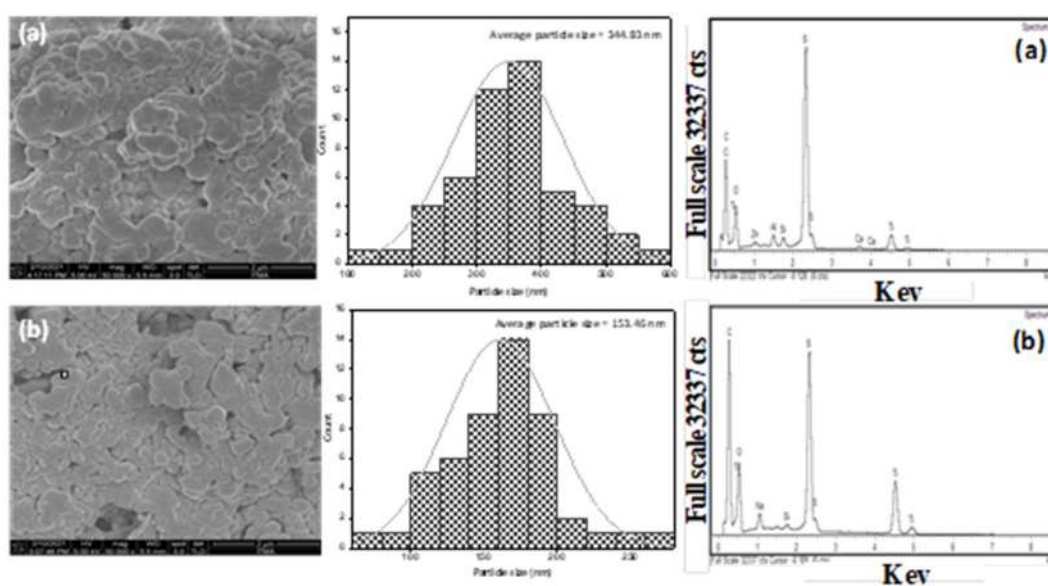


Fig 4. FESEM images and EDX of (a) RW and (b) SRW

RW (344.83 ± 82.61 nm), which was considerably larger than the particle size of SRW (153.46 ± 33.20 nm) as shown in Fig. 4(b). This might be because the RW material had been modified and undesirable elements had been removed.

The EDX spectrum of polymeric materials is depicted in Fig. 4(a) and (b). As shown in Fig. 4(a), the rubber waste (RW) contains a variety of elements, including carbon (C), oxygen (O), silicon (Si), sulfur (S), calcium (Ca), zinc (Zn), aluminum (Al), and titanium (Ti). The major constituents of RW were C, S, and O, while the remaining elements may be the product additives, as seen in Table 1. The EDX spectrum of SRW is displayed in Fig. 4(b), and the presence of C, O, S, Si, Ti and Na, as well as the percentage composition of the elements are shown in Table 1. The oxygen percentage composition increased, which might be attributed to sulfonation. Some of the elements in RW were not detected in SRW or decreased in percentage, which might be due to leaching during the acid treatment process [23]. The presence of sodium in SRW was attributed to the neutralization process after the acid treatment of RW. Furthermore, the percentage of sulfur ingredients in SRW had dropped. This could be attributed to the increased oxygen content of the RW material.

The Brunauer-Emmett-Teller (BET) surface area, total pore volume, and average pore size of RW and SRW that were determined by nitrogen adsorption-desorption are shown in Table 2. According to IUPAC, RW and SRW have a narrow pore distribution with an average pore size of 6.96 and 9.39 nm respectively and are considered as mesoporous materials. Both polymeric materials have a considerably high surface area compared to garlic peel (4.23 m²/g) [24] and Litchi peel biomass (3.73 m²/g) [25].

Adsorption Studies

A preliminary experiment was carried out for the adsorption of MB over unmodified rubber waste, and it was discovered that just 2.02% of the MB was removed. However, SRW demonstrated that MB was removed at more than 99.5%, due to the presence of a sulfonate group on the surface of SRW. Therefore, the following variables affecting the adsorption process were investigated:

Effect of contact time

The contact time is one of the most important elements that influence the removal percentage, adsorption capacity, and the time required to reach equilibrium [26]. A series of experiments were carried out

Table 1. Elemental compositions of RW and SRW

Element composition	Symbol	RW	SRW
		Atomic %	Atomic %
Carbon	C	70.43	69.72
Oxygen	O	17.18	20.24
Aluminum	Al	0.46	-
Silicon	Si	0.36	0.13
Sulphur	S	9.88	5.96
Calcium	Ca	0.15	-
Titanium	Ti	1.4	3.3
Zinc	Zn	1.14	-
Sodium	Na	-	0.66
Total		100	100

Table 2. The results of the BET analysis

Feature	RW	SRW
BET surface area (m ² /g)	7.87	5.94
Total pore volume (cm ³ /g)	0.01371	0.01398
Average Pore size (nm)	6.96	9.39

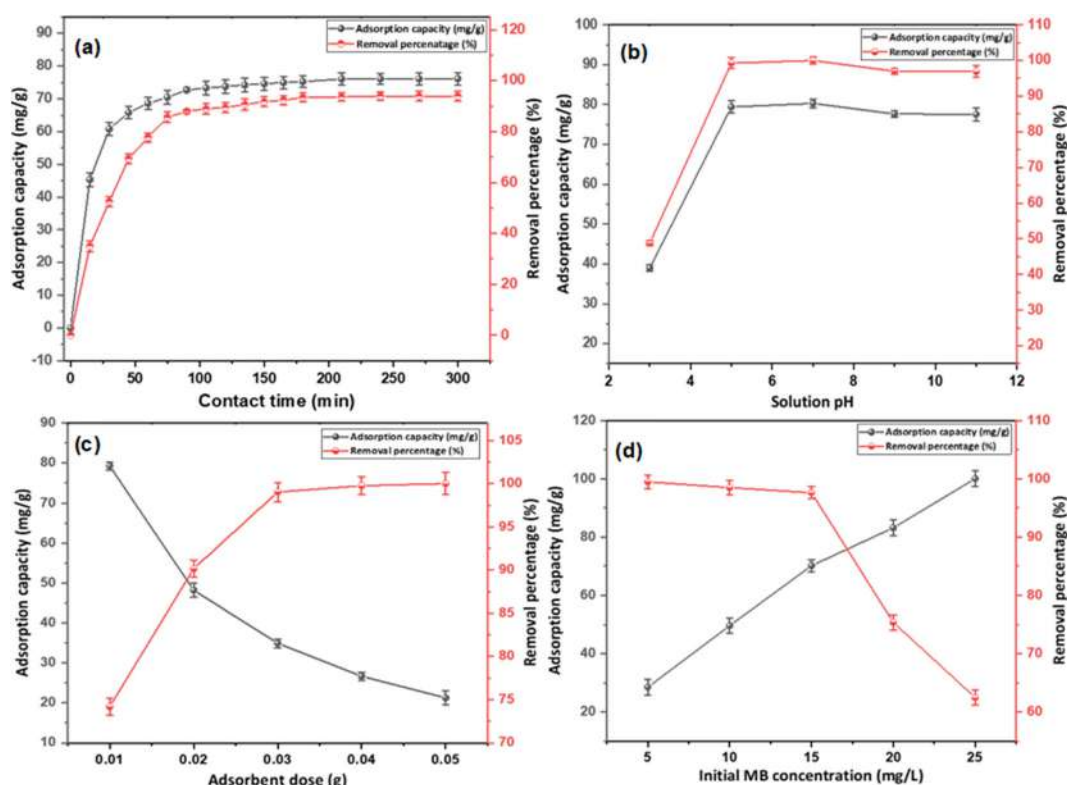


Fig 5. Effect of (a) contact time (b) solution pH (c) adsorbent dose and (d) initial concentration on adsorption of MB onto SRW

to evaluate the effect of contact time. As shown in Fig. 5(a), the adsorption capacity (Q_e) and removal percentage (%) are directly proportional to the adsorption time. As the adsorption time increased from 15 to 240 min, the adsorption capacity increased relatively rapidly from 45.33 to 76.08 mg/g, which could be due to the higher amount of active sites on SRW's surface that are vacant and available to interact with MB in the solution. However, within 300 min of the experiment, the vacant active sites on the surface of SRW was almost saturated or occupied, indicating that there is no increasing trend in adsorption capacity, and it becomes nearly constant. Therefore, the optimum adsorption equilibrium time of 300 min was chosen to be used throughout the adsorption experiments.

Effect of solution pH

The pH of a solution is an important parameter that affects the adsorption of adsorbate [2]. Fig. 5(b) illustrates the adsorption capacity and removal percentage of MB onto SRW (adsorbent) at various pH values under

experimental conditions. The adsorption capacity of SRW increased from 39 mg/g to 80.3 mg/g when the pH was increased from 3 to 7. Then, the adsorption capacity slightly decreased from 77.65 mg/g to 77.55 mg/g as the pH rose from 9 to 11. Therefore, the adsorption mechanism could be electrostatic interaction between positively charged MB and negatively charged functional groups on the SRW surface. Thus, the adsorption process prefers basic/neutral media. We observed a low adsorption capacity in alkaline solution, which could be attributed to the large concentration of hydroxyl groups in the solution, which can compete with MB to attach to the adsorbent during the adsorption process. Ultimately, pH 7 was selected as the optimal solution pH for the adsorption studies.

Adsorbent dose effect

Fig. 5(c) depicts the trend of the MB adsorptive capacity with adsorbent dosage. As shown in Fig. 5(c), the adsorption capacity of SRW decreased from 79.3 mg/g to 21.29 mg/g as the adsorbent dose increased

from 0.01 to 0.05 g. An excess of adsorbent in the solution may promote agglomeration, decreasing the adsorption capacity since active adsorption sites are not completely occupied [14]. On the other hand, as the adsorbent dose was raised from 0.01 to 0.03 g, the removal percentage increased significantly from 74.18 to 99.03%, which could be attributed to the presence of more active sites on the adsorbent's surface that can capture the MB in the solution. Furthermore, as the dose of adsorbent material increased from 0.04 to 0.05 mg, the removal percentage of MB did not significantly increase, the removal percentage of MB did not significantly increase, which was due to the presence of fewer MB molecules in the solution. Finally, 30 mg of SRW was chosen to be the optimal adsorbent dosage for the adsorption experiments.

Effect of initial MB concentration

As illustrated in Fig. 5(d), the adsorption capacity increased from 28.5 mg/g to 100.05 mg/g as the initial MB concentration increased from 5 mg/L to 25 mg/L because high concentrations of MB in a solution leads to a greater adsorption driving force. On the other hand, As the concentration of MB increased, the removal efficiency of MB began to decline. This could be due to the number of accessible adsorption sites at a given dose of SRW was inadequate to adsorb a large number of MB molecules. Nonetheless, the higher removal percentage in diluted solutions could be attributed to the presence of enough active sites on the adsorbent's surface to accommodate a smaller number of MB molecules [19].

Kinetic Adsorption

To understand more about the adsorption process,

the pseudo-first-order and pseudo-second-order reaction kinetic models were used to investigate the adsorption mechanisms of MB on SRW, as shown in Eq. (3) and (4).

$$\log(Q_e - Q_t) = \log Q_e - \frac{k_1}{2.303} t \quad (3)$$

$$\frac{t}{Q_t} = \frac{1}{Q_e} t + \frac{1}{k_2 Q_e^2} \quad (4)$$

where t (min) was the adsorption time, Q_e and Q_t (mg/g) were the adsorption capacity by SRW at equilibrium and time, respectively. And k_1 (1/min), and k_2 (g/(mg min)) were the pseudo-first-order and pseudo-second-order rate constants, respectively.

The kinetics of MB adsorption on SRW are depicted in Fig. 6(a) and (b). In addition, the experimental ($Q_{e, \text{exp}}$) and calculated ($Q_{e, \text{cal}}$) value of the adsorption capacity, adsorption kinetics parameters, and correlation coefficient are displayed in Table 3. As revealed, the correlation coefficient (R^2) for the pseudo-second-order model is higher than that pseudo-first-order one. The calculated adsorption capacity ($Q_{e, \text{cal}}$) obtained from pseudo-second-order is 78.78 mg/g which is close to the experimental adsorption capacity ($Q_{e, \text{exp}}$) of 77.21 mg/g. This indicates that the kinetics of MB adsorption by SRW is highly fitted with the pseudo-second-order of kinetics model.

Adsorption Isotherm

Adsorption isotherms describe the distribution of adsorbate molecules in the liquid phases at different equilibrium concentrations [10]. Finding an appropriate model that fits the adsorption data well yields important

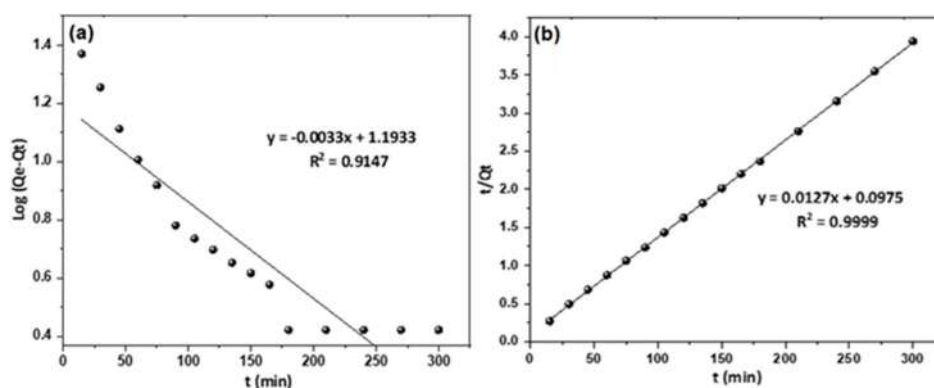


Fig 6. Adsorption kinetics; (a) Pseudo-first and (b) second-order kinetics

Table 3. Kinetic adsorption model parameters of adsorption MB onto SRW

$Q_{e, \text{exp}}$ (mg/g)	Pseudo-first order			Pseudo-second order		
	K_1 (min ⁻¹)	$Q_{e, \text{cal}}$ (mg/g)	R^2	K_2 (g/(mg min))	$Q_{e, \text{cal}}$ (mg/g)	R^2
77.21	0.0075	3.29	0.9147	0.0016	78.74	0.9999

insights into the adsorption process, such as how the interaction between adsorbent and adsorbate occurs. Langmuir [27] and Freundlich [10] are the most widely used adsorption models. These two models were used in their linear forms, as seen in Eq. (5) and (6):

$$\frac{C_e}{Q_e} = \frac{1}{Q_{\text{max}} K_L} + \frac{C_e}{Q_{\text{max}}} \tag{5}$$

$$\log Q_e = \log K_F + \frac{1}{n} \log C_e \tag{6}$$

where C_e (mg/L) is the equilibrium concentration of MB, Q_e (mg/g) is the amount of MB adsorbed per gram of adsorbent (SRW) under equilibrium, Q_{max} (mg/g) is the theoretical maximum adsorption capacity of SRW for MB, and K_L (L/mg) is a constant that describes the affinity in the Langmuir adsorption process; K_F (mg/g) is the Freundlich empirical constant that represents the SRW's relative adsorption capacity, and $1/n$ is a constant that represents the intensity of the Freundlich adsorption.

The adsorption equilibrium of MB onto SRW fits the Langmuir and Freundlich isotherms, as illustrated in Fig. 7(a) and (b), and the corresponding isotherm model constants and correlation coefficients (R^2) are reported in Table 4. The Langmuir isotherm model appropriately described the MB adsorption process on SRW due to the higher correlation coefficient ($R^2 = 0.9994$). Furthermore, the theoretical maximum adsorption capacity (Q_{max}) obtained from the Langmuir isotherm model was 119 mg/g, significantly greater than the experimental adsorption capacity. On the other hand, the correlation coefficient (R^2) of the Freundlich isotherm model was 0.9895, indicating that it was not suitable for portraying the adsorption process of MB onto SRW. The results revealed that MB adsorption onto SRW involves monolayer adsorption and that MB adsorption occurs on the energetically homogeneous surface of the SRW.

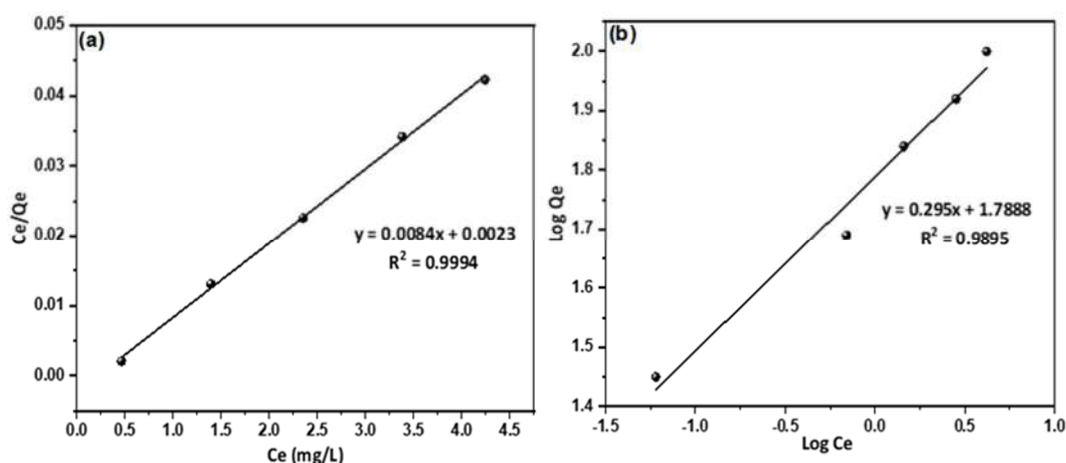


Fig 7. Adsorption isotherm; (a) Langmuir (b) Freundlich isotherms

Table 4. Langmuir and Freundlich isotherm parameter of MB adsorption onto SRW

Dye	Langmuir isotherm			Freundlich isotherm		
	Q_{max} (mg/g)	K_L (L/mg)	R^2	K_F (mg/g)	n	R^2
MB	119	3.65	0.9994	5.98	3.38	0.9895

The additional essential component in the Langmuir isotherm is a dimensionless constant known as the equilibrium parameter, which is as follows:

$$R_L = \frac{1}{1 + K_L C_o} \quad (7)$$

C_o denotes the initial MB concentration. The value of R_L shows whether the isotherm model is reversible ($R_L = 0$), unfavorable ($R_L > 1$), linear ($R_L = 1$), or favorable ($0 < R_L < 1$). We calculated the R_L value and obtained $R_L = 0.1448$, suggesting that the adsorption is favorable.

Comparison of SRW with Other Adsorbent Materials

Waste-based adsorbents have previously been utilized to remove pollutants such as pharmaceuticals, dyes, and heavy metal ions. Similarly, polymeric adsorbent-derived rubber was used in this study to remove methylene blue from an aqueous solution. Table 5 shows the maximum adsorption capacity of SRW (119 mg/g), which is high compared to other adsorbent materials.

Regeneration and Reusability

The reusability and regeneration of adsorbents are essential factors in the decontamination process. We used adsorption steps in the reusability investigation with MB as the model pollutant. The adsorption processes are the same as those described in the experimental section. The adsorbent material was separated after adsorption by filtration with Whatman filter paper. The used adsorbent was taken for future reuse. For desorption, distilled water, 0.1 M HCl, and 0.1 M NaOH were used to desorb MB from SRW. The finding results demonstrated that SRW could be reused up to four times after the desorption process.

As seen in Fig. 8, SRW desorbed with 0.1 M NaOH had a higher removal percentage after four cycles ($90.45 \pm 2.07\%$) compared to 0.1 M HCl ($42.32 \pm 1.58\%$) and distilled water ($12.34 \pm 1.22\%$). The desorption efficiency at basic conditions indicates that an electrostatic interaction exists between the dye molecules and the aqueous solution. The high concentration of H^+ ions in 0.1 M HCl (pH 1~2) destructed the adsorbent structure, resulting in functional group collapse [29]. Therefore, 0.1 M NaOH (pH 11~12) increased the alkalinity of the aqueous solution, separating the adsorbed MB dye molecule that had been adsorbed on the adsorbent, resulting in a high percentage of dye removal.

CONCLUSION

This study showed that using sulfonated rubber waste (SRW) as a polymeric-adsorbent material is a good strategy for producing a promising low-cost adsorbent to

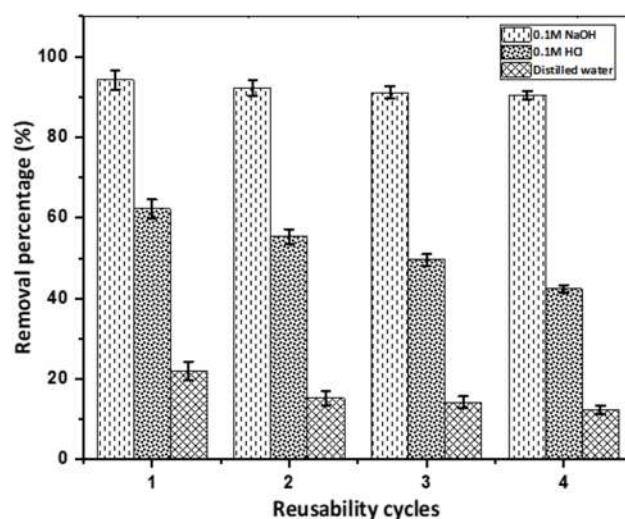


Fig 8. Reusability of SRW in 0.1 M NaOH, 0.1 M HCl, and distilled water

Table 5. Adsorption capacities toward methylene blue by some low-cost adsorbent materials

Adsorbent material	Adsorption capacity (mg/g)	References
R-NBR	60	[28]
Activated carbon	31.14	[2]
Cockle shells-treated banana pith	85.47	[17]
Spent rice biomass (SRB)	8.13	[9]
garlic peel	82.64	[24]
SRW	119	Present study

remove cationic MB dye from aqueous solutions, as well as a novel waste management method. After being modified with concentrated sulfuric acid, the sulfonate groups ($-\text{SO}_3^-$), was successfully added to the surface of SRW using a simple sulfonation method. The FESEM micrographs revealed that RW and SRW are spherical and irregular, with carbon, oxygen, and sulfur components dominating the elemental composition analysis (EDX). RW and SRW are both categorized as mesoporous materials based on their pore size distribution. The pH_{PZC} experiments revealed that RW and SRW have a neutral surface charge at pH 8.78 and 2.62, respectively. The experimental results revealed that SRW was highly dependent on operating parameters such as contact time, solution pH, adsorbent dose, and initial MB concentration. The parameters were optimized, and the data obtained were evaluated using various isotherm models (Langmuir and Freundlich) and kinetics models (pseudo-first and pseudo-second-order). Thus, the results of the adsorption experiments revealed that the Langmuir isotherm model was well fitted, with a maximum adsorption capacity of 119 mg/g and a better agreement with the pseudo-second-order kinetic model. Furthermore, SRW was proven to be highly reusable, with 0.1 M NaOH desorption being the optimal condition for reusability. Finally, SRW can be proposed as a cost-effective polymeric-adsorbent that can be used to treat dye-polluted wastewater.

■ ACKNOWLEDGMENTS

The authors would like to express their deepest gratitude to the management of Universiti Putra Malaysia and the Maikanya Foundation Hadejia for their generous support.

■ AUTHOR CONTRIBUTIONS

Muhammad Aliyu: Writing – review & editing.
Abdul Halim Abdullah: Writing – review & editing.
Mohamed Ibrahim Mohamed Tahir: Software.
Muhammad Aliyu: Methodology, writing – original draft.

■ REFERENCES

- [1] Nuzaimah, M., Sapuan, S.M., Nadlene, R., and Jawaid, M., 2018, Recycling of waste rubber as fillers: A review, *IOP Conf. Ser.: Mater. Sci. Eng.*, 368, 012016.
- [2] Mahapatra, U., Chatterjee, A., Das, C., and Manna, A.K., 2021, Adsorptive removal of hexavalent chromium and methylene blue from simulated solution by activated carbon synthesized from natural rubber industry biosludge, *Environ. Technol. Innovation*, 22, 101427.
- [3] Hirata, Y., Kondo, H., and Ozawa, Y., 2014, "Natural rubber (NR) for the tyre industry" in *Chemistry, Manufacture and Applications of Natural Rubber*, Woodhead Publishing, Cambridge, UK, 325–352.
- [4] Bang-iam, N., Udman, Y., and Masawat, P., 2013, Design and fabrication of artificial neural network-digital image-based colorimeter for protein assay in natural rubber latex and medical latex gloves, *Microchem. J.*, 106, 270–275.
- [5] Mohammadi, M., Man, H.C., Hassan, M.A., and Yee, P.L., 2010, Treatment of wastewater from rubber industry in Malaysia, *Afr. J. Biotechnol.*, 9 (38), 6233–6243.
- [6] Chakraborty, T.K., Islam, M.S., Zaman, S., Kabir, A.H.M.E., and Ghosh, G.C., 2020, Jute (*Corchorus olitorius*) stick charcoal as a low-cost adsorbent for the removal of methylene blue dye from aqueous solution, *SN Appl. Sci.*, 2 (4), 765.
- [7] Temel, F., Turkyilmaz, M., and Kucukcongar, S., 2020, Removal of methylene blue from aqueous solutions by silica gel supported calix[4]arene cage: Investigation of adsorption properties, *Eur. Polym. J.*, 125, 109540.
- [8] Jantawatchai, K., Jitpluem, S., Kerdlap, W., Phanawadee, P., Warakulwit, C., Chisti, Y., and Hansupalak, N., 2017, Production and characterization of a novel hierarchical porous silica adsorbent for removal of methylene blue dye from wastewaters, *Chem. Eng. Commun.*, 204 (12), 1452–1465.
- [9] Saif ur Rehman, M., Kim, I., and Han, J.I., 2012, Adsorption of methylene blue dye from aqueous solution by sugar extracted spent rice biomass, *Carbohydr. Polym.*, 90 (3), 1314–1322.

- [10] Olusegun, S.J., de Sousa Lima, L.F., and Mohallem, N.D.S., 2018, Enhancement of adsorption capacity of clay through spray drying and surface modification process for wastewater treatment, *Chem. Eng. J.*, 334.
- [11] Kubra, K.T., Salman, M.S., and Hasan, M.N., 2021, Enhanced toxic dye removal from wastewater using biodegradable polymeric natural adsorbent, *J. Mol. Liq.*, 328, 115468.
- [12] Huang, X.Y., Bu, H.T., Jiang, G.B., and Zeng, M.H., 2011, Cross-linked succinyl chitosan as an adsorbent for the removal of methylene blue from aqueous solution, *Int. J. Biol. Macromol.*, 49 (4), 643–651.
- [13] Karagöz, S., Tay, T., Ucar, S., and Erdem, M., 2008, Activated carbons from waste biomass by sulfuric acid activation and their use on methylene blue adsorption, *Bioresour. Technol.*, 99 (14), 6214–6222.
- [14] Islam, M.T., Saenz-Arana, R., Hernandez, C., Guinto, T., Ahsan, M.A., Bragg, D.T., Wang, H., Alvarado-Tenorio, B., and Noveron, J.C., 2018, Conversion of waste tire rubber into a high-capacity adsorbent for the removal of methylene blue, methyl orange, and tetracycline from water, *J. Environ. Chem. Eng.*, 6 (2), 3070–3082.
- [15] Du, J.J., Yuan, Y.P., Sun, J.X., Peng, F.M., Jiang, X., Qiu, L.G., Xie, A.J., Shen, Y.H., and Zhu, J.F., 2011, New photocatalysts based on MIL-53 metal-organic frameworks for the decolorization of methylene blue dye, *J. Hazard. Mater.*, 190 (1-3), 945–951.
- [16] Li, X., and Li, Y., 2019, Adsorptive removal of dyes from aqueous solution by KMnO_4 -modified rice husk and rice straw, *J. Chem.*, 2019, 8359491.
- [17] Hasan, R., Ying, W.J., Cheng, C.C., Jaafar, N.F., Jusoh, R., Jalil, A.A., and Setiabudi, H.D., 2020, Methylene blue adsorption onto cockle shells-treated banana pith: Optimization, isotherm, kinetic, and thermodynamic studies, *Indones. J. Chem.*, 20 (2), 368–378.
- [18] Bello, O.S., Adegoke, K.A., Olaniyan, A.A., and Abdulazeez, H., 2015, Dye adsorption using biomass wastes and natural adsorbents: Overview and future prospects, *Desalin. Water Treat.*, 53 (5), 1292–1315.
- [19] Hu, Z.P., Gao, Z.M., Liu, X., and Yuan, Z.Y., 2018, High-surface-area activated red mud for efficient removal of methylene blue from wastewater, *Adsorpt. Sci. Technol.*, 36 (1-2), 62–79.
- [20] Chan, W.H., Mazlee, M.N., Ahmad, Z.A., Ishak, M.A.M., and Shamsul, J.B., 2017, The development of low-cost adsorbents from clay and waste materials: A review, *J. Mater. Cycles Waste Manage.*, 19 (1), 1–14.
- [21] Troca-Torrado, C., Alexandre-Franco, M., Fernández-González, C., Alfaro-Domínguez, M., and Gómez-Serrano, V., 2011, Development of adsorbents from used tire rubber: Their use in the adsorption of organic and inorganic solutes in aqueous solution, *Fuel Process. Technol.*, 92 (2), 206–212.
- [22] Nethaji, S., Sivasamy, A., and Mandal, A.B., 2013, Adsorption isotherms, kinetics and mechanism for the adsorption of cationic and anionic dyes onto carbonaceous particles prepared from *Juglans regia* shell biomass, *Int. J. Environ. Sci. Technol.*, 10 (2), 231–242.
- [23] Ayodele, O.B., 2013, Effect of phosphoric acid treatment on kaolinite supported ferrioxalate catalyst for the degradation of amoxicillin in batch photo-Fenton process, *Appl. Clay Sci.*, 72, 74–83.
- [24] Hameed, B.H., and Ahmad, A.A., 2009, Batch adsorption of methylene blue from aqueous solution by garlic peel, an agricultural waste biomass, *J. Hazard. Mater.*, 164 (2-3), 870–875.
- [25] Foletto, V.S., Ferreira, A.B., da Cruz Severo, E., Collazzo, G.C., Foletto, E. L., and Dotto, G.L., 2017, Iron-based adsorbent prepared from Litchi peel biomass via pyrolysis process for the removal of pharmaceutical pollutant from synthetic aqueous solution, *Environ. Sci. Pollut. Res.*, 24 (11), 10547–10556.
- [26] Jusoh, N.W.C., Choo, T.Y., Masudi, A., and Ali, R.R., 2020, Waste tire carbon adsorbent for active removal of paracetamol in aqueous solution, *J. Phys.: Conf. Ser.*, 1447, 012050.
- [27] Dada, A.O., Olalekan, A.P., Olatunya, A.M., and Dada, O., 2012, Langmuir, Freundlich, Temkin and Dubinin–Radushkevich isotherms studies of equilibrium sorption of Zn^{2+} unto phosphoric acid

- modified rice husk, *IOSR J. Appl. Chem.*, 3 (1), 38–45.
- [28] Polat, K., and Bursalı, E.A., 2019, A promising strategy for the utilization of waste nitrile gloves: Cost-effective adsorbent synthesis, *J. Mater. Cycles Waste Manage.*, 21 (3), 659–665.
- [29] Oladipo, A.C., Tella, A.C., Clayton, H.S., Olayemi, V.T., Akpor, O.B., Dembaremba, T.O., Ogunlaja, A.S., Clarkson, G.J., and Walton, R.I., 2021, A zinc-based coordination polymer as adsorbent for removal of trichlorophenol from aqueous solution: Synthesis, sorption and DFT studies, *J. Mol. Struct.*, 1247, 131274.

Assessment of Multi-Nutrients and Heavy Metals in Inorganic Fertilizers Widely Used by Indonesian Farmers Using NAA

Sri Murniasih^{1,2}, Sri Juari Santosa^{1*}, and Roto Roto¹

¹Department of Chemistry, Faculty of Mathematics and Natural Sciences, Universitas Gadjah Mada, Sekip Utara, Yogyakarta 55281, Indonesia

²Center for Science and Accelerator Technology, The National Nuclear Energy Agency, Jl. Babarsari No. 21, Yogyakarta 55281, Indonesia

* **Corresponding author:**

tel: +62-8164262984

email: sjuari@ugm.ac.id

Received: October 22, 2021

Accepted: January 15, 2022

DOI: 10.22146/ijc.69908

Abstract: This research aims to determine the concentration of multi-nutrients and heavy metals and investigate the correlation among them in the seven inorganic fertilizers in Indonesia. Sample analysis was carried out using the NAA method. The highest concentrations of macro-nutrients were K (36.54 %) and Cl (18.09%) found in the KCl sample, while Ca (23.01%) was observed in the TSP sample. In the case of micro-nutrients, the highest concentrations of Se (0.36 mg/kg), Ti (597 mg/kg), Br (1.84%), and Ni (2.46 mg/kg) detected in the NPK sample. Meanwhile, the highest concentrations of Co (19.57 mg/kg) and Na (1.40%) were measured in the ZA sample, while Mg, with the highest concentration of 1.78%, was found in the KMgS sample. The micro-nutrients with the highest concentration detected in the TSP sample were Cr (45.96 mg/kg), Zn (342.6 mg/kg), and Mn (1331 mg/kg). Non-essential elements such as U, V, La, Sb, Sm, Th, Hf, Sr, Cs, Tb, Sc, Rb, Ta, and Eu were also detected in the fertilizer samples with the highest concentrations in the TSP sample. Statistical tests of multi-nutrient and heavy metals concentrations indicated that multi-nutrient and heavy metals in fertilizers are complex.

Keywords: inorganic fertilizer; multi-nutrients; heavy metals; essential elements; non-essential elements

■ INTRODUCTION

Plants require multi-nutrients to grow and develop properly [1]. The presence of multi-nutrients is naturally available in nature, or they can be added to increase soil fertility. The use of fertilizers as one of the efforts to increase soil fertility is commonly carried out by the community [2]. Thus, natural or synthetic fertilizers are chemical compounds used to provide additional amounts of multi-nutrients to the soil to stimulate the growth of plants [3].

The multi-nutrients needed by plants are categorized into three classes, namely macro, micro and trace elements. Macro-nutrient elements include calcium, phosphorus, sulfur, and chloride, while microelements include iron, copper, cobalt, potassium, magnesium, iodine, zinc, manganese, molybdenum, fluoride,

chromium, selenium, and boron. Macro elements are needed in amounts greater than 1000 mg/kg, and microelements are needed in amounts 10 – <1000 mg/kg, and trace elements are needed in amounts less than 10 mg/kg. Some micro-nutrients can be categorized as heavy metals for plants if their presence exceeds their needs [4-6].

Several micro and trace elements occur naturally in soil. Their presence is caused by the weathering of the parent material [7]. The use of fertilizer is one of the anthropogenic processes that can affect the amount of micro and trace elements in the soil. The high concentration of micro and trace elements causes environmental risks because they are accumulated in soil, plants, animals, and water. Furthermore, they can also reduce soil fertility [8]. A study by Wang et al.

showed that long-term use of organic and inorganic fertilizers caused a significant increase in the concentration of Cu, Zn, Pb, and Cd in the soil [9]. The use of phosphate mineral fertilizers has been proven to increase the content of trace elements in agricultural soil. There was a correlation between the increasing concentration of Cd, U, V, Sb, Cr, As, and Ni with the P concentration. This correlation indicates that these trace elements come from phosphate rocks used as raw material for mineral phosphate fertilizers [10]. The continuous utilization of inorganic fertilizers for 25 years has influenced the accumulation of Pb, Cd, Ni, Co, and Cr elements in agricultural soil [11]. The use of Zn fertilizers for eight years has increased the concentration of Zn in soil and wheat plants grown in this soil [12].

Additionally, the use of phosphate fertilizers for ten years continuously has increased 83.31% of Cd concentration in agricultural soil [13]. Qian et al. reported that synthetic fertilizers affected the concentrations of Fe, Co, Ni, Se, Rh, Eu, Pr, Tl, and Pt in the soil. In contrast, the use of pesticides affected the concentrations of Al, Ni, and Co in rice plants [14]. Extensive, excessive, and continuous use of fertilizers can lead to a more significant accumulation of heavy metals in the soil. Heavy metals originating from fertilizers can stay in the soil for a certain period and can be transferred and accumulated in plants [9,12,15].

Naturally, heavy metals can be found in the earth's crust. However, most cases of environmental heavy metal contamination are caused by anthropogenic activities such as industrial and agricultural activities that use fertilizers [16-17]. The accumulation of heavy metals and metalloids produced from natural and anthropogenic sources has indirectly become a public health problem [12-13]. The heavy metals in the soil that cause this accumulation can be transported and accumulated in the plants that grow on it. This problem increases the potential health and food safety risks and threatens human health safety [18-19]. Accordingly, this study was conducted to determine the concentration of multi-nutrient elements and heavy metals and investigate the correlation and relationship in commercial fertilizers used by farmers in Indonesia.

■ EXPERIMENTAL SECTION

Sample Collection

Seven inorganic fertilizers that are commonly used and commercially available were purchased at a local shop in Brebes District, Central Java–Indonesia, in February 2020. The fertilizer samples consist of NPK 15-15-15, Urea, Kamas (KMgS 30-11-17), Ammonium sulfate (ZA), Trubus (NPK+TE 35-7-8), Potassium chloride (KCl), and Triple superphosphate (TSP). All samples were obtained in small packages (500–1000 g), except for Trubus (NPK+TE 35-7-8) sample that was purchased in 500 mL bottle packages. The collected samples were in the granule form, except for the Trubus sample, liquid form.

Sample Preparation

The granules samples were refined using a Fritsch Pulverisette 5/2 Classic Grinding Planetary ball mill with 200 rpm. Then the sample was sieved to pass 200 mesh [20]. Short and long irradiation samples were weighed to 200 mg using a Sartorius BSA 42245-CW digital scale and inserted into EP 338 polyethylene vials to be later identified [21-22]. One milliliter of the liquid fertilizer sample was taken using an Eppendorf Research 1000 μL micropipette and inserted into EP 338 polyethylene vials and identified.

Sample Analysis

Sample analysis was performed using the Neutron Activation Analysis (NAA) method. Samples were irradiated using the Kartini reactor in the Center for Science and Accelerator Technology–National Nuclear Energy Agency with a thermal neutron flux of $2 \times 10^{11} \text{ n.s}^{-1}.\text{cm}^{-1}$. Elemental concentrations based on short-lived radionuclides, i.e., Cl, V, Mg, Ti, Al, Ca, and Mn, were determined by irradiation for three minutes in a pneumatic facility. In this process, one irradiation capsule contained one sample and was irradiated. After 5 and 15 min decays, the samples were measured for 5 min consecutively. The long-lived isotopes, namely Na, Sc, Cr, Fe, Co, Ni, Zn, As, Se, Rb, Sr, Zn, Sb, Cs, La, Sm, Eu, Tb, Hf, Ta, Th, and U were irradiated at the Lazy Susan facility of the Kartini reactor for 20 h. In this

process, one irradiation capsule consisted of six samples, one standard, one blank vial, and one SRM. Specifically, the irradiation of the Ni element was carried out for 2 h in the Lazy Susan facility and was measured after a cooling time of 2 h. The irradiated samples were wrapped in new plastic clips to avoid contamination of equipment and the addition of other elements to the sample being analyzed. Samples were measured twice after 3 and 15 days. The samples were measured using a gamma spectrometer equipped with an HPGe detector with an efficiency of 35% and Genie 2000 software. The measurements of Na, As, Br, K, Sm, La, and U isotopes were carried out for 20 min, while Sc, Cr, Fe, Co, Se, Rb, Sr, Zn, Sb, Cs, Eu, Tb, Hf, Ta, Th, and Zn isotopes were measured for 2 h. The measurement of the Ni element was conducted for 30 min after samples were irradiated for 2 h and cooled for 2 h. The sample measurement distances from the end-cap detector for short, medium, and long half-lives were 10, 4, and 2 cm, respectively. The distance setting of the sample measurement aims to consider dead time less than 20% [23], 10%, and 5% for short, medium, and long-lived elements, respectively [22].

Analytical Method Validation

The analytical performance of the method was checked by analysis of the certified reference materials NIST SRM 695— Trace Elements in Multi-Nutrient Fertilizer. NIST SRM 695 was chosen to determine the method's precision and accuracy because the reference material contained the certificate value of all analyzed elements. The relative error, expressed as the percentage of the standard deviation of the mean of three determinations [24], was below 10% for all elements. The Relative Standard Deviation (RSD) was given as the percentage deviation from the certified value material [25]. The value of RSD varied between 1 and 10%.

Statistical Analysis

The correlations among multi-nutrients and heavy metals in the fertilizer samples analyzed using NAA were determined using correlation coefficients analysis in the SPSS version 22 for Windows 10. The correlation coefficient values (r), which measured the strength of the linear and inter-relationship between each parameter that

ranged between -1 and $+1$, were determined. A correlation was assumed to be statistically significant at $\rho < 0.05$ and $\rho < 0.01$. In this study, the values of $\rho < 0.05$ and $\rho < 0.01$ indicate a significant and very significant correlation for one to other variables, respectively. The probability of incorrectly rejecting a true null hypothesis (H_0) is almost 23% for $\rho < 0.05$ and 7% for $\rho < 0.01$. Because of better precision, the two-tailed test was conducted assuming that these variables were higher than average mean or lower than average mean [26-28].

RESULTS AND DISCUSSION

Quality control is necessary to ensure the validity of the analysis results. A certified reference material, NIST SRM 695, was employed to validate the analytical method used. The relative errors and relative standard deviations obtained from 3 repetitions of the SRM analysis are shown in Table 1. As shown from the value of the relative error, the Ca, Fe, Mn, Na, Co, and V elements were smaller than 5%, while that of Mg, K, Zn, Al, As, Cr, Cu, Hg, Ni, and Se elements was below 10%. Since the deviation from the certificate value was less than 10% for all elements, the NAA method used in this case had good precision. This finding means that the NAA method can be used for analyzing samples and providing a valid value [24-25]. Furthermore, Table 1 also showed that the experimental values for all tested elements did not significantly differ from the certified values, indicating that the NAA used in this experiment was highly accurate.

The seven inorganic fertilizers widely used by Indonesian farmers were known to contain macro, micro, and trace nutrients and heavy metals (Table 2). The macro-nutrients detected were K, Mg, Ca, and Cl. The concentration of K (36.54%) and Cl (18.09%) was the highest in the KCl sample. The highest concentration of Mg (1.78%) was detected in the KMgS sample, while that of Ca (23.01%) was detected in the TSP sample. High concentrations of macro-nutrients in fertilizers are needed to support plant growth. The average concentration of K, Ca, Mg, and Cl elements necessarily needed for plants are 1, 0.5, 0.2, and 0.01%, respectively [29].

Table 1. Analytical results of the certified reference material, NIST SRM 695 (Trace Elements in Multi-Nutrient Fertilizer) by NAA method

Elements	Certified value	Experimental value	Relative error (%)	RSD (%)
Ca	2.26±0.04%	2.201±0.069%	2.61	3.13
Fe	3.99±0.08%	4.09±0.102%	2.51	2.49
Mg	1.79±0.05%	1.89±0.064%	5.59	3.52
Mn	0.305±0.005%	0.296±0.016%	2.95	5.41
Na	0.405±0.007%	0.389±0.022%	3.95	5.66
K	11.65±0.13%	12.298±0.512%	5.56	4.34
Zn	0.325±0.005%	0.301±0.023%	7.38	7.69
Al	0.61±0.03%	0.579±0.049%	5.08	8.46
As	200±0.2 mg/kg	215±6.12 mg/kg	7.50	2.85
Cr	244±6 mg/kg	227±8.98 mg/kg	6.97	3.96
Co	65.3±2.4 mg/kg	66.4± 1.42 mg/kg	1.68	2.15
Cu	1225±9 mg/kg	1125±43.45 mg/kg	8.16	3.86
Hg	1.955±0.036 mg/kg	2.119±0.119 mg/kg	8.39	5.89
Ni	135±2 mg/kg	124±8.43 mg/kg	8.15	6.80
V	122±3 mg/kg	116±5.93 mg/kg	4.92	5.11
Se	2.1±0.1 mg/kg	2.21±0.19 mg/kg	5.24	8.60

Table 2. Multi-nutrients and heavy metal concentrations in fertilizers widely used in Indonesia

Elements	KMgS ₃₀₋₁₁₋₁₇	KCl	Urea	NPK ₁₅₋₁₅₋₁₅	TSP	ZA	NPK + TE ₃₅₋₇₋₈
Macro (%)							
K	25.53±1.57	36.54±2.41	<0.002	19.126±1.11	0.45±0.03	0.75±0.04	0.39±0.02
Mg	1.78±0.12	<0.003	<0.003	0.34±0.02	0.31±0.02	<0.003	0.09±0.008
Ca	0.31±0.2	<0.0005	<0.0005	2.59±0.19	23.01±1.92	<0.0005	1.00±0.09
Cl	1.62±0.14	18.09±1.21	0.01±0.001	7.42±0.51	<0.001	<0.001	1.39±0.01
Micro-trace (mg/kg)							
Co	0.05±0.004	0.06±0.004	0.02±0.003	1.10±0.09	4.42±0.31	19.57±1.34	0.003±0.005
Ti	<0.1	<0.1	<0.1	596.86±41.37	179.64±18.78	<0.1	226.33±20.34
Br	1934.08±18.74	5050.03±45.27	<0.01	11398.73±251.32	37.21±2.54	37.88±2.27	0.25±0.01
Na	4357.91±23.98	9468.21±98.44	4.06±0.35	3891.75±198.23	1840.69±29.56	14129.73±130.84	2910.61±120.4
Cr	0.57±0.04	0.37±0.033	0.07±0.008	14.85±1.12	45.96±3.2	51.32±3.94	0.30±0.029
Al	106.76±7.92	10.67±1.85	<5	868.16±21.73	7249.74±60.85	<5	526.93±32.48
Fe	101.89±8.24	682.21±45.11	6.76±0.45	1070.41±79.38	7691.44±52.96	47521.57±214.2	136.37±7.12
Zn	1.97±0.14	3.08±0.31	2.53±0.22	257.18±17.37	342.60±38.34	90.25±7.25	4.51±0.35
Mn	<0.1	<0.1	<0.1	332.17±21.82	1331.17±27.92	<0.1	4.71±0.33
Ni	0.03±0.005	0.07±0.009	<0.01	2.46±0.28	0.06±0.009	<0.01	<0.01
Heavy metal (mg/kg)							
As	0.05±0.007	0.08±0.009	<0.01	<0.01	37.48±2.91	2.19±0.18	<0.01
Hg	0.03±0.006	0.03±0.005	0.05±0.007	<0.01	0.17±0.02	<0.01	0.004±0.001
Trace elements non-essential (mg/kg)							
Se	<0.01	<0.01	<0.01	0.36±0.042	0.27±0.03	0.20±0.015	0.02±0.004
U	1.01±0.1	6.16±0.79	<0.01	3.00±0.27	6.92±0.55	<0.01	<0.01
V	<0.01	<0.01	<0.01	16.42±1.91	26.20±2.34	<0.01	<0.01
La	0.06±0.008	0.06±0.009	<0.01	412.82±67.88	15.70±1.37	8.48±0.91	<0.01
Sb	<0.01	<0.01	<0.01	0.34±0.023	5.84±0.48	0.17±0.02	<0.01
Sm	0.01±0.002	<0.01	<0.01	31.022±5.32	3.28±0.41	<0.01	<0.01
Th	0.03±0.002	0.03±0.002	<0.01	7.97±0.68	2.30±0.19	3.78±0.32	0.03±0.004
Hf	0.01±0.002	0.02±0.003	0.01±0.002	0.21±0.019	0.37±0.033	3.02±0.27	<0.01

Table 2. Multi-nutrients and heavy metal concentrations in fertilizers widely used in Indonesia (*Continued*)

Elements	KMgS ₃₀₋₁₁₋₁₇	KCl	Urea	NPK ₁₅₋₁₅₋₁₅	TSP	ZA	NPK + TE ₃₅₋₇₋₈
Sr	60.34±5.54	<0.01	<0.01	2881.01±95.02	274.56±12.43	211.44±11.37	<0.01
Cs	0.02±0.004	0.01±0.005	<0.01	0.12±0.03	<0.01	1.65±0.21	<0.01
Tb	<0.03	<0.03	<0.03	3.92±0.41	0.46±0.05	0.35±0.05	<0.03
Sc	0.03±0.004	0.02±0.003	0.002±0.001	0.07±0.009	1.52±0.11	18.68±1.15	<0.001
Rb	29.42±2.45	139.84±9.87	<0.02	13.87±1.42	15.08±1.67	19.88±2.0	1.25±0.2
Ta	<0.1	<0.1	<0.1	0.23±0.03	0.03±0.009	0.23±0.004	<0.1
Eu	0.003±0.001	0.004±0.001	0.004±0.001	10.19±0.08	0.45±0.041	3.09±0.029	<0.001

The micro-nutrients detected in nearly all fertilizers were Co, Ti, Na, and Br. The highest concentration of Co (19.57 mg/kg) and Na (1.41%) was found in the ZA sample. The highest concentration of Se (0.36 mg/kg), Ti (597 mg/kg), and Br (1.84%) was found in the NPK samples. The titanium element is still not considered an essential micronutrient for plants. The addition of the Ti element has been proven to increase the absorption of several essential elements and improve the activity of several enzymes [30]. Leaf fertilization is the most efficient Ti supply because Ti has low mobility in the soil and deficient absorption. The use of large amounts of Ti has not been proven to impact plants negatively, but plants that have high contents of Ti have been proven to be dangerous for consumption [31]. The concentration of Co and Se in all fertilizer samples was still below the limits allowed by the Canadian standard trace metal safety guidelines, i.e., 150 and 14 mg/kg, respectively [8].

The presence of heavy metals in the soil does not always have a negative impact as long as they are within a specific concentration limit. The elements of Al, Co, Se, Na, and Si were considered functional elements to plants, although plants did not need them. They can support growth and are essential for the metabolism of certain plants, but their support depends on environmental conditions, their concentration, and the type of plant species [19].

The concentration of Hg and As heavy metals and Al, Cr, Fe, Mn, Ni, and Zn varied in the seven tested inorganic fertilizers. Among others, Al and Fe were the most dominant in all examined fertilizers. The highest concentrations of Al and Fe were detected in the TSP fertilizer. There are no safety standards set for Al and Fe in fertilizers.

Iron is an essential micronutrient for plant growth because it is a vital component for photosynthesis and respiration in plants. Iron is not readily available in neutral or alkaline soils. It makes plants become Fe deficient even though Fe is abundant in nature [32]. The addition of Fe through fertilizers is still needed since the requirement of Fe is considerably high for plants [8].

Aluminum is the most abundant metal in the earth's crust, but its availability depends on soil pH. Despite its abundance, Al has not been considered an essential element for plants. In plants and other organisms, Al may be considered either beneficial or toxic depending on its concentration and chemical form and the growing condition and species of the plant. Although there are no established guidelines for Al in fertilizers, Al can be accumulated in plant tissues and become toxic to plants. In plants, the first sign of Al accumulation is the discoloration of the roots, which causes a decrease in root permeability for water and nutrient absorption. In contrast, low concentrations of Al can stimulate plant root growth [33].

The highest concentrations of As, Hg, Cr, Zn, and Mn were found in the TSP fertilizer. Their concentrations were 37.47, 0.17, 45.96, 342.6, and 1331 mg/kg, respectively. The highest concentration of Ni was 2.46 mg/kg and was detected in the NPK fertilizer. Currently, no allowable limit is set as the standard safety guidelines for Mg in fertilizers. In plants, Mn is considered an essential element for growth and reproduction. The requirement of Mn in plants is only in small amounts, but it plays an important role in growth. The use of Mn fertilizers is a way to overcome the shortage of Mn availability. The availability of Mn in soil drastically decreases at high pH value because the soluble Mn

(Mn²⁺) is rapidly converted to insoluble Mn oxide, which is not needed by plants, especially in alkaline sandy soils [29]. In addition, spraying Mn on leaves is only effective for a limited period because Mn moves very little within the plant [31]. On the other hand, Mn toxicity can occur in poor drainage and highly acidic soils [20]. Indicators of Mn toxicity in plants can be observed by decreasing growth rate, chlorosis of the leaves, and the presence of necrotic leaf spots [32].

The detected concentrations of As, Hg, Cr, Zn, and Ni heavy metals in all samples of fertilizers were still below the allowable limits set in the Canadian standard trace metal safety guidelines, which are 75, 5, 1060, 1868, and 180 mg/kg, respectively [34]. In this study, non-essential elements were also detected in the inorganic fertilizers, namely U, V, La, Sb, Sm, Th, Hf, Sr, Cs, Tb, Sc, Rb, Ta, and Eu. The highest content of V was 26.2 mg/kg and was detected in the TSP fertilizer. This value is still below the allowable limit set in the Canadian standard trace metal safety guidelines, 656 mg/kg [34]. The content of U, La, Sb, Sm, Th, Hf, Sr, Cs, Tb, Sc, Rb, Ta, and Eu elements can be closely related to the raw material content of the mineral phosphate fertilizers [7]. It was proven that the content of U, V, La, Sb, Sm, Th, Hf, Sr, Cs, Tb, Sc, Rb, Ta, and Eu elements were dominantly detected in NPK and TSP fertilizers, where both fertilizers include mineral phosphate fertilizers.

The concentration of trace elements and heavy metals in fertilizers was strongly influenced by the main raw material used to make the fertilizers. Phosphorus, nitrogen, and potassium fertilizers contain more trace elements and heavy metals. In this study, fertilizers made from phosphorus, namely TSP with 46% phosphorus composition, contained more trace elements than the NPK fertilizer (15% of P) and NPK+TE fertilizer (7% of P), as shown in Table 2. This result follows the result of Molina et al. in which the concentration of trace elements in phosphorus fertilizer > K fertilizer > N fertilizer [35]. Based on the research by Gambuś and Wieczorek, it was observed that the concentration of phosphorus provided a higher correlation coefficient ($r=0.764$) to Cd, Cr, and Zn than that of N ($r=0.564$) and K ($r=-0.135$) [36]. This was consistent with the current study, where the

concentration of trace elements and heavy metals in the NPK fertilizer (N=15%, P=15% and K=15%) were higher than that in NPK+TE (N=35%, P=7% and K=8%). Nitrogen concentration in the NPK+TE fertilizer was twice higher than that in the NPK fertilizer, but phosphorus concentration in the NPK fertilizer was twice higher than that in the NPK+TE fertilizer.

Table 3 compares this study and other studies related to the concentration of multi-nutrients and heavy metals in fertilizer samples. The concentrations of Cr and Zn in the Indonesian urea fertilizers were not significantly different from those in Brunei Darussalam [8]. Still, they were much lower than those found in China [37], Iran [38], and Nigeria [39]. The concentrations of As, Hg, Cr, Al, Fe, Zn, and Ni in the Indonesian KCl fertilizer were not much different from those found in KCl fertilizers from China [40-41], Chile [35], Iran [38], and Nigeria [39]. The concentrations of Cr, Fe, and Mn elements in the Indonesian NPK fertilizer were similar to those in the Iran NPK fertilizer [38] but lower than those in Brunei Darussalam [8] and Lebanon [42]. The concentrations of Zn and Ca elements in NPK fertilizers in Indonesia were lower than in Lebanon [42]. The concentrations of As, Hg, Fe, and Mn in Indonesian TSP fertilizers were higher than those found in TSP fertilizers in Chile [35,43], Iran [43], Lebanon [42], Europe [10], and Nigeria [39]. The concentration of the Ca element in the Indonesian TSP fertilizer was much lower than that in Lebanon [42] and Europe [10]. Meanwhile, the concentrations of Ni and V elements in the Indonesian TSP fertilizer were much lower than those in Iran [38] and Europe [10]. The concentration of the Co element in the Indonesian TSP fertilizer was lower than that in Chile [35] and Europe [10] but lower than that in Iran [38]. The concentrations of U, K, and Mg in the Indonesian TSP fertilizer were much lower than those in Europe [10]. Meanwhile, the concentrations of Al, Na, and Sb in the Indonesian TSP fertilizer were higher than those in Europe [10]. The concentrations of As, Cr, Zn, and Co in the ZA fertilizer circulated in Indonesia were higher than those in ZA fertilizers found in China [37] and Iran [38]. Overall, the concentrations of Hg, Cr, Zn, and Ni elements in the

Table 3. Concentration of multi-nutrients and heavy metals in inorganic fertilizer samples used Indonesia farmers in comparison with results other studies

element	Urea (mg/kg)					KCl (mg/kg)					NPK ₁₅₋₁₅₋₁₅ (mg/kg)				
	This study	Nigeria [39]	Brunei Darussalam [8]	China [37]	Iran [38]	This study	China [41]	China [40]	Poland [36]	Iran [38]	Chile [35]	This study	Iran [38]	Brunei Darussalam [8]	Lebanon [42]
As	ND	0.0013	NA	0.0106	NA	0.08	NA	0.19060	NA	NA	12.1	ND	NA	NA	NA
Hg	0.05	NA	NA	9E-05	NA	0.03	NA	0.01004	0.011	NA	NA	ND	NA	NA	NA
Cr	0.07	NA	0.04	1.1677	7.6	0.37	NA	0.00	0.29	9.7	82.3	14.85	12.3	23.1	NA
Al	ND	NA	ND	0.0716	NA	10.67	3.83	NA	NA	NA	NA	868.16	NA	2916	NA
Fe	6.76	NA	ND	NA	3846	682.21	500.83	NA	NA	1265	8515	1070.41	1446	1987	1700
Zn	2.53	3.90	1.10	0.0645	51.3	3.08	0.21244	NA	45	1	63.5	257.18	387	NA	541
Mn	ND	NA	0.001	NA	119	ND	5.44	NA	NA	15	142	332.17	371	85.2	NA
Ni	ND	5.87	0.48	0.1886	12.7	0.07	0.06554	0.06554	0.55	7.9	4.9	2.46	8.5	4.5	NA
V	ND	1.53	NA	NA	NA	ND	NA	NA	NA	NA	47	16.42	NA	NA	NA
Co	0.02	NA	ND	NA	1.5	0.06	0.01312	NA	NA	7.2	2.8	1.10	5.2	7.3	NA
Mg	ND	NA	NA	NA	NA	ND	50.51	NA	NA	NA	NA	0.34	NA	NA	NA
Ca	ND	NA	NA	NA	NA	ND	1309.48	NA	NA	NA	NA	2.59	NA	NA	9200
Se	ND	NA	NA	NA	NA	ND	0.02325	NA	NA	NA	NA	0.36	NA	NA	NA
Na	9468.21	NA	NA	NA	NA	4357.91	25095.89	NA	NA	NA	NA	4.06	NA	NA	NA
Sb	ND	NA	NA	NA	NA	ND	NA	0.00297	NA	NA	NA	0.34	NA	NA	NA
Ti	ND	NA	NA	0.0054	NA	ND	NA	NA	NA	NA	NA	596.86	NA	NA	NA
K	ND	NA	NA	NA	NA	365400	NA	NA	NA	NA	NA	191260	NA	NA	NA
U	ND	NA	NA	NA	NA	6.16	NA	NA	NA	NA	NA	3	NA	NA	NA

elements	This study	TSP (mg/kg)					ZA (mg/kg)			KMgS ₃₀₋₁₁₋₁₇ (mg/kg)		NPK+TE ₃₅₋₇₋₈ (mg/kg)	
		Chile [35,43]	Nigeria [39]	Iran [38]	Lebanon [42]	Europe [10]	This study	China [37]	Iran [38]	This study	Poland [36]	This study	Poland [36]
As	37.48	17.9	0.0012	NA	NA	5.5	2.19	0.04254	NA	0.05	NA	ND	NA
Hg	0.17	NA	NA	NA	NA	NA	ND	0.0272	NA	0.03	0.446	0.0037	0.023
Cr	45.96	633	NA	110	NA	70	51.32	2.53927	13.4	0.57	475.4	0.30	0.35
Al	7249.74	NA	NA	NA	NA	1591	ND	1.34513	NA	106.76	NA	526.93	NA
Fe	7691.44	6003	NA	3092	1400	2321	47521.57	NA	926	101.89	NA	136.37	NA
Zn	342.60	600	15.91	178	239	251	90.25	0.27079	2.2	1.97	600	4.51	26
Mn	1331.17	67.7	NA	316	NA	227	ND	NA	13	ND	NA	4.71	NA
Ni	0.06	10.6	5.26	29.7	NA	16	ND	0.28726	7.7	0.03	460	ND	0.78
V	26.20	430	1.92	NA	NA	62	ND	NA	NA	ND	NA	ND	NA
Co	4.42	2.5	NA	7.4	NA	1.3	19.57	NA	3.1	0.05	NA	0.00	NA
Mg	0.31	NA	NA	NA	NA	7100	ND	NA	NA	1.78	NA	0.09	NA
Ca	23.01	NA	NA	NA	149300	57000	ND	NA	NA	0.31	NA	1.00	NA
Se	0.27	NA	NA	NA	NA	NA	0.20	NA	NA	ND	NA	0.02	NA
Na	6891.75	NA	NA	NA	NA	3800	1840.69	NA	NA	ND	NA	14129.73	NA
Sb	5.84	NA	NA	NA	NA	0.52	0.17	NA	NA	ND	NA	ND	NA
Ti	179.64	NA	NA	NA	NA	NA	ND	0.03512	NA	ND	NA	226.33	NA
K	4500	NA	NA	NA	NA	92000	7500	NA	NA	255300	NA	3900	NA
U	6.92	NA	NA	NA	NA	41	ND	NA	NA	1.01	NA	ND	NA

ND: no detected; NA: not available

Indonesian KMgS and NPK+TE fertilizers were much lower than those found in similar fertilizers distributed in Poland [36].

The correlation between multi-nutrients and heavy metals was tested using a correlation coefficient matrix. The correlation of two elements with a high positive or negative correlation coefficient (r close to +1 or -1)

indicates that these elements were bound to each other in a fertilizer. This correlation means that the change of concentration of one element will be accompanied by the change of concentration of the second element proportionally [8].

According to Table 4, the correlation coefficient matrix for elements in the urea fertilizer sample with a

confidence level value of less than 0.05 ($\rho < 0.05$) was $r = 0.816$ for Hg-Cl and $r = 0.792$ for Hf-Cr. Both had a significant positive correlation, while Na-Cl had a significant negative correlation $r = -0.835$. In the confidence level $\rho < 0.01$, Co-Cr and Co-Hf had a very significant positive correlation of 0.939 and 0.882, respectively, while Eu-Sc had a very significant negative correlation $r = -0.979$. This indication shows that Co, Cr, and Hf in urea fertilizer samples have a positive correlation, where Co affects the presence of Cr and Hf. Meanwhile, the presence of Cl was positively correlated with Hg, but it was negatively correlated to Na.

Almost all elements of multi-nutrients and heavy metals in the ZA fertilizer sample did not provide significant correlation coefficients, except Th-Hg and Sc-

Na. A perfect positive correlation ($r = 1.000$) with $\rho < 0.01$ was found for Th-Hg, while Sc-Na had a positive correlation coefficient ($r = 0.755$) with $\rho < 0.05$, as shown in Table 5.

The correlation coefficients of elements in NPK 35-7-8 fertilizers are given in Table 6 in which some of them show significant value with confidence level $\rho < 0.05$. Elements with $\rho < 0.05$ that have positive correlation coefficients were Na-Cl ($r = 0.873$), La-Na ($r = 0.763$), and Co-Br ($r = 0.803$), while those with negative correlation coefficients were Th-Mg ($r = -0.779$), Th-Ca ($r = -0.821$), Rb-Se ($r = -0.761$), Rb-Hg ($r = -0.780$), Fe-Cl ($r = -0.798$), Fe-Mn ($r = -0.831$), and Fe-Na ($r = -0.765$). The positive significant correlation coefficients with $\rho < 0.05$ were found for elements in the KCl fertilizer (Table 7)

Table 4. Matrix of correlation coefficient among multi-nutrients and heavy metal concentrations in urea sample

elements	Cl	Na	Hg	Cr	Hf	Sc	Fe	Zn	Co	Eu
Cl	1	-0.835*	.816*	0.450	0.615	-0.248	0.266	0.719	0.527	0.221
Na		1	-0.713	-0.190	-0.471	0.102	-0.641	-0.619	-0.318	-0.007
Hg			1	-0.007	0.189	-0.040	0.183	0.346	0.162	0.059
Cr				1	.792*	-0.383	-0.201	0.645	.939**	0.316
Hf					1	-0.143	0.317	0.695	.882**	0.113
Sc						1	0.016	0.140	-0.172	-.979**
Fe							1	0.090	-0.060	-0.065
Zn								1	0.691	-0.229
Co									1	0.114
Eu										1

* Correlation is significant at the 0.05 level (2-tailed)

** Correlation is significant at the 0.01 level (2-tailed)

Table 5. Matrix of correlation coefficient among multi-nutrients and heavy metal concentrations in ZA sample

elements	Na	Hg	Th	Cr	Hf	Sc	Fe	Zn	Co	Eu
Na	1	0.208	0.212	-0.474	0.168	.755*	-0.092	0.421	-0.365	0.085
Hg		1	1.000**	-0.570	0.457	0.083	-0.455	-0.306	0.132	0.165
Th			1	-0.570	0.460	0.081	-0.463	-0.299	0.124	0.170
Cr				1	0.060	-0.279	-0.035	0.179	-0.318	0.070
Hf					1	-0.076	0.011	0.090	0.017	0.328
Sc						1	-0.063	-0.118	-0.597	0.496
Fe							1	-0.087	0.556	-0.158
Zn								1	-0.097	-0.553
Co									1	-0.619
Eu										1

* Correlation is significant at the 0.05 level (2-tailed)

** Correlation is significant at the 0.01 level (2-tailed)

Table 6. Matrix of correlation coefficient among multi-nutrients and heavy metal concentrations in NPK₃₅₋₇₋₈ sample

elements	Ti	Mg	Cl	Al	Mn	Ca	Br	Na	K
Ti	1	-0.053	0.585	0.187	0.297	-0.517	-0.495	0.553	-0.221
Mg		1	-0.287	-0.307	0.312	0.423	0.652	-0.260	-0.443
Cl			1	0.251	0.459	0.018	-0.106	.873*	0.200
Al				1	-0.543	-0.490	0.000	0.147	-0.420
Mn					1	0.627	0.035	0.315	0.502
Ca						1	0.612	-0.066	0.505
Br							1	-0.009	-0.228
Na								1	0.178
K									1
La									
Se									
Hg									
Th									
Rb									
Fe									
Zn									
Co									

elements	La	Se	Hg	Th	Rb	Fe	Zn	Co
Ti	0.564	-0.048	0.155	0.172	-0.193	-0.387	-0.636	-0.534
Mg	0.319	-0.064	0.356	-.779*	0.290	-0.024	0.237	0.293
Cl	0.658	-0.225	-0.506	-0.022	0.310	-.798*	-0.387	-0.082
Al	0.152	-0.215	-0.433	0.546	0.368	0.247	-0.673	-0.125
Mn	0.485	-0.294	-0.121	-0.674	0.221	-.831*	0.076	0.047
Ca	0.155	-0.210	-0.270	-.821*	0.485	-0.478	0.551	0.603
Br	0.333	0.088	-0.051	-0.701	0.522	-0.096	0.485	.803*
Na	.763*	0.274	-0.122	-0.080	-0.043	-.765*	-0.076	0.194
K	-0.056	0.031	-0.244	-0.143	-0.125	-0.516	0.342	0.219
La	1	0.159	0.048	-0.488	0.189	-0.734	-0.106	0.352
Se		1	0.741	-0.033	-.761*	0.059	0.600	0.491
Hg			1	-0.157	-.780*	0.248	0.403	0.104
Th				1	-0.301	0.517	-0.536	-0.606
Rb					1	-0.203	-0.298	0.122
Fe						1	-0.063	-0.245
Zn							1	0.733
Co								1

* Correlation is significant at the 0.05 level (2-tailed)

** Correlation is significant at the 0.01 level (2-tailed)

namely Br-Al ($r=0.792$), La-Na ($r=0.859$), Cr-Th ($r=0.855$), Hf-Al ($r=0.866$), Cs-Al ($r=0.812$), Cs-Br ($r=0.784$), Rb-Br ($r=0.771$), and Eu-Hf ($r=0.815$). On the other hand, the negative significant correlation coefficients were obtained for Hg-Al ($r=-0.837$), Hg-Na ($r=-0.776$), Sc-Cr ($r=-0.810$), Co-Cr ($r=-0.789$), and Eu-Hg ($r=-0.803$).

There were positive correlation coefficients with $\rho < 0.05$ for elements in the KMgS fertilizer as illustrated in Table 8. Those elements were Br-Sm ($r=0.836$), Na-As ($r=0.783$), K-Mg ($r=0.809$), Sc-Th ($r=0.798$), Fe-Cr ($r=0.768$), Zn-As ($r=0.773$), Zn-Hg ($r=0.761$), Eu-U ($r=0.759$), and Eu-Cs ($r=0.790$), while negative correlation

Table 7. Matrix of correlation coefficient among multi-nutrients and heavy metal concentrations in KCl sample

elements	U	Cl	Al	Sm	Br	As	Na	K	La	Hg	Th
U	1	0.685	0.092	0.404	0.049	0.452	0.352	-0.451	0.462	0.136	0.325
Cl		1	-0.280	-0.072	-0.268	0.472	-0.218	-0.640	-0.061	0.570	0.481
Al			1	-0.293	.792*	-0.268	0.556	-0.278	0.428	-.837*	-0.139
Sm				1	-0.076	0.548	0.137	0.129	0.383	0.208	0.330
Br					1	0.041	0.062	-0.205	0.030	-0.441	0.233
As						1	-0.328	-0.508	-0.031	0.454	0.739
Na							1	0.027	.859*	-.776*	-0.501
K								1	-0.279	-0.048	-0.681
La									1	-0.560	-0.046
Hg										1	0.527
Th											1
Cr											
Hf											
Cs											
Sc											
Rb											
Fe											
Zn											
Co											
Eu											
Ni											

elements	Cr	Hf	Cs	Sc	Rb	Fe	Zn	Co	Eu	Ni
U	0.112	-0.271	-0.071	-0.051	-0.410	-0.512	-0.475	0.019	-0.376	0.039
Cl	0.414	-0.648	-0.539	-0.036	-0.736	-0.236	-0.007	0.023	-0.527	-0.457
Al	0.158	.866*	.812*	-0.623	0.669	-0.329	-0.294	-0.632	0.747	0.405
Sm	-0.161	-0.209	-0.100	0.154	-0.204	0.151	-0.660	0.185	-0.395	0.137
Br	0.453	0.585	.784*	-0.683	.771*	-0.178	-0.618	-0.680	0.576	0.568
As	0.397	-0.418	-0.489	-0.145	-0.484	0.089	-0.687	-0.099	-0.192	-0.156
Na	-0.528	0.603	0.418	0.024	0.148	-0.425	-0.054	0.024	0.308	0.231
K	-0.729	-0.026	0.129	0.702	0.378	-0.113	0.276	0.668	-0.035	0.539
La	-0.194	0.489	0.310	-0.253	-0.075	-0.041	-0.244	-0.241	0.069	-0.114
Hg	0.326	-.948**	-0.668	0.260	-0.596	0.271	0.045	0.293	-.803*	-0.379
Th	.855*	-0.326	-0.172	-0.602	-0.302	0.457	-0.557	-0.563	-0.348	-0.406
Cr	1	-0.087	0.087	-.810*	-0.016	0.389	-0.318	-.789*	-0.083	-0.366
Hf		1	.766*	-0.488	0.706	-0.025	-0.123	-0.527	.815*	0.309
Cs			1	-0.506	.879**	-0.130	-0.265	-0.523	0.469	0.549
Sc				1	-0.311	-0.346	0.389	.997**	-0.313	0.203
Rb					1	-0.110	-0.189	-0.347	0.632	0.705
Fe						1	0.095	-0.375	-0.218	-0.620
Zn							1	0.351	-0.119	-0.406
Co								1	-0.351	0.203
Eu									1	0.418
Ni										1

* Correlation is significant at the 0.05 level (2-tailed)

** Correlation is significant at the 0.01 level (2-tailed)

Table 8. Matrix of correlation coefficient among multi-nutrients and heavy metal concentrations in KMgS₃₀₋₁₁₋₁₇ sample

elements	U	Mg	Cl	Al	Ca	Sm	Br	As	Na	K	La	Hg
U	1	0.320	0.029	-0.534	0.468	0.690	0.375	0.384	-0.035	0.151	-0.129	-0.177
Mg		1	-0.112	-0.704	-0.183	0.423	0.719	-0.053	-0.078	.809*	-0.002	-.805*
Cl			1	0.437	0.709	0.116	0.022	-0.384	-0.169	-0.016	0.490	-0.034
Al				1	0.407	-0.754	-.853*	-0.351	-0.063	-0.386	0.466	0.411
Ca					1	0.134	-0.246	-0.093	-0.236	-0.183	0.530	0.166
Sm						1	.836*	0.295	-0.093	0.008	-0.207	-0.075
Br							1	0.039	-0.106	0.403	-0.312	-0.466
As								1	.783*	-0.295	0.153	0.350
Na									1	-0.042	0.300	0.111
K										1	-0.107	-.993**
La											1	0.170
Hg												1
Th												
Cr												
Hf												
Sr												
Cs												
Sc												
Rb												
Fe												
Zn												
Co												
Eu												
Ni												

elements	Th	Cr	Hf	Sr	Cs	Sc	Rb	Fe	Zn	Co	Eu
U	-0.450	0.057	0.144	0.204	0.502	-0.229	-0.089	-0.169	0.108	-0.389	.759*
Mg	-0.405	0.644	0.193	-0.716	0.410	-0.485	-0.202	0.652	-0.668	-0.191	0.382
Cl	-0.053	-0.264	-0.454	-0.068	-0.324	0.050	0.217	-0.067	-0.150	-0.378	0.006
Al	0.733	-0.177	0.089	0.189	-0.590	0.605	-0.207	-0.018	0.227	0.138	-0.453
Ca	0.139	-0.181	0.039	0.079	-0.268	0.359	-0.112	-0.033	0.128	-0.561	0.186
Sm	-.839*	-0.323	-0.488	-0.056	0.253	-0.418	0.571	-0.280	-0.058	-0.583	0.348
Br	-.874*	0.012	-0.472	-0.351	0.391	-0.696	0.477	0.041	-0.454	-0.344	0.287
As	0.110	-0.196	0.187	0.256	0.005	0.354	-0.012	-0.452	.773*	0.208	0.321
Na	0.358	0.015	0.174	0.189	-0.024	0.305	-0.185	-0.337	0.637	0.630	0.292
K	-0.183	.878**	0.350	-0.453	0.624	-0.595	-0.523	0.650	-0.720	0.222	0.543
La	0.604	0.006	0.202	-0.455	-0.712	0.743	-0.228	0.291	0.191	-0.205	-0.204
Hg	0.282	-.824*	-0.254	0.423	-0.655	0.675	0.440	-0.605	.761*	-0.170	-0.549
Th	1	0.213	0.615	-0.026	-0.494	.798*	-0.614	0.228	0.378	0.407	-0.277
Cr		1	0.737	-0.422	0.498	-0.259	-.829*	.768*	-0.537	0.350	0.430
Hf			1	-0.133	0.194	0.322	-.935**	0.526	0.044	0.319	0.294
Sr				1	0.296	-0.045	0.099	-.832*	0.622	0.356	0.286
Cs					1	-.795*	-0.282	-0.023	-0.286	0.325	.790*
Sc						1	-0.187	-0.016	0.614	-0.064	-0.439
Rb							1	-0.540	0.080	-0.434	-0.411
Fe								1	-0.723	-0.142	-0.107
Zn									1	0.248	0.018
Co										1	0.217
Eu											1
Ni											

* Correlation is significant at the 0.05 level (2-tailed)

** Correlation is significant at the 0.01 level (2-tailed)

Table 9. Matrix of correlation coefficient among multi-nutrients and heavy metal concentrations in NPK₁₅₋₁₅₋₁₅ sample

elements	U	Ti	Mg	V	Cl	Al	Mn	Ca	Sm	Br	Na	K	La	Se	Th	
U	1	.839*	0.595	-.761*	-0.516	0.463	0.035	-0.210	0.292	0.735	-0.312	-0.706	0.414	0.325	-0.221	
Ti		1	0.144	-.765*	-0.644	0.567	0.158	-0.076	0.276	0.365	-0.137	-.888**	0.422	0.593	-0.243	
Mg			1	-0.298	0.128	0.028	0.065	-0.045	0.132	0.641	-0.189	-0.020	0.098	-0.126	-0.003	
V				1	.847*	-.876**	0.378	0.568	-0.366	-0.287	0.101	0.543	-0.626	0.056	0.104	
Cl					1	-.912**	0.442	0.523	-0.068	-0.020	-0.030	0.408	-.768*	0.089	0.212	
Al						1	-0.345	-0.487	-0.007	-0.104	0.307	-0.332	0.677	-0.187	0.059	
Mn							1	.878**	-0.473	-0.054	0.447	-0.286	-0.358	.778*	0.165	
Ca								1	-0.596	-0.281	0.361	0.075	-0.173	0.641	-0.175	
Sm									1	0.443	-0.728	-0.373	-0.185	-0.056	-0.050	
Br										1	-0.629	-0.448	-0.081	0.132	-0.073	
Na											1	0.136	-0.030	0.017	0.543	
K												1	0.013	-0.691	-0.073	
La													1	-0.150	-0.639	
Se														1	-0.179	
Th															1	
Cr																
Hf																
Sr																
Cs																
Tb																
Sc																
Rb																
Fe																
Zn																
Co																
Ta																
Eu																
Sb																
Ni																

elements	Cr	Hf	Sr	Cs	Tb	Sc	Rb	Fe	Zn	Co	Ta	Eu	Sb	Ni
U	0.541	0.085	0.701	0.226	0.427	0.354	0.475	-.774*	-0.024	.946**	.831*	-0.627	-0.245	0.715
Ti	0.292	-0.047	0.670	0.167	0.151	0.357	0.151	-0.600	-0.213	.774*	0.598	-0.716	-0.460	.850*
Mg	0.339	0.346	0.348	0.102	0.667	0.166	0.415	-0.382	0.027	0.677	.843*	0.013	0.196	0.068
V	-0.750	-0.057	-0.606	-0.494	0.068	-0.210	-0.649	0.662	-0.378	-0.589	-0.567	.836*	0.107	-.868*
Cl	-0.753	0.312	-0.284	-0.276	0.332	0.126	-0.558	0.688	-0.418	-0.307	-0.098	.771*	0.089	-.878**
Al	0.733	-0.061	0.168	0.227	-0.409	-0.109	0.509	-0.515	0.375	0.266	0.206	-0.724	0.186	.885**
Mn	-0.652	0.105	-0.247	-.756*	0.269	0.051	-.802*	0.252	-.977**	0.234	0.162	0.366	0.014	-0.031
Ca	-.755*	-0.271	-0.375	-.837*	0.401	-0.314	-.860*	0.228	-.912**	0.070	-0.055	0.689	-0.131	-0.270
Sm	0.130	0.405	.840*	.922**	0.090	.765*	0.402	0.005	0.405	0.184	0.390	-0.504	-0.487	0.003
Br	0.375	0.307	0.611	0.327	0.525	0.546	0.498	-0.482	0.097	0.691	0.666	-0.357	-0.156	0.146
Na	-0.131	0.109	-0.728	-0.632	-0.503	-0.377	-0.421	0.331	-0.342	-0.306	-0.272	0.155	0.671	0.205
K	-0.095	-0.256	-0.613	-0.184	0.007	-0.662	0.004	0.285	0.312	-0.606	-0.493	0.735	0.377	-0.683
La	0.607	-0.689	0.164	0.015	0.140	-0.575	0.454	-.821*	0.297	0.388	0.141	-0.249	-0.195	0.595
Se	-0.531	-0.084	0.252	-0.389	0.297	0.293	-0.637	-0.035	-.856*	0.452	0.251	-0.043	-0.529	0.243
Th	-0.027	.828*	-0.355	-0.011	-0.596	0.405	-0.086	0.604	-0.001	-0.357	-0.078	-0.174	0.747	-0.024
Cr	1	-0.025	0.236	0.412	-0.145	-0.078	.927**	-0.701	0.723	0.322	0.266	-0.633	0.277	0.595
Hf		1	0.155	0.333	-0.201	.759*	0.070	0.483	0.024	-0.009	0.370	-0.270	0.430	-0.067
Sr			1	0.707	0.413	0.636	0.402	-0.426	0.158	0.657	0.699	-0.569	-0.668	0.333
Cs				1	-0.109	0.566	0.650	-0.086	0.715	0.046	0.260	-0.581	-0.278	0.085
Tb					1	-0.016	-0.007	-0.401	-0.321	0.663	0.614	0.373	-0.437	-0.207
Sc						1	0.078	0.229	-0.037	0.251	0.461	-0.522	-0.206	0.081
Rb							1	-0.601	.851*	0.274	0.312	-0.555	0.144	0.340
Fe								1	-0.223	-0.732	-0.446	0.405	0.262	-0.629
Zn									1	-0.242	-0.133	-0.377	0.183	0.042
Co										1	.881**	-0.361	-0.334	0.557
Ta											1	-0.329	-0.161	0.382

Table 9. Matrix of correlation coefficient among multi-nutrients and heavy metal concentrations in NPK₁₅₋₁₅₋₁₅ sample (Continued)

elements	Cr	Hf	Sr	Cs	Tb	Sc	Rb	Fe	Zn	Co	Ta	Eu	Sb	Ni
Eu												1	0.094	-.793*
Sb													1	-0.032
Ni														1

* Correlation is significant at the 0.05 level (2-tailed)

** Correlation is significant at the 0.01 level (2-tailed)

coefficients were detected for Br-Al ($r=-0.853$), Hg-Mg ($r=-0.805$), Th-Sm ($r=-0.839$), Th-Br ($r=-0.874$), Cr-Hg ($r=-0.824$), Sc-Cs ($r=-0.795$), and Rb-Cr ($r=-0.829$). For the confidence level $\rho < 0.01$, a very significant positive correlation coefficient was found for Cr-K ($r=0.878$), while a very significant negative correlation coefficient was found for Hg-K ($r=-0.993$) and Rb-Hf ($r=-0.935$).

According to Table 9, there were positive significant correlation coefficients with $\rho < 0.05$ in the NPK 15-15-15 fertilizer. Those elements were Ti-U ($r=0.839$), Cl-V ($r=0.847$), Se-Mn ($r=0.778$), Hf-Th ($r=0.828$), Sr-Sm ($r=0.840$), Sc-Sm ($r=0.765$), Sc-Hf ($r=0.759$), Zn-Rb ($r=0.851$), Co-Ti ($r=0.774$), Ta-U ($r=0.831$), Ta-Mg ($r=0.843$), Eu-V ($r=0.836$), Eu-Cl ($r=0.771$), Ni-Ti ($r=0.850$), and Ni-Al ($r=0.885$), while negative significant correlation coefficients were found for V-U ($r=-0.761$), V-Ti ($r=-0.765$), La-Cl ($r=-0.768$), Cl-Ca ($r=-0.755$), Cs-Mn ($r=-0.756$), Cs-Ca ($r=-0.837$), Rb-Mn ($r=-0.802$), Rb-Ca ($r=-0.860$), Fe-U ($r=-0.774$), Fe-La ($r=-0.821$), Zn-Se ($r=-0.856$), Ni-V ($r=-0.868$), and Ni-Eu ($r=-0.793$). For the

confidence level $\rho < 0.01$, very significant positive correlation coefficients were found for Ca-Mn ($r=0.847$), Cs-Sm ($r=0.922$), Rb-Cs ($r=0.927$), Co-U ($r=0.946$), and Ni-Al ($r=0.885$), while very significant negative correlation coefficients were detected in Al-V ($r=-0.876$), Al-Cl ($r=-0.912$), K-Ti ($r=-0.888$), Zn-Mn ($r=-0.977$), and Ni-Cl ($r=-0.878$).

In the TSP sample as shown in Table 10, significant positive correlation coefficients with $\rho < 0.05$ were found for V-U ($r=0.805$), As-Ca ($r=0.784$), Na-As ($r=0.788$), Na-Br ($r=0.839$), Hg-Al ($r=0.825$), Hg-Se ($r=0.811$), Th-Ti ($r=0.760$), Cr-Sm ($r=0.861$), Hf-Na ($r=0.841$), Co-As ($r=0.865$), Eu-Al ($r=0.824$), Eu-Sm ($r=0.755$), Eu-Se ($r=0.759$), and Eu-Hg ($r=0.869$), while significant negative correlation coefficients were detected for Al-Mg ($r=-0.847$), Mn-Al ($r=-0.765$), Br-U ($r=-0.813$), Na-U ($r=-0.766$), Cr-Ti ($r=-0.770$), Sr-Se ($r=-0.871$), Sr-Hg ($r=-0.852$), Tb-Se ($r=-0.799$), Sc-Al ($r=-0.866$), Eu-Tb ($r=-0.785$), Ni-Mn ($r=-0.775$), and Ni-Sr ($r=-0.796$). For the confidence level $\rho < 0.01$, there were very significant

Table 10. Matrix of correlation coefficient among multi-nutrients and heavy metal concentrations in TSP sample

elements	U	Ti	Mg	V	Al	Mn	Ca	Sm	Br	As	Na	K	La	Se	Hg
U	1	-0.197	0.160	.805*	0.098	-0.439	-0.287	0.146	-.813*	-0.014	-.766*	0.127	0.312	-0.025	0.272
Ti		1	-0.482	-0.378	0.157	-0.158	0.537	-0.474	-0.224	0.268	0.267	0.129	-0.421	-0.710	-0.353
Mg			1	0.338	-.847*	0.620	-0.347	-0.035	-0.007	0.271	-0.317	-0.438	-0.336	-0.149	-0.567
V				1	-0.064	0.024	-0.370	0.141	-0.540	-0.097	-0.686	0.350	0.366	-0.038	0.087
Al					1	-.765*	0.260	0.489	-0.067	-0.222	0.153	0.345	0.435	0.487	.825*
Mn						1	-0.316	-0.448	0.330	-0.086	0.009	-0.175	-0.432	-0.318	-0.714
Ca							1	0.295	0.380	.784*	.788*	0.405	0.092	-0.274	-0.170
Sm								1	0.290	0.306	0.242	0.091	0.427	0.702	0.562
Br									1	0.204	.839*	0.122	0.143	0.304	-0.094
As										1	0.477	0.083	-0.120	-0.381	-0.465
Na											1	0.255	0.073	0.020	-0.134
K												1	0.737	-0.148	0.133
La													1	0.429	0.589
Se														1	.811*
Hg															1
Th															
Cr															
Hf															

Table 10. Matrix of correlation coefficient among multi-nutrients and heavy metal concentrations in TSP sample (Continued)

elements	U	Ti	Mg	V	Al	Mn	Ca	Sm	Br	As	Na	K	La	Se	Hg
Sr															
Tb															
Sc															
Rb															
Fe															
Zn															
Co															
Ta															
Eu															
Sb															
Ni															
elements	Th	Cr	Hf	Sr	Tb	Sc	Rb	Fe	Zn	Co	Ta	Eu	Sb	Ni	
U	-0.340	0.289	-0.740	-0.147	-0.338	-0.002	0.249	0.527	-0.134	-0.049	0.347	0.242	-0.292	0.215	
Ti	.760*	-.770*	-0.062	0.533	0.733	-0.502	0.019	-0.749	-0.268	-0.115	-0.009	-0.367	-0.541	-0.109	
Mg	-0.135	0.405	-0.244	0.280	0.018	0.747	0.054	0.539	0.388	0.293	0.501	-0.448	0.466	-0.690	
V	-0.274	0.408	-0.588	-0.196	-0.484	0.171	0.612	0.452	-0.300	-0.079	0.430	0.286	-0.248	0.033	
Al	0.028	0.057	0.004	-0.635	-0.399	-.866*	0.154	-0.158	-0.320	-0.133	-0.150	.824*	-0.343	.954**	
Mn	0.104	-0.124	0.150	0.311	0.144	0.642	0.080	-0.203	-0.090	-0.002	0.150	-0.535	0.145	-.775*	
Ca	0.720	0.016	0.434	0.428	0.604	-0.470	0.353	-0.123	0.433	0.697	-0.052	-0.016	0.248	0.064	
Sm	-0.061	.861*	0.079	-0.556	-0.490	-0.376	0.370	0.628	0.405	0.570	0.271	.755*	0.487	0.612	
Br	0.119	0.253	.896**	0.018	0.104	0.137	0.010	-0.021	0.465	0.466	-0.366	0.022	0.689	-0.100	
As	0.615	0.287	0.130	0.602	0.617	-0.063	0.360	0.298	0.699	.865*	0.331	-0.276	0.489	-0.303	
Na	0.494	0.007	.841*	0.253	0.455	-0.234	0.074	-0.235	0.461	0.545	-0.354	-0.035	0.484	-0.002	
K	0.106	0.043	0.331	0.069	-0.004	-0.185	0.642	-0.095	-0.182	0.319	-0.353	0.301	-0.158	0.196	
La	-0.490	0.444	0.338	-0.332	-0.434	-0.019	0.290	0.405	0.093	0.239	-0.495	0.570	0.174	0.479	
Se	-0.584	0.611	0.169	-.871*	-.799*	-0.152	-0.168	0.440	0.122	-0.057	-0.132	.759*	0.347	0.689	
Hg	-0.516	0.324	-0.039	-.852*	-0.734	-0.485	-0.102	0.229	-0.179	-0.259	-0.240	.869*	-0.112	.943**	
Th	1	-0.298	0.016	0.479	0.647	-0.480	0.427	-0.489	-0.018	0.385	0.397	-0.237	-0.163	-0.204	
Cr		1	0.018	-0.414	-0.536	0.113	0.384	.877**	0.505	0.618	0.322	0.525	0.650	0.255	
Hf			1	0.165	0.249	0.153	-0.127	-0.133	0.426	0.340	-0.711	-0.073	0.560	-0.080	
Sr				1	.927**	0.365	-0.018	-0.193	0.349	0.320	-0.066	-.875**	0.120	-.796*	
Tb					1	0.071	-0.123	-0.386	0.330	0.267	-0.113	-.785*	0.066	-0.605	
Sc						1	-0.256	0.352	0.324	0.030	-0.174	-0.587	0.439	-0.743	
Rb							1	0.115	-0.166	0.565	0.464	0.356	-0.097	0.070	
Fe								1	0.619	0.492	0.232	0.248	0.636	0.077	
Zn									1	0.708	-0.079	-0.234	.910**	-0.240	
Co										1	0.228	0.029	0.679	-0.159	
Ta											1	0.075	-0.107	-0.091	
Eu												1	-0.088	.908**	
Sb													1	-0.221	
Ni														1	

* Correlation is significant at the 0.05 level (2-tailed)

** Correlation is significant at the 0.01 level (2-tailed)

positive correlation coefficients for Hf-Br ($r=0.896$), Tb-Sr ($r=0.927$), Fe-Cr ($r=0.877$), Tb-Zn ($r=0.910$), Ni-Al ($r=0.954$), Ni-Hg ($r=0.943$), and Ni-Eu ($r=0.908$), while a very significant negative correlation coefficient was found in Eu-Sr ($r=-0.875$). The TSP fertilizer, which has 46% phosphorus, positively correlates to U, Th, V, As, Cr, Co, Hg, Al, Ni, Fe, Zn, Ca, Na, Br, Br, Se, Ti, Sm, Tb, and Eu. This result is in line with the study of Verbeek et al., which

stated that the phosphorus content was positively correlated to Cd, U, V, Sb, Cr, As, and Ni elements [10].

Eighty-five percent of the world's TSP fertilizer production is made from sedimentary phosphate rock, where metals that initially exist in this rock and the manufacturing process highly affect the content of metals in TSP fertilizers [7]. Phosphate rock was proven to contain various metals as constituents in sediments

which can be easily transferred into fertilizers during the production process [42]. The long-term use of phosphorus fertilizer has been proven to increase the concentrations of As, Cd, and other trace elements in agricultural soil [35,43]. The long-term use of phosphorus fertilizers in Switzerland increased the concentration of U, Cd, and Th on the soil surface [10].

■ CONCLUSION

The NPK fertilizer contained the highest macro, micro, trace, and non-essential elements compared to other fertilizers. Meanwhile, the TSP fertilizer contained the highest concentration of heavy metals compared to other fertilizers. Fortunately, the concentration of macro, micro, trace, non-essential and heavy metals in all fertilizer samples tested here was within the allowable limits according to Canadian standards. Many of the multi-nutrients and heavy metals analyzed in each fertilizer sample were highly correlated. This finding indicates that those strongly correlated elements form a complex. Considering that some elements and heavy metals that originate from fertilizers can pollute and later accumulate in environmental matrices, it is necessary to monitor the long-term use of inorganic fertilizers against the increase of metal concentrations in the environment to reduce potential health risks to plants and humans. This research provides reliable data that policymakers can use regarding the content of multi-nutrients and heavy metals in fertilizers widely distributed in the market and used by many farmers.

■ ACKNOWLEDGMENTS

This research was supported by RISTEK-BRIN (grant number 2277/UNI/DITLIT/DIT-LIT/PT/2021). The authors are deeply indebted to all of the staff of the process technology division and the KARTINI reactor division - Center for Science and Accelerator Technology for assistance in the sample irradiation process.

■ REFERENCES

- [1] Dimkpa, C.O., Fugice, J., Singh, U., and Lewis, T.D., 2020, Development of fertilizers for enhanced nitrogen use efficiency – Trends and perspectives, *Sci. Total Environ.*, 731, 139113.
- [2] Vecino, X., Reig, M., Bhushan, B., Gibert, O., Valderrama, C., and Cortina, J.L., 2019, Liquid fertilizer production by ammonia recovery from treated ammonia-rich regenerated streams using liquid-liquid membrane contactors, *Chem. Eng. J.*, 360, 890–899.
- [3] Adiloglu, S., Acikgoz, F.E., Belliturk, K., Gurgan, M., Solmaz, Y., and Adiloglu, A., 2021, The effects of increasing amounts of vermicompost and a fixed amount of *Rhodobacter capsulatus* applications on macro and micro elements of plant and soil samples, *J. Plant Nutr.*, 44 (19), 2876–2884.
- [4] Baloch, S., 2021, Essential and non-essential elements in medicinal plants: A review, *Biomed. J. Sci. Tech. Res.*, 33 (4), 26098–26100.
- [5] Trziszka, T., Dobrzański, Z., Chojnacka, K., Bubel, A., Beń, H., Korczyński, M., Konkol, D., and Tronina, W., 2021, Assessment of macro-, micro-, trace, and ultratrace element concentration in green-legged partridge hens' eggs from a free-range system, *Agriculture*, 11 (6), 473.
- [6] Zote, L., Lalrammawia, K., Buragohain, A., Lalrinhlupuii, Kakki, B., Lalmuanpuii, R., Pachuau, Z., Vanlalhruaia, J., Muthukumar, R.B., Kumar, N.S., Jahau, L., Sudarshan, M., Yushin, N., Nekhoroshkov, P., Grozdov, D., Sergeeva, A., and Zinicovscaia, I., 2021, Macro-, micro-, and trace element distributions in areca nut, husk, and soil of northeast India, *Environ. Monit. Assess.*, 193 (2), 65.
- [7] Beygi, M., and Jalali, M., 2019, Assessment of trace elements (Cd, Cu, Ni, Zn) fractionation and bioavailability in vineyard soils from the Hamedan, Iran, *Geoderma*, 337, 1009–1020.
- [8] Zunaidi, A.A., Lim, L.H., and Metali, F., 2021, Assessments of heavy metals in commercially available fertilizers in Brunei Darussalam, *Agric. Res.*, 10 (2), 234–242.
- [9] Wang, X., Liu, W., Li, Z., Teng, Y., Christie, P., and Luo, Y., 2020, Effects of long-term fertilizer applications on peanut yield and quality and plant and soil heavy metal accumulation, *Pedosphere*, 30 (4), 555–562.
- [10] Verbeeck, M., Salaets, P., and Smolders, E., 2020,

- Trace element concentrations in mineral phosphate fertilizers used in Europe: A balanced survey, *Sci. Total Environ.*, 712, 136419.
- [11] Adhikari, T., Gowda, R.C., Wanjari, R.H., and Singh, M., 2021, Impact of continuous fertilization on heavy metals content in soil and food grains under 25 years of long-term fertilizer experiment, *Commun. Soil Sci. Plant Anal.*, 52 (4), 389–405.
- [12] Liu, Y.M., Liu, D.Y., Zhang, W., Chen, X.X., Zhao, Q.Y., Chen, X.P., and Zou, C.Q., 2020, Health risk assessment of heavy metals (Zn, Cu, Cd, Pb, As and Cr) in wheat grain receiving repeated Zn fertilizers, *Environ. Pollut.*, 257, 113581.
- [13] Li, H., Yang, Z., Dai, M., Diao, X., Dai, S., Fang, T., and Dong, X., 2020, Input of Cd from agriculture phosphate fertilizer application in China during 2006–2016, *Sci. Total Environ.*, 698, 134149.
- [14] Qian, L., Zhang, C., Zuo, F., Zheng, L., Li, D., and Zhang, A., and Zhang, D., 2019, Effects of fertilizers and pesticides on the mineral elements used for the geographical origin traceability of rice, *J. Food Compos. Anal.*, 83, 103276.
- [15] Ugulu, I., Ahmad, K., Khan, Z.I., Munir, M., Wajid, K., and Bashir, H., 2021, Effects of organic and chemical fertilizers on the growth, heavy metal/metalloid accumulation, and human health risk of wheat (*Triticum aestivum* L.), *Environ. Sci. Pollut. Res.*, 28 (10), 12533–12545.
- [16] Mirzaei, M., Marofi, S., Solgi, E., Abbasi, M., Karimi, R., and Bakhtyari, H.R.R., 2019, Ecological and health risks of soil and grape heavy metals in long-term fertilized vineyards (Chaharmahal and Bakhtiari province of Iran), *Environ. Geochem. Health*, 42 (1), 27–43.
- [17] Ali, H., Khan, E., and Ilahi, I., 2019, Environmental chemistry and ecotoxicology of hazardous heavy metals: Environmental persistence, toxicity, and bioaccumulation, *J. Chem.*, 2019, 6730305.
- [18] Tousi, E.T., 2022, Determining the mobility of some essential elements in saffron (*Crocus sativus* L.) by the neutron activation analysis, *Baghdad Sci. J.*, 19 (2), 283–296.
- [19] Tang, L., Deng, S., Tan, D., Long, J., and Lei, M., 2019, Heavy metal distribution, translocation, and human health risk assessment in the soil-rice system around Dongting Lake area, China, *Environ. Sci. Pollut. Res.*, 26 (17), 17655–17665.
- [20] Alejandro, S., Höller, S., Meier, B., and Peiter, E., 2020, Manganese in plants: From acquisition to subcellular allocation, *Front. Plant Sci.*, 11, 00300.
- [21] Zinicovscaia, I., Sturza, R., Gurmeza, I., Vergel, K., Gundorina, S., and Duca, G., 2019, Metal bioaccumulation in the soil-leaf-fruit system determined by neutron activation analysis, *J. Food Meas. Charact.*, 13 (1), 592–601.
- [22] Turra, C., Fernandes, E.A.D.N., Bacchi, M.A., Sarriés, G.A., and Reyes, A.E.L., 2020, Temporal variability of rare earth elements in Ultisol soil under citrus plants, *J. Radioanal. Nucl. Chem.*, 324 (1), 219–224.
- [23] Pavlov, S.S., Dmitriev, A.Y., and Frontasyeva, M.V., 2016, Automation system for neutron activation analysis at the reactor IBR-2, Frank Laboratory of Neutron Physics, Joint Institute for Nuclear Research, Dubna, Russia, *J. Radioanal. Nucl. Chem.*, 309 (1), 27–38.
- [24] Bouhila, Z., Azli, T., Boukhadra, D., Hadri, A., Bayou, N., Mazouzi, C., Benbouzid, S., and Lounici, H., 2021, Assessment of elemental composition in Algiers-Algeria, using instrumental neutron activation analysis on different environmental samples of lichens and tree barks, *J. Radioanal. Nucl. Chem.*, 329 (3), 1301–1311.
- [25] Silachyov, I., 2020, Elemental analysis of vegetation samples by INAA internal standard method, *J. Radioanal. Nucl. Chem.*, 324 (1), 97–108.
- [26] Colquhoun, D., 2017, The reproducibility of research and the misinterpretation of p-values, *R. Soc. Open Sci.*, 4 (12), 171085.
- [27] Cesana, B.M., 2018, What p-value must be used as the Statistical Significance Threshold? $P < 0.005$, $P < 0.01$, $P < 0.05$ or no value at all?, *Biomed. J. Sci. Tech. Res.*, 6 (3), 5310–5318.
- [28] Andrade, C., 2019, The P value and statistical significance: Misunderstandings, explanations,

- challenges, and alternatives, *Indian J. Psychol. Med.*, 41 (2), 138–143.
- [29] Etienne, P., Diquelou, S., Prudent, M., Salon, C., Maillard, A., and Ourry, A., 2018, Macro and micronutrient storage in plants and their remobilization when facing scarcity: The case of drought, *Agriculture*, 8 (1), 14.
- [30] Carbajal-Vázquez, V.H., Gómez-Merino, F.C., Herrera-Corredor, J.A., Contreras-Oliva, A., Alcántar-González, G., and Trejo-Téllez, L.I., 2020, Effect of titanium foliar applications on tomato fruits from plants grown under salt stress conditions, *Not. Bot. Horti Agrobot. Cluj-Napoca*, 48 (2), 924–937.
- [31] Bacilieri, F.S., de Vasconcelos, A.C.P., Lana, R.M.Q., Mageste, J.G., and Torres, J.L.R., 2017, Titanium (Ti) in plant nutrition - A review, *Aust. J. Crop Sci.*, 11 (04), 382–386.
- [32] El-Desouky, H.S., Islam, K.R., Bergefurd, B., Gao, G., Harker, T., Abd-El-Dayem, H., Ismail, F., Mady, M., and Zewail, R.M.Y., 2021, Nano iron fertilization significantly increases tomato yield by increasing plants' vegetable growth and photosynthetic efficiency, *J. Plant Nutr.*, 44 (11), 1649–1663.
- [33] Muhammad, N., Zvobgo, G., and Zhang, G., 2019, A review: The beneficial effects and possible mechanisms of aluminum on plant growth in acidic soil, *J. Integr. Agric.*, 18 (7), 1518–1528.
- [34] Anonymous, 2021, *T-4-93 - Safety standards for fertilizers and supplements*, Canadian Food Inspection Agency, Ontario, Canada, 1–20.
- [35] Molina, M., Aburto, F., Calderón, R., Cazanga, M., and Escudey, M., 2009, Trace element composition of selected fertilizers used in Chile: Phosphorus fertilizers as a source of long-term soil contamination, *Soil Sediment Contam.*, 18 (4), 497–511.
- [36] Gambuś, F., and Wieczorek, J., 2012, Pollution of fertilizers with heavy metals, *Ecol. Chem. Eng. A*, 19 (04), 353–360.
- [37] Rui, Y.K., Shen, J.B., and Zhang, F.S., 2008, Application of ICP-MS to determination of heavy metal content of heavy metals in two kinds of N fertilizer, *Guangpuxue Yu Guangpu Fenxi*, 28 (10), 2425–2427.
- [38] Latifi, Z., and Jalali, M., 2018, Trace element contaminants in mineral fertilizers used in Iran, *Environ. Sci. Pollut. Res.*, 25 (32), 31917–31928.
- [39] Benson, N.U., Anake, W.U., and Etesin, U.M., 2013, Trace metals levels in inorganic fertilizers commercially available in Nigeria, *J. Sci. Res. Rep.*, 3 (4), 610–620.
- [40] Rui, Y., Shen, J., Zhang, F., Yan, Y., Jing, J., and Meng, Q., 2008, Application of ICP-MS to detecting ten kinds of heavy metals in KCl fertilizer, *Guangpuxue Yu Guangpu Fenxi*, 28 (10), 2428–2430.
- [41] Xu, F., Rui, Y., Lin, Q., and Zhang, F.S., 2009, The content of nutrient elements of plant in KCl fertilizer, *Guangpuxue Yu Guangpu Fenxi*, 29 (3), 822–823.
- [42] Azzi, V., Kazpard, V., Lartiges, B., Kobeissi, A., Kalso, A., and El Samrani, A.G., 2017, Trace Metals in Phosphate Fertilizers Used in Eastern Mediterranean Countries, *Clean: Soil, Air, Water*, 45 (1), 201500988.
- [43] Molina-Roco, M., Escudey, M., Antilén, M., Arancibia-Miranda, N., and Manquían-Cerda, K., 2018, Distribution of contaminant trace metals inadvertently provided by phosphorus fertilisers: movement, chemical fractions and mass balances in contrasting acidic soils, *Environ. Geochem. Health*, 40 (6), 2491–2509.

Synthesis and Cytotoxic Test of Halogen-Substituted Chalcone Against MCF-7 Breast Cancer Cells

Eti Meirina Brahmana^{1,2,3}, Jamaran Kaban^{2*}, Ginda Haro⁴, and Mimpin Ginting²

¹Postgraduate School, Department of Chemistry, Faculty of Mathematics and Natural Sciences, Universitas Sumatera Utara, Jl. Bioteknologi No. 1, Medan 20155, Indonesia

²Department of Chemistry, Faculty of Mathematics and Natural Sciences, Universitas Sumatera Utara, Jl. Bioteknologi No. 1, Medan 20155, Indonesia

³Biology Study Program, Faculty of Teaching Training and Education, Universitas Pasir Pengaraian, Riau 28557, Indonesia

⁴Department of Pharmaceutical Chemistry, Faculty of Pharmacy, Universitas Sumatera Utara, Jl. Tri Dharma No. 5, Medan 20155, Indonesia

* **Corresponding author:**

email: jamarankaban@yahoo.com

Received: October 26, 2021

Accepted: March 7, 2022

DOI: 10.22146/ijc.69991

Abstract: A series of chalcones was synthesized to be (E)-1-(4-chlorophenyl)-3-p-tolylprop-2-en-1-on (1), (E)-1-(4-chlorophenyl)-3-(4-tolylpropenyl) prop-2-en-1-on (2), (E)-1-(3-bromophenyl)-3-p-tolylprop-2-en-1-on (3), and (E)-1-(3-bromophenyl)-3-(4-isopropyl phenyl) prop-2-en-1-on (4) using irradiate microwave method with reaction time from 3, 6, and 8 min at 800 °C and 700 W. The compounds were characterized using TLC, UV-Vis, FTIR, ¹H-NMR, and evaluated MCF-7 cancer cell cytotoxic test with Presto Blue™. All compounds produced were in the form of yellow crystals. The results showed that compounds 2, 3, and 4 were potentially a Como prevention agent and inhibit cell proliferation with IC₅₀ values of 37.24, 422.22, and 22.41 ppm, respectively. While compound 1 had IC₅₀ 1,484.75 and no cytotoxic effect. Further tests should be carried out for compounds 2, 3, and 4 against normal cells to measure the compound's safety for normal cells.

Keywords: breast cancer; chalcones; MCF-7 cancer cell

■ INTRODUCTION

Chalcones are aromatic compounds found from ferns to higher plants and have been used in traditional herbal medicine for centuries. They have an unsaturated side chain and are often cytotoxic in vitro. They also have a highly pleiotropic molecule that can interact with huge molecular targets and have a broad biological spectrum and pharmacological activities [1-2]. As an important class of natural compounds belonging to the flavonoid family, chalcone and its derivative gain significant attention from researchers to be antifungal, anti-inflammatory, antituberculosis, antihyperglycemic, antimalarial, antileishmanial, and anticancer. Its structure consists of two aromatic rings (A-ring and B-ring) linked by a three-carbon alpha, beta-unsaturated carbonyl system [3-4].

The general structure of chalcones consists of coumarin chalcones (III) acting as anticancer agents in the treatment and prevention of cervical, oral squamous, lung, prostate carcinoma, and brain tumors without harming normal cells [5]. Furthermore, chalcones have anticancer activity due to having a similar mode of action to the structurally related natural combretastatin A-4. The methoxy substituent in A ring is used in pharmacology for anticancer potency by inhibiting tubulin polymerization. Anticancer activity is significantly changed by introducing different substituents on aromatic rings of chalcone [3].

Cancer is an uncontrolled cell growth that occurs in invasion into surrounding tissues and spreads (metastatic) to other parts of the body [6]. The number of cancers in Indonesia is still high, ranking 8 in

Southeast Asia, while in Asia is at 23. Global Observatory data 2018 from the World Health Organization (WHO) shows that the most common cancer case in Indonesia is breast cancer, 16.7% of the total 348,809 cancer cases [7]. Therefore, there is a continuous need to develop anticancer drugs that provide maximum therapeutic effect without causing resistance. In plants, the content of chalcone is low, and it is difficult to isolate in large quantities. Besides that, the variation of the structure of chalcone is limited.

Wang et al. [3] synthesized a derivative chalcone containing diaryl ether moiety. They found that a compound with 4-methoxy substitution on the right aromatic ring has a high activity on MCF-7, HepG2, and HCT1 16 cancer lines, with IC_{50} values of 3.44 ± 0.19 , 4.64 ± 0.23 , and 6.31 ± 0.27 μ M, respectively. Luo et al. [8] synthesized a series of novel ligustrazine-chalcone hydrides and evaluated in vitro and in vivo antitumor activities. It showed that these compounds exhibited significant in vitro cytotoxicity against MDA-MB-231, MCF-7, A549, and HepG2 cell lines with IC_{50} values as low as sub-micromole. These hydrides showed both in vitro and in vivo proliferation inhibition potency against breast cancer. Anwar et al. [9] produced derivative chalcones from hydroxy acetophenone and benzaldehyde in the presence of 50% KOH and found that it was active against breast cell line (T47D). A previous study synthesized several chalcones using the Microwave Assisted Organic Synthesis (MAOS) method through the aldol condensation process of aromatic ketone and aldehyde under alkaline conditions using NaOH catalyst [10]. The process has advantages such as short reaction times, pure reaction products, and higher yields. However, the test for breast cancer is still not reported yet.

In this study, chalcone was synthesized to be (E)-1-(4-chlorophenyl)-3-p-tolylprop-2-en-1-on (1), (E)-1-(4-chlorophenyl)-3-(4-tolylpropenyl) prop-2-en-1-on (2), (E)-1-(3-bromophenyl)-3-p-tolylprop-2-en-1-on (3), and (E)-1-(3-bromophenyl)-3-(4-isopropyl phenyl) prop-2-en-1-on (4) using the Claisen-Schmidt condensation method by aldol condensation, in which new products of chalcone were synthesized from aldehyde and ketone

aromatic by eco-friendly method (the method microwave radiation irradiated). The Vero cell was developed, the bioactivity was investigated using a cytotoxic test with the addition of Presto Blue™, and absorbance measurements were performed using MCF-7 cell lines.

■ EXPERIMENTAL SECTION

Materials

The materials were 4-chloroacetophenone, 4-methylbenzaldehyde, 4-isopropylbenzaldehyde, 3-bromoacetophenone, 2-methyl acetophenone. 4-chlorobenzaldehyde was used as aromatic ketone, and aldehyde was purchased from Merck (Darmstadt, Germany). KOH, HCl, *n*-hexane, ethyl acetate, methanol, ethanol, acetonitrile, distilled water, agar nutrient, broth nutrient, and KLT GF₂₅₄ was obtained from Merck. In addition, some materials used were positive control (Doksorubisin), cell line cancer MCF-7, medium Rosewell Park memorial institute (RPMI) 1640 (GIBCO BRL), phosphate-buffered saline (PBS), prestoBlue™ cell viability reagent, fetal bovine serum (FBS), trypsin-EDTA, trypan Blue, and Cisplatin.

Procedure

Synthesis of (E)-1-(4-chlorophenyl)-3-p-tolylprop-2-en-1-on (1)

The amount of 5 mmol (0.7730 g) of 4-chloroacetophenone as aromatic ketone and 5 mmol (0.6001 g) 4-methyl benzaldehyde as aromatic aldehyde was mixed in an Erlenmeyer glass and dissolved in 15 mL of ethanol. The mixture was added with 10 mL of KOH (5%) as a catalyst dropwise and homogenized using a magnetic stirrer. After that, it was irradiated using a microwave for 3 min at 800 °C and 700 W with an interval of 10 s to avoid evaporation. The reaction process was observed using TLC with *n*-hexane/ethyl acetate as the mobile phase. After that, the mixture was allowed for 20 h at room temperature to maximize the yield. 15 mL of distilled water was added and neutralized with 10% HCl. The precipitation formed was then filtered using a Buchner funnel, washed with cold *n*-hexane, and put in a vacuum oven [11].

Synthesis of (E)-1-(4-chlorophenyl)-3-(4-isopropilfenil) prop-2-en-1-on (2)

The same procedure above was carried out for the synthesis of E-1-(4-chlorophenyl)-3-(4-isopropilfenil) prop-2-en-1-on (2) with a slight modification in which 5 mmol (0.7410 g) of 4-isopropilbenzaldehyd was used as an aldehyde aromatic and the irradiation time was performed for 6 min at 80 °C and 700 W.

Synthesis of (E)-1-(3-bromofenil)-3-p-tolilprop-2-en-1-on (3)

The amount of 5 mmol (0.9952 g) 3-bromoacetophenon and 5 mmol (0.6001 g) of 4-methyl benzaldehyde were used as aromatic ketone and aromatic aldehyde, respectively. It was mixed in an Erlenmeyer and added with 15 mL of ethanol with 10 mL KOH (50%) as a catalyst. The mixture was irradiated in a microwave for 8 min at 80 °C and 700 W using an interval time of 10 s to avoid solvent evaporation. The following procedure was carried out as above.

Synthesis of (E)-1-(3-bromofenil)-3-(4-isopropilfenil) prop-2-en-1-on (4)

The compound of (E)-1-(3-bromofenil)-3-(4-isopropilfenil) prop-2-en-1-on was synthesized using 5 mmol (0.9952 g) 3-bromoacetophenon and 5 mmol (0.7410 g) of 4-isopropilbenzaldehyd as aromatic ketone and aromatic aldehyde, respectively. It was mixed in an Erlenmeyer and added with 15 mL of ethanol with 10 mL KOH (50%) as a catalyst. The mixture was irradiated in a microwave for 8 min at 80 °C and 700 W using an interval time of 10 s to avoid solvent evaporation. The following procedure was carried out as above.

Purification of the compound

Compound 1-4 in the form of a yellow solid was dissolved with hot ethyl acetate in a dropwise fashion. The solution was filtered, and the filter was collected. It was then cooled to form a crystal, filtered using a Buchner funnel, washed using *n*-hexane, vacuumed, and characterized using TLC analysis.

Characterization

The eluent was prepared with a ratio of ethyl acetate:*n*-hexane (2:8, 1:9, 0.5:9.5, 0:10) and allowed to

evaporate in a closed chamber to saturate the vapor. Compounds 1-4 were dissolved in ethyl acetate and spotted using a capillary tube at a distance of 0.7 cm from the lower edge of the silica gel plate GF254. The plate was inserted into the chamber, and the eluent was allowed to rise to the finish line. The plates were removed, and the strains were viewed with a UV lamp at wavelengths of 254 and 366 nm. The compound was pure if there was only one strain. TLC analysis with different eluent ratios was used to examine the purity of the compound, then the R_f value was determined. In addition, the structure of the compound 1-4 was analyzed using a UV/VIS spectrophotometer (UV-2610, China), FTIR (Nicolet 380, Thermo Scientific, Boston, USA), and $^1\text{H-NMR}$ (Agilent Technology, Santa Clara, CA, USA).

Cytotoxic analysis

Cytotoxicity as an anticancer in this study used cell lines MCF-7 and Vero cells which were developed at the University of Padjadjaran, Indonesia. Cell cultures used in 96 well plates were then incubated (at 37 °C and 5% CO_2 until the percentage of cells reached 70%), then the cells were treated with samples and incubated for 48 h at 37 °C and 5% CO_2 and added presto blue to the cell. The absorbance measurement used a Multimode reagent [12].

In this study, Presto Blue™ was used as a-based solution resazurin, which used live-cell reduction capabilities to measure cell proliferation quantitatively. Resazurin was added to the cells, and the absorbance was measured using a multimode reader. When cells were alive, they maintained a reducing environment in their cytosol. Upon entering living cells, Presto Blue™ was reduced to a red color, highly fluorescent resorufin. A healthy cell could be monitored by changes in fluorescent. Metabolically active cells were constantly changing Presto Blue™. On the other hand, non-viable cells could not reduce the indicator dye and therefore did not produce a signal change. The higher the intensity of the purple formed, the greater the number of living cells. In addition, the breast cancer cells used were MCF-7 cells derived from breast tissue of a 69-year woman with blood type O, Rh-positive, in the form of cells that were attached and could be grown in media.

RESULTS AND DISCUSSION

The final products of the synthesis of chalcone (C) 1-4 were yellow crystals with melting point of 156–157, 77–78, 131–132, and 66–68 °C, and the yield obtained was 1.1142 (87.03%), 0.9202 (64.80%), 0.9349 (62.32%), and 0.9075 g (55.32%), respectively. The R_f value for compound 1 at a ratio of 2:8; 1:9; 0.5:9.5; and 0:10 was 0.82, 0.77, 0.69 and 0.45, respectively. Using the same ratio, compound 2 had the R_f value 0.94, 0.87, 0.68, and 0.48. Meanwhile, compound 3 had 0.88, 0.78, 0.58, and 0.35, compound 4 was 0.88, 0.81, 0.54, and 0.20. A good R_f value was in the range from 0.2 to 0.8 [13].

The UV-Vis spectra of compounds 1-4 is shown in Fig. 1. Identification using a UV-Vis spectrophotometer provides information about the presence of conjugated bonds (double bonds), chromophore, and auxochrome of the synthesized chalcone. The results showed that compounds 1, 3, and 4 had three bands, at 286, 292, and 327 nm, while compound 2 had one band at 327 nm. The maximum absorption of the compounds was due to the π - π^* transition indicating the presence of a conjugated C=C chromophore [14]. Compounds 1-4 produced K bands or conjugated bands because they contained carbonyl compounds and produced B bands or benzenoid bands, indicating the presence of double bonds in the aromatic benzene ring.

FTIR spectra for compounds 1-4 are shown in Fig. 2. For compound 1, the presence of the C-Cl group, C=C group of benzene, and C=O ketone was seen at 812, 1512, and 1598 cm^{-1} , respectively. The band at 2916, 3028, and 3487 cm^{-1} are attributed to the presence of $-\text{CH}_3$, C-H of benzene, and overtone of C=O [15]. Compound 2 had an absorption at 817, 1512, and 1604 cm^{-1} indicating the presence of C-Cl group, C=C group of benzene, and the presence of C=O of ketones with a relatively constant number, intensity high, and generally free of distracting bands, making the band the most easily recognizable. The band at 2866 cm^{-1} is attributed to $-\text{CH}_3$ (asymmetric stretching), while symmetric stretching of $-\text{CH}_3$ and overtone of C=O were seen at 2962 and 3448 cm^{-1} , respectively [15]. FTIR spectra of compound 3 showed that absorption at 792, 1512, and 1604 cm^{-1} contributed to the presence of C-Br group, C=C group of benzene, and

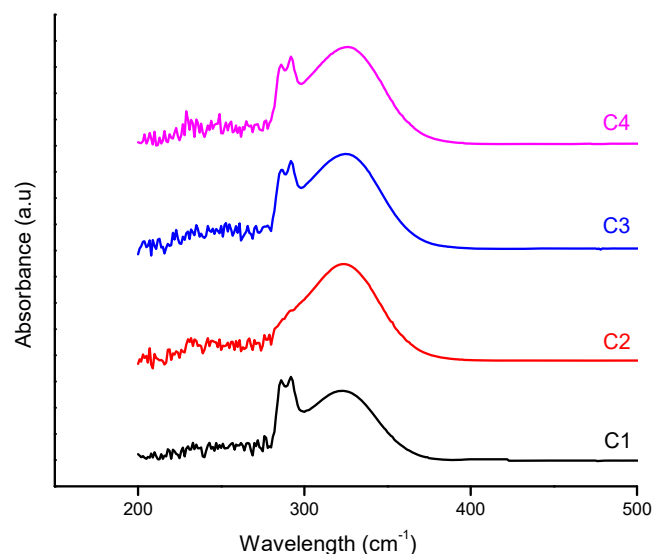


Fig 1. UV-Vis spectra of compounds: (C1) (E)-1-(4-chlorophenyl)-3-p-tolylprop-2-en-1-on, (C2) (E)-1-(4-chlorophenyl)-3-(4-tolylphenyl) prop-2-en-1-on, (C3) (E)-1-(3-bromophenyl)-3-p-tolylprop-2-en-1-on, and (C4) (E)-1-(3-bromophenyl)-3-(4-isopropylphenyl) prop-2-en-1-on

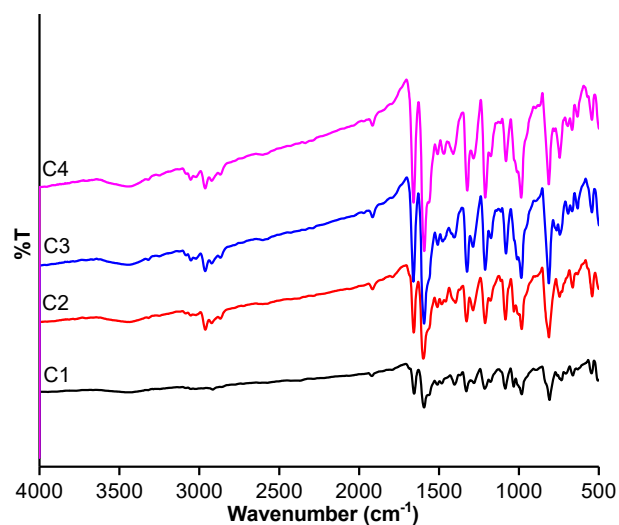


Fig 2. FTIR spectra for (C1) (E)-1-(3-bromofenil)-3-(4-isopropilfenil) prop-2-en-1-on, (C2) (E)-1-(3-bromofenil)-3-p-tolilprop-2-en-1-on, (C3) (E)-1-(4-chlorophenil)-3-(4-isopropilfenil) prop-2-en-1-on, and (C4) (E)-1-(4-chlorophenil)-3-p-tolilprop-2-en-1-on

the presence of C=O of ketones, respectively. The presence of C-Br, C-H of benzene, and C=O were informed at 2362, 2960, and 3468 cm^{-1} , respectively [15].

Finally, compound 4 had the band at 790,1510, and 1604 cm^{-1} , corresponding to the presence of C-Br group, C=C group of benzene, and C=O of the ketone. The band at 2866, 2958, and 3485 cm^{-1} , respectively, attributed to the presence of $-\text{CH}_3$ (asymmetric), $-\text{CH}_3$ (symmetrical), and C=O [15-16].

Spectrum $^1\text{H-NMR}$ (CDCl_3 , 500 MHz) of common chalcone derivatives showed a typical chemical shift, namely the appearance of a double peak with a coupling constant of around 15–16 Hz due to the presence of protons in C_α (δ_{H} : 7.22–7.67 ppm) and C_β (δ_{H} : 7.49–7.94 ppm) to indicate trans configuration (E). The duplet peak at 6.5–8.2 ppm H chemical shift indicated H-aromatic resonance. Proton signal H 7.74 ppm (d, 1H) $J = 16$ Hz indicated H-signals H-aliphatic close to C-carbonyl, and H 7.89 ppm (d, 1H) $J = 16$ Hz corresponded ($\text{H}_\beta = \text{H}$ -aliphatic far from C-carbonyl). The duplet signal at H 7.74 ppm was for one neighboring H atom. The signal at H 2.36 ppm (singlet) had the integrity of 3 protons, which especially characterized the presence of a methyl group ($-\text{CH}_3$) attached to an aromatic ring. H 1.5–2.5 ppm was a proton

bound to the carbon next to the unsaturated bond. H 6.5–8 ppm, the protons in the aromatic ring (aryl protons) were strongly shielded by the orbitals on the ring and absorbed in this typical low field range [17-18]. The $^1\text{H-NMR}$ spectra of compounds 1-4 are shown in Fig. 3, and the measurement results are presented in Table 1.

MCF-7 Cancer Cell Cytotoxic Test with Presto Blue™

The cytotoxic test in this study used the colorimetric method due to color change caused by the oxidation-reduction reaction. Resazurin as a blue indicator is reduced to pink resorufin, and color change indicates cell activity. Cells that were still actively dividing carried out metabolic activities, resulting in enzymes derived from mitochondrial cell organelles and reduced resazurin.

The IC_{50} value was obtained from linear regression analysis between the log concentrations compound with percent inhibition of MCF-7 cell proliferation. The IC_{50} calculation data from compounds 1-4 are summarized in Table 2.

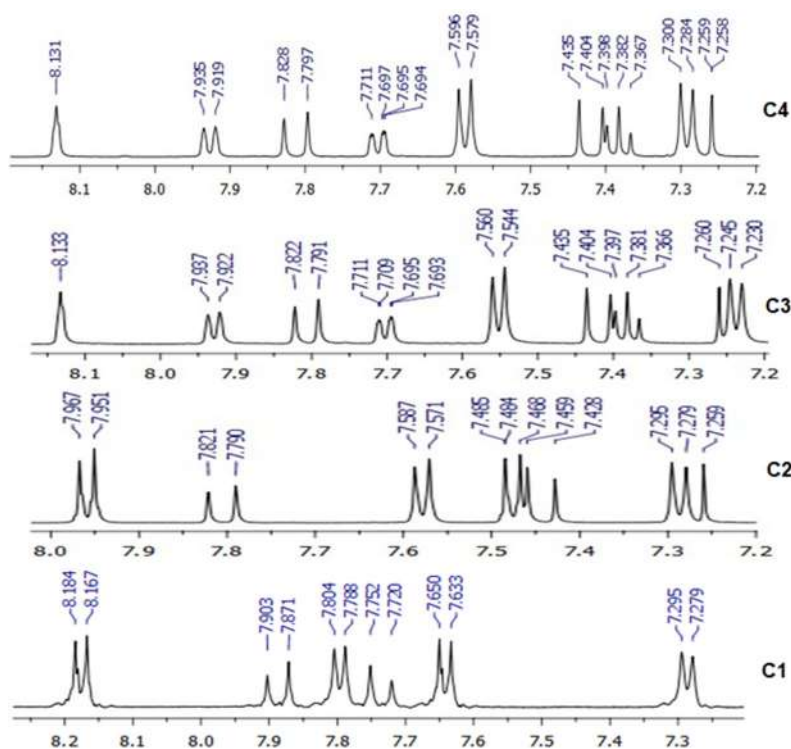
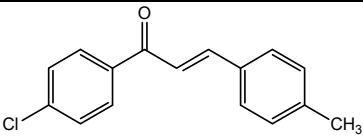
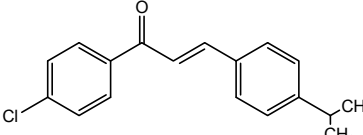
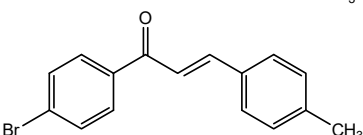
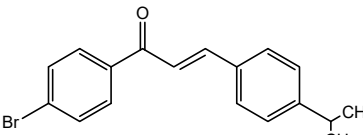


Fig 3. $^1\text{H-NMR}$ spectra of compounds (C1) (E)-1-(4-chlorophenyl)-3-p-tolylprop-2-en-1-on, (C2) (E)-1-(4-chlorophenyl)-3-(4-tolylphenyl) prop-2-en-1-on, (C3) (E)-1-(3-bromophenyl)-3-p-tolylprop-2-en-1-on, and (C4) (E)-1-(3-bromophenyl)-3-(4-isopropylphenyl) prop-2-en-1-on

Table 1. ¹H-NMR of compounds 1-4

Number atom	C1 δ_H (ppm)	C2 δ_H (ppm)	C3 δ_H (ppm)	C4 δ_H (ppm)
1	-	-	-	-
2	7.80 (d, 1H) $J = 8$ Hz	7.58 (d, 1H) $J = 8$ Hz	7.55 (d, 1H) $J = 8$ Hz	7.59 (d, 1H) $J = 8.5$ Hz
3	7.29 (d, 1H) $J = 8$ Hz	7.29 (d, 1H) $J = 8$ Hz	7.24 (d, 1H) $J = 7.5$ Hz	7.29 (d, 1H) $J = 8$ Hz
4	-	-	-	-
5	7.29 (d, 1H) $J = 8$ Hz	7.29 (d, 1H) $J = 8$ Hz	7.24 (d, 1H) $J = 7.5$ Hz 7.55 (d, 1H) $J = 8$ Hz	7.29 (d, 1H) $J = 8$ Hz 7.59 (d, 1H) $J = 8.5$ Hz
6	7.80 (d, 1H) $J = 8$ Hz	7.58 (d, 1H) $J = 8$ Hz	7.42 (d, 1H) $J = 715.5$ Hz	7.42 (d, 1H) $J = 15.5$ Hz
C α	7.74 (d, 1H) $J = 16$ Hz	7.44 (d, 1H) $J = 15.5$ Hz	7.81 (d, 1H) $J = 15.5$ Hz	7.81 (d, 1H) $J = 15.5$ Hz
C β	7.89 (d, 1H) $J = 16$ Hz	7.81 (d, 1H) $J = 15.5$ Hz	-	-
1'	-	-	8.13 (s, 1H)	8.13 (s, 1H)
2'	8.18 (d, 1H) $J = 8.5$ Hz	7.96 (d, 1H) $J = 8$ Hz	-	-
3'	7.64 (d, 1H) $J = 8.5$ Hz	7.48 (d, 1H) $J = 8.25$ Hz	7.70 (dd, 1H) $J_a = 8$ Hz, $J_b = 1$ Hz	7.70 (td, 1H) $J_a = 8$ Hz, $J_b = 1$ Hz
4'	-	-	7.38 (t, 1H) $J = 8$ Hz	7.38 (t, 1H) $J = 8$ Hz 7.93 (d, 1H) $J = 8$ Hz
5'	7.64 (d, 1H) $J = 8.5$ Hz	7.48 (d, 1H) $J = 8.25$ Hz	7.93 (d, 1H) $J = 7.5$ Hz	1.27 (d, 6H) $J = 7$ Hz 2.95 (sep, 1H)
6'	8.18 (d, 1H) $J = 8.5$ Hz	7.96 (d, 1H) $J = 8$ Hz	2.40 (s, 3H)	
CH ₃	2.36 (s, 3H)	1.27 (d, 6H) $J = 7$ Hz		
CH(CH ₃) ₂		2.950 (sep, 1H)		

Table 2. The structure and IC₅₀ calculation of compounds 1-4

Compound	Structure	Linear regression equation	X = IC ₅₀ (ppm) ^a
1		$y = -0.0002x + 0.587$	1,484.75
2		$y = -0.0114x + 0.7209$	37.24
3		$y = -0.0091x + 0.6673$	42.22
4		$y = -0.0228x + 0.8112$	22.41

According to the National Cancer Institute [19], a compound has cytotoxic activity if IC₅₀ 20 g/mL. Meanwhile, Meiyanto et al. [20] reported that the IC₅₀ 100

g/mL in the compound showed anticancer activity that inhibited cell proliferation and was very potential as a Como prevention agent, as a compound to prevent the

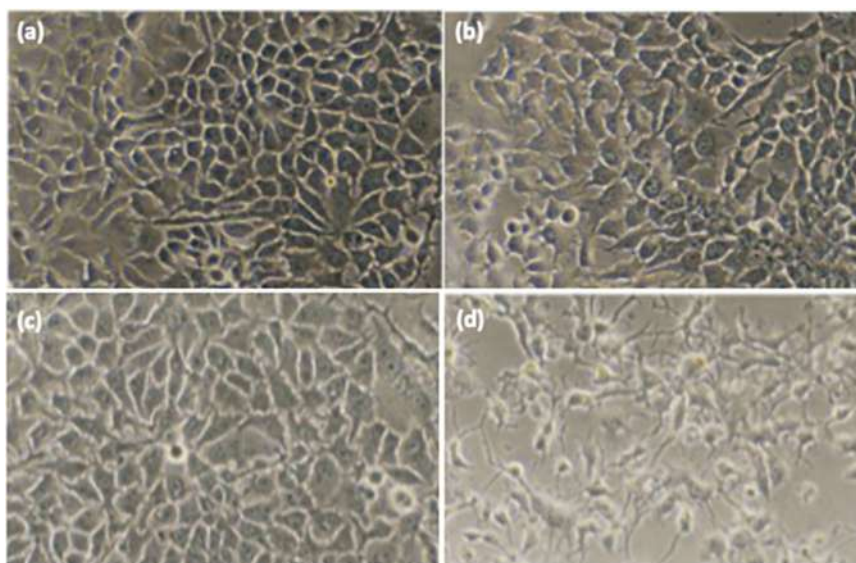


Fig 4. Morphology images of MCF7 for: (a) (E)-1-(4-chlorophenyl)-3-p-tolylprop-2-en-1-on; (b) (E)-1-(4-chlorophenyl)-3-(4-tolylpropenyl) prop-2-en-1-on; (c) (E)-1-(3-bromophenyl)-3-p-tolylprop-2-en-1-on; and (d) (E)-1-(3-bromophenyl)-3-(4-isopropylphenyl) prop-2-en-1-on with a concentration of 7.81 $\mu\text{g/mL}$

carcinogenesis process of triggers cancer. Compounds 2-4 had an IC_{50} of 100 $\mu\text{g/mL}$ so that it was able to inhibit cell proliferation and was potential as a Como prevention agent. Meanwhile, compound 1 had no effect cytotoxic with LC_{50} of 1,484.75 $\mu\text{g/mL}$.

In addition, IC_{50} indicates the concentration that produces resistance cell growth of 50% of the population and the potential of a compound as cytotoxic. The greater the IC_{50} value, the more the compound is non-toxic [21]. Cells with compound treatment showed morphological changes that lead to the characteristics of apoptotic cells in the form of shrinkage of cell dimensions (shrinkage) and cytoplasmic compaction, as well as extracellular matrix damage. Possible cytotoxic activity of compounds induces apoptosis and inhibits cell migration leading to antimetastatic [21]. The measurement of cell death for compounds 1-4 was indicated by changes in the morphology of the cell nucleus MCF-7 to be black, as seen in Fig. 4 (a-d).

Living cells appeared to have an elongated shape and were also attached to the base plate, while the dead cells were small, round, and floated. Activity test compound against MCF-7 breast cancer cells decreased the number of living cells with increasing concentration. The higher the concentration, the lower the number of living cells

[22]. The biological activity of chalcone compounds in this study was influenced by the presence of α,β -unsaturated carbonyl groups and substituents bonded to the aromatic ring present in this compound.

■ CONCLUSION

The synthesized of chalcone into four compounds: (E)-1-(4-chlorophenyl)-3-p-tolylprop-2-en-1-on (1); (E)-1-(4-chlorophenyl)-3-(4-tolylpropenyl) prop-2-en-1-on (2); (E)-1-(3-bromophenyl)-3-p-tolylprop-2-en-1-on (3); and (E)-1-(3-bromophenyl)-3-(4-isopropylphenyl) prop-2-en-1-on (4) has been carried out and the yield of chalcone derivative from aromatic aldehyde compounds with halogen-substituted aromatic ketones by microwave radiation method are 87.03%, 64.80%, 62.32%, and 55.32%, respectively. Cytotoxic bioactivity of halogen-substituted chalcone analogue compounds 1-4 against MCF-7 breast cancer cells was 1,484.75 $\mu\text{g/mL}$, 37.24 $\mu\text{g/mL}$, 42.22 $\mu\text{g/mL}$, 22.41 $\mu\text{g/mL}$. The results shows that compound 2, 3 and 4 is potential as a Como prevention agent and able to inhibit cell proliferation.

■ ACKNOWLEDGMENTS

The authors thank the Indonesian Ministry of Education through DRPM provides the research grant

with contract number 49/UN5.2.3.1/PPM/KP-DRPM/2019.

■ AUTHOR CONTRIBUTIONS

EMB conducted the experiment, JK and GH conducted the characterization, and EMB, JK, and MP wrote and revised the manuscript. All authors agreed to the final version of this manuscript.

■ REFERENCES

- [1] Ahmad, M.R., Sastry, V.G., Bano, N., and Anwar, S., 2016, Synthesis of novel derivatives by conventional and microwave irradiation methods and their pharmacological activities, *Arabian J. Chem.*, 9, S931–S935.
- [2] Wang, G., Liu, W., Gong, Z., Huang, Y., Li, Y., and Peng, Z., 2019, Design, synthesis, biological evaluation and molecular docking studies of new chalcone derivatives containing diaryl ether moiety as potential anticancer agents and tubulin polymerization inhibitors, *Bioorg. Chem.*, 95, 103565.
- [3] Wang, G., Peng, Z., and Li, Y., 2020, Synthesis, anticancer activity and molecular modelling studies of novel chalcone derivatives containing indole and naphthalene moieties as tubulin polymerization inhibitors, *Chem. Pharm. Bull.*, 67 (7), 725–728.
- [4] Harmastuti, N., Herowati, R., Susilowati, D., Pranowo, H.D., and Mubarika, S., 2012, Synthesis and cytotoxic activity of chalcone derivatives on human breast cancer cell lines, *Indones. J. Chem.*, 12 (3), 261–267.
- [5] Adnan, D., Singh, B., Mehta, S.K., Kumar, V., and Kataria, R., 2020, Simple and solvent free practical procedure for chalcones: An expeditious, mild and greener approach, *Curr. Res. Green Sustainable Chem.*, 3, 100041.
- [6] Iqbal, J., Abbasi, B.A., Mahmood, T., Kanwal, S., Ali, B., Shah, S.A., and Khalil, A.T., 2017, Plant-derived anticancer agents: A green anticancer approach, *Asian Pac. J. Trop. Biomed.*, 7 (12), 1129–1150.
- [7] World Health Organization, 2018, *Latest Global Cancer Data: Cancer Burden Rises to 18.1 Million New Cases and 9.6 Million Cancer Deaths in 2018*, World Health Organization, Geneva.
- [8] Luo, Y., Wu, W., Zha, D., Zhou, M., Wang, C., Huang, J., Chen, S., Yu, L., Li, Y., Huang, Q., Zhang, J., and Zhang, C., 2021, Synthesis and biological evaluation of novel ligustrazine-chalcone derivatives as potential anti-triplet breast cancer agents, *Bioorg. Med. Chem. Lett.*, 47, 128230.
- [9] Anwar, C., Prasetyo, Y.D., Matsjeh, S., Haryadi, W., Sholikhah, E.N., and Nendrowati, N., 2018, Synthesis of chalcone derivatives and their in vitro anticancer test against breast (T47D) and colon (WiDr) cancer cell line, *Indones. J. Chem.*, 18 (1), 102–107.
- [10] Brahmana, E.M., Adel, Z., and Hilwan, Y.T., 2013, Sintesis dan uji toksisitas (E)-1-(2-chlorophenyl)-3-p-tolylprop-2-en-1-on, *Indones. Chem. Acta*, 4 (1), 21–25.
- [11] Uddin, M.N., M.Knock, N.H., Uzzaman, M.M.H., Bhuiyyan, M., Sanaullah, A.F.M., Shumi, W., and Sadrul Amin, H.M., 2020, Microwave assisted synthesis, characterization, molecular docking and pharmacological activities of some new 2'-hydroxychalcone derivatives, *J. Mol. Struct.*, 1206, 127678.
- [12] Maqsood, M., Qureshi, R., Ikram, M., Ahmad, M.S., Jabeen, B., Asi, M.R., Khan, J.A., Ali, S., and Lilge, L., 2018, *In vitro* anticancer activities of *Withania coagulans* against HeLa, MCF-7, RD, RG2, and INS-1 cancer cells and phytochemical analysis, *Intergr. Med. Res.*, 7 (2), 184–191.
- [13] Wulandari, L., 2011, *Kromatografi Lapis Tipis*, PT Taman Kampus Presindo, Jember.
- [14] Fesseden, J.S., and Fesseden, R.J., 2010, *Dasar-dasar Kimia Organik*, PT. Binarupa Aksara, Tangerang.
- [15] Kriz, G.S., Lampman, G.M., Vyvyan, J.A., and Pavia, D.L., 2014, *Introduction to Spectroscopy*, Cengage Learning, US.
- [16] Modwi, A., Ali, M.K.M., Taha, K.K., Ibrahim, M.A., El-Khair, H.M., Eisa, M.H., Elamin, M.R., Aldaghri, O., Alhathloul, R., and Ibnaouf, K.H., 2017, Structural and optical characteristic of chalcone doped ZnO nanoparticles, *J. Mater. Sci.: Mater. Electron.*, 29 (4), 2791–2796.

- [17] Yadav, V.R., Prasad, S., Sung, B., and Aggarwal, B.B., 2011, The role of chalcones in suppression of NF- κ B-mediated inflammation and cancer, *Int. Immunopharmacol.*, 11 (3), 295–309.
- [18] Vh, E.S., Matsjeh, S., Mustofa., and Wahyuningsih, T.D., 2014, Improved synthesis of 2',6'-dihydroxy-3,4-dimethoxy chalcone by grinding technique to synthesize 5-hydroxy-3'-4'-dimethoxy flavone, *Indones. J. Chem.*, 14 (2), 174–178.
- [19] National Cancer Institute, 2015, *Tumor Markers Fact Sheet*, National Cancer Institute US Department of Health and Human Services, Maryland, US.
- [20] Meiyanto, E., Putri, D.D.P., Susidarti, R.A., Murwanti, R., Sadjiman, Fitriyani, A., Husnaa, U., Purnomo, H., and Kawaichi, M., 2014, Curcumin and its analogues (PGV-0 and PGV-1) enhance sensitivity of resistant MCF-7 cells to doxorubicin through inhibitions of HER2 and NF- κ B activation, *Asian Pac. J. Cancer Prev.*, 15 (1), 179–184.
- [21] Zhu, M., Wang, J.B., Xie, J.W., Chen, L.P., Wei, X.Y., and Jiang, X., 2018, Design, synthesis, and evaluation of chalcone analogues incorporate α,β -unsaturated ketone functionality as anti-lung, cancer agents via evoking ROS to induce pyroptosis, *Eur. J. Med. Chem.*, 157, 1395–1405.
- [22] Ramos, A., Carvalho, B., Sena, M., Dethoup, T., Buttachon, S., Kijjoa, A., and Rocha, E., 2016, Crude extract of marine-derived and soil fungi of the genus *Neosartorya* exhibit selective anticancer activity by inducing cell death in colon, breast, and skin cancer cell lines, *Pharmacogn. Res.*, 8 (1), 8–15.

Codoping Effect of Nitrogen (N) to Iron (Fe) Doped Zirconium Titanate (ZrTiO₄) Composite toward Its Visible Light Responsiveness as Photocatalysts

Rizka Hayati¹, Rian Kurniawan², Niko Prasetyo¹, Sri Sudiono¹, and Akhmad Syoufian^{1*}

¹Department of Chemistry, Faculty of Mathematics and Natural Sciences, Universitas Gadjah Mada, Sekip Utara, Yogyakarta 55281, Indonesia

²Institute of Chemical Technology, Universität Leipzig, Linnéstr. 3, 04103 Leipzig, Germany

* **Corresponding author:**

email: akhmadsyoufian@ugm.ac.id

Received: November 1, 2021

Accepted: February 19, 2022

DOI: 10.22146/ijc.70146

Abstract: Iron (Fe) and nitrogen (N) were introduced as dopants into zirconium titanate (ZrTiO₄) in order to study the codoping effects of nitrogen on iron-doped zirconium titanate (Fe,N-codoped ZrTiO₄) composite. Titanium tetraisopropoxide (TTIP), zirconia (ZrO₂), urea, and iron(II) sulfate heptahydrate were used as the source of TiO₂, semiconductor supports, source of nitrogen, and iron, respectively. A specific amount of iron (1, 3, 5, 7, and 9 wt.%) and a fixed nitrogen content (10 wt.%) were doped into the ZrTiO₄ lattice. Various calcination temperatures (from 500 to 900 °C) were also applied to investigate the crystal structure of the composite. The composites were characterized by X-ray powder diffractometer (XRD), Fourier-transform infrared spectrophotometer (FT-IR), scanning electron microscope with energy dispersive X-Ray spectrometer (SEM-EDX), and specular reflectance UV-Vis (SR-UV). The lowest bandgap energy of 2.62 eV was obtained in the composite with 3 wt.% of Fe and 10 wt.% of N calcined at 500 °C.

Keywords: codoping; Fe,N-codoped ZrTiO₄; composite; iron; nitrogen

■ INTRODUCTION

Titanium dioxide (TiO₂) has been extensively studied as a semiconductor photocatalyst, attributed to its eminent photocatalytic activity, high chemical stability, high redox ability, photo-corrosion resistance, non-toxicity, and low-price [1-3]. Three major polymorphs of TiO₂ exist in nature, namely anatase, rutile, and brookite [4]. Although the bandgap of anatase (3.2 eV) is slightly higher than rutile (3.0 eV), it exhibits superior photoactivity under UV light irradiation to that of rutile [5]. However, the bandgap of TiO₂ is too large to permit electron excitation under solar light that comprises only about 5% UV energy [6]. Therefore, many efforts have been made to enhance the photocatalytic activity of TiO₂ under the remaining spectrum of solar light, the visible light irradiation.

Modification of TiO₂ can be done by transition metal doping. The interaction of the 3d orbitals of the metal dopant with Ti causes distortion of the surrounding structure and affects the conduction band of the

semiconductor [7]. It creates an energy level of impurity within the electronic structure that activates TiO₂ at a low energy wavelength (visible light) [8]. Fe³⁺ species has been considered a favorable candidate among other metal ions due to its similar ionic radii (0.64 Å) to Ti⁴⁺ (0.68 Å). Thus, Fe³⁺ ions can be easily incorporated into the TiO₂ crystal lattice and decrease the bandgap width, making them more efficient for visible light absorption [9]. Zhang et al. [10] reported in their study that the addition of Fe³⁺ ions to the TiO₂ matrix acts as an electron-hole trap and reduces the recombination rate of the pairs, resulting in the extension of the light absorption band. Nevertheless, there are some drawbacks of using metal dopants, i.e. photo-corrosion and thermal instability. Hence, deep-level defects may form as recombination centers, lowering photocatalytic efficiency [11-12].

The addition of non-metal as codopant has received much interest due to its synergistic impact on improving the visible light absorption [13]. Nitrogen is the most suitable and frequently used as a non-metal doping

element [14]. Nitrogen as a non-metal dopant has many advantages, including chemical stability, low ionization energy, and the atomic size similarity to oxygen. Incorporation of N dopant into the TiO₂ lattice can occur at substitutional or interstitial positions, affecting electron density and charge distribution, thus leading to increased photocatalytic ability [1]. Sinhmar et al. [15] prepared Ni and N codoped TiO₂ catalyst by surface impregnation method and revealed a high performance for photodegradation of phenol under visible light irradiation. It was reported that 2p states of N mixed with O 2p states lead to bandgap narrowing [16]. Di Valentin et al. [17] confirmed that N 2p states occupy slightly above the O 2p valence band, causing a redshift in the valence band edge.

Zirconia (ZrO₂) is another semiconductor with several advantages: predominant thermal properties, high refractive index, high optical transparency, and polymorphic nature [18-19]. Hybrid material of TiO₂ with ZrO₂ is investigated and expected to improve the thermal stability of TiO₂. Syoufian et al. [20] successfully combined ZrO₂ and TiO₂ using sulfonated polystyrene as a template, resulting a hollow spheres material called zirconium titanate (ZrTiO₄). According to Kim et al. [21], the coupling of ZrO₂/TiO₂ enhances the photocatalytic activity, owing to its relatively large surface area, small crystalline size, and well-crystallized anatase phase. Incorporating Zr⁴⁺ into TiO₂ can create lattice defects that allow higher photoactivity than pure oxides. The defects prevent charge recombination by acting as charge-trapping sites [22].

Several methods have been reported for preparing undoped and doped TiO₂ composites, including hydrothermal, sol-gel, microwave, and impregnation [10,23-25]. The utilization of lower reaction temperatures is a typical aspect of these approaches. The reaction processes conducted in the gas or liquid phase allow substantially quicker diffusion than typical solid-state techniques. Among those, the sol-gel process is the most commonly used method because of its many advantages such as simplicity, precise composition control, inexpensive, and ability to produce high purity products [26-27]. The sol-gel method mixes components homogeneously at the molecular level, which is convenient

Table 1. Bandgap value of M-ZrTiO₄ at the optimum condition (M = Fe, Cu, Zn, and Co)

Material	Eg (eV)
7% Fe-ZrTiO ₄ 500 °C	2.83 [30]
5% Cu-ZrTiO ₄ 500 °C	2.87 [31]
5% Zn-ZrTiO ₄ 900 °C	2.87 [32]
3% Co-ZrTiO ₄ 500 °C	2.94 [33]

for the dopant incorporation process in the material matrix [28]. Ning et al. [29] observed the presence of Ti–O–Zr links in ZrTiO₄ gel produced using the sol-gel process, which possesses a higher oxygen vacancy concentration that enhances photocatalytic activity.

Previous studies of doping on ZrTiO₄ composite materials with transition metals Fe, Cu, Zn, and Co have been done. The optimum conditions for the dopant content and calcination temperature obtained for each transition metal are shown in Table 1. Zirconium titanate with 7 wt.% of Fe and calcination temperature of 500 °C has the lowest bandgap value of 2.83 eV. In this work, iron and nitrogen codoped zirconium titanate composite (Fe,N-codoped ZrTiO₄) was prepared by the sol-gel method. It has the potential to provide a synergistic effect by expanding the light absorption edge and increasing the efficiency of photocatalysis. Titania was grown on the surface of zirconia to form a material with higher thermal stability compared to pure TiO₂. Both metal and non-metal dopants, i.e., Fe and N, were incorporated into the ZrTiO₄ system in order to shift the absorption ability of the material to the visible range. Various dopant contents and calcination temperatures were applied to observe the absorption shift and crystal structures.

■ EXPERIMENTAL SECTION

Materials

Titanium(IV) tetraisopropoxide (TTIP) (97%, Sigma-Aldrich) and ZrO₂ fine powder (Jiaozuo Huasu) were used as the precursor of TiO₂ and supporting semiconductor, respectively. Iron(II) sulfate heptahydrate (FeSO₄·7H₂O) (Merck) and urea (PA, Merck) were chosen as the dopant sources. Absolute ethanol (PA, Merck) and demineralized water (Jaya Sentosa) were used as solvents.

Instrumentation

X-ray powder diffractometer (XRD) PANalytical X'Pert PRO MRD (Cu K α radiation $\lambda = 1.54 \text{ \AA}$, 40 kV, 30 mA) was used to examine the crystalline structure of the materials. Fourier transform infrared spectrophotometer (FTIR, Thermo Nicolet Is10) was utilized to observe vibrational spectra of functional groups in the materials. The morphology and elemental composition of materials were analyzed using a scanning electron microscope with an energy dispersive X-Ray spectrometer (SEM-EDX). The bandgap was determined from the absorption spectra, obtained using specular reflectance UV-Vis spectrometer UV 1700 Pharmaspec (SR-UV).

Procedure

Fe,N-codoped ZrTiO₄ was synthesized by the sol-gel method. All sol-gel processes were performed at room temperature. First, 2.5 mL of TTIP as Ti precursor was dissolved in 25 mL of absolute ethanol and stirred for 10 min at 700 rpm, resulting in a colorless and transparent Ti solution. Meanwhile, 1 g of ZrO₂ powder, 86.61 mg of urea (10 wt.%), and FeSO₄·7H₂O with different loadings (20.11, 60.34, 100.55, 140.78 and 181.01 mg) for 0, 1, 3, 5, 7, and 9 wt.% Fe/Ti ratios were dissolved together in 25 mL of demineralized water, then added dropwise into the Ti precursor with delicate stirring. The solution was further

stirred over 30 min homogeneously and then separated by centrifugation at 1500 rpm for 1 h. The solid was aged in the open air for 48 h before being heated at 50 °C for 24 h. Finally, the material was calcined at 500 °C for 4 h under atmospheric conditions. Additionally, composite with 5 wt.% of Fe dopant was calcined at 700 and 900 °C. The composite materials are denoted as α Fe- β N-ZT- γ , in which Fe, N, and ZT represent iron dopant, nitrogen dopant, and zirconium titanate composite, respectively. Moreover, α and β are the percentage of iron and nitrogen dopants, respectively, and γ is the calcination temperature in °C. All samples were characterized using XRD, FTIR, SRUV, and SEM-EDX.

RESULTS AND DISCUSSION

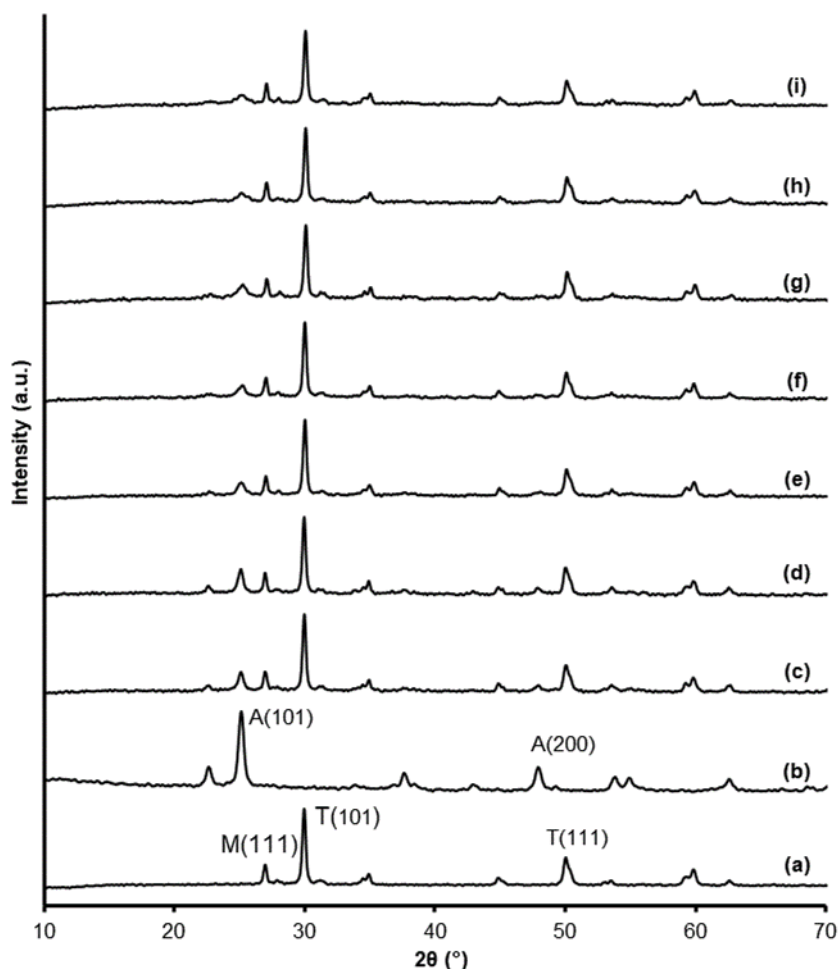
X-ray diffraction patterns of Fe-10N-ZT with various amounts of Fe after calcination at 500 °C are shown in Fig. 1. The reference materials were TiO₂, ZrO₂, ZT-500 (undoped ZrTiO₄), and 10N-ZT-500 (N-doped ZrTiO₄). The crystallite size of Fe-10N-ZT and references were calculated by using Debye-Scherrer equation [12] and presented in Table 2. The diffraction pattern of pure TiO₂ exhibits major peaks at 25° (d101) and 48° (d200), indicating TiO₂ in the anatase phase (ICDD: 00-021-1272). On the other hand, pure ZrO₂ reveals tetragonal phase appeared at 30° (d101), 50° (d112), and 60° (d211) (ICDD: 00-042-1164). Small peaks

Table 2. Crystallite size of ZrO₂, TiO₂, ZT-500, 10N-ZT-500 and various Fe-10N-ZT composites

Material	Crystal phase	hkl	2 θ (°)	FWHM (°)	L (nm)
ZrO ₂	Tetragonal	101	29.93	0.20	28.24
TiO ₂	Anatase	101	25.11	0.32	17.65
ZT-500	Tetragonal	101	29.95	0.20	28.70
	Anatase	101	25.08	0.30	18.99
10N-ZT-500	Tetragonal	101	29.93	0.19	29.44
	Anatase	101	25.05	0.32	17.58
1Fe-10N-ZT-500	Tetragonal	101	29.99	0.20	28.88
	Anatase	101	25.11	0.44	12.86
3Fe-10N-ZT-500	Tetragonal	101	29.99	0.20	28.99
	Anatase	101	25.16	0.39	14.54
5Fe-10N-ZT-500	Tetragonal	101	30.06	0.20	28.08
	Anatase	101	25.26	0.38	14.78
7Fe-10N-ZT-500	Tetragonal	101	30.05	0.19	29.81
	Anatase	101	25.15	0.41	13.91

Table 2. Crystallite size of ZrO₂, TiO₂, ZT-500, 10N-ZT-500 and various Fe-10N-ZT composites (*Continued*)

Material	Crystal phase	hkl	2θ (°)	FWHM (°)	L (nm)
9Fe-10N-ZT-500	Tetragonal	101	30.04	0.20	28.27
	Anatase	101	25.00	0.29	19.56
5Fe-10N-ZT-700	Tetragonal	101	29.91	0.19	29.93
	Anatase	101	25.10	0.10	54.26
	Rutile	110	27.16	0.21	27.24
5Fe-10N-ZT-900	Tetragonal	101	30.03	0.19	30.67
	Rutile	110	27.30	0.18	31.56

**Fig 1.** Diffraction patterns of (a) ZrO₂, (b) TiO₂, (c) ZT-500, (d) 10N-ZT-500, (e) 1Fe-, (f) 3Fe-, (g) 5Fe-, (h) 7Fe-, and (i) 9Fe-10N-ZT-500

around 27° (d111) and 51° (d220) correspond with the monoclinic phase (ICDD: 00-037-1484). The diffraction peak of 10N-ZT-500 at 25° (d101) shifts slightly to a lower angle than the ZT-500. This can be related to the insertion of a nitrogen atom into the crystal lattice, which has a higher ionic radius than the oxygen atom, destabilizing the crystalline structures [34]. The iron pattern was hardly

observed in the XRD pattern, indicating the inclusion of Fe³⁺ replacing Ti⁴⁺ in the crystal lattice. This is confirmed by a shift to a higher angle in the anatase diffraction peak (101) in comparison to pure TiO₂ [35].

In comparison to pure TiO₂, the full width of half maximum (FWHM) at the diffraction peak corresponding to the anatase phase of TiO₂ (101) in the

ZT-500 sample was reduced. As a result, the crystal size increased from 17.65 nm to 18.99 nm, suggesting that ZrO_2 presence slightly enhances the formation of anatase from amorphous. Furthermore, the FWHM value of the diffraction peak corresponding to the anatase TiO_2 phase was slightly higher after N doping and increased significantly after the Fe and N codoping. These results indicate that codoping with Fe and N hinders TiO_2 crystal growth, resulting in smaller anatase crystals [36].

Fig. 2 presents the XRD patterns of 5Fe-10N-ZT calcined at various temperatures. After calcined at 700 °C, 5Fe-10N-ZT-700 displays typical rutile pattern (ICDD: 00-021-1276) at 27° (d110), 36° (d101), 41° (d111), and 54° (d211), whereas anatase pattern intensity at 25° (d101) and 48° (d200) diminish. The diffraction pattern of 5Fe-10N-ZT-900 shows an apparent rutile phase. Anatase peaks at 25° (d101) and 48° (d200) are still observable, but with considerably lower intensity. This confirms that the presence of ZrO_2 , which is prominent as a supporting material, can impede the transition of anatase to rutile [25]. No rutile peaks were seen in 10N-ZT-500, indicating that doping with nitrogen does not promote the phase transition from anatase to rutile at 500 °C. As reported in the literature, using urea as a nitrogen precursor retards the transition from anatase to rutile [37].

Fig. 3 shows FT-IR spectra of various iron dopant

contents in Fe-10N-ZT with ZrO_2 , TiO_2 , and 10N-ZT-500 as references. All the materials were calcined at 500 °C. A vibration around 3400 cm^{-1} appearing in all samples is recognized as O–H stretching vibration [38]. Vibration peaks at 512 cm^{-1} and 1635 cm^{-1} are related to Zr–O and Zr–OH vibrations, respectively, which confirms the presence of ZrO_2 [39]. Comparing 10N-ZT-500 with ZrO_2 and TiO_2 , the peak intensity in the frequency of 1640 cm^{-1} becomes strong and sharp. This discrepancy confirms the existence of the N dopant in the crystal lattice [40]. In addition, this also shows that the concentration of the OH group is getting stronger, which can increase the photocatalytic ability because it acts as a hole trap and suppresses the electron-hole recombination process [41]. The broadband of all Fe-10N-ZT-500 in the range of 400–800 cm^{-1} can be attributed to the Ti–O and Fe–O stretching vibration [3]. A vibrational band was observed and increased around 1080 cm^{-1} as a percentage of iron arose, which might potentially be the vibration Fe–O–Zr or Fe–O–Ti, or both.

The FTIR spectra of 5Fe-10N-ZT following calcination at various temperatures are shown in Fig. 4. Higher calcination temperatures lower the intensity of O–H vibration at 3400 cm^{-1} . This is mainly due to the reduced water content caused by high-temperature

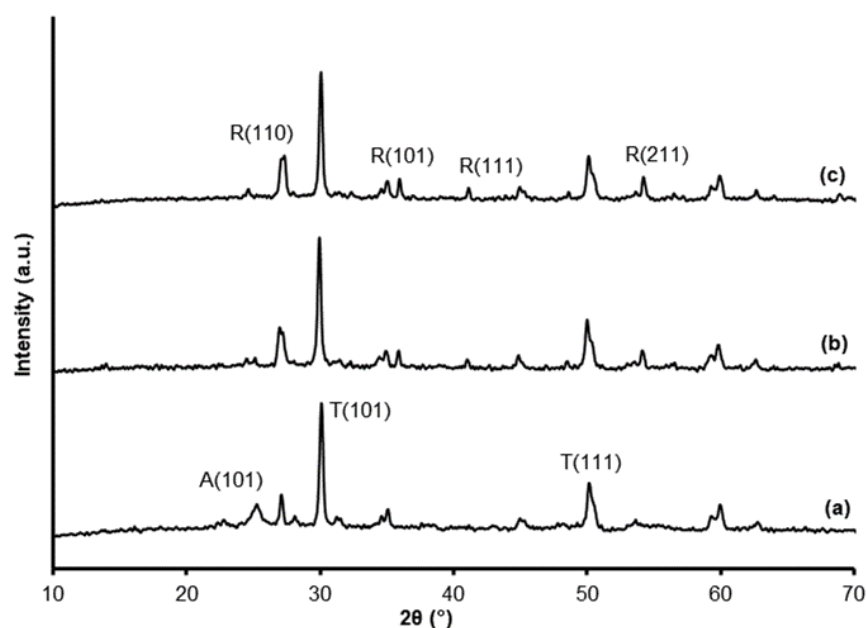


Fig. 2. Diffraction patterns of 5Fe-10N-ZT (a) -500, (b) -700, and (c) -900

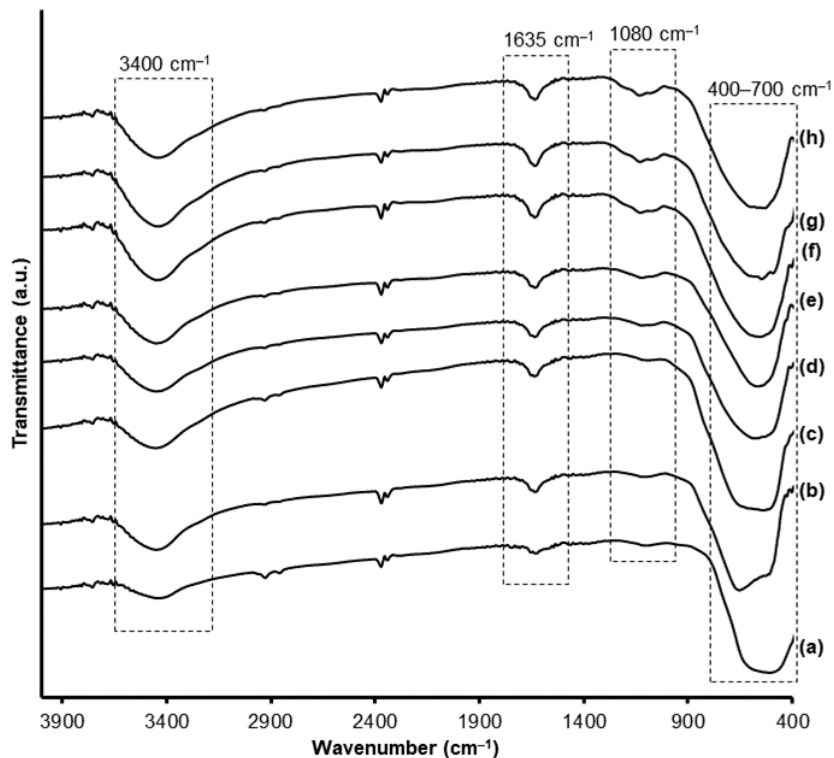


Fig 3. FT-IR spectra of (a) ZrO_2 , (b) TiO_2 , (c) 10N-ZT-500, (d) 1Fe-, (e) 3Fe-, (f) 5Fe-, (g) 7Fe-, and (h) 9Fe-10N-ZT-500

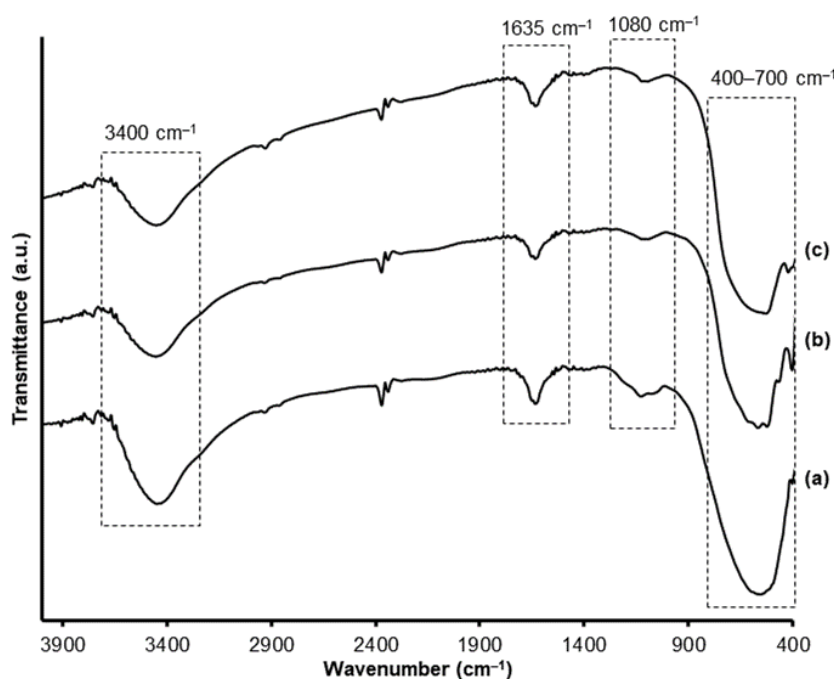


Fig 4. FTIR spectra of 5Fe-10N-ZT (a) -500, (b) -700, and (c) -900

calcination. The band of iron dopants at 1080 cm^{-1} decreases as the calcination temperature rises. This might be because the iron dopants are sintered at higher

temperatures, lowering the Fe–O vibration. A sharp tip was noticed at 508 cm^{-1} after calcination at 700 and 900 °C, attributed to vibrations of the O–Ti–N or

N–Ti–N bonds. At a calcination temperature of 500 °C, the peak is less significant. Thus, it suggests that the Ti–N bond has not formed at 500 °C [42].

Table 3 lists the calculated bandgap (E_g) of various Fe-10N-ZT composites with TiO_2 as a reference. The bandgap was determined by analyzing the UV-Vis absorption spectra shown in Fig. 5. The regression method was used to obtain the turning point as the minimum absorbance, which will be calculated for the bandgap. All Fe-10N-ZT composites have E_g values below pure TiO_2 (3.12 eV). This proves that the presence of Fe and N dopants allows the absorption edge to shift to the visible light region (wavelength > 400 nm). It can be seen that the bandgap energy value of all Fe-10N-ZT samples is lower than that of 10N-ZT-500. The addition of 3 of wt.% Fe and 10 of wt.% N dopants is the optimal condition that gives the lowest bandgap value of 2.62 eV. The bandgap values increased as Fe content increased from 3 to 9 wt.% with a fixed amount of nitrogen. This might be owing to the agglomeration of iron that eliminates the doping effect. The result proves that codoping of ZrTiO_4 with Fe and N gives a significantly lower E_g value compared to the results of single transition metal doping in the previous work [30–33]. Possibly, this result occurred due to the contribution of Fe 3d and N 2p orbitals forming a new electron state above VB in the crystal lattice [43].

After calcined at 700 and 900 °C, the bandgap of 5Fe-10N-ZT showed a lower value. Based on the diffraction data, it can be seen that the TiO_2 phase transformation from anatase to rutile occurs at 700 °C. The rutile phase has a lower bandgap value than anatase, thus increasing the calcination temperature decreases the bandgap value. However, at 900 °C, the value of E_g is greater (2.81 eV) than at 700 °C (2.79 eV). This is probably because of the sintering effect, which leads to dopant agglomeration so that the dopant effect diminishes.

The morphology and particle size of the composites were identified through characterization by SEM-EDX. SEM images of ZrO_2 and 3Fe-10N-ZT-500 materials with a magnification of 15,000 times are shown in Fig. 6, along with their respective EDX spectra. Uniformly and spherical morphologies are seen in both the 3Fe-10N-ZT-500 and

Table 3. Bandgap data of various Fe-10N-ZT composites and TiO_2

Material	E_g (eV)
TiO_2	3.12
10N-ZT-500	2.78
1Fe-10N-ZT-500	2.67
3Fe-10N-ZT-500	2.62
5Fe-10N-ZT-500	2.82
5Fe-10N-ZT-700	2.79
5Fe-10N-ZT-900	2.81
7Fe-10N-ZT-500	2.88
9Fe-10N-ZT-500	2.91

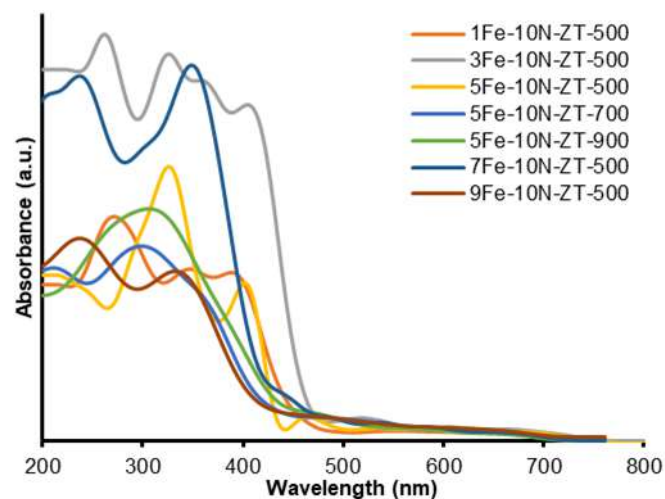


Fig 5. UV-Vis absorption spectra of various Fe-10N-ZT composites

and ZrO_2 . There are agglomerations in some locations due to calcination. The 3Fe-10N-ZT-500 composite has a coarser surface than pure ZrO_2 , while the particle size is similar with an estimated diameter of 0.2 μm .

The mass percentage of each element by EDX analysis is shown in Table 4. The results of the EDX spectra prove the presence of the main elements of the synthesized material. Ti is present on the surface of ZrO_2 , indicated by the Zr-to-O ratio of 3Fe-10N-ZT-500 to be lower than that of ZrO_2 . The 3Fe-10N-ZT-500 composite contained 1.5 and 2.8 wt.% of Fe and N dopants, respectively. Low quantities of dopants were used because a high amount of dopant may act as a recombination sites for photogenerated charges, decreasing the photocatalytic activity [44]. Despite the fact that the percentage is small, it does influence the

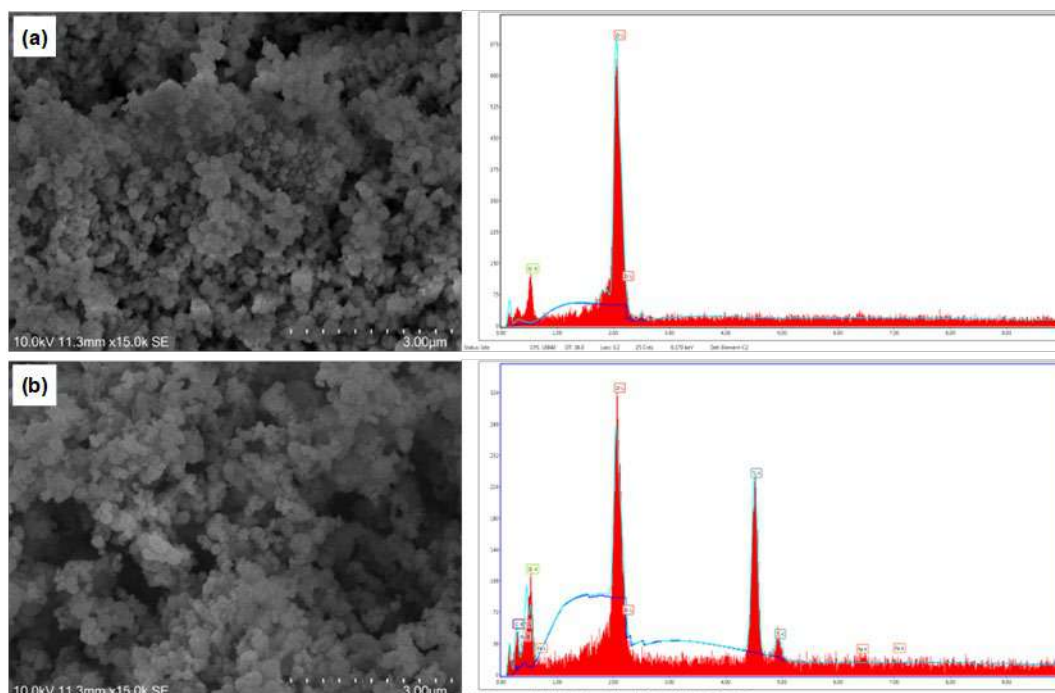


Fig 6. SEM images captured with 15,000× magnification and the corresponding EDX spectra of (a) ZrO_2 and (b) 3Fe-10N-ZT-500

Table 4. Elemental composition of ZrO_2 and 3Fe-10N-ZT-500 surfaces measured by X-ray energy dispersive spectroscopy

Material	% Mass						Total
	Zr	O	Ti	Fe	N	C	
ZrO_2	52.8	47.2	-	-	-	-	100
3Fe-10N-ZT-500	19.7	43.8	15.1	1.5	2.8	17.2	100

crystallite structure and light absorption of the material, as shown by XRD and SR-UV characterization.

■ CONCLUSION

The Fe,N-codoped $ZrTiO_4$ composites were successfully prepared through the sol-gel method. The incorporation of Fe and N dopants into $ZrTiO_4$ shifts the bandgap to the visible region and influences the crystal phase transformation. The composite with the lowest bandgap (2.62 eV) was obtained with 3 wt.% of Fe and 10 wt.% of N contents calcined at 500 °C. Furthermore, the XRD analysis proves that the presence of ZrO_2 prevents the anatase-to-rutile transformation at higher calcination temperatures than 500 °C. Fe,N-codoped $ZrTiO_4$ can be considered as a potentially active photocatalyst under visible light.

■ REFERENCES

- [1] Huang, W.C., and Ting, J.M., 2017, Novel nitrogen-doped anatase TiO_2 mesoporous bead photocatalysts for enhanced visible light response, *Ceram. Int.*, 43 (13), 9992–9997.
- [2] Zhang, J., Li, L., Xiao, Z., Liu, D., Wang, S., Zhang, J., Hao, Y., and Zhang, W., 2016, Hollow sphere TiO_2 - ZrO_2 prepared by self-assembly with polystyrene colloidal template for both photocatalytic degradation and H_2 evolution from water splitting, *ACS Sustainable Chem. Eng.*, 4 (4), 2037–2046.
- [3] Song, J., Wang, X., Bu, Y., Wang, X., Zhang, J., Huang, J., Ma, R.R., and Zhao, J., 2017, Photocatalytic enhancement of floating

- photocatalyst: Layer-by-layer hybrid carbonized chitosan and Fe-N-codoped TiO₂ on fly ash cenospheres, *Appl. Surf. Sci.*, 391, 236–250.
- [4] Kalantari, K., Kalbasi, M., Sohrabi, M., and Royae, S.J., 2017, Enhancing the photocatalytic oxidation of dibenzothiophene using visible light responsive Fe and N co-doped TiO₂ nanoparticles, *Ceram. Int.*, 43 (1), 973–981.
- [5] Zhang, J., Zhou, P., Liu, J., and Yu, J., 2014, New understanding of the difference of photocatalytic activity among anatase, rutile and brookite TiO₂, *Phys. Chem. Chem. Phys.*, 16 (38), 20382–20386.
- [6] Lin, H.Y., and Shih, C.Y., 2015, Efficient one-pot microwave-assisted hydrothermal synthesis of M (M = Cr, Ni, Cu, Nb) and nitrogen co-doped TiO₂ for hydrogen production by photocatalytic water splitting, *J. Mol. Catal. A: Chem.*, 411, 128–137.
- [7] Wang, J., Zhao, Y.F., Wang, T., Li, H., and Li, C., 2015, Photonic, and photocatalytic behavior of TiO₂ mediated by Fe, Co, Ni, N doping and co-doping, *Phys. B*, 478, 6–11.
- [8] Zou, M., Feng, L., Ganeshraja, A.S., Xiong, F., and Yang, M., 2016, Defect induced nickel, nitrogen-codoped mesoporous TiO₂ microspheres with enhanced visible light photocatalytic activity, *Solid State Sci.*, 60, 1–10.
- [9] Barkhade, T., and Banerjee, I., 2019, Optical properties of Fe doped TiO₂ nanocomposites synthesized by sol-gel technique, *Mater. Today: Proc.*, 18, 1204–1209.
- [10] Zhang, Y., Shen, Y., Gu, F., Wu, M., Xie, Y., and Zhang, J., 2009, Influence of Fe ions in characteristics and optical properties of mesoporous titanium oxide thin films, *Appl. Surf. Sci.*, 256 (1), 85–89.
- [11] Basavarajappa, P.S., Patil, S.B., Ganganagappa, N., Reddy, K.R., Raghu, A.V., and Reddy, C.V., 2020, Recent progress in metal-doped TiO₂, non-metal doped/codoped TiO₂ and TiO₂ nanostructured hybrids for enhanced photocatalysis, *Int. J. Hydrogen Energy*, 45 (13), 7764–7778.
- [12] Cong, Y., Zhang, J., Chen, F., and Anpo, M., 2007, Synthesis and characterization of nitrogen-doped TiO₂ nanophotocatalyst with high visible light activity, *J. Phys. Chem. C*, 111 (19), 6976–6982.
- [13] Shen, J.H., Tang, Y.H., Jiang, Z.W., Liao, D.Q., and Horng, J.J., 2021, Optimized preparation and characterization of Co-N codoped TiO₂ with enhanced visible light activity: An insight into effect of dopants on surface redox reactions of photogenerated charge carriers for hydroxyl radical formation, *J. Alloys Compd.*, 862, 158697.
- [14] Linnik, O., Shestopal, N., Smirnova, N., Eremenko, A., Korduban, O., Kandyba, V., Kryshchuk, T., Socol, G., Stefan, N., Popescu-Pelin, G., Ristoscu, C., and Mihailescu, I.N., 2015, Correlation between electronic structure and photocatalytic properties of non-metal doped TiO₂/ZrO₂ thin films obtained by pulsed laser deposition method, *Vacuum*, 114, 166–171.
- [15] Sinhmar, A., Setia, H., Kumar, V., Sobti, A., and Toor, A.P., 2020, Enhanced photocatalytic activity of nickel and nitrogen codoped TiO₂ under sunlight, *Environ. Technol. Innovation*, 18, 100658.
- [16] Farkas, B., Budai, J., Kabalci, I., Heszler, P., and Geretovszky, Z., 2008, Optical characterization of PLD grown nitrogen-doped TiO₂ thin films, *Appl. Surf. Sci.*, 254 (11), 3484–3488.
- [17] Di Valentin, C., Pacchioni, G., and Selloni, A., 2004, Origin of the different photoactivity of N-doped anatase and rutile TiO₂, *Phys. Rev. B: Condens. Matter Mater. Phys.*, 70 (8), 085116.
- [18] Gurushantha, K., Anantharaju, K.S., Nagabhushana, H., Sharma, S.C., Vidya, Y.S., Shivakumara, C., Nagaswarupa, H.P., Prashantha, S.C., and Anilkumar, M.R., 2015, Facile green fabrication of iron-doped cubic ZrO₂ nanoparticles by *Phyllanthus acidus*: Structural, photocatalytic and photoluminescent properties, *J. Mol. Catal. A: Chem.*, 397, 36–47.
- [19] de Moraes, N.P., de Azeredo, C.A.S.H., Bacetto, L.A., da Silva, M.L.C.P., and Rodrigues, L.A., 2018, The effect of C-doping on the properties and photocatalytic activity of ZrO₂ prepared via sol-gel route, *Optik*, 165, 302–309.

- [20] Syoufian, A., Manako, Y., and Nakashima, K., 2015, Sol-gel preparation of photoactive srilankite-type zirconium titanate hollow spheres by templating sulfonated polystyrene latex particles, *Powder Technol.*, 280, 207–210.
- [21] Kim, J.Y., Kim, C.S., Chang, H.K., and Kim, T.O., 2010, Effects of ZrO₂ addition on phase stability and photocatalytic activity of ZrO₂/TiO₂ nanoparticles, *Adv. Powder Technol.*, 21 (2), 141–144.
- [22] Chang, S.M., and Doong, R.A., 2006, Characterization of Zr-doped TiO₂ nanocrystals prepared by a nonhydrolytic sol-gel method at high temperatures, *J. Phys. Chem. B*, 110 (42), 20808–20814.
- [23] Wan, L., Gao, Y., Xia, X.H., Deng, Q.R., and Shao, G., 2011, Phase selection and visible light photo-catalytic activity of Fe-doped TiO₂ prepared by the hydrothermal method, *Mater. Res. Bull.*, 46 (3), 442–446.
- [24] Kumar, K.D., Kumar, G.P., and Reddy, K.S., 2015, Rapid microwave synthesis of reduced graphene oxide-supported TiO₂ nanostructures as high performance photocatalyst, *Mater. Today: Proc.*, 2 (4-5), 3736–3742.
- [25] Abdelhaleem, A., Chu, W., and Liang, X., 2019, Diphenamid degradation via sulfite activation under visible LED using Fe (III) impregnated N-doped TiO₂ photocatalyst, *Appl. Catal., B*, 244, 823–835.
- [26] Saidani, T., Zaabat, M., Aida, M.S., Benaboud, A., Benzitouni, S., and Boudine, A., 2014, Influence of annealing temperature on the structural, morphological and optical properties of Cu doped ZnO thin films deposited by the sol-gel method, *Superlattices Microstruct.*, 75, 47–53.
- [27] Sharon, M., Modi, F., and Sharon, M., 2016, Titania based nanocomposites as a photocatalyst: A review, *AIMS Mater. Sci.*, 3 (3), 1236–1254.
- [28] Aba-Guevara, C.G., Medina-Ramírez, I.E., Hernández-Ramírez, A., Jáuregui-Rincón, J., Lozano-Álvarez, J.A., and Rodríguez-López, J.L., 2017, Comparison of two synthesis methods on the preparation of Fe, N-Co-doped TiO₂ materials for degradation of pharmaceutical compounds under visible light, *Ceram. Int.*, 43 (6), 5068–5079.
- [29] Ning, Q., Zhang, L., Liu, C., Li, X., Xu, C., and Hou, X., 2021, Boosting photogenerated carriers for organic pollutant degradation via in-situ constructing atom-to-atom TiO₂/ZrTiO₄ heterointerface, *Ceram. Int.*, 47 (23), 33298–33308.
- [30] Kurniawan, R., Sudiono, S., Trisunaryanti, W., and Syoufian, A., 2019, Synthesis of iron-doped zirconium titanate as a potential visible-light responsive photocatalyst, *Indones. J. Chem.*, 19 (2), 454–460.
- [31] Andita, K.R., Kurniawan, R., and Syoufian, A., 2019, Synthesis and characterization of Cu-doped zirconium titanate as a potential visible-light responsive photocatalyst, *Indones. J. Chem.*, 19 (3), 761–766.
- [32] Alifi, A., Kurniawan, R., and Syoufian, A., 2020, Zinc-doped titania embedded on the surface of zirconia: A potential visible-responsive photocatalyst material, *Indones. J. Chem.*, 20 (6), 1374–1381.
- [33] Sulaikhah, E.F., Kurniawan, R., Pradipta, M.F., Trisunaryanti, W., and Syoufian, A., 2020, Cobalt doping on zirconium titanate as a potential photocatalyst with visible-light-response, *Indones. J. Chem.*, 20 (4), 911–918.
- [34] Lee, H.U., Lee, S.C., Choi, S., Son, B., Lee, S.M., Kim, H.J., and Lee, J., 2013, Efficient visible-light induced photocatalysis on nanoporous nitrogen-doped titanium dioxide catalysts, *Chem. Eng. J.*, 228, 756–764.
- [35] Wang, Q., Jin, R., Zhang, M., and Gao, S., 2017, Solvothermal preparation of Fe-doped TiO₂ nanotube arrays for enhancement in visible light induced photoelectrochemical performance, *J. Alloys Compd.*, 690, 139–144.
- [36] Suwannaruang, T., Hildebrand, J.P., Taffa, D.H., Wark, M., Kamonsuangkasem, K., Chirawatkul, P., and Wantala, K., 2020, Visible light-induced degradation of antibiotic ciprofloxacin over Fe–N–TiO₂ mesoporous photocatalyst with

- anatase/rutile/brookite nanocrystal mixture, *J. Photochem. Photobiol., A*, 391, 112371.
- [37] Suwannaruang, T., Kidkhunthod, P., Chanlek, N., Soontaranon, S., and Wantala, K., 2019, High anatase purity of nitrogen-doped TiO₂ nanorice particles for the photocatalytic treatment activity of pharmaceutical wastewater, *Appl. Surf. Sci.*, 478, 1–14.
- [38] Realpe Jimenez, A., Nuñez, D., Rojas, N., Ramirez, Y., and Acevedo, M., 2021, Effect of Fe–N codoping on the optical properties of TiO₂ for use in photoelectrolysis of water, *ACS Omega*, 6 (7), 4932–4938.
- [39] Arafati, A., Borhani, E., Nourbakhsh, S.M.S., and Abdoos, H., 2019, Synthesis and characterization of tetragonal/monoclinic mixed phases nanozirconia powders, *Ceram. Int.*, 45 (10), 12975–12982.
- [40] Di, K., Zhu, Y., Yang, X., and Li, C., 2006, Electrorheological behavior of urea-doped mesoporous TiO₂ suspensions, *Colloids Surf., A*, 280 (1-3), 71–75.
- [41] Neppolian, B., Wang, Q., Yamashita, H., and Choi, H., 2007, Synthesis and characterization of ZrO₂-TiO₂ binary oxide semiconductor nanoparticles: Application and interparticle electron transfer process, *Appl. Catal., A*, 333 (2), 264–271.
- [42] Nolan, N.T., Synnott, D.W., Seery, M.K., Hinder, S.J., Van Wassenhoven, A., and Pillai, S.C., 2012, Effect of N-doping on the photocatalytic activity of sol-gel TiO₂, *J. Hazard. Mater.*, 211-212, 88–94.
- [43] Li, Z., Wang, X., Jia, L., and Chi, B., 2014, Synergistic effect in Fe/N co-doped anatase TiO₂ (101) surface and the adsorption of di-, tri- and polyatomic gases: A DFT investigation, *J. Mol. Struct.*, 1061, 160–165.
- [44] Jaiswal, R., Bharambe, J., Patel, N., Dashora, A., Kothari, D.C., and Miotello, A., 2015, Copper and nitrogen co-doped TiO₂ photocatalyst with enhanced optical absorption and catalytic activity, *Appl. Catal., B*, 168-169, 333–341.

Design, Synthesis, and Anti-mycobacterial Evaluation of New 3,5-Disubstituted-pyrazole-1-carbothioamides

Kok Tong Wong¹, Hasnah Osman¹, Thaigarajan Parumasivam², Muhammad Solehin Abd Ghani¹, Mohd. Zaheen Hassan^{1,3}, Unang Supratman⁴, and Mohamad Nurul Azmi Mohamad Taib^{1*}

¹School of Chemical Sciences, Universiti Sains Malaysia, 11800 Minden, Penang, Malaysia

²School of Pharmaceutical Sciences, Universiti Sains Malaysia, 11800 Minden, Penang, Malaysia

³College of Pharmacy, King Khalid University, Abha, Kingdom of Saudi Arabia

⁴Department of Chemistry, Faculty of Mathematics and Natural Sciences, Universitas Padjadjaran, Jatinangor 45363, Indonesia

* **Corresponding author:**

tel: +60-4653-3562

email: mnazmi@usm.my

Received: November 5, 2021

Accepted: February 9, 2022

DOI: 10.22146/ijc.70243

Abstract: Two series of new 3,5-disubstituted-pyrazole-1-carbothioamides (**4a-f** and **5a-e**) were designed and synthesized through condensation reaction between chalcones and thiosemicarbazides under alkaline condition via cyclocondensation reaction. The structures have been elucidated by Fourier-transform infrared (FTIR), High-resolution mass spectrometry (HRMS), one- and two-dimensional nuclear magnetic resonance (NMR) analyses. These compounds were assayed for in vitro anti-tuberculosis activity against *Mycobacterium tuberculosis* H37Ra using the Tetrazolium microplate assay (TEMA) method. As a result, six compounds (i.e., **4a**, **4d**, **4f**, **5a**, **5c**, and **5d**) showed a weak activity with minimum inhibition concentration (MIC) between 650–530 μ M, and other compounds showed no inhibition against MTB. In addition, all tested compounds also did not show any cidal effects for minimum bactericidal concentration (MBC), even at the highest test concentration.

Keywords: 3,5-disubstituted-pyrazole-1-carbothioamide; pyrazolines; *Mycobacterium tuberculosis*; antitubercular agents; anti-mycobacterial

■ INTRODUCTION

Tuberculosis (TB) is one of the global major health problems, in which these microbial infections could potentially cause the death of human beings. Although its incidence has been diminished significantly in the industrially more developed countries, it remains out of control in many developing nations [1]. It was estimated that 1.3 million lives among human immunodeficiency virus (HIV)-negative people died of TB in 2016, which surpassed the number of deaths caused by HIV. In addition, about 374,000 death cases of TB were coinfecting with HIV [2]. In 2006, Corbett et al. reported that the emergence of anti-TB resistance and HIV are vital contributors to death by TB [3]. Recently, several drugs in the market were used for TB treatment, including isoniazid (INH), rifampicin, pyrazinamide, and delamanid,

all of which possess a nitrogen atom in their ring structure [4]. The problem is commonly known that *Mycobacterium tuberculosis* (MTB) has developed resistance to any of these drugs [5]. Oxygen and nitrogen-containing heterocyclic moieties have been reported as active compounds against herpes simplex virus-1 (HSV), and HIV thus exhibited a potential diversity of biological activities [6-9]. In particular, electron-rich nitrogen heterocycles play a vital role in various pharmacological activities [10]. Pyrazoline was first discovered by Knorr in the year 1883 [11-12]. Pyrazolines are dihydropyrazole, heterocycles having an endocyclic double bond with two adjacent nitrogen atoms at positions 1- and 2- within the five-membered ring, are the most studied group of compounds in the azole family [13]. Pyrazoline derivatives are reported as new potent compounds possessing biological activities;

anticancer [14], antimalarial [15], antitumor [16], anti-cardiovascular [17], monoamine oxidase (MAO) inhibitors [18-19], antiamebic [20], and anticonvulsant activities [21-23]. Meanwhile, a previous study reported that a new set of pyrazoline derivatives were synthesized and exhibited significant anti-mycobacterial activity [24]. This information has prompted us to synthesize a new pyrazoline derivative with possible anti-TB activity against MTB H37Ra. These derivatives may reduce the duration of the TB therapy and consequently minimize the adverse effects of the medication.

■ EXPERIMENTAL SECTION

Materials

Chemicals were purchased from Sigma-Aldrich Co., Acros Organics, QReC, and Merck Chemical Co. All chemicals and solvents were of reagent grade and were used without further purification. Column chromatography was performed using Merck silica gel (40–63 μm).

Instrumentation

The reactions were monitored on Merck pre-coated aluminum Thin-layer chromatography (TLC) plates 60 F254, and the products were visualized under a UV radiation lamp ($\lambda_{\text{max}} = 254 \text{ nm}$). Melting points were determined on open capillary tubes. Infrared (FTIR-ATR) spectra were recorded on a Perkin-Elmer RX1 spectrometer. Bruker Advance 500 MHz FT-NMR spectrometer (Bruker Bioscience, Billerica, MA, USA) equipped with ultra-shield were recorded the NMR analyses of ^1H (500 MHz) and ^{13}C (125 MHz) using CDCl_3 and CD_3COCD_3 as the solvents and tetramethylsilane (TMS) as internal standard. Chemical shifts were reported in part per million (δ -scale), and the coupling constants J are reported in Hertz (Hz). The HRMS mass spectra were obtained from the Waters Xevo QTOF MS system.

Procedure

General procedure for preparation of chalcone derivatives

All the synthesized chalcone derivatives (**3a-f**) were prepared through Claisen-Schmidt condensation. A mixture of acetophenone (**1**) (1.17 mL, 0.01 mol) and

benzaldehydes (**2a-f**) (0.015 mol) was dissolved in methanol (10 mL) and refluxed in the presence of piperidine for 72 h [25-26]. After filtration, the solid was washed, recrystallized, and dried to give the desired chalcone derivatives (**3a-f**). The spectroscopic data were compared with the literature (Refer supporting information) [27-30].

General procedure for the preparation of 3,5-disubstituted-pyrazole-1-carbothioamide (**4a-f** and **5a-e**)

The reaction scheme was depicted in Scheme 1. In a round-bottomed flask, chalcone derivatives (**3a-f**) (1 mmol) and 4-methyl-3-thiosemicarbazide (0.1576 g, 1.5 mmol)/4-ethyl-3-thiosemicarbazide (0.1788 g, 1.5 mmol) were dissolved in ethanol (6 mL). The reaction mixture was then heated and stirred. Sodium hydroxide (0.12 g, 3 mmol) was then slowly added to the reaction mixture and continued refluxed under vigorous stirring for 3–8 h at 100 °C. Upon completing, the mixture was allowed to cool and stirred at room temperature overnight. On the next day, crushed ice was added into the reaction mixture to precipitate the final products. The precipitate was filtered and dried at room temperature. Purification by column chromatography using silica gel (*n*-hexane:ethyl acetate) or recrystallization with ethanol to afford compounds **4a-f** and **5a-e**.

Spectral data for synthesized compounds

5-(4-methylphenyl)-*N*-methyl-3-phenyl-4,5-dihydro-1*H*-pyrazole-1-carbothioamide (**4a**).

Yellowish crystals; yield: 0.0845 g (26%); mp: 180–184 °C; FTIR (ATR) $\nu_{\text{max}} \text{ cm}^{-1}$: 3361 (N–H), 3042 (C_{sp^2} –H), 2958 (C_{sp^3} –H), 1516, 1427 (aromatic C=C), 1403 (C=S); ^1H -NMR (δ /ppm, 500 MHz, CDCl_3): δ 2.32 (3H, s, 9- CH_3), 3.18 (1H, dd, $J = 4.0 \text{ Hz}$ and 17.5 Hz , 4 α - CH), 3.22 (3H, s, 8- CH_3), 3.81 (1H, dd, $J = 11.5 \text{ Hz}$ and 17.5 Hz , 4 β - CH), 6.07 (1H, dd, $J = 3.5 \text{ Hz}$ and 11.5 Hz , 5- CH), 7.14 (4H, m, H-2', H-3', H-5' and H-6'), 7.45 (3H, m, H-3'', H-4'' and H-5''), 7.74 (2H, dd, $J = 1.5 \text{ Hz}$ and 7.5 Hz , H-2'' and H-6''); ^{13}C -NMR (δ /ppm, 125 MHz, CDCl_3): δ 21.1 (9- CH_3), 31.4 (8- CH_3), 42.6 (4- CH_2), 63.3 (5- CH), 125.4 (C-2'' and C-6''), 126.8 (C-2' and C-6'), 128.8 (C-3'' and C-5''), 129.5 (C-3' and C-5'), 130.7 (C-4''), 131.1 (C-1''), 137.1 (C-4'), 139.6 (C-1'), 154.4 (3- $\text{C}=\text{N}$), 177.0

(6-C=S); HRMS: 310.1380 [M+H]⁺ {calcd. 309.1378 for C₁₈H₂₀N₃S}.

5-(4-methoxyphenyl)-N-methyl-3-phenyl-4,5-dihydro-1H-pyrazole-1-carbothioamide (4b).

Yellowish crystals; yield: 0.1528 g (47%); mp: 152–155 °C; FTIR (ATR) ν_{\max} cm⁻¹: 3371 (N-H), 3066 (C_{sp}²-H), 2997 (C_{sp}³-H), 1614 (C=N), 1510, 1428 (aromatic C=C), 1402 (C=S), 1246 (C-O); ¹H-NMR (δ /ppm, 500 MHz, CDCl₃): δ 3.19 (4H, m, 4 α -CH and 8-CH₃), 3.79 (4H, m, 4 β -CH and 9-OCH₃), 6.05 (1H, dd, J = 3.5 Hz and 11.5 Hz, 5-CH), 6.86 (2H, d, J 9.0 Hz, H-3' and H-5'), 7.18 (2H, d, J = 8.5 Hz, H-2' and H-6'), 7.45 (3H, m, H-3'', H-4'' and H-5''), 7.75 (2H, dd, J = 1.5 Hz and 7.5 Hz, H-2'' and H-6''); ¹³C-NMR (δ /ppm, 125 MHz, CDCl₃): δ 31.4 (8-CH₃), 42.5 (4-CH₂), 55.2 (9-OCH₃), 63.0 (5-CH), 114.2 (C-3' and C-5'), 126.8 (C-2' and C-6'), 126.8 (C-2'' and C-6''), 128.8 (C-3'' and C-5''), 130.7 (C-4''), 131.1 (C-1''), 134.7 (C-1'), 154.5 (3-C=N), 158.9 (C-4'); HRMS: 326.1326 [M+H]⁺ {calcd. 326.1327 for C₁₈H₂₀N₃OS}.

5-(4-chlorophenyl)-4,5-dihydro-N-methyl-3-phenyl-1H-pyrazole-1-carbothioamide (4c). Yellow powder; yield: 0.1924 g (53%); mp: 184–188 °C; FTIR (ATR) ν_{\max} cm⁻¹: 3358 (N-H), 3041 (C_{sp}²-H), 1594 (C=N), 1522, 1429 (aromatic C=C), 1402 (C=S); ¹H-NMR (δ /ppm, 500 MHz, CDCl₃): δ 3.15 (1H, dd, J 4.0 Hz and 17.5 Hz, 4 α -CH), 3.21 (3H, d, J = 4.5 Hz, 8-CH₃), 3.83 (1H, dd, J 11.5 Hz and 18.0 Hz, 4 β -CH), 6.06 (1H, dd, J = 4.0 Hz and 11.5 Hz, 5-CH), 7.18 (2H, d, J 8.5 Hz, H-2' and H-6'), 7.30 (2H, m, H-3' and H-5'), 7.46 (3H, m, H-3'', H-4'' and H-5''), 7.74 (2H, dd, J = 1.0 Hz and 8.0 Hz, H-2'' and H-6''); ¹³C-NMR (δ /ppm, 125 MHz, CDCl₃): δ 31.4 (8-CH₃), 42.4 (4-CH₂), 62.9 (5-CH), 126.8 (C-2'' and C-6''), 127.0 (C-2' and C-6'), 128.9 (C-3'' and C-5''), 129.0 (C-3' and C-5'), 130.8 (C-4''), 130.8 (C-1''), 133.2 (C-4'), 141.0 (C-1'), 154.3 (3-C=N), 177.1 (6-C=S); HRMS: 352.0646 [M+Na]⁺ {calcd. 352.0651 for C₁₇H₁₆ClN₃SNa}.

5-(2,4-dichlorophenyl)-4,5-dihydro-N-methyl-3-phenyl-1H-pyrazole-1-carbothioamide (4d).

Yellowish crystals; yield: 0.3051 g (84%); mp: 166–170 °C; FTIR (ATR) ν_{\max} cm⁻¹: 3365 (N-H), 3064 (C_{sp}²-H), 2934 (C_{sp}³-H), 1592 (C=N), 1520, 1470 (aromatic C=C), 1399 (C=S); ¹H-NMR (δ /ppm, 500 MHz, CD₃COCD₃): δ 3.12 (3H, d, J 5.0 Hz, 8-CH₃), 3.17 (1H, dd, J = 4.5 Hz and 18.5

Hz, 4 α -CH), 4.07 (1H, dd, J = 12.0 Hz and 18.0 Hz, 4 β -CH), 6.27 (1H, dd, J = 4.5 Hz and 12.0 Hz, 5-CH), 7.07 (1H, d, J = 8.5 Hz, H-6'), 7.31 (1H, dd, J = 2.0 Hz and 8.0 Hz, H-5'), 7.46 (3H, m, H-3'', H-4'' and H-5''), 7.52 (1H, d, J = 2.5 Hz, H-3'), 7.87 (2H, dd, J = 1.5 Hz and 8.0 Hz, H-2'' and H-6''), 8.38 (1H, s, 7-NH); ¹³C-NMR (δ /ppm, 125 MHz, CD₃COCD₃): δ 30.9 (8-CH₃), 40.5 (4-CH₂), 61.1 (5-CH), 126.9 (C-2'' and C-6''), 127.4 (C-5' and C-6'), 128.7 (C-3'' and C-5''), 129.1 (C-3'), 130.5 (C-4''), 131.3 (C-1''), 132.0 (C-2'), 136.4 (C-4'), 139.5 (C-1'), 154.3 (3-C=N), 177.4 (6-C=S); HRMS: 364.0445 [M+H]⁺ {calcd. 364.0442 for C₁₇H₁₆Cl₂N₃S}.

5-(2-chlorophenyl)-4,5-dihydro-N-methyl-3-phenyl-1H-pyrazole-1-carbothioamide (4e).

Yellowish crystals; yield: 0.0400 g (12%); mp: 242–245 °C; FTIR (ATR) ν_{\max} cm⁻¹: 3366 (N-H), 3040 (C_{sp}²-H), 2937 (C_{sp}³-H), 1572 (C=N), 1523, 1471 (aromatic C=C), 1400 (C=S); ¹H-NMR (δ /ppm, 500 MHz, CDCl₃): δ 3.12 (3H, d, J = 5.0 Hz, 8-CH₃), 3.17 (1H, dd, J = 4.5 Hz and 18.5 Hz, 4 α -CH), 4.07 (1H, dd, J = 12.0 Hz and 18.0 Hz, 4 β -CH), 6.27 (1H, dd, J = 4.5 Hz and 12.0 Hz, 5-CH), 7.07 (1H, m, H-5'), 7.22 (2H, dd, J = 3.5 Hz and 7.5 Hz, H-3' and H-6'), 7.43 (4H, m, H-4', H-3'', H-4'' and H-5''), 7.75 (2H, dd, J = 1.5 Hz and 8.0 Hz, H-2'' and H-6''); ¹³C-NMR (δ /ppm, 125 MHz, CDCl₃): δ 31.0 (8-CH₃), 41.3 (4-CH₂), 61.3 (5-CH), 126.8 (C-2'' and C-6''), 127.2 (C-6'), 128.6 (C-3'), 128.8 (C-5', C-3'' and C-5''), 130.0 (C-4'), 130.8 (C-4''), 130.9 (C-2'), 131.3 (C-1''), 139.3 (C-1'), 154.7 (3-C=N), 176.1 (6-C=S); HRMS: 330.0816 [M+H]⁺ {calcd. 330.0832 for C₁₇H₁₇ClN₃S}.

5-(2-methoxyphenyl)-4,5-dihydro-N-methyl-3-phenyl-1H-pyrazole-1-carbothioamide (4f).

Light brown crystals; yield: 0.0549 g (17%); mp: 172–175 °C; FTIR (ATR) ν_{\max} cm⁻¹: 3380 (N-H), 3048 (C_{sp}²-H), 2835 (C_{sp}³-H), 1600 (C=N), 1518, 1432 (aromatic C=C), 1401 (C=S), 1237 (C-O); ¹H-NMR (δ /ppm, 500 MHz, CD₃COCD₃): δ 3.06 (1H, dd, J = 3.5 Hz and 18.0 Hz, 4 α -CH), 3.14 (3H, d, J = 4.5 Hz, 8-CH₃), 3.90 (3H, t, J = 7.5 Hz, 4 β -CH and 9-OCH₃), 6.26 (1H, dd, J = 3.5 Hz and 11.5 Hz, 5-CH), 6.84 (1H, t, J = 7.5 Hz, H-5'), 6.95 (1H, d, J = 7.5 Hz, H-3'), 7.01 (1H, d, J = 8.5 Hz, H-6'), 7.22 (1H, m, H-4'), 7.44 (3H, m, H-3'', H-4'' and H-5''), 7.84 (2H, dd, J = 1.5 Hz and 8.0 Hz, H-2'' and H-6''), 8.26

(1H, s, 7-NH); $^{13}\text{C-NMR}$ (δ/ppm , 125 MHz, CD_3COCD_3): δ 30.8 (8-CH₃), 41.0 (4-CH₂), 55.1 (9-OCH₃), 59.5 (5-CH), 111.0 (C-6'), 120.1 (C-5'), 125.7 (C-3'), 126.8 (C-2'' and C-6''), 128.1 (C-4'), 128.6 (C-3'' and C-5''), 130.2 (C-4''), 130.5 (C-1''), 131.7 (C-1'), 154.8 (3-C=N), 156.1 (C-2'), 176.1 (6-C=S); HRMS: 326.1325 [M+H]⁺ {calcd. 326.1327 for C₁₈H₂₀N₃OS}.

5-(4-methylphenyl)-4,5-dihydro-N-ethyl-3-phenyl-1H-pyrazole-1-carbothioamide (5a). Yellowish oil; yield: 0.1875 g (58%); FTIR (ATR) ν_{max} cm⁻¹: 3375 (N-H), 3022 (C_{sp}²-H), 2970 (C_{sp}³-H), 1571 (C=N), 1514, 1448 (aromatic C=C), 1407 (C=S); $^1\text{H-NMR}$ (δ/ppm , 500 MHz, CD_3COCD_3): δ 1.20 (3H, t, $J = 7.0$ Hz, 9-CH₃), 2.26 (3H, s, 10-CH₃), 3.14 (1H, dd, $J = 4.0$ Hz and 18 Hz, 4 α -CH), 3.66 (2H, m, 8-CH₂), 3.92 (1H, dd, $J = 11.5$ Hz and 17.5 Hz, 4 β -CH), 6.01 (1H, dd, $J = 4.0$ Hz and 11.5 Hz, 5-CH), 7.09 (4H, m, H-2', H-3', H-5', and H-6'), 7.44 (3H, m, H-3'', H-4'' and H-5''), 7.85 (2H, d, $J = 9.5$ Hz, H-2'' and H-6''), 8.21 (1H, s, 7-NH); $^{13}\text{C-NMR}$ (δ/ppm , 125 MHz, CD_3COCD_3): δ 14.1 (9-CH₃), 20.2 (10-CH₃), 38.9 (8-CH₂), 42.0 (4-CH₂), 63.3 (5-CH), 125.5 (C-2'' and C-6''), 126.8 (C-2', and C-6'), 128.7 (C-3'' and C-5''), 129.0 (C-3' and C-5'), 130.3 (C-4''), 131.6 (C-1''), 136.3 (C-4'), 140.6 (C-1'), 154.1 (3-C=N), 176.4 (6-C=S); HRMS: 324.1436 [M+H]⁺ {calcd. 324.1534 for C₁₉H₂₂N₃S}.

5-(4-methoxyphenyl)-4,5-dihydro-N-ethyl-3-phenyl-1H-pyrazole-1-carbothioamide (5b). Yellow crystals; yield: 0.1900 g (56%); mp: 145–148 °C; FTIR (ATR) ν_{max} cm⁻¹: 3324 (N-H), 3050 (C_{sp}²-H), 2979 (C_{sp}³-H), 1610 (C=N), 1525, 1445 (aromatic C=C), 1383 (C=S), 1245 (C-O); $^1\text{H-NMR}$ (δ/ppm , 500 MHz, CDCl_3): δ 1.31 (3H, t, $J = 7.5$ Hz, 9-CH₃), 3.17 (1H, dd, $J = 3.5$ Hz and 18.0 Hz, 4 α -CH), 3.76 (6H, m, 4 β -CH, 10-OCH₃ and 8-CH₂), 6.06 (1H, dd, $J = 3.5$ Hz and 11.5 Hz, 5-CH), 6.86 (2H, d, $J = 8.5$ Hz, H-3'' and H-5''), 7.17 (2H, d, $J = 8.5$ Hz, H-2' and H-6'), 7.45 (3H, m, H-3'', H-4'' and H-5''), 7.75 (2H, dd, $J = 2.0$ Hz and 7.5 Hz, H-2'' and H-6''); $^{13}\text{C-NMR}$ (δ/ppm , 125 MHz, CDCl_3): δ 14.6 (9-CH₃), 39.5 (8-CH₂), 42.5 (4-CH₂), 55.2 (10-OCH₃), 62.9 (5-CH), 114.2 (C-3' and C-5'), 126.8 (C-2', C-6', C-2'' and C-6''), 128.8 (C-3'' and C-5''), 130.7 (C-4''), 131.1 (C-1''), 134.7 (C-1'), 154.4 (3-C=N), 158.8 (C-4'), 175.9 (6-C=S); HRMS: 340.1490 [M+H]⁺ {calcd. 340.1484 for C₁₉H₂₂N₃OS}.

5-(4-chlorophenyl)-4,5-dihydro-N-ethyl-3-phenyl-1H-pyrazole-1-carbothioamide (5c). Yellowish needle; yield: 0.1874 g (55%); mp: 173–175 °C (lit. 164–166 °C) [31]; FTIR (ATR) ν_{max} cm⁻¹: 3375 (N-H), 3062 (C_{sp}²-H), 2927 (C_{sp}²-H), 1596 (C=N), 1518, 1445 (aromatic C=C), 1381 (C=S); $^1\text{H-NMR}$ (δ/ppm , 500 MHz, CDCl_3): δ 1.31 (3H, t, $J = 7.5$ Hz, 9-CH₃), 3.14 (1H, dd, $J = 3.5$ Hz and 18.0 Hz, 4 α -CH), 3.72 (2H, m, 8-CH₂), 3.82 (1H, dd, $J = 11.5$ Hz and 17.5 Hz, 4 β -CH), 6.07 (1H, dd, $J = 4.0$ Hz and 11.5 Hz, 5-CH), 7.18 (2H, d, $J = 8.5$ Hz, H-2' and H-6'), 7.30 (2H, t, $J = 8.5$ Hz, H-3' and H-5'), 7.46 (3H, m, H-3'', H-4'' and H-5''), 7.74 (2H, dd, $J = 2.0$ Hz and 8.0 Hz, H-2'' and H-6''); $^{13}\text{C-NMR}$ (δ/ppm , 125 MHz, CDCl_3): δ 14.5 (9-CH₃), 39.6 (8-CH₂), 42.3 (4-CH₂), 62.8 (5-CH), 126.8 (C-2'' and C-6''), 127.0 (C-2' and C-6'), 128.9 (C-3'' and C-5''), 129.0 (C-3' and C-5'), 130.8 (C-1'' and C-4''), 132.2 (C-4'), 142.1 (C-1'), 154.2 (3-C=N), 176.0 (6-C=S); HRMS: 344.1048 [M+H]⁺ {calcd. 344.0988 for C₁₈H₁₉ClN₃S}.

5-(2,4-dichlorophenyl)-4,5-dihydro-N-ethyl-3-phenyl-1H-pyrazole-1-carbothioamide (5d). Yellowish needle; yield: 0.1577 g (42%); mp: 136–139 °C; FTIR (ATR) ν_{max} cm⁻¹: 3364 (N-H), 3066 (C_{sp}²-H), 2931 (C_{sp}³-H), 1588 (C=N), 1518, 1446 (aromatic C=C), 1382 (C=S); $^1\text{H-NMR}$ (δ/ppm , 500 MHz, CD_3COCD_3): δ 1.23 (3H, t, $J = 7.0$ Hz, 9-CH₃), 3.16 (1H, dd, $J = 4.0$ Hz and 18.0 Hz, 4 α -CH), 3.68 (2H, m, 8-CH₂), 4.06 (1H, dd, $J = 12.0$ Hz and 18.0 Hz, 4 β -CH), 6.28 (1H, dd, $J = 4.5$ Hz and 12.0 Hz, 5-CH), 7.06 (1H, d, $J = 8.5$ Hz, H-6'), 7.31 (1H, dd, $J = 2.0$ Hz and 8.5 Hz, H-5'), 7.46 (3H, m, H-3'', H-4'' and H-5''), 7.52 (1H, d, $J = 2.0$ Hz, H-3'), 7.87 (2H, dd, $J = 1.5$ Hz and 8.0 Hz, H-2'' and H-6''), 8.38 (1H, s, 7-NH); $^{13}\text{C-NMR}$ (δ/ppm , 125 MHz, CD_3COCD_3): δ 14.0 (9-CH₃), 39.1 (8-CH₂), 40.5 (4-CH₂), 61.0 (5-CH), 126.9 (C-2'' and C-6''), 127.4 (C-6'), 128.7 (C-5', C-3'' and C-5''), 129.1 (C-3'), 130.5 (C-4''), 131.3 (C-1''), 131.9 (C-2'), 132.7 (C-4'), 139.5 (C-1'), 154.4 (3-C=N), 176.3 (6-C=S); HRMS: 378.0565 [M+H]⁺ {calcd. 378.0598 for C₁₈H₁₈Cl₂N₃S}.

5-(2-chlorophenyl)-4,5-dihydro-N-ethyl-3-phenyl-1H-pyrazole-1-carbothioamide (5e). Yellowish crystals; yield: 0.1521 g (44%); mp: 176–179 °C; FTIR (ATR) ν_{max} cm⁻¹: 3359 (N-H), 3055 (C_{sp}²-H), 2967 (C_{sp}³-

H), 1600 (C=N), 1520, 1445 (aromatic C=C), 1379 (C=S); $^1\text{H-NMR}$ (δ/ppm , 500 MHz, CDCl_3): δ 1.34 (3H, t, $J = 7.5$ Hz, 9- CH_3), 3.10 (1H, dd, $J = 4.0$ Hz and 17.5 Hz, 4 α - CH), 3.76 (2H, m, 8- CH_2), 3.91 (1H, dd, $J = 11.5$ Hz and 18.0 Hz, 4 β - CH), 6.40 (1H, dd, $J = 4.0$ Hz and 12.0 Hz, 5- CH), 7.07 (1H, m, H-5'), 7.22 (2H, dd, $J = 3.5$ Hz and 7.5 Hz, H-3' and H-6'), 7.43 (4H, m, H-4', H-3'', H-4'' and H-5''), 7.75 (2H, dd, $J = 1.5$ Hz and 8.0 Hz, H-2'' and H-6''); $^{13}\text{C-NMR}$ (δ/ppm , 125 MHz, CDCl_3): δ 14.6 (9- CH_3), 39.6 (8- CH_2), 41.3 (4- CH_2), 61.3 (5- CH), 126.8 (C-2'' and C-6''), 127.2 (C-6'), 128.6 (C-3'), 128.8 (C-5', C-3'' and C-5''), 130.0 (C-4'), 130.8 (C-4''), 130.9 (C-2'), 131.3 (C-1''), 139.3 (C-1'), 154.7 (3- $\text{C}=\text{N}$), 176.1 (6- $\text{C}=\text{S}$); HRMS: 344.0909 $[\text{M}+\text{H}]^+$ {calcd. 344.0988 for $\text{C}_{18}\text{H}_{19}\text{ClN}_3\text{S}$ }.

Screening of anti-tuberculosis activity against *M. tuberculosis* H37Ra

The Tetrazolium microplate assay (TEMA) method was performed to evaluate the anti-mycobacterial activity of the derivatives as described by Amilah et al. [32] with minor modification. The assay was carried out in 96-well plates in duplicate and at least three times independently. The derivatives were dissolved in DMSO and serially diluted to the desired concentration in complete Middlebrook 7H9 media to reduce the DMSO concentration below 1%. A log phase MTB ATCC 25177 was added and incubated at 37 °C and 5% CO_2 for 5 days. On the fifth day, 50 μL of tetrazolium reagent mixture was added into all wells and re-incubated for 24 h. The MIC is defined as the lowest drug concentration that prevented the color change from yellow to purple. A small volume of the culture from the 96-well plate was transferred into Middlebrook 7H10 agar media, and the plates were incubated at 37 °C and 5% CO_2 for 28 days. The MBC is defined as the lowest concentration of compound that did not show any bacterial colonies.

Molecular docking studies

Molecular docking studies were performed using AutoDock v. 4.2.2 to identify appropriate binding modes and the conformation of the ligand molecule. The crystal structure of dihydrofolate reductase complexed with novel 7-aryl-2,4-diaminoquinazolines (PDB code: 3SRQ) was retrieved from the RCSB protein data bank in PDB format [33]. The structures of all the ligands were drawn

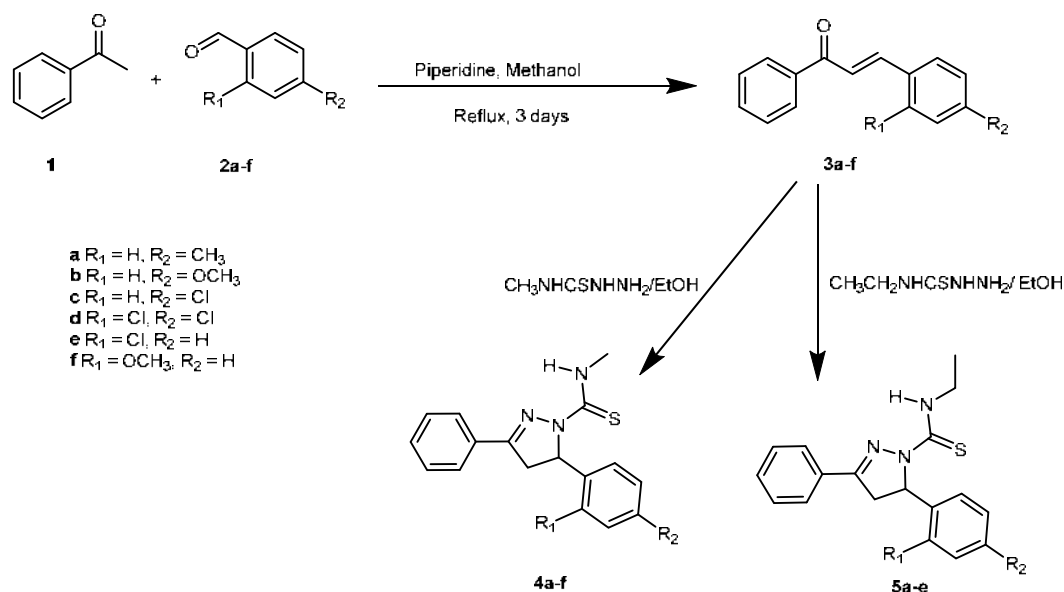
using ChemDraw Ultra 13.0 and converted into 3D structures using Hyperchem Pro 8.0 software (www.hyper.com). Autodock Tools (ADT) version 1.5.6 (www.autodock.scrips.edu) was used for molecular docking. The active site was considered as a rigid molecule, while the ligands were treated as being flexible. Using default parameters, grid-based docking studies were carried out, and docking was performed on all compounds using standard ligand 7-aryl-2,4-diaminoquinazolines. The best binding conformation was selected from the docking log (dlg) file for each ligand, and further interaction analysis was performed using PyMol and Discovery Studio Visualizer 4.0.

RESULTS AND DISCUSSION

Chemistry

The synthesis of 3,5-disubstituted-4,5-dihydro-*N*-alkyl-1*H*-pyrazole-1-carbothioamides (**4a-f** and **5a-e**) was achieved by condensation reaction between chalcones (**3a-f**) with 4-methyl-3-thiosemicarbazide/4-ethyl-3-thiosemicarbazide under the alkaline condition (Scheme 1). Chalcone derivatives (**3a-f**) were synthesized through Claisen-Schmidt condensation. Compound **4a** was taken as an example to describe the obtained data. Compound **4a** was obtained yellowish crystals with a melting point 180–184 °C. The HRMS spectrum of **4a** revealed molecular ion peak $[\text{M}+\text{H}]^+$ at m/z 310.1380, which is consistent with the molecular formula $\text{C}_{18}\text{H}_{20}\text{N}_3\text{S}$ (calcd. 310.1378). The important absorption bands in the FTIR spectrum were observed at 3361 cm^{-1} (N-H stretching), 1590 cm^{-1} (C=N stretching), 1516 cm^{-1} and 1427 cm^{-1} (C=C stretching of the aromatic), and 1403 cm^{-1} (C=S stretching). The absence of C=O and C=C bands, as well as the appearance of new C=N and C=S bands in the IR spectra, suggested the complete formation of the compound **4a** via the cyclocondensation reaction between chalcone **3a** and 4-methyl-3-thiosemicarbazide (Scheme 1).

The $^1\text{H-NMR}$ spectrum of compound **4a** showed two singlet signals at the region of δ_{H} 2.32 and 3.22 ppm indicating the presence of two methyl protons, 9- CH_3 and 8- CH_3 , respectively. Two geminal protons, H-4 α and H-4 β of the methylene group, were resonated as



Scheme 1. Synthesis of chalcone and pyrazoline derivatives

doublet of doublets at δ_{H} 3.18 and 3.81 ppm, respectively. The appearance of these two signals could be attributed to the non-equivalent nature of the two geminal protons with J coupling constant of $J_{4\alpha 4\beta} = 17.5$ Hz, $J_{4\alpha 5} = 4.0$ Hz, and $J_{4\beta 5} = 11.5$ Hz. Meanwhile, the vicinal proton (H-5) also appeared as a doublet of doublets at a slightly downfield region, δ_{H} 6.07 ppm, due to the vicinal coupling with the two neighboring geminal protons of methylene group at position-4 of the pyrazoline ring. In compound **4a**, some aromatic protons such as H-3'', H-4'', and H-5'' were observed at the same chemical shift, δ_{H} 7.45 ppm, due to the overlapping of peaks in a similar environment. The absence of one board signal in the thioamide (7-N-H) of compound **4a** due to the deuterium proton will exchange with the proton of the synthesized compound by intermolecular proton transfer [34]. The ^{13}C -NMR spectrum of carbothioamide compound **4a** was showed fourteen carbons signals. One carbon signal each at δ_{C} 42.6 and 63.3 ppm suggested the presence of the pyrazoline ring carbons, which are assigned to 4-CH₂ and 5-CH, respectively. Also, a signal at δ_{C} 154.4 ppm was attributed to 3-C=N in the pyrazoline ring, which is a carbon attached to electronegative nitrogen by a double bond also to a benzene ring. Besides, a signal at δ_{C} 177.0 ppm was indicated to 6-C=S. The 2D-NMR correlation of ^1H - ^1H COSY and ^1H - ^{13}C HMBC spectra were used to

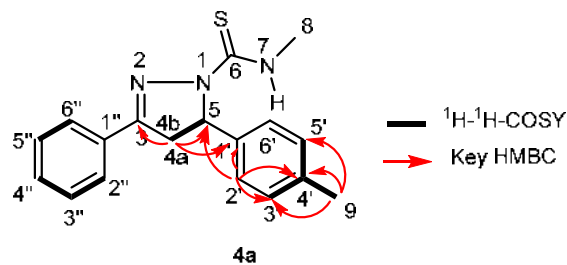


Fig 1. 2D-COSY and 2D-HMBC correlations of compound **4a**

assign the aromatic signals, especially in the case of the pyrazoline ring. The analysis of ^1H - ^1H COSY the cross peak of 9-CH₃ with H-3'-H-5', 4 α -CH with 5-CH-4 β -CH, and H-2''-H-6'' with H-3''-H-4''-H-5'' (Fig. 1). The ^1H - ^{13}C HMBC spectrum of **4a** shows the cross-correlations of 4 α -CH with carbons 5-CH, C-1', and 3-C=N, and H-2' with 5-CH, C-3', C-4' and C-1' (Fig. 1). Additionally, the cross-correlation of 9-CH₃ with C-3', C-5', and C-4'. According to the above spectra data analysis, compound **4a** was identified as a new 2-pyrazoline compound named 5-(4-methylphenyl)-4,5-dihydro-*N*-methyl-3-phenyl-1*H*-pyrazole-1-carbothioamide.

Anti-tuberculosis Activity

Eleven synthesized pyrazoline derivatives **4a-f** and **5a-e** were screened for anti-TB activity against MTB

H37Ra using the TEMA method. The INH was used as a positive control. The following Table 1 depicts the results of the anti-TB activity of these compounds based on their MIC and MBC values. Among the eleven tested compounds, six exhibited promising activity against MTB H37Ra with MIC values in the range 530 to 647 μM . Compounds **4a**, **4d**, **4f**, **5a**, **5c** and **5d** showed weak activity with MICs of 647 μM (200 $\mu\text{g/mL}$), 551 μM (200 $\mu\text{g/mL}$), 615 μM (200 $\mu\text{g/mL}$), 619 μM (200 $\mu\text{g/mL}$), 583 μM (200 $\mu\text{g/mL}$) and 530 μM (200 $\mu\text{g/mL}$), respectively. Meanwhile, other compounds **4b**, **4c**, **4e**, **5b**, and **5e** showed no inhibition against MTB H37Ra. The six compounds (**4a**, **4d**, **4f**, **5a**, **5c**, and **5d**) were further evaluated for their bactericidal activity against MTB H37Ra. As the results for MBC, all tested compounds did not show any cidal effects against MTB H37Ra, even at the highest test concentration of 200 $\mu\text{g/mL}$. The *in vitro* anti-TB evaluation revealed that the compounds containing *para* methoxy substituted (**4b** and **5b**) in both series showed no inhibition against MTB H37Ra even at the highest tested concentration of 200 $\mu\text{g/mL}$. This is not surprising as the previous studies reported that (OCH₃) group substitution at phenyl ring in pyrazoline analog worsens the anti-TB activity [35].

Molecular Docking Analysis

To gain further support regarding the antibacterial effect of the most promising pyrazole derivative **5d** against TB, a molecular docking study was carried out on the dihydrofolate reductase (DHFR) enzyme (PDB ID: 3SRQ) using the AutoDock program [33]. AutoDock 4.2.2 with a Lamarckian genetic algorithm-implemented program suite was employed to identify appropriate binding modes and the conformations of the ligand molecules. DHFR catalyzes the NADPH-dependent reduction of dihydrofolate to tetrahydrofolate, which is essential for the synthesis of purines, some amino acids, and thymidine required for bacterial growth and proliferation. Thus, DHFR represents an attractive antifolate drug target that produces antibacterial action by selectively disrupting the folate pathway. The docking protocol was validated by redocking the co-crystallized ligand 7-aryl-2,4-diaminoquinazoline at the active site (RMSD 0.10). The results of docking studies clearly showed that all compounds fit nicely into the active site and form van der Waals, alkyl, π - π , and π -alkyl interactions with the active site residues. The binding free energy of compounds **5d** was found to be -8.2 kcal/mol, indicating

Table 1. *In vitro* anti-tuberculosis activities of pyrazoline derivatives **4a-e** and **5a-f** against *Mycobacterium tuberculosis* H37Ra

Compounds	MIC		MBC	
	($\mu\text{g/mL}$)	(μM)	($\mu\text{g/mL}$)	(μM)
4a	200	647	> 200	> 647 (NC)
4b	> 200	> 615	> 200	> 615
4c	> 200	> 608	> 200	> 608
4d	200	551	> 200	> 551 (NC)
4e	> 200	> 608	> 200	> 608
4f	200	615	> 200	> 615 (NC)
5a	200	619	> 200	> 619 (NC)
5b	> 200	> 590	> 200	> 590 (NC)
5c	200	583	> 200	> 583 (NC)
5d	200	530	> 200	> 530 (NC)
5e	> 200	> 583	> 200	> 583
Isoniazid (Control)	0.625	5	0.625	5

Results are mean values of duplicate and independently thrice. NC = No cidal effect at high concentration

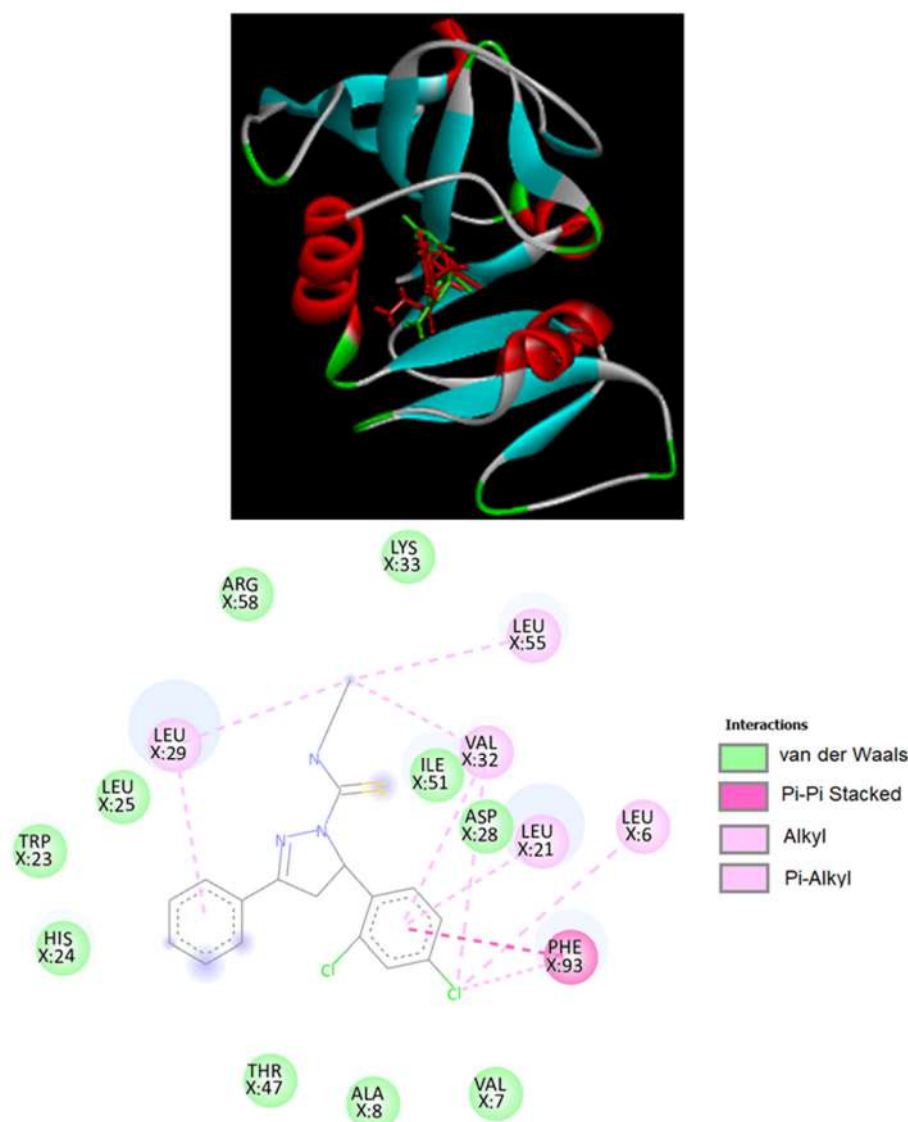


Fig 2. Overlay of the co-crystallized ligand 1-[3-(2,4-diamino-6-methylquinazolin-7-yl)phenyl]ethanone (green) with the compounds **5d** (red) at the same active site of DHFR and 2D binding interactions of **5d**

sufficient affinity between the oxadiazole analog and the enzyme. The 3D and 2D docked conformations of the most active ligand **5d** bound to the active site of DHFR are shown in Fig. 2. Lipophilicity also appears to play a crucial role in the antibacterial activity of **5d**, as the phenyl ring positioned itself into the lipophilic pocket of the binding site and formed π - π interactions with the Phe93 residues. Based on the above study, it can be proved that pyrazole derivatives possess potential DHFR inhibitory activity.

CONCLUSION

In the present study, eleven compounds from a series of 3,5-disubstituted-4,5-dihydro-*N*-alkyl-1*H*-pyrazole-1-carbothioamides (**4a-f** and **5a-e**) have been successfully synthesized via Claisen-Schmidt condensation reaction. All compounds were elucidated using FTIR, 1D- & 2D-NMR, and HRMS, and also tested for their anti-tuberculosis activity by *in vitro* study against *Mycobacterium tuberculosis* H37Ra. Our

preliminary data indicate that the assessed, newly synthesized compounds showed a partial inhibitory effect against *Mycobacterium tuberculosis* H37Ra at a 200 µg/mL concentration.

■ ACKNOWLEDGMENTS

The authors would like to acknowledge the Universiti Sains Malaysia RUI grant (1001/PKIMIA/8011072). Ministry of Higher Education of Malaysia under MyBrain15 Scheme – MyPhD for the scholarship.

■ AUTHOR CONTRIBUTIONS

Conceptualization, HO, TP, and MNA; methodology, KTW, HO, TP, and MNA; software, MZH; validation, HO, TP, and MNA; formal analysis, KTW, MZH, MSAG, and US; investigation, KTW, MSAG, and US; resources, HO, TP, and MNA; data curation, KTW, and MSAG; writing-original draft preparation, KTW, MSAG, MZH, TP, and MNA; writing-review and editing, HO, MNA, US, TP, and MZH; visualization, KTW, and MNA; supervision, HO, TP, and MNA; project administration, HO, and MNA; funding acquisition, HO, and MNA; All authors have read and agreed to the published version of the manuscript.

■ REFERENCES

- [1] Harikrishna, N., Isloor, A.M., Ananda, K., Obaid, A., and Fun, H.K., 2016, Synthesis, and antitubercular and antimicrobial activity of 1'-(4-chlorophenyl)pyrazole containing 3,5-disubstituted pyrazoline derivatives, *New J. Chem.*, 40 (1), 73–76.
- [2] WHO, 2017, *Global Tuberculosis Report 2017*, World Health Organization, Geneva.
- [3] Corbeet, E., Marston, B., Churchyard, G.J., and De Cock, K.M., 2006, Tuberculosis in sub-Saharan Africa: Opportunities, challenges, and change in the era of antiretroviral treatment, *Lancet*, 367 (9514), 926–937.
- [4] Dixit, S.R., Joshi, S.D., Kulkarni, V.H., Jalalpure, S.S., Kumbar, V.M., Mudaraddi, T.Y., Nadagouda, M.N., and Aminabhavi, T.M., 2017, Pyrrolyl pyrazoline carbaldehydes as enoyl-ACP reductase inhibitors: Design, synthesis and antitubercular activity, *Open Med. Chem. J.*, 11, 92–108.
- [5] Yar, M.S., Siddiqui, A.A., and Ali, M.A., 2007, Synthesis and anti-mycobacterial activity of novel heterocycles. *J. Serb. Chem. Soc.*, 72 (1), 5–11.
- [6] Oglah, M.K., Mustafa, Y.F., Bashir, M.K., and Jasim, M.H., 2020, Curcumin and its derivatives: A review of their biological activities, *Syst. Rev. Pharm.*, 11 (3), 472–81.
- [7] Bashir, M.K., Mustafa, Y.F., and Oglah, M.K., 2020, Antitumor, antioxidant, and antibacterial activities of glycosyl-conjugated compounds: A review, *Syst. Rev. Pharm.*, 11 (4), 175–187.
- [8] Mustafa, Y.F., and Abdulaziz, N.T., 2020, Biological potentials of hymecromone-based derivatives: A systematic review. *Syst. Rev. Pharm.*, 11 (11), 438–452.
- [9] Mustafa, Y.F., Abdulaziz, N.T., and Jasim, M.H., 2021, 4-Methylumnelliferone and its derived compounds: A brief review of their cytotoxicity, *Egypt. J. Chem.*, 64 (4), 1807–1816.
- [10] Cai, D., Zhang, Z.H., Chen, Y., Yan, X.J., Zou, L.J., Wang, Y.X., and Liu, X.Q., 2015, Synthesis, antibacterial and antitubercular activities of some 5H-thiazolo[3,2-a]pyrimidin-5-ones and sulfonic acid derivatives, *Molecules*, 20 (9), 16419–16343.
- [11] Jadhav, S.A., Kulkarni, K.M., Patil, P.B., Dhole, V.R., and Patil, S.S., 2016, Design, synthesis and biological evaluation of some novel pyrazoline derivatives, *Pharma Chem.*, 8 (3), 38–45.
- [12] Knorr, L., 1883, Einwirkung von acetessigester auf phenylhydrazin, *Ber. Dtsch. Chem. Ges.*, 16 (2), 2597–2599.
- [13] Korrouchi, K., Radi, S., Ramli, Y., Taoufik, J., Mabkhot, Y.N., Al-Aizari, F.A., and Ansar, M., 2018, Synthesis and pharmacological activities of pyrazole derivatives: A review, *Molecules*, 23 (1), 134.
- [14] Ramirez-Prada, J., Robledo, S.M., Velez, I.D., Crespo, M.D.P., Quiroga, J., Abonia, R., Montoya, A., Svetaz, L., Zacchino, S., and Insuasty, B., 2017, Synthesis of novel quinoline-based 4,5-dihydro-

- 1*H*-pyrazoles as potential anticancer, *Eur. J. Med. Chem.*, 131, 237–240.
- [15] Kumar, G., Tanwar, O., Kumar, J., Akhter, M., Sharma, S., Pillai, C.R., Alam, M.M., and Zama, M.S., 2018, Pyrazole-pyrazoline as promising novel antimalarial agents: A mechanistic study, *Eur. J. Med. Chem.*, 149, 139–147.
- [16] Montoya, A., Quiroga, J., Abonia, R., Nogueras, M., Cobo, J., and Insuasty, B., 2014, Synthesis and *in vitro* antitumor activity of a novel series of 2-pyrazoline derivatives bearing the 4-aryloxy-7-chloroquinoline fragment, *Molecules*, 19 (11), 18656–18675.
- [17] Malhotra, V., Pathak, S., Nath, R., Mukerjee, D., and Shanker, K., 2002, Substituted pyrazolines and their cardiovascular activity, *Indian J. Chem. Sect. B*, 41 (6), 1310–1313.
- [18] Nayak, B.V., Ciftci-Yabanoglu, S., Jadav, S.S., Jagrat, M., Sinha, B.N., Ucar, G., and Jayaprakash, V., 2013, Monoamine oxidase inhibitory activity of 3,5-biaryl-4,5-dihydro-1*H*-pyrazole-1-carboxylate derivatives, *Eur. J. Med. Chem.*, 69, 762–767.
- [19] Upadhyay, S., Tripathi, A.C., Paliwal, S., and Saraf, S.K., 2017, 2-Pyrazoline derivatives in neuropharmacology: Synthesis, ADME prediction, molecular docking and *in vivo* biological evaluation, *EXCLI J.*, 16, 628–649.
- [20] Abid, M., Bhat, A.R., Athar, F., and Azam, A., 2009, Synthesis, spectral studies and antiamebic activity of new 1-*N*-substituted thiocarbamoyl-3-phenyl-2-pyrazolines, *Eur. J. Med. Chem.*, 44 (1), 417–425.
- [21] Beyhan, N., Kocyigit-Kaymakcioglu, B., Gümrü, S., and Aricioglu, F., 2017, Synthesis and anticonvulsant activity of some 2-pyrazolines derived from chalcones, *Arabian J. Chem.*, 10 (Suppl. 2), S2071–S2081.
- [22] Bhandari, S., Tripathi, A.C., and Saraf, S.K., 2013, Novel 2-pyrazoline derivatives as potential anticonvulsant agents, *Med. Chem. Res.*, 22 (11), 5290–5296.
- [23] Rao, G.S., Kalaichelvan, V.K., and Rao, G.S., 2015, Synthesis and anticonvulsant activity of certain chalcone based pyrazoline compounds, *Int. J. Pharm. Res.*, 5 (8), 179–185.
- [24] Ahmad, A., Husain, A., Khan, S.A., Mujeed, M., and Bhandari, A., 2016, Synthesis, antimicrobial and antitubercular activities of some novel pyrazoline derivatives, *J. Saudi Chem. Soc.*, 20 (5), 577–584.
- [25] Bhasker, N., Prashanthi, N., and Subba Reddy, B.V., 2015, Piperidine mediated synthesis of new series of prenyloxy chalcones, flavanones and comparative cytotoxic study, *Pharm. Lett.*, 7, 8–13.
- [26] Desai, V., Desai, S., Gaonkar, S.N., Palyekar, U., Joshi, S.D., and Dixit, S.K., 2017, Novel quinoxalanyl chalcone hybrid scaffolds as enoyl ACP reductase inhibitors: Synthesis, molecular docking and biological evaluation, *Bioorg. Med. Chem. Lett.*, 27 (10), 2174–2180.
- [27] Zhang, L., Wang, A., Wang, W., Huang, Y., Liu, X., Miao, S., Liu, J., and Zhang, T., 2015, Co-N-C Catalyst for C-C coupling reactions: On the catalytic performance and active sites, *ACS Catal.*, 5 (11), 6563–6572.
- [28] Mellado, M., Madrid, A., Reyna, M., Weinstein-Oppenheimer, C., Mella, J., Salas, C.O., Sanchez, E., and Cuellar, M., 2018, Synthesis of chalcones with antiproliferative activity on the SH-SY5Y neuroblastoma cell line: Quantitative structure-activity relationship models, *Med. Chem. Res.*, 27 (11), 2414–2425.
- [29] Davey, W., and Gwilt, J.R., 1957, Chalcones and related compounds. Part I. Preparation of nitro-, amino-, and halogeno-chalcones, *J. Chem. Soc.*, 0, 1008–1014.
- [30] Suwito, H., Jumina, J., Mustofa, M., Pudjiastuti, P., Fanani, M.Z., Kimata-Arigo, Y., Katahira, R., Kawakami, T., Fujiwara, T., Hase, T., Mohd Sirat, H., and Tri Puspaningsih, N.N., 2014, Design and synthesis of chalcone derivatives as inhibitors of the Ferredoxin-Ferredoxin-NADP⁺ reductase interaction of *Plasmodium falciparum*: Pursuing new antimalarial agents, *Molecules*, 19 (12), 21473–21488.
- [31] Weber, F.G., and Brosche, K., 1972, Über 1-Thiocarbamoyl- und 1-Carbamoyl-3, 5-diaryl- Δ^2 -pyrazoline, *Z. Chem.*, 12 (4), 132–133.

- [32] Wan Abdul Wahab, W.N.A., Yahaya, M.L., Md Noor, S.S., and Noor Jamil, N.I., 2016, Direct tetrazolium microplate assay (TEMA) for rapid drug susceptibility test screening of *Mycobacterium tuberculosis*, *Trop. Biomed.*, 33 (4), 814–823.
- [33] Li, X., Hilgers, M., Cunningham, M., Chen, Z., Trzoss, M., Zhang, J., Kohnen, L., Lam, T., Creighton, C., Kedar, G.C., Nelson, K., Kwan, B., Stidham, M., Brown-Driver, V., Shaw, K.J., and Finn, J., 2011, Structure-based design of new DHFR-based antibacterial agents: 7-Aryl-2,4-diaminoquinazolines, *Bioorg. Med. Chem. Lett.*, 21 (18), 5171–5176.
- [34] Aly, S.M., Usman, A., AlZayer, M., Hamdi, G.A., Alarousu, E., and Mohammed, O.F., 2015, Solvent-dependent excited-state hydrogen transfer and intersystem crossing in 2-(2'-hydroxyphenyl)-benzothiazole, *J. Phys. Chem. B*, 119 (6), 2596–2603.
- [35] Rathod, A.S., Godipurge, S.S., and Biradar, J.S., 2017, Synthesis of indole, coumarinyl and pyridinyl derivatives of isoniazid as potent antitubercular and antimicrobial agents and their molecular docking studies, *Int. J. Pharm. Pharm. Sci.*, 9 (12), 233–240.

Trace Element Content and Food Safety of Traditional Crackers (*Kerupuk*) Collected from Java Island, Indonesia

Indah Kusmartini*, Diah Dwiana Lestiani, Syukria Kurniawati, Endah Damastuti, Natalia Adventini, Woro Yatu Niken Syahfitri, Dyah Kumala Sari, Djoko Prakoso Dwi Atmodjo, and Muhayatur Santoso

National Agency for Research and Innovation (BRIN), Center for Applied Nuclear Research and Technology, Jl. Tamansari 71, Bandung 40213, Indonesia

* **Corresponding author:**

email: indahkusmartini@gmail.com

Received: November 8, 2021

Accepted: January 11, 2022

DOI: 10.22146/ijc.70294

Abstract: In this study, trace elements in crackers were determined using Instrumental Neutron Activation Analysis (INAA) to assess their intake, food safety, and health contribution. The 62 samples of crackers were collected and purchased from local markets in five provinces of Java during 2013–2014. The validation method was performed using SRM Wheat Flour 1567a, with 80–110% accuracy (% recovery) and precision less than 10% (% RSD). The concentration of trace elements such as Cr, Co, Fe, and Zn was analyzed and found in the range of 0.03–1.4, 0.01–0.32, 14.49–85.70, 0.15–17.26 µg/g, respectively. Daily intake of elements in crackers contributes less than 1% to Recommended Dietary Allowances (RDA). Based on food safety evaluation through the calculation of Hazard Quotient, the value of Cr, Co, Fe, and Zn is less than 1, indicating that the crackers are safe for consumption and do not possess non-carcinogenic health risks due to heavy metals content. Therefore, the crackers in all Java provinces meet the current standards and are safe for consumption.

Keywords: crackers; trace element; intake; food safety; INAA

■ INTRODUCTION

Crackers are a popular snack in several Southeast Asian countries, including Indonesia. They are also known as keropok in Malaysia, keawkrab pla in Thailand, and banh phongtom in Vietnam [1]. Indonesians commonly consume crackers as supplementary food or snacks, particularly those living on Java Island. Traditionally, crackers are made of gelatinizing starch. Ingredients of cracker dough include tapioca flour, salt, sugar, monosodium glutamate, and water [2-4]. Cracker drying is a technique used to preserve the freshness of crackers during storage. The method is traditional for food preservation in which the water content is reduced to a safe level to prevent the growth of bacteria, yeast, and fungi [5]. Since crackers are still produced on a small scale using home-based methods, sun-drying usually occurs in people's yards. Crackers are dried in the sun, but this method takes longer, has a higher moisture content, and is unhygienic. Moreover, there are several months of the rainy season in Java Island (due to the transition period

from the monsoon winds). The meteorological conditions affect the drying process, which involves the cleanliness and hygiene of the produced crackers [6].

In addition, foods containing diseases caused by microorganisms and other food contaminants pose a serious health threat in developing and developed countries. World Health Organization (WHO) estimates that less than 10% of cases of congenital disease have been reported, compared to less than 1% of cases in developing countries [7]. This study conducts a food safety risk assessment to ensure customers' safety. According to Jiang et al., nutrients consist of necessary and non-essential components in the human body [8]. The content of inorganic substances in food is essential, such as minerals found in all tissues and body fluids needed to maintain several physicochemical processes in the body. Mineral nutrients classify into primary, secondary, micro, or trace elements needed by humans. Deficiency and excess of these minerals can cause health problems [9]. Some trace elements such as Cr, Co, Fe,

and Zn, present in sufficient concentrations, play an essential role in ensuring consistent physiological activities. On the other hand, excessive intake of crucial elements with different biochemical functions has harmful effects on the body [8].

Chromium (Cr) is an important mineral in the body since it stimulates insulin action and is a major hormone in the metabolism of carbs (which helps to regulate blood sugar levels), lipids (which helps to prevent heart disease), and protein (fertility and fetal growth) [10]. Low chromium concentrations can be carried down through vegetables or plant products. According to Salau and Hasan, most plant meals, such as white flour and sugar, have been refined to have minimum Cr content [11].

Cobalt (Co) is an essential element present in considerable concentrations in bones, kidneys, and liver and found throughout all body tissues in a normal distribution. Cobalt is also essential for red blood cell development and is an active vitamin B12 to make cobalamin, which is important for nerve function. Heart failure, goiter, hypothyroidism, vomiting, and diarrhea are all symptoms of cobalt insufficiency, commonly known as vitamin B12 deficiency [12].

Recommended Dietary Allowance (RDA) for iron (Fe) in adult males is 8 mg/day, whereas the RDA for adult females is 18 mg/day; the value of Fe contribution in males is higher than in females. Due to Fe loss during the menstrual month, Fe in adult females is lower than in men. Fe is found in hemoglobin, myoglobin, ferritin, hemosiderin, and cytochrome enzymes. Hemoglobin is a protein that carries oxygen to all body tissues. A lack of iron in the blood causes anemia, poor cognitive development, and impaired immune function [13-14].

Zinc (Zn) is an essential element of biochemical activities in the body, such as immune system function, protein synthesis, nucleic acid synthesis, muscular contraction, and insulin production. People with diabetes frequently suffer from zinc insufficiency. Furthermore, Zn deficiency causes malabsorption syndromes, liver and renal illness, and inflammatory bowel disease in children, inducing growth retardation. Acrodermatitis enteropathica is a hereditary disorder affecting zinc absorption and transport in the intestines [15-16].

Nasreddine et al. [16] conducted a risk assessment procedure for toxic trace elements in the food to determine the influence of intake on food safety in calculating the level of information consumed every day. Risk assessment for nutrition is defined by the association between excessive consumption toxicity and the relationship between excessive intake and nutritional deficiency. Dietary References Intake (DRI), which includes Recommended Daily Intake, has assisted medical institutions in the food and nutrition sector in the United States overcome nutritional deficiencies and trace element toxicity. Reference values for nutrition and toxicity utilizing as benchmarks in food risk assessment [16]. Due to low element content in crackers, a high precision and sensitivity method is required, such as Instrumental Neutron Activation Analysis (INAA). INAA method is qualitative and quantitative for evaluating elements in samples, has a low detection limit, and determines elements in small amounts, such as trace elements in food samples [14]. This project aims to determine the concentration of elements (Cr, Co, Fe, and Zn) present in crackers, estimate the daily nutrient intake in crackers, and assess potential health risks to determine food safety consumed by Javanese.

■ EXPERIMENTAL SECTION

Sample Collection

The 62 samples were collected and purchased from local markets in five provinces of Java during 2013–2014. Five provinces are West Java (n = 8), Central Java (n = 23), East Java (n = 23), Special Capital Region of Jakarta (n = 5), Special Region of Yogyakarta (n = 3). The sampling location can be seen in Fig. 1-3. Java is a very dense island with more than half of Indonesia's population or about 160 million countries, and 241 million people reside.

The ingredients for making *kerupuk* are starch or sago flour and spices (pepper, garlic, salt, sugar, monosodium glutamate). Crackers are manufactured on a small and large scale. The quality of cracker products is inconsistent depending on the type of raw material and the difference in the cracker manufacturing process [17]. According to Mubarok's study [18], the consumption of



Fig 1. Sampling location in West Java and Special Capital Region of Jakarta (source: google earth)



Fig 2. Sampling location in Central Java and Special Region of Yogyakarta (source: google earth)



Fig 3. Sampling location in East Java (source: google earth)

Indonesian people per capita of crackers in 2003 was 0.166 ounces/month. On the other hand, based on the National Bureau of Statistics, the average consumption of crackers data was 0.093 ounces/week in 2015 [19].

Sample Preparation and Standards

The Materials used in this activity include Standard Reference Material (SRM), Wheat Flour 1567a from the National Institute of Standards and Technology, and demineralized water ($> 18 \text{ M}\Omega \text{ cm}^2$). Other materials used in this activity are a standard multi-elemental E-Merck tritisol solution and a polyethylene vial.

The crackers were weighted and then mashed in an agate mortar for homogenization. The sample was then weighed again and placed in the oven. Moisture content was determined by drying the sample in a forced air oven at $100 \text{ }^\circ\text{C}$ for 8 h [4]. A total of 60 mg of cracker samples weighed with analytical balance (AG 245 Mettler Toledo Ltd., Melbourne, Australia) were inserted into a polyethylene vial of 0.3 mL and then sealed with heating.

The standard solution ICP multi-element VI E-Merck was prepared with elements concentrations of Cr, Co, Fe, and Zn, which were 1, 1, 49.9, and 10 μg , respectively. A total of 100 μL of the standard solution was piped and placed into a 0.3 mL polyethylene vial, dried with an infra-red lamp, then sealed with heating. Validation of the NAA method using SRM NIST Wheat Flour 1567a was done by weighing as much as 60 mg into a polyethylene vial of 0.3 mL, then sealed by heating.

Irradiation, Counting, and Data Analysis

Samples, NIST Wheat Flour reference material (SRM), and multi-element ICP standards were irradiated for 2 h using thermal neutron sources with a neutron flux of $10^{13} \text{ n}\cdot\text{cm}^{-2}\cdot\text{s}^{-1}$ in rabbit systems at the G.A. Siwabessy multipurpose reactor facility in Serpong. Sample decay was performed for one month, then the sample, SRM, and ICP standards were measured for ± 50000 sec using Gamma spectrometer, Canberra USA, and multi-channel Analyzer (MCA). The spectrum of ^{51}Cr , ^{60}Co , ^{59}Fe , and ^{65}Zn have gamma energy characteristics 320.08, 1332.50, 1099.25, 1115.52 keV, respectively, and determined by Genie 2000 software.

The calculation of the concentration of this element was carried out using a comparative method, namely comparing the concentration of elements in the sample with a standard with a known concentration. Elemental content in the sample was calculated following the formula. In this method, standard ICP (W_{std}) and sample (W_{spl}) have a known value weight concentration, are simultaneously irradiated, and measured under the same conditions. The concentration of elements in the sample was determined by comparing the activity between the sample ($A0_{\text{spl}}$) and the ICP standard ($A0_{\text{std}}$) in the formula [20]:

$$C = \frac{A0_{\text{spl}}}{A0_{\text{std}}} \times \frac{W_{\text{std}}}{W_{\text{spl}}} \quad (1)$$

where $A0_{\text{spl}}$: Activity of sample (cps), $A0_{\text{std}}$: Activity of standard (cps), W_{std} : Weight of standard (μg), W_{spl} : Weight of sample (g), C: Concentration of element ($\mu\text{g/g}$).

Quality Assurance of the INAA Method

Standard reference material is used to assess data validation quality control. The SRM result value measured is compared to the value of the certificate whose concentration is known. Accuracy and precision were evaluated by calculating % recovery and % RSD (Relative Standard Deviation). Accuracy measures the degree of agreement between the concentration of the determination result and the actual concentration of the element. Accuracy can be defined as a measure of a result that is close to the true value, while precision can be expressed as a measure of the repeatability and reproducibility of results. Accuracy can be defined as %Rec. Recovery is a comparison of the measurement results with the certificate value and is expressed by the following formula:

$$\% \text{Rec} = \frac{X_{\text{test}}}{X_{\text{cert}}} \times 100\% \quad (2)$$

with X_{test} is the result of the analysis value, and X_{cert} is the certificate value.

Precision is a measure that indicates the degree of conformity between individual test results, measured through the dissemination of individual results from the average. Precision tests are counted as standard

deviations or relative standard deviations (RSD) obtained through formula (3) [11] with SD_{test} is the standard deviation testing, $\text{mean}_{\text{test}}$ is the average test scores, and RSD is relative standard deviation:

$$\text{RSD} = \frac{SD_{\text{test}}}{\text{Mean}_{\text{test}}} \times 100\% \quad (3)$$

Estimated Daily Intake of Crackers and Their Contribution to Recommended Dietary Allowance (RDA)

The daily intake of each element depends on the concentration of elements in the diet and the intake consumed daily. Estimated daily intake is calculated based on the following formula [21]:

$$\text{EDI} = C \text{ metal} \times D \text{ food intake} \quad (4)$$

EDI is the daily intake estimation of elements in mg/day or $\mu\text{g}/\text{day}$ of each element. C metal is the concentration of elements in food samples (mg/kg wet weight), whereas D food intake is the average amount consumed per day [14]. In this activity, the average consumption per capita of crackers in Indonesia, based on the National Statistics Agency data, was 0.093 ounces/week; therefore, the average daily consumption of crackers consumed was 1.33 g/day [19].

Risk Assessment

The term human health risk assessment refers to determining the carcinogenic and non-carcinogenic effects of chemicals that enter the body. The HI (Hazard Index) is the sum of each metal's Hazard Quotient (HQ), estimating various heavy metals' overall potential non-carcinogenic health consequences in diets. Quantifying non-cancerous health implications, HQ is used, followed by HI [22]. A formula can be used to calculate the daily intake of each element (g/kg bw/day):

$$\text{Daily intake} = \frac{\sum C \times I}{Bw} \quad (5)$$

$$\text{Hazard Quotient} = \frac{\text{Daily intake}}{\text{TDI}} \quad (6)$$

where C: concentration of element ($\mu\text{g}/\text{g}$), I: the average consumption rate (g/day) of Indonesians for crackers of 1.33 g/day, Bw: the average body weight of Indonesian adults, as 60 kg.

By comparing daily intake with Tolerable Daily Intake (TDI), Hazard Quotient (HQ) can be calculated (Formula 6). TDI is the value of a daily intake tolerance approach for all harmful compounds that humans are exposed to daily without causing harm [23].

RESULTS AND DISCUSSION

Quality Control and Assurance

In this activity, the method was validated by assessing the accuracy and precision of the results using SRM NIST 1567a Wheat Flour. SRM used has a similar matrix and was determined using the same measurement settings as the sample. The results of the determination of trace elements in SRM are shown in Table 1. The table shows a good agreement with the certificate. The precision values characterized by the percentage value RSD were in the range of 4–6%, while the accuracy values described by the percentage recovery were in the field of 99–101%. According to the Association of Official Agricultural Chemists (AOAC) International Guidelines, analytical accuracy and precision are acceptable [24]. Thus, the elemental analysis results in SRM NIST 1567a Wheat Flour have good accuracy and precision. Hence, the analytical method used is valid, and the data obtained can be trusted.

Previously, the method validation using SRM WF 1567a to determine selenium in tempeh using the INAA technique was carried out by Kuniawati et al. [20]. Another researcher, Syahfitri et al., analyzed the trace element content in tofu with INAA using SRM WF 1567a

Table 1. Determination of quality control using SRM NIST 1567a wheat flour

Element	SRM NIST Wheat Flour 1567a			Acceptable		
	Result ($\mu\text{g}/\text{g}$)	Certified value ($\mu\text{g}/\text{g}$)	Accuracy (% recovery)	Precision (% RSD)	Accuracy range (% recovery)	Precision (% RSD)
Co	0.006	0.006	100	6	80–110	5.66
Fe	14.2±1.63	14.1±0.5	101	4	80–110	4.00
Zn	11.5±0.23	11.6±0.4	99	4	80–110	4.00

to validate the method [25]. Meanwhile, the validation of the technique with other SRM WF was carried out by Kurniawati et al. in selected trace elements of cassava [26]. According to research conducted by Pompa et al., SRM Wheat Flour 1567b NIST flour was used and treated the same way as the analyzed test samples for quality control (accuracy and precision); in Pb and Hg recovery study, SRM was spiked to 0.020 ppm [27]. From several studies that have been carried out, SRM WF 1567a can be used to validate the INAA method, and the result showed good agreement and was acceptable for accuracy and precision values.

Element Characterization in Traditional Crackers (Kerupuk)

In analytical techniques, determining a food sample's moisture content or water content is a crucial first step. INAA technique analyzes solid and dry samples. Therefore, the water content of cracker samples must be determined [20]. The water content of crackers in this activity was 3.12–16.43%, with an average of $6.5 \pm 2.16\%$. According to Indonesian National Standards, the moisture content of crackers is 12%. In this study, the water content of crackers showed no significant differences from the water content allowed by Indonesian National Standards [28]. The dry weight was carried out to quantify the number of elements present in crackers. Element concentrations are converted to wet weight by measuring the water content in each sample to obtain daily consumption recommended levels. According to a recent study by Suseno et al., water content is controlled by various factors, including methods and product quality. The water content in a product can affect its resistance to microbial and enzymatic activities and be harmful [4].

The determination of Cr, Co, Fe, and Zn elements in crackers from Java Island can be seen in Table 2. The results showed the concentration of cracker samples followed the order $Fe > Zn > Cr > Co$. The average concentration of each element in crackers was multiplied by the amount of crackers consumed by Indonesians to calculate daily consumption. According to food consumption data, the average cracker consumed is 1.33 g/day [19]. Estimated daily trace element intake was then calculated and compared to the recommended

dietary allowance (RDA). RDA is a number that represents the average daily requirement for nutrients for all people of a certain age, gender, degree of physical activity, and physiological circumstances. As a benchmark for determining the adequacy of daily intake, RDA meets the dietary requirements of (97–98%) of healthy people [11,22]. Discussion of results obtained as well as comparison of data reported in other studies on the concentration of elements in crackers are as follows:

The highest concentration of Cr in a crackers sample cracker was 0.46 $\mu\text{g/g}$ in Central Java, and the lowest was 0.06 $\mu\text{g/g}$ in the Special Capital Region of Jakarta, as seen in Table 2 and Fig. 4. Previous studies by Salau and Hasan compared these found the amount of Cr in crackers was 0.55 $\mu\text{g/g}$, which seems similar to the concentration found in this study [11]. However, the average concentration of Cr in West Java and the Special Region of Yogyakarta are lower than crackers in Malaysian studies. The estimated daily intake of trace elements in crackers and their contribution to the nutritional adequacy rate are shown in Table 3. The chromium estimated daily consumption of 0.47 $\mu\text{g/day}$ resulted in RDA values for males and females being 0.001%, respectively.

Table 2 and Fig. 5 present the data of cobalt concentrations in crackers. East Java and the Special Capital Region of Jakarta have similar cobalt values of 0.14 and 0.11 $\mu\text{g/g}$, respectively. Central Java and the 0.09 $\mu\text{g/g}$, as shown in Table 2. West Java has the lowest concentration of Co, which is 0.07 $\mu\text{g/g}$. Cobalt concentration in crackers was also compared to the Malaysian study and was found to have a value of 0.17 $\mu\text{g/g}$, which is similar to East Java in this report's results [11]. Meanwhile, West Java, Central Java, and the Special Region of Yogyakarta have lower results than Malaysian studies. Due to there being no RDA for cobalt, the value is determined from the Upper-Level Intake (UL).

In this activity, the determination of iron concentration in crackers is given in Table 2 and shown in Fig. 6. Central Java has the highest Fe concentration of 52.3 $\mu\text{g/g}$, while the lowest concentration of Fe in crackers was found in the Special Region of Yogyakarta.

Table 2. The concentration of the elements in *kerupuk* from Java Island ($\mu\text{g/g}$)

Province	Concentration ($\mu\text{g/g}$)							
	Cr		Co		Fe		Zn	
	Range	Mean	Range	Mean	Range	Mean	Range	Mean
West Java	0.11–0.35	0.19 \pm 0.03	0.06–0.20	0.07 \pm 0.004	29.94–62.18	42.81 \pm 2.98	1.78–17.26	5.01 \pm 0.2
Central Java	0.10–1.40	0.46 \pm 0.04	0.01–0.32	0.09 \pm 0.004	20.93–85.70	52.3 \pm 3.05	0.15–16.06	5.02 \pm 0.2
East Java	0.06–1.06	0.34 \pm 0.07	0.01–0.29	0.14 \pm 0.01	14.49–84.59	48.72 \pm 4.11	0.51–12.07	4 \pm 0.26
Special Capital Region of Jakarta*	0.03–0.09	0.06 \pm 0.04	0.10–0.13	0.11 \pm 0.01	32.55–60.38	45.03 \pm 4.70	3.22–7.48	5.34 \pm 0.24
Special Region of Yogyakarta	0.09–0.20	0.13 \pm 0.03	0.07–0.10	0.09 \pm 0.004	20.62–45.51	33.96 \pm 3.04	1.98–4.05	3.1 \pm 0.13

*Kurniawati et al. [29]

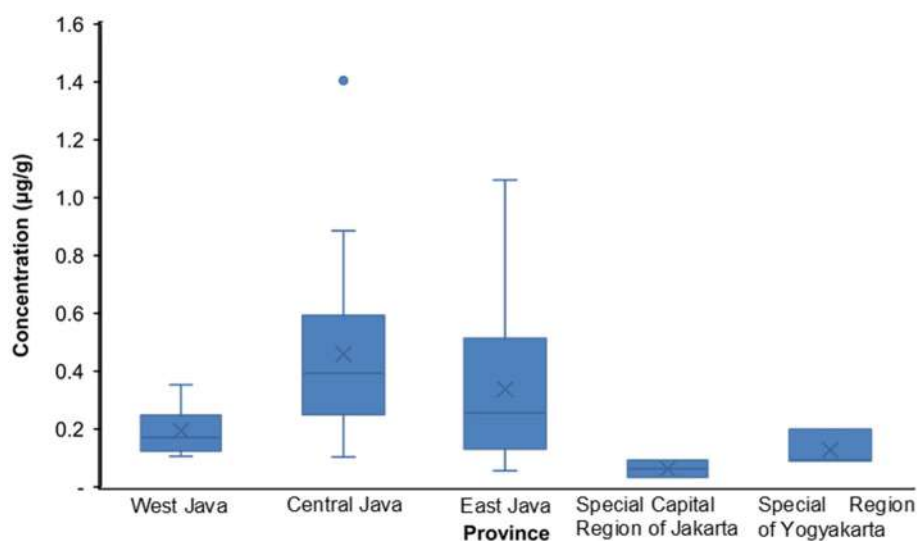
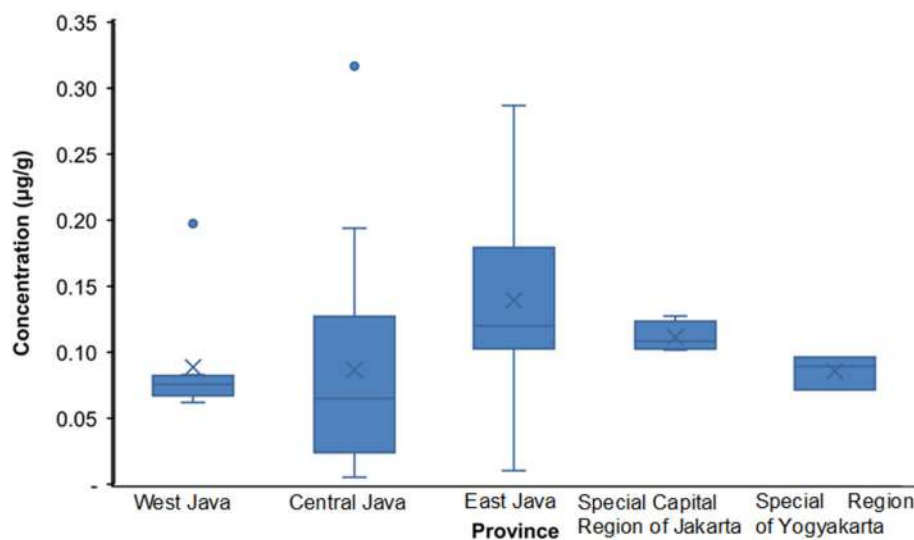
**Fig 4.** The concentration of chromium in crackers from Java Island**Fig 5.** The concentration of cobalt in crackers from Java Island

Fig. 6 showed that West Java and the Special Capital Region of Jakarta have similar concentrations, i.e., 42.81 and 45.03, respectively. In a previous study in Malaysia

reported by Salau and Hasan, the concentration of trace elements in Lekor crackers measurement are similar in composition to the crackers in this study. The Fe

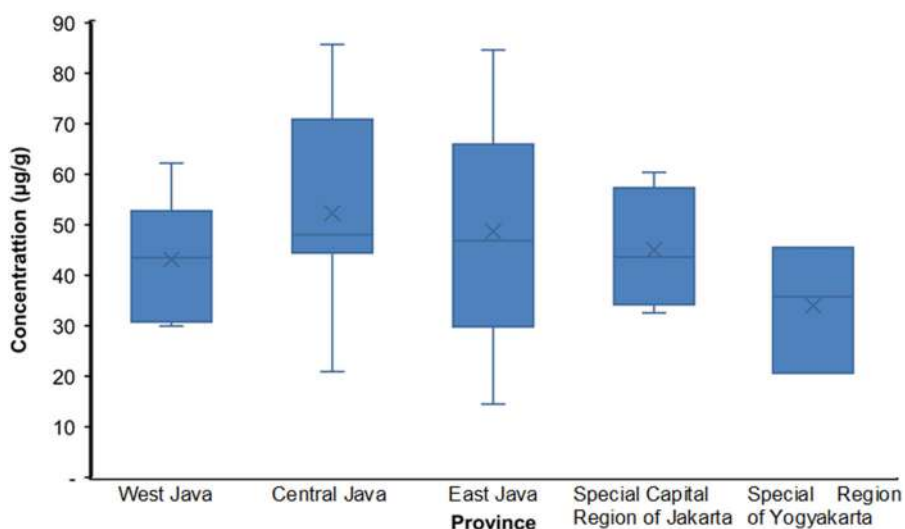


Fig 6. The concentration of iron in crackers from Java Island

concentration of Lekor crackers was $0.063 \mu\text{g/g}$ [30]. The Fe value of Lekor crackers was lower than in this study. Iron is the most prevalent element in the human body. Fe's estimated daily intake value is $59.4 \mu\text{g/day}$, with RDA contribution values for males and females being 0.33 and 0.74%, respectively, as seen in Table 3.

Determination of Zink content in crackers is shown in Fig. 7 and given in Table 2. Zn concentrations in West Java, Central Java, and the Special Capital Region of Jakarta have similar concentrations, i.e., 5.01, 5.02, and $5.34 \mu\text{g/g}$, respectively; these are the highest concentrations of Zn in Java. The lowest concentration is in the Special Region of Yogyakarta. This result is higher than in previous studies conducted by Salau and Hassan was $0.012 \mu\text{g}/\mu\text{g}$ [30]. Zn has estimated daily intakes were $5.90 \mu\text{g/day}$ and provided less than 0.1% of RDA.

Starch is the main ingredient for making crackers and plays an essential role in determining the quality of crackers. Previous research by Liu Q., and Liu K., stated that starch is extensively used as a thickener, stabilizer, gelling, gelling, binding, or water-retaining agent for numerous meals products [31]. Commercial crackers are manufactured with flour that contains starch, mainly in the form of amylose and pectin. The composition and quality of various types of starch derived from plant products will significantly impact trace element content in crackers. Cassava and sago starches are processed into flour. Therefore, the composition and quality of various

types of starch obtained from plant products will influence the elemental content of crackers in several parts of Java Island. Consequently, soil conditions and planting methods significantly impact cracker elemental composition. Organic matter in starch, soil conditions, pH, and chemical inputs, including fertilizers and insecticides, all affect the element composition in the sample [20,32].

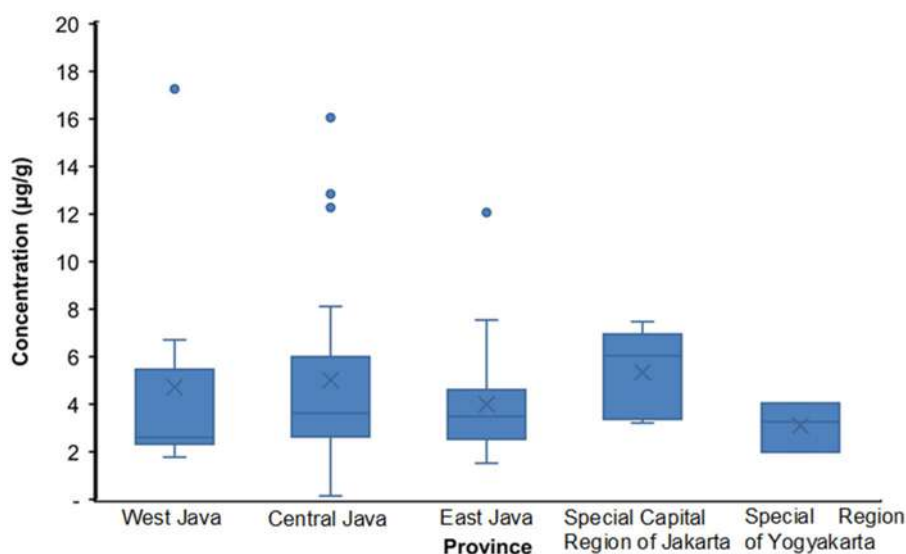
Related to RDA values for these trace elements in crackers were not contributed significantly ($< 1\%$). Taewee, T.K., conducted previous research that crackers are considered healthy foods, including carbohydrates and protein. However, the concentration of vitamins and micronutrients has restrictions influenced by high frying temperatures [32].

Risk Assessment

A safety risk assessment is carried out to ensure the safety of products consumed by the public [12]. According to the World Health Organization, food safety is a science that deals with the preparation, handling, and storage of food and beverages to keep them free of physical, chemical, and biological contaminants. The purpose is to prevent food or drinks from being contaminated and limit the risk of foodborne illnesses[23,31]. Mostly, trace elements are essential micronutrients, such as Cr, Co, Fe, and Zn. On the other hand, these trace elements are considered heavy metals

Table 3. The estimation of daily nutrient intake (EDI) and contribution to RDA

Element	Mean ($\mu\text{g/g}$)	Consumption rate (g/day) [19]	EDI ($\mu\text{g/day}$)	RDA (%)	
				Female	Male
Cr	0.24	1.33	0.31	0.001	0.001
Co	0.10	1.33	0.14	0.690	0.690
Fe	44.63	1.33	59.4	0.330	0.740
Zn	4.44	1.33	5.90	0.074	0.054

**Fig 7.** The concentration of zinc in crackers from Java Island

and potentially, such as Cr and Co, harmful if their concentration in the body exceeds a certain level, causing health problems.

Table 4 showed the hazard quotient values in a trace element Cr, Co, Fe, and Zn were 0.01; 0.002; 0.98; 0.09, respectively. Therefore, the hazard quotient for cracker samples from cities/districts on Java Island is less than 1 ($HQ < 1$). Trace elements Cr, Co, Fe, and Zn, found in crackers, are safe to consume and present no health hazards. It can be seen in Table 4 that the summary of the Hazard Index was 0.31. The concentration of elements in the HQ is measured as a Hazard Index with a value less than one ($HI < 1$) overall. These results indicate that the intake of crackers consumed by the population still reaches an acceptable level for the four basic parameters. Health risk estimation showed that the consumption of crackers is safe for the population if no more than two pieces are consumed per day, with an average per capita consumption of 1.33 g/day, based on statistical data on Indonesian food consumption in 2015 [19]. However, the

Table 4. Health risk assessment of trace elements in crackers

Element	TDI (mg/day)	Daily intake (mg/day)	HQ	HI
Cr	0.2*	0.01	0.026	$\Sigma 0.31 < 1$
Co	0.02*	0.002	0.115	
Fe	6**	0.98	0.165	
Zn	6.8**	0.09	0.002	

*Mulyaningsih et al. [13]

**Al-Fartusie and Mohssan [33]

HI number may increase if the crackers consumed exceed the recommended cracker consumption limit.

Toxic substances include biological (particularly pathogenic bacteria), chemical, and other (physical) toxic substances or pose a risk to human health. Healthy and safe food consumption are essential for improving public health. This trace element content of crackers is safe for consumption since fresh or processed food contains at least illegal and toxic chemical residues [34-36].

According to WHO, 70% of the world's 1.5 billion people are affected by foodborne illness. The model of a single agency, as found in the United States under the name of the US Food and Drug Administration (US FDA) or in China under the name of the China FDA, can serve as a model or reference for a food control system under the social, cultural and geographical conditions in Indonesia [36]. Therefore, investigating trace elements in crackers as a first step in determining the adequacy and safety of food consumed by the urban Javanese population regarding the aspects under study will serve as a foundation for future monitoring studies.

■ CONCLUSION

Assessment of trace element content in crackers widely consumed by local Javanese people has been carried out. A total of four trace elements (Cr, Co, Fe, and Zn) were determined in the 62 samples collected and purchased from local markets in five provinces of Java during 2013–2014. It was found that the concentration of elements in crackers from Java Island follows the order of $Fe > Zn > Cr > Co$. The highest levels of Fe were also found in Central Java and East Java, while the highest levels of Zn concentration were in West Java. East and Central Java Province have the highest Cr content, while the highest Co content was found in Central Java. RDA value was not significantly contributed by the daily intake of these elements in crackers. The results of this study have confirmed that the carcinogenic and non-carcinogenic trace elements are indicated by the Hazard Quotient (HQ) and the hazard index value. Both have less than 1, which means trace elements in consumed crackers are still within the permissible value. These results show that the intake of crackers is safe for the population if no more than three pieces are consumed per day, with an average per capita consumption of 1.33 g/day. Overall, the health risks assessment indicates crackers consumed by Java Island residents are safe and meet specific food safety requirements. Further study related to the potential health risks of trace elements such as Pb, As, Cd, Cu, and Se from crackers needs to be done for more comprehensive results.

■ ACKNOWLEDGMENTS

The authors are grateful for financial support from the National Nuclear Energy Agency (BATAN) budget for the national research project 2016 – 2021 and thanks to technical staff in the GA Siwabessy research reactor in Serpong.

■ AUTHOR CONTRIBUTIONS

The main contributor to this paper is Indah Kusmartini in sampling, preparation, samples measurement and data analysis, drafting, and finalizing the manuscript. Natalia Adventini, Woro Yatu Niken, Dyah Kumala Sari, and Djoko Prakoso Dwi Atmodjo conducted the sampling, sample preparation, and samples measurement. Endah Damastuti has conducted the sampling, correcting grammar/spelling errors in the manuscript. Syukria Kurniawati has conducted sampling and spectrum analysis. Diah Dwiana Lestiani conducted the data analysis, checked the QA and QC of the data, provided the conceptualization, revised and supervised the drafting of the manuscript, and Muhayatun Santoso designed the research. All authors agreed to the final version of this manuscript.

■ REFERENCES

- [1] Rames, R., Shakila, R.J., Sivaraman, B., Ganesan, P., and Velayutham, P., 2018, Optimization of the gelatinization conditions to improve the expansion and crispiness of fish crackers using RSM, *LWT--Food Sci. Technol.*, 89, 248–254.
- [2] Neiva, C.R.P., Machado, T.M., Tomita, R.Y., Furlan, É.F., Lemos Neto, M.J., and Bastos, D.H.M., 2011, Fish crackers development from minced fish and starch: An innovative approach to a traditional product, *Cienc. Tecnol. Aliment. (Campinas, Braz.)*, 31 (4), 973–979.
- [3] Ahmed, Z.S., and Abozed, S.S., 2015, Functional and antioxidant properties of novel snack crackers incorporated with *Hibiscus sabdariffa* by-product, *J. Adv. Res.*, 6 (1), 79–87.
- [4] Suseno S.H., Hayati, S., Saraswati, and Izaki, A.F., 2014, Chemical characteristics of traditional

- aquatic products collected from wet market in Banten province, Indonesia, *World J. Fish Mar. Sci.*, 6 (5), 424–428.
- [5] Abdullah, S., Musa, N., Rukunudin, I.H., and Shaari, A.R., 2019, Drying characteristics of fish cracker under different drying techniques, *Food Res.*, 3 (4), 357–361.
- [6] Dilbar Shah, S.S., 2013, Improvement of Drying Process in Fish Cracker Production, *Undergraduate Thesis*, Faculty of Mechanical Engineering, University Malaysia Pahang, Malaysia.
- [7] Fung, F., Wang, H.S., and Menon, S., 2018, A review: food safety in the 21st century, *Biomed. J.*, 41 (2), 88–95.
- [8] Jiang, J., Lu, S., Zhang, H., Liu, G., Lin, K., Huang, W., Luo, R., Zhang, X., Tang, C., and Yu, Y., 2015, Dietary intake of human essential elements from a total diet study in Shenzhen, Guangdong province, China, *J. Food Compos. Anal.*, 39, 1–7.
- [9] Orecchio, S., Amorello, D., Raso, M., Barreca, S., Lino, C., and Di Gaudio, F., 2014, Determination of trace elements in gluten-free food for celiac people by ICP-MS, *Microchem. J.*, 116, 163–172.
- [10] Londonio, A., Morzán, E., and Smichowski, P., 2019 Determination of toxic and potentially toxic elements in rice and rice-based products by inductively coupled plasma-mass spectrometry, *Food Chem.*, 284, 149–154.
- [11] Salau, R.B., and Hasan, M.N., 2019, Quantitative and chemometric study of patterns distributions and health status of chromium, cobalt, nickel, and molybdenum in selected Malaysian dishes, *J. Sci. Technol. Math. Educ.*, 15 (1), 8–22.
- [12] Sadiq N.W., and Beauchemin, D., 2017, Simultaneous speciation analysis of arsenic, chromium, and selenium in the bioaccessible fraction for realistic risk assessment of food safety, *Anal. Chem.*, 89 (24), 13299–13304.
- [13] Mulyaningsih, R., Istanto, I., Yusuf, S., and Suprpti, S., 2010, Analisis unsur toksik dan makro-mikro nutrien dalam bahan makanan dengan metode analisis aktivasi neutron, *J. Iptek Nuklir Ganendra*, 13, (1), 46–55.
- [14] Damastuti, E., Kurniawati, S., Syahfitri, W.Y.N., Adventini, N., Lestiani, D.D., and Santoso, M., 2020, Determinations of minerals composition of rices in Java Island, Indonesia, *J. Nutr. Sci. Vitaminol.*, 66, S479–S485.
- [15] Dutta, T.K., and Mukta, V., 2012, Trace elements, *Med. Update*, 22, 353–357.
- [16] Nasreddine, L., Nashalian, O., Naja, F., Itani, L., Parent-Massin, D., Nabhani-Zeidan, M., and Hwalla, N., 2010, Dietary exposure to essential and toxic trace elements from a total diet study in an adult Lebanese urban population, *Food Chem. Toxicol.*, 48 (5), 1262–1269.
- [17] Sharma, V., Sharma, P.C., and Kumar, V., 2015, A mini-review on pyridoacridines: Prospective lead compounds in medicinal chemistry, *J. Adv. Res.*, 6 (1), 63–71.
- [18] Mubarak, N., 2009, Faktor-Faktor yang Mempengaruhi Produksi Kerupuk Ikan di Sentra Produksi Kerupuk Desa Kenanga Kecamatan Sindang Kabupaten Indramayu Provinsi Jawa Barat, *Undergraduate Thesis*, Faculty of Science and Technology, Universitas Islam Negeri Syarif Hidayatullah Jakarta, Indonesia.
- [19] Anonymous, 2015, Statistik Konsumsi Pangan Tahun 2015, Center for Agricultural Data and Information System, Ministry of Agriculture Republic of Indonesia, Jakarta, Indonesia, 1–129.
- [20] Kurniawati, S., Lestiani, D.D., Damastuti, E., and Santoso, M., 2019, The selenium content of Tempeh in Indonesia and its potential contribution to the dietary selenium requirements for adults, *J. Food Compos. Anal.*, 82, 103222.
- [21] Bargellini, A., Venturelli, F., Casali, E., Ferrari, A., Marchesi, I., and Borella, P., 2018, Trace elements in starter infant formula: Dietary intake and safety assessment, *Environ. Sci. Pollut. Res.*, 25 (3), 2035–2044.
- [22] Jeevanaraj, P., Ahmad Foat, A., Tholib, H., and Ahmad, N.I., 2020, Heavy metal contamination in processed seafood and the associated health risk for Malaysian women, *Br. Food J.*, 122 (10), 3099–3114.
- [23] Syahfitri, W.Y.N., Kurniawati, N., and Damastuti, E., 2011, Penentuan logam Berat Cr, Co, Zn, dan Hg pada Padi dan Kedelai Daerah Kota Bandung, *Proceedings of the National Seminar on Nuclear*

- Science and Technology*, PTNBR–BATAN, Bandung, June 11, 2011, 213–219.
- [24] Gustavo González, A., and Ángeles Herrador, M., 2007, A practical guide to analytical method validation, including measurement uncertainty and accuracy profiles, *TrAC, Trends Anal. Chem.*, 26 (3), 227–238.
- [25] Syahfitri., W.Y.N., Kurniawati, S., Adventini N., Atmodjo, D.P.D, Kusmartini, I., Damastuti, E., Lestiani, D.D., and Santoso, M., 2020, Characterization of micronutrients in tofu from several cities in Java Island Indonesia, *J. Nutr. Sci. Vitaminol.*, 66, S262–S266.
- [26] Kurniawati, S., Damastuti, E., Lestiani, D.D., Adventini, N., Syahfitri, W.Y.N., Kusmartini, I., Sari, D.K., and Santoso, M., 2021, Determination of several trace elements in cassava using nuclear analytical technique, *AIP Conf. Proc.*, 2381, 020032.
- [27] Pompa, C., D'Amore, T., Miedico, O., Preite, C., and Chiaravalle, A.E., 2021, Evaluation and dietary exposure assessment of selected toxic trace elements in durum wheat (*Triticum durum*) imported into the Italian market: Six years of official controls, *Foods*, 10 (4), 775.
- [28] Andriani, D.P., Rizky, D.A., and Setiaji, U., 2017, Pengendalian kualitas kadar air produk kerupuk udang berbasis SNI menggunakan statistical quality control method, *Seminar dan Konferensi Nasional IDEC 2017*, Universitas Sebelas Maret, May 8-9, 2017, Surakarta, Indonesia, 8–9.
- [29] Kurniawati, S., Damastuti, E., Adventini, A., Syahfitri, W.Y.N., Kusmartini, I., Lestiani, D.D., and Santoso, M., 2021, Determination of several heavy metals in staple foods from traditional markets in Jakarta using neutron activation analysis, *AIP Conf. Proc.*, 2349, 020054.
- [30] Salau, R.B., and Hasan, M.N., 2013, Preliminary investigation of Malaysian foods for sourcing essential mineral micronutrients, *Proceedings of 4th International Graduate Conference on Engineering, Science and Humanities (IGCESH)*, 1007–1016.
- [31] Liu, K., and Liu, Q., 2020, Enzymatic determination of total starch and degree of starch gelatinization in various products, *Food Hydrocolloids*, 103, 105639.
- [32] Taewee, T.K., 2011, Cracker 'Keropok': A review on factors influencing expansion, *Int. Food Res. J.*, 18 (3), 855–866.
- [33] Al-Fartusie F.S., and Mohssan, S.N., 2017, Trace elements and their vital roles in human body, *Indian J. Adv. Chem. Sci.*, 5 (3), 127–136.
- [34] Maulidah, W.U., and Wahyuni, H.C., 2021, Food safety and halal risk mitigation in fish crackers supply chain with FMECA and AHP, *Procedia Eng. Life Sci.*, 1, 1.
- [35] Moelyaningrum, A.D., 2019, Boric acid and hazard analysis critical control point (HACCP) on kerupuk to improve the Indonesian's traditional foods safety, *Int. J. Sci. Technol. Res.*, 8 (6), 50–54.
- [36] Lestari, T.R.P., 2020, Keamanan pangan sebagai salah satu upaya perlindungan hak masyarakat sebagai konsumen, *Aspirasi: Jurnal Masalah-Masalah Sosial*, 11 (1), 57–72.

Synthesis of Mesoporous Silica from Beach Sand by Sol-Gel Method as a Ni Supported Catalyst for Hydrocracking of Waste Cooking Oil

Siti Salamah¹, Wega Trisunaryanti^{2*}, Indriana Kartini², and Suryo Purwono³

¹Department of Chemical Engineering, Faculty of Industrial Technology, Universitas Ahmad Dahlan, Jl. Kapas No. 9, Semaki, Umbulharjo, Yogyakarta 55166, Indonesia

²Department of Chemistry, Faculty of Mathematics and Natural Sciences, Universitas Gadjah Mada, Sekip Utara, Yogyakarta 55281, Indonesia

³Department of Chemical Engineering, Faculty of Engineering, Universitas Gadjah Mada, Jl. Grafika No. 2, Yogyakarta 55281, Indonesia

* **Corresponding author:**

tel: +62-811256055

email: wegats@ugm.ac.id

Received: November 13, 2021

Accepted: March 15, 2022

DOI: 10.22146/ijc.70415

Abstract: Mesoporous silica (MS) supported by nickel was synthesized from Parangtritis beach sand and assessed for its activity and selectivity as catalysts in hydrocracking waste cooking oil into biofuel. The synthesis of MS was done by the sol-gel method. Ni/MS catalysts using Ni weight variations of 1, 5, and 10 wt.% were denoted as Ni/MS1, Ni/MS5, and Ni/MS10 and were compared to standard mesoporous silica (Ni/SBA-15). The catalysts were characterized using FTIR, XRD analysis, N₂ gas sorption analysis, SEM-EDX, and TEM. Catalyst Ni/MS1, Ni/MS5, Ni/MS10, and Ni/SBA-15 have specific surface areas of 130.5, 195.9, 203.9, and 381.2 m²/g and the average pores of 12.30, 9.80, 11.12, and 8.70 nm, respectively. The hydrocracking was run four times to evaluate the catalyst reusability. The hydrocracking WCO has 95.8, 82.4, and 85.2%, respectively. While Liquid fractions produced were 38.8, 43.2, and 50.2 wt.%, each of which contains gasoline of 37.09, 39.76, and 44.27 wt.%, Ni/MS10 has the highest liquid products of 50.2 wt.% and was selective to gasoline fractions up to 44.27%. Therefore, the catalyst synthesized from Parangtritis beach sand is selective for gasoline-fraction hydrocarbon and has hydrocracking activity up to 4 runnings.

Keywords: beach sand; catalyst; hydrocracking; mesoporous silica; gasoline selective

■ INTRODUCTION

The waste of cooking oil (WCO), one of the most frequently used cooking oils with over 3.5 MT/annum consumption (2.5% of world vegetable cooking oil production), can be considered a promising alternative for renewable energy sources [1]. The population growth per year led to increased cooking oil usage and, in turn, resulted in the accumulation of its waste in the environment [2]. Waste cooking oil (WCO) contains fatty acid methyl ester (FAME), which can be used as a biofuel. WCO can be environmentally friendlier than those made from food crops, such as palm oil. A suitable performing catalyst is required to convert a sufficiently high methyl ester content in WCO. The hydrocarbon produced from

this process has similar compounds to those found in petroleum fuel, in which there is a higher energy density, lower viscosity, and higher stability [3].

Conversion of waste cooking oil into hydrocarbon requires an acidic catalyst with optimal activity, stability at high temperatures, and high selectivity for the desired product. Among many catalysts available, mesoporous silica has drawn much attention in recent years because of its high porosity properties and better performance [4]. However, the availability of MS and other synthetic silica materials is limited and may be expensive. The alternative is to use naturally occurring silica materials, such as beach sand. Beach sand is an example of carbonate sand with a silicon dioxide content of 72–84% [5], though the silica composition varies depending on

the geographical location. Parangtritis beach sand, located in Yogyakarta, Indonesia, abounds with silica [6]. For this reason, this research used silica extracted from Parangtritis beach sand as a material to synthesize mesoporous silica catalysts. However, no research has yet to confirm whether catalyst produced from beach sands has high activity and selectivity to hydrocarbon gasoline fraction.

Metal precursors are required to increase the number of active sites in a catalyst, thus increasing the activity and selectivity of the catalyst. This study impregnated nickel as metal precursors to support mesoporous silica catalysts. By impregnating nickel, it is expected to increase the number of active sites and the catalyst's ability, thereby increasing the catalytic performance. Nickel is also abundant, low cost, and environmentally benign.

This paper studied the synthesis of mesoporous silica from Parangtritis beach sand as a Ni-supported catalyst. The synthesis was done using a dodecyl-amine (DDA) template by sol-gel method, chosen for its relatively fast processing time, in addition to its low-temperature requirement, among other syntheses in the research study by Salamah et al. and Thahir et al. [6-7]. The nickel was then impregnated using the wet impregnation method with variations of nickel content weight of 1, 5, and 10 wt.%. The catalysts were assessed for the activity and selectivity in the hydrocracking process of waste cooking oil into gasoline fraction. The results were compared to the catalyst from standard synthetic mesoporous silica (SBA-15).

■ EXPERIMENTAL SECTION

Materials

The materials used in this study were silica extracted from Parangtritis beach sand, dodecyl amine supplied by Fisher Scientific, distilled water, HCl produced by Mallinckrodt, NaOH produced by VWR Chemicals, AgNO₃, C₅H₅N, Nickel nitrate, and silica standard produced by Sigma Aldrich, and SBA-15 produced by Green Stone Swiss Co. Ltd. Waste cooking oil was obtained collectively from the food shop.

Instrumentation

The functional group in silica, as well as the presence and disappearance of the DDA template from silica, was observed and analyzed using Fourier-Transform Infra-Red Spectrometer (FTIR) in combination with the KBr disc technique [8]. Surface Area & Pore Size Analyzer is from Quantachrome NOVA touch. The mesoporous silica crystallinity was analyzed using X-ray diffraction analysis, XRD-6000 Shimadzu. Morphology of mesoporous silica was characterized by Scanning Electron Microscope (SEM-EDX) mapping and Transmission Electron Microscope (TEM) JEOL JEM-1400 to analyze its pore structure [8]. The acidity of sand, silica, and mesoporous silica were analyzed using gravimetric base adsorption and hydrocracking WCO with a semi-fixed batch hydrocracking reactor.

Procedure

Extraction of silica from Parangtritis beach sand

The silica used was extracted from Parangtritis beach sand using the reflux method. The synthesis steps washed the sand to remove excess Cl and impurities. The washed sands were then sieved with 100 mesh, refluxed with 6 M HCl at 90 °C for 4 h, filtered, and washed with distilled water until the pH was 7. The neutralized sand was then dried at 120 °C for 2 h. Silica was extracted from the sand sample by refluxing each sample with 6 M NaOH at a constant temperature of 80 °C for 4 h, then filtered and washed. Concentrated HCl was added dropwise into the filtrate until the pH reached 12 and the solution turned white. The solution was then stored for 24 h until the gel was formed. Afterward, the gel was separated and washed until the filtrate had no Cl. The synthesized silica dried in an oven at 120 °C for 4 h [6].

Synthesis of mesoporous silica (MS)

Mesoporous silica was synthesized using the sol-gel method with DDA surfactant as a template [6]. First, powder SiO₂ was dissolved in a solution of 1.5 M NaOH and stirred at a temperature of 40 °C for 30 min to obtain soluble sodium silicate. Next, sodium silicate was added dropwise to 0.05 M DDA solution under rotation speed

of 120 rpm at room temperature and stirred for 40 min. The solution was left under a static condition at room temperature for 18 h [9]. The product was then filtered and washed with distilled water until the filtration reached a pH value of 6. Finally, it was dried at 50 °C for 4 h. The dried product was then calcined at 600 °C for 5 h with a heating rate of 5 °C/min to remove the surfactant template.

Synthesis of Ni/MS catalyst

The synthesized Nickel mesoporous silica (MS) catalyst was divided into three samples: Ni/MS1, Ni/MS5, and Ni/MS10, Ni/SBA-15 for the standard. The first sample, MS1, used Ni impregnation of 1 wt.%. Ni/MS5 and Ni/MS10 used nickel impregnation of 5 and 10 wt.%, respectively. The catalyst Ni/MS from mesoporous silica (MS) was prepared by impregnating nickel nitrate into MS for 24 h at 30 °C. The material was then dried in the oven for 24 h at 100 °C. Next, the catalyst was calcined at a temperature of 500 °C for 5 h under the flow of nitrogen gas (20 mL min⁻¹) and reduced for 4 h at 450 °C under the flow of H₂ (20 mL min⁻¹) for 3 h and then characterized by FTIR.

Sample characterization

The functional group in catalyst Ni/MS and the presence and disappearance functional group from MS were observed and analyzed using Fourier-Transform Infrared Spectrometer (FTIR) combined with the KBr disc technique, the sample used for analysis was 2–5 mg.

The acidity of catalyst Ni/MS was analyzed using gravimetric with pyridine as an adsorbate. An empty crucible was first dried in the oven at 100 °C for 1 h and weighed as W1. As much as 0.1 g of the catalyst sample was put into the crucible, reheated at 100 °C for 1 h, and weighed as W1. As much as 0.1 g of the catalysts sample was put into the 100 °C for 1 h. The mass measured after this process was labeled as W2. The catalyst's crucible was then put into a closed desiccator and flowed with pyridine for 24 h. The mass of the sample obtained was considered W3. Total acidity is calculated using the following formula [10].

$$\text{Total Acidity} = \frac{W3 - W2}{(W2 - W1)Mr_{C_5H_5N}} \times 1000$$

The catalyst was characterized using SEM, TEM, Surface Area, and Pore Size Analyzer.

The catalytic performance in hydrocracking waste cooking oil

Hydrocracking of waste cooking oil was done by putting 0.1 g of Ni/MS and 10 g of waste cooking oil into the oil container. The waste cooking oil sample and catalyst were put into a semi-fixed batch hydrocracking reactor [11]. The reactor with OD 25 cm, ID = 5 cm, length = 36 cm, holder feed at 10 cm long, OD 5 cm.

The catalytic activity of mesoporous silica was evaluated in hydrocracking waste cooking oil by a reactor. The reactor was set at a temperature of 450 °C, 1 atm, per 2 h, with a hydrogen gas flow at 20 mL/min. The liquid produced by hydrocracking waste cooking oil was further analyzed by Gas Chromatography-Mass Spectrometer (GC-MS, Shimadzu QP2010S) to determine the components of compounds in liquid products.

The reactant yield was determined gravimetrically by using calculation as written in the equation below [12]:

$$\text{Liquid fraction (LF) (wt.\%)} = \frac{W_P}{WF} \times 100\% \quad (1)$$

$$\text{Residue (wt.\%)} = \frac{WR}{WF} \times 100\% \quad (2)$$

$$\text{Coke (wt.\%)} = \frac{WC2 - WC1}{WF} \times 100\% \quad (3)$$

$$\text{Gas} = 100 - (\text{LF} + \text{coke} + \text{residue}) \quad (4)$$

$$\text{Total result (\%)} = (100 - \text{residue}) \quad (5)$$

$$\text{Selectivity (wt.\%)} = \frac{Ac}{AT} \times 100\% \quad (6)$$

where W_p is the weight of the product, WF is the weight feed, WR is the unconverted weight product (g), WC1 is the weight of catalyst before hydrocracking (g), WC2 is the weight of catalyst after hydrocracking (g), Ac is GC-MS area of the gasoline or diesel fraction or free fatty, aldehydes/ketones, alcohols and other oxygenates, and AT is the total GC-MS area.

RESULTS AND DISCUSSION

Characterization of Ni/Mesoporous Silica Catalyst

Functional Groups contracting all catalyst materials in this study were analyzed using FTIR, as shown in Fig. 1.

The broadband at a wavenumber of 460 cm^{-1} showed bending vibration, indicating the presence of Si–O–Si [13]. An influentially strong intensity band at 1090 cm^{-1} represented Si–O–Si stretching; this is due to the interaction of the O–H group originating from the water found on the Ni/MS surface through hydrogen bonds. It was generally known that the $450\text{--}1300\text{ cm}^{-1}$ range was the unique silica band [6]. The broadband at a wavenumber of 1632 cm^{-1} showed bending Si–OH as there were new bands at 1635 cm^{-1} and a strong band at 3437 cm^{-1} . This phenomenon follows a previous study by Qiu et al. and Komaruzzaman et al. [14–15]. The broadband at a wavenumber of spectra MS and Ni/SBA-15 represented water O–H bending and O–H stretching, as well as silanol (Si–OH) and Siloxane functional (Si–O–Si), respectively [16]. The impregnation process of Ni does not destroy or affect the functional group of MS.

The materials used are mesoporous silica (either MS or SBA-15) which contains Si. Therefore the FTIR results show the presence of a Si bond toward OH (Si–OH) or Si–O–Si. A comparison of FTIR result analysis of MS with the Ni-supported catalyst does not show any significant difference. Similarly, the impregnation of Ni does not change the structure of MS. In addition, the FTIR result does not show any Ni peak because metal elements will only appear in the fingerprint area [16–17].

Acidity analysis

Ni/MS catalyst surface acidity was determined using pyridine as a base probe molecule in gravimetric analysis.

The results were 0.71 mmol/g for sand, 0.9 mmol/g for silica, 1.02 mmol/g for MS, 1.34 mmol/g for Ni/MS1 and 1.55 mmol/g for Ni/MS5, Ni/MS10 1.74 and Ni/SBA-15 2.09 mmol/g . The higher acidity of Ni/SBA-15 and Ni/MS10 showed potential as a catalyst that requires acid sites, such as hydrocracking. The greater the nickel impregnation, the higher the acidity was. This property was due to the uneven distribution of the pores on the layer surface of the material [14,18–19].

The data show that the Ni/MS catalyst had a higher total acidity value than the MS. The increase in total acidity was caused by metals deposited on the carrier, resulting in more acidic sites. The number of acidic sites affected pyridines adsorbed on the catalyst surface. In addition, the increased metal contents led to more acidic sites, which in turn increased the probability of pyridine adsorption on the catalyst surface. This phenomenon showed that Ni/MS catalysts could be used as hydrocracking catalysts.

Catalyst crystallinity analysis

The catalyst crystallinity was examined using XRD (Fig. 1). Sand and silica have crystalline, Excluding Ni/MS1, Ni/MS5, and Ni/SBA-15. It was found that MS has an amorphous silica mesoporous phase [16]. In contrast, the catalyst with impregnated Ni 10 wt.% showed crystals. This crystalline structure was because the increase in the metal content of Ni produced a crystal diffractogram pattern with crystal peaks appearing at $2\theta = 44, 52,$ and 76° (111), (200) and (220) (JCPDS card

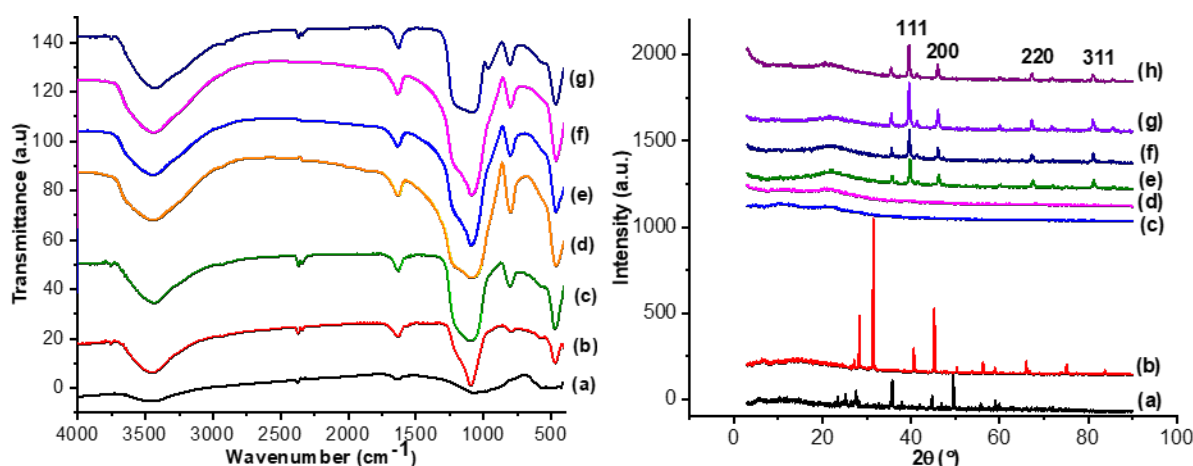
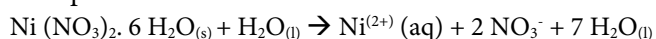


Fig 1. Infra-red spectra (left) and diffraction pattern (right) of (a) Sand, (b) Silica, (c) MS, (d) Ni/MS1, (e) Ni/MS5, (f) Ni/MS10, and (g) Ni/SBA-15 catalyst

no. 00-004-0850). These results indicate that these peaks are characteristic of Ni where the presence of sufficient nickel oxide forms face-centered cubic Ni crystals, which aligns with a research study by Sudhasree et al. [16]. When the Ni impregnation on MS is conducted, this stage can be explained as follows:



When immersed in the carrier system, Ni precursors in the form of cations (Ni^{2+}) with high mobility were adsorbed into MS solids due to the chemical potential difference between the solution and MS solids. Subsequently, the cations interacted with MS (carrier) and were distributed in the material. There was a coordinated covalent bond between the Ni^{2+} ion and the oxygen atom on the MS surface (carrier 0 to form NiO) after the calcination treatment. The reduction treatment using H_2 gas resulted in a great NiO bonded to the MS surface being reduced to aggregate Ni particles [19-20],

$$\text{NiO}(s) + \text{H}_2(g) \rightarrow \text{Ni}(s) + \text{H}_2\text{O}(g)$$

Morphology of Ni/MS1, Ni/MS5, Ni/MS10 catalyst

SEM was used to further confirm the morphological structure of the synthesized material at a magnification of 5000 times with an energy of 15 kV. EDX was used to determine the amount of impregnated Ni concentration. The morphology of sand, silica, MS, Ni/MS1, Ni/MS5, Ni/MS10, and Ni/SBA-15 are shown in Fig. 2, Table 1, and Fig. 3.

The SEM image catalyst in Fig. 2. shows the morphology of (a) sand, (b) silica sand, (c) mesoporous silica, (d) Ni/MS1, (e) Ni/MS5, (f) Ni/MS10, and (g) Ni/SBA-15, which are uniformly bundled macroscopic structures. The figure reveals that the surface of the catalyst material is rough and consists of a relatively uniform arrangement of particle aggregates. The shape is almost spherical (semispherical), in which the agglomeration of the particle aggregates containing Ni is higher than that of MS. Typical particle agglomerates in the form of granules formed on the Ni/MS5 catalyst are

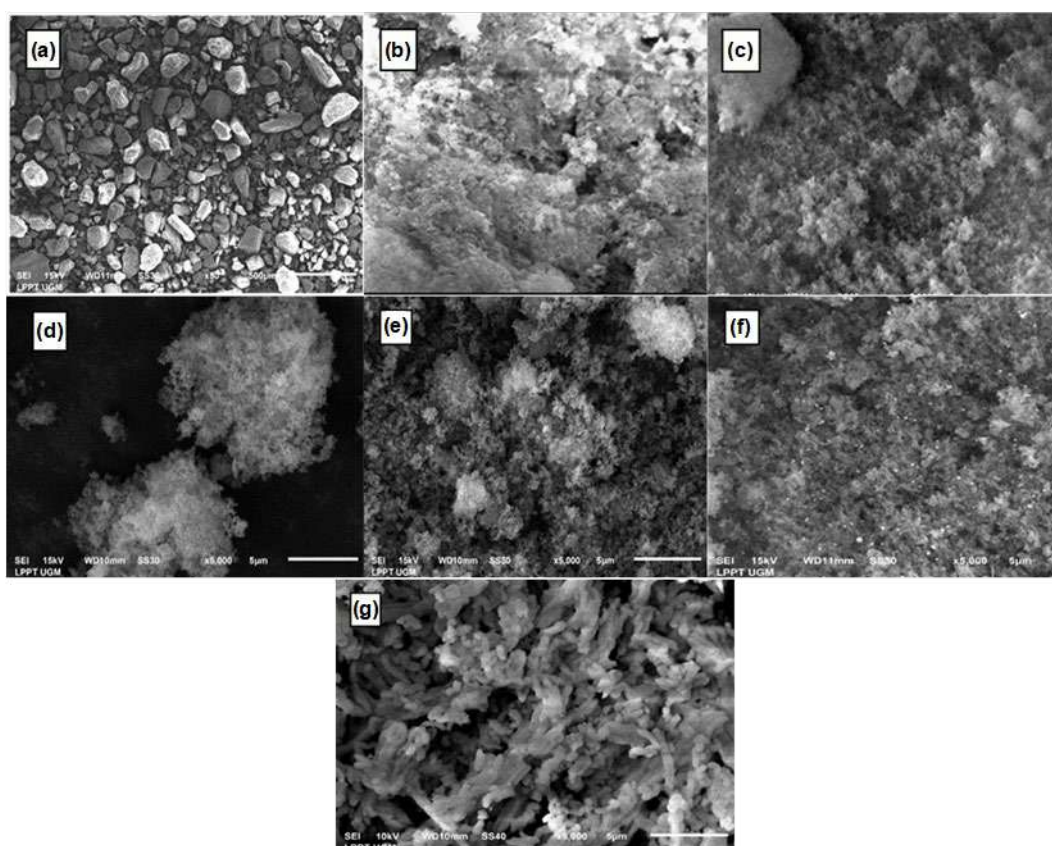


Fig 2. Morphology of catalyst (a) Sand, (b) Silica, (c) MS, (d) Ni/MS1, (e) Ni/MS5, (f) Ni/MS10, (g) Ni/SBA-15

larger and more non-uniform than those on MS. Small particles tend to form strong agglomerates, which require very high specific energy inputs to overcome the adhesion forces between particles.

The morphology type of MS is an aggregate shaped like a coral, while the morphological type of Ni/SBA-15 is an aggregate that is shaped like a rod [19]. On the surface of the MS catalyst, all MS pores are visible, which is characteristic of amorphous carrier material. In the Ni/MS1 and Ni/MS5 pictures, agglomeration of the impregnated metal appears to occur.

In Ni/MS10, the impregnated Ni metal enters the pores and spreads evenly on the catalyst surface. This phenomenon is related to the results of the XRD analysis that the metal-bearing Ni is 10%, as also evidenced in the previous research by Komaruzzaman et al. [15]. The characteristics of Ni have embedded in a porous material forms Ni, which is in the pores and on the surface of the pores, causing agglomeration [19]. The element on the surface of Ni/MS1, Ni/MS5, Ni/MS10, and Ni/SBA-15 were analyzed by EDX mapping, as shown in Table 1 and Fig. 3.

Not all the Ni content on the surface of the impregnated mesoporous silica can be deposited. At 1% impregnation Ni, 0.87% impregnated Ni, the higher the

impregnated Ni, the lower the impregnated metal was. This effect was probably due to the agglomeration of Ni metal and the amount of Ni on their surface, which were dramatically different. This indicated that most Ni in Ni/MS5 entered and filled the pores or the internal surface of the materials, and hence, they did not appear on the surfaces [20].

The EDX mapping is a beneficial method for examining the distribution of each type of atom on the catalyst's surface. As shown in Fig. 3. the EDX spectra confirm that the main elements of the analyzed material are Silica (Si), Oxygen (O), and Nickel (Ni). The EDX data shows that the Ni/MS catalyst material contains several elements. The ratio of the mass percent of the elements Si, O, and Ni are presented in Table 1. The catalyst material prepared with the highest concentration contains 5.96% Ni. The EDX analysis data

Table 1. Element contents of catalyst

Sample	Element composition (wt.%)				
	Si	O	C	Na	Ni
Ni/MS1	27.31	48.72	22.3	0.73	0.87
Ni/MS5	27.21	67.56	0	1.21	0.64
Ni/MS10	33.19	54.47	0	1.41	5.96
Ni/SBA-15	33.50	50.91	13.89	0	0.46

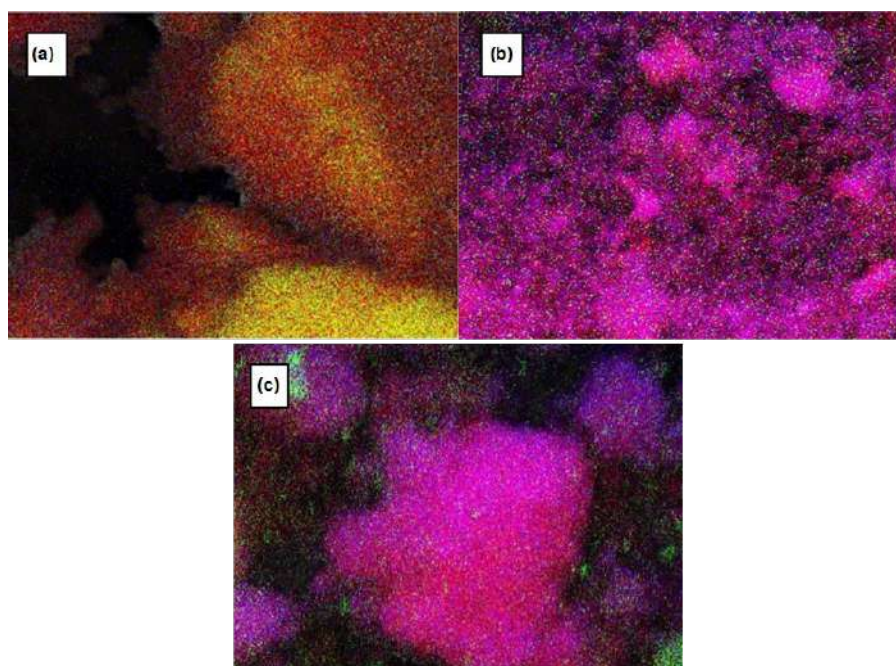


Fig 3. EDX-Mapping morphology of (a) Ni/MS1, (b) Ni/MS5, and (c) Ni/MS10 catalyst

listed in the picture (which is colorful) is a mapping of the distribution of Si, O, and Ni elements on the surface of the Ni/MS catalyst material. The mapping shows that the dispersion of silica and oxygen, and Ni on the catalyst's surface is relatively homogeneous, and agglomeration occurs.

In the Ni/MS1 catalyst, the red, green, and blue colored dots are identified as silica, oxygen, and nickel. The Ni is evenly distributed. In the Ni/MS5 and Ni/MS10 catalysts, the red, blue, and green colored dots are identified as silica, oxygen, and nickel. This shows that the Ni atoms are evenly distributed. However, there is an agglomeration of the Ni atoms in clusters. The agglomeration is not expected because it reduces the surface area of the catalyst, which is expected to interact with the feed during the catalyst activity test. This finding is in line with previous studies by Qiu et al. [14] and Wang et al. [19]. Ni atom precursors are difficult to direct into the mesoporous channels. Ni is detected both inside and outside the pores, causing poor dispersion due to redistribution and agglomeration. This finding is in line with previous studies by Pauly et al. [21].

Gas sorption analysis catalyst

The synthesized catalyst Ni/MS were analyzed using Gas Sorption Analyzer (GSA) to determine their porosity character. In this analysis, the isotherm graph and specific surface area were calculated using the BET equation. Pore volume, average pore diameter, and pore size distribution were calculated using BJH.

The characterization of GSA produced the classification of mesoporous materials based on their pore size according to the material classification [22-23]. The results of the characterization of GSA can be seen in Table 2.

The results show that Ni/MS catalysts and MS have a larger surface area than sand and silica. MS also shows 122.8 m²/g, which indicates that it is a mesoporous material. Based on this data, it can be concluded that the synthesis of MS from the DDA template and Parangtritis beach sand was successfully carried out.

The Ni impregnation into MS increases the surface area of MS; the more significant the Ni is carried, the wider the surface area becomes. For example, for 10 wt.% Ni, there is an increase of 60% in the surface area. Ni/MS10 has a surface area of 203.9 m²/g, while Ni/SBA-15 has 381.2 m²/g. As the surface area increases, more reactants are adsorbed, and the possibility of a reaction occurring is more significant. The impregnation of Ni causes an increase in the physical properties of the catalyst into the MS pores as the entry of Ni into the carrier increases the active site. The acidity triggers the increase. The higher the Ni content is, the more the active sites are formed.

Similarly, the greater the total Ni content is, the wider the surface area becomes, as well as the greater pore volume. This phenomenon is probably due to the Ni being evenly distributed in the carrier system even though there is a slight buildup at certain pore channel positions. The adsorption-desorption isotherm of N₂ gas on the surface of the Ni/MS catalyst is shown in Fig. 4. The desorption isotherm shows a hysteresis loop starting at a P/P₀ relative pressure of about 0.5. This fact indicates that the relative pressure is brought to 0.5. Nitrogen gas is adsorbed on the monolayer. When the relative pressure starts to be in the range of 0.5 to 1, a multilayer arrangement of nitrogen gas occurs on the active Ni/MS surface. The adsorption isotherm is typical of a reversible type IV with hysteresis loop based on the

Table 2. The porosity property of the Ni/MS catalyst

Samples	Specific surface area (m ² /g)	Total pore volume (cm ³ /g)	Average pore diameter (nm)
Sand	1.08	0.003	2.47
Silica (S)	9.4	0.006	19.12
MS	122.8	0.14	4.65
Ni/MS1	130.5	0.37	12.30
Ni/MS5	195.9	0.47	9.80
Ni/MS10	203.9	0.52	11.12
Ni/SBA-15	381.2	0.80	8.70

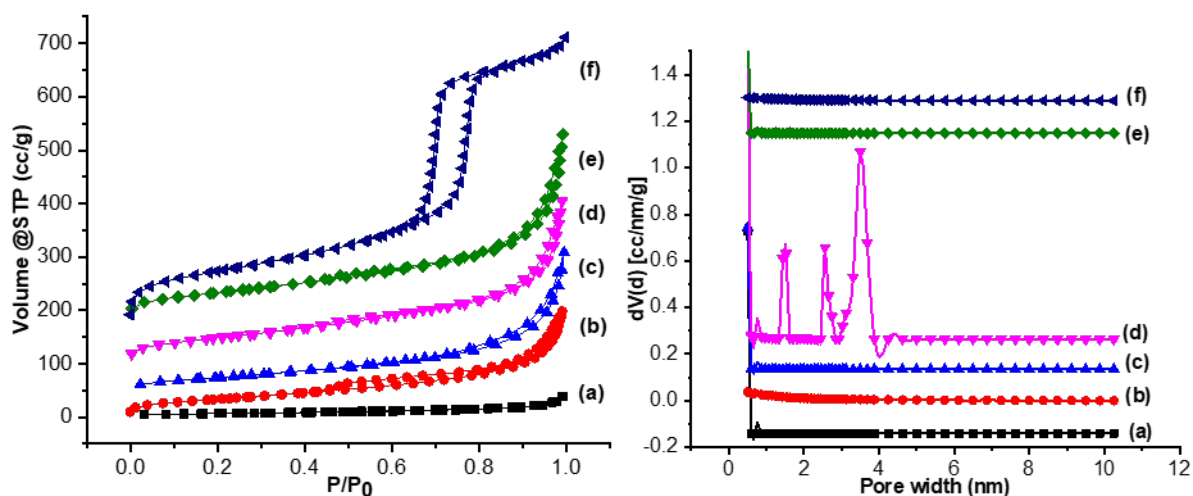


Fig 4. Adsorption-desorption isotherm graphs (left) and pore size distribution graphs (right) of the (a) Silica, (b) MS, (c) Ni/MS1, (d) Ni/MS5, (e) Ni/MS10, and (f) Ni/SBA-15 catalyst

IUPAC classification Schemer for Mesoporous materials [14,23] is shown in Fig. 4.

The hysteresis loop formed in the desorption adsorption isotherm has an HIV pattern. The HIV hysteresis loop indicates that the Ni/MS catalyst has a smaller pore mouth size than the pore body size, referred to as a bottle-shaped pore. The bottle-shaped pore causes the nitrogen gas desorption process to run faster. As a result, the amount of nitrogen gas adsorbed and adsorbed at the same pressure is much different. The increase in pore diameter is caused by the space between the layers of the crystal lattice planes, which increases the distance between the crystal lattice planes and causes an increase in the pore diameter. The expansion of the metallic Ni in MS causes the diameter range to increase and allows more gas molecules to enter, thus causing the formation of a more porous structure between layers and contributing to an increase in surface area and porosity. All the three catalysts have the same mesoporous, which is characterized by the presence of a hysteresis loop [22-23].

As shown in Fig. 4, the Ni/MS1, Ni/MS5, and Ni/MS10 catalysts have a reasonably wide pore size distribution, ranging from 1–10 nm. This pore size corresponds to the pore size range of the mesoporous material, which is 2–50 nm [23]. The pore size distribution is the relative abundance of each pore size based on the sample volume represented as dv/r , where

this function has a value that is proportional to the combined volume of all pores whose effective radius is in a minimal range and centered on r . The Ni/MS pore size distribution profile synthesized with variations in Ni mass indicated the presence of a small number of pore fractions with a pore diameter of 4–12.3 nm. The catalyst Ni/MS1, Ni/MS10, and Ni/SBA-15 showed a homogeneous pore distribution of solids. As for the Ni/MS5 catalyst, the pore size distribution is tapered at a diameter of 1–4 nm and slopes at 4–9.8 nm. This catalyst is characterized by mesoporous solids with the most abundant heterogeneous pore distribution at 2–4 nm in diameter. The presence of micropores causes a decrease in pore diameter, which becomes smaller than the Ni/MS10 catalyst. This is probably due to the Ni/MS5 catalyst, where many impregnated Ni agglomeration occurs on the catalyst's surface. The pore distribution is more diminutive than Ni/MS1 and Ni/MS5, as supported by SEM EDX data. This data indicates that the Ni/MS5 obtained is micropore and mesopore-sized, referred to as hierarchical mesoporous [16]. These types follow the data in Fig 3.

Characterization using TEM

TEM image is required to ensure that the synthesized MS has pore gaps according to the results of the GSA analysis. The TEM image in Fig. 5 appears to have clear pores like wormholes. The use of nickel made

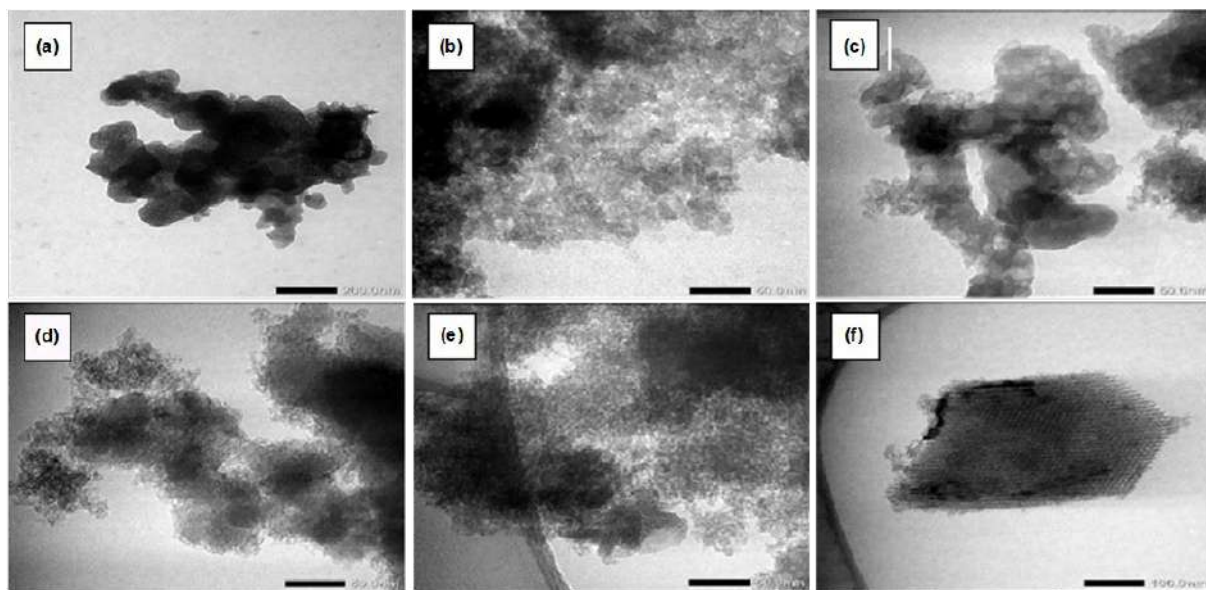


Fig 5. Morphology TEM of (a) silica, (b) MS, (c) Ni/MS1, (d) Ni/MS5, (e) Ni/MS10 and (f) Ni/SBA-15 catalyst

the pore structure of Ni/MS irregular. Pores with a wormhole-like structure were obtained [4,24]. TEM images are required to ensure that the synthesized Ni/MS has a pore gap according to the results of the GSA analysis.

The presence of Ni forms more pores with an irregular pore shape similar to a wormhole, as revealed in previous research studies [4,24]. As a result, the surface area becomes more prominent, and the pore radius increases. The number of pores formed due to the spread of Ni leads to the increasing pore volume in proportion to the added Ni. The study results using variations in the percentage of Ni showed a significant change in the catalyst's performance obtained. As shown in Fig. 3, a severe degree of agglomeration occurs with the addition of 10% Ni. In the results of Ni, which was impregnated with SBA-15, it was also seen that the metal agglomerated in several places.

Catalytic Performance in Hydrocracking of Waste Cooking Oil

This study tested the catalytic activity of MS, Ni/MS1, Ni/MS5, and Ni/MS10 catalysts. The bait used in this research was waste cooking oil. The hydrocracking process was carried out at a temperature of 450 °C and with the weight ratio of catalyst: feed 1:100 and H₂ gas flowed with a flow rate of 20 mL/min to find the catalyst with the best activity and selectivity. The catalytic activity

can be seen in Table 3. The Ni/MS10 has a higher surface area than silica, Ni/MS1, and Ni/MS5. Ni/MS1, Ni/MS5, and Ni/MS10 shows a liquid fraction of 38.8, 43.2, and 50.2 wt. %.

The Ni/MS 10 catalyst produces the highest liquid product. This result is due to the entry of Ni into the pores of MS. Furthermore, Ni/MS has an active site that helps the hydrocracking process. Ni in the hydrocracking process is used as the active site due to its unpaired electrons in the d orbitals. The unpaired electron in the d orbital homolitically dissociates hydrogen gas required in the hydrocracking process and functions as an active hydrogenation site and a Brønsted-Lowry acid site [15]. The Ni/MS10 catalyst has a higher liquid product than the MS due to its higher acidity value. The higher acidity value of a catalyst results in a higher liquid product. This is because an increase in the total acidity of a catalyst causes an increase in the number of acid sites. Whereas the number of acid sites also attracts hybrid ions (H⁺), which play a role in the initial stage of the hydrocracking process. This finding aligns with the previous research study by Qiu et al. [14], who state that a high total acidity increases the liquid product in the hydrocracking process.

Similarly, the presence of Ni reduces the gas product. The used waste cooking oil has been successfully

Table 3. Hydrocracking products of waste cooking oil

Hydrocracking catalyst	Result (wt.%)				Total result (wt.%)
	Liquid product	Gas product	Residue	Coke	
Thermal	15.2	57.3	27.5	0	72.5
MS	41.2	51.2	6.2	1.4	93.7
Ni/MS1	38.8	55.3	4.2	1.7	95.8
Ni/MS5	43.2	37.8	17.5	1.9	82.4
Ni/MS10	50.2	33.3	14.8	1.7	85.2
Ni/SBA15	46.7	40.3	11.3	1.7	88.7

converted into a liquid product [25]. Therefore, the Ni/MS1 catalyst decreases while the amount of gas formed increases. This is probably due to the metal Ni/MS1 catalyst not being well distributed. During the agglomeration, the waste cooking oil, as the feed, cannot be desorbed by the catalyst or is retained on the catalyst so that it causes gas formation. This finding aligns with the previous studies on catalytic performance [13,20].

The main components of used waste cooking oil are petroselinic acid and palmitic acid, where C18 and C16 of the two fatty acids are cracked into shorter hydrocarbon chains if the oxygen is removed, or vice versa, creating shorter fatty acid chains [8]. In the hydrocracking process, the waste cooking oil is converted into liquid, gas, and coke fractions, as shown in Table 3. Ni/MS10 catalyst shows superior performance in producing liquid fraction while retaining its ability to avoid over-cracking, as indicated by the relatively low gas fraction produced. This phenomenon can be caused by the excellent catalyst pore structure, where the mesopores on the catalyst surface allow the feed to enter the catalyst while releasing the product easily.

Liquid product produced in thermal cracking is less compared to catalytic hydrocracking. Thermal cracking produces more gas products compared to catalytic hydrocracking as a result of radical ion formation affected by relatively high temperatures. Radical ions formed in the initiation stage of thermal cracking break the carbon bond and form a new radical compound with fewer carbon atoms; hence, more gas product is produced than catalytic hydrocracking. According to Kusumastuti et al. [24], catalyst Ni/MS10 produces the most liquid product of 50.2 wt.%. This occurrence is due to the penetration of the optimum metal composition of Ni to the MS pores. Ni

also has active sites, which helps the hydrocracking process. In the hydrocracking process, Ni is used as the active site because of unpaired electrons in the d-orbital. Unpaired electrons in the d-orbital will dissociate hydrogen gas homolytically, which is required in the hydrocracking process, and function as active hydrogenation sites and as acid sites of Brønsted-Lowry.

The study shows that the surface area was higher, and the location of the acid site could be responsible for this phenomenon, where the acid site of Ni/MS may reside deep beneath the catalyst. While the feed and product could come in and out easily, the chance of the feed finding the active site before they exit the catalyst becomes slimmer. This hypothesis seems to be responsible for the relatively high amount of oxygenated product [24,26]. The more Ni is impregnated, the more the active sites will be. However, the increase of Ni impregnated can cover the catalyst pore, which causes Lewis's acid site to be clogged, which causes agglomeration. This agglomeration process makes it difficult for the feed in the hydrocracking process to find the active site on the catalyst, compared to the condition of evenly distributed metal and minimal agglomeration. The evenly distributed metal causes the feed to be on the active surface of the catalyst, which may cause the breaking of the C=O bond to produce alcohol as an intermediate. Further hydrogenation of the alcohol produces long-chain hydrocarbons via the hydrodeoxygenation mechanism, as revealed in previous research studies [27]. The Ni/MS catalyst is the most optimal as it has 50.2 wt.% in the liquid fraction, and the thermal reaction has a liquid product of 15.2 wt.%. The results of the analysis of liquid products from hydrocracking show that thermal cracking produces

Table 4. Selectivity of the Ni/MS1, Ni/MS5, and Ni/MS10 catalyst

Hydrocracking catalyst	Liquid fraction (wt.%)					
	Gasoline (C ₅ -C ₁₂)	Diesel (C ₁₃ -C ₁₇)	Free fatty acids	Aldehydes/Ketones	Alcohols	Other oxygenates
Thermal	1.08	7.64	0.00	3.36	3.13	0.00
MS	22.9	1.00	5.34	5.60	5.69	0.66
Ni/MS1	37.09	0.00	0.17	0.41	0.24	0.78
Ni/MS5	39.76	0.24	0.63	0.38	0.24	1.96
Ni/MS10	44.27	0.51	2.57	1.37	1.46	0.00
Ni/SBA15	31.10	0.77	4.94	5.59	1.06	3.25

Gasoline is hydrocarbons containing C₅ to C₁₂ atoms,

Diesel is hydrocarbons containing C₁₃ to C₁₇ atoms,

Oxygenates contain ether, silane, epoxy

1.08% gasoline and 7.64% diesel. Hydrocracking with a catalyst, there is an increase in liquid products containing gasoline from 31.1 to 44.27%. This increase shows that the impregnation of Ni influences the cracking process and that Ni carriers in MS can undergo deoxygenation, decarboxylation, and decarbonylation reactions [26,28-29].

In this study, the liquid product was analyzed using GC-MS (see Table 4). The Gas Chromatography (GC) serves as a separator, while the Mass Spectrometer (MS) was used to detect liquid fraction. The analysis of the chromatogram data produced by the gas chromatography shows the number of components that were separated from the liquid fraction and were detected using a mass spectrometer (MS). The liquid product was obtained from the hydrocracking process of waste cooking oil. This finding is in line with previous studies by Nugraha et al. [25].

The catalyst obtained in this synthesis is selective for the gasoline fraction, the most selective being the Ni/MS10 catalyst. It is probably due to the large surface area and high acidity. The increase in total acidity occurs because the Ni deposited on the carrier provides acidic sites. The acidity and contribution of different catalysts create catalysts with different activities and selectivity. A suitable condenser is required for the hydrogenation of oxygen-containing components. The pore size in the mesoporous catalyst region helps the reactants and intermediates overcome the limited diffusion of adsorption at the Ni sites [9,13].

Several reactions coincide in the cracking process with a catalyst. The cracking occurs by breaking the C-C

bond in the compound. According to Yıldız et al. [3] and Chen et al. [29], the cracking reaction of used waste cooking oil goes through 3 stages, namely decarboxylation, decarbonylation, and hydrodeoxygenation, as shown from the reaction pathway in Fig. 6 [29].

Furthermore, through decarboxylation, CO₂ by-products are formed. The decarboxylation and hydrodeoxygenation reactions often occur through a catalyst following the fatty acid deoxygenation process. The decarboxylation and hydrodeoxygenation reactions coincide to form alkane and alkene products. The number of particular products for the chain gasoline fraction with carbon atoms is from 5 to 12 (C₅-C₁₂). These products show that the hydrodeoxygenation and decarboxylation reactions may occur with hydrogen gas flow at a rate of 20 mL/min [19,26]. The results of the hydrocracking process are in Table 4 and Fig. 7. Hydrocracking with a catalyst, there is an increase in liquid products containing gasoline from 31.1 to 44.27%.

In thermal cracking, relatively few gasoline compounds are formed compared to diesel, and aldehyde and alcohol were formed. In the hydrocracking of WCO with a Ni/MS1 catalyst, several alkane compounds are isomers of hydrocarbon compounds. At peak numbers 15, 19, 20, and 25, a compound with the molecular formula C₁₁H₂₂ is 2-Undecene (Z), 1-Undecane, 3-Undecane (Z), and 3-Undecane. At peak 27, 34, and 36 are compounds with the molecular formula C₁₂H₂₄, namely 5-5-Dodecane, E1-Dodecane, and Cyclohexane. According to Chen et al. [29], the

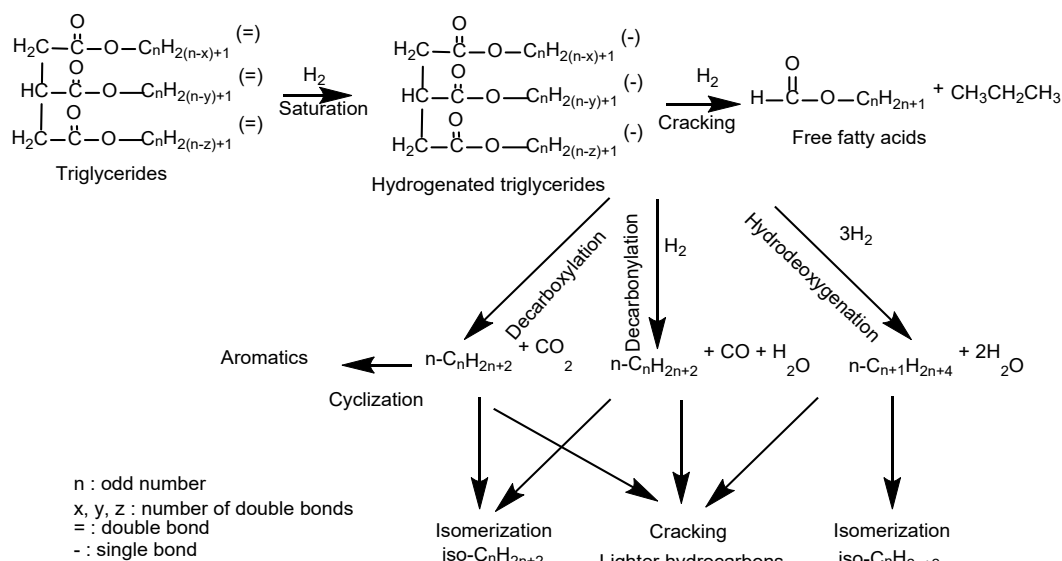


Fig 6. The possible hydrocracking pathway

Table 5. Distribution of catalyst reusability in hydrocracking WCO

Catalyst	Result (wt.%)				Total result (wt.%)
	Liquid product	Gas product	Residue	Coke	
Ni/MS1 ¹	38.8	55.3	4.2	1.7	95.8
Ni/MS1 ²	38.3	27.6	32.1	2	67.9
Ni/MS1 ³	39.9	32.1	26.1	2	73.9
Ni/MS1 ⁴	49	34.8	12.4	3.8	87.6
Ni/MS5 ¹	43.2	37.8	17.5	1.9	82.4
Ni/MS5 ²	37.7	33.8	27.2	1.3	72.8
Ni/MS5 ³	46	28.9	22.5	2.6	77.5
Ni/MS5 ⁴	41.8	42	15.9	0.3	84.1
Ni/MS10 ¹	50.2	33.3	14.8	1.7	85.2
Ni/MS10 ²	37.8	29.8	31.5	0.9	68.5
Ni/MS10 ³	25.5	52.7	20.9	0.9	79.1
Ni/MS10 ⁴	40.7	19	34.1	1.3	81
Ni/SBA15 ¹	46.7	40.3	11.3	1.7	88.7
Ni/SBA15 ²	48.9	27.9	21.1	2.1	78.9
Ni/SBA15 ³	46.6	30	22.3	1.1	77.7
Ni/SBA15 ⁴	43.1	52.6	2	2.3	98

¹The first hydrocracking; ²The second hydrocracking; ³The third hydrocracking;⁴The fourth hydrocracking

formation of this isomer is due to the decarboxylation and hydrodeoxygenation processes.

The reusability of Ni/MS1, Ni/MS5, and Ni/MS10 catalyst for hydrocracking of WCO

The stability test of the Ni/MS catalyst was conducted 4 times for hydrocracking using WCO at a

temperature of 450 °C and a weight ratio of 1:100 catalyst: feed. Throughout 4 testing runs, the Ni/MS1, Ni/MS5, and Ni/MS10 catalysts produced optimum activity and selectivity with high conversion rates. The results of the reusability of the catalyst can be seen in Table 5. The Ni/MS5 catalyst activity increased with the use of the catalyst throughout the four runs. The GC-MS

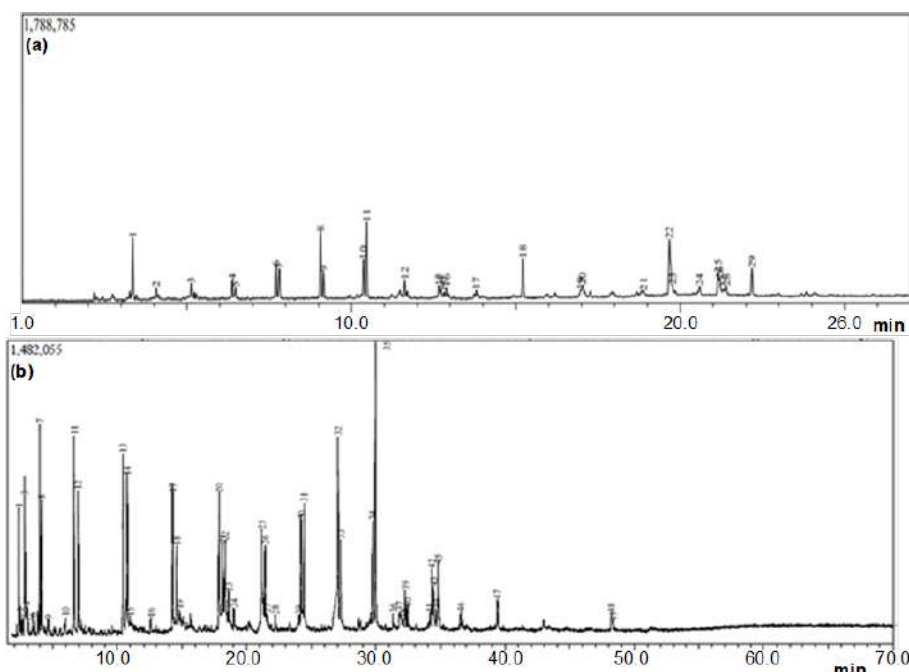


Fig 7. The Gas chromatograms of (a) thermal cracking WCO and (b) hydrocracking WCO with Ni/MS1

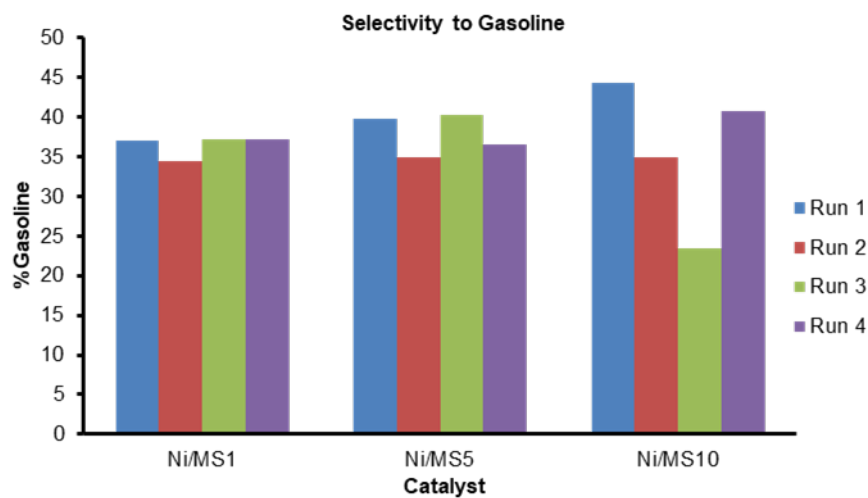


Fig 8. The reusability of catalyst from hydrocracking of WCO

analysis of reusability results can be seen in Fig. 8.

The stability test results of GC-MS analysis on selectivity in the gasoline fraction show that the Ni/MS5 and Ni/MS10 catalyst is relatively stable throughout the four runs. This stabilization effect is probably due to the overall character of the catalyst, namely Ni properties, acidity, surface area, pore volume, pore diameter, and reaction mechanism. The Ni/MS10 catalyst has the highest acidity and surface area. Coke formation was also

seen to decrease, indicating stability against coke poisoning. Increasing the amount of coke on the catalyst's surface can cover the catalyst's active site where the deoxygenation mechanism occurs. The deactivation of the catalyst that occurs is caused by the formation of coke deposited on the active site of the catalyst. The residue increased with the reuse of the Ni/MS catalyst.

The results of the repetition of the Ni/MS10 catalyst were seen decreasing in the 1st, 2nd, and 3rd run and

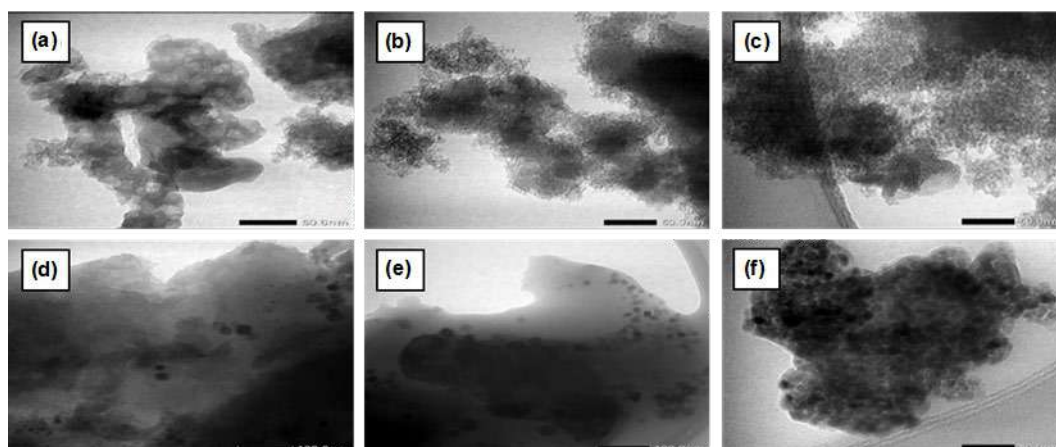


Fig 9. Morphology TEM of catalyst before and after hydrocracking

they were increasing in the 4th run. According to Trisunaryanti et al. [27] and Rodiansono and Trisunaryanti [28], after repeated use of the catalyst, the active sites decrease either due to coke or temperature. The reduction of the active site causes the hydrocracking reaction to be more dominantly affected by temperature than by the catalyst. At the same time, this increase is due to the polymerization reaction of lighter components into components with a more significant number of carbon atoms. Although still going through the mechanism of free radical formation, these radicals combine to form more significant hydrocarbon compounds.

The morphological structure of the Ni/MS catalyst before and after the stability test in this study was characterized using a Transmission Electron Microscope (TEM) observed at 100 nm magnification. The Ni/MS catalyst before and after hydrocracking is shown in Fig. 9. As can be seen, Fig. 9(a-c) are the catalysts before hydrocracking when the agglomeration has not occurred. Fig. 9(d-f) shows the condition after the fourth use when black spots and clumping appear. Clumping that occurs indicates the presence of a sintering process. The sintering process can occur due to too high a temperature, which causes the aggregation of Ni [24-25]. The black stain that is visible comes from the nickel getting darker. It indicates that coke formation affects the deactivation of the catalyst [12]. This result also follows the coke level in Table 3, which shows the increasing amount of coke, and in Fig. 9(e) and 9(f), which indicate quite dark black spots. Coke

formation was also seen to increase, indicating stability against coke poisoning. Increasing the amount of coke on the catalyst surface can cover the active catalyst site where the deoxygenation mechanism occurs. The deactivation of the catalyst that occurs is caused by the formation of coke deposited on the active site of the catalyst. The residue increased with the reuse of the Ni/MS catalyst.

Coke is a by-product formed during the hydrocracking process. Coke can reduce the activity of the catalyst because coke can cover the active site of the catalyst, causing the breakdown of long-chain hydrocarbons to be lower. This produced coke causes a decrease in the activity of the catalyst, as can be seen in the picture on the stability test. Trisunaryanti et al. [12] reused the catalyst as several acid sites became shields from the coke deposit.

■ CONCLUSION

The Ni/mesoporous silica catalyst was successfully synthesized from Parangtritis Beach sand using dodecyl Amina as a template. The catalysts were synthesized by impregnating MS with Ni metal of 1, 5, and 10 wt.% weight variations and were denoted as Ni/MS1, Ni/MS5, and Ni/MS10. These catalysts had specific surface areas of 130.5, 195.9, and 203.9 m²/g, while standard Ni/SBA-15 had 381.2 m²/g. The average pores were 12.30, 9.8, and 11.12 nm, while Ni/SBA-15 had 8.7 nm. The hydrocracking WCO has 95.8, 82.4, and 85.2 wt.%, and Ni/SBA-15 88.7 wt.%. The activity catalyst produced

liquid fractions recorded at 38.8, 43.3, 50.2, and 46.7 wt.%. They respectively contain gasoline (C₅-C₁₂) of 37.09, 39.76, and 44.27% and Ni/SBA-15 has 31.10%. Therefore, it could be deduced that Ni/MS10 has exceptional performance with reusability until 4 times running and still produce gasoline of 40.73 wt.%. Therefore, the catalyst synthesized from Parangtritis beach sand is selective for gasoline-fraction hydrocarbon and has hydrocracking activity up to 4 runnings.

■ ACKNOWLEDGMENTS

The authors would like to express the deepest gratitude to the General Director of Higher Education, Ministry of Education and Culture Indonesia, for the financial support under the scheme of Universitas Gadjah Mada Doctoral Dissertation Research (PDD) grant with a contract number 208/UN.1/DITLIT/DITLIT/PT/2021).

■ AUTHOR CONTRIBUTIONS

The first author conducted the experiment, data collection, and analysis and drafted the manuscript. The corresponding author wrote the manuscript and proofread it. The co-author worked as a data analysis consultant. All authors contributed to the shape of the research, research analysis, and manuscript and agreed to the final version of this manuscript.

■ REFERENCES

- [1] Trisunaryanti, W., Larasati, S., Triyono, T., Santoso, N.R., and Paramesti, C., 2020, Selective production of green hydrocarbons from the hydrotreatment of waste cooking oil over Ni- and NiMo- supported on amine-functionalized mesoporous silica, *Bull. Chem. React. Eng. Catal.*, 15 (2), 415–431.
- [2] Nanda, S., Rana, R., Hunter, H.N., Fang, Z., Dalai, A.K., and Kozinski, J.A., 2020, Hydrothermal catalytic processing of waste cooking oil for hydrogen-rich syngas production, *Chem. Eng. Sci.*, 195, 935–945.
- [3] Yildiz, A., Goldfarb, J.L., and Ceylan, S., 2019, Sustainable hydrocarbon fuels via “one-pot” catalytic deoxygenation of waste cooking oil using inexpensive, unsupported metal oxide catalysts, *Fuel*, 263, 116750.
- [4] Nuntang, S., Yousatit, S., Yokoi, T., and Ngamcharussrivichai, C., 2019, Tunable mesoporosity and hydrophobicity of natural rubber/hexagonal mesoporous silica nanocomposites, *Microporous Mesoporous Mater.*, 275, 235–243.
- [5] Irzon, R., 2018, Komposisi kimia pasir pantai di selatan Kulon Progo dan implikasi terhadap provenance, *JGSM*, 19 (1), 31–46.
- [6] Salamah, S., Trisunaryanti, W., Kartini I., and Purwono, S., 2021, Synthesis and characterization of mesoporous silica from beach sand as silica source, *IOP Conf. Ser.: Mater. Sci. Eng.*, 1053, 012027.
- [7] Thahir, R., Wahab, A.W., Nafie, N.L., and Raya, I., 2019, Synthesis of mesoporous silica SBA-15 through surfactant set-up and hydrothermal process, *Rayasan J. Chem.*, 12 (3), 1117–1126.
- [8] Salamah, S., Trisunaryanti, W., Kartini, I., and Purwono, S., 2021, Hydrocracking of waste cooking oil into biofuel using mesoporous silica from Parangtritis Beach sand synthesis by sonochemistry, *Silicon*, 14, 3583–3590.
- [9] Miyao, T., Sakurabayashi, S., Shen, W., Higashiyama, K., and Watanabe, M., 2015, Preparation and catalytic activity of mesoporous Silica-coated Ni-Alumina base catalyst for selective CO methanation, *Catal. Commun.*, 58, 93–96.
- [10] Wijaya, K., Kurniawan, A.H., Saputri D., Trisunaryanti, W., Mirzan, M., Harjani, P.L., and Tjkoalu A.D., 2021, Synthesis of nickel catalyst supported on ZrO₂/SO₄ pillared bentonite and its application for conversion of coconut oil into gasoline via hydrocracking process, *J. Environ. Chem. Eng.*, 9 (4), 105399.
- [11] Levenspiel, O., 1999, “Chemical Reaction Engineering,” in *Chemical Reaction Engineering*, 3rd Ed., John Wiley & Sons, New York, US, 90–119.
- [12] Trisunaryanti, W., Sumbogo, S.D., Mukti, R.R., Kartika, I.A., Hartati, and Triyono, 2021, Performance of low-content Pd and high-content Co, Ni supported on hierarchical activated carbon for the hydrotreatment of *Calophyllum inophyllum* oil (CIO), *React. Kinet., Mech. Catal.*, 134 (1), 259–272.
- [13] Wijaya, K., Saputri, W.D., Aziz, I.T.A., Wangsa, Heraldly, E., Hakim, L., Suseno, A., and Utami, M.,

- 2021, Mesoporous silica preparation using sodium bicarbonate as template and application of the silica for hydrocracking of used waste cooking oil into biofuel, *Silicon*, 14 (4), 1583–1591.
- [14] Qiu, S., Zhang, Q., Lv, W., Wang, T., Zhang, Q., and Ma, L., 2017, Simply packaging Ni nanoparticles inside SBA-15 channels by co-impregnation for dry reforming of methane, *RSC Adv.*, 7, 24551–24560.
- [15] Komaruzzaman, M.F., Taufik-Yap, Y.H., and Derawi D., 2020, Green diesel production from palm fatty acid distillate over SBA-15 supported nickel/cobalt catalyst, *Biomass Bioenergy*, 134, 105476.
- [16] Sudhasree, S., Banu, A.S., Brinda, P., and Kurian, G.A., 2014, Synthesis of nickel nanoparticles by chemical and green route and their comparison in respect to biological effect and toxicity, *Toxicol. Environ. Chem.*, 96 (5), 743–754.
- [17] Lin, H.Y., and Chen, Y.W., 2005, Preparation of spherical hexagonal mesoporous silica, *J. Porous Mater.*, 12 (2), 95–105.
- [18] Lin S., Shi, L., Ribeiro Carrott, M.M.L., Carrott, P.J.M., Rocha, J., Li, M.R., and Zou, X.D., 2011, Direct synthesis without addition of acid of Al-SBA-15 with controllable porosity and high hydrothermal stability, *Microporous Mesoporous Mater.*, 142 (2-3), 526–534.
- [19] Wang, N., Yu, X., Shen, K., Chu, W., and Qian, W., 2013, Synthesis, characterization and catalytic performance of MgO-coated Ni/SBA-15 catalysts for methane dry reforming to syngas and hydrogen, *Int. J. Hydrogen Energy*, 38 (23), 9718–9731.
- [20] Amin, A.K., Wijaya, K., and Trisunaryanti, W., 2020, Physico-chemical properties of nickel promoted sulfated zirconia powder prepared using different procedures, *Asian J. Chem.*, 32 (3), 555–560.
- [21] Pauly, T.R., Liu, Y., Pinnavaia, T.J., Billinge, S.J.L., and Rieker, T.P., 1999, Textural mesoporosity and the catalytic activity of mesoporous molecular sieves with wormhole framework structures, *J. Am. Chem. Soc.*, 121 (38), 8835–8842.
- [22] Sotomayor, F.J., Cychosz, K.A., and Thommes, M., 2018, Characterization of micro/mesoporous materials by physisorption: Concepts and case studies, *Acc. Mater. Surf. Res.*, 3 (2), 34–50.
- [23] Coasne, B., 2016, Multiscale adsorption and transport in hierarchical porous materials, *New J. Chem.*, 40 (5), 4078–4094.
- [24] Kusumastuti, H., Trisunaryanti, W., Falah, I.I., and Marsuki, M.F., 2018, Synthesis of mesoporous silica-alumina from Lapindo mud as support of Ni and Mo metals catalysts for hydrocracking of pyrolyzed α -cellulose, *Rasayan J. Chem.*, 11 (2), 522–530.
- [25] Nugraha, A., and Nandiyanto, A.B.D., 2021, How to read and Interpret GC/MS spectra, *IJOMR*, 1 (2), 171–206.
- [26] Li, L., Ding, Z., Li, K., Xu, J., Liu, F., Liu, S., Yu, S., Xie, C., and Ge, X., 2016, Liquid hydrocarbon fuels from catalytic cracking of waste cooking oils using ultrastable zeolite USY as catalyst, *J. Anal. Appl. Pyrolysis*, 117, 268–272.
- [27] Trisunaryanti, W., Larasati, S., Bahri, S., Ni'mah, Y.L., Efiyanti, L., Amri, K., Nuryanto, R., and Sumbogo, S.D., 2020, Performance comparison of Ni-Fe loaded on NH₂-functionalized mesoporous silica and beach sand in the hydrotreatment of waste palm cooking oil, *J. Environ. Chem. Eng.*, 8 (6), 104477.
- [28] Rodiansono, and Trisunaryanti, W., 2005, Activity test and regeneration of NiMo/Z catalyst for hydrocracking of waste plastic fraction to gasoline fraction, *Indones. J. Chem.*, 5 (3), 261–268.
- [29] Chen, R.X., and Wang, W.C., 2019, The production of renewable aviation fuel from waste cooking oil. Part I: Bio-alkane conversion through hydro-processing of oil, *Renewable Energy*, 135, 819–835.

Evaluation of Influencing Factors and Technological Processes for the Production of Orange Essential Oil (*Citrus sinensis*) on Equipment Semi-industrial Distillation

Tran Thien Hien^{1,2*}, Hoang Quang Binh^{1,2}, Huynh Bao Long³, and Xuan Tien Le^{4,5}

¹Institute of Environmental Technology and Sustainable Development, Nguyen Tat Thanh University, Ho Chi Minh City 700000, Vietnam

²Faculty of Food and Environmental Engineering, Nguyen Tat Thanh University, Ho Chi Minh City 700000, Vietnam

³Faculty of Chemical Engineering, Ho Chi Minh City University of Food Industry, Ho Chi Minh City 700000, Vietnam

⁴Faculty of Chemical Engineering, Ho Chi Minh City University of Technology, Ho Chi Minh City 700000, Vietnam

⁵Vietnam National University Ho Chi Minh City, Ho Chi Minh City 700000, Vietnam

* **Corresponding author:**

tel: +84-375643345

email: hientt@ntt.edu.vn

Received: November 15, 2021

Accepted: February 17, 2022

DOI: 10.22146/ijc.70467

Abstract: In recent years, essential oils extracted from different plant species have become increasingly popular in the production of pharmaceuticals, cosmetics, and foods. The essential oil from orange (*Citrus sinensis*) is important in large-scale applications due to its antibacterial, antioxidant activities, and pleasant aroma. In this study, factors affecting the production of orange essential oil on a distillation device with an operating capacity of 50 L/batch, including the ratio of material to water, temperature, and time distillation, have been surveyed. Through the survey, it was found that the raw materials were pureed, the materials: water ratio was 1:3 g/g, the water heating temperature was 130 °C, and the distillation time was 140 min. The yield of the essential oil was 1.8 mL/g with compounds limonene accounting for 98%, α -Pinene (0.655–0.734%), and β -Pinene (1.114 and 1.163%) by the GC-MS method. The review also found that the hydrodistillation equipment was designed to be suitable for the semi-industrial scales of orange essential oil due to its stable yield and volatile compounds contained in the essential oil.

Keywords: *Citrus sinensis*; hydrodistillation; limonene; essential oil

■ INTRODUCTION

Aromatic substances in general or essential oils have been associated with human life and civilization for thousands of years. Essential oils are the very small, quintessential, most concentrated drops of herbs. Sometimes it's just aromatic molecules formed through regulatory functions in the stems of plants that make them attractive, seduce, bring vitality, freshness, and bring richness to life [1-3]. It is a mixture of soluble organic substances with a characteristic odor. Essential oils are widely used in the cosmetic industry, especially in the production of various perfumes [4], shower gels, hair creams, shampoos [5], as a component of disinfectants in pharmaceuticals [6], and as pesticides in the field of insecticides from natural substances [7-8]. Phenolic

constituents, which are present in essential oils, are known to have antibacterial activity, and some are generally recognized as safe substances [9-11]. Therefore, it is used to prevent the growth of bacteria and contaminants in food [6,12-13].

In recent years, the use of herbs in production in many fields has become more and more popular. Various studies illustrate the activities and effectiveness of compounds derived from medicinal plants. Orange tree (*Citrus sinensis*) is grown mainly in different Asian countries such as Vietnam and Thailand. Orange fruits have great potential for scientific research due to the presence of a large number of bioactive compounds with antibacterial and antioxidant activities [14-17]. Previous research showed that there are different compounds obtained from orange peels essential oil, such as

limonene (main compound accounting for over 70%), myrcene, terpinolene, etc., which are among the important components of oranges, help prevent carcinogenic, antibacterial, and aromatherapy properties in physiotherapy [12,18-19]. Orange essential oil (OEO) has an important role in aromatherapy and cosmetic applications due to its antibacterial activities. The quality of OEO was evaluated based on the analytical method GC-MS. Among the extraction methods of essential oils, the hydrodistillation method has been widely used, especially for commercial production, because of its low cost, ease of operation, and efficient recovery stable, the high-quality essential oil obtained [4,20-21].

In Vietnam, the value of orange raw materials changes with great variability from time to time, thus making the value of this product unstable and making life difficult for farmers. Enhancing the economic value of agricultural products is of interest, and the production of essential oils from these agricultural products is a promising option that can enhance the value of these agricultural products. Studies on hydrodistillation methods as well as optimization of technological parameters to recover essential oil from orange peel have been carried out for a long time. However, most of the studies have been done in flasks, at the laboratory scale, with few published studies on the semi-industrial or industrial scale. It's a long way from laboratory-scale research to industrial-scale application. Differences in production scale will significantly affect the yield and quality of essential oils. Pilot-scale studies are needed to make it easy to apply in practice.

The purpose of this study is to investigate the influencing factors and technological process of producing OEO (*Citrus sinensis*) by a 50-L hydrodistillation device. Specifically, surveying the conditions affecting the content of OEO (ratio of water/material, temperature, distillation time); evaluating the chemical composition of the optimized essential oil sample, and the performance of a 50-L hydrodistillation device.

■ EXPERIMENTAL SECTION

Materials

This study was conducted on the subject of oranges

(*Citrus sinensis*) in Hau Giang province (9° 45'52" N 105° 38'25" E) harvested in July 2021. Oranges purchased must be fresh, not damaged, have the characteristic green color of oranges, no strange smell. In addition, sodium sulfate (Na_2SO_4 , Sigma Aldrich) was used for the anhydrous process of the essential oil after it was obtained.

Instrumentation

Equipment used in the study includes a distillation device with a volume of 50 L (diameter = 300 mm, thickness = 3 mm, height = 650 mm) heated by thermal oil (140–160 °C), imported capacity raw material from 20 to 25 kg/batch (Fig. 1). The equipment is made of stainless steel and inox 304. In addition, the unit is equipped with a horizontal beam tube condensing system cooled by water, a condensate recovery device, temperature control and sensing system, and pressure gauge.

Procedure

Hydrodistillation

After being harvested, the oranges are pre-treated, damaged materials removed, and peeled and flesh separated. The peels were grounded into small pieces and put into the material tank of the device 50 L. The amount of water was added in accordance with each experiment and put into the distillation system at a ratio of 1:2–1:5 (g/g). The heating temperature is at 120–150 °C,



Fig 1. Hydrodistillation equipment 50 L/batch

and the distillation time was calculated from the moment the first drop of liquid appears until the amount of essential oil remains constant. After the essential oil extraction process, a mixture of water and essential oil was obtained after passing through the condenser to recover the essential oil. Then, Na_2SO_4 salt was added to remove the water content in the essential oil. After the water removal process, pure essential oil was obtained.

The yield of essential oil in orange peel is determined as in Eq. (1):

$$Y\left(\frac{\text{mL}}{\text{g}}\right) = \frac{V}{m} \times 100\% \quad (1)$$

where V: volume of obtained essential oil (mL), m: weight of fresh orange peel (g)

Analysis of compounds by Gas Chromatography-Mass Spectrometry (GC-MS)

The chemical composition of the essential oils was determined by GC-MS analysis using the Agilent 6890 N GC instrument in combination with an inert HP5-MS and MS 5973 column. Head column pressure is 9.3 psi. Twenty-five μL of essential oils were added with 1 mL of *n*-hexane and dehydrated with Na_2SO_4 . The flow rate is constant at 1 mL/min. Nozzle temperature is 250 °C, and the division rate is 30. Heating program for samples: 50 °C is held for 2 min, increase 2 °C/min to 80 °C, continues to increase 5 °C/min to 150 °C, keep increasing at 10 °C/min to 200 °C, increase 20 °C/min to 300 °C, and hold for 5 min.

Statistical analysis

Each experimental data was presented as mean \pm standard deviation in three replicates. Statistical analysis was carried out by using SPSS software (SPSS Inc, Chicago, USA). The analysis of variance (ANOVA) and Tukey HSD analysis were used to compare the significant difference among analyzed groups at the significant level of 5%.

RESULTS AND DISCUSSION

Conditions Affecting the Yield of the Orange Essential Oil (OEO)

The influence of the raw materials and water ratio

During the hydrodistillation process, at the boiling point, the essential oils in the plant cells diffuse out to the

surface of the material and are carried away by the steam. At the same time, water enters the material in the opposite direction, and the oil continues to be entrained in the water. The process continues until the essential oil in the tissues is completely drained out. Therefore, determining the percentage of water in the raw material is necessary for the extraction process to achieve maximum yield. Experiments were carried out on two-weight scales of orange peels material, 3 kg and 5 kg. The results presented in Fig. 2(a-b) show that when increasing the ratio of raw materials and water, the yield of the obtained essential oil tends to increase to a certain value, and then this yield decreases. Accordingly, at the ratio of 1:2 (g/g), the low amount of essential oil obtained is due to the insufficient amount of water needed to dissolve the colloidal film surrounding the essential oil bag. This leaves a large amount of residual essential oil in the material, reducing the efficiency of the essential oil distillation process. On the other hand, at a higher ratio of 1:5 (g/g), the amount of essential oil obtained is not high because excess water can dissolve or form an oil emulsion and oil loss in the tube collection, reducing the efficiency of the hydrodistillation process. In practical terms, the large volume of water also leads to longer distillation times and higher operating costs. Therefore, the highest yield of essential oil was obtained at 1.63 (mL/g) with a ratio of material:water of 1:3 (g/g). This ratio is also consistent with previous studies on the distillation of Citrus essential oils, such as Tran et al. [13] on the distillation of *Citrus latifolia* essential oil; or by Ngo et al. [22] on the distillation of *Citrus aurantifolia* essential oil.

For the 5 kg weight, the yield of orange oil obtained on the 50 L/batch device did not change significantly compared to the 3 kg weight. Accordingly, the ratio of 1:3 (g/g) still gave the highest yield, accounting for 1.67 (mL/g), followed by the ratio of 1:2 (1.5 mL/g), 1:4 (1.54 mL/g), and 1:5 (1.44 mL/g). Therefore, through the survey results, it was found that with 3 kg and 5 kg of input materials, there was no significant change in the efficiency, and the optimal ratio was still chosen as 1:3 (g/g).

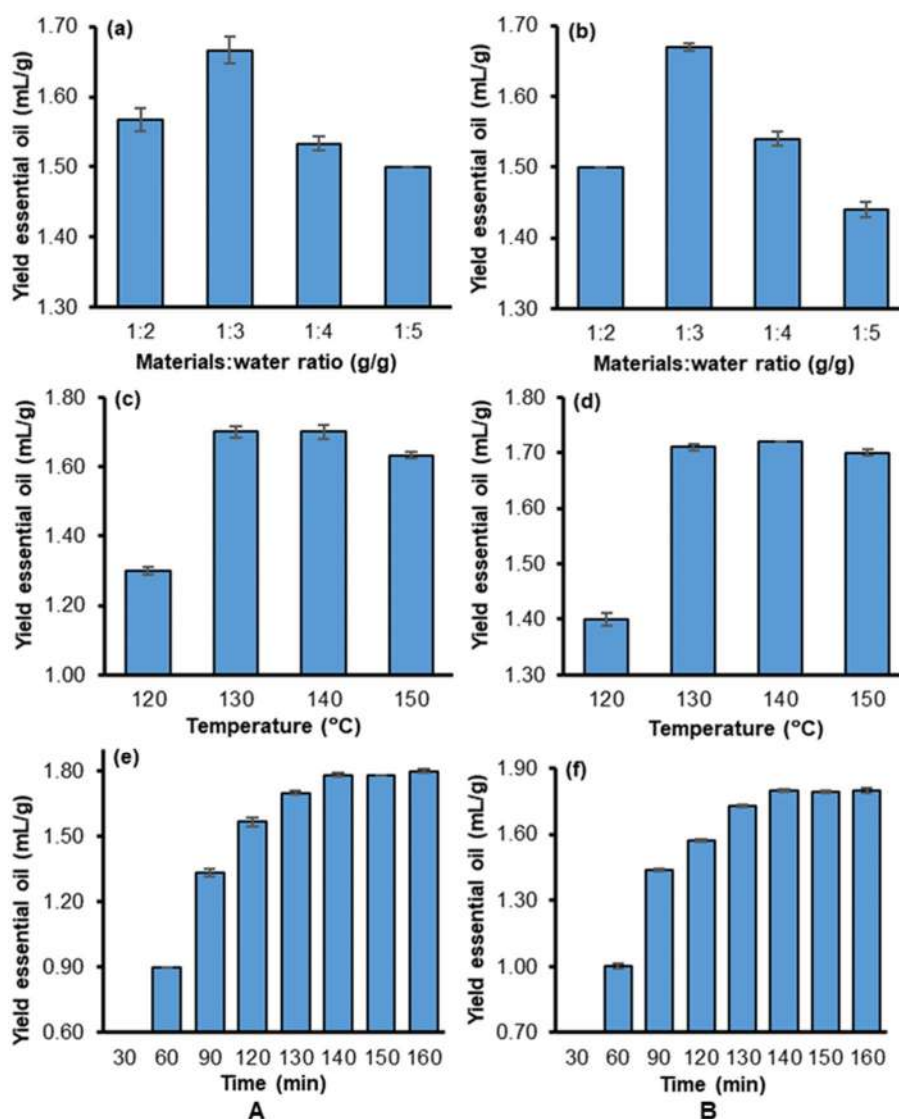


Fig 2. Factors affecting the hydrodistillation of orange essential oil on a 50L/batch device (A. 3kg scales, B. 5kg scales)

The influence of hydrodistillation temperature

One of the main factors affecting the hydrodistillation process is temperature. Fig. 2(c-d) was presented the surveying temperature conditions from 120 to 150 °C, which is consistent with many previous studies on optimizing the extraction process of Citrus essential oils such as Tran et al. [13], Ngo et al. [22], and Phat et al. [23]. The results from Fig. 2(b) show that high temperature leads to better oil yield, but only to a certain point. When the temperature exceeds the optimum point, the yield will decrease afterward. Specifically, in both 3 kg and 5 kg materials, the yield of essential oil increased from 1.3 to 1.63 mL/g (3 kg of material). It increased from 1.4

to 1.7 mL/g (5 kg of material) when the temperature was increased from 120 to 140 °C. However, when analyzing each temperature, at 130 °C, the oil yield reached the highest value of 1.7 mL/g (3 kg) and 1.71 mL/g (5 kg). In contrast, at the temperature of 140–150 °C, the yield of essential oil decreased, accounting for 1.63 and 1.72 mL/g. This can be explained because the high temperature makes the heat transfer and mass transfer from the outside to the material faster due to the weakening of the surface tension and the viscosity of the water. On the other hand, at too high temperature, there are also some limitations. Some components of essential oils are sensitive to decomposition temperature, adversely

affecting extraction efficiency, essential oil quality, and production cost due to when the high temperature will increase energy consumption. Comparing the difference between 3 kg and 5 kg materials/batch, there is no significant change, and the efficiency is 1.7–1.71 mL/g, still highest at 130 °C. Therefore, the temperature chosen for that period is 130 °C.

The influence of hydrodistillation time

Extraction time is the third factor affecting the hydrodistillation of orange essential oil. The long enough time for water to diffuse the essential oil from the raw materials into the environment increased the yield of essential oils. In contrast, water exposed to heat for a long time generates heat and high pressure, which can degrade the yield of essential oil due to heat-sensitive compounds in essential oils, thermal decomposition, energy consumption, and cost manufacturing. Fig. 2(e-f) shows that the effect of time on the yield of essential oils tends to increase with increasing time from 30 to 60 min. This trend is true for both 3 kg and 5 kg scales. The highest yield of the 3 kg scale was 1.78 mL/g, while the 5 kg scale was 1.8 mL/g at 140 min. Therefore, to optimize the time factor of hydrodistillation of orange essential oil, 140 min is the extraction time selected to bring the highest efficiency.

Assessment of the Chemical Composition of Optimized OEO Samples

The factors affecting the hydrodistillation process of orange essential oil on equipment with a capacity of 50 L/batch after optimal investigation include: the size of the peels to be grounded, the materials and water ratio is 1:3 (g/g), hydrodistillation temperature of 130 °C, hydrodistillation time of 140 min with yields reaching 1.78 mL/g (3 kg scales) and 1.8 mL/g (5 kg scales). After running under optimal conditions to obtain essential oil, this essential oil was anhydrous with Na₂SO₄ and evaluated for chemical composition by the GC-MS method. Analytical results are presented in Table 1, Fig. 3, and Fig. 4. In this study, the essential oil of orange was analyzed and found to have 3 components, with limonene compound as the main component accounting for very high content of 98%, then β -Pinene (1.143 and 1.193%),

and α -Pinene (0.720–0.785%). When comparing the analytical results between the 3 kg and 5 kg samples, there was no difference in the composition of the compounds, although there was no significant change in the content. This can also be explained by the fact that the essential oils are made from the same raw materials,

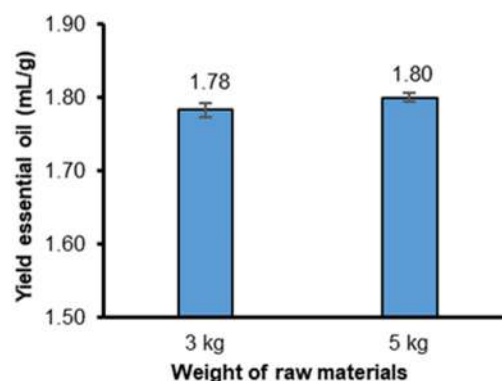


Fig 3. Comparison of the yield of essential oils obtained between 3 kg and 5 kg

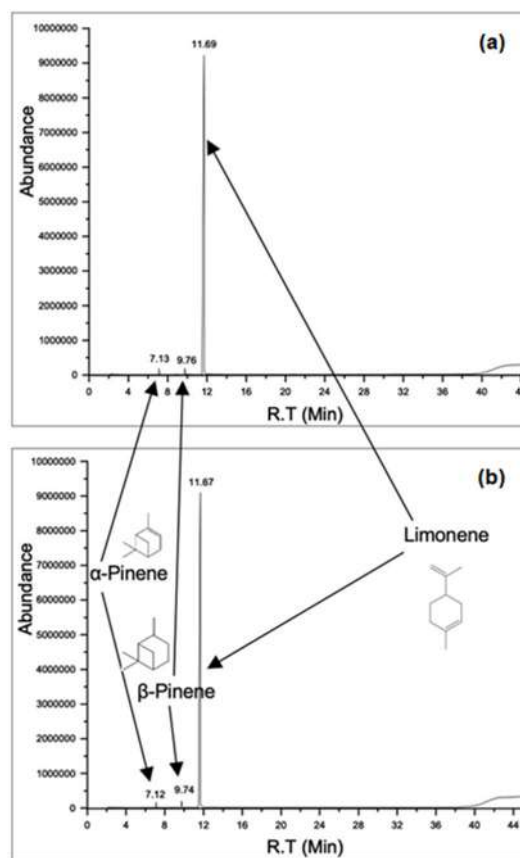
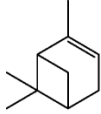
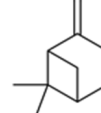
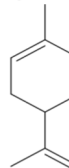


Fig 4. GC-MS spectrum of the composition of OEO (a) 3 kg scales (b) 5kg scales)

Table 1. Composition and content of compounds in orange essential oil

Peak	R.T (min)	Name compounds	Molecular formula	Structure formula	Content (%)	
					3 kg scales	5 kg scales
1	7.125	α -Pinene	C ₁₀ H ₁₆		0.785	0.720
2	9.760	β -Pinene	C ₁₀ H ₁₆		1.143	1.193
3	11.695	Limonene	C ₁₀ H ₁₆		98.072	98.087

the same time of harvest, the same methods, conditions, and distillation equipment.

In addition, in Table 2–6, the content of volatile compounds in orange essential oil is compared in this study with essential oils of the Citrus family such as orange, lemon, grapefruit, and sweet mandarin. In these tables, only the content of compounds contained in this study is compared with other studies in many countries at different harvest times. In general, essential oils hydrodistillation from the fresh peels of Citrus trees often have limonene as the main compound, accounting for the highest content (over 70%). In addition, it can be seen that the Limonene compounds in Table 2–6 in different studies have the highest concentration in oranges (most of which account for more than 80% of the remaining compounds) compared with other types of citrus fruits.

Specifically, in Table 2, a comparison of the same species of *Citrus sinensis* shows that the Limonene compound accounts for a high content from 61.08 to 95.54%, followed by β -pinene accounted for from 0.25 to 5.45%, and α -pinene accounted for range from 0.3 to 5.98%. However, it is easy to see that the content of the main compound Limonene in this study is considered to be the highest compared to the cited studies. This is also understandable because the quality of the essential oil depends a lot on the changing factors such as the growing conditions of the orange trees, the harvesting conditions of the fruits, and the factors affecting the distillation method [24–25]. This was even more pronounced when

the cultivars were changed by comparing the concentrations of compounds in the essential oils of orange (*Citrus sinensis*) and orange (*Citrus aurantium*). Results from Table 3 showed that limonene remained the main compound. However, the content is still lower than that of the essential oil distilled from orange peel (*Citrus sinensis*).

On the other hand, the study also compared the content of compounds in orange (*Citrus sinensis*) and lemon (*Citrus limon*) essential oils, with other lemon essential oils, with grapefruit (*Citrus paradisi*) and mandarin (*Citrus reticulata*), as shown in Table 4, 5 and 6. The results show that limonene is still the main compound, although there are many significant changes in some studies. That changes in the study of Kaskoos [1], Gomes et al. [41], Atti-Santos et al. [20], Smeriglio et al. [46], Sreepian et al. [47] when the content of the main compound Limonene accounted for less than 50% in the essential oils of lemons. This is the opposite in the essential oils of *Citrus paradisi* peels and *Citrus reticulata* peels, the main compounds in these peels all account for high content of over 80%.

Therefore, the main compound present in orange essential oil in Vietnam in this study is limonene, accounting for more than 98%, higher than in previous studies. This also helps other studies to show that oranges contain high amount of limonene, which has good fragrance, antibacterial and antioxidant properties in food, cosmetics, and pharmaceutical products [26–27].

Table 2. Comparison of compounds in orange essential oil (*Citrus sinensis*)

In this study	<i>Citrus sinensis</i>												
	2006 [28]	2009 [29]	2012 [30]	2017 [17]	2017 [31]	2019 [32]	2020 [15]	2020 [14]	2020 [33]	2020 [34]	2020 [35]	2021 [36]	
	Vietnam	Pakistan	India	Tunisia	Nigeria	Turkey	China	Iran	South Africa	Algeria	Turkey	Egypt	China
α -Pinene	0.785	0.84–1.26	0.291–0.390	0.07–0.44	0.7	0.9	5.98	1.85	0.9	0.53	0.32	0.3–1.4	0.33
β -Pinene	1.143	5.45	3.043–3.443	0.97–1.80	2.7	0.05	-	-	-	0.25	-	-	1.9
Limonene	98.072	61.08–76.2	35.060–76.68	81.52–86.43	92.14	92.01–93.32	90.75	71.54	80.5	95.54	88.90	74.5–82.1	88.25

Table 3. Comparison of compounds in the essential oils of orange (*Citrus sinensis*) and orange (*Citrus aurantium*)

	<i>Citrus aurantium</i>					
	In this study	2016 [37]	2018 [18]	2019 [5]	2019 [38]	2021 [10]
	Vietnam	Iran	Croatia	Bulgaria	Iran	Turkey
α -Pinene	0.785	0.30	0.8	1.29	1.32	-
β -Pinene	1.143	0.65	0.8	0.07	0.97	0.26–0.28
Limonene	98.072	94.81	91.1	85.22	85.49	72.51–95.70

Table 4. Comparison of compounds in orange (*Citrus sinensis*) and lemon (*Citrus limon*) essential oils

	<i>Citrus limon</i>								
	In this study	2006 [27]	2010 [39]	2012 [30]	2019 [1]	2019 [3]	2020 [40]	2020 [41]	2021 [42]
	Vietnam	Pakistan	Korea	Tunisia	Iraq	Sardegna	India	Brazil	Bulgaria
α -Pinene	0.785	2.63	2.6	0.13–5.9	2.25	0.43	00.17	2.4	-
β -Pinene	1.143	10.80	15.7	0.63–31.49	23.89	-	-	23.01	1.5
Limonene	98.072	53.61	64.54	37.63–69.71	29.52	77.44	55.40	44.75	82.96

Table 5. Comparison of compounds in orange essential oil (*Citrus sinensis*) and other lemon essential oils

In this study	<i>Citrus meyerii</i>	<i>Citrus latifolia</i>	<i>Citrus karna</i>	<i>Citrus limettioides</i>	<i>Citrus bergamia</i>	<i>Citrus lumia</i>	<i>Citrus hystrix</i>	<i>Citrus aurantifolia</i>	
	2005 [43]	2005 [20]	2009 [29]	2012 [44]	2012 [45]	2018 [46]	2019 [47]	2020 [22]	
	Vietnam	Italy	Brazil	India	India	Tunisia	Italy	Thailand	Vietnam
α -Pinene	0.785	1.33–2.25	1.9	1.227	0.865	0.48	0.62	2.22	1.855
β -Pinene	1.143	1.04–16.90	12.4	1.8	2.933	4.38	6.89	21.10	11.287
Limonene	98.072	51.95–79.7	47.5	92.310	89.089	59.21	48.91	25.28	65.988

Table 6. Comparison of compounds in the essential oils of orange (*Citrus sinensis*), *Citrus paradise*, and *Citrus reticulata*

In this study	<i>Citrus paradise</i>						<i>Citrus reticulata</i>				
	2006 [27]	2010 [39]	2015 [9]	2020 [48]	2020 [21]	2021 [42]	2021 [49]	2012 [30]	2021 [42]	2021 [36]	
	Vietnam	Pakistan	Korea	Argentina	China	Algeria	Bulgaria	Algeria	Tunisia	Bulgaria	China
α -Pinene	0.785	1.26	1.0	0.60	0.76	0.89	-	1.08	0.39–1.25	-	0.62–1.22
β -Pinene	1.143	-	-	-	0.05	1.06	1.13	-	0.06–1.59	1.01	2.00
Limonene	98.072	86.27	94.20	92.60	93.33	87.51	91.78	67.22	51.81–69.0	84.88	79.13–91.54

In addition, this can also be shown that because each geographical region, climatic conditions, farming, and harvesting conditions will greatly affect the quality as well as the content of volatile compounds present in the plants.

Assessment of Performance of Hydrodistillation Equipment 50 L/Batch

In order to evaluate the stable operation of the oil hydrodistillation equipment with the capacity of 50 L/batch, this study carried out 3 times of 5 kg scales with optimal conditions. The yield of the obtained essential oil was 1.8–1.81 mL/g. The results shown in Fig. 5 and Table 7 show that after 3 times of hydrodistillation at 5 kg, the yield of the obtained essential oil did not change significantly (almost 1.8 mL/g) due to errors in the extraction process, making the essential oil anhydrous. In terms of color and scent, the essential oils obtained through 3 times of applications have the same color and characteristic scent of orange. When analyzing the content of compounds in orange essential oil by GC-MS method, 3 components were detected, with Limonene compound being the main component accounting for a high content of 98.144–98.182%, α -pinene (0.655–0.734%) and β -pinene (1.114 and 1.163%). Most of these compounds changed insignificantly over the measurements. This shows that this 50 L capacity essential oil distiller works stably and obtains good quality and content without changing the yield and volatile compounds content.

Through the process of orange essential oil hydrodistillation on this equipment 50 L, it was found that the equipment is easy to operate, stable, does not cause noise, and recovers the yield of the essential oil between scales. However, the device still has some shortcomings, such as the small input material space, which makes it difficult to input peels, and the small place where the

residue is left after distillation, so the process of getting the residue is still hindered.

CONCLUSION

This study investigated the factors affecting the hydrodistillation of orange essential oil on a 50 L/batch device with a weight scale of 3 kg and 5 kg. The results show that after pre-treatment, the orange peels are ground into small pieces, put into the raw material tank of the distillation device, the amount of water is added to the distillation system at a ratio of 1:3 (g/g) at a heating temperature of 130 °C and a distillation time of 140 min. A comparison of the content of the essential oil compounds obtained on the 3 kg and 5 kg scales is also provided. The results show that at the above optimal conditions, the yield of the obtained essential oil did not change significantly (about 1.8 mL/g), and the volatile components in the essential oils of these two scales also did not change in composition and content. Accordingly, Limonene compounds are the main compounds accounting for over 98%. Therefore, the device is rated as easy to operate, stable, does not cause noise, and recovers a stable yield of essential oil between implementation times.

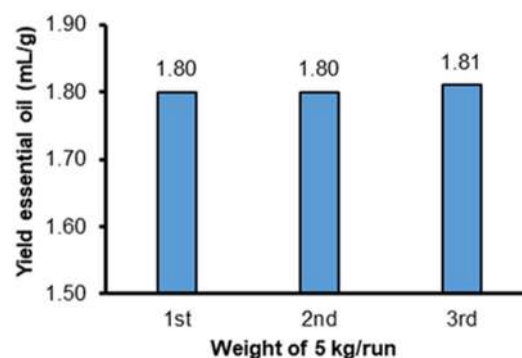


Fig 5. The yield of essential oil obtained after 3 times by 5 kg scales

Table 7. Composition and content of compounds in orange essential oil at 5 kg scales

Peak	R.T (min)	Compounds	Content (%)		
			1	2	3
1	7.136	α -Pinene	0.717	0.655	0.734
2	9.781	β -Pinene	1.114	1.163	1.123
3	11.705	Limonene	98.170	98.182	98.144

■ ACKNOWLEDGMENTS

This research was funded by Nguyen Tat Thanh University, Ho Chi Minh City, Vietnam.

■ REFERENCES

- [1] Kaskoos, R.A., 2019, Essential oil analysis by GC-MS and analgesic activity of *Lippia citriodora* and *Citrus limon*, *J. Essent. Oil Bear. Plants*, 22 (1), 273-281.
- [2] Gaff, M., Esteban-Decloux, M., and Giampaoli, P., 2020, Bitter orange peel essential oil: A review of the different factors and chemical reactions influencing its composition, *Flavour Fragrance J.*, 35 (3), 247-269.
- [3] Flamini, G., Pistelli, L., Nardoni, S., Ebani, V.V., Zinnai, A., Mancianti, F., Ascricchi, R., and Pistelli, L., 2019, Essential oil composition and biological activity of 'Pompia', a Sardinian citrus ecotype, *Molecules*, 24 (5), 908.
- [4] Tran, T.H., Nguyen, D.T., Phu, T.N.N., Ho, V.T.T., Vo, D.V.N., Bach, L.G., and Nguyen, T.D., 2019, Research on lemongrass oil extraction technology (Hydrodistillation, microwave-assisted hydrodistillation), *Indones. J. Chem.*, 19 (4), 1000-1007.
- [5] Teneva, D., Denkova-Kostova, R., Goranov, B., Hristova-Ivanova, Y., Slavchev, A., Denkova, Z., and Kostov, G., 2019, Chemical composition, antioxidant activity and antimicrobial activity of essential oil from *Citrus aurantium* L zest against some pathogenic microorganisms, *Z. Naturforsch., C: Biosci.*, 74 (5-6), 105-111.
- [6] Ngo, T.C.Q., Dao, T.P., Tran, T.H., Le, T.H.N., Pham, M.Q., Nguyen, N.H., Tran, Q.T., 2020, Application of response surface methodology in the process of extracting essential oil from the Calamondin (*Citrus microcarpa*) peels, *IOP Conf. Ser.: Mater. Sci. Eng.*, 736, 022062.
- [7] Idoko, J.E., and Ileke, K.D., 2020, Comparative evaluation of insecticidal properties of essential oils of some selected botanicals as bio-pesticides against Cowpea bruchid, *Callosobruchus maculatus* (Fabricius) [Coleoptera: Chrysomelidae], *Bull. Natl. Res. Cent.*, 44 (1), 119.
- [8] Isman, M.B., 2020, Bioinsecticides based on plant essential oils: A short overview, *Z. Naturforsch., C: Biosci.*, 75 (7-8), 179-182.
- [9] Vasek, O.M., Cáceres, L.M., Chamorro, E.R., and Velasco, G.A., 2015, Antibacterial activity of *Citrus paradisi* essential oil, *J. Nat. Prod.*, 8, 16-26.
- [10] Sevindik, E., Aydın, S., Sujka, M., Apaydın, E., Yıldırım, K., and Palas, G., 2021, GC-MS analysis and evaluation of antibacterial and antifungal activity of essential oils extracted from fruit peel of *Citrus aurantium* L. (Rutaceae) grown in the West Anatolian area, *Erwerbs-Obstbau*, 63, 135-142.
- [11] Mohan, L., Negi, A., Melkani, A.B., and Dev, V., 2011, Chemical composition and antibacterial activity of essential oil from *Salvia mukerjeei*, *Nat. Prod. Commun.*, 6 (12), 1949-1952.
- [12] Kamal, G.M., Anwar, F., Hussain, A.I., Sarri, N., and Ashraf, M.Y., 2011, Yield and chemical composition of Citrus essential oils as affected by drying pre-treatment of peels, *Int. Food Res. J.*, 18 (4), 1275-1282.
- [13] Tran, T.K.N., Ngo, T.C.Q., Tran, T.H., Tran, T.T., Huynh, X.P., Do, V.D., Nguyen, K.T., Nguyen, M.V., and Bach, L.G., 2020, Yields and composition of Persian lime essential oils (*Citrus latifolia*) from Hau Giang province, Vietnam extracted by three different extraction methods, *IOP Conf. Ser.: Mater. Sci. Eng.*, 991, 012130.
- [14] Matuka, T., Oyedeji, O., Gondwe, M., and Oyedeji, A., 2020, Chemical composition and *in vivo* anti-inflammatory activity of essential oils from *Citrus sinensis* (L.) osbeck growing in South Africa, *J. Essent. Oil Bear. Plants*, 23 (4), 638-647.
- [15] Caputo, L., Cornara, L., Bazzicalupo, M., De Francesco, C., De Feo, V., Trombetta, D., and Smeriglio, A., 2020, Chemical composition and biological activities of essential oils from peels of three citrus species, *Molecules*, 25 (8), 1890.
- [16] Farahmandfar, R., Tirgarian, B., Dehghan, B., and Nemati, A., 2020, Changes in chemical composition and biological activity of essential oil from Thomson navel orange (*Citrus sinensis* L. osbeck) peel under freezing, convective, vacuum, and

- microwave drying methods, *Food Sci. Nutr.*, 8 (1), 124–138.
- [17] Oboh, G., Ademosun, A.O., Olumuyiwa, T.A., Olasehinde, T.A., Ademiluyi, A.O., and Adeyemo, A.C., 2017, Insecticidal activity of essential oil from orange peels (*Citrus sinensis*) against *Tribolium confusum*, *Callosobruchus maculatus* and *Sitophilus oryzae* and its inhibitory effects on acetylcholinesterase and Na⁺/K⁺-ATPase activities, *Phytoparasitica*, 45 (4), 501–508.
- [18] Radan, M., Parčina, A., and Burčul, F., 2018, Chemical composition and antioxidant activity of essential oil obtained from bitter orange peel (*Citrus aurantium* L.) using two methods, *Croat. Chem. Acta*, 91 (1), 125–128.
- [19] Gioffrè, G., Ursino, D., Labate, M.L.C., and Giuffrè, A.M., 2020, The peel essential oil composition of bergamot fruit (*Citrus bergamia*, Risso) of Reggio Calabria (Italy): A review, *Emir. J. Food Agric.*, 32 (11), 835–845.
- [20] Atti-Santos, A.C., Rossato, M., Serafini, L.A., Cassel, E. and Moyna, P., 2005, Extraction of essential oils from lime (*Citrus latifolia* Tanaka) by hydrodistillation and supercritical carbon dioxide, *Braz. Arch. Biol. Technol.*, 48 (1), 155–160.
- [21] Nour el Houda, A.K., Ali, B., Ahmed, A., Salah, O., and Yazid, F.C., 2020, Chemical composition, antimicrobial and insecticidal activities of *Citrus paradisi* peel essential oil from Algeria, *J. Microbiol., Biotechnol. Food Sci.*, 9 (6), 1093–1098.
- [22] Ngo, T.C.Q., Tran, T.K.N., Dao, T.P., Tran, T.H., Ngo, H.D., Huynh, X.P., Tran, T.T., and Mai, H.C., 2020, Yield and composition analysis of Vietnamese lemon (*Citrus aurantifolia*) essential oils obtained from hydrodistillation and microwave-assisted hydrodistillation, *IOP Conf. Ser.: Mater. Sci. Eng.*, 991, 012123.
- [23] Phat, D.T., Tuyen, K.C., Huynh, X.P and Truc, T.T., 2020, Extraction process optimization and characterization of the pomelo (*Citrus grandis* L.) peel essential oils grown in Tien Giang Province, Vietnam, *Nat. Volatiles Essent. Oils*, 7 (4), 26–33.
- [24] Hudz, N., Makowicz, E., Shanaida, M., Bialoń, M., Jasicka-Misiak, I., Yezerska, O., Svydenko, L., and Wieczorek, P.P., 2020, Phytochemical evaluation of tinctures and essential oil obtained from *Satureja montana* herb, *Molecules*, 25 (20), 4763.
- [25] Gömöri, C., Vidács, A., Kerekes, E.B., Nacsafarkas, E., Böszörményi, A., Vágvölgyi, C., and Krisch, J., 2018, Altered antimicrobial and anti-biofilm forming effect of thyme essential oil due to changes in composition, *Nat. Prod. Commun.*, 13 (4), 483–487.
- [26] Ibáñez, M.D., Sanchez-Ballester, N.M., and Blázquez, M.A., 2020, Encapsulated limonene: A pleasant lemon-like aroma with promising application in the agri-food industry. A review, *Molecules*, 25 (11), 2598.
- [27] Heydari, M., Rostami, O., Mohammadi, R., Banavi, P., Farhoodi, M., Sarlak, Z., and Rouhi, M., 2021, Hydrodistillation ultrasound-assisted green extraction of essential oil from bitter orange peel wastes: Optimization for quantitative, phenolic, and antioxidant properties, *J. Food Process. Preserv.*, 45 (7), e15585.
- [28] Ahmad, M.M., Ur-Rehman, S., Iqbal, Z., Anjum, F.M., and Sultan, J.I., 2006, Genetic variability to essential oil composition in four citrus fruit species, *Pak. J. Bot.*, 38 (2), 319–324.
- [29] Malhotra, S., Suri, S., and Tuli, R., 2009, Antioxidant activity of citrus cultivars and chemical composition of *Citrus karna* essential oil, *Planta Med.*, 75 (1), 62–64.
- [30] Bourgo, S., Rahali, F.Z., Ourghemmi, I., and Tounsi, M.S., 2012, Changes of peel essential oil composition of four Tunisian citrus during fruit maturation, *Sci. World J.*, 2012, 528593.
- [31] Bozkurt, T., Gülnaz, O., and Kaçar, Y.A., 2017, Chemical composition of the essential oils from some citrus species and evaluation of the antimicrobial activity, *IOSR J. Environ. Sci., Toxicol. Food Technol.*, 11 (10), 1–8.
- [32] Zhang, L.L., Yang, Z.Y., Fan, G., Ren, J.N., Yin, K.J., and Pan, S.Y., 2019, Antidepressant-like effect of *Citrus sinensis* (L.) Osbeck essential oil and its main

- component limonene on mice, *J. Agric. Food Chem.*, 67 (50), 13817–13828.
- [33] Benazzouz, K., Belkahla, H., Hamiche, S., and El Hattab, M., 2020, Effect of *Citrus* stubborn disease (*Spiroplasma citri*) on chemical composition of orange (*Citrus sinensis* (L) Osbeck) essential oil fruits, *Int. J. Fruit Sci.*, 20 (Suppl. 3), S1360–S1372.
- [34] Eliuz, E.A.E., Yabalak, E., and Sicak, Y., 2020, Chemical composition and antimicrobial activity of essential oil of *Citrus sinensis*: Interaction with ampicillin and fluconazole, *Rev. Roum. Chim.*, 65 (10), 899–907.
- [35] Khalid, K.A., and Ahmed, A.M.A., 2020, Agriculture locations induced variations in the essential oil of Valencia orange, *J. Essent. Oil Bear. Plants*, 23 (6), 1438–1449.
- [36] Lin, X., Cao, S., Sun, J., Lu, D., Zhong, B., and Chun, J., 2021, The chemical compositions, and antibacterial and antioxidant activities of four types of citrus essential oils, *Molecules*, 26 (11), 3412.
- [37] Sanei-Dehkordi, A., Sedaghat, M.M., Vatandoost, H., and Abai, M.R., 2016, Chemical compositions of the peel essential oil of *Citrus aurantium* and its natural larvicidal activity against the malaria vector *Anopheles stephensi* (Diptera: Culicidae) in comparison with *Citrus paradisi*, *J. Arthropod Borne Dis.*, 10 (4), 577–585.
- [38] Farahmandfar, R., Tirgarian, B., Dehghan, B., and Nemati, A., 2019, Comparison of different drying methods on bitter orange (*Citrus aurantium* L.) peel waste: Changes in physical (density and color) and essential oil (yield, composition, antioxidant and antibacterial) properties of powders, *J. Food Meas. Charact.*, 14 (2), 862–875.
- [39] Yang, S.A., Jeon, S.K., Lee, E.J., Shim, C.H., and Lee, I.S., 2010, Comparative study of the chemical composition and antioxidant activity of six essential oils and their components, *Nat. Prod. Res.*, 24 (2), 140–151.
- [40] Paw, M., Begum, T., Gogoi, R., Pandey, S.K., and Lal, M., 2020, Chemical composition of *Citrus limon* L. Burmf peel essential oil from North East India, *J. Essent. Oil Bear. Plants*, 23 (2), 337–344.
- [41] Gomes, P.R.B., de Sousa, D.A., Everton, G.O., Fontenele, M.A., e Marques, J.N.L., de Freitas, A.C., Hunaldo, V.K.L., Louzeiro, H.C., de Paula, M.L., Reis, J.B., Melo, A.V., de Lima, H.S., and Filho, V.E.M., 2020, Chemical composition and larvicidal activity of *Citrus limonia* Osbeck bark essential oil, *J. Med. Plants Res.*, 14 (7), 354–358.
- [42] Denkova-Kostova, R., Teneva, D., Tomova, T., Goranov, B., Denkova, Z., Shopska, V., Slavchev, A., and Hristova-Ivanova, Y., 2021, Chemical composition, antioxidant and antimicrobial activity of essential oils from tangerine (*Citrus reticulata* L.), grapefruit (*Citrus paradisi* L.), lemon (*Citrus lemon* L.) and cinnamon (*Cinnamomum zeylanicum* Blume), *Z. Naturforsch., C: Biosci.*, 76 (5-6), 175–185.
- [43] Verzera, A., Trozzi, A., Zappalá, M., Condurso, C., and Cotroneo, A., 2005, Essential oil composition of *Citrus meyerii* Y. Tan and *Citrus medica* L. cv. Diamante and their lemon hybrids, *J. Agric. Food Chem.*, 53 (12), 4890–4894.
- [44] Vasudeva, N., and Sharma, T., 2012, Chemical Composition and antimicrobial activity of essential oil of *Citrus limettioides* Tanaka, *J. Pharm. Technol. Drug Res.*, 1, 2.
- [45] Nabiha, B., Abdelfatteh, E.O., Faten K., Herve, C., and Moncef, C.M., 2010, Chemical composition of bergamot (*Citrus bergamia* Risso) essential oil obtained by hydrodistillation, *J. Chem. Chem. Eng.*, 4 (4), 60–62.
- [46] Smeriglio, A., Alloisio, S., Raimondo, F.M., Denaro, M., Xiao, J., Cornara, L., and Trombetta, D., 2018, Essential oil of *Citrus lumia* Risso: Phytochemical profile, antioxidant properties and activity on the central nervous system, *Food Chem. Toxicol.*, 119, 407–416.
- [47] Sreepian, A., Sreepian, P.M., Chanthong, C., Mingkhwancheep, T., and Prathit, P., 2019, Antibacterial activity of essential oil extracted from *Citrus hystrix* (Kaffir Lime) peels: An *in vitro* study, *Trop. Biomed.*, 36 (2), 531–541.
- [48] Deng, W., Liu, K., Cao, S., Sun, J., Zhong, B., and Chun, J., 2020, Chemical composition,

antimicrobial, antioxidant, and antiproliferative properties of grapefruit essential oil prepared by molecular distillation, *Molecules*, 25 (1), 217.

[49] Kaanin, G., Fatiha, B., Magdalena, B., Hadjal, S.,

Madani, K., and Nerín, C., 2021, *Citrus × paradisi* essential oil as a promising agent for margarine storage stability: Composition and antioxidant capacity, *J. Food Process. Preserv.*, 45 (5), e15374.

Supplementary Data

This supplementary data is a part of paper entitled “Potential *Adenostemma lavenia* and *Muntingia calabura* Extracts to Inhibit Cyclooxygenase-2 Activity as a Therapeutic Strategy for Anti-inflammation: Experimental and Theoretical Studies”.

Suppl. 1. Lists of *M. calabura* compounds used for docking

Code	CID	Name
1	5272653	(2S)-5'-hydroxy-7,3',4'-trimethoxyflavan
2	23730738	(2S)-7,8,3',4',5'-pentamethoxyflavan
3	44567046	(2S)-2'-hydroxy-7,8,3',4',5'-pentamethoxyflavan
4	44567047	(2S)-5'-hydroxy-7,8,3',4'-tetramethoxyflavan
5	44567048	(2S)-8-hydroxy-7,3',4',5'-tetramethoxyflavan
6	44567055	(2S)-8,2'-dihydroxy-7,3',4',5'-tetramethoxyflavan
7	44567056	(2S)-8,5'-dihydroxy-7,3',4'-trimethoxyflavan
8	24750458	7,8,3',4',5'-pentamethoxyflavone
10	9950661	5'-hydroxy-7,8,3',4'-tetramethoxyflavone
12	44257590	8,5'-dihydroxy-7,3',4'-trimethoxyflavone
13	639682	(2R,3R)-7-methoxy-3,5,8-trihydroxyflavanone
14	688857	(2S)-7-hydroxyflavanone
15	31013944	(2S)-5,7-dihydroxyflavanone
16	73202	(2R,3R)-3,5,7-trihydroxyflavanone
17	73201	(2S)-5-hydroxy-7-methoxyflavanone
18	5281894	7-hydroxyflavone
19	5281607	5,7-dihydroxyflavone
23	5378823	3,5-dihydroxy-7,4'-dimethoxyflavone
24	5491798	3,5-dihydroxy-7,8-dimethoxyflavone
25	21632881	5-hydroxy-3,7,8-trimethoxyflavone
27	-	5-hydroxy-3,7,8,4'-tetramethoxyflavone
28	6433293	2',4'-dihydroxychalcone
29	77520393	4,2',4'-trihydroxychalcone
30	5376891	7-hydroxyisoflavone
31	628528	7,3',4'-trimethoxyisoflavone
32	20977489	2',4'-dihydroxydihydrochalcone
33	370	3,4,5-trihydroxybenzoic acid
34	92158	lupenone
35	73659	2 α ,3 β -dihydroxy-olean-12-en-28-oic acid
36	129847689	8-hydroxy-7,3',4',5'-tetramethoxyflavone
37	102169932	8,4'-dihydroxy-7,3',5'-trimethoxyflavone
39	88881	5,7-dimethoxyflavone
40	13291608	3,5-dihydroxy-6,7-dimethoxyflavone
41	60123241	β -sitostenone
43	521199	β -sitosterol
44	10742	syringic acid
45	8468	vanillic acid

Suppl. 1. Lists of *M. calabura* compounds used for docking (Continued)

Code	CID	Name
50	129847697	2',4'-dihydroxy-3'-methoxydihydrochalcone
52	5272653	(2S)-(-)-5'-hydroxy-7,3',4'-trimethoxyflavanone
54	5281954	5-hydroxy-7-methoxyflavone
55	5748697	3,7-dimethoxy-5-hydroxyflavone
57	5318691	3,5-dihydroxy-7-methoxyflavone
58	-	8-methoxy-3,5,7-trihydroxyflavone
59	9972910	5,7-dihydroxy-3,8-dimethoxyflavone
60	5281616	galangin
61	5281607	chrysin
62	42607832	7-hydroxy-8-methoxyflavanone
63	10265122	4'-hydroxy-7-methoxyflavanone
64	71935	2',4'-dihydroxy-3'-methoxychalcone
65	145706584	[2,3-dihydroxy-4,3',4',5'-tetramethoxydihydrochalcone
66	21722167	4,2',4'-trihydroxy-3'-methoxydihydrochalcone
67	145706492	(2R,3R)-(-)-3,5-dihydroxy-6,7-dimethoxyflavanone
68	5280794	stigmaterol
69	466268	7-methoxyflavone
70	5281946	5,7-dihydroxy-3-methoxyflavone
71	5320315	5,7-dihydroxy-6-methoxyflavone
72	5318869	5,4'-dihydroxy-3,7-dimethoxyflavone
73	23730738	(2S)-7,8,3',4',5'-pentamethoxyflavan
74	44567047	(2S)-5'-hydroxy-7,8,3',4'-tetramethoxyflavan
75	-	methyl 4-hydrobenzoate
76	12575	isovanillic acid
77	980	p-nitrophenol
78	7428	methyl gallate
79	5319562	trans-methyl p-coumarate
80	12306160	β -amyrenone
81	-	α -tocopherylquione
85	145706471	5-hydroxy-3,8-dimethoxyflavone
86	5378234	3,5,7-trihydroxy-8-methoxyflavone
87	129848348	8-hydroxy-6-methoxyflavone

Suppl. 2. Lists of *A. lavenia* compounds used for docking

Code	CID	Name
101	226486	4-Allyl-2,6-Dimethoxyphenol
102	1549095	coniferyl alcohol
103	5280450	linoleic acid
104	575987	5h-1-Pyridine
105	6736	3-methylindole
106	102527619	1-cyano-3-methylisoquinoline
107	579053	6,7-Dihydro-3-Nitro-5h-Cyclopenta[B]Pyridin-2(1h)-One
108	551125	5,10-Diethoxy-2,3,7,8-Tetrahydro-1h,6h-Dipyrrolo[1,2-A;1',2'-D] Pyrazine
109	637542	p-Coumaric acid
110	5362796	Z-Cycloundecene
111	5362790	E_Cycloundecene
112	572128	3,5-Heptadien-2-ol, 2,6-dimethyl-
113	5365626	(Z)6-Pentadecen-1-ol
114	15304	3,6-Dimethylphenanthrene
115	603766	1-Iodo-4-Phenylbicyclo(2
116	6660	Corylon
117	533622	2,5-Methano-2h-Furo[3,2-B] -8-One, Hexahydro-
118	23415	2-Methyldecane
119	9602952	Carbamic Acid, 3-Pentylidene-, Ethyl Ester
120	445639	Oleic Acid
121	8183	Adacene 12
122	5283361	Trans-2-Dodecenal
123	30874	1,12-Tridecadiene
124	606063	1a,9b-Dihydro-1h-Cyclopropa[A]Anthracene
125	9817754	9,12-Octadecadienoyl Chloride,
126	8142	1-Chlorooctane
127	9248	Epoxy cyclododecane
128	5368351	Cis-3-Undecene-1,5-Diyne
129	5282714	2-Octenoic Acid (Cas)
130	5364492	cis-9-Octadecenal
131	5362688	trans-Dodec-5-enal
132	535532	6-Oxa-Bicyclo[3,1,0]Hexan-3-One
133	83742	2-Imidazolidinone, 1,3-Diethenyl-
134	713	Methanamide
135	6436740	N-Phenyl-N'-Furaldehyde Hydrazone
136	87568	Pentadecanonitrile
137	996	Phenol (Cas)
138	335	O-Cresol
139	460	460_Guaiacol
140	2879	2879_P-Cresol
141	6997	O-Ethylphenol
142	10364	Carvacrol
143	7041	2,6-Dimethoxyphenol
144	12462	1,2,3-Trimethoxybenzene

Suppl. 2. Lists of *A. lavenia* compounds used for docking (*Continued*)

Code	CID	Name
145	2724705	1,6-Anhydro-Beta-D-Glucopyranose; Levoglucosan
146	17198	Acetosyringone
147	5374088	2,4-Hexadienedioic Acid, 3,4-Diethyl-, Dimethyl Este
148	561602	5-beta,8-beta-Epoxy-3,5,8,8a-tetrahydro-1H-2-benzopyran
149	43551	Biphenyl, 3,4-Diethyl
150	3033	diclofenac
151	444899	arachidonic acid
152	-	ent-11 α -hydroxy-15-oxo-kaur-16-en-19-oic acid

Potential *Adenostemma lavenia* and *Muntingia calabura* Extracts to Inhibit Cyclooxygenase-2 Activity as a Therapeutic Strategy for Anti-inflammation: Experimental and Theoretical Studies

Bagaskoro Tuwalaid¹, Dyah Iswantini^{1,2}, and Setyanto Tri Wahyudi^{3*}

¹Department of Chemistry, Faculty of Mathematics and Natural Sciences, IPB University, Bogor 16680, Indonesia

²Tropical Biopharmaca Research Center, IPB University, Taman Kencana Campus, Bogor 16128, Indonesia

³Department of Physics, Faculty of Mathematics and Natural Sciences, IPB University, Bogor 16680, Indonesia

* Corresponding author:

email: stwahyudi@apps.ipb.ac.id

Received: November 28, 2021

Accepted: February 18, 2022

DOI: 10.22146/ijc.70794

Abstract: Continuous inflammation can cause new and more severe diseases, thus effective treatments are needed. One of the common inflammation treatments is given by reducing prostaglandins' production through the inhibition of COX-2 activity. This experiment aims to examine the potential application of plant extracts of *Adenostemma lavenia* and *Muntingia calabura* (Jamaica cherry) as anti-inflammatory agents in inhibiting COX-2 activity through in silico and in vitro assays. Molecular docking and molecular dynamics simulation were accomplished to evaluate the stability of the complex between COX-2 and ligands. The COX-2 inhibition was determined using the COX-2 Inhibitor Screening Assay KIT. Based on the docking results, the active compound from *A. lavenia*, ligand 1a,9b-dihydro-1H-cyclopropa[a]anthracene, has the lowest binding energy of -8.7 kcal/mol. In comparison, *M. calabura* contains 7-hydroxyflavone ligand with a Gibbs free energy of -9.1 kcal/mol. The molecular dynamics study demonstrates that COX-2 maintains its stability when forming interactions with selected compounds from all the tested extracts. The results of the COX-2 inhibition test showed that 96% EtOH extract of *A. Lavenia* at concentrations of 25 and 100 ppm had an inhibitory activity of 98%; meanwhile, 70% and 96% EtOH extracts of *M. calabura* at 1000 ppm concentration could inhibit COX-2 activity up to 100%. The results demonstrate that both plants show potential anti-inflammatory activity.

Keywords: anti-inflammatory; herbal medicine; in vitro; molecular docking; molecular dynamics

■ INTRODUCTION

Inflammation is a biological response of the immune system triggered by some factors, such as exogenous substances, pathogens, damaged cells, and toxic compounds that enter the body. These factors can cause acute or chronic inflammatory responses in the body that may end up in serious diseases such as rheumatoid arthritis, lung, cancer, and heart disease [1]. Inflammation is usually suffered by patients infected with Covid-19. Several studies concluded that the hyperinflammatory response of SARS-CoV-2 is a significant cause of illness severity and death in infected

patients [2]. Furthermore, continuous inflammation can cause new problems in the area where inflammation occurs and can trigger the proliferation of cancer cells. Therefore, prevention and treatment efforts to reduce inflammation in the body are needed [3].

Inflammation is usually triggered by several inflammatory mediators, one of which is prostaglandins. Prostaglandins are produced from arachidonic acid metabolism catalyzed by the COX-2 enzyme. Therefore, one of the efforts to prevent inflammation is to inhibit COX-2 activity [4]. The drugs that can inhibit COX-2 activity are classified as non-steroidal anti-inflammatory drugs. Non-steroidal anti-inflammatory drugs are one of

the generally prescribed ache medications. Unfortunately, long-term use can cause more harmful side effects such as gastrointestinal bleeding, cardiovascular side effects, and nephrotoxicity [5]. Therefore, it is preferable to use drugs derived from natural products to minimize the side effects. Searching for drug compounds that can inhibit COX-2 can be carried out using the molecular docking method and continued with molecular dynamics studies.

Molecular docking is a process in which small molecules are anchored into macromolecular structures such as proteins, polysaccharides, carbohydrates, and double-helical DNA structures to assess their complementary value at the binding site [6]. The molecular docking technique aims to predict the most suitable binding mode of the ligand to the receptor. This method can estimate the binding affinity between the ligand and protein and the protein-ligand complex structure [7]. Receptors in molecular docking can be assumed to be rigid molecules (immobile) and might also be considered flexible molecules similar to their natural state [8]. The stability of receptor binding with ligands resulting from the docking process can be calculated using molecular dynamics simulations. Molecular dynamics (MD) is a computational physics method to study and analyze the interactions and movements of atoms and molecules based on Newton's laws. The force field is used to estimate the forces between the interacting particles and calculate the system's total energy consisting of bond energy, angular energy, dihedral energy, electrostatic energy, and van der Waals energy [9]. MD is commonly carried out using the AMBER20 program because this program is non-periodic simulations, the use of a generalized Born or numerical Poisson-Boltzmann implicit solvent model, free-energy calculations use thermodynamic integration, and there may be widespread assistance for trajectory evaluation and active post-processing [10]. The root means square deviation (RMSD), a radius of gyration residue (Rg), the root means square fluctuation (RMSF), and the total energy of the molecular dynamics simulation path are the basic parameters to measure the stability of a system.

Anti-inflammatory drugs circulating in public tend to have dangerous side effects, so an alternative that can

be used is by utilizing herbal medicines derived from plants. The use of herbal medicines is expected to contain safe therapeutic compounds, the resulting side effects are not destructive, and the treatment of inflammation is more effective. The plants that would have been tested for anti-inflammatory activity as herbal medicine in this study are *Adenostemma lavenia* (sticky daisy, *legetan warak*) and *Muntingia calabura* (*Jamaica cherry, kersen*). Compounds in the ethanolic extract of *A. lavenia* have been reported to inhibit COX-2 activity [11]. The active compound in the root is 11-hydroxylated kauranic acids, which are beneficial as an anti-inflammatory, improve lung and liver function, and relieve pain [12]. Increasing the concentration of *M. calabura* fruit extract has been known to reduce prostaglandins concentration in the body [13]. This study was designed to examine the potential of these two plants as anti-inflammatory agents in inhibiting COX-2 activity through *in silico* and *in vitro* experiments.

■ EXPERIMENTAL SECTION

Materials

The material used for the *in silico* test is a 3D structure of COX-2 protein with the PDB code 5IKR. The ligands used were 49 compounds in *A. lavenia*, and 68 compounds in *M. calabura*. Materials for *in vitro* tests were 50%, 70%, and 96% ethanol extracts from leaves of the respective species, provided by the Tropical Biopharmaca Research Center Laboratory, Bogor City, Indonesia.

Procedure

Preparation of molecular docking

The receptor used is the human co-crystal structure of the COX-2 protein with the PDB code 5KIR. The 3D structure is obtained from the Protein Data Bank (PDB) database in a *.pdb file on www.rcsb.org. The 3D structure of the COX-2 protein was then examined for completeness of the residue using the UCSF-Chimera software [14]. The last preparation was removing the ligands and water present in the receptor and adding Gasteiger charge and polar hydrogen using AutodockTools 1.5.6.rc3 [15]. The ligands were 49

compounds in *A. Lavenia* leaves, and 68 compounds in *M. calabura* leaves based on literature studies (Suppl. 1 and 2), encompassing polar and semipolar compounds. The 3D structures of the compounds were obtained from the <https://pubchem.ncbi.nlm.nih.gov/>. Each ligand structure was optimized using quantum mechanics (QM) calculations using the xTB program. Finally, each compound was charged, and the torque was adjusted using AutodockTools 1.5.6.rc3 software. The ligands that gave the most negative Gibbs free energy value were determined by their physicochemical properties using Lipinski's rule.

Running and evaluation of molecular docking

The grid box was determined based on the shape of a protein with the appropriate X, Y, and Z-axis values. The grid box parameters used for each process are shown in Table 1. Next, the target protein and ligand docking simulation were performed in *.pdbqt format. Molecular docking was processed using Autodock Vina software with an exhaustiveness value of 8. Each ligand was flexible and would interact with the receptor in strict conditions. Afterward, a docked output ligand structure file (out.pdbqt) and a text file (log.txt) appeared containing data on the energy value of the affinity of the ligand to the receptor for each ligand conformational mode. The final step was assessing the molecular docking results using the DS visualizer software. The hydrogen bonds and the contact residues between ligands and target protein were observed using DS visualizer software with *.pdb format [16]. Finally, with the lowest Gibbs free energy (ΔG), the docked ligand compounds were tested for toxicity using Data Warrior software.

Molecular dynamics simulation and evaluation of the results

Molecular dynamics simulations were carried out on COX-2 protein and the five best ligands based on molecular docking results. Each complex molecule was provided with a folder for running molecular dynamics

simulations. Before running the simulation, the proteins and the ligands were prepared. The ligands and the target proteins were combined to form protein-ligand complexes using AutodockTools. The complexes were then processed using the Pdb4amber program to remove water and hydrogen molecules. Next, the hydrogens were added to the complex and neutralized the pH to 7 using a webserver (<http://biophysics.cs.vt.edu/H++>) [17-19]. The results of the H++ webserver were in the form of topology files and coordinates. Next, the protein and the ligand files were combined to form a ligand-protein complex PDB file parameterized by tLEaP using the Amber FF14SB and GAFF2 force field for proteins and ligands, respectively. At tLEaP, the system was also neutralized by adding sodium and chlorine ions. The preparation produced a topology file and the final coordinates of the protein.

Furthermore, minimization was carried out to minimize energy in the system, avoid inappropriate van der Waals contacts (bad contact), and minimize high-energy steric effects to obtain molecules with minimum energy. Energy minimization was carried out using the steepest descent and conjugate gradient algorithms. Minimization was carried out in five steps. The first step was a dynamic constraint of 10 kcal/mol on all atoms. A dynamic constraint of 10 kcal/mol was applied to all atoms except hydrogen in the second step. In the third step, 10 kcal/mol dynamic constraints were applied to the backbone atoms of carbon, alpha carbon (CA), oxygen, and nitrogen. In the fourth step, a dynamic constraint of 10 kcal/mol was applied to the CA atom. Finally, the last step was carried out without any constraints, and the molecules moved freely.

The next stage in this simulation is heating, following the Langevin protocol. This stage uses the NVT dynamic ensemble. The heating was carried out with six temperature ranges, 0–50, 50–100, 100–150, 150–200, 200–250, and 250–300 K. The next stage was an

Table 1. Grid box parameters used for the molecular docking process

Protein target	Grid size A			Spacing (A)	Coordinate		
	x	y	z		x	y	z
COX-2	20	20	20	1.00	-19.163	74.728	33.837

equilibration to stabilize the protein from thermodynamic disturbances in the simulation. The resulting equilibration output was then depicted in a density graph against time using the `mdout_analyzer.py` command in the Amber20 program. The last stage of the simulation was the production run using the NPT ensemble. The simulation stage of molecule production was made in a natural state without restraints. The production run was carried out for 250 ns.

MD simulations were performed for 250 ns for each COX-2-ligand complex. The atomic coordinates in the complex system were stored at 0.2-ns time intervals during the simulation. Using the initial structure of the MD simulation as the reference structure, the CPPTRAJ module from AmberTools20 was used to determine the RMSD value to validate the convergence of the MD simulation process for calculating hydrogen bonds formed in the ligand-complex during the simulation. In addition, the structural flexibility of the protein was estimated by calculating the fluctuating root-mean-square (RMSF) values. Also, the simulation results were analyzed using binding affinity using molecular mechanics energies with the Poisson-Boltzmann surface area method (MM/PBSA) [20].

Measurement of the inhibitory activity of *A. lavenia* and *M. calabura* extracts on COX-2 activity

The inhibition activity measured toward COX-2 was 50, 70, and 96% ethanol extracts of *A. lavenia* and *M. calabura*. Various extracting compositions were carried out to obtain semipolar and polar compounds from the samples. *In vitro* studies could be followed by *in silico* studies related to the compounds to be tested computationally. All extracts were measured for their inhibitory activity toward COX-2 *in vitro* using COX-2 (Human) Inhibitor Screening Assay KIT (Cayman Chemical Item No. 701080). The kit directly read PGF_{2α} by measuring PGH₂ reduction by SnCl₂. PGH₂ was produced from a reaction catalyzed by COX-2. Prostanoid products were confirmed by enzyme immunoassay (ELISA) using a broad specific antiserum that binds all major prostaglandin compounds.

The test method following the kit protocol includes a COX-2 reaction procedure consisting of the preparation

of a COX-2 reagent and a COX-2 reaction process. The reaction process began with inactivating the COX-2 enzyme by heating it in boiling water for 3 min. Then 950 μL of the reaction buffer was pipetted and put into the initial tube activity and all test tubes. During the process, 10 μL of heme and 10 μL inactive COX-2 were added to tube background, added 10 μL of active COX-2 to tube initial activity and all test tubes, added 10 μL of arachidonic acid to all test tubes, then vortexed and incubated for 2 min before adding 50 μL of 1 M HCl. The test tube contains sample extracts with various concentrations. Into each test tube, 100 μL of SnCl₂ solution was added and incubated back for 5 min at room temperature before centrifuging at 4000 rpm to obtain a clear supernatant. The resulting supernatant was diluted before being measured by the ELISA procedure. The ELISA procedure includes preparation of buffer solution, special test reagents, dilution of COX-2 reagent, application to 96 well-plates, and measurements using ELISA spectrophotometer at 405–420 nm wavelengths. A more detailed procedure was in the guidebook COX-2 (Human) Inhibitor Screening Assay kit (Cayman Chemical Item No. 701080).

RESULTS AND DISCUSSION

Receptors and Ligands Used

Determination of receptors is the first step in the docking process, which is the COX-2 enzyme in this study. This enzyme plays a pivotal role in synthesizing prostanoids involving prostaglandins and thromboxane from arachidonic acid substrates [21]. The 3D structure of COX-2 was obtained from the Protein Data bank website with the PDB code 5IKR. The structure has two chains, namely the A and B chains with 551 amino acid sequences, and still forms a complex with the mefenamic acid ligand so that it needs to be separated to obtain a pure structure of COX-2 protein [22]. Separating COX-2 protein with ligands has been successfully carried out using VMD software. At this stage, water molecules, solvents, and small non-protein molecules were removed to produce a pure protein structure of COX-2 in the *.pdb format. The COX-2 structural model is shown in Fig. 1. The amino acid residues produced from

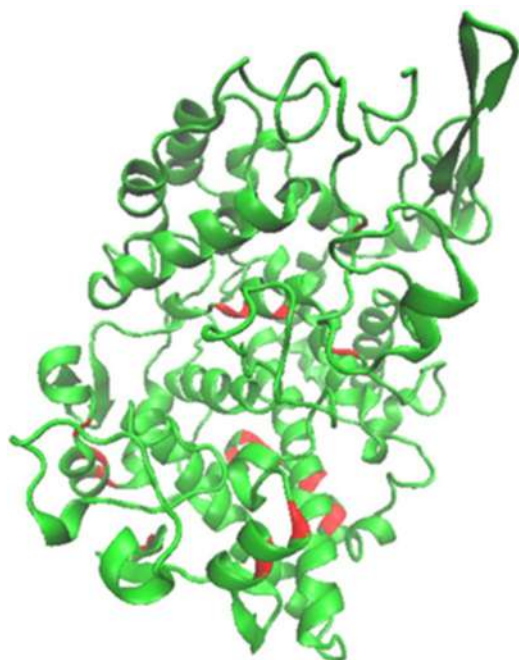


Fig 1. The 3D structure of chain A COX-2 (the red color is the active site of the protein)

the COX-2 structure showed no missing amino acid residues so the COX-2 protein could be used for the docking process. The compounds in *A. Lavenia* and *M. calabura* were referred to in literature [23-24]. Flavonoids, steroids, terpenoids, and saponins are observed in both plants [25].

Molecular Docking Result

Molecular docking is one of the most widely used virtual screening methods by utilizing the 3D structure of a protein, carbohydrates, and nucleic acids. This method can predict the binding affinity between the ligand and protein and the protein-ligand complex structure [7]. The docking process begins with determining the grid box parameters to be used. A grid box is a space or area that will be a place for interaction between ligands and target

receptors. Determination of the grid box aims to determine a receptor's active site [26]. Based on the results of docking *A. lavenia* compounds with COX-2, it seems that some compounds have a lower Gibbs free energy value than arachidonic acid, with a binding energy of -7.4 kcal/mol. Arachidonic acid is the main component of lipids in cell membranes. The COX-2 enzyme can metabolize arachidonic acid into various metabolites that trigger an inflammatory response, such as prostaglandins [4].

The results of the COX-2 docking analysis on *A. lavenia* gave the five best compounds with the lowest binding energies (Table 2). The ligands 124 and 149 have the lowest Gibbs free energy among the other test ligands, with a value of -8.7 kcal/mol. It indicates that there has been a strong interaction between COX-2 and these two ligands. The lower the Gibbs free energy value, the more robust and the more stable the interaction between the ligand and the receptor [27]. The energy values of the two ligands were lower than diclofenac. Diclofenac is a positive control used in this study with an -8.1 kcal/mol energy value. Thus, it is shown that the compounds in *A. lavenia* are potential COX-2 inhibitors. Diclofenac is a non-steroidal anti-inflammatory drug from the phenylacetic acid class with anti-inflammatory, analgesic, and antipyretic properties. Diclofenac has high enough selectivity to inhibit COX-2 with greater potency than COX-1 [28].

The results of COX-2 docking with ligands from *M. calabura* are shown in Table 3. The Gibbs free energy of the *M. calabura* ligand has a lower value than the positive control and ligands from *A. lavenia*, meaning higher potential as a COX-2 inhibitor. Ligand 18 has the lowest Gibbs free energy with -9.1 kcal/mol. These results agreed with previous reports that ligand 18 could

Table 2. Gibbs free energy of compound *A. lavenia* with COX-2

Number	Code	Compound	Energy (kcal/mol)
1	124	1a,9b-Dihydro-1H-cyclopropa[a]anthracene	-8.7
2	149	Biphenyl, 3,4-diethyl	-8.7
3	114	3,6-Dimethylphenanthrene	-8.3
4	150	Diclofenac	-8.1
5	110	Z-cyclodecene	-7.2
6	103	Linoleic acid	-7.0

Table 3. Gibbs free energy of compound *M. calabura* with COX-2

Number	Code	Compound	Energy (kcal/mol)
1	18	7-Hydroxyflavone	-9.1
2	30	7-Hydroxyisoflavone	-9.0
3	87	8-Hydroxy-6-methoxyflavone	-9.0
4	14	(2S)-7-Hydroxyflavanone	-8.9
5	19	5,7-Dihydroxyflavone	-8.9
6	150	Diclofenac	-8.1

reduce the production of prostaglandins and other pro-inflammatory mediators in cells induced by lipopolysaccharide [29]. The binding energy values obtained are almost similar to previous studies, which reported that the result of docking COX-2 with eutypoid A compound using Autodock Vina has a binding energy of -9.0 kcal/mol [30]. It indicates that the ligand binds strongly and is very stable to the COX-2 receptor.

Five ligands from Table 3 with the lowest binding energies are compounds that belong to flavonoids. These results agree with previous *in silico* studies related to the docking of flavonoid molecules to COX-2. Quercetin and its derivatives are predicted to have inhibitory activity against COX-2 so that it can be used as an anti-inflammatory [31]. Most flavonoids are known to have anti-inflammatory activity. For example, flavonoids from *Lotus plumule* have been reported to inhibit the production of inflammatory mediators such as NO radicals, PGE₂, and TNF- α , as well as pro-inflammatory cytokines IL-1 β and IL-6 [1]. The *S. alopecuroides* extract enriched with flavonoids can inhibit the release of lipopolysaccharide-induced NO, PGE₂, TNF- α , interleukin-6, and interleukin-1 β , and can reduce the expression of iNOS and COX-2 proteins [32]. A mixture of flavonoids and isolated compounds from *Boldoa*

purpurascens leaves has been shown to have an anti-inflammatory impact because it can reduce the expression of COX-2 when induced with lipopolysaccharides [33].

Characteristic of ligands according to Lipinski's rule

Lipinski's rule concerns the absorption or permeation of a drug molecule. A drug molecule that has a deviation from the Lipinski rule can have poor absorption in the body. Lipinski's rules include that the molecular weight should not exceed 500 g/mol, have a log *P* value not greater than five, have a hydrogen bond donor of less than five, and a hydrogen acceptor of less than 10 [34]. Based on Table 4, three compounds of *A. lavenia*, namely ligands 114, 124, and 149, have Lipinski rule deviations related to the log *P* value of more than five. The log *P* value indicates the lipophilicity of a molecule [35]. Lipophilicity affects solubility and affects permeability, potency, selectivity, distribution, metabolism, excretion, and toxicity. Its high lipophilicity (log *P* > 5) often contributes to its low solubility and poor drug absorption. In addition, highly lipophilic compounds tend to bind to hydrophobic molecules in the body other than their intended targets, increasing the risk of toxicity to cells or tissues [36]. According to Lipinski's rule, ligands 18, 30, and 87 have good properties

Table 4. Ligand characteristic of *A. lavenia* and *M. calabura* based on Lipinski's rule

Compound	Molecular weight (g/mol)	Log <i>P</i>	Number of hydrogen bond donors	Number of hydrogen bond acceptors
18	238.24	1.66	1	3
30	238.24	1.66	1	3
87	268.26	1.33	1	4
114	206.28	5.67	0	0
124	192.26	5.15	0	0
149	210.31	5.83	0	0

as drug molecules. The three ligands do not have Lipinski rule deviations to have good absorption or permeation in the body as drug molecules.

Prediction of ligand toxicity

A new drug molecule is expected to have better activity and lower toxicity than the existing drugs. Therefore, the ligands with the three lowest binding energies of *A. lavenia* and *M. calabura* were determined first for their toxicity. Then, a ligand toxicity test was carried out using Data Warrior software. Several studies have used this software to find new medicinal compounds, such as cancer and antidepressant drugs [37-38]. The results of the predictive analysis of ligand toxicity using Data Warrior are shown in Table 5 [39]. The ligands 18, 30, and 87 of *M. calabura*, and ligand 124 of *A. lavenia*, have no mutagenic, tumorigenic, irritant, and

reproductive effects. Therefore, it indicates that the two plants have potential as COX-2 inhibitor agents. However, ligands 114 and 149 have a low tumorigenic effect, so they can cause cancer if taken for a long time as a drug.

Ligand-receptor interaction analysis

The ligand-receptor interaction was carried out on the ligands with the lowest binding energies of the two plants. Ligand interaction analysis was performed using DS Visualizer. This analysis was carried out to see the active site and the type of bond between the ligand and the amino acid residues contained in COX-2. Interactions are hydrogen bonds, electrostatic interactions, and van der Waals interactions. The interaction between ligand 18 and COX-2 amino acid residues is shown in Fig. 2. The interaction of ligand 18

Table 5. Ligand properties of *A. lavenia* and *M. calabura* based on toxicity

Compound	Effect			
	Mutagenic	Irritant	Tumorigenic	Reproductive
18	None	None	None	None
30	None	None	None	None
87	None	None	None	None
114	Low	None	Low	None
124	None	None	None	None
149	None	None	Low	None

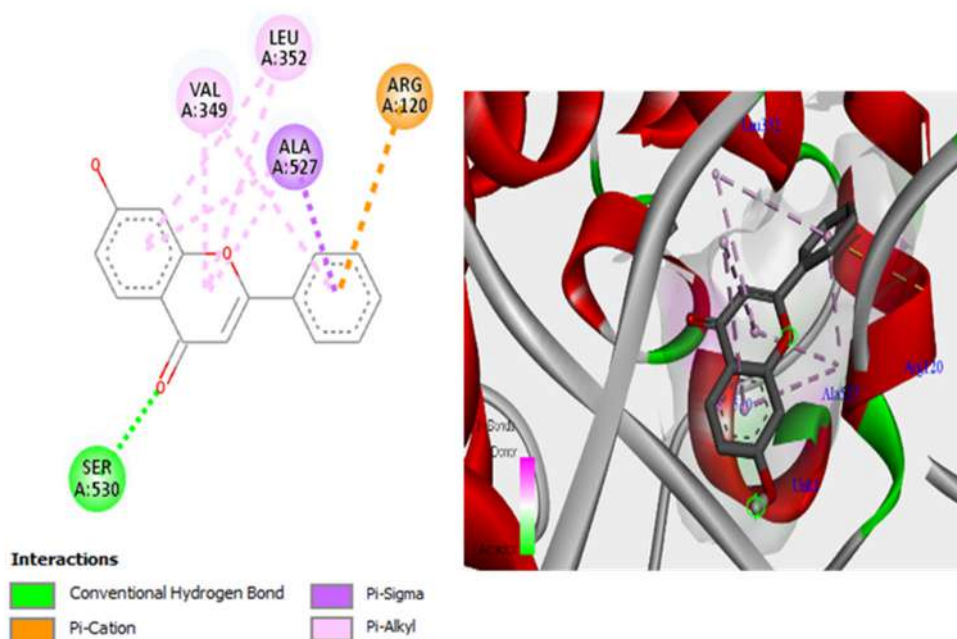


Fig 2. Ligand 18 interaction with COX-2 in 2D (left) and 3D (right)

produces hydrogen bonds at the Ser530 residue, in addition to hydrogen bonding, hydrophobic interactions at residues Arg120, Val349, Leu352, and Ala527. The results so far are still in line with previous studies related to the active site of COX-2. The results of previous studies reported that COX-2 protein has an active site on the amino acid residues Ser530, Ala527, Gly526, Met522, and Leu352 [40]. The binding between the ligand and the active site of COX-2 can change the secondary or tertiary structure of the COX-2 protein. Changes in the protein structure make COX-2 unable to recognize its substrate to produce prostaglandin inflammatory mediators [41]. An article reported that arachidonic acid interacts with COX-2 at the amino acid residues Tyr385, Ser530, Arg120, Leu531, Val349, Ser353, Ile523, Ala527, Leu352, Gly526, Phe205, Phe209, Val-228, Val-344, Ile-377, Phe-381, Gly533, and Leu-534 [42]. Tyr-385 is a critical catalytic residue that donates a hydrogen atom to heme during enzyme activation. In addition, the amino acid residue Ser530 has a vital role in the inhibition of COX-2 activity [43].

The analysis of ligand 124 with COX-2 (Fig. 3) shows hydrophobic interactions at the amino acid residues Val349, Leu352, Trp387, Phe518, Met522, Val523, Gly526, and Ala527. Hydrophobic interactions are between the ligand molecule's non-polar group and the receptor's non-polar region. Hydrophobic interactions can stabilize the ligand-receptor interaction

by lowering the value of the Gibbs free energy because the interaction is a combination of weakly interacting bonds such as van der Waals, dipole-dipole, and electrostatic bonds [44]. Therefore, the Gibbs free energy value of ligand 18 is lower due to the hydrogen interaction at the amino acid residue Ser530 than ligand 124, which does not have hydrogen interactions.

Molecular Dynamics Result

A total of 10 ligands consisting of five ligands each from *A. lavenia* and *M. calabura* (Table 6) were selected based on the lowest binding energy resulting from the molecular docking process for stability through MD

Table 6. List of ligands selected for MD simulation of stability

Number	Code	Compound
1	14	(2S)-7-Hydroxyflavanone
2	18	7-Hydroxyflavone
3	19	5,7-Dihydroxyflavone
4	30	7-Hydroxyisoflavone
5	87	8-Hydroxy-6-methoxyflavone
6	103	Linoleic acid
7	110	Z-cyclodecene
8	114	3,6-Dimethylphenanthrene
9	124	1a,9b-Dihydro-1H-cyclopropa[a]anthracene
10	149	Biphenyl, 3,4-diethyl

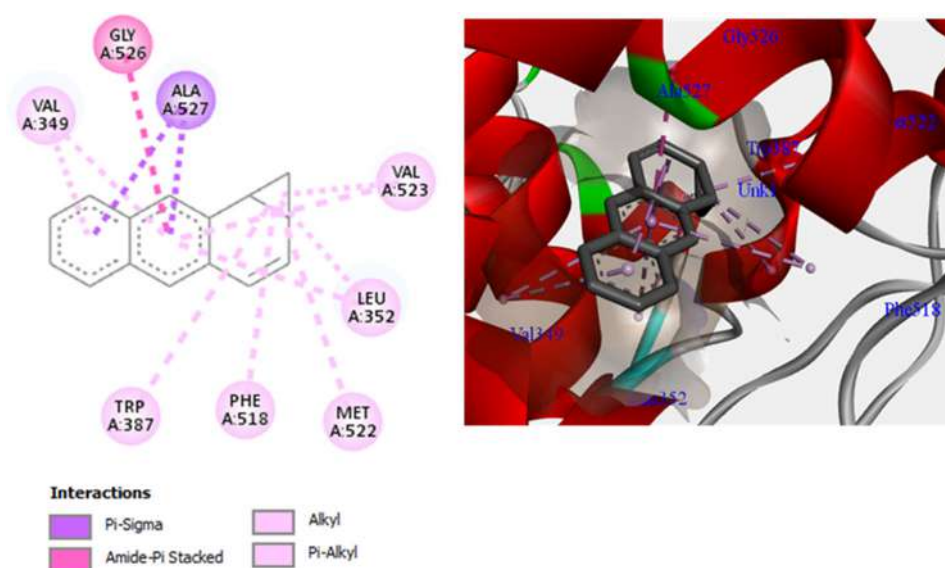


Fig 3. Ligand 124 interaction with COX-2 in 2D (left) and 3D (right)

simulation for 250 ns. The RMSD values for compounds from *A. lavenia* increased during the first 50 ns. After that phase, the five ligands experienced simple fluctuations in the range of 1.5–2.5 Å and had an average RMSD below 2 Å (Fig. 4). Overall, in the 250 ns period, the COX-2 complex structure with five selected *A. lavenia* ligands converged because the fluctuations in the RMSD value produced were not too large (not exceeding 1.5 Å). It indicates that the complex formed is stable during the simulation [45]. Based on Fig. 5, the COX-2 complex with the *M. calabura* ligand looks stable at the beginning of the simulation until it reaches a simulation time of 125 ns, the RMSD value increases until the end of the simulation, especially in the 8-hydroxy-6-methoxyflavone ligand. The COX-2 complex with 8-hydroxy-6-methoxyflavone ligand

has the most considerable fluctuation in the RMSD value among the other four ligand complexes with a range of 0.96–3.14 Å. Fig. 5 exhibits a decrease in the stability of the COX-2 complex with 8-hydroxy-6-methoxyflavone at the end of the simulation. However, overall, the five ligand complexes of *M. calabura* have good stability during the simulation because the fluctuations produced are not too large (still close to 1.5 Å).

The RMSF value indicates the flexibility of the receptor amino acid residues. Changes in the RMSF value can explain fluctuations in each residue in the protein structure and protein flexibility during the MD simulation. RMSF of the two species ligands has almost the same value seen from the peaks and valleys formed (Fig. 6). RMSF value fluctuates at amino acid residues

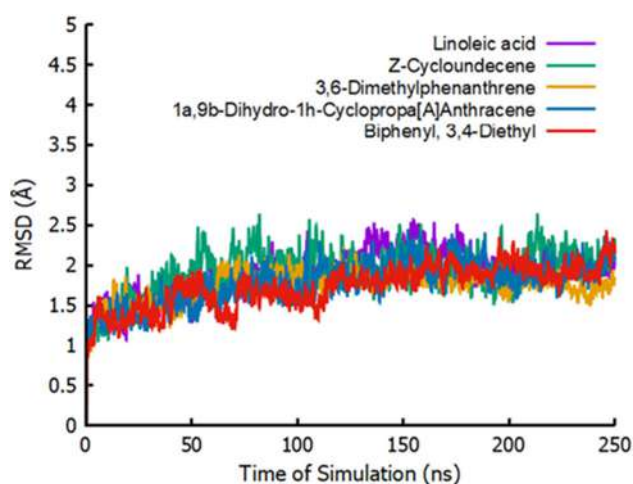


Fig 4. RMSD of the protein-ligand complex from *A. lavenia* at 250 ns

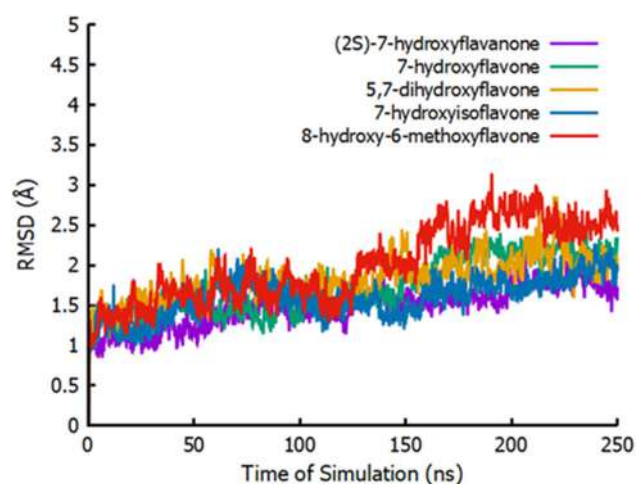


Fig 5. RMSD of the protein-ligand complex from *M. calabura* at 250 ns

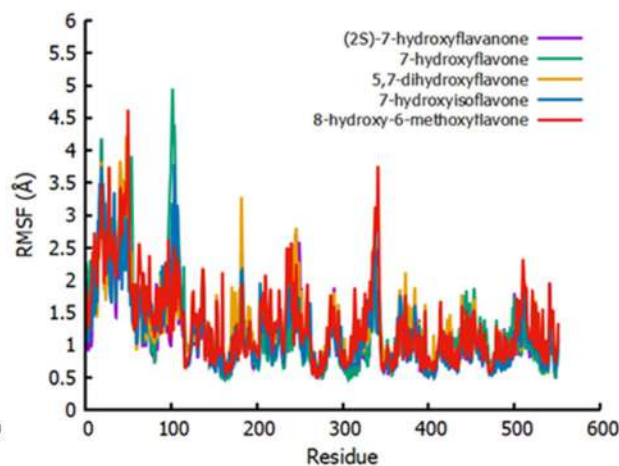
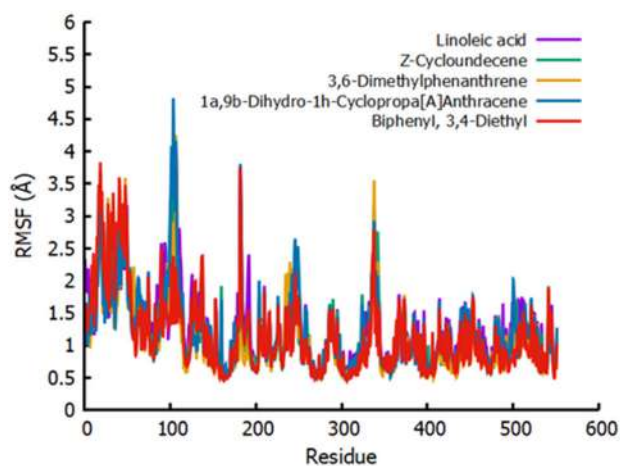


Fig 6. RMSF of the protein-ligand complex from *A. lavenia* (left) and *M. calabura* (right) at 250 ns

15–30, 40–54, 100–110, and 335–342. Higher RMSF values indicate greater flexibility during MD simulations [46]. Amino acid residues 100–110 give the highest RMSF fluctuations peaks because they do not bond with the ligands, causing the amino acid residues to become more flexible.

In comparison, the valleys indicate that the ligand interacts with the residue causing the COX-2 protein to become more rigid [47]. Residues above 350 are also related to the active site of COX-2, which is in the amino acid residues Ser530, Ala527, Gly526, Met522, and Leu352 [39]. In all complexes, the RMSF value for each residue surrounding the ligand has a lower value of less than 1 Å, as shown in residues above 350. The interaction between the ligand and protein is relatively stable during the MD simulation.

The calculation of the binding energy of the protein-ligand complex was carried out using the MMPBSA technique. This calculation technique can provide information about the stability of the bond between the ligand and COX-2 as a complex structure. Based on Fig. 7, the linoleic acid compound had the lowest MMPBSA value with an average energy of -48.605 kcal/mol. The Z-cycloundecene ligand had the highest binding energy with an average energy of -28.733 kcal/mol. It shows a very different order of results from the Gibbs free energy in the molecular docking step, as clearly seen in Table 7 and 8. The difference in the data can represent that molecular

docking data needs to be validated using molecular dynamics simulations because logarithms and conditions applied in molecular docking simulations with Autodock Vina are more straightforward and more rigid.

In contrast, the receptors are flexible in molecular dynamics simulations. Hence, more parameters are required, and the logarithm of applied calculations is more complex than in molecular docking. The parameters used in the computation of MMPBSA that do not exist in the molecular docking include the dielectric constant, parameters for non-polar energy, polar solvation energy, radius, electrostatic energy, and entropy of the system used. As a result, the calculation of the MMPBSA value has better accuracy than the calculation by molecular docking [48]. Meanwhile, the results of MMPBSA with *M. calabura* ligand (Fig. 8) have energy that is almost similar to energy fluctuations ranging from -30 to -40 kcal/mol. Ligand 8-hydroxy-6-methoxyflavone has the most negative average binding energy of -38.346 kcal/mol. The negative Gibbs free energy value indicates that the receptor has an attractive interaction with the ligand. Furthermore, the value of the Gibbs free energy of the ligand pair in each conformation is negative, signifying that the receptor with the ligand has a stable bond [49].

Hydrogen bond analysis was also performed on the MD Trajectory to calculate the number of hydrogen bonds formed in each complex during the simulation.

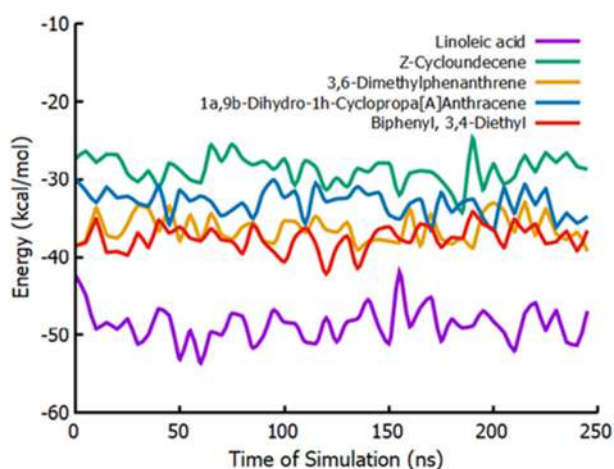


Fig 7. MM-PBSA of the protein-ligand complex from *A. lavenia* at 250 ns

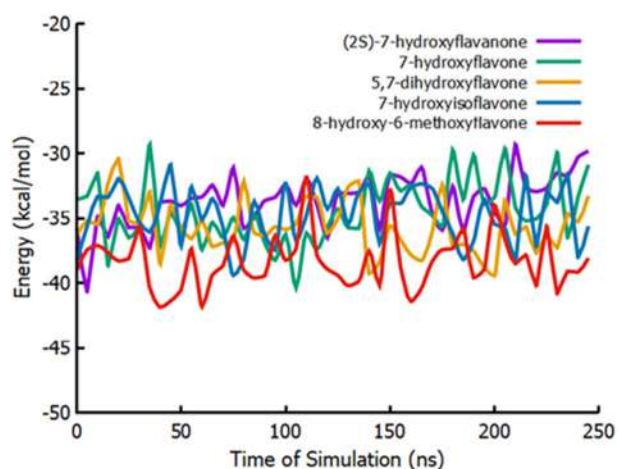


Fig 8. MM-PBSA of the protein-ligand complex from *M. calabura* at 250 ns

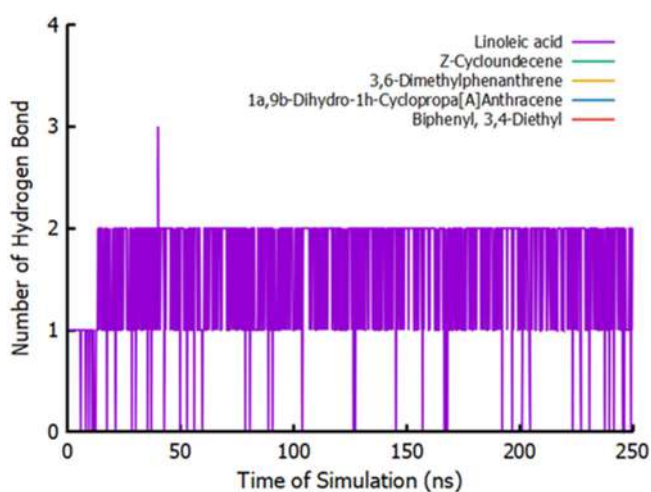
Table 7. Comparison of energy from Autodock Vina and MMPBSA from *A. lavenia*

Code	Compound	Energy (kcal/mol)	
		Autodock Vina	MMPBSA
124	1a,9b-Dihydro-1H-cyclopropa[a]anthracene	-8.7	-33.0
149	Biphenyl, 3,4-diethyl	-8.7	-37.6
114	3,6-Dimethylphenanthrene	-8.3	-36.3
110	Z-cyclodecene	-7.2	-28.7
103	Linoleic acid	-7.0	-48.6

Table 8. Comparison of energy from Autodock Vina and MMPBSA from *M. calabura*

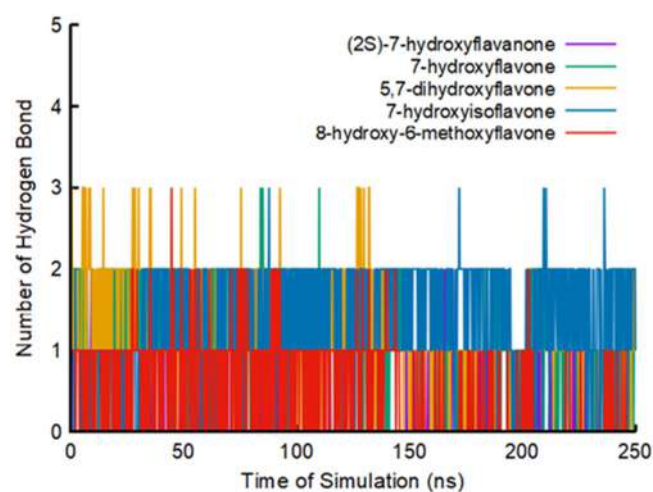
Code	Compound	Energy (kcal/mol)	
		Autodock Vina	MMPBSA
18	7-Hydroxyflavone	-9.1	-34.5
30	7-Hydroxyisoflavone	-9.0	-34.7
87	8-Hydroxy-6-methoxyflavone	-9.0	-38.3
14	(2S)-7-Hydroxyflavanone	-8.9	-33.6
19	5,7-Dihydroxyflavone	-8.9	-35.7

From *A. lavenia*, only linoleic acid ligands form hydrogen bonds with two hydrogen bonds on average (Fig. 9). The other four ligands do not show hydrogen bonding. The hydrogen bond is not formed presumably because the position of the donor atom and the hydrogen acceptor are far apart at the time of docking, avoiding hydrogen bonds between COX-2 and the ligand. It makes linoleic acid ligands have the lowest binding energy than the other four due to hydrogen bonds with COX-2. Hydrogen bonds can strengthen the interactions between ligands and proteins.

**Fig 9.** Number of hydrogen bonds formed for the MD simulation trajectory for the COX-2 enzyme with selected ligand from *A. lavenia*

H-bonds are critical for protein folding and protein-ligand interactions [50]. These results are consistent with the docking analysis that the ligand 1a,9b-dihydro-1H-cyclopropa[a]anthracene does not form hydrogen interactions with COX-2 but forms hydrophobic interactions to stabilize the complex structure formed.

In contrast to the ligands from *A. lavenia*, varying hydrogen bonds are formed between the ligands on *M. calabura* and COX-2 (Fig. 10). Ligands (2S)-7-hydroxyflavanone and 8-hydroxy-6-methoxyflavone

**Fig 10.** Number of hydrogen bonds formed for the MD simulation trajectory for the COX-2 enzyme with selected ligand from *M. calabura*

formed one hydrogen bond with COX-2 from the beginning of the simulation to the end of the MD simulation. The 7-hydroxyisoflavone ligand most often forms two hydrogen bonds during the simulation, and sometimes three hydrogen bonds can be formed even if only temporarily. Meanwhile, according to the molecular docking analysis, 7-hydroxy flavone only formed one hydrogen bond. The 5,7-dihydroxyflavone ligand formed two hydrogen bonds at the beginning of the simulation and three hydrogen bonds formed during the MD simulation.

In vitro Extract Inhibition Test against COX-2

The samples measured for their inhibitory activity on COX-2 were single extracts of *A. lavenia* and *M. calabura* with 25, 100, and 1000 ppm concentrations. The extract was produced by macerating the samples for 3×24 h in 50, 70, and 96% ethanol as the solvent. Referring to Fig. 11, the 50% EtOH extract does not show inhibition of COX-2 activity. The inhibitory activity of 70% EtOH extract is only seen at a concentration of 100 ppm with an inhibition value of 6%, and 1000 ppm is equal to 81%. The 96% EtOH extract gives a high inhibitory power to COX-2 activity. The 96% EtOH extract of *A. lavenia* with 25 and 100 ppm concentrations produced an inhibitory power of about 98%. These results are consistent with the previous *in vivo* studies that *A. lavenia* extract can treat the pathogenesis of pneumonia in LPS-induced rats. In addition, the extract can reduce MAPK and NF- κ B activity to suppress the production of pro-inflammatory cytokines [11]. The compound ent-11 α -hydroxy-15-oxo-kaur-16-en-19-oic-acid in *A. lavenia* is also reported to inhibit NF- κ B expression in the treatment of colorectal cancer [51]. Several groups of compounds that have been known to have potential as COX-2 inhibitors include acetogenins [52], alkaloids [53], and sterol derivatives [54].

The inhibitory power of EtOH single extract of *M. calabura* is shown in Fig. 12. In contrast to *A. lavenia*, 50% EtOH extract with a concentration of 25 ppm could inhibit COX-2. It showed the highest inhibitory power of 50% EtOH extract of 51% at a concentration of 1000 ppm. The inhibitory activity above 50% is given by 70% and 96% EtOH extracts. At 25 ppm concentration, both 70

and 96% EtOH extracts can provide inhibition power approaching 80 and 84%, respectively. EtOH 70 and 96% extracts may inhibit COX-2 activity up to 100% at 1000 ppm concentration. Compared with the other two EtOH extracts, the inhibitory power of 96% EtOH extract shows a higher potential for COX-2 inhibition.

The positive control employed in this study is diclofenac, a synthetic drug commonly used as an anti-inflammatory. Based on the research results, diclofenac has a COX-2 inhibition percentage of 88% at a concentration of 0.75 ppm (Fig. 13). The inhibitory activity produced by all tested extracts was able to compete

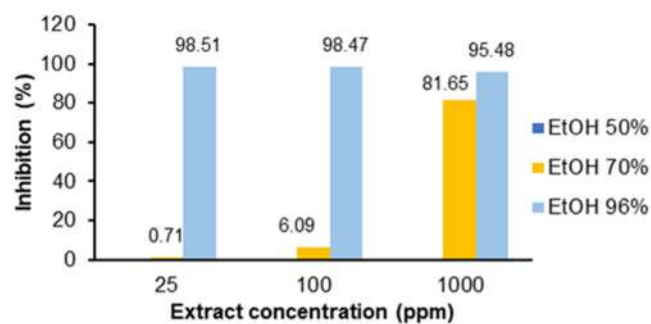


Fig 11. Inhibition of EtOH extract of *A. lavenia* on COX-2 activity

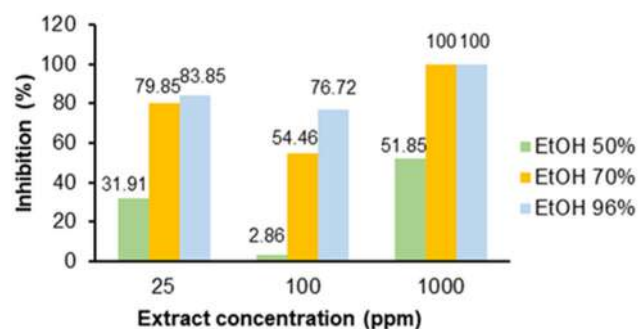


Fig 12. The inhibitory activity of the EtOH extract of *M. calabura* on COX-2

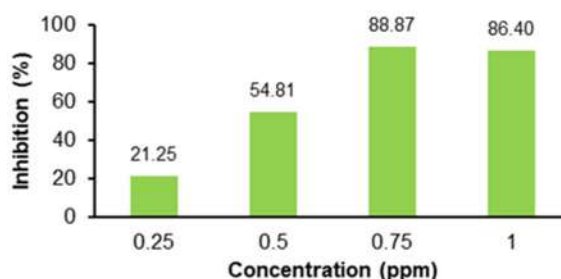


Fig 13. The inhibitory activity of diclofenac on COX-2

with diclofenac as a positive control even though the concentration of the extract used was relatively different. The anti-inflammatory activity becomes better if the required concentration is getting smaller. Based on the measurement of the inhibition of COX-2, both plants have the potential to be anti-inflammatory.

The active compounds found in extracts of *A. lavenia* and *M. calabura*, which act as anti-inflammatory through inhibition of COX-2 activity, are flavonoids and steroids. Following *in silico* results, the five compounds from *M. calabura*, with the lowest Gibbs free energy, belong to flavonoids. Flavonoids can suppress COX gene expression through cell signaling pathways such as the NF-B pathway and tyrosine kinase, but the mechanism has not been determined with certainty [55]. However, based on the *in silico* results, it can be predicted that the compounds contained in the extracts of *A. lavenia* and *M. calabura* will interact with COX-2 in the body. It happens because, in the inflammatory process, COX-2 production will increase so that the potential for binding between the active compounds in the extracts of these two species with COX will be even more significant. This interaction can inhibit COX-2 in binding arachidonic acid so that the catalysis process does not occur and can result in changes in the structure and active site of the enzyme so that COX-2 cannot catalyze the formation of prostaglandins.

■ CONCLUSION

We conclude that *A. lavenia* and *M. calabura* extracts have the potency to inhibit the performance of COX-2, which affects the regulation of inflammation *in vitro*. The computational simulations agree with the *in vitro* experiment results that show an interaction between the compounds in both plants and the active site of the COX-2 enzyme. Furthermore, the MD simulations show that the interactions between COX-2 and ten selected compounds formed a stable protein-ligand complex. These results provide an urgently needed opportunity to develop new therapeutic drug design and discovery strategies to treat inflammation.

■ ACKNOWLEDGMENTS

The authors would like to thank the Ministry of

Education and Culture, Research and Technology of the Republic of Indonesia for granting this work through *Penelitian Terapan Kompetitif Nasional* scheme (Grant Number 2052/IT3.L1/PN/2021). The Authors also acknowledge computational resources provided by the HPC Lab of Theoretical Physics Division, Department of Physics, IPB University.

■ AUTHOR CONTRIBUTIONS

Bagaskoro Tuwalaid, Dyah Iswantini, and Setyanto Tri Wahyudi conducted the experiment. Bagaskoro Tuwalaid wrote the manuscript and conducted the scoring docking analysis and simulation of molecular dynamics. Dyah Iswantini and Setyanto Tri Wahyudi supervised the experimental and revised the manuscript. All authors agreed to the final version of this manuscript.

■ REFERENCES

- [1] Chen, L., Deng, H., Cui, H., Fang, J., Zuo, Z., Deng, J., Li, Y., Wang, X., and Zhao, L., 2018, Inflammatory responses and inflammation-associated diseases in organs, *Oncotarget*, 9 (6), 7204–7218.
- [2] Merad, M., and Martin, J.C., 2020, Author correction: Pathological inflammation in patients with COVID-19: A key role for monocytes and macrophages, *Nat. Rev. Immunol.*, 20 (7), 448.
- [3] Syahputra, G., Ambarsari, L., and Sumaryada, T., 2014, Simulasi docking kurkumin enol, bisdemetoksikurkumin dan analognya sebagai inhibitor enzim 12-lipoksigenase, *J. Biofisika*, 10 (1), 55–67.
- [4] Wang, T., Fu, X., Chen, Q., Patra, J.K., Wang, D., Wang, Z., and Gai, Z., 2019, Arachidonic acid metabolism and kidney inflammation, *Int. J. Mol. Sci.*, 20 (15), 3683.
- [5] Wongrakpanich, S., Wongrakpanich, A., Melhado, K., and Ranganwami, J., 2018, A comprehensive review of non-steroidal anti-inflammatory drug use in the elderly, *Aging Dis.*, 9 (1), 143–150.
- [6] Saikia, S., and Bordoloi, M., 2019, Molecular docking: Challenges, advances and its use in drug discovery perspective, *Curr. Drug Targets*, 20 (5), 501–521.

- [7] Salmaso, V., and Moro, S., 2018, Bridging molecular docking to molecular dynamics in exploring ligand-protein recognition process: An overview, *Front. Pharmacol.*, 9, 923.
- [8] Ravindranath, P.A., Forli, S., Goodsell, D.S., Olson, A.J., and Sanner, M.F., 2015, AutoDockFR: Advances in protein-ligand docking with explicitly specified binding site flexibility, *PLOS Comput. Biol.*, 11 (12), e1004586.
- [9] De Vivo, M., Masetti, M., Bottegoni, G., and Cavalli, A., 2016, Role of molecular dynamics and related methods in drug discovery, *J. Med. Chem.*, 59 (9), 4035–4061.
- [10] Case, D.A., Cheatham, T.E., Darden, T., Gohlke, H., Luo, R., Merz, K.M., Onufriev, A., Simmerling, C., Wang, B., and Woods, R.J., 2005, The Amber biomolecular simulation programs, *J. Comput. Chem.*, 26 (16), 1668–1688.
- [11] Chen, J.J., Deng, J.S., Huang, C.C., Li, P.Y., Liang, Y.C., Chou, C.Y., and Huang, G.J., 2019, *p*-Coumaric acid-containing *Adenostemma lavenia* ameliorates acute lung injury by activating AMPK/Nrf2/HO-1 signaling and improving the anti-oxidant response, *Am. J. Chin. Med.*, 47 (7), 1483–1506.
- [12] Cheng, P.C., Hufford, C.D., and Doorenbos, N.J., 1979, Isolation of 11-hydroxyated kauranic acids from *Adenostemma lavenia*, *J. Nat. Prod.*, 42 (2), 183–186.
- [13] Lin, J.T., Chang, Y.Y., Chen, Y.C., Shen, B.Y., and Yang, D.J., 2017, Molecular mechanisms of the effects of the ethanolic extract of *Muntingia calabura* Linn. fruit on lipopolysaccharide-induced pro-inflammatory mediators in macrophages, *Food Funct.*, 8 (3), 1245–1253.
- [14] Pettersen, E.F., Goddard, T.D., Huang, C.C., Couch, G.S., Greenblatt, D.M., Meng, E.C., and Ferrin, T.E., 2004, UCSF Chimera—A visualization system for exploratory research and analysis, *J. Comput. Chem.*, 25 (13), 1605–1612.
- [15] Morris, G.M., Huey, R., and Olson, A.J., 2008, Using AutoDock for Ligand-Receptor Docking, *Curr. Protoc. Bioinf.*, 24 (1), 8.14.1–8.14.40.
- [16] Zubair, M.S., Anam, S., Maulana, S., and Arba, M., 2021, *In vitro* and *in silico* studies of quercetin and daidzin as selective anticancer agents, *Indones. J. Chem.*, 21 (2), 310–317.
- [17] Gordon, J.C., Myers, J.B., Folta, T., Shoja, V., Heath, L.S., and Onufriev, A., 2005, H++: A server for estimating pK_as and adding missing hydrogens to macromolecules, *Nucleic Acids Res.*, 33 (Suppl. 2), W368–W371.
- [18] Myers, J., Grothaus, G., Narayanan, S., and Onufriev, A., 2006, A simple clustering algorithm can be accurate enough for use in calculations of pK_s in macromolecules, *Proteins: Struct., Funct., Bioinf.*, 63 (4), 928–938.
- [19] Anandakrishnan, R., Aguilar, B., and Onufriev, A.V., 2012, H++ 3.0: Automating pK prediction and the preparation of biomolecular structures for atomistic molecular modeling and simulations, *Nucleic Acids Res.*, 40 (W1), W537–W541.
- [20] Radwan, A., and Mahrous, G.M., 2020, Docking studies and molecular dynamics simulations of the binding characteristics of waldiomycin and its methyl ester analog to *Staphylococcus aureus* histidine kinase, *PLoS One*, 15 (6), e0234215.
- [21] Rawat, C., Kukal, S., Dahiya, U.R., and Kukreti, R., 2019, Cyclooxygenase-2 (COX-2) inhibitors: Future therapeutic strategies for epilepsy management, *J. Neuroinflammation*, 16 (1), 197.
- [22] Orlando, B.J., and Malkowski, M.G., 2016, Substrate-selective inhibition of cyclooxygenase-2 by fenamic acid derivatives is dependent on peroxide tone, *J. Biol. Chem.*, 291 (29), 15069–15081.
- [23] Fauzan, A., Praseptianga, D., Hartanto, R., and Pujiastanto, B., 2018, Characterization of the chemical composition of *Adenostemma lavenia* (L.) Kuntze and *Adenostemma platyphyllum* Cass, *IOP Conf. Ser.: Earth Environ. Sci.*, 102, 012029.
- [24] Mahmood, N.D., Nasir, N.L.M., Rofiee, M.S., Tohid, S.F.M., Ching, S.M., Teh, L.K., Salleh, M.Z., and Zakaria, Z.A., 2014, *Muntingia calabura*: A review of its traditional uses, chemical properties, and pharmacological observations, *Pharm. Biol.*, 52 (12), 1598–1623.
- [25] Krishnaveni, M., and Dhanalakshmi, R., 2014, Qualitative and quantitative study of

- phytochemicals in *Muntingia calabura* L. leaf and fruit, *World J. Pharm. Res.*, 3 (6), 1687–1696.
- [26] Rachmania, R.A., Supandi, S., and Cristina, F.A.D., 2016, Analisis penambatan molekul senyawa flavonoid buah mahkota dewa (*Phaleria macrocarpa* (Scheff.) Boerl.) pada reseptor α -glukosidase sebagai antidiabetes, *Pharm. J. Indones.*, 13 (2), 239–251.
- [27] Legiawati, L., Fadilah, F., Bramono, K., and Indriatmi, W., 2018, *In silico* study of *Centella asiatica* active compounds as anti-inflammatory agent by decreasing IL-1 and IL-6 activity, promoting IL-4 activity, *J. Pharm. Sci. Res.*, 10 (9), 2142–2147.
- [28] Altman, R., Bosch, B., Brune, K., Patrignani, P., and Young, C., 2015, Advances in NSAID development: Evolution of diclofenac products using pharmaceutical technology, *Drugs*, 75 (8), 859–877.
- [29] Jin, Z., Yang, Y.Z., Chen, J.X., and Tang, Y.Z., 2017, Inhibition of pro-inflammatory mediators in RAW264.7 cells by 7-hydroxyflavone and 7,8-dihydroxyflavone, *J. Pharm. Pharmacol.*, 69 (7), 865–874.
- [30] Taidi, L., Maurady, A., and Britel, M.R., 2022, Molecular docking study and molecular dynamic simulation of human cyclooxygenase-2 (COX-2) with selected eutypoids, *J. Biomol. Struct. Dyn.*, 40 (3), 1189–1204.
- [31] Kartasasmita, R.E., Herowati, R., Harmastuti, N., and Gusdinar, T., 2009, Quercetin derivatives docking based on study of flavonoids interaction to cyclooxygenase-2, *Indones. J. Chem.*, 9 (2), 297–302.
- [32] Guo, C., Yang, L., Wan, C.X., Xia, Y.Z., Zhang, C., Chen, M.H., Wang, Z.D., Li, Z.R., Li, X.M., Geng, Y.D., and Kong, L.Y., 2016, Anti-neuroinflammatory effect of Sophoraflavanone G from *Sophora alopecuroides* in LPS-activated BV2 microglia by MAPK, JAK/STAT and Nrf2/HO-1 signaling pathways, *Phytomedicine*, 23 (13), 1629–1637.
- [33] González Mosquera, D.M., Hernández Ortega, Y., Fernández, P.L., González, Y., Doens, D., Vander Heyden, Y., Foubert, K., and Pieters, L., 2018, Flavonoids from *Boldoa purpurascens* inhibit proinflammatory cytokines (TNF- α and IL-6) and the expression of COX-2, *Phytother. Res.*, 32 (9), 1750–1754.
- [34] Lipinski, C.A., Lombardo, F., Dominy, B.W., and Feeney, P.J., 2001, Experimental and computational approaches to estimate solubility and permeability in drug discovery and development settings, *Adv. Drug Delivery Rev.*, 46 (1-3), 3–26.
- [35] Gao, Y., Gesenberg, C., and Zheng, W., 2017, "Oral Formulations for Preclinical Studies: Principle, Design, and Development Considerations" in *Developing Solid Oral Dosage Forms*, 2nd Ed., Eds. Qiu, Y., Chen, Y., Zhang, G.G.Z., Yu, L., and Mantri, R.V., Academic Press, Boston, US, 455–495.
- [36] Hughes, J.D., Blagg, J., Price, D.A., Bailey, S., DeCrescenzo, G.A., Devraj, R.V., Ellsworth, E., Fobian, Y.M., Gibbs, M.E., Gilles, R.W., Greene, N., Huang, E., Krieger-Burke, T., Loesel, J., Wager, T., Whiteley, L., and Zhang, Y., 2008, Physicochemical drug properties associated with *in vivo* toxicological outcomes, *Bioorg. Med. Chem. Lett.*, 18 (17), 4872–4875.
- [37] Ajay Kumar, T.V., Kabilan, S., and Parthasarathy, V., 2017, Screening and toxicity risk assessment of selected compounds to target cancer using QSAR and pharmacophore modelling, *Int. J. PharmTech Res.*, 10 (4), 219–224.
- [38] Sultan, M.A., Galil, M.S.A., Al-Qubati, M., Omar, M.M., and Barakat, A., 2020, Synthesis, molecular docking, druglikeness analysis, and ADMET prediction of the chlorinated ethanoanthracene derivatives as possible antidepressant agents, *Appl. Sci.*, 10 (21), 7727.
- [39] Sander, T., Freyss, J., von Korff, M., and Rufener, C., 2015, DataWarrior: An open-source program for chemistry aware data visualization and analysis, *J. Chem. Inf. Model.*, 55 (2), 460–473.
- [40] Reddy, K.K., Vidya Rajan, V.K., Gupta, A., Aparoy, P., and Reddanna, P., 2015, Exploration of binding site pattern in arachidonic acid metabolizing enzymes, cyclooxygenases and lipoxigenases, *BMC Res. Notes*, 8 (1), 152.
- [41] Wang, B., Wu, L., Chen, J., Dong, L., Chen, C., Wen,

- Z., Hu, J., Fleming, I., and Wang, D.W., 2021, Metabolism pathways of arachidonic acids: Mechanisms and potential therapeutic targets, *Signal Transduction Targeted Ther.*, 6 (1), 94.
- [42] Rouzer, C.A., and Marnett, L.J., 2020, Structural and chemical biology of the interaction of cyclooxygenase with substrates and non-steroidal anti-inflammatory drugs, *Chem. Rev.*, 120 (15), 7592–7641.
- [43] Deb, P.K., Mailabaram, R.P., Al-Jaidi, B., and Saadh, M.J., 2017, "Molecular Basis of Binding Interactions of NSAIDs and Computer-Aided Drug Design Approaches in the Pursuit of the Development of Cyclooxygenase-2 (COX-2) Selective Inhibitors" in *Nonsteroidal Anti-Inflammatory Drugs*, Eds. Al-kaf, A.G., IntechOpen, Rijeka, Croatia.
- [44] Syahputra, G., 2014, Simulasi Docking Senyawa Kurkumin dan Analognya sebagai Inhibitor Enzim 12-Lipoksigenase, *Thesis*, Institut Pertanian Bogor.
- [45] Mahapatra, M.K., Bera, K., Singh, D.V., Kumar, R., and Kumar, M., 2018, *In silico* modelling and molecular dynamics simulation studies of thiazolidine based PTP1B inhibitors, *J. Biomol. Struct. Dyn.*, 36 (5), 1195–1211.
- [46] Zhao, Y., Zeng, C., and Massiah, M.A., 2015, Molecular dynamics simulation reveals insights into the mechanism of unfolding by the A130T/V mutations within the MID1 zinc-binding Bbox1 domain, *PLoS One*, 10 (4), e0124377.
- [47] Khan, S., Farooq, U., and Kurnikova, M., 2017, Protein stability and dynamics influenced by ligands in extremophilic complexes – A molecular dynamics investigation, *Mol. Biosyst.*, 13 (9), 1874–1887.
- [48] Genheden, S., and Ryde, U., 2015, The MM/PBSA and MM/GBSA methods to estimate ligand-binding affinities, *Expert Opin. Drug Discovery*, 10 (5), 449–461.
- [49] Botelho, F.D., dos Santos, M.C., Gonçalves, A.S., Kuca, K., Valis, M., LaPlante, S.R., França, T.C.C., and de Almeida, J.S.F.D., 2020, Ligand-based virtual screening, molecular docking, molecular dynamics, and MM-PBSA calculations towards the identification of potential novel ricin inhibitors, *Toxins*, 12 (12), 746.
- [50] Al-Thiabat, M.G., Mohd Gazzali, A., Mohtar, N., Murugaiyah, V., Kamarulzaman, E.E., Yap, B.K., Abd Rahman, N., Othman, R., and Wahab, H.A., 2021, Conjugated β -Cyclodextrin Enhances the Affinity of Folic Acid towards FR α : Molecular Dynamics Study, *Molecules*, 26 (17), 5304.
- [51] Ye, H., Wu, Q., Guo, M., Wu, K., Lv, Y., Yu, F., Liu, Y., Gao, X., Zhu, Y., Cui, L., Liang, N., Yun, T., Li, L., and Zheng, X., 2016, Growth inhibition effects of ent-11 α -hydroxy-15-oxo-kaur-16-en-19-oic-acid on colorectal carcinoma cells and colon carcinoma-bearing mice, *Mol. Med. Rep.*, 13 (4), 3525–3532.
- [52] Soekaryo, E., Simanjuntak, P., and Setyahadi, S., 2016, Uji Inhibisi Enzim Siklooksigenase-2 (COX-2) dari Ekstrak Daun Sirsak (*Annona muricata* Linn.) sebagai Antiinflamasi, *The 4th Univesity Research Coloquium 2016*, STIKES Muhammadiyah Pekajangan, Pekalongan, 485–492.
- [53] Hashmi, M.A., Khan, A., Farooq, U., and Khan, S., 2018, Alkaloids as cyclooxygenase inhibitors in anticancer drug discovery, *Curr. Protein Pept. Sci.*, 19 (3), 292–301.
- [54] Joy, M., and Chakraborty, K., 2018, Previously undisclosed bioactive sterols from corbiculid bivalve clam *Villorita cyprinoides* with anti-inflammatory and antioxidant potentials, *Steroids*, 135, 1–8.
- [55] Lago, J.H.G., Toledo-Arruda, A.C., Mernak, M., Barrosa, K.H., Martins, M.A., Tibério, I.F.L.C., and Prado, C.M., 2014, Structure-activity association of flavonoids in lung diseases, *Molecules*, 19 (3), 3570–3595.

A New Flow Injection System with Merging-Zone Technique for the Determination of Copper(II) by Neocuproine Reagent in Aqueous Solution

Ahmed Saleh Farhood^{1*} and Dakhil Nassir Taha²

¹Department of Chemistry, College of Science, University of Babylon, Hilla 51002, Iraq

²Department of Chemistry, College of Sciences for Women, University of Babylon, Hilla 51002, Iraq

* **Corresponding author:**

email: sci.ahmed.saleh@uobabylon.edu.iq

Received: November 29, 2021

Accepted: February 1, 2022

DOI: 10.22146/ijc.70799

Abstract: A fast, simple, and high throughput sample merging-zone flow injection design was developed to determine copper(II) in an aqueous solution. The procedure is based on the reduction of copper(II) to copper(I) by uric acid followed by a direct reaction with Neocuproine reagent (NC). The orange-yellow complex that forms absorbs light at 454 nm. All conditions of the new flow injection unit were investigated. The analytical curve of copper(II) was linear with an r^2 value of 0.9978, in the range of 0.4 to 40 mg/L with a detection limit of 0.1 mg/L and a quantification limit of 0.3 mg/L. The molar absorptivity was 1.661×10^5 L/mol cm, and the recovery range was between 104.9 and 97%. The homemade acrylic valve was low-cost with zero dead volume and high repeatability ($n = 7$) with an RSD of 2.31%. The dispersion coefficient values were 1.8, 1.62, and 1.31 for the concentrations of 5, 15, and 25 mg/L, respectively. The sample throughput was 69 h^{-1} .

Keywords: merging-zone; copper(II); Neocuproine; homemade valve; dead volume

■ INTRODUCTION

Copper is one of the major trace elements in many biological and industrial processes, organic fertilizers, electroplating, nanotechnology, and sewage sludge [1-3]. Cu(II) is directly reduced by uric acid (UA), ascorbic acid (AA), and or other reducing agents [4-5]. Copper(I) reacts with 2,9-Dimethyl-1,10-phenanthroline (NC) to produce a complex that absorbs light at 454 nm [6]. The merging-zone flow injection method has low consumption of chemicals during analysis [7]. Consequently, a homemade valve can be used to determine copper with NC reagent by merging-zone FIA technique.

The Cu(I)-NC complex has high stability constant [8]. The complexation ratio of Cu(I)-NC is 1:2 with an optimum pH of 7 [9]. Based on Cu-NC complex represents a new Redox mediator, and it is used as an electrode [10]. Cu(I) is determined in the form of Cu(I)-BCS (bathocuproine_disulfonicacid) complex when Cu is accumulated by electrolysis of a plating solution [11]. Based on the reduction of Cu(II)-NC by ascorbic acid, the

Cu(I) is formed and then reacts with NC reagent to produce an orange-yellow colored complex, then ascorbic acid was determined [12-13]. Cu in water is determined by using the interaction between Cu(I) with one derivative of Neocuproine immobilized on modified silica based on the adsorption-photometric method [14].

The flow injection analysis (FIA) method was used for the Neocuproine-copper complex on a modified surfactant electrode to determine hydrazine [15]. The FIA unit was used to determine Cu with a low sample throughput value at 15 h^{-1} ; the reaction time for one analysis was 4 min [16]. The reaction between Cu(II) and reducing sugars in the presence of NC reagent was used for determining sugars. This novel principle is based on flow injection analysis and is considered as a fast, simple, analytically versatile, and accurate method [17]. An FIA method based on the reaction of Cu(II) with NC reagent was designed to determine *N*-acetyl-L-cysteine, with a maximum sample throughput of 180 h^{-1} [18]. Stop FIA was applied in the determination of Cu(II) by 4-(2-pyridylazo)resorcinol reagent as a carrier

solution at 525 nm [19]. The hybrid flow system based on the reaction between *N*-acetyl-L-cysteine and Cu(II)-NC was applied to determine *N*-acetyl-L-cysteine. An orange-yellow complex of Cu(I)-NC was obtained at 458 nm with a throughput sample of 100 h⁻¹ [20]. Cu(II) was determined by flow injection analysis depending on the reaction of *N,N'*-*o*-phenylene-bis(3-methoxysalicylidene imine) with Cu(II) at a sample throughput more than 60 h⁻¹ [21]. The automatic FIA unit was used to determine the total antioxidant capacity in urine and serum samples based on the reduction of Cu(II)-NC to colored Cu(I)-NC [22].

This paper describes a new merging-zone technique for copper determination by flow injection. This method is a simple, high throughput, and high precision method for copper(II) determination in an aqueous solution with an inexpensive homemade valve. In this novel technique, Cu(II) is reduced directly by uric acid to Cu(I) that reacts with a specific Neocuproine reagent to form an orange-yellow complex that absorbs light at 454 nm.

■ EXPERIMENTAL SECTION

Materials

2,9-Dimethyl-1,10-phenanthroline (Neocuproine Reagent)(Merck), Uric acid (BDH), copper(II) chloride anhydrous (BDH), sodium hydroxide (Merck), hydrochloric acid (Chem-Lab), and absolute ethanol(Chem-Lab) were used. The chemicals and reagents used were of analytical grade. The water used was deionized and distilled.

Instrumentation

A 4-channel Peristaltic pump from Ismatec (Germany) with their tubing was used for thrusting the carrier solution. A manual flow injection valve, made of plastic, acrylic, and a three-way dispenser, was used for loading and injecting the sample, reagent, and reference carrier solution in the flow injection unit. UV-VIS spectra were acquired using a single-beam APEL, PD-303 (Japan) UV spectrophotometric for spectrometric measurements by flow injection analysis. The spectrophotometer was connected to the Kompensograph recorder C1032 Siemens (Germany) to obtain data as a peak height. The

flow cell (1 cm optical path) was obtained from Helmma (UK) with two vents for input and output with a volume capacity of 450 μL. The pH meter Philips Pw 9421 (Germany) was used to measure pH. The double-beam spectrophotometer Shimadzu UV-1700 (Japan) was used to determine the maximum wavelength.

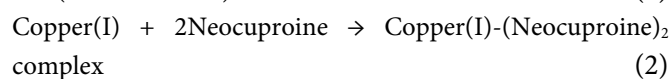
Procedure

Solutions and reagents

A stock solution of copper(II) 250 mg/L was prepared in distilled water. The working solution of copper(II) was acquired by diluting the stock solution with a suitable volume of distilled water. A stock solution of uric acid 250 mg/L was prepared by dissolving 0.025 g of uric acid in 5 mL of 0.1 M sodium hydroxide solution [23]. Then the volume was completed to 100 mL by distilled water. The working solution of uric acid was acquired by diluting the stock solution with a suitable distilled water volume, and then pH was adjusted using 0.1 M hydrochloric acid or 0.1 M sodium hydroxide. A stock solution of NC reagent 1000 mg/L was prepared in 10% (v/v) of absolute ethanol [24]. Working solutions of NC reagent were prepared by dilution in distilled water.

Method principle

The copper(II) determination method that is used in this article is based on the redox properties of uric acid and copper(II). The reactions which occur are as follows: Copper(II) + Uric acid(reduced form) → Copper(I) + Uric acid(oxidized form) (1)



Uric acid is colorless in the oxidized form, but when the positively charged Cu(I)-Neocuproine complex forms, the color becomes orange-yellow and absorbs light at 455 nm. The combination ratio is Cu(I) 1:2 Neocuproine [25-26], as shown in Fig. 1.

Analysis module of merging-zone flow injection

The merging-zone of the flow injection unit with spectrophotometric detection to determine Cu(II) in an aqueous solution with a simple and fast flow injection system is shown in Fig. 2, where: C is the carrier solution (uric acid 150 mg/L), P is the peristaltic pump (flow rate

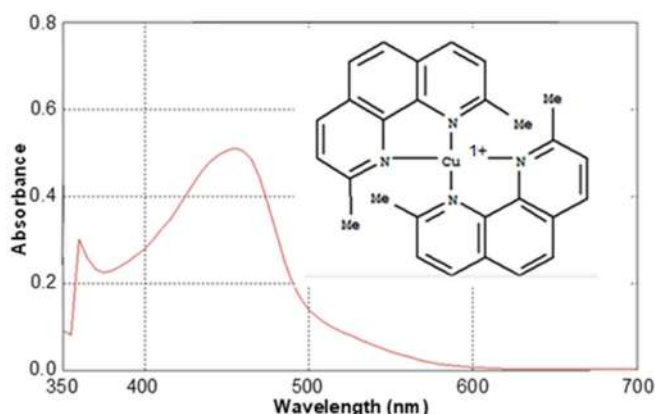


Fig 1. Absorption spectra of Cu(I)-NC complex. Wavelength 455 nm at Cu(II) 15 mg/L, NC reagent 600 mg/L, Uric acid concentration 150 mg/L, and pH 7

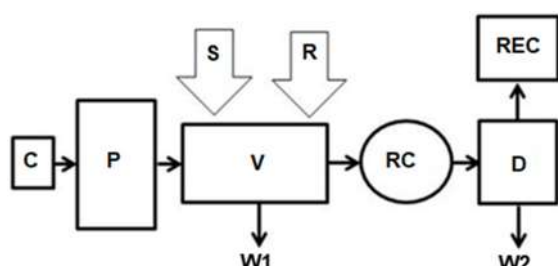


Fig 2. Schematic diagram of the flow-injection unit for determination copper(II), where: C- uric acid carrier, P- peristaltic pump, V- injector valve, S- sample loop, R- Neocuproine loop, W1- injection waste, RC- tubular reaction coil, D- UV-VIS spectrophotometer, REC- Kompensograph and W2- unit waste

of 6.5 mL/min), V is the injector valve with two loops (homemade), S is the sample solution loop (78.5 μ L of copper(II)), R is the reagent solution loop (157 μ L of 600 mg/L Neocuproine), W1 is the injection waste (sample and reagent), RC is the tubular reaction coil 150 cm, D is the UV-VIS spectrophotometer 454 nm, REC is the Kompensograph at 0.2 volts, and W2 is the unit waste.

Mechanical operation diagram of the homemade valve

The schematic diagram of the homemade working valve shows in Fig. 3. The first stage involved the suction of 150 mg/L of uric acid (adjusted at pH 7) as the carrier solution to all the parts of the unit by a peristaltic pump at a flow rate of 6.5 mL/min. Uric acid represents the reference solution (blank solution) and reducing agent.

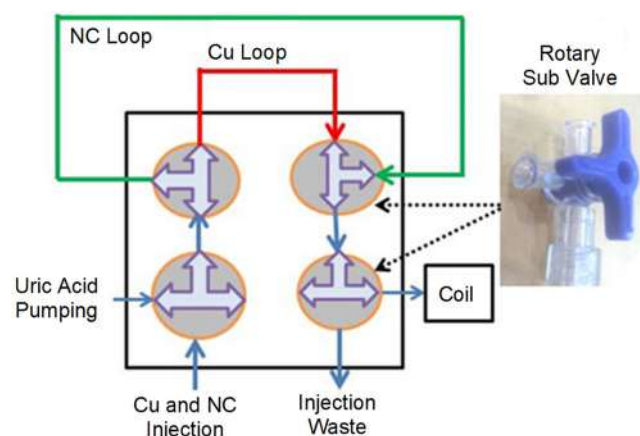


Fig 3. Schematic diagram of the homemade valve working

The second and third stage includes stopping the pump and injecting 157 μ L of 600 mg/L NC reagent solution in the specific loop (represented by the green line in Fig. 3 and injecting 78.5 μ L of the Cu(II) sample solution in the loop (represented by the red line in Fig. 3). Then uric acid carries the copper and NC from loops to the tubular reaction coil (150 cm). At first, uric acid reduces Cu(II) to Cu(I). Subsequently, the NC reagent reacts with Cu(I) to form an orange-yellow complex that absorbs light at 454 nm. The change in peak height of the Kompensograph was proportional to the Cu(II) sample concentration/reference carrier solution (uric acid).

RESULTS AND DISCUSSION

The Effect of Uric Acid Concentration

The effect of uric acid concentration on the height of the peak was studied in the range of 25–250 mg/L. The conditions of the study were: pH = 10 of uric acid 117.00 μ L of 400 mg/L NC reagent, a flow rate of 3.8 mL/min, reaction coil length of 100 cm, and 47.1 μ L of 15 mg/L Cu(II) solution. The preferred peak height of 2.7 cm was obtained at a uric acid concentration of 150 mg/L, as shown in Fig. 4.

The pH Effect of the Carrier Solution

The effect of pH was studied in the range of 3–10. The study was conducted using the selected concentration of uric acid (150 mg/L). The other conditions of the study include 117.00 μ L of 400 mg/L NC reagent, a flow rate of 3.8 mL/min, reaction coil length of 100 cm, and

47.1 μL of 15 mg/L Cu(II) solution. As shown in Fig. 5, the optimal pH was seven at a peak height of 5 cm. The consequence obtained in this study corresponds to the results of Gaál et al. [9] and Ribeiro et al. [16].

The Effect of the Flow Rate of Uric Acid Solution

The effect of the flow rate of the carrier solution on the height of the peak was studied at 0.9, 2.3, 3.8, 5.2, 6.5, and 7.8 mL/min. Optimum parameters were used in the study, which includes: 150 mg/L uric acid concentration at pH 7, 117.00 μL of 400 mg/L NC reagent, reaction coil length of 100 cm, and 47.1 μL of 15 mg/L of Cu(II) solution. The best peak height was 3.6 cm at the carrier solution flow rate of 6.5 mL/min, as shown in Fig. 5. Although the response at low flow rates was greater than the higher flow rates, the shape of the peak was wide and double. For this reason, the flow rate of 6.5 mL/min was selected because the response was sharp and dependable. Authors found that low flow rates cause double, distorted, and wide peaks, while the fast flow rates decrease the response.

The Effect of the Cu(II) Sample Volume

The optimal conditions of the flow rate of the carrier solution, pH, and uric acid concentration were fixed at 6.5 mL/min, 7, and 150 mg/L, respectively. The effect of the Cu(II) sample volume on the shape and sensitivity of the peak height was studied at 47.1, 78.5, 117, 157, and 196.25 μL using 117.00 μL of 400 mg/L NC reagent, reaction coil length of 100 cm, and 15 mg/L of Cu(II) solution. It was observed that the highest response of 4 cm was obtained at 78.5 μL of Cu(II) sample solution, as shown in Fig. 6. In comparison, Dakhil and Zuhair found that the response decreased when using a very high sample volume because of the dilution process [27].

The Effect of the Neocuproine Reagent Volume

The effect of the NC reagent volume on the peak height was studied at values of 117, 157, 196.25, and 235.5 μL at optimal conditions as follows: flow rate of carrier solution of 6.5 mL/min, pH 7, the uric acid concentration of 150 mg/L, and 78.5 μL of 15 mg/L Cu(II) sample solution concentration, 400 mg/L of NC reagent

and reaction coil length of 100 cm. As a result, it was observed that the highest response of 4.3 cm was obtained at 157 μL of NC reagent volume, as shown in Fig. 6.

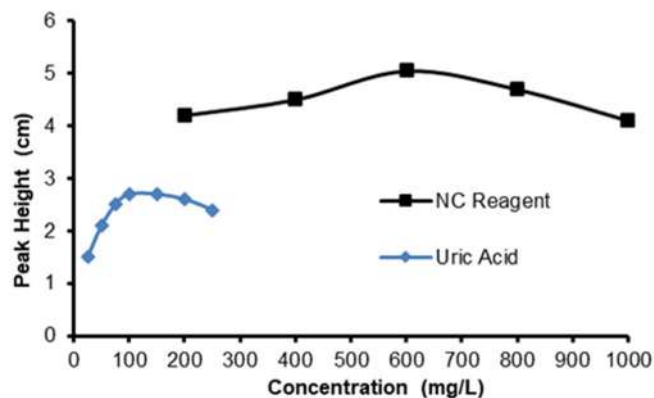


Fig 4. Effect of NC and uric acid concentration on the peak height

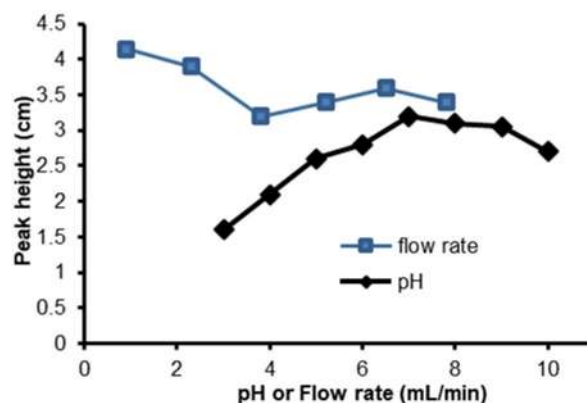


Fig 5. Effect of pH and flow rate on the peak height

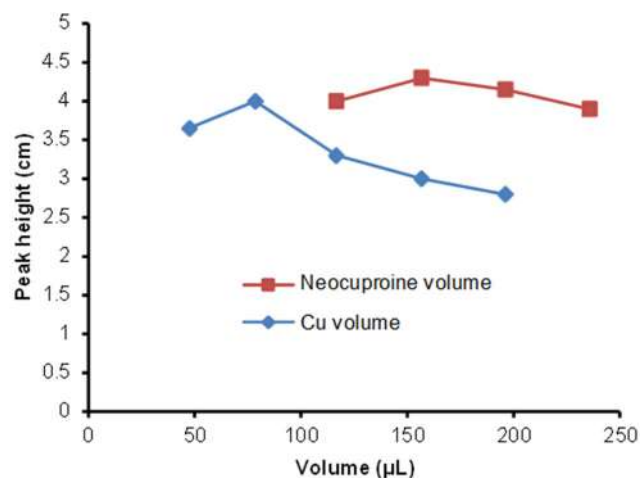


Fig 6. The relationship between the volume of Cu(II) and NC on the peak height

The Effect of Reaction Coil Length

The effect of the reaction coil length was studied at values of 50, 100, 150, and 200 cm (with a Teflon tube diameter of 0.5 mm), which produced peak height values of 4, 4.25, 4.5, and 3.65 cm, respectively. The study was conducted under optimum parameters: flow rate of carrier solution of 6.5 mL/min, pH 7, the uric acid concentration of 150 mg/L, 78.5 μ L of 15 mg/L Cu(II) sample solution, and 157 μ L of 400 mg/L NC reagent. It is clear from the results in Fig. 7 that the optimum coil length was 150 cm at the highest peak of 4.5 cm. The authors found that the increasing reaction coil length leads to an increase in the response because it facilitates good mixing for the components of the reaction. On the other hand, using very long reaction coils decreases response as the dispersion effect is happened but increases the time required for one analysis.

Neocuproine Reagent Concentration

The effect of the NC reagent concentration on the peak height was determined at values of 200, 400, 600, 800, and 1000 mg/L, in which the responses were 4.2, 4.5, 5.05, 4.7, and 4.1 cm, respectively, at the optimal conditions: flow rate of carrier solution of 6.5 mL/min, pH 7, the uric acid concentration of 150 mg/L, 78.5 μ L of 15 mg/L Cu(II) sample solution, 157 μ L of the NC reagent and reaction coil length of 150 cm. As shown in Fig. 4, it was observed that the highest response of 5.05 cm was obtained at the NC reagent concentration of 600 mg/L.

Compared to other techniques that are based on the reaction between Cu(II) and the NC reagent, there are several advantages that can be obtained by using the flow injection unit designed to determine Cu(II). It is

important to show that this work is characterized by utilizing a low concentration of NC reagent of 600 mg/L and a small volume of NC at 157 μ L. Furthermore, the current merging-zone flow injection unit requires a tiny volume of the Cu(II) sample of 78.5 μ L. Table 1 shows the comparison between the current non-consumptive new analysis unit for the determination of copper with other methods that are based on the same reaction.

The optimal conditions required by the new unit designed to determine Cu(II): the appropriate voltage of recorder, uric acid concentration, pH of the carrier solution, flow rate, Cu and NC volume, reaction coil length, and NC concentration are shown in Table 2.

Calibration Curve

The Cu(II) calibration curve was constructed by performing measurements at the optimal conditions. A series of Cu(II) concentrations were prepared to calculate the calibration graph, as shown in Fig. 8. The calibration curve indicated linearity of the Beer's law over

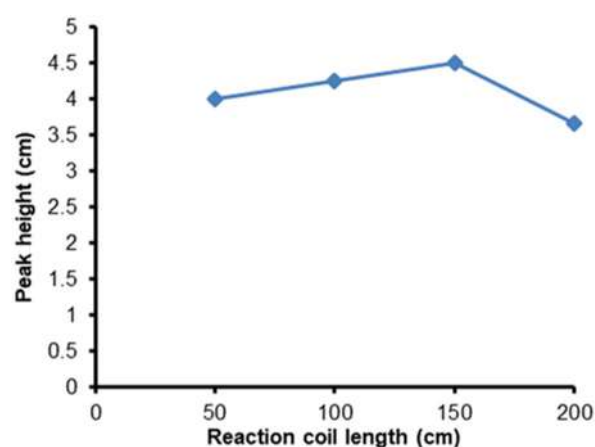


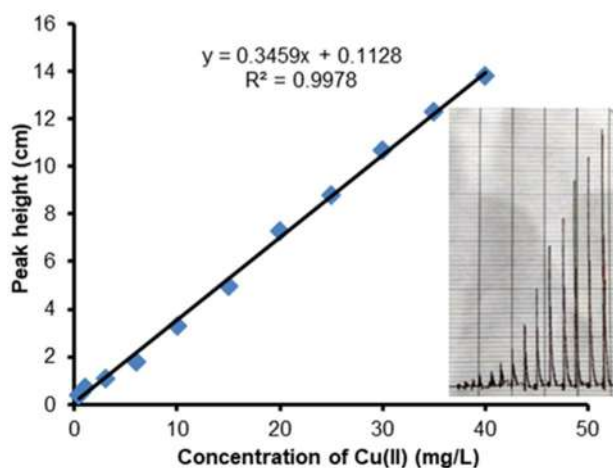
Fig 7. The relationship between reaction coil length and peak height

Table 1. Comparison of the present FIA unit to other analytical techniques for the determination of copper(II)

Method	Reagent (mg/L)	Reagent (μ L)	Cu (μ L)	Range (mg/L)	Ref.
Thermal lensing	1040	1000	500	0.6–63	[8]
FIA	832	400	100	-	[10]
Spectrophotometric	4160	219	220	-	[11]
Spectrophotometric	160	1000	1000	0.006–0.3	[28]
LLE-Spectrophotometric	880	250	5000	2.2–12.2	[29]
Merging-Zone FIA	600	157	78.5	0.4–40	current work

Table 2. Parameters estimate to optimize the FIA unit for determining Cu(II)

Parameter	Estimate range	Selected value
The recorder voltage (volt)	0.2–2	0.2
Uric acid concentration (mg/L)	25–250	150
The pH of the carrier solution	3–10	7
Flow rate (mL/min)	0.9–7.8	6.5
copper(II) volume (μL)	47.1–196.25	78.5
Neocuproine volume (μL)	117–235.5	157
Length of reaction coil (cm)	50–200	150
Neocuproine (mg/L)	200–1000	600

**Fig 8.** Calibration curve at optimum conditions: flow rate of carrier solution (6.5) mL/min, pH (7), the uric acid concentration 150 mg/L, 78.5 μL of Cu(II) sample solution, 157 μL of 600 mg/L NC reagent and reaction coil length 150 cm

the range of 0.4–40 mg/L ($r^2 = 0.9978$) with average standard deviation of 0.037 and average RSD of 1.14%. The detection limit ($S/N = 3$) was 0.1 mg/L, and the quantification limit ($S/N = 10$) was 0.3 mg/L. Molar absorptivity and Sandell's sensitivities were 1.661×10^5 L/mol cm and $0.0028 \mu\text{g}/\text{cm}^2$, respectively.

Repeatability

Repeatability was determined by repeating injections of the Cu(II) sample at least five times. The target of this study was to determine the precision of the measurement and the unit's efficiency. Using the optimum conditions, seven consecutive injections of the copper solution concentration 5, 15, and 25 mg/L of

Cu(II) were used to study the repeatability of injections. For these concentrations, the relative standard deviation values were 2.31, 0.63, and 0.50%, respectively. The obtained results shown in Table 3 display the efficiency and precision of the new flow injection unit design for the determination of Cu(II).

Dispersion Coefficient (D)

At optimum conditions, two measurements were done to determine the dispersion coefficient. The first experiment involved mixing the reaction components in a beaker outside the flow injection unit while keeping the volume ratio at 1:2 of Cu(II):NC reagent. Then 15 mL of 150 mg/L uric acid was added to prepare a suitable amount of carrier solution for aspiration into the flow injection unit. In this situation, the response represented H^0 . The second experiment involved the injection of the components of the reaction into their specified loops in the valve, in which the carrier solution was 150 mg/L of uric acid. The response was referred to as H_{max} and was considered as the original peak produced from the injection process. The coefficient of dispersion (D) was calculated by dividing H^0 by H_{max} [30-31]. The values of the dispersion coefficient were 1.8, 1.627, and 1.318 for the three concentrations of Cu(II), namely 5, 15, and 25 mg/L, respectively, as shown in Table 4.

Table 3. Repeatability ($n = 7$) at 5, 15, 25 mg/L of Cu(II)

Cu(II) (mg/L)	5	15	25
Peak height (cm)	1.6	5.05	8.8
	1.6	5	8.8
	1.5	5.05	8.7
	1.55	5.1	8.75
	1.6	5	8.8
	1.6	5.05	8.7
	1.55	5.05	8.8
SD	0.036	0.031	0.044
RSD%	2.31	0.63	0.50

Table 4. Dispersion coefficient

The concentration of Cu(II) (mg/L)	5	15	25
Peak height (cm), (H^0)	2.7	8.3	11.6
Peak height (cm), (H_{max})	1.5	5.1	8.8
Dispersion coefficient	1.80	1.62	1.31

Table 5. Comparison sampling throughput of the present FIA unit to other analytical techniques for determination of Cu(II)

Method	Sampling throughput (h ⁻¹)	Reaction time (min)	Ref.
Spectrophotometric	-	1	[28]
FIA-SPE- FAAS	25	2	[35]
SPE- FAAS	12	5	[36]
SFODME-FI-FAAS	6	10	[37]
Voltammetry	4	15	[38]
ICP-MS	10	-	[39]
Merging-zone FIA	69	52 sec	Present work

Table 6. Recovery and percentage error for determination Cu(II)

Taken (mg/L)	Response (cm)	Found (mg/L)	E	E%	Recovery
30	10.6	30.318	-0.010	-1.061	98.93
20	7.2	20.489	-0.024	-2.445	97.55
10	3.4	9.503	0.049	4.96	104.96

Dead Volume

The first step to determine the dead volume was the loading of the distilled water instead of the Cu(II) sample solution. The second step was loading distilled water instead of NC reagent solution in their loops. In these two steps, no peak was observed, but when the reaction components were injected into the loops, the peak was clearly noticeable. The carrier solution in both steps was 150 mg/L of uric acid under the optimum conditions. Therefore, this study indicates that no volume of Cu(II) sample solution or NC reagent solution remained in their loops before the loading of the next measurement. Therefore, the homemade valve worked with zero dead volume, indicating that this new flow injection unit is highly efficient. In previous articles, many designs of homemade valves accomplished operation with zero dead volume [32-34].

Sampling Throughput

The injection of all reaction components in the loops of the homemade valve required 25 sec. The required time for the peak to start from the baseline to the maximum peak height and back again to the baseline by the washing process was 52 sec (including injection of the components). Therefore, the sampling rate of the flow injection unit was 69 samples per hour. The comparison

of the sampling of the current FIA unit to other analytical techniques for the determination of Cu(II) is shown in Table 5.

Application in Aqueous Solution

The purpose of this experiment was to develop an application to determine copper in aqueous solutions. The prepared samples were taken without treatment and were analyzed with the new merging-zone flow injection technique. Table 6 shows satisfactory results for three prepared concentrations at a relative standard deviation of less than 5%. In addition, the table also shows a good agreement between the actual concentrations of Cu(II) and the concentration obtained from the calibration curve of the designed unit at the recovery rate of 100% ± 4.9.

CONCLUSION

A simple, fast, inexpensive, and feasible unit was developed to determine Cu(II) using the flow injection system with the merging-zone technique. The simplicity and speed of this new design involved a direct redox reaction between Cu(II) and uric acid, followed by an instantaneous reaction of Cu(I) with the NC reagent. The unit had good sampling throughput compared to other techniques. The homemade valve included a merging zone that reduced the volume of the Cu(II)

sample and NC reagent. The homemade valve was observed to have many advantages, namely: easy handling, high precision, low-cost, zero dead volume, and nearly no maintenance. The repeatability of measurements for this system was accurate at a very low relative standard deviation. Therefore, this new unit is dependable for determining Cu(II) in aqueous solution samples at a wide concentration range.

■ REFERENCES

- [1] Abdel-Raouf, M.S., and Abdul-Raheim, A.R., 2017, Removal of heavy metals from industrial waste water by biomass-based materials: A review, *J. Pollut. Eff. Control*, 5 (1), 1000180.
- [2] Ghorpade, A., and Ahammed, M.M., 2018, Water treatment sludge for removal of heavy metals from electroplating wastewater, *Environ. Eng. Res.*, 23 (1), 92–98.
- [3] Yu, J.S., Kim, S.H., Man, M.T., and Lee, H.S., 2018, Synthesis and characterization of water soluble fluorescent copper nanoparticles, *Appl. Sci. Convergence Technol.*, 27 (4), 75–77.
- [4] Jiang, T., Xie, D., Wu, J., He, H., Wang, H., Wang, N., Zhu, Z., Wang, Y., and Yang, T., 2020, Association between serum copper levels and prevalence of hyperuricemia: A cross-sectional study, *Sci. Rep.*, 10 (1), 8687.
- [5] Krivorotova, T., and Sereikaite, J., 2014, Determination of fructan exohydrolase activity in the crude extracts of plants, *Electron. J. Biotechnol.*, 17 (6), 329–333.
- [6] Dontha, S., 2016, A review on antioxidant methods, *Asian J. Pharm. Clin. Res.*, 9 (8), 14–32.
- [7] Zhang, G.Q., Li, Y.S., and Gao, X.F., 2018, An asynchronous-alternating merging-zone flow-injection gold nanoparticles probe method for determining anti-diabetic pioglitazone hydrochloride medicine, *New J. Chem.*, 42 (6), 4337–4343.
- [8] Proskurnin, M.A., Chernysh, V.V., Pakhomova, S.V., Kononets, M.Y., and Sheshenev, A.A., 2002, Investigation of the reaction of copper(I) with 2,9-dimethyl-1,10-phenanthroline at trace level by thermal lensing, *Talanta*, 57 (5), 831–839.
- [9] Gaál, A., Garay, T.M., Horváth, I., Máthé, D., Szöllősi, D., Veres, D.S., Mbuotidem, J., Kovács, T., Tóvári, J., Bergmann, R., Strelci, C., Szakács, G., Mihály, J., Varga, Z., and Szoboszlai, N., 2020, Development and in vivo application of a water-soluble anticancer copper ionophore system using a temperature-sensitive liposome formulation, *Pharmaceutics*, 12 (5), 466.
- [10] Emir, G., Dilgin, Y., and Apak, R., 2020, A new redox mediator (cupric-neocuproine complex)-modified pencil graphite electrode for the electrocatalytic oxidation of H₂O₂: A flow injection amperometric sensor, *ChemElectroChem*, 7 (3), 649–658.
- [11] Koga, T., Sakata, Y., and Terasaki, N., 2019, Accumulation and analysis of cuprous ions in a copper sulfate plating, *J. Visualized Exp.*, 145, e59376.
- [12] Skrovankova, S., Mlcek, J., Sochor, J., Baron, M., Kynicky, J., and Jurikova, T., 2015, Determination of ascorbic acid by electrochemical techniques and other methods, *Int. J. Electrochem. Sci.*, 10, 2421–2431.
- [13] Morosanova, M.A., and Morosanova, E.I., 2017, Silica-titania xerogel doped with Mo,P-heteropoly compounds for solid phase spectrophotometric determination of ascorbic acid in fruit juices, pharmaceuticals, and synthetic urine, *Chem. Cent. J.*, 11 (1), 3.
- [14] Losev, V.N., Didukh, S.L., Trofimchuk, A.K., and Zaporozhets, O.A., 2014, Adsorption–photometric and test determination of copper using silica gel sequentially modified with polyhexamethylene guanidine and bathocuproinedisulphonic acid, *Adsorpt. Sci. Technol.*, 32 (6), 443–452.
- [15] Ayaz, S., Dilgin, Y., and Apak, R., 2020, Flow injection amperometric determination of hydrazine at a cupric-Neocuproine complex/anionic surfactant modified disposable electrode, *Microchem. J.*, 159, 105457.
- [16] Ribeiro, J.P.N., Magalhães, L.M., Reis, S., Lima, J.L.F.C., and Segundo, M.A., 2011, High-throughput total cupric ion reducing antioxidant

- capacity of biological samples determined using flow injection analysis and microplate-based methods, *Anal. Sci.*, 27 (5), 483–488.
- [17] Brasil, M.A.S., and Reis, B.F., 2017, An automated multicommuted flow analysis procedure for photometric determination of reducing sugars in wine employing a directly heated flow-batch device, *J. Braz. Chem. Soc.*, 28 (10), 2013–2020.
- [18] Kukoc-Modun, L., Tsikas, D., Biocic, M., and Radić, N., 2015, Flow injection analysis of *N*-acetyl-L-cysteine based on the reduction of copper(II)-neocuproine reagent, *Anal. Lett.*, 49 (5), 607–617.
- [19] Chandramouleeswaran, S., and Ramkumar, J., 2018, Insight of spectrophotometric determination using 4-(2-pyridylazo) resorcinol: Application of stop flow injection analysis, *Chem. Sin.*, 9 (2), 605–608.
- [20] Kraljević, T., Jelić-Knezović, N., Marković Boras, M., and Ćurlin, M., 2020, Spectrophotometric hybrid flow system for determination of *N*-acetyl-L-cysteine in pharmaceuticals, *IOSR J. Appl. Chem.*, 13 (5), 27–34.
- [21] Omarova, S., Demir, S., and Andac, M., 2018, Development of a new spectrophotometric based flow injection analysis method for the determination of copper (II), *J. Taibah Univ. Sci.*, 12 (6), 820–825.
- [22] Segundo, M.A., Tóth, I.V., Magalhães, L.M., and Reis, S., 2015, “Automatic flow injection analysis (FIA) determination of total reducing capacity in serum and urine samples” in *Advanced Protocols in Oxidative Stress III*, Armstrong, D., Eds., Humana Press, New York, 277–284.
- [23] Marques, S.S., Magalhães, L.M., Tóth, I.V., and Segundo, M.A., 2014, Insights on antioxidant assays for biological samples based on the reduction of copper complexes—the importance of analytical conditions, *Int. J. Mol. Sci.*, 15 (7), 11387–11402.
- [24] da Silva, P.A.B., de Souza, G.C.S., Paim, A.P.S., and Lavorante, A.F., 2018, Spectrophotometric determination of reducing sugar in wines employing in-line dialysis and a multicommuted flow analysis approach, *J. Chil. Chem. Soc.*, 63 (2), 3994–4000.
- [25] Viganor, L., Howe, O., McCarron, P., McCann, M., and Devereux, M., 2017, The antibacterial activity of metal complexes containing 1,10-phenanthroline: Potential as alternative therapeutics in the era of antibiotic resistance, *Curr. Top. Med. Chem.*, 17 (11), 1280–1302.
- [26] da Silva, J.C., Suarez, W.T., and de Oliveira Krambeck, F.M., 2018, Flow-injection spectrophotometric determination of methimazole in pharmaceuticals using a charge-transfer complex Cu(I)-neocuproine, *J. Anal. Chem.*, 73 (3), 243–248.
- [27] Taha, D.N., and Obaid, Z.S., 2016, Designing flow injection unit for chromates determining, *Res. J. Pharm., Biol. Chem. Sci.*, 7 (6), 2242–2251.
- [28] Babayeva, K., Demir, S., and Andac, M., 2017, A novel spectrophotometric method for the determination of copper ion by using a salophen ligand, *N,N*-disalicylidene-2,3-diaminopyridine, *J. Taibah Univ. Sci.*, 11 (5), 808–814.
- [29] Çağlar, Y., and Saka, E.T., 2017, Ionic liquid based dispersive liquid-liquid microextraction procedure for the spectrophotometric determination of copper using 3-dimethylamino rhodanine as a chelating agent in natural waters, *Karbala Int. J. Mod. Sci.*, 3 (4), 185–190.
- [30] Kulkarni, A.A., and Vaidya, I.S., 2015, Flow injection analysis: An overview, *J. Crit. Rev.*, 2 (4), 19–24.
- [31] Yaseen, S.M., Qassim, B.B., and Al-Lami, N.O., 2020, Spectrophotometric determination of Co(II) in vitamin B12 using 2-(biphenyl-4-yl)-3-((2-(2,4-dinitrophenyl) hydrazono)methyl) imidazo [1,2-a]pyridine as ligand by flow injection–merging zone analysis, *Al-Nahrain J. Sci.*, 23 (3), 24–38.
- [32] Farhood, A.S., Majeed, A.S., Ali, L.A.M., and Taha, D.N., 2017, Semi-automated flow injection method for the determination of iron (II) by 1,10-phenanthroline, *Orient. J. Chem.*, 33 (6), 3112–3120.
- [33] Farhood, A.S., Ali, L.A.M., and Ali, F.F., 2017, Determination of aniline blue dye by flow injection analysis with home made valve, *Orient. J. Chem.*, 33 (2), 944–950.
- [34] Majeed, A.S., Farhood, A.S., Ali, L.A.M., and Taha, D.N., 2017, Home-made micro valve for determining malachite green dye by flow injection analysis, *Indones. J. Chem.*, 17 (2), 248–255.

- [35] Cassella, R.J., Magalhães, O.I., Couto, M.T., Lima, E.L.S., Neves, M.A.F.S., and Coutinho, F.M.B., 2005, Synthesis and application of a functionalized resin for flow injection/F AAS copper determination in waters, *Talanta*, 67 (1), 121–128.
- [36] Mashhadizadeh, M.H., Pesteh, M., Talakesh, M., Sheikhshoae, I., Ardakani, M.M., and Karimi, M.A., 2008, Solid-phase extraction of copper (II) by sorption on octadecyl silica membrane disk modified with a new Schiff base and determination with atomic absorption spectrometry, *Spectrochim. Acta, Part B*, 63 (8), 885–888.
- [37] Şahin, Ç.A., and Tokgöz, İ., 2010, A novel solidified floating organic drop microextraction method for preconcentration and determination of copper ions by flow injection flame atomic absorption spectrometry, *Anal. Chim. Acta*, 667 (1-2), 83–87.
- [38] Mohadesi, A., and Taher, M.A., 2007, Voltammetric determination of Cu(II) in natural waters and human hair at a meso-2,3-dimercaptosuccinic acid self-assembled gold electrode, *Talanta*, 72 (1), 95–100.
- [39] Wainwright, P., Wadey, D., and Cook, P., 2018, An inductively coupled plasma mass spectrometry method for relative free copper determination and generation of a paediatric reference interval, *Ann. Clin. Biochem.*, 55 (4), 485–490.

Ion Impregnation Effect of Fe, Cu, Cr-attributed Mordenite on Stearic Acid Cracking

Abdulloh Abdulloh, Ulfa Rahmah, Satya Candra Wibawa Sakti, Alfa Akustia Widati, Ahmadi Jaya Permana, Rochadi Prasetya, Musbahu Adam Ahmad, and Mochamad Zakki Fahmi*

Department of Chemistry, Faculty of Science and Technology, Airlangga University, Surabaya 60115, Indonesia

* Corresponding author:

email: m.zakki.fahmi@fst.unair.ac.id

Received: December 10, 2021

Accepted: March 28, 2022

DOI: 10.22146/ijc.71126

Abstract: The improvement in the design of mordenite-based catalysts focuses on the present study to fulfill the massive demand for bio-aviation fuel (BAF) as renewable energy. Modification of the mordenite through ionic impregnation of Fe, Cu, and Cr, has supported the mordenite to perform with better efficiency and activity in catalyzing the cracking process of stearic acid. The adjustment on catalytic activity was carried out by simply reacting the catalyst with stearic acid at 190 °C and investigating cracking products with Gas Chromatography-Mass Spectroscopy. The results of the GC-MS test of the cracking product showed the formation of alkane-alkene and aromatic compounds. BAF was selectively obtained (30.27%) when the reaction was catalyzed by FeCuCr/mordenite catalyst. The BAF derived from FeCuCr/mordenite contained hydrocarbons that include xylene, mesitylene, dodecane, tridecane, tetradecane, and pentadecane. However, reduced selectivity was realized (19.85%) when the reaction was catalyzed by nano FeCuCr/mordenite. Its hydrocarbon constituents include benzene, tetradecane, and pentadecane compounds.

Keywords: mordenite; stearic acid; metal impregnation; cracking

■ INTRODUCTION

The massive development of transportation technology increases the need for fuel that mostly comes from unrenowned oil sources. This condition emerges the need for an alternative source to reduce such problems by using renewable materials, such as BAF and biodiesel. Blakey et al. explained that aviation fuel is a hydrocarbon with a range of carbon chains C₈-C₁₆ [1]. The hydrocarbon component in aviation fuel consists of paraffin (alkane), naphthalene (alkenes), cycloparaffine (cycloalkanes), and/or aromatic hydrocarbon. Sabarman et al. produced aviation fuel compounds from palm fatty acid distillate (PFAD) through hydrotreating and hydrocracking. All these methods were catalyzed by NiMo/ γ -Al₂O₃ catalyst at a temperature of 400 °C. In this study, the production of hydrocarbons with high C₁₅ carbon chains was reported. The production was influenced significantly by 3% (wt.%) catalyst loading [2]. Also, other catalysts based on Ni-Mo/SiO₂ and NiMo/zeolite were also reported to increase BAF production and activity [3-4]. In the case of zeolite

application, Carli et al. reported the synthesis of aviation fuel from oleic acid through hydrodeoxygenation reaction of NiMo/zeolite at temperature and pressure conditions were 375 °C and 15 bar, respectively. The catalyst results in the production the aviation fuel, whose yield was up to 36.32% for a 2.5 h reaction time [4]. The above reports indicated that the compounds of aviation fuel could be produced from fatty acid-based compounds, and zeolite can contribute to the reaction as a supported catalyst.

Well-known as an excellent and suitable material as a catalyst, zeolite showed excellent properties, such as stability at high temperatures, good activity, microporous, and high acid sites. The industries, as well as other researchers, preferred using heterogeneous catalysts because they are less prone to multi-step neutralization and also due to their economic advantages [5-6]. The first aspect is the crystallinity of the zeolite, which can affect the catalytic activity [7]. Besides the crystallinity, the acid sites and zeolite pore also determine its performance. The last two factors are

quite crucial in setting a good catalyst and allowing researchers to do modifications by increasing the acid site or restructuring the zeolite to get high porosity on it. To get the acid site strengthened, the catalyst could be modified by adding a metal element that would possibly enhance the activity of the catalyst [5]. The cationic metals can serve as Lewis acid sites. This site will capture H atoms from hydrogen gas which will be transferred to hydrocarbon compounds that have been cracked by Bronsted acid sites on the catalyst [8]. Therefore, this study proposes the application of modified mordenite to produce Aviation fuel from stearic acid. Stearic acid is a common compound found in vegetable oils. It can be found in palm oil coarse (CPO) by 5% [9], 35% in brown [10], 4.9–8.6% in kapok seed oil [11], and 12.66% in the seeds of the rubber [12]. In animal sources, stearic acid can also be found in beef fat as much as 20–25%, pork fat at 12–16% [13], and chicken fat at 17.55% [14].

The importance of metals in modifying new properties of mordenite is interesting to be explored. Some studies proposed the addition of metal by chemical interaction with mordenite support to make the struggle mode of the catalyst. One of the chemical interactions is impregnation. The impregnation method is the most advantageous as it maximizes the use of the active component with the lowest dosage [15]. The impregnation of Ni to HZSM-5/SBA resulted in a bimodal structure and demonstrated efficient performance capable of producing 40% aromatics and 80% cyclic hydrocarbons conversion products, which are important components of jet fuel [16]. Impregnation of trimethyl phosphate on HZSM-5 nano zeolite was able to increase hydrothermal stability so that there was an increase in catalytic performance in the conversion of olefin into gasoline [17]. Impregnation of CuCo catalyst with carbon nanotubes (CNT) was successfully synthesized and could convert stearic acid into biodiesel with a selectivity of 94.82% [18]. Impregnation of Ni into the HZSM-5 catalyst was made by immersing HZSM-5 in a solution of nickel nitrate ($\text{Ni}(\text{NO}_3)_2$), which resulted in the enhanced catalytic performance of the catalysts in trimerization of *n*-butane [19]. Catalytic conversion of methanol to valuable products like *p*-Xylene impregnated with zinc

[20–21]. Impregnation can reduce BAS (Brønsted acid sites) and increase LAS (Lewis acid sites) in the pores of the zeolite [21]. This property, coupled with appropriate reaction conditions, resulted in an increase in selective conversion to *p*-Xylene [21]. The purpose of this method is to fill the pores of the support layer with a precursor solution containing a sufficient concentration of metal salts to achieve the desired loading [22]. Even though several studies also report the application of impregnation (physical binding) on introducing metal on the zeolite and it successfully obtains aviation fuel components from oleic acid compound [4]. However, the inclusion of metal on zeolite through impregnation to convert the fatty acid into aviation fuel has not been well explored previously. The present study will try to overcome the above gap by modifying raw mordenite (as zeolite class abundantly found in nature) from commercial cat sand with simple metal impregnation. Trimetallic catalysts made from transition metals are common [23]. Some metals such as iron (Fe), copper (Cu), and chromium (Cr) were also introduced to mordenite to support the cracking process of stearic acid in obtaining aviation fuel components. Besides the characterization of the catalyst, further observation is focused on evaluating selectivity towards obtaining aviation fuel compounds. The selectivity of producing alkane and the conversion percentage of stearic acid were also studied. Overall, the study investigated the effect of metal impregnation and catalyst size reduction on catalytic performance.

■ EXPERIMENTAL SECTION

Materials

The materials used in the present study consist of commercial cat sand purchased from a local market in Surabaya, Indonesia. Other chemicals such as Hydrofluoric Acid (HF, 40%), Hydrochloric Acid (HCl, 37%), Ammonium Chloride (NH_4Cl , 99%), Silver Nitrate (AgNO_3), Stearic Acid, Iron(III) Chloride Hexahydrate ($\text{FeCl}_3 \cdot 6\text{H}_2\text{O}$, 97%), Chromium(III) Chloride (CrCl_3 , 99%), and Copper(II) Chloride Dihydrate ($\text{CuCl}_2 \cdot 2\text{H}_2\text{O}$, 99%) were all purchased from Sigma Aldrich (St. Louise, USA). Ethanol and *n*-hexane as solvents were purchased

from Bratachem Ltd (Surabaya, Indonesia). All chemicals are used without particular purification.

Procedure

Preparation of catalyst

The catalyst preparation was done by following a number of stages. Firstly, the cat sand was soaked in a solution of HF 1% for 30 min to remove the non-framework silica (quartz-free) and washed with distilled water to reach neutral pH. Furthermore, the quartz-free mordenite was immersed in 6 M of HCl for 30 min at a temperature of 50 °C, followed by washing with distilled water. The obtained material was then submerged in NH₄Cl 1 N with a set temperature of 90 °C and stirred the mixture roughly for 3 h, followed by curing the mixture over seven days. The solid was then filtered and washed with distilled water to get Cl-free, then the sample was dried in an oven at a temperature of 110 °C for 3 h. Then, the obtained sample was sieved to a size of 140 mesh, and the solid obtained was called H-mordenite.

Secondly, impregnation of metal ions was done. Experimentally, the above-resulted sample was mixed with a 10% aqueous solution of CrCl₃ and refluxed at 50 °C for 30 min. The pH was set between a range of 10–12 following the addition of hydrazine (6 mL). This sample was then washed with flowing distilled water to get a Cl-free sample and dried at 110 °C for 24 h. It continued by calcining at 500 °C for 5 h with nitrogen flow. The obtained product was marked as Cr/mordenite. This protocol was repeated by changing the Cr source with Fe and Cu to produce the other ion-modified mordenite. Thirdly, the size of the catalyst was reduced. Experimentally, the impregnated mordenite (25 g) was added to agate jars and treated on a ball-milling machine BKBM-V2S (Biobase, China) at 300 rpm for 5 h. The mordenite with reduced size was subsequently used to catalyze the cracking of the stearic acid.

The activity of the catalyst

The cracking reaction of stearic acid is mediated on a fractional distillation set, including a fractionation column, condenser, and thermocouple. The FeCuCr/mordenite and stearic acid (1:50) are inserted into the reaction flask and heated at 190 °C to initiate a

cracking reaction (under a vacuum condition). After a reaction proceeded, at adjusted times, about 0.1 mL of the product was collected and dissolved in 10 mL of *n* hexane-ethanol mixture (1:1). At the end of the cracking process, the catalyst was collected and separated from the liquid phase by centrifugation. The conversion of stearic acid and selectivity to BAF were calculated based on the following equations:

$$\text{Stearic acid conversion (\%)} = 100\% - \% \text{ stearic acid area}$$

$$\text{BAF Selectivity (\%)} = \frac{\text{bioavtur area}}{\text{stearic acid converted}} \times 100\%$$

Characterizations

Several instruments were used to characterize the catalyst, including X-ray Diffraction (XRD) Phillips Analytical JOEL JDX-3530, X-ray Fluorescence (XRF) PANalytical Epsilon 4, Scanning Electron Microscopy (SEM) Zeiss Evo 40 Series, and Fourier Transform Infrared (FTIR) Shimadzu 84005. Characterization for the resulting BAF was confirmed by Gas Chromatography-Mass Spectrometry (GC-MS) Agilent GCMS 5977B.

X-ray diffraction analysis was carried out using a solid powder sample placed on a glass plate and analyzed with Cu K α radiation ($\lambda = 1.5405 \text{ \AA}$) at 2θ between 10°–80°. The results obtained are in the form of diffractogram peaks, and from these peaks, a material can be identified as having a crystal structure or not.

Determination of the type and number of acid sites in the catalyst using the pyridine-FTIR method. The working process is that the sample is heated at 400 °C for 2 h and cooled and then put into a glass tube which has a place to drain N₂ gas and drip pyridine. Then it was put into a tubular furnace and heated at 150 °C for 30 min while N₂ gas was flowing. Then pyridine was added from the tube through the faucet, and N₂ gas was still flowing. After the pyridine liquid dries, the N₂ gas flow is closed, and the end of the tube is clamped. The sample was cooled at room temperature. Then the sample was tested for acid sites using FTIR at a wavenumber of 1540–1545 cm⁻¹, indicating the presence of a Brønsted acid site, and at a wavenumber of 1440–1452 cm⁻¹, indicating the presence of a Lewis acid site. The number of the acid side of Brønsted and Lewis can be calculated based on the following equation [25]:

$$C_L = \frac{\pi}{\text{IMEGC}_L} \times \frac{r^2}{w} \times A_{1450} \quad (1)$$

$$C_B = \frac{\pi}{\text{IMEC}_B} \times \frac{r^2}{w} \times A_{1540} \quad (2)$$

where C_L and C_B are the concentration of Lewis (L) and Brønsted (B) acid sites in mmol g^{-1} ; A_{1450} and A_{1540} are integrated areas of bands at 1450 and 1540 cm^{-1} ; IMEC_L and IMEC_B are molar extinction coefficients of 2.22 and 1.67 $\text{cm } \mu\text{mol}^{-1}$, respectively. The r value refers to pellet radius in cm, and w is the pellet weight in mg.

In the morphological assessment by SEM method, the sample is inserted into a brass stub sample holder using a double stick carbon tape, then sputtered with Au for 15 min, with a pressure of 6×10^2 mBar. Next, the sample holder is placed on the instrument, and an analysis is carried out.

Observation of the composition of the catalyst was measured using the direct exposure of powder solids to X-ray Fluorescence (XRF). The analysis was carried out with the sample that had been finely inserted into the sample tube and pressed until the surface was flat. Then placed in the instrument and analyzed.

RESULTS AND DISCUSSION

FeCuCr/Mordenite

The catalysts that were successfully synthesized were then characterized using X-ray Diffraction (XRD), X-ray Fluorescence (XRF), Scanning Electron Microscopy (SEM), and Fourier Transform Infrared (FTIR). The characterization of the resulting BAF was confirmed by Gas Chromatography-Mass Spectrometry (GC-MS).

The XRD was firstly carried out to observe the crystal structure of the obtained zeolite. From Fig. 1, it can be seen that there is a similarity in the peak of bare mordenite with other modified mordenites even though there are some additional peaks. The diffractogram changes could be observed by the appearance of new peaks and the change of d-spacing. The XRD diffractogram of the bare mordenite was confirmed by X'Pert HighScore (JCPDS #01-073-1490), where it showed particular peaks with 2θ at 20.79, 22.19, 25.52, 26.56, 27.72, and 35.58°; whereas H-mordenite showed peaks at 2θ of 20.78, 22.20, 25.60, 26.53, 27.66, and 36.45°. The results clarify the

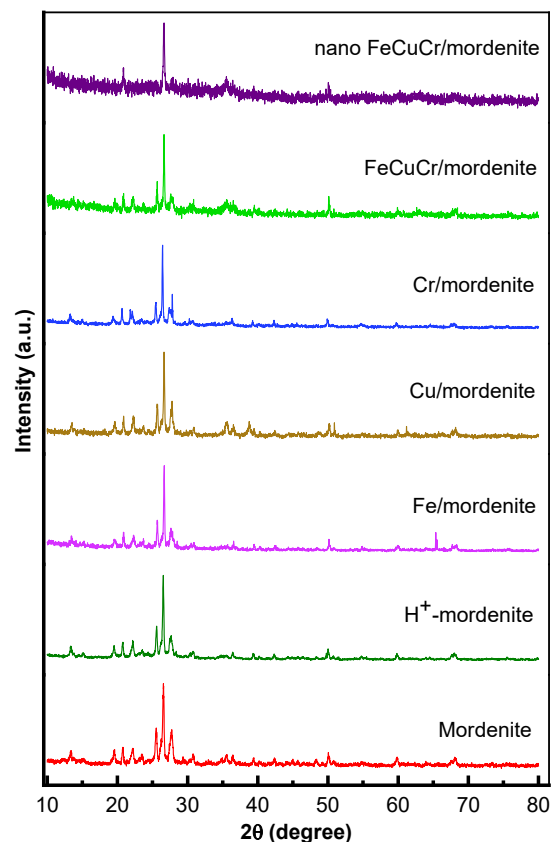


Fig 1. XRD patterns of mordenite, H-mordenite, Fe/mordenite, Cu/mordenite, Cr/mordenite, and FeCuCr/mordenite

the diffractogram of H-mordenite has not undergone significant changes compared with bare mordenite because the peaks on the bare mordenite re-emerged on the H-mordenite pattern. The d-spacing comparison of both samples also does not make a difference much. However, the quartz composition decreased from 10.6% (in mordenite) to 8.5% (in H-mordenite). This indicates that after HF and HCl treatment, silica-free mordenite was obtained.

Further impregnation of metals into the mordenite with varied metal combinations affected the diffractogram, however, each sample still maintains the crystalline structure by performing sharp peak patterns. In particular, the diffractogram pattern of Fe/mordenite has peaks at 2θ values of 20.87, 22.31, 25.68, 26.65, 27.64, and 36.55°. The peaks have relative intensities of 17.93, 14.25, 30.78, 100, 22.54, and 7.64%, which shows there is mordenite in the sample. The diffractogram of the

Cu/mordenite has a peak at 2θ values of 20.86, 22.29, 25.68, 26.64, 27.78, and 36.50°, and each has a relative intensity of 19.15, 18.95, 35.11, 100, 33.81, and 8.69%. The diffractogram of the Cr/mordenite in the 2θ region of 25°–28° has a relatively less intense peak compared to the H-mordenite. It smoothly indicates the crystallinity of Cr/mordenite was decreased. The results of three metal combination mordenite showed its similarity with bare mordenite, which indicated the existing mordenite phase in the samples. The d-spacing comparison on the Cr/mordenite on the peak area of 9.49, 19.37, and 22.10° shifts the peak to the right. This shifting indicated that metal ion impregnation into the mordenite was successful. The diffractogram of FeCuCr/mordenite owing 2θ peaks at 20.86, 26.63, and 35.54° with relative intensities of 15.38, 100, and 9.44%, respectively, which indicated the existence of individual mordenite in the sample. The diffractogram of nano FeCuCr/mordenite showed a peak at 2θ values of 20.86, 26.62, and 35.48° with relative intensities of 23.12, 100, and 10.92%, thus, also indicating the existence of mordenite in the sample. The increased intensity indicates that the nano-sized FeCuCr/mordenite was more crystalline when compared to FeCuCr/mordenite. The XRD showed the impregnation of 3 metals into mordenite, which resulted in the loss of some peaks at around $2\theta = 13.45^\circ$. The peak around $2\theta = 26.62^\circ$ did not reappear in the nano FeCuCr/mordenite. The peak intensity of grinded-

FeCuCr/mordenite was lower than FeCuCr/mordenite, while increased noise peaks were observed on the diffractogram of nano FeCuCr/mordenite. This observation showed the influence of the grinding process on FeCuCr/mordenite. The lower peak intensity could be attributed to the reduced size crystallites of mordenite due to the grinding process.

The X-ray Fluorescence technique was used to observe the elemental composition before and after the impregnation of metal in mordenite. Table 1 shows Fe element is not detected on both bare mordenite and H-mordenite due to the small amount of this element. Furthermore, the Fe signal increases drastically when the impregnation of H⁺-mordenite by Fe metal with a percentage up to 33.71%; and revealed the catalyst impregnation of Fe/mordenite was successfully prepared with the presented protocol. Similarly, the composition of the Cu and Cr that were initially absent on bare mordenite comes to a high percentage (up to 50.18 and 51.9%, respectively) after its impregnations. The impregnation of 10% metals in a ratio of (1:1:1) produces XRF data that corresponds to the percent composition of Fe:Cu:Cr (28.0%:22.8%:23.8%). In addition, there are also the elements that declined in the composition, namely K, Ca, and Ti, but are not completely gone after the impregnation. This result can be assumed that the metal was replaced by impregnating metals through substitution isomorphic. Thus, the data

Table 1. Elemental composition of mordenite, H-mordenite, Fe/mordenite, Cu/mordenite, Cr/mordenite, FeCuCr/mordenite, nano FeCuCr/mordenite

Composition (%)	Sample						
	Mordenite	H-mordenite	Fe/mordenite	Cu/mordenite	Cr/mordenite	FeCuCr/mordenite	Nano FeCuCr/mordenite
Al	8.80	6.60	6.98	0.30	4.03	2.50	-
Si	58.00	70.60	52.21	43.60	32.40	18.4	18.30
K	4.96	5.49	3.36	2.26	1.82	1.10	1.00
Ca	16.10	4.78	1.94	1.66	1.18	0.63	1.00
Ti	1.60	1.40	0.95	0.63	0.56	0.32	0.28
Fe	-	-	33.71	-	-	28.00	27.6
Cu	-	-	-	50.27	-	22.80	30.0
Cr	1.00	-	0.52	0.71	51.90	23.80	21.0
Mn	5.90	5.20	0.27	0.35	7.10	0.480	0.27

reveals a successful impregnation process of the metal on the zeolite. The Si/Al ratio in FeCuCr/mordenite was 7.36 and then increased in size, reducing FeCuCr/mordenite by 17.89. The Si/Al ratio is the ratio of the amount of silica to aluminum contained in the sample. The increase in the Si/Al ratio affects the reactivity and stability of the zeolite. A large number of Si/Al ratios can affect the acidity of mordenite, where the greater the ratio value, the higher the acidity.

Fig. 2 shows the FTIR spectra of the Fe/mordenite, Cu/mordenite, Cr/mordenite, FeCuCr/mordenite and nano FeCuCr/mordenite. The peaks at 787–799 cm^{-1} referred to the presence of vibrational bending of the T–O–H for the metal binding, whereas the vibrational stretching of Al–OH is on wavenumber 3590–3642 cm^{-1} . The peaks at 1057–1122 cm^{-1} showed the vibrational stretching of Si–O–Si, and the peaks at 1224–1231 cm^{-1} showed the vibrational stretching of Si–O–Al [24]. The peaks at 1622–1636 cm^{-1} indicate the presence of vibration of OH molecules of water, and peak vibration bending Si–O–Si or Si–O–Al appears in the wavenumber 460–480 cm^{-1} [25]. This data supports the above XRD and XRF data which claimed a successful metal impregnation on the zeolite.

Pyridine-FTIR method for determining the type and amount of acid sites in the obtained catalyst was carried out. In this protocol, the acid sites on the sample are banded at 1540–1545 cm^{-1} for Brønsted acid and 1440–1452 cm^{-1} for Lewis acid [26]. From the data, FeCuCr/mordenite catalyst emerges Brønsted acid site observed at wavenumbers 1546 cm^{-1} and Lewis acid site on the 1441 cm^{-1} . Moreover, nano FeCuCr/mordenite also presented Brønsted acid around 1547 and 1442 cm^{-1} for the Lewis acid (Fig. 3). After the calculation, the number of the Brønsted site on FeCuCr/mordenite and nano FeCuCr/mordenite were 964.36 and 1356.87 $\mu\text{mol g}^{-1}$, respectively. Then, the number of Lewis acid sites of FeCuCr/mordenite and size-reduced FeCuCr/mordenite were 213.65 and 249.33 $\mu\text{mol g}^{-1}$, respectively. The number of acid sites of nano FeCuCr/mordenite was found to be greater than that of FeCuCr/mordenite. These results revealed that decreasing the size of the catalyst will increase the number of acid sites. This leads to a resulted

increase in active surfaces on the catalyst, thus resulting in better catalytic ability. In addition, the number of Brønsted and Lewis acids was also affected by the ratio of Si/Al as informed by previous XRF data, thus, increasing of Si/Al ratio will promote the acidity of the Brønsted-Lewis.

SEM analysis of the modified catalyst is shown in Fig. 4. The morphology of bare mordenite (Fig. 4(a)) shows irregular granules as a common zeolite-based catalyst. Moreover, further size modification on size-reduced FeCuCr/mordenite results in more homogenous granules that tend to be smaller particles.

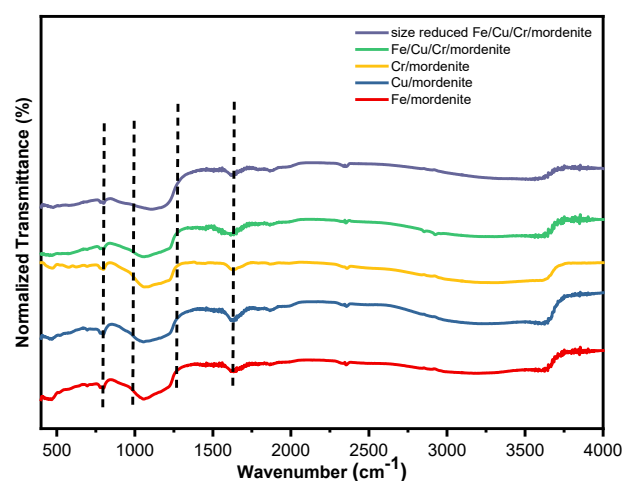


Fig 2. FTIR spectra of (a) Fe/mordenite, (b) Cu/mordenite, (c) Cr/mordenite, (d) FeCuCr/mordenite, and (e) Nano FeCuCr/mordenite

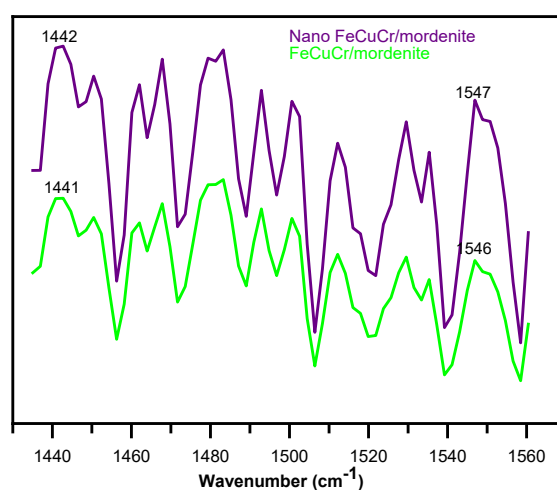


Fig 3. The acidity of FeCuCr/mordenite and Nano FeCuCr/mordenite

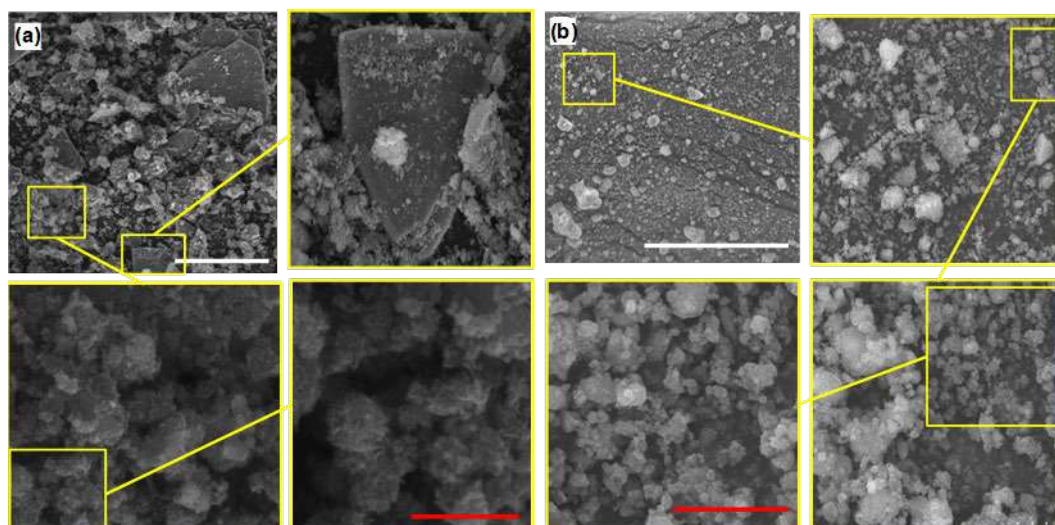


Fig 4. SEM images of (a) FeCuCr/mordenite and (b) size reduced FeCuCr/mordenite. The magnification of the adjusted area is indicated with yellow squares. White and red bars represent 100 μm and 2 μm , respectively

The result showed that the ball-milling process successfully decreased the diameter of the catalyst and increased acid sites, as previously discussed while describing pyridine-FTIR data.

Performance of the Catalyst

The chromatogram results of the sample after the cracking reaction for an initial 3 h showed the presence of

several formed compounds, namely alkanes, alkenes, alkynes, carboxylic acids, aromatic and other compounds (non-hydrocarbon) (Fig. 5). The formation of hydrocarbons (alkanes, alkenes, alkynes) through a decarboxylation reaction of stearic acid with the catalyst will produce heptadecane. A decarboxylation reaction that occurs mainly was affected by the Lewis acid site in

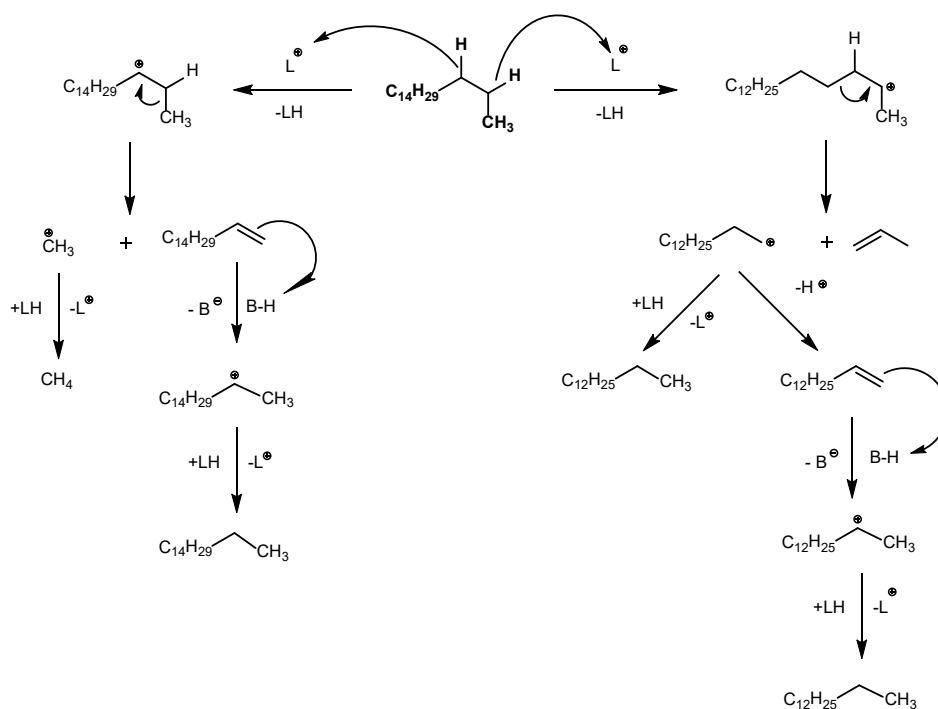


Fig 5. Mechanism of catalytic cracking reaction of heptadecane obtained from stearic acid decarboxylation reaction

the catalyst. It is thought that the oxygen attacks the Lewis acid sites on the carbonyl stearic acid, resulting in temporary binding. Subsequently, stearic acid rearranges ions, releasing the hydrogen ion. A carbon atom at the alpha (α) binding position of the hydrogen atoms obtains the heptadecane compound. This compound reacts with the acid sites again and lets the following cracking produce shorter hydrocarbon fragments (Fig. 5). Optimization of the catalytic process for producing aviation fuel components and alkane components through modification on single metal impregnation, combined metal impregnation, and size-reduced catalyst (Fig. 6–8). The cracking results of stearic acid with Fe/mordenite can be seen in Fig. 5. After the reaction for 0.5 h, 83.78% of stearic acid was converted, after 1 h up to 90.22% were converted, and after 2 to 3 h, stearic acid was completely converted to the product (Fig. 8). Method optimization for the selective production of aviation fuel by the Fe/Mordenite was done over a range of reaction times. After half an hour of the reaction time, 16.64% of the BAF was selectively produced. After 1 h, selectivity increased to 28.92%, while as high as 55.98% selective production was realized after 2 h. However, beyond 2 h of reaction time, a decrease in selectivity was observed. Therefore, it could be considered that the optimum time for the production of BAF by Fe/Mordenite catalyst is when the reaction is allowed to take place for 2 h. The components of the BAF were characterized and found to be hexadecane, pentadecane, tetradecane, tridecane, dodecane, undecane, decane, nonane, cyclohexadecane, cyclopentadecane, decylbenzene, nonylbenzene, and ethylbenzene. The Cu/mordenite catalyzed cracking of stearic acid to yield aviation fuel having the yield of 7.01, 7.16, 17.19, 30.56, 40.17, and 42.72% for 0.5, 1, 1.5, 2, 2.5, and 3 h, respectively (Fig. 6), the hydrocarbons that were produced as avtur compound are dodecane, pentadecane, and hexadecane. The conversion of stearic acid with Cr/mordenite also increased from 0.5 to 3 h, and the product components of aviation fuel also became higher (Fig. 6). The resulting fractions from Cr/mordenite catalysis included a BAF whose components are tridecane, (E)-2-tetradecane, tetradecane, 1-pentadecene, pentadecane, cetene, hexadecane, and decylbenzene. In Fig. 6, it was

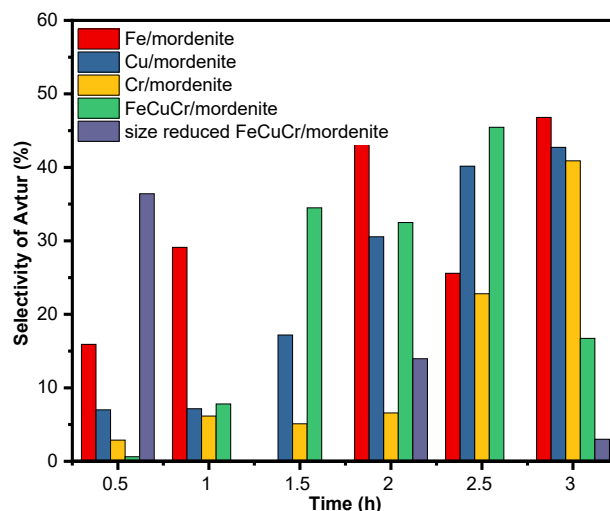


Fig 6. Comparison of the selectivity of the results of the aviation fuel from the reaction of cracking using the 5 variations of the catalyst

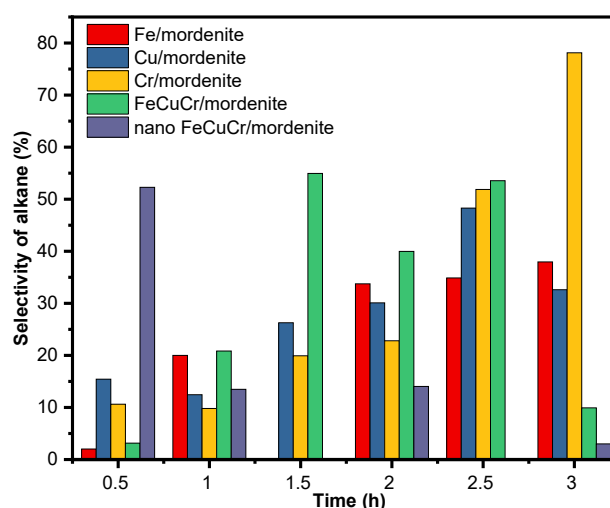


Fig 7. Comparison of the selectivity of alkanes from the reaction of cracking using the 5 variations of the catalyst

revealed that Cr/mordenite catalysts resulted in superior alkane conversion when compared to the remaining catalysts for reaction done for 3 h. All the data obtained suggest that the metals under study could influence the catalytic nature of mordenite in stearic acid conversions. Moreover, by using the metal combined catalyst, stearic acid's selectivity to produce aviation fuel was less effective at the initial reaction time but reached optimum after 2 h (up to 55.2%). Similarly, optimum alkane conversion was reached at 1.5 h (up to 54.9%). Although the conversion could not reach a desirable

optimum condition for Fe/mordenite catalyst (in terms of its selectivity towards alkane conversion) and Cr/mordenite catalyst (in terms of its selectivity towards aviation fuel conversion), however, it could be seen that FeCuCr/mordenite showed stable and selective performance (on both aviation fuel and alkane) as the reaction process reached 1.5 h. As could be seen from the above findings, the addition of metals to Mordenite could affect its selectivity. Also, the combination of the three metals affects the catalytic nature of the Mordenite. Therefore, it could be assumed that the catalytic process of mordenite could be enhanced by the addition of metal ions. Moreover, subsequent evaluation on using size-reduced FeCuCr/mordenite opens the possibility of a new way in catalytic processes. From Fig. 6 and 7, it can be observed that smaller particles of the FeCuCr/mordenite tend to have higher selectivity of aviation fuel and alkane on initial time reaction. This indicates that the nano FeCuCr/mordenite catalysts were active at the initial reaction time, however, became deactivated as the reaction took longer than 0.5 h. This statement is also supported by conversion data of all modified catalysts (Fig. 8). Components of BAF produced from FeCuCr/mordenite conversion include xylene, mesitylene, dodecane, tridecane, tetradecane, and pentadecane. Constituents of BAF produced by nano FeCuCr/mordenite catalyst include benzene, tetradecane, and pentadecane. While all of the catalysts increased the percentage of stearic acid conversion over time, the size reduced performed optimum conversion at the initial time (100% conversion at 0.5 h). Reducing the size of the catalyst caused an increase in the active sites. The increasing effectivity was common and be main reason application of nanotechnology in many fields, including the catalytic process [27-29]. As such, the cracking

process was more efficient, leading to a higher percentage of selective production of BAF.

In addition to determining the composition, fuel specifications and performance requirements are also needed (Table 2). The specifications required for aircraft fuel are (1) maximum permissible viscosity, (2) maximum pour point, (3) cloud point, (4) minimum allowable flashpoint, and (5) maximum amount of sulfur. The results showed that the kinetic viscosity of 0.46 cSt was smaller than the characteristic viscosity at 40 °C for aircraft fuel according to ASTM of 1.6–7 cSt. Pour point values, total sulfur, and ash (< -30 °C, 0.08%, 0.004%) have characteristics for aircraft fuel according to ASTM of a maximum of 15 °C, 1%, and 0.01%, respectively. The compound produced from this cracking reaction burns at room temperature. According to ASTM, the minimum flash point tolerance is 38 °C. The cloud point obtained is very low (< -30 °C). This is a necessary condition for fuel performance because the lower the temperature,

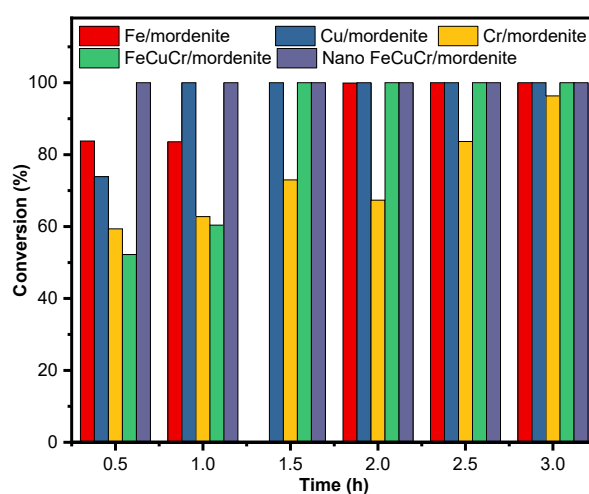


Fig 8. Comparison of the conversion of the reaction cracking with stearic acid using 5 variations of the catalyst

Table 2. Specifications for the obtained aviation-fuel

Type of test	Result	Unit	Test method
Kinematic viscosity (40 °C)	0.46	cSt	ASTM D 445-97
Pour point	< -30	°C	ASTM D 97-85
Cloud point	< -30	°C	ASTM D 2500
Flash point	burns at room temperature (around 25)	°C	ASTM D 93-00
Sulfur content	0.08	%	SNI 7431:2015
Ash content	0.004	%	ASTM D 482

the longer the liquid fuel solidifies, so it is not easy to clog the filter and fuel injectors in the engine.

■ CONCLUSION

The present study successfully reveals the impregnation of Fe, Cu, and Cr onto mordenite through several characterizations. The modified catalyst performs good stearic acid cracking, even with single metal and combined metal impregnation. The size modification on the catalyst helps very well in increasing acid sites upon the catalyst. The cracking reaction changes stearic acid into several compounds, including alkanes, alkenes, alcohols, ketones, cycloalkanes, and benzene containing aviation fuel components. It also shows that Fe/mordenite, Cu/mordenite, Cr/mordenite, and FeCuCr/mordenite have optimum catalytic activity mostly over a 1.5 h reaction. At the same time, the size reduced FeCuCr/mordenite showed good activity at the initial reaction. Selective production of BAF compound in the present study reached up to 30.27% by using FeCuCr/mordenite catalyst. The BAF constituents included xylene, mesitylene, dodecane, tridecane, tetradecane, and pentadecane. On the other hand, 19.85% selectivity was obtained when nano FeCuCr/mordenite catalyst was used to produce BAF, which contains benzene, tetradecane, and pentadecane.

■ ACKNOWLEDGMENTS

The authors thank the Ministry of Research, Technology, and Higher Education, Republic Indonesia, for financial support and Universitas Airlangga through PUF research funding under contract 1900/UN 3.1.8/LT/2018.

■ REFERENCES

- [1] Blakey, S., Rye, L., and Wilson, C.W., 2011, Aviation gas turbine alternative fuels: A review, *Proc. Combust. Inst.*, 33 (2), 2863–2885.
- [2] Sabarman, J.S., Legowo, E.H., Widiputri, D.I., and Siregar, A.R., 2019, Bioavtur synthesis from palm fatty acid distillate through hydrotreating and hydrocracking processes, *Indones. J. Energy*, 2 (2), 99–110.
- [3] Zanata, M., Amelia, S.T.W., Mumtazy, M.R., Kurniawansyah, F., and Roesyadi, A., 2019, Synthesis of bio jet fuel from crude palm oil by HEFA (Hydroprocessed Esters and Fatty Acids) using Ni-Mo catalyst supported by rice husk ash-based SiO₂, *Mater. Sci. Forum*, 964, 193–198.
- [4] Carli, M.F., Susanto, B.H., and Habibie, T.K., 2018, Synthesis of bioavtur through hydrodeoxygenation and catalytic cracking from oleic acid using NiMo/zeolite Catalyst, *E3S Web Conf.*, 67, 02023.
- [5] Abdulloh, A., Purkan, P., and Hardiansyah, N., 2017, Reparasi dan karakterisasi alfa-Fe₂O₃/zeolit Y untuk reaksi perengkahan asam palmitat, *Jurnal Kimia Riset*, 2 (2), 69–76.
- [6] Abdulloh, A., Widati A.A., and Tamamy F., 2016, Hidrolisis minyak jarak pagar menjadi asam lemah bebas menggunakan katalis CaO, *Jurnal Kimia Riset*, 1 (1), 1–6.
- [7] Saxena, S.K., and Viswanadham, N., 2017, Enhanced catalytic properties of mesoporous mordenite for benzylation of benzene with benzyl alcohol, *Appl. Surf. Sci.*, 392, 384–390.
- [8] Chai, M., Liu, R., and He, Y., 2020, Effects of SiO₂/Al₂O₃ ratio and Fe loading rate of Fe-modified ZSM-5 on selection of aromatics and kinetics of corn stalk catalytic pyrolysis, *Fuel Process. Technol.*, 206, 106458.
- [9] Bahadi, M.A., Japir, A.W., Salih, N., and Salimon, J., 2016, Free fatty acids separation from Malaysian high free fatty acid crude palm oil using molecular distillation, *Malays. J. Anal. Sci.*, 20 (5), 1042-1051.
- [10] Tuminah, S., 2010, Efek perbedaan sumber dan struktur kimia asam lemak jenuh terhadap kesehatan, *Bul. Penelit. Kesehat.*, 38 (1), 43–51.
- [11] Widiyanto, W., Suranto, S., Kusumanti, E., and Mulyono, M., 2016, The influence of protected kapok seed oil supplementation on in vitro ruminal fermentability and linoleic acid status with Etawah crossbred goat rumen fluid and elephant grass as feed, *Afr. J. Agric. Res.*, 11 (14), 1237–1244.
- [12] Chaikul, P., Lourith, N., and Kanlayavattanukul, M., 2017, Antimelanogenesis and cellular antioxidant

- activities of rubber (*Hevea brasiliensis*) seed oil for cosmetics, *Ind. Crops Prod.*, 108, 56–62.
- [13] Srinivasan, G.R., and Jambulingam, R., 2018, Comprehensive study on biodiesel produced from waste animal fats-A review, *J. Environ. Sci. Technol.*, 11 (3), 157–166.
- [14] Purandaradas, A., Silambarasan, T., Murugan, K., Babujanarthanam, R., Gandhi, A.D., Dhandapani, K.V., Anbumani, D., and Kavitha, P., 2018, Development and quantification of biodiesel production from chicken feather meal as a cost-effective feedstock by using green technology, *Biochem. Biophys. Rep.*, 14, 133–139.
- [15] Permata, M.L., and Trisunaryanti, W., 2020, The effect of nickel content impregnated on zeolite toward catalytic activity and selectivity for hydrotreating of cashew nut shell liquid oil, *Rasayan J. Chem.*, 13 (1), 772–779.
- [16] Weng, Y., Qiu, S., Ma, L., Liu, Q., Ding, M., Zhang, Q., Zhang, Q., and Wang, T., 2015, Jet-fuel range hydrocarbons from biomass-derived sorbitol over Ni-HZSM-5/SBA-15 catalyst, *Catalysts*, 5 (4), 2147–2160.
- [17] Zhao, Y., Liu, J., Xiong, G., and Guo, H., 2017, Enhancing hydrothermal stability of nanosized HZSM-5 zeolite by phosphorus modification for olefin catalytic cracking of full-range FCC gasoline, *Chin. J. Catal.*, 38 (1), 138–145.
- [18] Liang, J., Zhang, Z., Wu, K., Shi, Y., Pu, W., Yang, M., and Wu, Y., 2019, Improved conversion of stearic acid to diesel-like hydrocarbons by carbon nanotubes-supported CuCo catalysts, *Fuel Process. Technol.*, 188, 153–163.
- [19] Zhang, X., Zhong, J., Wang, J., Zhang, L., Gao, J., Liu, A., 2009, Catalytic performance and characterization of Ni-doped HZSM-5 catalysts for selective trimerization of *n*-butene, *Fuel Process. Technol.*, 90 (7-8), 863–870.
- [20] Li, J., Tong, Z., Xi, Y., Hu, Z., and Zhu, Z., 2016, Highly-efficient conversion of methanol to *p*-xylene over shape-selective Mg-Zn-Si-HZSM-5 catalyst with fine modification of pore-opening and acidic properties, *Catal. Sci. Technol.*, 6 (13), 4802–4813.
- [21] Zambare A.S., Ou, J., Wong, D.S.H., Yao, C.W., and Jang, S.S., 2019, Controlling the product selectivity in the conversion of methanol to the feedstock for phenol production, *RSC Adv.*, 9 (41), 23864–23875.
- [22] Fani, K., Lycourghiotis, S., Bourikas, K., and Kordouli, E., 2021, Biodiesel upgrading to renewable diesel over nickel supported on natural mordenite catalysts, *Ind. Eng. Chem. Res.*, 60 (51), 18695–18706.
- [23] Anderson, J.A., 2011, *Supported Metals in Catalysis*, 2nd Ed., Imperial College Press, London, UK.
- [24] Jia, Y., Wang, J., Zhang, K., Feng, W., Liu, S., Ding, C., and Liu, P., 2017, Nanocrystallite self-assembled hierarchical ZSM-5 zeolite microsphere for methanol to aromatics, *Microporous Mesoporous Mater.*, 247, 103–115.
- [25] Stuart, B., 2004, *Infrared Spectroscopy: Fundamentals and Applications*, John Wiley & Sons Inc., Chichester, UK.
- [26] Narayan, S., Vijaya, J.J., Sivasanker, S., Alam, M., Tamizhdurai, P., and Kennedy, L.J., 2015, Characterization and catalytic reactivity of mordenite – Investigation of selective oxidation of benzyl alcohol, *Polyhedron*, 89, 289–296.
- [27] Girma, W.M., Fahmi, M.Z., Permadi, A., Abate, M.A., and Chang, J.Y., 2017, Synthetic strategies and biomedical applications of I–III–VI ternary quantum dots, *J. Mater. Chem. B*, 5 (31), 6193–6216.
- [28] Aung, Y.Y., Wibrianto, A., Sianturi, J.S., Ulfa, D.K., Sakti, S.C., Irzaman, I., Yulianto, B., Chang, J.Y., Kwee, Y., and Fahmi, M.Z., 2021, Comparison direct synthesis of hyaluronic acid-based carbon nanodots as dual active targeting and imaging of HeLa cancer cells, *ACS Omega*, 6 (20), 13300–13309.
- [29] Fahmi, M.Z., and Chang, J.Y., 2014, A facile strategy to enable nanoparticles for simultaneous phase transfer, folate receptor targeting, and cisplatin delivery, *RSC Adv.*, 4 (100), 56713–56721.

Synthesis of Cassava Starch-Grafted Polyacrylamide Hydrogel by Microwave-Assisted Method for Polymer Flooding

Maudy Pratiwi Novia Matovanni, Sperisa Distantina*, and Mujtahid Kaavessina

Department of Chemical Engineering, Faculty of Engineering, Universitas Sebelas Maret,
Jl. Ir. Sutami 36A, Kentingan, Surakarta 57126, Indonesia

* Corresponding author:

email: sperisa_distantina@staff.uns.ac.id

Received: December 18, 2021

Accepted: April 5, 2022

DOI: 10.22146/ijc.71343

Abstract: Cassava starch-grafted polyacrylamide (CS-g-PAM) hydrogels were synthesized using a microwave-assisted method and $K_2O_8S_2$ (KPS) as an initiator. In this study, we studied the influence of the amount of acrylamide and irradiation time on the properties of CS-g-PAM. The characterization of CS-g-PAM obtained was shown by Fourier-transform infrared (FTIR) and Scanning Electron Microscope (SEM) analysis. To predict the behavior of the samples under reservoir conditions, the properties of CS-g-PAM, such as swelling ratio, water-solubility, and viscosity were determined as a function of temperature, salt concentration, and aging time. The FTIR spectra and SEM analysis of the CS-g-PAM confirmed that the polyacrylamide chains were successfully grafted onto the cassava starch backbone. The results showed that the increasing amount of acrylamide and the longer irradiation time improved the properties of CS-g-PAM. Preparation of CS-g-PAM with 10 g of acrylamide and 180 s of irradiation time resulted in the highest grafting percentage and water solubility, which was 1565.53 and 96.06%, respectively. Its viscosity also exceeded 97% after 15 days of aging. The results showed that CS-g-PAM expressed properties such as good thickening, temperature resistance, and salt resistance according to reservoir conditions. This finding indicated that CS-g-PAM has good potential for oil recovery applications.

Keywords: hydrogel; cassava starch; polyacrylamide; microwave-assisted; enhanced oil recovery

■ INTRODUCTION

Enhanced oil recovery (EOR) technology is urgently needed in the midst of a worsening energy crisis, such as declining oil production, high crude prices and ineffective primary production methods [1]. In the field of oil production, several methods are used to increase the recovery of the amount of oil and gas from the field. The most frequently injected fluid into oil wells is water, but water flooding still leaves around 60–70% of the oil contained in the reservoir [2]. Polymer flooding in the EOR system has evolved into a very efficient and cost-effective method. Polymer flooding is a process that has been used effectively in various oil fields across the world. Field investigations have indicated that polymer flooding can improve crude oil recovery by 5–30% from the original oil in place (OOIP) and by 3% following water

flooding. The efficiency of polymer flooding ranges from 0.7 to 1.75 lb of polymer per bbl of remaining oil output [3-4]. Even at extremely low concentrations, the polymer solution is injected with water to improve its viscosity and affect the mobility of the oil and reduce the permeability of the core [5]. Hydrogel is a polymer that can be used as polymer injection in EOR technology. However, hydrogel in high temperature and high salinity environments is usually affected by syneresis problems, which cause water to escape from the hydrogel phase [6]. Consequently, improving hydrogel stability is key to enhancing hydrogel performance for polymer flooding applications in difficult reservoir conditions.

The hydrogel can be made from natural or synthetic polymers or both. Graft copolymerization of natural polymers with functional synthetic polymers

results in modified products that combine the desired features of both the natural and the synthetic polymer in a single molecule [7]. The synthetic polymer commonly used for EOR applications is partially hydrolyzed polyacrylamide (HPAM). Synthetic polymers provide high flexibility in controlling the chemical structure of the polymer to increase the strength of the hydrogel and absorption capabilities [8]. However, the HPAM chain will collapse and disrupt the three-dimensional network structure of the polymer solution under high salinity and high temperature conditions [9]. Therefore, the viscosity of the HPAM solution will decrease drastically under difficult reservoir conditions (e.g., high temperature, high pressure, high salinity) leading to non-compliance with oilfield engineering application standards [10]. The use of synthetic polymers also has an adverse effect on the environment due to the toxicity and carcinogenicity of the residual monomers [11].

As a natural and renewable raw material with abundant supplies and no contamination, polysaccharides (xanthan, cellulose, and starch) can be used as raw materials for hydrogel synthesis and widely applied in polymer flooding procedures. Natural polymers have a greater resistance to salinity and temperature because of their unusual helical structure (triple or double), stiffness, and charge-free chains, which gives them excellent thickening and stability in adverse conditions reservoirs [11-12]. Natural polymers are cheap, readily available, biocompatible, biodegradable, and environmentally friendly [13]. Therefore, the synthesis of hydrogels from natural and synthetic materials can be an alternative to polymer synthesis that is environmentally friendly, inexpensive and has good resistance to reservoir conditions.

Several previous studies have reported hydrogel synthesis from a combination of natural and synthetic polymers for potential EOR. Previous studies have reported the synthesis of guar gum-based hydrogel by graft copolymerization using acrylamide and 2-acrylamido-2-methylpropane sulfonic acid (AMPS) and cross-linked using *N,N'*-methylene bisacrylamide (MBA) and potassium persulfate (KPS) as initiator. Guar gum-based hydrogel showed higher thermal stability than the

native guar gum [14]. Composite from rice straw waste, acrylamide (AM), vinyl methacrylate (VMA) was synthesized by free-radical emulsion polymerization using MBA as crosslinker and KPS as initiator. According to flooding experiments, the obtained composite has good resistance to thermal and ionic degradation [15]. Chitosan-modified polymer was synthesized by free radical polymerization with acrylic acid (AA) and acrylamide (AM). The solution properties of the polymer obtained showed better thickening ability and temperature and salt resistance than HPAM [16]. All syntheses mentioned above were done by polymerization using conventional thermal heating. Previous studies showed that natural and synthetic polymer modification successfully improved hydrogel stability.

According to several previous studies, grafting was performed by utilizing microwave energy, and the obtained hydrogel, CS-g-PAM hydrogel, may have the potential to be a candidate for EOR application. It has never been reported previously. The use of microwave increases the formation of copolymers, resulting in higher polymer products with a very short time required for polymer formation compared to conventional heating methods. To control the percentage of grafting, the microwave power and irradiation exposure time are controlled electronically [17].

In this study, we explore the influence of acrylamide amounts and irradiation time on the tolerance of reservoir properties of CS-g-PAM obtained as indicated by the swelling ratio of the hydrogel in water with various salt concentrations and temperatures, the viscosity of the polymer solution under reservoir conditions as a thickening agent, and the viscosity resistance of the polymer solution for 15 days. The successful grafting of polyacrylamide chains onto the backbone of cassava starch was characterized using Fourier-transform infrared (FTIR) and Scanning Electron Microscopy (SEM) analysis.

■ EXPERIMENTAL SECTION

Materials

Cassava starch was obtained from a local market in Surakarta, Indonesia. Acrylamide (> 99%) and $K_2O_8S_2$

(KPS) (> 99%) were purchased from E. Merck, Germany. Acetone (technical) was purchased from Saba Kimia, Surakarta, Indonesia. Sodium chloride (technical) was purchased from PT. Polimikro Berdikari Nusantara, Surakarta. All chemicals and reagents are used without additional treatment.

Instrumentation

FTIR analysis was conducted on a Frontier FTIR spectrophotometer (Shimadzu, IRSpirit). The surface morphology was determined by JEOL Benchtop Scanning Electron Microscopy JCM 7000. Viscosity measurement was carried out on the Brookfield Viscometer DV2T.

Procedure

Synthesis of cassava starch-grafted polyacrylamide

In this experiment, hydrogel polymer was synthesized by reacting cassava starch and acrylamide using KPS as the initiator and utilizing energy from domestic microwave radiation (Krisbow 20 L). CS-g-PAM was synthesized by varying the amount of acrylamide and the irradiation time, as shown in Table 1. One gram of cassava starch was added in 50 mL distilled water, then a certain amount of acrylamide and 0.3 g of KPS were added. The solution mixture of cassava starch, acrylamide, and KPS was put into a 1000 mL beaker and irradiated by microwave at 364 W. Microwave irradiation was carried out for 30 s until the solution approached the boiling temperature at < 70 °C, then the solution was cooled by immersing the beaker in cold water until the solution approached room temperature. Microwave irradiation – cooling cycle was repeated until a gel was formed and the irradiation time was determined (180 s or

6 cycles). There were 2 types of irradiation time. The first was stopped when the gel was formed and changed according to the amount of acrylamide. The second was the determined irradiation time (180 s), which was the same for all acrylamide amounts. The microwave irradiation – cooling cycle was carried out to minimize homopolymer formation reactions and to avoid vapors containing acrylamide monomers. After the microwave-assisted grafting process was completed, the gel material was allowed to stand for 24 h to complete the grafting reaction process. The gel material in the reaction vessel was soaked with excess acetone until a precipitate was formed. The CS-g-PAM precipitate was dried in an oven at 50 °C for 24 h. The percentage of grafting of CS-g-PAM obtained was calculated by the Eq. (1):

$$\% \text{grafting} = \frac{\text{mass of polyacrylamide grafted cassava starch} - \text{mass of cassava starch}}{\text{mass of cassava starch}} \times 100\% \quad (1)$$

The details of the synthesis of CS-g-PAM hydrogel are shown in Table 1.

Fourier transform infrared spectroscopy

FTIR spectra of cassava starch and CS-g-PAM (A–F) were analyzed on a Frontier FTIR spectrophotometer (Shimadzu, IRSpirit). CS-g-PAM obtained from various conditions was analyzed directly without forming pellets with KBr.

Scanning electron microscopy

The surface microstructure of cassava starch and CS-g-PAM (A–F) was determined by using JEOL Benchtop Scanning Electron Microscopy JCM 7000. The specimens were coated with gold and observed at 500–5000× magnification. The cassava starch had been gelatinized before SEM measurement.

Table 1. Various compositions for the synthesis of CS-g-PAM hydrogel

Code	Mass of cassava starch (g)	Mass of acrylamide (g)	Mass of KPS (g)	Irradiation time (s)	% Grafting
A	1	2	0.3	300	112.20
B	1	2	0.3	180	71.25
C	1	5	0.3	60	360.29
D	1	5	0.3	180	575.58
E	1	10	0.3	30	1237.32
F	1	10	0.3	180	1565.53

Swelling test

The dried CS-g-PAM was weighed and recorded as W_1 (g). The swelling test was determined by soaking W_1 in 100 mL of distilled water with various swelling times, NaCl concentrations, and temperatures according to reservoir conditions. The swollen CS-g-PAM was measured as W_2 (g). The swelling ratio was calculated using Eq. (2):

$$S = \frac{W_2 - W_1}{W_1} \quad (2)$$

Water solubility measurement

One gram of CS-g-PAM was mixed in 100 mL of distilled water for 1 h, then filtered. The precipitated filter paper was dried in an atmospheric oven at 50 °C to a constant weight. The percentage of CS-g-PAM solubility in water was calculated by Eq. (3).

$$\text{Water solubility \% (w / w)} = \frac{W_0 - W_{\text{ins}}}{W_0} \quad (3)$$

where W_0 is the initial weight of the CS-g-PAM (1 g), and W_{ins} is the weight of dried precipitated CS-g-PAM.

Thickening ability

The dried CS-g-PAM was powdered and dissolved in distilled water at room temperature. The viscosity of polymer solutions with a concentration of 1 wt.% was measured in various NaCl concentrations and temperatures according to reservoir conditions. After preparing the polymer solution, viscosity measurement was carried out on the Brookfield Viscometer DV2T.

Anti-aging ability

The viscosity of polymer solutions with a concentration of 1 wt.% was measured for 15 days in distilled water. Apparent viscosity was measured with a Brookfield Viscometer DV2T.

■ RESULTS AND DISCUSSION

Synthesis of Cassava Starch-Polyacrylamide Hydrogel

The mechanism of the microwave-assisted grafting method consists of initiation, propagation, termination, and homopolymer formation (side reaction) [18]. The initiation phase occurs when a certain amount of initiator is added, and a microwave irradiates the reaction mixture.

The formation of complexes between the hydroxyl groups of polysaccharides and oxidants occurs due to the KPS mechanism that produces free radicals. Microwave radiation twists and stretches the bonds of acrylamide molecules. The electrons from the pi bond, where the C-C double bond will be extended, split into two locations (i.e., the free radical side of the constituent carbon atom). When free radical sites are formed in cassava starch (i.e., polymer backbone), monomers are added by chain propagation until the free radical sites are terminated via the termination step [19]. The termination step occurs when acetone is added to form a precipitate of the resulting CS-g-PAM. Here, microwave selectively excited polar bonds unlike heat energy and high energy radiation [18,20]. CS-g-PAM was synthesized through the interaction between free radical sites generated in the cassava starch backbone (by KPS) and free radical sites generated in acrylamide (by microwave radiation) through free radical reactions.

The microwave-assisted method with various initial conditions is shown in Table 1, where we can see that the irradiation time required for the gel to form decreased as the amount of acrylamide increased. The irradiation time required for the gel formation decreased from 300 to 30 s as the content of the acrylamide monomer increased from 2 to 10 g. Meanwhile, for the case of CS-g-PAM C, D, E, and F, when the irradiation time was extended to 180 s, the percentage of grafting obtained also increased. For the case of CS-g-PAM A and B, it had not yet formed a gel when the irradiation time was 180 s. Therefore, the irradiation time was extended, and the gel formation time was 300 s. The higher amount of acrylamide and the longer irradiation time increased the grafting percentage. The grafting percentage increased from 71.25 to 1565.53% as the amount of acrylamide increased from 2 to 10 g. The increase in grafting percentage and the decrease of irradiation time for the gel formation was due to the availability of excess monomer molecules to be grafted onto the polymer backbone at the propagation step.

In addition, because the proportion of cassava starch was smaller than acrylamide, the percentage of grafting was quite high. More homopolymerization

reactions occurred, and some of the homopolymers and grafted products were overlapped, entangled, or even twisted. Acetone extraction could not entirely remove these homopolymers [21].

Fourier Transform Infrared Spectroscopy

The FTIR spectra of cassava starch (CS) and CS-g-PAM are shown in Fig. 1. The FTIR results of CS show the main absorption peaks, including: 3304.71 cm^{-1} (OH strain vibration), 2916.76 cm^{-1} (CH strain vibration), and C–O–C strain vibrations at 1141.03 cm^{-1} , 1069.72 cm^{-1} , and 1016.94 cm^{-1} .

All grafted products displayed identical profiles on the FTIR spectrum. Therefore, the discussion was carried out for CS-g-PAM A only as a representative for the entire grafted sample. In CS-g-PAM A, the O–H strain vibration of the starch hydroxyl group and the N–H strain vibration of the PAM amide group overlapped and led to a peak at 3356.06 cm^{-1} and a shoulder peak at 3197.74 cm^{-1} . A small peak at 2929.60 cm^{-1} is associated with the C–H strain vibration. The peak at 1019.80 cm^{-1} is assigned to the C–O–C strain vibration. The appearance of a sharp peak at 1645.99 cm^{-1} is associated with C=O stretching while the peak at 1596.02 cm^{-1} is associated with N–H. Furthermore,

another additional peak in the graft product at 1336.43 cm^{-1} , indicates C–N stretching.

Fig. 1. shows that the peaks of O–H groups in CS-g-PAM is not as sharp compared to the CS. It was similar to FTIR spectra of starch-g-polyacrylamide [22] and cassava starch-polydiallyldimethylammonium chloride (polyDADMAC) [23]. It may be explained that the presence of O–H groups was replaced by polyacrylamide chains [22]. The presence of strain vibrations C=O, N–H, and C–N at $-\text{CONH}_2$ also indicates the success of the grafting process. The FTIR spectra shown in Fig. 1. show that the graft copolymer is generated by the interaction between the free radical generated in the backbone of CS and polyacrylamide through the free radical reaction mechanism.

To support our data, the comparison of the FTIR spectra between CS-g-PAM A and other hydrogels from previous studies is shown in Table 2. In the FTIR spectra of the synthesis of cassava starch-graft-polyacrylamide using the reactive blending method, there was a stretch of the C=O bond associated with a peak at 1667 cm^{-1} , and the same vibration for the N–H and C–N bonds was associated with a peak centered on 1611 and 1407 cm^{-1} [24].

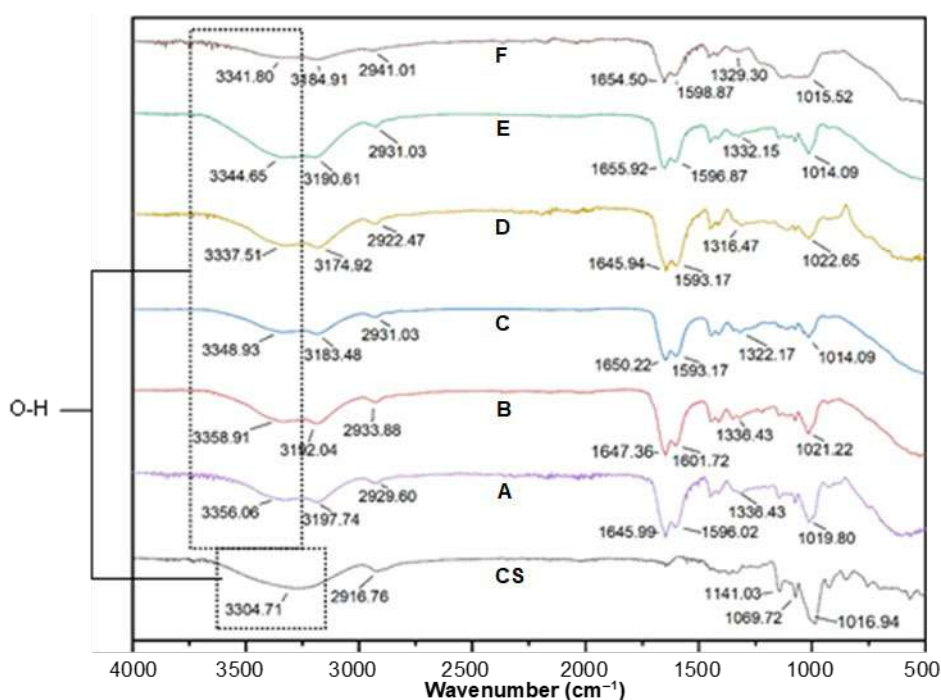


Fig 1. FTIR of CS and CS-g-PAM (A–F)

Table 2. Comparison FTIR spectra between CS-g-PAM hydrogel and previous report

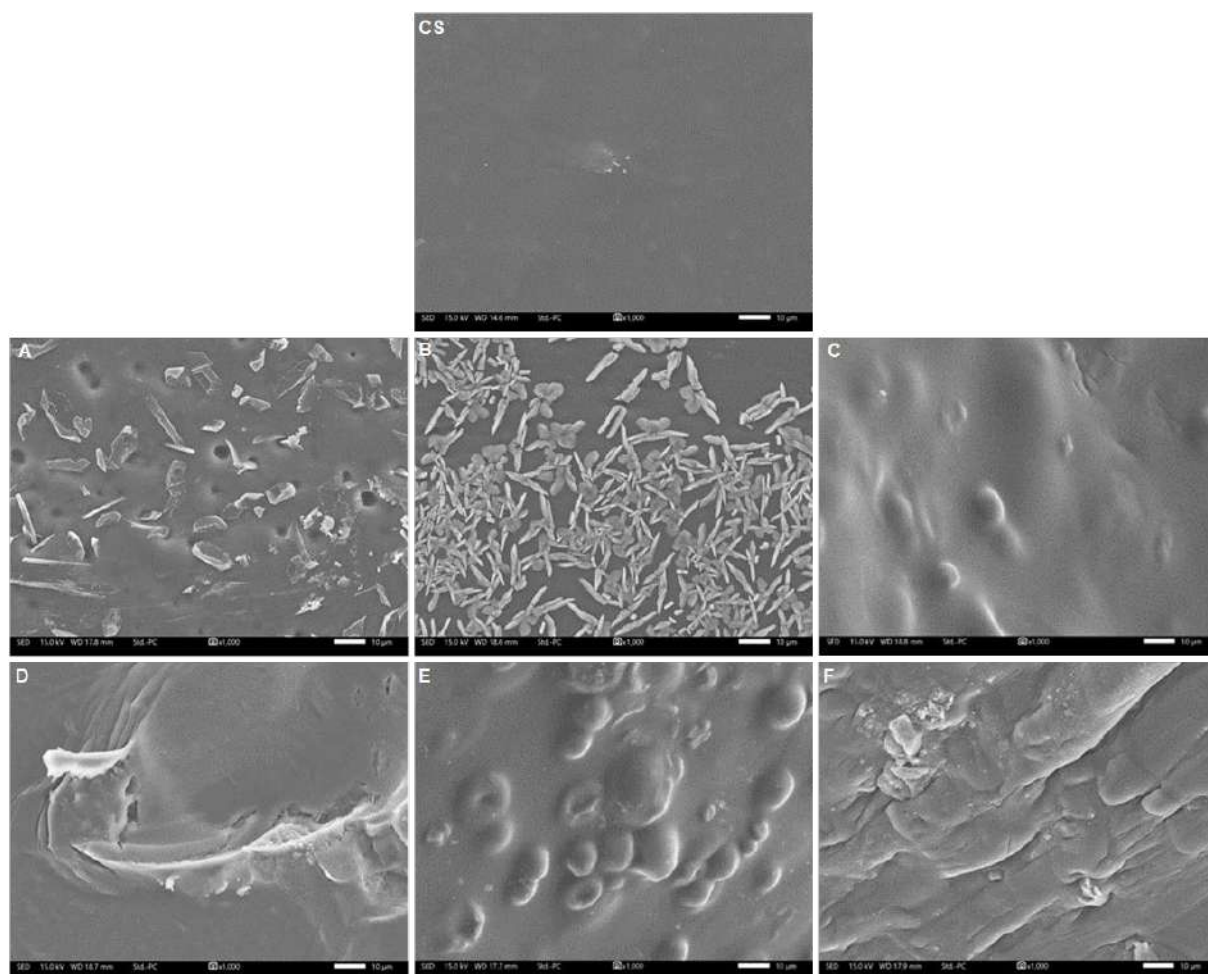
Spectrum	Peak (cm ⁻¹)		
	CS-g-PAM A	Cassava starch-graft-polyacrylamide [24]	Polyacrylamide grafted xanthan [25]
C=O	1645.99	1667	1675
N-H	1596.02	1611	1615
C-N	1336.43	1407	1410

In the FTIR spectra of the synthesis of polyacrylamide grafted xanthan there was a stretch of the C=O bond associated with a peak at 1675 cm⁻¹, and the same vibration for the N-H and C-N bonds was associated with a peak centered on 1615 and 1410 cm⁻¹ [25]. These peaks appeared in the FTIR spectra of CS-g-PAM (A-F). Thus, the presence of additional peaks in the case of CS-g-PAM (A-F) compared to CS confirmed the success of grafting acrylamide chains in the backbone of CS.

Scanning Electron Microscope

The microstructure of the surface of CS and CS-g-PAM can be determined by SEM. The SEM photographs of CS and CS-g-PAM are shown in Fig. 2. The SEM of CS-g-PAM shows that it has different surface morphology compared to CS.

The SEM image of CS-g-PAM showed smooth, coarse and rough surfaces. The SEM of CS-g-PAM (B, D, F) with a higher amount of acrylamide, appeared to have a more rough surface. Likewise, with CS-g-PAM (C

**Fig 2.** SEM images of CS and CS-g-PAM hydrogel (A-F)

and D or E and F) with a longer irradiation time. This observation indicated that the higher the amount of acrylamide and the longer irradiation time, the more polyacrylamide chains were grafted onto the backbone of CS.

The SEM of images CS-g-PAM C and E have similar surface morphology, which was caused when the irradiation time stopped and the gel mass was formed. However, E had a rougher surface than C because of the higher amount of acrylamide. The SEM image of CS-g-PAM D and F showed more rough surfaces when the irradiation time was extended to 180 s. The higher the acrylamide amount and the longer the irradiation time caused more polyacrylamide to be grafted onto the backbone of CS, causing more rough surfaces in the morphology results.

The SEM images of CS-g-PAM A and B show that these materials contained granules with shape irregularities, consisting of a number of faces (polyhedral) and relatively sharp edges. Although most of the granules were still separated, some of the granules were connected to each other via the outer layer of the grafted polyacrylamide chain. The irregular structure in the form of connected grains and sharp edges was due to the low acrylamide content. The polyacrylamide grafted onto the backbone of CS was low [26].

The binding of hydroxyl groups, which establish hydrogen and covalent connections between starch chains, causes granules to aggregate, allowing the development of pores suitable for water absorption [27]. CS-g-PAM has a

coarse and broad network and slightly rough surfaces. Coarse, rough and porous surfaces seem to be related to water absorption abilities [24]. The SEM photographs of CS-g-PAM exhibit a coarse and broad network with a rough surface. It was similar to the SEM photograph of chitosan-grafted-polyacrylamides [28] and cassava waste pulp-acrylamide [29]. The morphological differences between CS and CS-g-PAM further supported the successful grafting of polyacrylamide side chains onto the starch backbone.

Swelling Ratio Measurement

The swelling ratio of CS-g-PAM in distilled water is shown in Fig. 3. The swelling ratio increased from 0 to 120 m of swelling time. The longer irradiation time and the higher amount of acrylamide improved the swelling ratio. The measurement of the swelling ratio aims to determine the potential of hydrogels to decrease reservoir heterogeneity, hence enhancing sweep efficiency during profile improvements in a typical reservoir [30].

The swelling ratio of CS-g-PAM A and B increased from 1.39 to 2.83 g/g as irradiation time increased from 180 to 300 s. The swelling ratio of CS-g-PAM C, D, E, and F increased as the irradiation time for the gel to form was extended to 180 s. These results showed that the swelling ratio of CS-g-PAM is affected by irradiation time.

In the case of CS-g-PAM B, D, and F with an irradiation time of 180 s, the swelling ratio increased from 1.39 to 9.58 g/g as the amount of acrylamide increased from 2 to 10 g. This phenomenon indicated

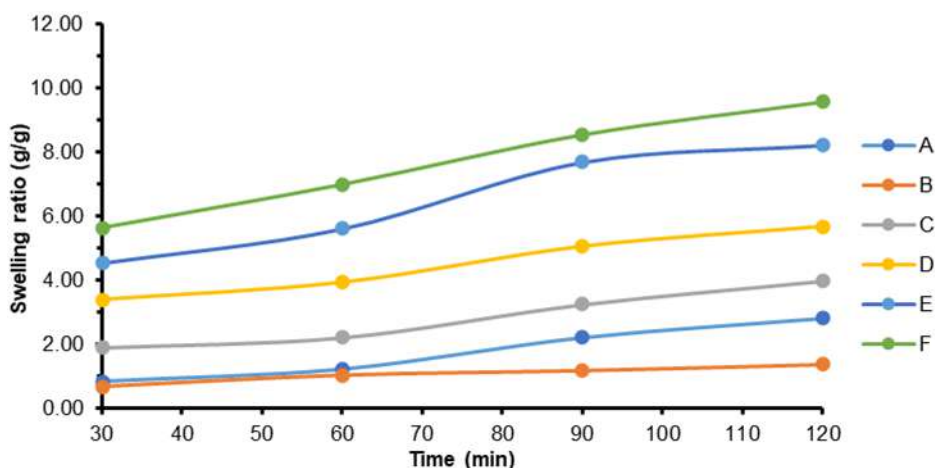


Fig 3. Swelling ratio of CS-g-PAM hydrogel (A-F) in distilled water

that the swelling ratio of CS-g-PAM is influenced by the amount of acrylamide.

The highest swelling ratio was obtained in CS-g-PAM F at 9.58 g/g. The longer irradiation time and the higher amount of acrylamide, the more polyacrylamide will be grafted onto CS. It can be proven in the morphology results that F had the roughest and broadest surface compared to the other products.

Preformed particle gel (PPG) that was synthesized from acrylamide-*N,N*-dimethyl acrylamide-2-acrylamido-2-methylpropane sulfonic sodium salt (AMPSNa)-*N*-vinylpyrrolidone as a plugging agent in reservoirs had a swelling ratio of about 28 g/g in distilled water at room temperature [31]. Hydrogel synthesis from lutensol AT 25 E - methacrylate as chemical enhanced oil recovery (CEOR) had a swelling ratio of 3.1 g/g [32]. From the previous studies of the swelling ratio of CS-g-PAM for EOR applications that have been carried out, it is proven that CS-g-PAM can be applied for EOR.

According to reservoir conditions, the swelling ratio was measured at NaCl concentrations from 0 to 250,000 ppm [31]. The swelling ratio of CS-g-PAM at various concentration of saline water (NaCl) are shown in Fig. 4. The swelling ratio decreased as the NaCl concentration was increased from 0 to 250,000 ppm.

The decrease of the swelling ratio of CS-g-PAM as the NaCl concentration was increased, was indicated by

the interaction between the negatively charged groups and the hydrophilic groups connected to the backbone of CS. When the salt content is increased, the contact between the negatively charged polymer chains with the cationic metal results in incomplete electrostatic interactions, which reduces the osmotic pressure difference between the hydrogel network and the external solution [31-32]. Thus, the swelling ratio of CS-g-PAM decreased at high salinity concentrations.

This well-known phenomenon is frequently observed in ionic hydrogel swelling. The presence of amide groups influences hydrogel swelling (non-ionic). The high charge screening effect and complexing with cations resulted in a decreased swelling capacity in the salt solution [33]. Thus the production of homopolymer decreases the swelling ratio significantly. In the case of CS-g-PAM E and F, the increase in the amount of acrylamide and irradiation time could also promote the production of homopolymers and decrease the swelling ratio more significantly than other CS-g-PAM.

According to reservoir conditions, the swelling ratio was measured at temperatures from 25 to 90 °C in laboratory experiments. The swelling ratio of CS-g-PAM in distilled water at various temperatures is shown in Fig. 5. The swelling ratio of CS-g-PAM decreased from the temperature of 25 to 90 °C. The behavior of decreasing swelling ratio of CS-g-PAM in high temperatures can be

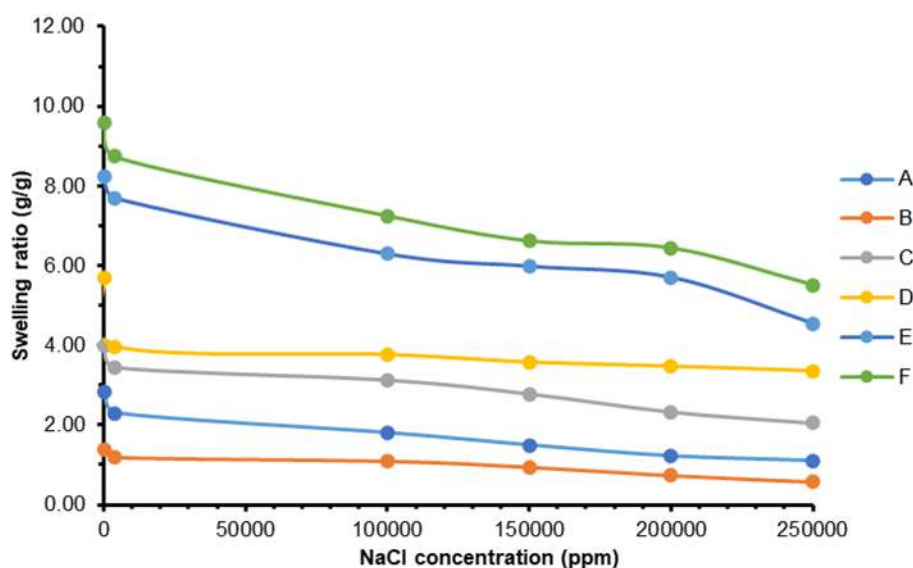


Fig 4. Swelling ratio of CS-g-PAM hydrogel (A-F) at various NaCl concentrations (Swelling time = 120 min)

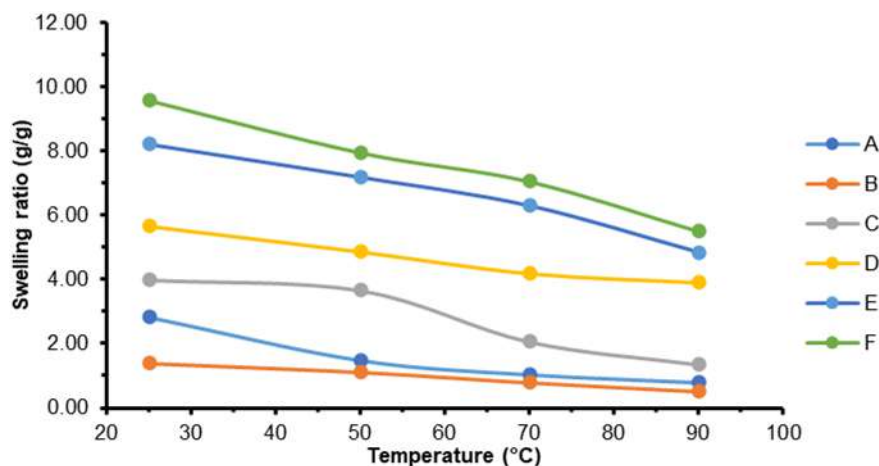


Fig 5. Swelling ratio of CS-g-PAM hydrogel (A-F) at various temperatures (Swelling time = 120 min)

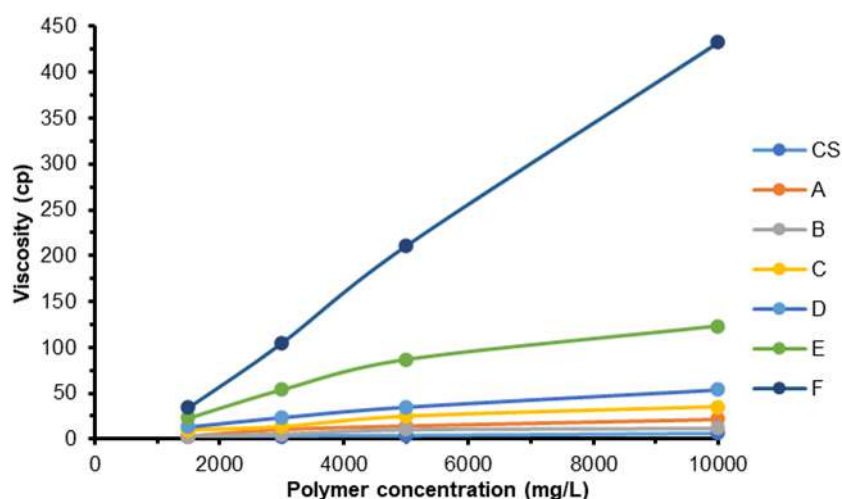


Fig 6. Effect of concentration on CS and CS-g-PAM (A-F) viscosity in distilled water

significantly affected by hydrogen bonding. With increasing temperature, the water molecules trapped in the network are exposed freely when the hydrogen bond interactions become weak or disintegrate and the hydrophobic carbon group interactions become completely dominant [31,34].

In general, the solubility of the polyacrylamide network decreases with increasing temperature and as a consequence the network collapses and the swelling ability is reduced [35]. In the case of CS-g-PAM E and F, the decreasing swelling ratio is significantly caused by the production of homopolymer.

Water Solubility Measurement

Solubility in the water of CS-g-PAM improved by increasing the amount of acrylamide. Water solubility

increased from 26.72 to 96.06% as the amount of acrylamide increased from 2 to 10 g. The solubility in water also increased with a longer irradiation time. The solubility in water of CS-g-PAM E and F increased from 81.51 to 96.06% with increased irradiation time from 30 to 180 s. Increasing acrylamide concentrations and irradiation time cause improved solubility of the polyacrylamide side chains that lead to a less aggregated and stable grafted starch solution [36].

Thickening Ability

The viscosity of the polymer solution is an important feature for mobility control. The polymer solution can improve water viscosity and decrease the water-oil mobility ratio, enhancing sweep efficiency [37]. The viscosity of CS and CS-g-PAM that gradually

improved with the concentration of polymer solution are shown in Fig. 6. The polymer in the solution exists as single molecules in the dilution zone, and the viscosity gradually increases. Polymer molecules entangle and even create network structures as polymer concentration increases. The internal frictional motion of the molecules also increased, resulting in increased flow resistance and a significant increase in the viscosity of the polymer solution [16].

The viscosity of the polymer solution increased as the amount of acrylamide and irradiation time increased. The viscosity of CS-g-PAM was several times higher than the viscosity of CS, in the whole polymer concentration range that was investigated. Therefore, grafting polyacrylamide chains onto the CS backbone led to a viscosity increase of the polymer solution. The addition of polyacrylamide increases the viscosity and hence the hydrodynamic volume of CS-g-PAM in water, which may be expressed by destroying the strong intra-hydrogen bonds between the acrylamide units [38].

The viscosity of CS-g-PAM B was slightly higher than the viscosity of CS solution, indicating the small amount of polyacrylamide grafted onto the backbone of CS. This might also indicate that CS-g-PAM B had lower water solubility than the other CS-g-PAM, with water solubility obtained at 26.72%.

The viscosity of the CS-g-PAM solution at various concentrations of NaCl is shown in Fig. 7. For all samples of CS-g-PAM solution, the viscosity decreased with

increasing NaCl concentration. This phenomenon occurred as a result of the addition of a small molecule electrolyte to the system, which modified the polarity of the solution and protected the electrostatic attraction forces within the molecules [16].

CS-g-PAM solution containing polyacrylamide in a low ratio (A, B, C, D) showed a relatively stable viscosity profile compared to NaCl concentration. For CS-g-PAM solution containing polyacrylamide in a high ratio (E, F), a decreasing trend was significant as NaCl concentration was increased. This is due to the "salt out" effect of NaCl on the homopolymer unit of the CS-g-PAM, which causes a shrinkage of the hydrodynamic volume of the polymer and thus lowers the viscosity [38].

A similar observation of the decreased viscosity of polymer solution in saline water is found in the literature, such as the viscosity of the chitosan-AA-AM polymer that decreased from 100 to 20 cp with increasing NaCl concentration from 0 to 40000 mg/L [16]. Starch-g-(PAM-co-PNIPAM) viscosity decreased from 300 to 100 cp with increasing NaCl concentration from 0 to 100,000 ppm [38], which further supports our finding.

The viscosity of CS-g-PAM solution at various temperatures is shown in Fig. 8. The viscosity of CS-g-PAM solution decreased with increasing temperature. Water molecules' thermal mobility increases as the temperature rises and chemical bonds in molecular chains are easily disrupted. Furthermore, the internal rotation of the single bonds in the molecule increased,

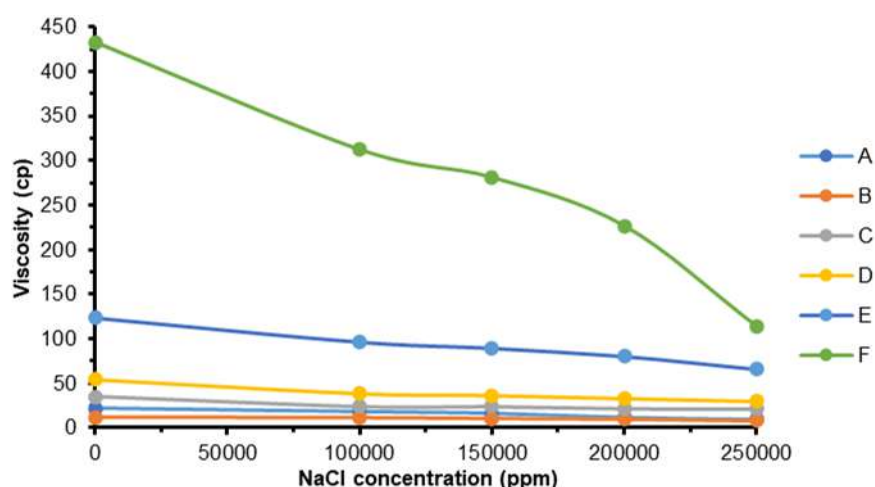


Fig 7. NaCl effects on CS-g-PAM (A-F) viscosity

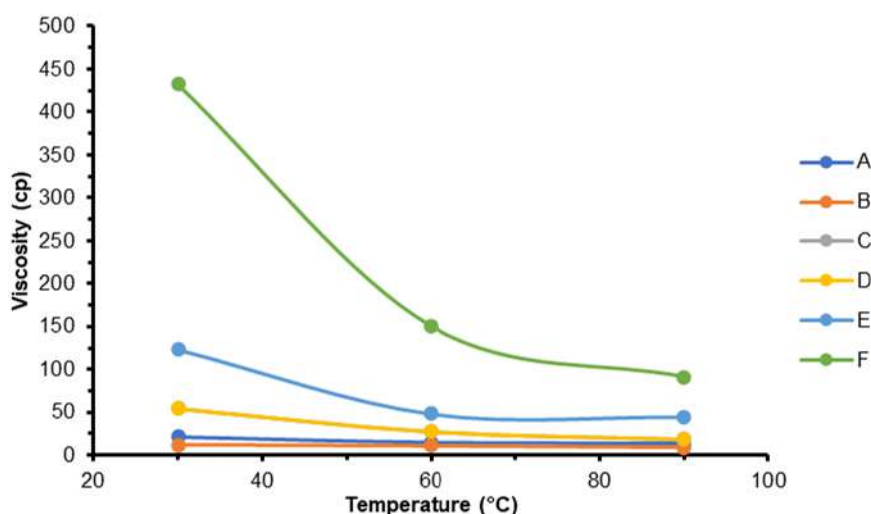


Fig 8. Effect of temperature on CS-g-PAM (A-F) viscosity in distilled water

causing the molecular chain to bend and the associated hydrodynamic radius to decrease [16]. On the other hand, CS-g-PAM solution is susceptible to hydrolysis at high temperatures, which causes a decrease in the viscosity of CS-g-PAM solution. This thermo-responsive behavior is related to breaking strong intra-molecular hydrogen bonds at high temperatures, which is promising for hydrodynamic volume improvement [38].

In the case of CS-g-PAM solution containing polyacrylamide at high ratios (E and F), a decreasing trend was significant as the temperature increased. When the amount of acrylamide and irradiation time in the grafting process are increased, the network between monomers

and CS is strengthened. As a result, the value of grafting percentage increased. However, the increase in the amount of acrylamide and irradiation time could also accelerate the formation of homopolymers and reduce viscosity significantly [39].

A similar observation of the decreased viscosity of polymer solution at various temperatures is found in the literature, such as the viscosity of chitosan-AA-AM polymer that decreased from 350 to 220 cp with increasing temperature from 30 to 90 °C [16]. Starch-g-PAM viscosity decreased from 100 to 60 cp with increasing temperature from 24 to 80 °C [34], further supporting our finding.

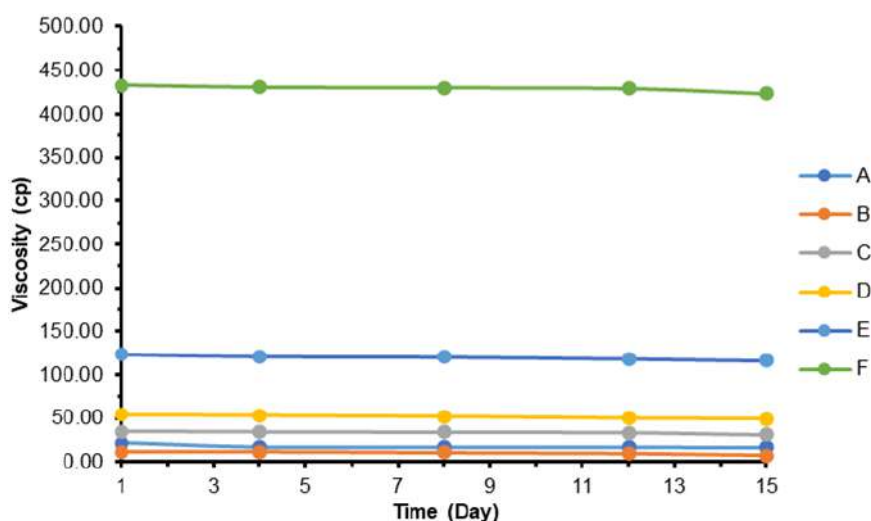


Fig 9. Anti-aging of CS-g-PAM (A-F) solution

Anti-aging Ability

The viscosity of CS-g-PAM solution in 15 days is shown in Fig. 9. The viscosity of CS-g-PAM solution decreased with increasing aging time. The viscosity of CS-g-PAM solution at 15 days for CS-g-PAM A was 77.66%, CS-g-PAM B was 62.24%, CS-g-PAM C was 88.42%, CS-g-PAM D was 91.24%, CS-g-PAM E was 94.20%, and CS-g-PAM F was 97.85% of CS-g-PAM solution on the first day. This showed that CS-g-PAM F has a good anti-aging ability. The main reason for decreasing the viscosity is that the long molecular polymer chains are broken in the polymer degradation process [40]. As can be seen, with the higher acrylamide amount and longer irradiation time, the viscosity of CS-g-PAM solution was constant with an increasing number of days. Thus, grafting polyacrylamide onto the CS backbone gives a copolymer that has a high and stable viscosity. In other words, grafting polyacrylamide onto starch greatly provides starch resistance to biodegradation [36].

CONCLUSION

The synthesis of CS-g-PAM by microwave-assisted grafting method and KPS as the initiator has been performed. The FTIR spectra and SEM morphology of CS and CS-g-PAM confirmed the success of polyacrylamide grafted onto the CS backbone by utilizing energy from a domestic microwave.

The results showed that the increasing amount of acrylamide and irradiation time improved the swelling ratio, water-solubility, thickening ability, and anti-aging ability of CS-g-PAM. The data indicated that CS-g-PAM has good thickening, temperature resistance, and salt resistance properties.

CS-g-PAM F prepared with 10 g acrylamide and 180 s of irradiation time exhibited the highest performance compared to the other CS-g-PAM samples. CS-g-PAM F had the highest grafting percentage and water solubility, which was 1565.53 and 96.06%, respectively. CS-g-PAM F had the highest swelling ratio in distilled water which was 9.58 g/g, and still offered the highest swelling ratio at various NaCl concentrations and temperatures. The viscosity of CS-g-PAM F also showed the highest result compared to the other CS-g-PAM samples and exceeded

97% after 15 days of aging, which indicated that CS-g-PAM F has a good performance as a thickening agent and has a good anti-aging ability.

Considering the inexpensive CS, easy synthesis, and resistance of CS-g-PAM to various NaCl concentrations and temperatures according to reservoir conditions, CS-g-PAM can be a good candidate for EOR applications.

ACKNOWLEDGMENTS

The authors sincerely thank The Directorate General of Higher Education, Indonesia, for financial support of this work through *Penelitian Fundamental* 2021 PNPB Universitas Sebelas Maret with contract number 260/UN27.22/HK.07.00/2021.

REFERENCES

- [1] Sun, X., Zhang, Y., Chen, G., and Gai, Z., 2017, Application of nanoparticles in enhanced oil recovery: A critical review of recent progress, *Energies*, 10 (3), 345.
- [2] Xu, X., Saeedi, A., and Liu, K., 2017, An experimental study of combined foam/surfactant polymer (SP) flooding for carbone dioxide-enhanced oil recovery (CO₂-EOR), *J. Pet. Sci. Eng.*, 149, 603–611.
- [3] Wei, B., Romero-Zerón, L., and Rodrigue, D., 2014, Mechanical properties and flow behavior of polymers for enhanced oil recovery, *J. Macromol. Sci., Part B: Phys.*, 53 (4), 625–644.
- [4] Lee, K.S., 2011, Performance of a polymer flood with shear-thinning fluid in heterogeneous layered systems with crossflow, *Energies*, 4 (8), 1112–1128.
- [5] Samanta, A., Ojha, K., Sarkar, A., and Mandal, A., 2013, Mobility control and enhanced oil recovery using partially hydrolyzed polyacrylamide (PHPA), *Int. J. Oil, Gas Coal Technol.*, 6 (3), 245–258.
- [6] Chen, L., Zhu, X., Fu, M., Zhao, H., Li, G., and Zuo, J., 2019, Experimental study of calcium-enhancing terpolymer hydrogel for improved oil recovery in ultradeep carbonate reservoir, *Colloids Surf., A*, 570, 251–259.
- [7] Singh, R., and Mahto, V., 2017, Synthesis, characterization and evaluation of polyacrylamide

- graft starch/clay nanocomposite hydrogel system for enhanced oil recovery, *Pet. Sci.*, 14 (4), 765–779.
- [8] Haruna, M.A., Nourafkan, E., Hu, Z., and Wen, D., 2019, Improved polymer flooding in harsh environments by free-radical polymerization and the use of nanomaterials, *Energy Fuels*, 33 (2), 1637–1648.
- [9] Viken, A.L., Skauge, T., Svendsen, P.E., Time, P.A., and Spildo, K., 2018, Thermo-thickening and salinity tolerant hydrophobically modified polyacrylamides for polymer flooding, *Energy Fuels*, 32 (10), 10421–10427.
- [10] Ghosh, P., and Mohanty, K.K., 2019, Study of surfactant–polymer flooding in high-temperature and high-salinity carbonate rocks, *Energy Fuels*, 33 (5), 4130–4145.
- [11] Pu, W., Shen, C., Wei, B., Yang, Y., and Li, Y., 2018, A comprehensive review of polysaccharide biopolymers for enhanced oil recovery (EOR) from flask to field, *J. Ind. Eng. Chem.*, 61, 1–11.
- [12] Mohd, T.A.T., Manaf, S.F.A., Naim, M.A., Shayuti, M.S.M., and Jaafar, M.Z., 2020, Properties of biodegradable polymer from terrestrial mushroom for potential enhanced oil recovery, *Indones. J. Chem.*, 20 (6), 1382–1391.
- [13] Junlapong, K., Maijan, P., Chaibundit, C., and Chantarak, S., 2020, Effective adsorption of methylene blue by biodegradable superabsorbent cassava starch-based hydrogel, *Int. J. Biol. Macromol.*, 158, 258–264.
- [14] Elsaheed, S.M., Zaki, E.G., Omar, W.A.E., Ashraf Soliman, A., and Attia, A.M., 2021, Guar gum-based hydrogels as potent green polymers for enhanced oil recovery in high-salinity reservoirs, *ACS Omega*, 6 (36), 23421–23431.
- [15] El-hoshoudy, A.N., Hosny, R., Fathy, M., Abdelraheem, O.H., Gomaa, S., and Desouky, S.M., 2019, Enhanced oil recovery using polyacrylates/ACTF crosslinked composite: Preparation, characterization and coreflood investigation, *J. Pet. Sci. Eng.*, 181, 106236.
- [16] Chen, Q., Ye, Z., Tang, L., Wu, T., Jiang, Q., and Lai, N., 2020, Synthesis and solution properties of a novel hyperbranched polymer based on chitosan for enhanced oil recovery, *Polymers*, 12 (9), 2130.
- [17] Nagarpita, M.V., Roy, P., Shruthi, S.B., and Sailaja, R.R.N., 2017, Synthesis and swelling characteristics of chitosan and CMC grafted sodium acrylate-co-acrylamide using modified nanoclay and examining its efficacy for removal of dyes, *Int. J. Biol. Macromol.*, 102, 1226–1240.
- [18] Singh, A.V., Nath, L.K., and Guha, M., 2011, Microwave assisted synthesis and characterization of *Phaseolus aconitifolius* starch-g-acrylamide, *Carbohydr. Polym.*, 86 (2), 872–876.
- [19] Mishra, S., Rani, G.U., and Sen, G., 2012, Microwave initiated synthesis and application of polyacrylic acid grafted carboxymethyl cellulose, *Carbohydr. Polym.*, 87 (3), 2255–2262.
- [20] Mishra, S., Mukul, A., Sen, G., and Jha, U., 2011, Microwave assisted synthesis of polyacrylamide grafted starch (St-g-PAM) and its applicability as flocculant for water treatment, *Int. J. Biol. Macromol.*, 48 (1), 106–111.
- [21] Zhou, P., Ru, X., Yang, W., Dai, Z., Ofori, M.A., Chen, J., Hou, J., Zhong, Z., and Jin, H., 2022, Study on preparation of cationic flocculants by grafting binary monomer on cellulose substrate by γ -ray co-irradiation, *J. Environ. Chem. Eng.*, 10 (2), 107138.
- [22] Kaavessina, M., Fatimah, I., and Soraya, S., 2018, Performance test of starch-g-polyacrylamide synthesized through grafting as a flocculant in artificial wastewater treatment, *EJChE*, 2 (1), 17–23.
- [23] Razali, M.A.A., Ismail, H., and Ariffin, A., 2015, Graft copolymerization of polyDADMAC to cassava starch: Evaluation of process variables via central composite design, *Ind. Crops Prod.*, 65, 535–545.
- [24] Nakason, C., Wohmang, T., Kaesaman, A., and Kiatkamjornwong, S., 2010, Preparation of cassava starch-graft-polyacrylamide superabsorbents and associated composites by reactive blending, *Carbohydr. Polym.*, 81 (2), 48–357.
- [25] Chami, S., Joly, N., Bocchetta, P., Martin, P., and Aliouche, D., 2021, Polyacrylamide grafted xanthan: Microwave-assisted synthesis and

- rheological behavior for polymer flooding, *Polymers*, 13 (9), 1484.
- [26] Lele, V., 2015, Morphological study of graft copolymers of maize starch with acrylamide and methacrylamide, *Int. J. Curr. Res.*, 7 (9), 19991–19994.
- [27] Soto, D., Urdaneta, J., Pernia, K., León, O., Muñoz-Bonilla, A., and Fernández-García, M., 2016, Itaconic acid grafted starch hydrogels as metal remover: Capacity, selectivity and adsorption kinetics, *J. Polym. Environ.*, 24 (4), 343–355.
- [28] Monyake, K.C., and Alagha, L., 2022, Enhanced separation of base metal sulfides in flotation systems using chitosan-grafted-polyacrylamides, *Sep. Purif. Technol.*, 281, 119818.
- [29] Mas'ud, Z.A., Khotib, M., Sari, N., and Nur, A., 2013, Synthesis of cassava waste pulp-acrylamide super absorbent: Effect of initiator and cross-linker concentration, *Indones. J. Chem.*, 13 (1), 66–71.
- [30] El-hoshoudy, A.N., Mohammedy, M.M., Ramzi, M., Desouky, S.M., and Attia, A.M., 2019, Experimental, modeling and simulation investigations of a novel surfmer-co-poly acrylates crosslinked hydrogels for water shut-off and improved oil recovery, *J. Mol. Liq.*, 277, 142–156.
- [31] Farasat, A., Sefti, M.V., Sadeghnejad, S., and Saghafi, H.R., 2017, Effects of reservoir temperature and water salinity on the swelling ratio performance of enhanced preformed particle gels, *Korean J. Chem. Eng.*, 34 (5), 1509–1516.
- [32] Czarnecka, E., and Nowaczyk, J., 2020, Semi-natural superabsorbents based on starch-g-poly(acrylic acid): Modification, synthesis and application, *Polymers*, 12 (8), 1794.
- [33] Sadeghi, M., and Yarahmadi, M., 2011, Swelling and characterization behavior of anti-salt superabsorbent based on carboxymethyl cellulose-g-PAA-co-BuMC hydrogel, *Orient. J. Chem.*, 27 (2), 435–444.
- [34] Abidin, A.Z., Puspasari, T., and Graha, H.P.R., 2014, Utilization of cassava starch in copolymerisation of superabsorbent polymer composite (SAPC), *J. Eng. Technol. Sci.*, 46 (3), 286–298.
- [35] Wedel, B., Hertle, Y., Wrede, O., Bookhold, J., and Hellweg, T., 2016, Smart homopolymer microgels: influence of the monomer structure on the particle properties, *Polymers*, 8 (4), 162.
- [36] Eutamene, M., Benbakhti, A., Khodja, M., and Jada, A., 2009, Preparation and aqueous properties of starch-grafted polyacrylamide copolymers, *Starch/Staerke*, 61 (2), 81–91.
- [37] Chen, Y., He, H., Yu, Q., Liu, H., Chen, L., Ma, X., and Liu, W., 2021, Insights into enhanced oil recovery by polymer-viscosity reducing surfactant combination flooding in conventional heavy oil reservoir, *Geofluids*, 2021, 7110414.
- [38] Fan, Y., Boulif, N., and Picchioni, F., 2018, Thermo-responsive starch-g-(PAM-co-PNIPAM): Controlled synthesis and effect of molecular components on solution rheology, *Polymers*, 10 (1), 92.
- [39] Wang, Z., Shi, H., Wang, F., Wang, A., He, Q., and Cuan, S., 2021, Synthesis of cassava starch-g-acrylic acid/dimethylaminopropyl methacrylamide: A new hydrogel for brine solution, *Carbohydr. Polym.*, 266, 118109.
- [40] Xin, X., Yu, G., Chen, Z., Wu, K., Dong, X., and Zhu, Z., 2018, Effect of polymer degradation on polymer flooding in heterogeneous reservoirs, *Polymers*, 10 (8), 857.

Effect of Solution pH on the Photo-Oxidation of 4-Chlorophenol by Synthesized Silver-Zinc Oxide Photocatalyst

Nur Syafiqah Hazirah Razali¹, Hayati Mohamad Mukhair², Kian Mun Lee³, Mohd Izham Saiman¹, and Abdul Halim Abdullah^{1,2*}

¹Department of Chemistry, Faculty of Science, Universiti Putra Malaysia, 43300 UPM Serdang, Selangor Malaysia

²Institute of Nanoscience and Nanotechnology, Universiti Putra Malaysia, 43400 UPM Serdang, Selangor, Malaysia

³Nanotechnology and Catalysis Research Centre (NANOCAT), University of Malaya, 50603 Kuala Lumpur, Malaysia

* **Corresponding author:**

tel: +603-97696777

email: halim@upm.edu.my

Received: January 4, 2022

Accepted: April 11, 2022

DOI: 10.22146/ijc.71763

Abstract: Due to its toxicity, 4-chlorophenol (4CP) must be removed from the wastewater before discharging into open water. In this work, ZnO and Ag-ZnO photocatalysts were prepared via a solvothermal method under mild conditions (150 °C), followed by calcination at 300 °C and then characterized. The addition of Ag resulted in a change of the ZnO morphologies, which exhibited wurtzite structure, from irregular to rod-like shape, lower bandgap energy, and a lower electron-hole recombination rate. The 0.6 Ag-ZnO catalyst showed the highest efficiency in the photooxidation of 4CP under UV irradiation. Molecular 4CP exists in acidic and near-neutral conditions (pH 4 and 6) and is stable towards UV irradiation. Photooxidation of 2.3×10^{-4} mol/L 4CP by 0.8 g of 0.6% Ag-ZnO resulted in 67% removal of molecular 4CP at pH 6 with a rate constant of $4.0 \times 10^{-3} \text{ min}^{-1}$. Under similar conditions, a complete photooxidation of the anionic 4CP was observed at pH 11 with a rate constant of $1.4 \times 10^{-2} \text{ min}^{-1}$. The holes and superoxide radicals are the species responsible for molecular 4CP photooxidation, while hydroxyl radicals are the dominant species for anionic 4CP. The prepared Ag/ZnO photocatalyst exhibit good potential to efficiently oxidize 4CP in both acidic and alkaline conditions.

Keywords: Ag-ZnO; photooxidation; 4-chlorophenol; endocrine disruptor chemicals; photocatalyst

■ INTRODUCTION

Semiconductor photocatalysis has been extensively studied to degrade non-biodegradable and highly persistent pollutants [1]. In principle, when a semiconductor photocatalyst absorbs light energy greater than or equal to its bandgap energy, it produces electron-hole pairs, which generate free radicals through a series of reactions. These free radicals are responsible for degrading organic pollutants to harmless by-products such as H₂O and CO₂ [2]. TiO₂, ZnO, CdS, CeO₂, GaN, WO₃, and ZnS, are the most frequently used semiconductors. Although TiO₂ is the most widely studied photocatalyst, several studies have reported that it has exhibited a significantly lower degradation rate than ZnO since the latter has higher light absorption efficiency

over a significant fraction of the solar spectrum [2-4]. However, the efficiency of ZnO is low due to its fast electron-hole recombination rate.

To suppress the recombination rate and enhance the photocatalytic activity, several researchers have modified the surface of ZnO via doping with C₃N₄, silver, gold, copper, and cobalt [5-9]. The photocatalytic activity of the doped ZnO was superior to pure ZnO due to the lower electron-hole recombination rate [10]. Silver, Ag, one of the best dopants for ZnO, can act as an electron sink, reducing the recombination rate and improving the photocatalyst's performance [11].

Various methods, including sol-gel [12-13], hydrothermal [14-15], co-precipitation [16-18], and thermal treatment [19], have been used to prepare Ag-

ZnO photocatalysts. Although the Ag-ZnO performance, under various reaction conditions, has been widely evaluated via photodegradation of dyes [20], reports on the degradation of chlorophenols by Ag-ZnO are limited. Chlorophenols are toxic and recalcitrant compounds harmful to human health and aquatic life [21]. The production of chlorophenol compounds has increased recently with the worldwide increase in industrial and agricultural activities. They are widely used to produce insecticides, pesticides, and wood preservatives. Their presence has been detected in soils, groundwater [1], and industrial wastewater [3]. 4CP, a known endocrine disruptor chemical, is widely used in manufacturing [2,22]. Due to its toxicity and non-biodegradable, removing 4CP from the wastewater is imperative. Recently, the removal of 4CP via photocatalysis using ZnO/ZnS/ carbon xerogel [23] and CuO-ZnO-PANI [24] was reported. In this study, ZnO and Ag-ZnO photocatalysts were prepared via a solvothermal method to photooxidize 4CP under different pH solutions. This study aims to investigate the photooxidation of 4CP at various pH solutions. At different pH levels, 4CP can exist as a parent molecule and anionic 4CP molecules. As of now, there has been no report on the photooxidation of anionic 4CP available in the literature.

■ EXPERIMENTAL SECTION

Materials

In preparing the ZnO and Ag/ZnO photocatalysts, zinc acetate dihydrate (99%, Merck, Germany) and silver nitrate (99.5%, Bendosen, Norway) were used as starting materials with isopropanol (98%, Merck, Germany) as the solvent. A stock solution of 4CP (98%, Fluka Chimie, Switzerland), prepared by dissolving 1.0 g of 4CP in 1.0 L deionized water, was diluted to produce the working solutions for the photooxidation studies. HCl and NaOH solutions were added to the 4CP working solution to adjust its pH (pH 6) to the desired pH values.

Instrumentation

A box furnace (Carbolite, USA) is used to prepare the catalyst. Powder X-ray diffractometer (X'pert Pro PanAnalytical, Philips), Belsorp Mini I Surface Area

Analyzer, Perkin Elmer Lambda 35 UV-Vis-NIR, and LS 55 Perkin Elmer fluorescence spectrophotometer were used to characterize the catalyst. A custom-made photo-reactor with a volume capacity of 1.2 L (Fig. 1) is used in the photocatalytic oxidation experiment. Perkin Elmer Lambda 35 UV-Vis-NIR was also used to determine the concentration of 4CP solution.

Procedure

Preparation of ZnO and Ag-ZnO photocatalysts

In preparing Ag-ZnO photocatalyst, a homogeneous solution containing 0.0–0.27 g of silver nitrate (0 to 2.0 mol), 14.70 g of zinc acetate dihydrate and 200 mL of isopropanol was prepared and sonicated for 1 h. The solution was placed into stainless steel autoclaves and heated at 150 °C for 3 h. The precipitate formed was collected via centrifugation, washed twice with ethanol, oven-dried at 80 °C for 24 h, and calcined at 300 °C for 2 h. A similar procedure was employed to synthesize ZnO particles.

Catalysts characterization

The XRD pattern of the photocatalysts was recorded at $2\theta = 2\text{--}60^\circ$ using a powder X-ray diffractometer (CuK α radiation at $\lambda = 1.540 \text{ \AA}$, 30 kV, and 30 mA) at the scanning rate of $2^\circ/\text{min}$. The surface area was measured by nitrogen adsorption at $-196 \text{ }^\circ\text{C}$ using the Belsorp mini I instrument. The UV diffuse-reflectance spectrum was recorded using Perkin Elmer

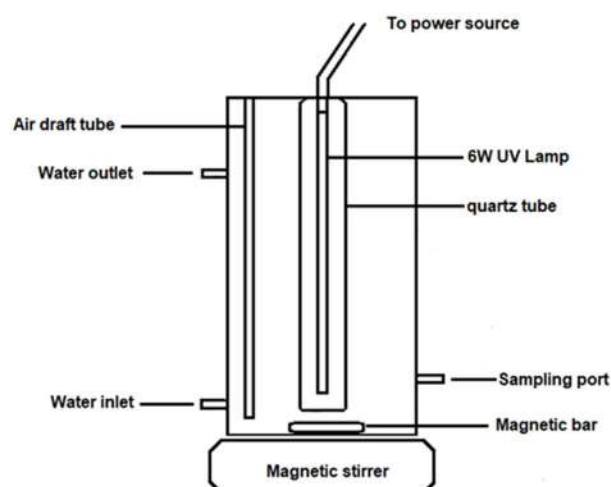


Fig 1. The schematic diagram of the photocatalytic reactor

Lambda 35 UV-Vis-NIR spectrophotometer and used to determine the bandgap energy of the photocatalysts. The electron-hole recombination was analyzed by LS 55 Perkin Elmer fluorescence spectrophotometer (PL) with an excitation wavelength set at 300 nm. A field emission-scanning electron microscope (Hitachi SU 8000) was used to capture the morphology of the photocatalyst.

Photocatalytic activity test

The photocatalytic degradation experiments were conducted using a custom-made photo-reactor equipped with water circulation to keep its temperature at 28 °C. A certain amount of catalyst ranging from 0.2 to 1.0 g was added into the photoreactor, containing a 1 L 4CP solution of known concentration ranging from 1.56×10^{-4} to 2.3×10^{-4} mol/L. After stirring the reaction mixture in the dark for 30 min to achieve adsorption-desorption equilibrium, the 6 W UV-A lamp (365 nm, Hitachi) was switched on to irradiate the solution for 240 min under a continuous supply of air. At regular intervals, 10 mL of sample were withdrawn from the bulk solution and filtered through a 0.45 μm cellulose nitrate filter to remove the catalysts. The residual concentration of 4CP during the photocatalytic oxidation experiments at solution pH of 4–9 and pH 11 was determined at λ_{max} of 225 nm and 244 nm,

respectively, using a UV-Vis spectrophotometer. The percentage of 4CP photocatalytic oxidation (PCO) was calculated as follows (Eq. (1)):

$$4\text{CP PCO (\%)} = \frac{C_o - C_t}{C_o} \times 100\% \quad (1)$$

where C_o and C_t are the concentration of 4CP initially and at time t , respectively.

RESULTS AND DISCUSSION

Catalyst Characterization

The XRD patterns of the prepared photocatalysts, shown in Fig 2, displayed a diffraction pattern matching the wurtzite structure of zinc oxide (JCPDS 036-1451). Besides, diffraction peaks observed at $2\theta = 38.1$ and 44.3° at Ag loading of 0.6 % corresponded to Ag (JCPDS 4-0783). Close examination of the XRD pattern (Fig. 2(b)) showed no significant shift in peak positions, which indicates the segregation of Ag particles in the grain boundaries of ZnO and may have formed interstitial as a second phase clusters around the ZnO lattices [25-26]. Furthermore, the Ag^+ ions cannot substitute the Zn^{2+} ions in the crystal lattice due to the difference in the oxidation states and ionic radius ($r(\text{Ag}^+) = 0.126$ nm, $r(\text{Zn}^{2+}) = 0.076$ nm) [27].

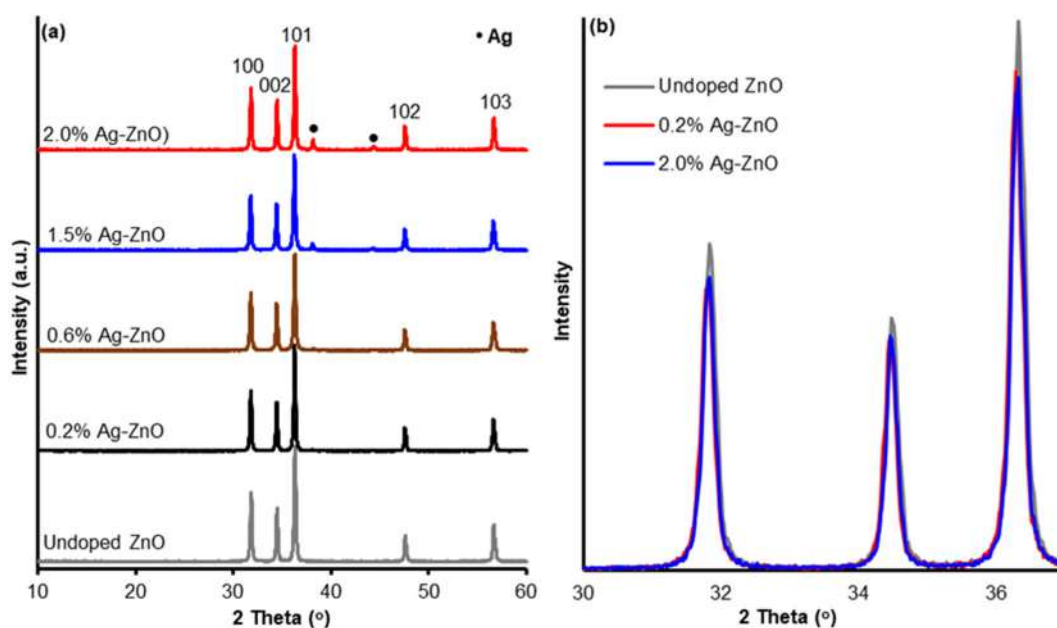


Fig 2. X-ray diffraction pattern of (a) ZnO and Ag-ZnO photocatalysts and (b) comparison of (100), (002), and (101) peaks for ZnO, 0.2% Ag-ZnO and 2.0% Ag-ZnO

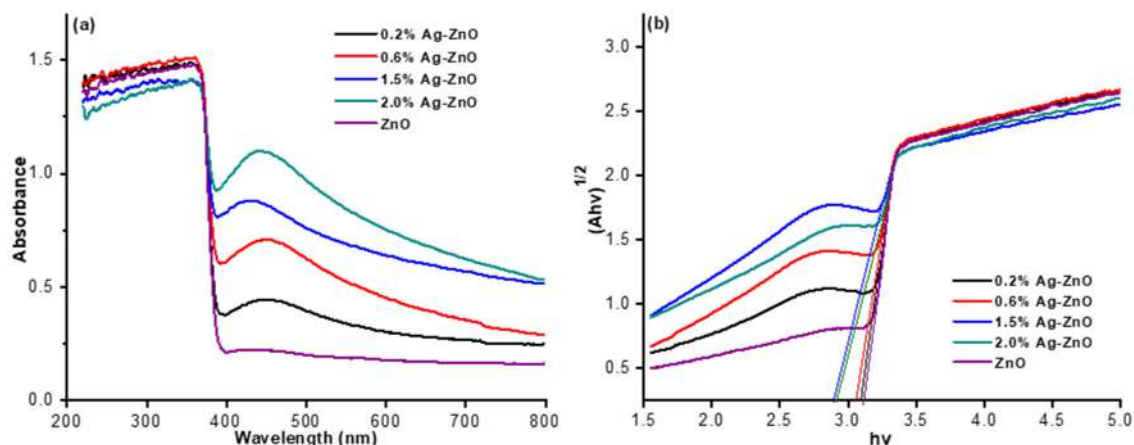


Fig 3. (a) UV-Vis spectra and (b) Tauc plot for determination of bandgap energy of ZnO and Ag-ZnO photocatalysts

The bandgap energy and surface area play an influential role in the photocatalytic activity of a photocatalyst [28]. Fig. 3 displays the UV-vis diffuse reflectance spectra and the Tauc's plot of the photocatalysts. The Ag surface plasmon resonance peak was observed at about 470 nm [29]. The peak intensity increases with the increase of Ag content, confirming that Ag has been successfully deposited on the surface of ZnO. The photocatalyst's bandgap energy, estimated from the intercept of the x-axis of the $(Ah\nu)^{1/2}$ versus $h\nu$ plot, are listed in Table 1. The addition of silver shifted the bandgap energy to 2.84 eV, changing the catalyst's optical properties from UV-activated to visible light-activated catalyst. However, the surface area of the photocatalysts was not affected by the addition of silver.

The photoluminescence (PL) study was conducted to identify the transfer, separation, and recombination of photogenerated electron-hole pairs of ZnO and Ag-ZnO. Lower PL intensity indicates a lower recombination rate of charge carriers, leading to higher photocatalytic activity. The PL spectra of ZnO and Ag-loaded ZnO are depicted in Fig. 4. Pure ZnO exhibited two emission bands at 380 nm and 420 nm. The former was attributed to the ultraviolet emission of the ZnO particles, while the latter is due to the charge carrier relaxation through the surface-related trap states [30]. As the amount of Ag increased, the PL intensity decreased significantly. The efficient interfacial charge transfer from ZnO to Ag acts as an electron sink that enhances the lifetime of the

Table 1. Surface area and bandgap energy of ZnO and Ag-ZnO photocatalysts

Photocatalyst	Surface area (m^2g^{-1})	Bandgap energy (eV)
ZnO	6.54	3.12
0.2% Ag-ZnO	6.49	3.04
0.6% Ag-ZnO	8.65	3.00
1.5% Ag-ZnO	7.71	2.84
2.0% Ag-ZnO	6.51	2.85

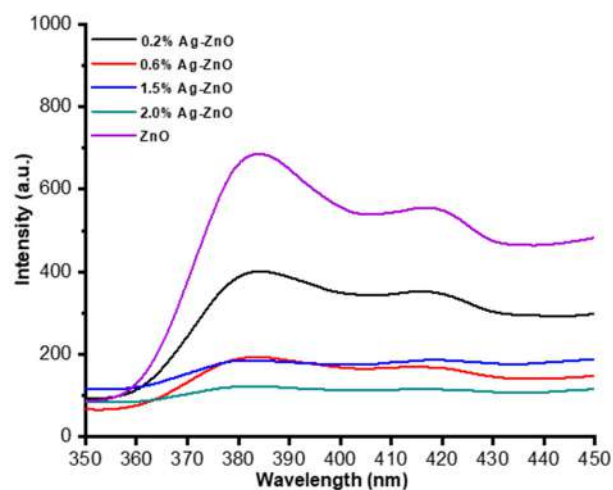


Fig 4. PL spectra of ZnO and Ag-ZnO photocatalysts

photogenerated charge carriers [31]. The morphology of the photocatalysts, depicted in Fig. 5, changed with the addition of Ag into ZnO from irregularly shaped particles (ZnO) to rod-like particles (2% Ag-ZnO). The morphological changes showed that the crystal growth of the photocatalyst is affected by the presence of Ag.

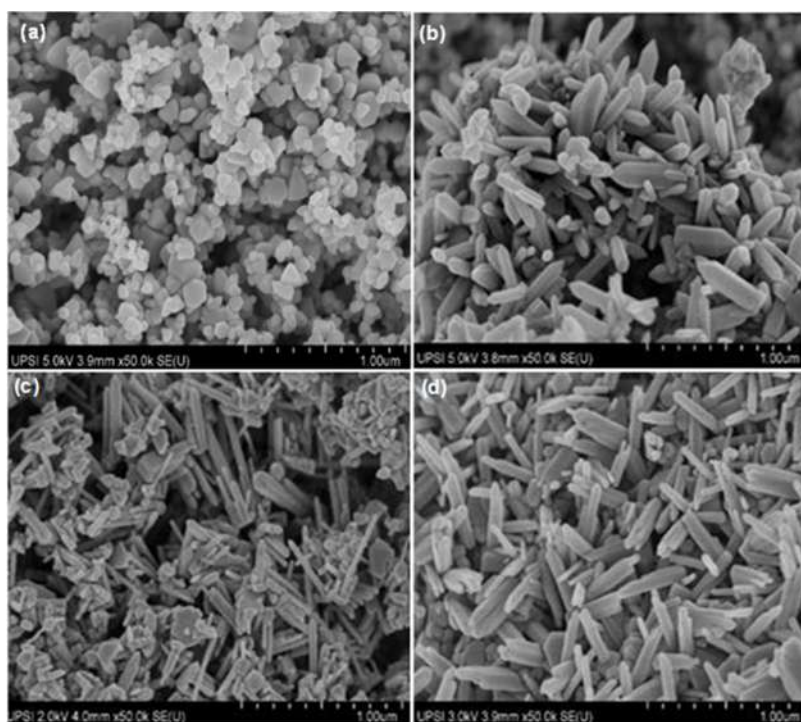


Fig 5. Micrographs of (a) ZnO (b) 0.2% (c) 0.6% (d) 2.0% Ag-ZnO photocatalysts

Photocatalytic Oxidation Activity

Fig. 6 shows the performance of ZnO and Ag-ZnO photocatalyst in the photocatalytic oxidation of 4CP. The percentage of 4CP photocatalytic oxidation increased with increasing Ag content up to 0.6% but then decreased at higher Ag content, indicating the optimum Ag loading of 0.6%. The improvement in the photocatalytic oxidation

of 4CP was due to the capability of the Ag to trap the photogenerated electron hence a better charge separation for Ag-ZnO than pure ZnO. However, excessive silver may act as recombination centers and filters that reduce the light from reaching the ZnO surface, consequently decreasing the photogeneration of charge carriers [32].

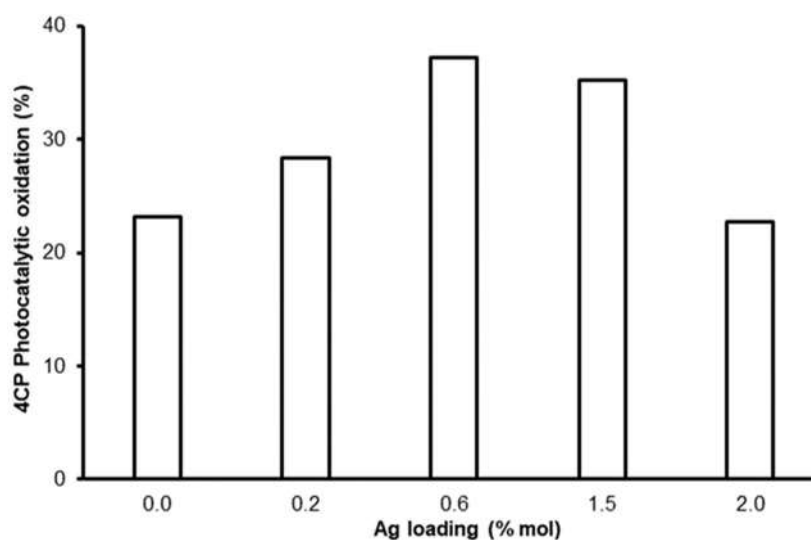


Fig 6. Photo-oxidation of 4CP by ZnO and Ag-ZnO photocatalysts (Conditions: 0.2 g photocatalysts, 1.94×10^{-4} mol/L 4CP, pH 6.0)

The influence of the mass of 0.6% Ag-ZnO photocatalyst on photo-oxidation of 4CP is shown in Fig. 7. The efficiency of the photo-oxidation increases with increasing mass up to 0.8 g (97.12%) and then decreases at a higher mass. Increasing the mass of the photocatalyst will increase photocatalytic sites, thus enhancing the photogeneration of electron and hole pairs. Consequently, more hydroxyl and superoxide radicals are produced, leading to higher photo-oxidation of 4CP [33]. However, when the mass of photocatalyst is higher than

0.8 g, the solution becomes turbid, thus reducing the light penetration into the solution, subsequently reducing the photo-oxidation of the 4CP.

The photocatalytic oxidation of 4CP, at various solution pHs, is affected by the surface charge and the stability of the catalyst, and the form of the 4CP molecule. The UV-Vis spectra of 4CP solution at different initial pH were recorded (Fig. 8) before performing the photocatalytic oxidation studies. Two peaks observed at λ_{\max} of 225 and 280 nm showed the 4CP

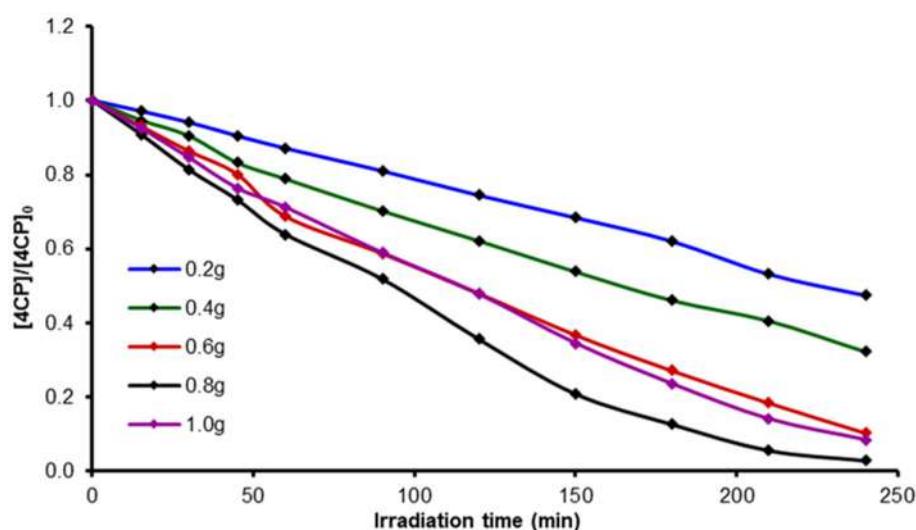


Fig 7. Photo-oxidation of 4CP by various amount of 0.6% Ag-ZnO photocatalyst (Conditions: 1.56×10^{-4} mol/L 4CP, pH 6.0)

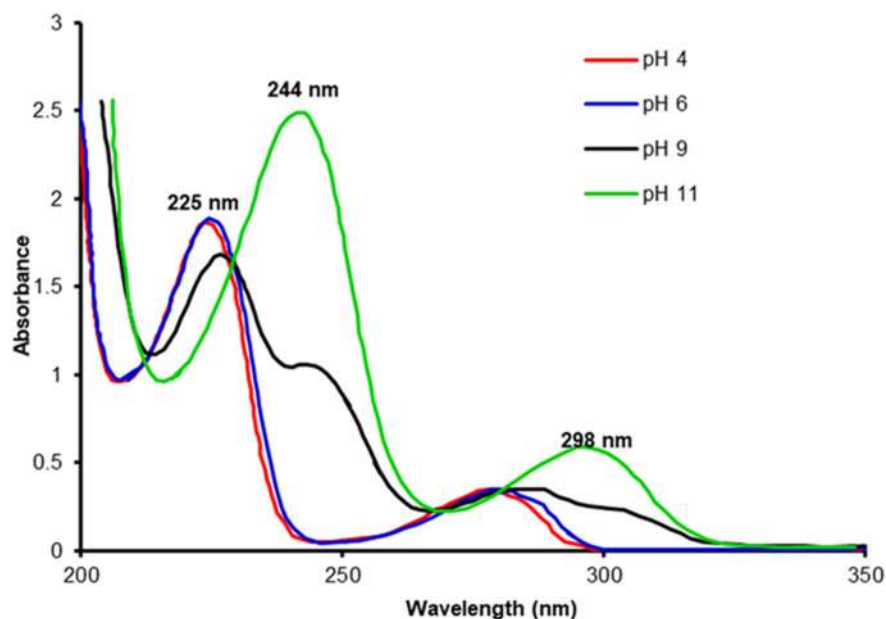


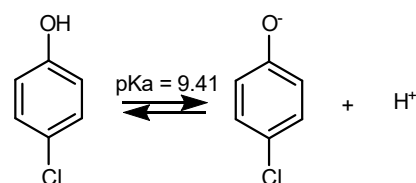
Fig 8. UV-Vis absorption spectra of 4CP with different pH solution

in its molecular form under acidic and near-neutral conditions (pH 4 and 6).

When the pH of the solution increased to 9, the 225 nm peak intensity decreased while the 280 nm peak became broader and red-shifted to 287 nm. Moreover, two shoulders appeared at 244 and 298 nm, showing partial dissociation of 4CP to its anionic form. The UV-Vis spectrum of 4CP at pH 11 displayed only the peaks at 244 and 298 nm, indicating that 4CP has completely dissociated from its anionic form [34]. These observations follow the pKa of 4CP, which is 9.4 (Scheme 1). Thus, the concentration of 4CP during the photocatalytic oxidation experiments at solution pH of 4-9 and pH 11 was then determined at λ_{\max} of 225 and 244 nm, respectively.

The photocatalytic oxidation of the 4CP molecule is also dependent on the surface charge of the catalyst. The pH of the point of zero-charge (pH_{pzc}) of the Ag-ZnO catalyst, as determined by the pH drift method [35], was 7.15. Hence, the Ag-ZnO surface is positively and negatively charged at pH below and above 7.15, respectively. The effect of the initial pH solution, ranging from pH 4 to 11, on the photocatalytic oxidation of 4CP is shown in Fig. 9. The photocatalytic oxidation increased up to pH 6, decreased slightly at pH 9, then increased significantly at pH 11. The lowest photocatalytic oxidation of 4CP, was observed at pH 4.

The progress of the 4CP photocatalytic oxidation at pH 6 to 11 is shown in Fig. 10. A steady decrease in the band intensity reflected the photocatalytic oxidation of 4CP. In the acidic and near-neutral conditions, the interaction between the positively charged Ag-ZnO and the p electron of the 4CP molecule may facilitate the photocatalytic oxidation of 4CP. At pH 9, the initial spectra of 4CP consist of 4 peaks at 225, 244 (shoulder), 287, and 298 (shoulder) nm. After the adsorption process, the 244 and 298 nm peaks were slightly visible, while the 225 nm peak became more intense. The pH of the solution also changed to 7. These changes indicate that the acidic site of the Ag-ZnO catalyst may have reacted with the added OH^- . Hence, it reduces the solution pH and causes some of the anionic 4CP molecules to return to their molecular form. The loss of acidic sites may have contributed to a slight decrease in photocatalytic oxidation of 4CP. However, at pH 11, complete photocatalytic oxidation of 4CP was observed



Scheme 1. Dissociation of 4CP and its corresponding pKa value

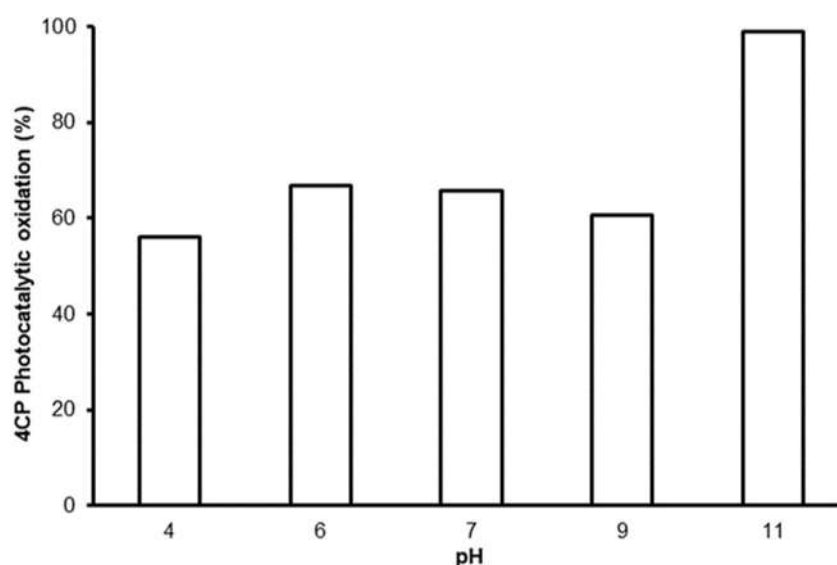


Fig 9. Photo-oxidation of 4CP under different pH of initial solution (Condition: 2.3×10^{-4} mol/L 4CP, 0.8 g of 0.6% Ag-ZnO photocatalyst)

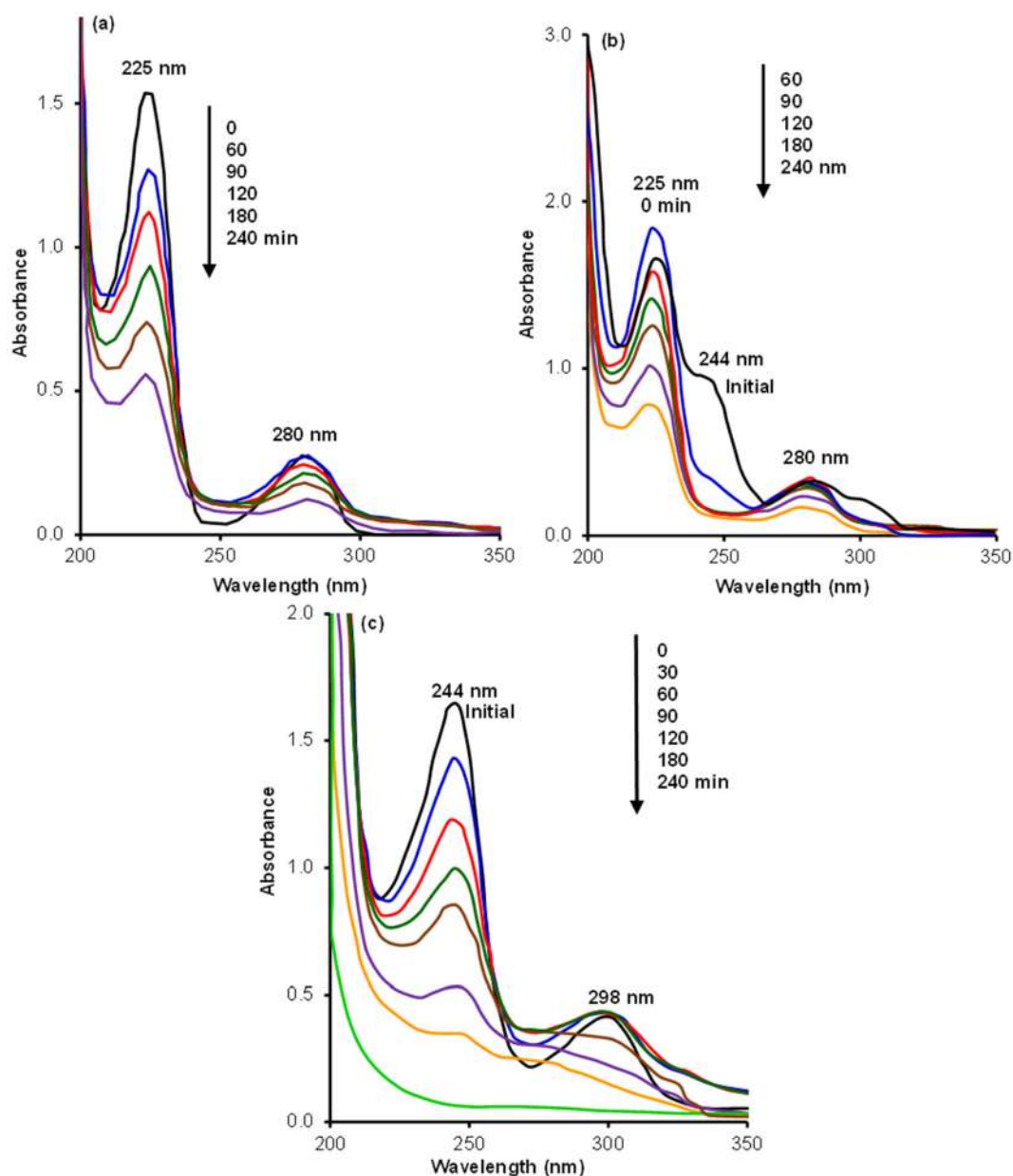


Fig 10. Progressive photo-oxidation of 4CP at (a) pH 6, (b) pH 9 and (c) pH 11

after 240 min of reaction. Theoretically, a reduction in photocatalytic oxidation of 4CP is expected in basic conditions. The reduction is due to (i) repulsion between the 4CP anion with the negatively charged surface of the catalyst and (ii) reduction in the formation of hydroxyl radicals, which is due to the competitive reaction between the hole (h^+) with the 4CP anion, H_2O and OH^- . Photolysis experiments were conducted at pH 6 and 11 to confirm that the photo-oxidation of 4CP is due to the photocatalytic reaction. The results showed that the

molecular 4CP was stable towards photolysis at pH 6, while 25% of the anionic 4CP photolyzed at pH 11. Thus, the photo-oxidation of anionic 4CP at pH 11 is due to both photolysis and photocatalytic activity.

The experimental data, fitted to the Langmuir-Hinshelwood kinetic model (Fig. 11), showed that the photocatalytic oxidation of 4CP followed the pseudo-first-order reaction. The apparent rate constants, k_{app} , were determined from the slope of the plot and are shown in the inset. The photocatalytic oxidation rate of the 4CP

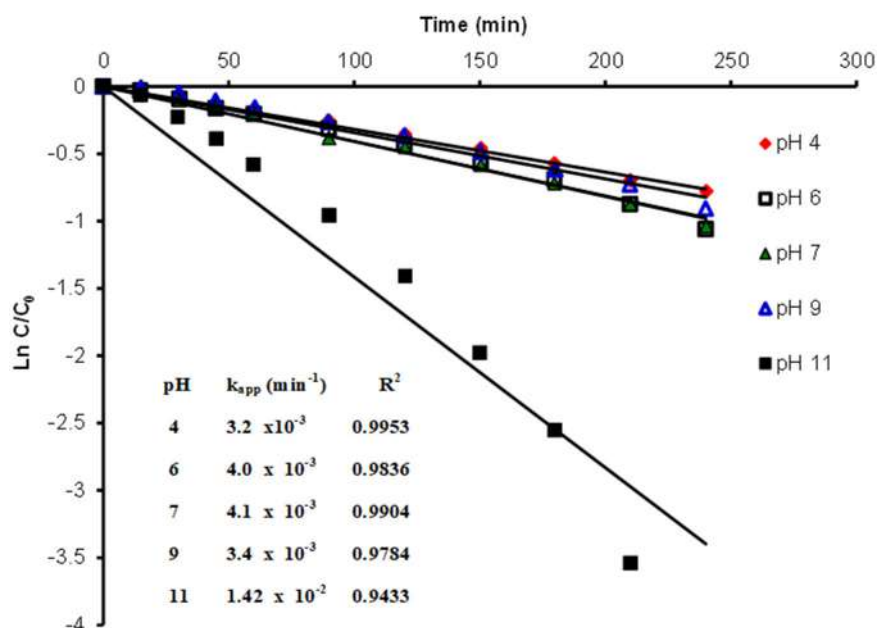


Fig 11. First-order kinetic for photo-oxidation of 4CP at different pH and its corresponding rate constant (inset)

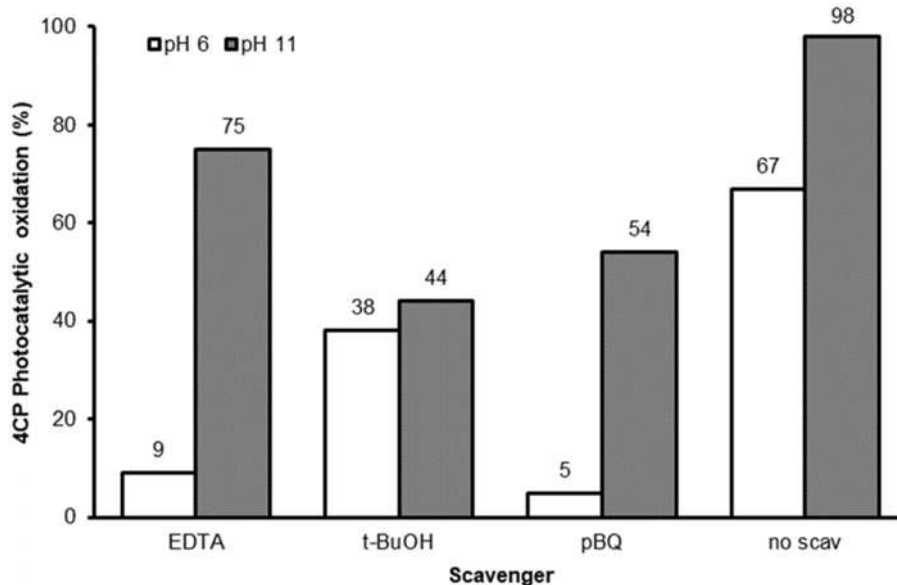


Fig 12. The effect of radical scavengers on 4CP oxidation at pH 6 and 11

molecule increased with increasing pH up to pH 6 and then decreased slightly at pH 9. The photo-oxidation rate of the anionic 4CP is approximately 4 times faster than that of molecular 4CP. Hence, the anionic 4CP is more reactive than the molecular 4CP towards photo-oxidation.

The effect of radical and hole scavengers in photocatalytic activity was conducted at pH 6 and 11 to determine the reactive species responsible for the photooxidation of 4-CP, and the results are shown in Fig.

12. Tert-butanol (t-BuOH) was used as scavengers for hydroxyl radical ($\bullet\text{OH}$), p-benzoquinone (BQ) for superoxide radical ($\bullet\text{O}_2^-$), and EDTA sodium (Na-EDTA) for the hole (h^+). The degradation of 4-CP without any scavengers was 67% at pH 6 and 98% at pH 11. At pH 6, the addition of BQ and Na-EDTA scavengers led to a significant decrease in the photooxidation of 4-CP compared to the addition of t-BuOH, indicating that both the $\bullet\text{O}_2^-$ and h^+ are the main

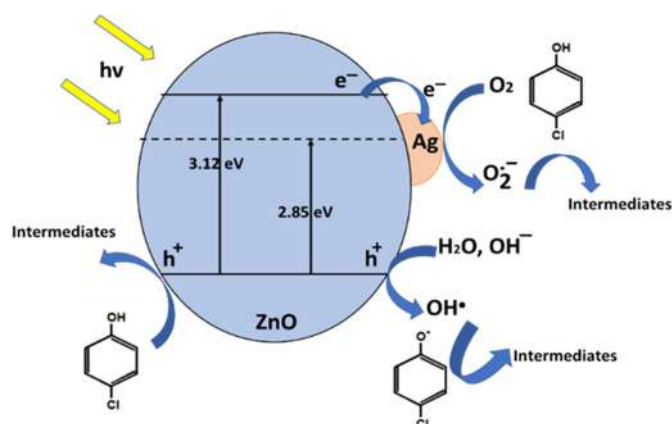


Fig 13. Proposed reaction mechanism for the photo-oxidation of molecular and anionic 4CP over Ag-ZnO catalyst

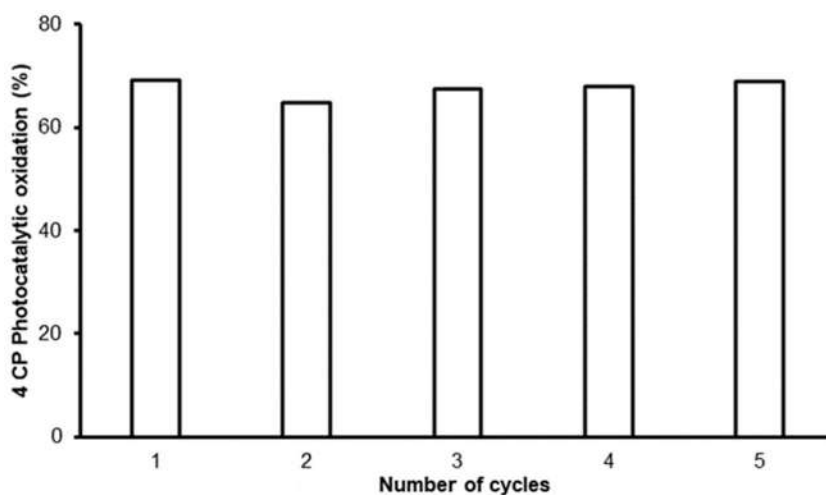


Fig 14. Reusability of 0.6% Ag-ZnO in photocatalytic oxidation of 4CP (Condition: 0.8 g photocatalyst, 2.3×10^{-4} mol/L 4CP, pH 6)

reactive species involved in the reaction system. However, a different pattern can be seen at pH 11. The photooxidation of anionic 4CP became less efficient in the presence of t-BuOH and BQ scavengers than Na-EDTA, suggesting that the $\bullet\text{OH}$ and $\bullet\text{O}_2^-$ are the active species in the reaction at pH 11. The photodegradation reaction mechanism route for molecular and anionic 4CP is different. As illustrated in Fig. 13, the photo-oxidation of molecular 4CP proceeded via reaction with the holes and superoxide radicals, while photooxidation of anionic 4CP occurs via reaction with hydroxyl radicals.

Reusability

The reusability test of the photocatalyst was investigated at optimum photo-oxidation conditions i.e.

0.8 g of 0.6% Ag-ZnO catalyst, 2.3×10^{-4} mol/L 4CP solution at natural pH (pH 6). At the end of the experiment, the catalyst was recovered by filtration, washed with deionized water, and then used to degrade a fresh 4CP solution. As shown in Fig. 14, no significant difference in the percentage of 4CP photo-oxidation was observed up to 5 cycles of photo-oxidation experiment, thus indicating the Ag-ZnO photocatalyst's stability during the photo-oxidation of the 4CP molecules.

CONCLUSION

ZnO and Ag-ZnO photocatalysts with hexagonal wurtzite ZnO structures were successfully synthesized under mild solvothermal conditions. The performance of ZnO in the photocatalytic oxidation of 4CP was

enhanced by the presence of Ag, with 0.6% Ag-ZnO exhibiting the highest photocatalytic activity. The photocatalytic oxidation of 4CP is affected by the pH of the 4CP solution. Approximately 68% of molecular 4CP was photo oxidized at pH 6, while a nearly complete photo-oxidation of anionic 4CP was observed at pH 11 when oxidizing 2.3×10^{-4} mol/L 4CP using 0.8 g catalyst, indicating a higher reactivity of the anionic 4CP towards photolysis and photocatalysis. The photocatalytic oxidation of 4CP followed the Langmuir-Hinshelwood first-order kinetic model. The stability and the reusability studies showed that the prepared Ag/ZnO photocatalyst has good potential to efficiently oxidize molecular and anionic 4CP in acidic and alkaline conditions, hence can be used to photo-oxidize other chlorophenol compounds.

■ ACKNOWLEDGMENTS

The authors also acknowledged the Ministry of Higher Education, Malaysia, for the financial assistance under grant project FRGS/FASA1-2011/(SG)/(UPM)/(02/38) and MyBrain Scholarship to NSHR, respectively. The authors also acknowledged the Faculty of Science, and Institute of Advanced Technology, Universiti Putra Malaysia, for providing the research facilities.

■ AUTHOR CONTRIBUTIONS

Abdul Halim Abdullah, Mohd Izham Saiman, Lee Kian Mun and Nur Syafiq Hazirah Razali proposed and designed the project. Nur Syafiq Hazirah Razali and Hayati Mukhair conducted the experiments and write the original draft. Abdul Halim Abdullah, Nur Syafiq Hazirah Razali and Hayati Mukhair analyzed and validated the data. Abdul Halim Abdullah, Mohd Izham Saiman, Lee Kian Mun reviewed and revised the manuscript. All authors agreed to the final version of this manuscript.

■ REFERENCES

- [1] Castañeda, C., Tzompantzi, F., Gómez, R., and Rojas, H., 2016, Enhanced photocatalytic degradation of 4-chlorophenol and 2,4-dichlorophenol on in situ phosphated sol-gel TiO₂, *J. Chem. Technol. Biotechnol.*, 91 (8), 2170–2178.
- [2] Lavand, A.B., and Malghe, Y.S., 2015, Visible light photocatalytic degradation of 4-chlorophenol using C/ZnO/CdS nanocomposite, *J. Saudi Chem. Soc.*, 19 (5), 471–478.
- [3] Mahrouqi, H.K.N., Nawi, M.A., and Nawawi, W.I., 2014, Photodegradation of 4-chlorophenol using carbon coated TiO₂ under solar irradiation, *Int. J. Sci. Res. Publ.*, 4 (6), 1–7.
- [4] Munshi, G.H., Ibrahim, A.M., and Al-Harbi, L.M., 2018, Inspired preparation of zinc oxide nanocatalyst and the photocatalytic activity in the treatment of methyl orange dye and paraquat herbicide, *Int. J. Photoenergy*, 2018, 5094741.
- [5] Li, L., Sun, S.Q., Wang, Y.X., and Wang, C.Y., 2018, Facile synthesis of ZnO/g-C₃N₄ composites with honeycomb-like structure by H₂ bubble templates and their enhanced visible light photocatalytic performance, *J. Photochem. Photobiol., A*, 355, 16–24.
- [6] Mendoza-Mendoza, E., Nuñez-Briones, A.G., García-Cerda, L.A., Peralta-Rodríguez, R.D., and Montes-Luna, A.J., 2018, One-step synthesis of ZnO and Ag/ZnO heterostructures and their photocatalytic activity, *Ceram. Int.*, 44 (6), 6176–6180.
- [7] Kavitha, R., and Kumar, S.G., 2019, A review on plasmonic Au-ZnO heterojunction photocatalysts: Preparation, modifications and related charge carrier dynamics, *Mater. Sci. Semicond. Process.*, 93, 59–91.
- [8] Jefri, S.N.S., Abdullah, A.H., and Muhamad, E.N., 2019, Response surface methodology: photodegradation of methyl orange by CuO/ZnO under UV light irradiation, *Asian J. Green Chem.*, 3 (2), 271–287.
- [9] He, R., Hocking, R.K., and Tsuzuki, T., 2012, Co-doped ZnO nanopowders: Location of cobalt and reduction in photocatalytic activity, *Mater. Chem. Phys.*, 132 (2-3), 1035–1040.
- [10] Ravishankar, T.N., Manjunatha, K., Ramakrishnappa, T., Nagaraju, G., Kumar, D., Sarakar, S., Anandakumar, B.S., Chandrappa, G.T., Reddy, V., and Dupont, J., 2014, Comparison of the

- photocatalytic degradation of trypan blue by undoped and silver-doped zinc oxide nanoparticles, *Mater. Sci. Semicond. Process.*, 26, 7–17.
- [11] Sopian, N.A.M., Nor, R.M., Rafaie, H.A., Sani, S.F.A., and Osman, Z., 2018, Photocatalytic degradation of methylene blue with silver doped ZnO nanoparticles grown on microscopic sand particles, *Malays. J. Anal. Sci.*, 22 (2), 270–278.
- [12] Chitradevi, T., Lenus, A.J., and Jaya, N.V., 2020, Structure, morphology and luminescence properties of sol-gel method synthesized pure and Ag-doped ZnO nanoparticles, *Mater. Res. Express*, 7, 015011.
- [13] AL-Jawad, S.M.H., Sabeeh, S.H., Taha, A.A., and Jassim, H.A., 2018, Studying structural, morphological and optical properties of nanocrystalline ZnO:Ag films prepared by sol-gel method for antimicrobial activity, *J. Sol-Gel Sci. Technol.*, 87 (2), 362–371.
- [14] Alshamsi, H.A.H., and Hussein, B.S., 2018, Hydrothermal preparation of silver doping zinc oxide nanoparticles: Study, characterization and photocatalytic activity, *Orient. J. Chem.*, 34 (4), 1898–1907.
- [15] Behera, T.K., Pradhan, S., Satapathy, P.K., and Mohapatra, P., 2021, Synthesis and characterization of ZnO-Ag plasmonic nanocomposite: An efficient photocatalyst for the degradation industrial pollutant, *Mater. Today: Proc.*, 47, 1159–1162.
- [16] Singh, R., Barman, P.B., and Sharma, D., 2017, Synthesis, structural and optical properties of Ag doped ZnO nanoparticles with enhanced photocatalytic properties by photo degradation of organic dyes, *J. Mater. Sci.: Mater. Electron.*, 28 (8), 5705–5717.
- [17] Shojaei, A.F., Tabatabaeian, K., Zanjanchi, M.A., Moafi, H.F., and Modirpanah, N., 2015, Synthesis, characterization and study of catalytic activity of silver doped ZnO nanocomposite as an efficient catalyst for selective oxidation of benzyl alcohol, *J. Chem. Sci.*, 127 (3), 481–491.
- [18] Rasaki, S.A., Zhao, C., Wang, R., Wang, J., Jiang, H., and Yang, M., 2019, Facile synthesis approach for preparation of robust and recyclable Ag/ZnO nanorods with high catalytic activity for 4-nitrophenol reduction, *Mater. Res. Bull.*, 119, 110536.
- [19] Xu, Z., Liu, N., Han, Y., Zhang, P., Hong, Z., and Li, J., 2021, Preparation of Ag/ZnO microspheres and study of their photocatalytic effect on dichloromethane, *Desalin. Water Treat.*, 216, 162–169.
- [20] Ong, C.B., Ng, L.Y., and Mohammad, A.W., 2018, A review of ZnO nanoparticles as solar photocatalysts: Synthesis, mechanisms, and applications, *Renewable Sustainable Energy Rev.*, 81 (1), 536–551.
- [21] Igbinosa, E.O., Odjadjare, E.E., Chigor, V.N., Igbinosa, I.H., Emoghene, A.O., Ekhaize, F.O., and Idemudia, O.G., 2013, Toxicological profile of chlorophenols and their derivatives in the environment: The public health perspective, *Sci. World J.*, 2013, 460215.
- [22] Byrne, C., Subramanian, G., and Pillai, S.C., 2018, Recent advances in photocatalysis for environmental applications, *J. Environ. Chem. Eng.*, 6 (3), 3531–3555.
- [23] de Moraes, N.P., Marins, L.G.P., de Moura Yamanaka, M.Y., Bacani, R., da Silva Rocha, R., and Rodrigues, L.A., 2021, Efficient photodegradation of 4-chlorophenol under solar radiation using a new ZnO/ZnS/carbon xerogel composite as a photocatalyst, *J. Photochem. Photobiol., A*, 418, 113377.
- [24] Rajendran, S., Pachaiappan, R., Hoang, T.K.A., Karthikeyan, S., Gnanasekaran, L., Vadivel, S., Soto-Moscoso, M., and Gracia-Pinilla, M.A., 2021, CuO-ZnO-PANI a lethal p-n-p combination in degradation of 4-chlorophenol under visible light, *J. Hazard. Mater.*, 416, 125989.
- [25] Welderfael, T., Yadov, O.P., Taddesse, A.M., and Kaushal, J., 2013, Synthesis, characterization and photocatalytic activities of Ag-N-codoped ZnO nanoparticles for degradation of methyl red, *Bull. Chem. Soc. Ethiop.*, 27 (2), 221–232.
- [26] Lupan, O., Chow, L., Ono, L.K., Cuenya, B.R., Chai, G., Khallaf, H., Park, S., and Schulte, A., 2010,

- Synthesis and characterization of Ag- or Sb-doped ZnO nanorods by a facile hydrothermal route, *J. Phys., Chem. C*, 114 (29), 12401–12408.
- [27] Jung, D., 2010, Syntheses and characterization of transition metal-doped ZnO, *Solid State Sci.*, 12 (4), 466–470.
- [28] Fatima, S., Ali, S.I., Iqbal, M.Z., and Rizwan, S., 2017, The high photocatalytic activity and reduced band gap energy of La and Mn co-doped BiFeO₃/graphene nanoplatelet (GNP) nanohybrids, *RSC Adv.*, 7 (57), 35928–3593.
- [29] Murali, A., Sarswat, P.K., Perez, J.P.L., and Free, M.L., 2020, Synergetic effect of surface plasmon resonance and schottky junction in Ag-AgX-ZnO-rGO (X= Cl & Br) nanocomposite for enhanced visible-light driven photocatalysis, *Colloids Surf., A*, 595, 124684.
- [30] Patil, S.S., Mali, M.G., Tamboli, M.S., Patil, D.R., Kulkarni, M.V., Yoon, H., Kim, H., Al-Deyab, S.S., Yoon, S.S., Kolekar, S.S., and Kale, B.B., 2016, Green approach for hierarchical nanostructured Ag-ZnO and their photocatalytic performance under sunlight, *Catal. Today*, 260, 126–134.
- [31] Zhang, X., Wang, Y., Hou, F., Li, H., Yang, Y., Zhang, X., Yang, Y., and Wang, Y., 2017, Effects of Ag loading on structural and photocatalytic properties of flower-like ZnO microspheres, *Appl. Surf. Sci.*, 391, 476–483.
- [32] Jia, Z., Peng, K., Li, Y., and Zhu, R., 2012, Preparation and photocatalytic performance of porous ZnO microrods loaded with Ag, *Trans. Nonferrous Met. Soc. China*, 22 (4), 873–878.
- [33] Dehdar, A., Asgari, G., Leili, M., Madrakian, T., and Seid-mohammadi, A., 2021, Step-scheme BiVO₄/WO₃ heterojunction photocatalyst under visible LED light irradiation removing 4-chlorophenol in aqueous solutions, *J. Environ. Manage.*, 297, 113338.
- [34] Matafonova, G., Philippova, N., and Batoev, V., 2011, The effect of wavelength and pH on the direct photolysis of chlorophenols by ultraviolet excilamps, *Eng. Lett.*, 19 (1), 20–23.
- [35] Kumar, T.K.M.P., Mandlimath, T.R., Sangeetha, P., Sakthivel, P., Revathi, S.K., Kumar, S.K.A., and Sahoo, S.K., 2015, Highly efficient performance of activated carbon impregnated with Ag, ZnO, and Ag/ZnO nanoparticle as antimicrobial materials, *RSC Adv.*, 5 (130), 108034–108043.

Gamma-Irradiated Bacterial Cellulose as a Three-Dimensional Scaffold for Osteogenic Differentiation of Rat Bone Marrow Stromal Cells

Farah Nurlidar^{1*}, Mime Kobayashi², Ade Lestari Yunus¹, Muhamad Yasin Yunus¹, Tita Puspitasari¹, and Darmawan Darwis¹

¹Center for Research and Technology of Isotopes and Radiation Application, The National Research and Innovation Agency, Jl. Lebak Bulus Raya No. 49, Jakarta Selatan 12440, Indonesia

²Nara Institute of Science and Technology, 8916-5 Takayama, Ikoma, Nara 630-0192, Japan

* Corresponding author:

tel: +62-21-7690709

email: farah@batan.go.id

Received: January 3, 2022

Accepted: March 20, 2022

DOI: 10.22146/ijc.71823

Abstract: The effect of gamma-irradiation on bacterial cellulose (BC) was investigated in terms of improving its properties as scaffolds for tissue engineering. BC pellicles were exposed to 25, 50, and 75 kGy gamma-ray irradiation, and X-ray diffraction analyses showed that the crystallinity of the BC decreased as stronger irradiation accelerated BC's degradation. Fourier transform infrared spectroscopy of the irradiated BC revealed the appearance of a new peak at 1724 cm⁻¹, indicating the formation of a new carbonyl group due to the cleavage of glycosidic linkages of the BC. Rat bone marrow stromal cells seeded on the gamma-irradiated BC incubated in an osteogenic medium for 14 days produced calcium, a late marker for osteogenic differentiation, as shown by Alizarin Red S (ARS) staining. Gamma-irradiated BC with higher irradiation doses showed intense ARS staining indicating higher calcium deposition. These findings demonstrate the feasibility of using gamma-irradiated BC as a cytocompatible 3D scaffold for bone tissue regeneration.

Keywords: bacterial cellulose; gamma-irradiation; Alizarin Red S staining; osteogenic differentiation; calcium deposition

■ INTRODUCTION

Hydrogels are promising cross-linked three-dimensional (3D) polymeric networks for tissue engineering because of their hydrophilic structure and ability to encapsulate cells and bioactive molecules [1-4]. In addition, the physical, chemical, and biological properties of the hydrogels can be easily tailored to support cell growth and functions [3].

Bacterial cellulose (BC) has shown promise as a 3D scaffold for stem cell encapsulation based on its high purity, high mechanical properties, and excellent biocompatibility [5-6]. BC has also been shown to be an excellent biomaterial for wound healing [5,7-8]. Despite the fact that native BC has extraordinary inherent properties, to enhance the potential of BC, various methods to improve the physical and chemical properties of native BC have been investigated [9-13]. Modified BC, hyaluronic acid, and gelatin scaffolds showed promising

results when they were used as scaffolds for a human glioblastoma cancer cell line [11]. In addition, modification of BC with the succinyl group has been shown to enhance BC's ability to incorporate bone-like hydroxyapatite [14].

Gamma irradiation has been mainly used to sterilize biomedical devices and pharmaceutical products [15-16]. However, irradiation affects the physicochemical characteristics of the irradiated substances. The degradation of polymers is one of the main negative effects [16]. At the same time, other functional properties may be improved. Criado et al. showed that gamma-irradiation of cellulose nanocrystals (CNCs) caused an increase in antioxidant properties of the materials due to the cleavage of glycosidic linkages in the CNCs [9].

The combination of BC and stem cells has the potential to be used for medical applications, especially for bone tissue regeneration. However, BC has high

crystallinity, limiting the diffusion of nutrients, oxygen, and waste, an essential property as a cell culture scaffold. Gamma-ray irradiation on the BC mainly results in the decomposition of the cellulose [9,17-18]. This process changes the physical and chemical properties of cellulose, such as mechanical properties and porosity. Darwis et al. observed that electron beam irradiation influenced the mechanical properties of dried BC that led to its degradation [19]. Previous studies have demonstrated the effect of high-energy irradiation on the degradation of BC, but few studies have evaluated the potential of gamma-irradiated BC in tissue engineering. In this study, the BC pellicle was gamma-irradiated, and changes in the physical, chemical, and thermal properties of the BC were investigated and discussed. Importantly, the effect of gamma irradiation on the cytotoxicity of the BC and its potential as a 3D scaffold for tissue engineering was also investigated.

■ EXPERIMENTAL SECTION

Materials

Ammonium sulfate, sodium hydroxide, and glacial acetic acid were purchased from Merck GmbH, Germany. Potassium bromide (KBr; FTIR grade) was acquired from Sigma-Aldrich (St. Louis, MO, USA). Water-soluble tetrazolium salt (WST-8) was obtained from Dojindo Molecular Technologies Inc. Kumamoto, Japan. All reagents were used without any additional processing.

Instrumentation

Gamma-ray irradiation was conducted in a gamma cell facility (cobalt-60; Gamma Cell 220 Upgraded, Izotop, Hungaria) at the Center for Research and Technology of Isotopes and Radiation Application (The National Research and Innovation Agency, Indonesia). X-ray diffraction (XRD) analysis was carried out with a RINT-TTR III X-ray diffractometer (Rigaku, Tokyo, Japan). Fourier transform infrared (FTIR) spectra were recorded using a Prestige-21 FTIR spectrometer (Shimadzu, Kyoto, Japan). A DSC-60 differential scanning calorimeter (DSC; Shimadzu, Kyoto, Japan) was used for thermal analysis.

Procedure

Preparation of BC

Bacterial cellulose (BC) was prepared using coconut water as a fermentation medium. Briefly, 1 L of fresh coconut water medium containing 50 g of sucrose (5% w/v) and 5 g of ammonium sulfate (0.5% w/v) was boiled. The pH of the medium was adjusted to pH 4 using glacial acetic acid. The medium was then equilibrated to room temperature prior to use. Ten percent of the pre-culture medium containing *Acetobacter xylinum* was then added into the flask containing the coconut water medium. The mixture was incubated at room temperature under static conditions for 3–4 days. The obtained BC pellicles were then washed with distilled water and immersed in 0.1 M sodium hydroxide at 60 °C for 4 h to remove any residual bacteria. Finally, the BC pellicles were rinsed with distilled water at room temperature to achieve a neutral pH. The pellicles of pure BC were then immersed in distilled water and kept at 4 °C prior to use.

Gamma-irradiation of BC

BC pellicles were placed in the polyethylene plastic bag and then irradiated in a gamma cell facility at a dose rate of 5.5 kGy/h. The irradiation doses were 0, 25, 50, and 75 kGy. After gamma-irradiation, the BC pellicles were extensively washed with distilled water to remove any soluble degradation products and freeze-dried to obtain dried BC.

XRD of gamma-irradiated BC

XRD analysis of the freeze-dried BC was carried out with an X-ray diffractometer in a 2θ range between 10° and 40° with a scanning step of 0.05°. The degree of crystallinity of the BC was evaluated by deconvolution of the XRD diffractogram after a peak-fitting process performed by Fityk 0.9.8 software [20-21]. The degree of crystallinity was calculated as the ratio of the area of crystalline peaks to the total area [20,22].

FTIR analysis of gamma-irradiated BC

FTIR spectra of the freeze-dried BC were recorded in the range of 400–4000 cm^{-1} based on the KBr method

with 45 scans and a resolution of 2 cm⁻¹. All samples were ground with KBr before measurement.

Thermal characteristics of gamma-irradiated BC

DSC was used to study the thermal characteristics of BC before and after gamma-irradiation. All DSC measurements were carried out with a crimped empty pan (aluminum pan, Shimadzu, Tokyo, Japan) as a reference. The reference and crimped pans containing samples were measured at the heating rate of 15 °C/min under a nitrogen atmosphere at a temperature range of 30–500 °C.

Cytotoxicity of gamma-irradiated BC

HeLa cells were cultured in an alpha-minimum essential medium (alpha-MEM; Gibco Invitrogen Corp. Grand Island, NY, USA) containing 10% fetal calf serum (FCS; HyClone, Logan, UT, USA) and cultured in a 25 cm² tissue culture flask (163371; Nalge Nunc International, Roskilde, Denmark) at 37 °C under 5% CO₂. After three days, the attached cells were washed with PBS and treated with an aliquot of 0.02% ethylenediaminetetraacetic acid (EDTA) and 0.25% trypsin. After centrifugation at 1,200 rpm for 5 min, the supernatant was removed, and the cell pellet was suspended in 10% FCS/alphaMEM. The HeLa cell suspension was then prepared at a density of 25,000 cells/mL.

One hundred microliters of cell suspension containing 2,500 cells were cultured in wells of a 96-well plate (Nunc, Denmark) and incubated for 24 h at 37 °C under 5% CO₂. After 24 h, gamma-irradiated BC was added into well-containing cells. The same number of cells without any addition of the BC was used as a 2D control. According to the manufacturer's instructions, the viable cells on days 1 and 2 were quantified using WST-8 reagent. The optical density at 450 nm was measured using a SpectraFluor Plus microplate reader (Tecan, Männedorf, Switzerland). The relative cell viability was calculated, as defined by Eq. (1):

$$\text{Cell viability (\%)} = \frac{(\text{OD}_{450} \text{ sample} - \text{OD}_{450} \text{ medium})}{(\text{OD}_{450} \text{ control} - \text{OD}_{450} \text{ medium})} \times 100\% \quad (1)$$

Encapsulation of rat bone marrow stromal cells on gamma-irradiated BC

Bone marrow cells (BMCs) were harvested from the femora of a six-week-old female Wistar rat. The obtained

rBMSCs were suspended in 20% FCS/alpha-MEM and cultured in an 80 cm² tissue culture flask (153732; Nalge Nunc International) at 37 °C under 5% CO₂ atmosphere. After three days, the attached cells were washed with PBS and treated with an aliquot of 0.02% EDTA and 0.25% trypsin. After centrifugation at 1,200 rpm for 5 min, the supernatant was removed, and the cell pellet was re-suspended in 10% FCS/alpha-MEM. The rBMSC suspension was prepared at a density of 5 × 10⁶ cells/mL. The gamma-irradiated BC scaffolds were put on 24 well-plate. The rBMSC suspension was then seeded on the BC scaffolds at a density of 5 × 10⁴ cells/scaffold and incubated at 37 °C under 5% CO₂. After three hours, 1 mL of medium was added to the dish containing the scaffold. On day 1, the medium was supplemented with an osteogenic supplement of 10 nM dexamethasone, 100 μM L-ascorbic acid-2-phosphate, and 10 mM beta-glycerophosphate, and incubated at 37 °C under 5% CO₂ atmosphere for 14 days. Half of the medium was replaced with a fresh osteogenic medium every two or three days.

The osteogenic differentiation of the rBMSCs in the scaffold was observed using Alizarin Red S (ARS) staining. The BC containing rBMSCs were washed three times with demineralized water and freeze-dried. The dried BC was then incubated in 2% of ARS staining solution for 30 min at room temperature. The BC was then washed four times with demineralized water to remove the excess stain, dried at room temperature, and observed with an optical microscope.

Statistical analysis

All statistical analyses were carried out using the one-way analysis of the variance routine of KaleidaGraph v. 4.5 (Synergy Software, Reading, PA, USA). Tukey's honest significant difference test was used to determine whether or not there were any differences between groups. A value of $p < 0.05$ was accepted as statistically significant. All data were expressed as mean ± standard deviation, with $n = 3$.

RESULTS AND DISCUSSION

XRD Analysis of Gamma-Irradiated BC

XRD analysis was conducted to investigate the influence of gamma-irradiation on the microstructures

of the BC. XRD diffractograms of BC before and after gamma-irradiation showed three main peaks located at $2\theta = 14.4^\circ$, 16.7° , and 22.6° (Fig. 1), which correspond to the $(1\bar{1}0)$, (110) , and (200) plane of cellulose I β , respectively [23-24]. These results are consistent with previous reports of BC production using the static culture method [25].

The degree of crystallinity of the BC was evaluated using the XRD deconvolution method [22]. An example of an XRD diffractogram after a curve fitting process using a Gaussian function is presented in Fig. 2. One amorphous and five crystalline peaks are observed in the XRD deconvolution spectra of BC and gamma-irradiated

BC. Table 1 shows the degree of crystallinity of the gamma-irradiated and native BC. The degree of crystallinity of BC irradiated at 25, 50, and 75 kGy shows a significant decrement compared to native BC ($p < 0.001$). This study revealed that the crystalline area of the BC was disrupted by the gamma irradiation. Similar results have shown that the crystallinity of cellulose was reduced significantly after high-energy radiation [26-27].

FTIR of Gamma-Irradiated BC

FTIR measurement was conducted to observe the influence of gamma-irradiation on the chemical structure

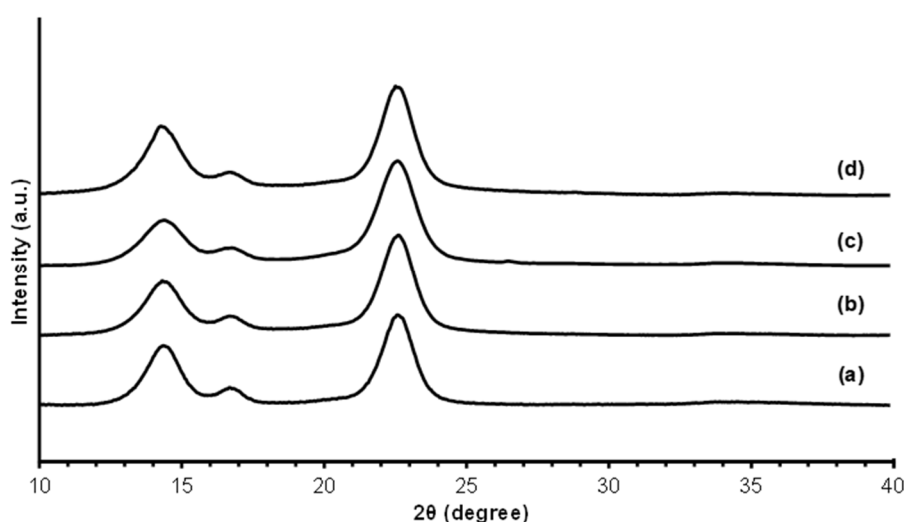


Fig 1. XRD diffraction patterns of native BC (a) and gamma-irradiated BC at 25 (b), 50 (c), and 75 (d) kGy

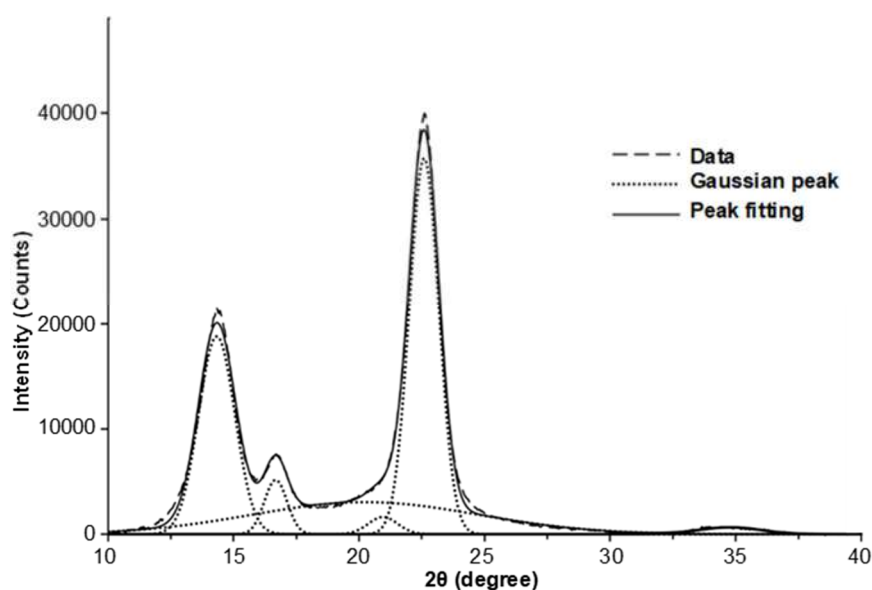


Fig 2. XRD deconvolution peak using a Gaussian function of gamma-irradiated BC 25 kGy with an R^2 value of 0.99766

Table 1. Degree of crystallinity of gamma-irradiated BC ($p < 0.001$)

Irradiation dose (kGy)	Degree of crystallinity (%)
0	82.16 ± 0.73
25	74.21 ± 2.81
50	72.17 ± 0.26
75	64.51 ± 2.65

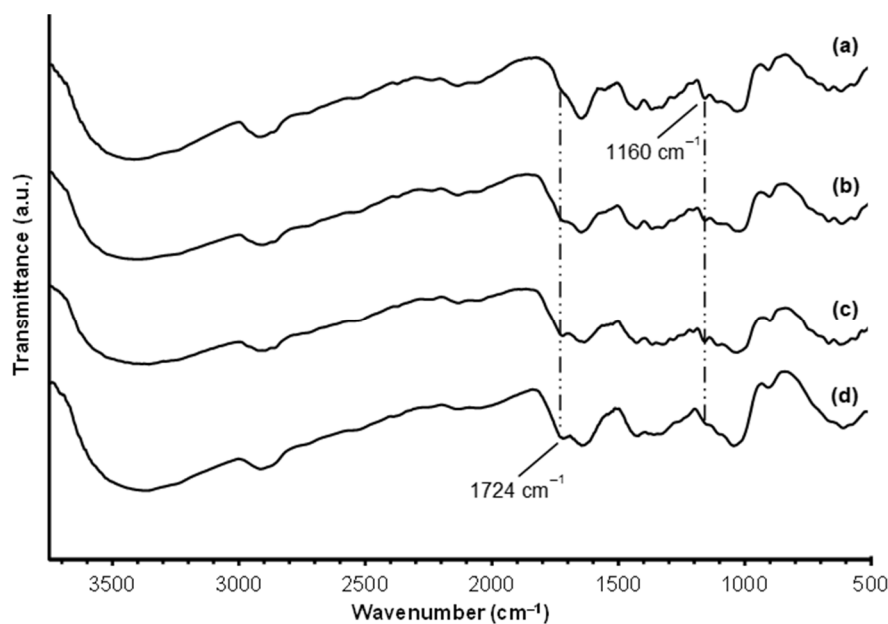
of the BC. Fig. 3 shows the FTIR spectra of BC before and after gamma irradiation. From the spectra, we can see the appearance of a new peak at 1724 cm^{-1} , which correlated to the formation of a new carbonyl group in the gamma-irradiated BC, similar to previous research [9,17-18,27]. It can also be seen from Fig. 3 that the intensity of the peak at 1724 cm^{-1} increased as the irradiation dose increased. In addition, Fig. 3 also shows the disappearance of the peak at 1160 cm^{-1} that correlated to the stretching vibration of the C–O–C glycosidic linkage in the BC structure.

Many authors reported that gamma-irradiation led to cleavage of the glycosidic linkage and the formation of carbonyl groups in the cellulose structure [9,17-18,27]. Bouchard et al. also reported a linear relationship between carbonyl concentration and the irradiation doses [18]. This study confirmed that gamma-irradiation might cause

the breakage of glycosidic linkage and the formation of the carbonyl group in the BC structure.

Thermal Behavior of Gamma Irradiated BC

Thermal properties of the native and gamma-irradiated BC were investigated by DSC, and the results are presented in Fig. 4. The exothermic peak of gamma-irradiated BC at 0, 25, 50, and 75 kGy were 358.57 , 330.12 , 324.50 , and $322.77 \text{ }^\circ\text{C}$, respectively. These peaks indicate the thermal decomposition of the BC [25,28]. The results showed that the degradation temperature of native BC (0 kGy) is higher than that of the gamma-irradiated BC. The decrease in the degradation temperature of the gamma-irradiated BC could be attributed to the radiation-induced degradation of the polymer chains in the BC. It can also be associated with the cleavage of the glycosidic linkage in the BC structure, as confirmed by the FTIR results. Furthermore, it is well known that the degradation induced by high-energy irradiation may destroy the structure of BC. Thus, the irradiation may have enhanced the amorphous peak in the BC structure, as indicated by the XRD results. These results implicated that irradiation doses have a significant contribution to the physical and chemical properties of the BC.

**Fig 3.** FTIR spectra of gamma-irradiated BC at 0 (a), 25 (b), 50 (c), and 75 (d) kGy

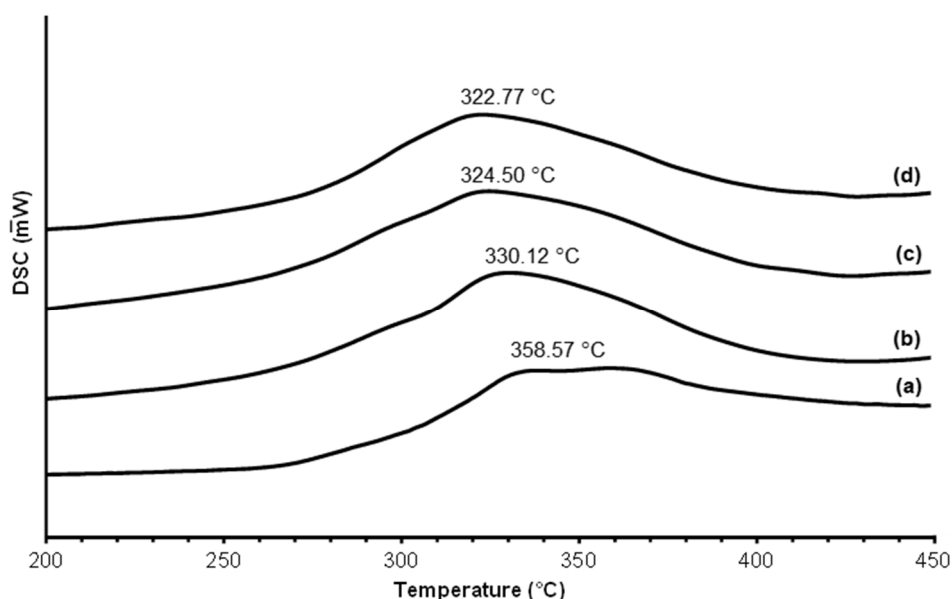


Fig 4. DSC spectra of BC irradiated with 0 (a), 25 (b), 50 (c), and 75 (d) kGy

Cytotoxicity Assay of Gamma-Irradiated BC

Cytotoxicity is an important characteristic of a material intended for biomedical applications. Cytotoxicity test of the gamma-irradiated BC was conducted using HeLa cells and the WST-8 assay, which is based on the conversion of a water-soluble tetrazolium salt to a water-soluble formazan dye upon reduction by dehydrogenases in the presence of an electron carrier [29].

The WST-8 assay of the adherent cell in the presence of the gamma-irradiated BC demonstrated low viability of the adherent cells after 24 h of incubation (Fig. 5). However, after 48 h of incubation, the adherent cells showed improved cell viability compared to those on day 1, indicating no cytotoxic effects of gamma-irradiated BC for cell proliferation. A previous report showed that the BC scaffold did not show any toxicity effect on BMSCs, while it increased cell viability [30].

Osteogenic Differentiation of rBMSCs on Gamma-Irradiated BC

To evaluate the potential of gamma-irradiated BC as a 3D scaffold for bone tissue regeneration, rBMSCs were seeded on BC scaffolds and incubated for 14 days in the presence of an osteogenic medium. The osteogenic differentiation of the rBMSCs was then evaluated by assessing calcium deposition on irradiated BC by ARS

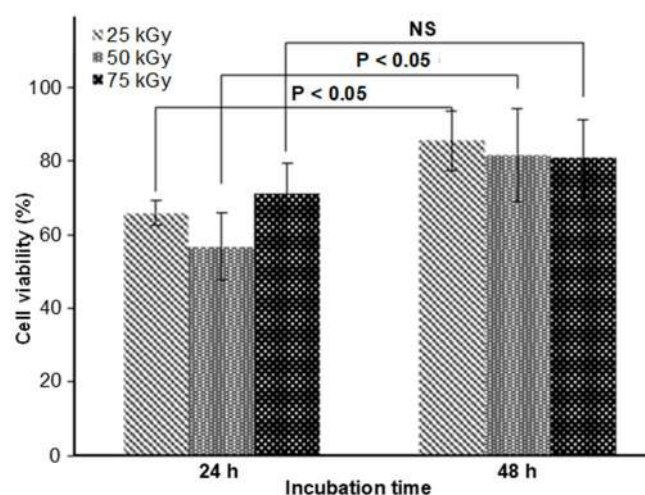


Fig 5. Cytotoxicity assay of gamma-irradiated BC against HeLa Cells. NS = not significant

staining. ARS compound reacts with calcium ions to form an ARS-calcium complex in a chelation process [30].

After 14 days of incubation, ARS staining revealed that BC scaffolds with higher irradiation doses showed intense staining indicating higher calcium deposition (Fig. 6). The difference in the ARS staining of the gamma-irradiated BC is probably due to the change of crystallinity of the BC caused by gamma irradiation, as confirmed by the XRD results. A previous report showed that the amorphous poly(caprolactone-co-glycolide) (PCL/PGA)

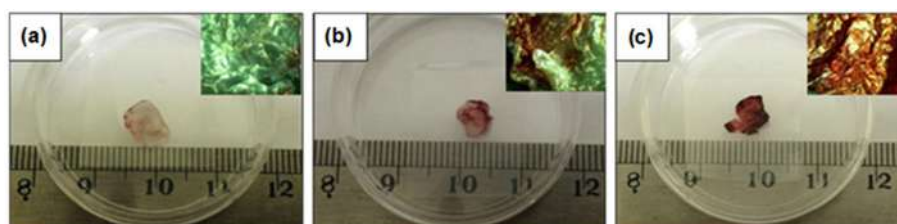


Fig 6. ARS staining of rBMSCs cultured on gamma-irradiated BC. BC pellicles exposed to 25 (a), 50 (b), or 75 (c) kGy of gamma irradiation were used

scaffold was significantly efficient in supporting osteoblast growth compared to highly crystalline and rigid PCL and PGA scaffolds [31]. However, it is not fully understood how crystallinity affects stem cell behavior [32]. Another possibility is from the increase of the carbonyl group in the gamma-irradiated BC, as confirmed by the FTIR measurement. The FTIR spectra showed that the intensities of the carbonyl peak of gamma-irradiated BC increased with increasing irradiation dose. It has already been known that functional groups of the scaffold may affect cell behaviors [33]. Carboxylic acid and carbonyl groups on the surface of PLGA/HA matrices containing graphene oxide improved bioactivity and osteogenic differentiation of MC3T3-E1 cells encapsulated in the matrices [34].

This study revealed that gamma-irradiated BC supported osteogenic differentiation of rBMSCs, as shown by ARS staining. However, the biodegradation properties and *in vitro* cell behavior inside the gamma-irradiated BC were not used in this study to investigate the basic characterization in terms of the application of gamma-irradiated BC as 3D scaffolds for tissue regeneration, which is the next step we need to investigate.

■ CONCLUSION

Our findings show that gamma-irradiation has a significant effect on the physical, chemical, and thermal properties of BC, as confirmed by FTIR, XRD, and DSC analyses. ARS staining demonstrated that rBMSCs seeded on gamma-irradiated BC and incubated in an osteogenic medium for 14 days produce calcium as a late marker for osteogenic differentiation. Higher irradiation doses of gamma-irradiated BC showed intense ARS staining, indicating higher calcium deposition. These findings show that gamma-irradiation can be used to create a

cytocompatible 3D scaffold for tissue engineering. An additional investigation should be conducted to further analyze interactions between cells and gamma-irradiated BC.

■ ACKNOWLEDGMENTS

This research was supported in part by the NAIST global collaboration project (FY2016-2018) funded by MEXT, Japan, and DIPA (2019) from the Center for Research of Radiation Processing Technology, National Nuclear Energy Agency. In addition, we thank Shohei Katao for his assistance in XRD measurements.

■ REFERENCES

- [1] Caliari, S.R., and Burdick, J.A., 2016, A practical guide to hydrogels for cell culture, *Nat. Methods*, 13 (5), 405–414.
- [2] Choe, G., Park, J., Park, H., and Lee, J.Y., 2018, Hydrogel biomaterials for stem cell microencapsulation, *Polymers*, 10 (9), 1–17.
- [3] Li, X., Sun, Q., Li, Q., Kawazoe, N., and Chen, G., 2018, Functional hydrogels with tunable structures and properties for tissue engineering applications, *Front. Chem.*, 6, 499.
- [4] Torgbo, S., and Sukyai, P., 2018, Bacterial cellulose-based scaffold materials for bone tissue engineering, *Appl. Mater. Today*, 11, 34–49.
- [5] Pang, M., Huang, Y., Meng, F., Zhuang, Y., Liu, H., Du, M., Ma, Q., Wang, Q., Chen, Z., Chen, L., Cai, T., and Cai, Y., 2020, Application of bacterial cellulose in skin and bone tissue engineering, *Eur. Polym. J.*, 122, 109365.
- [6] Hickey, R.J., and Pelling, A.E., 2019, Cellulose biomaterials for tissue engineering, *Front. Bioeng. Biotechnol.*, 7, 45.

- [7] Portela, R., Leal, C.R., Almeida, P.L., and Sobral, R.G., 2019, Bacterial cellulose: A versatile biopolymer for wound dressing applications, *Microb. Biotechnol.*, 12 (4), 586–610.
- [8] Cherng, J.H., Chou, S.C., Chen, C.L., Wang, Y.W., Chang, S.J., Fan, G.Y., Leung, F.S., and Meng, E., 2021, Bacterial cellulose as a potential bio-scaffold for effective re-epithelialization therapy, *Pharmaceutics*, 13 (10), 1592.
- [9] Criado, P., Frascini, C., Jamshidian, M., Salmieri, S., Safrany, A., and Lacroix, M., 2017, Gamma-irradiation of cellulose nanocrystals (CNCs): Investigation of physicochemical and antioxidant properties, *Cellulose*, 24 (5), 2111–2124.
- [10] Gorgieva, S., and Trček, J., 2019, Bacterial cellulose: Production, modification and perspectives in biomedical applications, *Nanomaterials*, 9 (10), 1352.
- [11] Unal, S., Arslan, S., Yilmaz, B.K., Oktar, F.N., Sengil, A.Z., and Gunduz, O., 2021, Production and characterization of bacterial cellulose scaffold and its modification with hyaluronic acid and gelatin for glioblastoma cell culture, *Cellulose*, 28 (1), 117–132.
- [12] Bayir, E., Bilgi, E., Hames, E.E., and Sendemir, A., 2019, Production of hydroxyapatite–bacterial cellulose composite scaffolds with enhanced pore diameters for bone tissue engineering applications, *Cellulose*, 26 (18), 9803–9817.
- [13] Popa, L., Ghica, M.V., Tudoroiu, E.E., Ionescu, D.G., and Dinu-Pîrvu, C.E., 2022, Bacterial cellulose–A remarkable polymer as a source for biomaterials tailoring, *Materials*, 15 (3), 1054.
- [14] Nurlidar, F., and Kobayashi, M., 2019, Succinylated bacterial cellulose induce carbonated hydroxyapatite eposition in a solution mimicking body fluid, *Indones. J. Chem.*, 19 (4), 858–864.
- [15] da Silva Aquino, K.A., 2012, "Sterilization by Gamma Irradiation" in *Gamma Radiation*, Eds. Adrovic, F., IntechOpen, Rijeka, Croatia.
- [16] Pérez Davila, S., González Rodríguez, L., Chiussi, S., Serra, J., and González, P., 2021, How to sterilize polylactic acid based medical devices?, *Polymers*, 13 (13), 2115.
- [17] Baccaro, S., Carewska, M., Casieri, C., Cemmi, A., and Lepore, A., 2013, Structure modifications and interaction with moisture in γ -irradiated pure cellulose by thermal analysis and infrared spectroscopy, *Polym. Degrad. Stab.*, 98 (10), 2005–2010.
- [18] Bouchard, J., Méthot, M., and Jordan, B., 2006, The effects of ionizing radiation on the cellulose of woodfree paper, *Cellulose*, 13 (5), 601–610.
- [19] Darwis, D., Khusniya, T., Hardiningsih, L., Nurlidar, F., and Winarno, H., 2012, In-vitro degradation behaviour of irradiated bacterial cellulose membrane, *Atom Indones.*, 38 (2), 78–82.
- [20] Ferro, M., Mannu, A., Panzeri, W., Theeuwes, C.H.J., and Mele, A., 2020, An integrated approach to optimizing cellulose mercerization, *Polymers*, 12 (7), 1559.
- [21] Wojdyr, M., 2010, Fityk: A general-purpose peak fitting program, *J. Appl. Crystallogr.*, 43 (5-1), 1126–1128.
- [22] Park, S., Baker, J.O., Himmel, M.E., Parilla, P.A., and Johnson, D.K., 2010, Cellulose crystallinity index: Measurement techniques and their impact on interpreting cellulase performance, *Biotechnol. Biofuels*, 3 (1), 10.
- [23] Wada, M., Sugiyama, J., and Okano, T., 1993, Native celluloses on the basis of two crystalline phase (I α /I β) system, *J. Appl. Polym. Sci.*, 49 (8), 1491–1496.
- [24] Ju, X., Bowden, M., Brown, E.E., and Zhang, X., 2015, An improved X-ray diffraction method for cellulose crystallinity measurement, *Carbohydr. Polym.*, 123, 476–481.
- [25] Luo, H., Li, W., Yang, Z., Ao, H., Xiong, G., Zhu, Y., Tu, J., and Wan, Y., 2018, Preparation of oriented bacterial cellulose nanofibers by flowing medium-assisted biosynthesis and influence of flowing velocity, *J. Polym. Eng.*, 38 (3), 299–305.
- [26] Eo, M.Y., Fan, H., Cho, Y.J., Kim, S.M., and Lee, S.K., 2016, Cellulose membrane as a biomaterial: From hydrolysis to depolymerization with electron beam, *Biomater. Res.*, 20 (1), 16.
- [27] Liu, Y., Chen, J., Wu, X., Wang, K., Su, X., Chen, L., Zhou, H., and Xiong, X., 2015, Insights into the effects of γ -irradiation on the microstructure, thermal stability and irradiation-derived

- degradation components of microcrystalline cellulose (MCC), *RSC Adv.*, 5 (43), 34353–34363.
- [28] Soares, S., Camino, G., and Levchik, S., 1995, Comparative study of the thermal decomposition of pure cellulose and pulp paper, *Polym. Degrad. Stab.*, 49 (2), 275–283.
- [29] Chamchoy, K., Pakotiprapha, D., Pumirat, P., Leartsakulpanich, U., and Boonyuen, U., 2019, Application of WST-8 based colorimetric NAD(P)H detection for quantitative dehydrogenase assays, *BMC Biochem.*, 20 (1), 4.
- [30] Vadaye Kheiry, E., Parivar, K., Baharara, J., Fazly Bazzaz, B.S., and Iranbakhsh, A., 2018, The osteogenesis of bacterial cellulose scaffold loaded with fisetin, *Iran. J. Basic Med. Sci.*, 21 (9), 965–971.
- [31] Cui, H., and Sinko, P.J., 2012, The role of crystallinity on differential attachment/proliferation of osteoblasts and fibroblasts on poly (caprolactone-co-glycolide) polymeric surfaces, *Front. Mater. Sci.*, 6 (1), 47–59.
- [32] Kaivosoja, E., Barreto, G., Levón, K., Virtanen, S., Ainola, M., and Konttinen, Y.T., 2012, Chemical and physical properties of regenerative medicine materials controlling stem cell fate, *Ann. Med.*, 44 (7), 635–650.
- [33] Klecker, C., and Nair, L.S., 2017, "Matrix Chemistry Controlling Stem Cell Behavior" in *Biology and Engineering of Stem Cell Niches*, Eds. Vishwakarma, A., and Karp, J.M., Academic Press, Boston, US, 195–213.
- [34] Fu, C., Bai, H., Zhu, J., Niu, Z., Wang, Y., Li, J., Yang, X., and Bai, Y., 2017, Enhanced cell proliferation and osteogenic differentiation in electrospun PLGA/hydroxyapatite nanofibre scaffolds incorporated with graphene oxide, *PLoS One*, 12 (11), e0188352.

Effect of Calcium Carbonate Content on the Mechanical and Thermal Properties of Chitosan-Coated Poly(urethane) Foams

Elvi Kustiyah, Achmad Nandang Roziyanto, Majid Amrullah,
Dedi Priadi, and Mochamad Chalid*

Department of Metallurgical and Material Engineering, Faculty of Engineering, Universitas Indonesia, Depok 16424, Indonesia

* **Corresponding author:**

tel: +62-81384360765

email: chalid@metal.ui.ac.id

Received: January 11, 2022

Accepted: May 13, 2022

DOI: 10.22146/ijc.72135

Abstract: In this work, the effect of chitosan and CaCO_3 coating on polyurethane (PU) foam on the mechanical and thermal properties was studied. PU-foams were soaked in a mixture of chitosan- calcium carbonate solution at different concentrations, i.e., 0.1–0.4%. The molecular behaviors due to the incorporation of chitosan/ CaCO_3 into the PU-foam matrix were investigated by Fourier-Transform Infrared (FTIR) spectroscopy. Field Emission Scanning Electron Microscope (FE-SEM) was utilized to study the effect of chitosan/ CaCO_3 coat on the pore structure of PU-foam. FTIR spectra show changes in the peak of 1446 and 1413 cm^{-1} , which serve as evidence of molecular interaction between PU and chitosan/ CaCO_3 . FE-SEM images show that the addition of chitosan/calcium carbonate cells was starting to close together, probably due to the increased dispersion of calcium carbonate on the entire surface of PU-foams/chitosan, which indicates that reducing the size of the cell will increase mechanical properties. From this study, it was found that PU-foam soaked in 0.4% CaCO_3 had the highest tensile strength. Coating PU-foam with 0.4% CaCO_3 also improved its thermal stability, indicated by an increase in its residual mass compared to neat PU-foam.

Keywords: coating; polyurethane; chitosan; calcium carbonate

■ INTRODUCTION

Polyurethane (PU) foams are polymers formed by a reaction between the hydroxyl group of polyol and the polyisocyanate functional group, which has a highly cross-linked three-dimensional closed-cell structure. PU-foams are highly porous, making this material have low density, high energy absorption capabilities, and low thermal conductivity. Because of the low density, good mechanical properties, high energy absorption capabilities, and low thermal conductivity, PU-foams have been used in furniture, bedding, carpet underlay, packaging, and automotive [1].

Automotive applications have shown great attention to the thermal insulation properties of the materials used in the interior design of vehicles, such as headliners. The characteristics of material required for headliners are high rigidity, good thermal insulation, and sufficient thermal stability [2]. PU-foams consist of a soft segment and a hard segment. PU-foams soft segments are usually

composed of polyols with a relatively low glass transition temperature, whereas hard segments are generally composed of diisocyanates with a relatively high glass transition temperature [3]. PU-foams are used for crash pads, mattresses, packaging, and automotive interior. The thermal stability of PU-foams is influenced strongly by their chemical and physical properties. Highly porous PU-foams tend to have less rigidity and low thermal stability [4]. The porous structure of PU-foam can provide better insulation properties against heat. Moreover, their lower thermal conductivity is a highly desired property in automotive applications. However, their porous structure makes PU-foams become less rigid and has low thermal stability. Surface modification of PU-foams on coating can increase their rigidity and thermal stability [5].

Chitosan is a deacetylate chitin product and a polysaccharide randomly substituted D-glucosamine and N-acetyl-D-glucosamine in β -(1-4) linkage and the

second most abundant natural-based biopolymer after cellulose [6]. D-glucosamine monomer is a rigid unit that makes it potential material for surface coating, and on the other hand, it can increase its crystallinity [7]. Chitosan has been used as a material that can improve polymers' mechanical and thermal properties and diminish their strength to absorb water [8]. The modification of the PU surface to get PU properties both thermally and mechanically by combining PU with chitosan has been studied by Kara et al. [5]. The reaction of chitosan coating to PU showed better compatibility and tensile properties in PU-foams. Previous research using chitosan coating to increase the performance of PU-foam chitosan has been carried out by Centenaro et al., which explained that coated chitosan in PU-foam for absorbent applications gave an excellent performance and was able to reduce costs, but in this study not observed the improvement of the mechanical properties of coated PU-foam [9]. Carosio et al. have studied chitosan-PU foam on cellulose nanofibrils layer products for flame retardant applications. Chitosan coating and the addition of nanofibril cellulose reduce the combustion rate by up to 30%, but the mechanical properties are still not studied [10].

Furthermore, some researchers add inorganic material, such as clay [6], to increase the mechanical and thermal properties of PU. The other inorganic material used is calcium carbonate which is cost-effective and easy to obtain. It has also been widely used as surface coating and applied in the plastic composite industry to improve its thermal properties and rigidity. Researchers have investigated the effect of adding calcium carbonate and chitosan onto polycaprolactone and enhancing the thermal and mechanical properties [11]. Many studies investigated the advantages of blending calcium carbonate into polymers. However, its agglomeration enormously decreases the composite's physical properties, limiting its applications [12]. Conventional surface modification by solution coating can involve interactions between chitosan with calcium carbonate to induce the calcium carbonate's nucleation on the chitosan-coated surfaces [13]. This research aimed to study the effect of adding calcium carbonate in the PU-

foams/chitosan coating to increase the thermal stability of PU-foams.

■ EXPERIMENTAL SECTION

Materials

The PU-foams materials with a density of 16 kg/m³ were produced by Inoac Polytecno Indonesia with the formula composed of polyols, isocyanates, catalyst, blowing agent, and some other additives. Chitosan powder material was obtained from Marine Natural Product, Ltd., Indonesia. Acetic acid with a purity of 99.98% was obtained from Sigma Aldrich.

Instrumentation

Fourier transform infrared (FTIR) analysis

The composite products were characterized using FTIR Perkin Elmer 90325 (Perkin Elmer Inc., Waltham, MA, USA) to study functional groups of molecules in the PU-foams, PU-foams/chitosan, and PU-foams/chitosan/calcium carbonate with various concentrations of calcium carbonate. FTIR spectral analysis was performed within the wavenumber range of 500–4000 cm⁻¹ and 30 scans.

Field emission-scanning electron microscope (FE-SEM)

The effect of calcium carbonate and chitosan coating on PU-foam surfaces was investigated by characterizing the composite products' morphology. The morphology observation was carried out using FE-SEM FEI Inspect F50 (FEI Company, Hillsboro, Oregon, USA).

Thermogravimetric analysis (TGA)

The coated PU thermal degradation behavior was recorded using thermogravimetric analyzer STA PerkinElmer STA6000 (PerkinElmer Inc., Waltham, MA, USA), N₂ gas atmosphere, from 40 °C to 500 °C with a heating rate of 10 °C/min.

Procedure

Preparation of coated PU-foams

In the preparation of the coating solution in Fig. 1, chitosan and calcium carbonate were diluted with 5% acetic acid. Chitosan with a concentration of 4% by weight

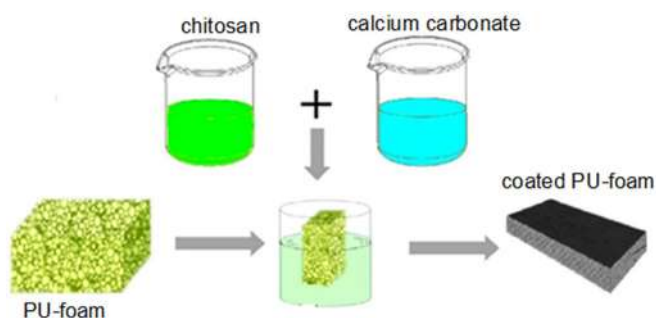


Fig 1. Schematic description of the process preparation of coated PU-foams. Chitosan solution and calcium carbonate were mixed in controlled conditions, then PU-foams cubes were immersed until completely covered

and calcium carbonate concentration ranging from 0.1 to 0.3% by weight are added together, and then the solution is stirred at a temperature of 75 °C until homogeneous. Furthermore, PU-foams were immersed in the solution for 3 min and exposed to air for a few moments. The results were then dried in an oven at 60 °C for 60 min and then cured at 120 °C for 90 min.

■ RESULTS AND DISCUSSION

Molecular Interaction in Coating

The FTIR analysis confirmed distinct groups of PU-foams, chitosan groups, and intermolecular O–H bond groups due to the coating reaction. The groups confirmed to be present before the reaction, namely neat PU-foams, are N–H and C=O, while the FTIR spectrum from the chitosan will be ascertained as hydroxyl, methyl, primary amide, and glycoside [14]. Meanwhile, after the coating reaction occurs, a new group appears, namely the intermolecular hydrogen bond between –O from PU and –H from chitosan, at wavenumbers of 3200–2700 cm^{-1} [15].

Fig. 2 shows a vibrational area characteristic of the urethane group at 2868–3280 cm^{-1} , which is the N–H group region, and the wavenumber of 1640–1718 cm^{-1} corresponding to the C=O group stretching vibration. These test results were in line with the research results by Chalid et al. [16]. Chitosan FTIR spectrum peak has strong and broad at a wavenumber of 3359 cm^{-1} , indicating the presence of O–H that overlaps with the N–H group. Meanwhile, the wavenumber of 1637, 1561, and 1375 cm^{-1}

show groups of C=O stretching (primary amide), N–H bending (secondary amide), and C–N (tertiary amide) stretching vibrations, and a weak intensity signal that is a characteristic of the hydrogen bond between O and H [17]. The FTIR results of chitosan-coated PU (Fig. 2) indicate the possibility of the overlapping between characteristic peaks of PU-foams and chitosan structure. A band at 3280 cm^{-1} and 1072 cm^{-1} related to the –NH₂ and –OH groups of chitosan, respectively [9].

After PU-foams were coated with chitosan, the result indicated increasing properties by producing intermolecular hydrogen bonds. Furthermore, calcium carbonate is added as a reinforcing additive in PU-foams/chitosan. With this addition, it is expected that its mechanical properties to increase. The compatibility between carbonate groups of calcium carbonate with PU-foams/chitosan with carbonate ions was determined and characterized using FTIR. Carbonate groups in the FTIR spectrum will appear at wavenumbers around 1446 and 1413 cm^{-1} , which is the vibrations of the bending O–H group, according to the report by Reig et al. [18]. This was demonstrated by the presence of these

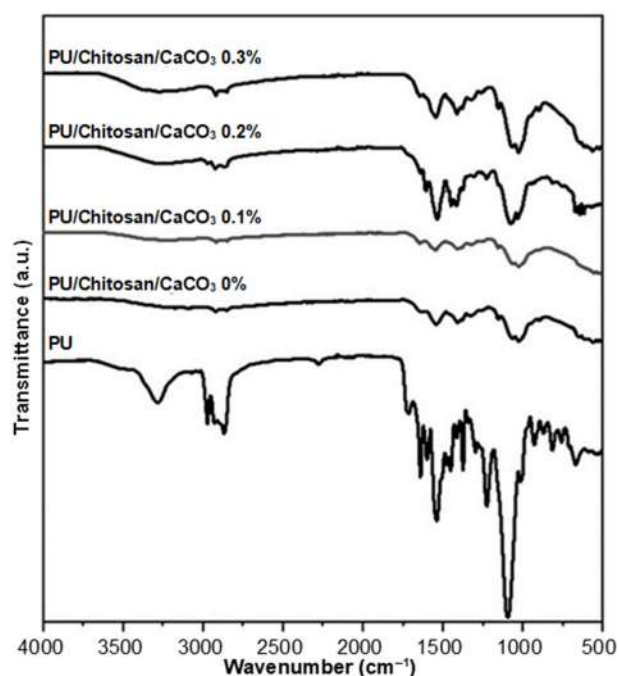


Fig 2. FTIR spectrum of PU-foams, PU-foams/chitosan, and PU-foams/chitosan/calcium carbonate with various concentrations of calcium carbonate

OH groups in all PU/chitosan/calcium carbonate spectrum. The results also explained that there was no shift from the peak of the N-H group and the C=O group by adding calcium carbonate because calcium carbonate was only deposited on the surface of PU-foams, and there was no chemical reaction to form new compounds. It was in accordance with research conducted by Dinararum et al. [19]. Fig. 3 shows the possible interaction between PU-foams, chitosan, and calcium carbonate. From FTIR results, the possible hydrogen bond was between H from chitosan and O from PU-foams and O from carbonyl groups in calcium carbonate with H from hydroxyl groups in chitosan.

Morphological Behavior of Coating

Characterization was then carried out using FE-SEM to understand the details of the coating mechanism and compatibility in PU-foams/chitosan coating materials and the effect of adding calcium carbonate. The presence of solid chitosan particles in the PU-foams matrix network affected PU-foam's morphology. A study showed that chitosan's presence affected PU-foams' porosity and surface roughness [20].

Fig. 4(a) showed the 250× magnification result for PU-foams having a stretchy and porous surface. The resulting pores had a large size and were open cells. Furthermore, PU-foams were coated with chitosan, resulting in a cell structure shown in Fig. 4(b). The pore size was smaller compared to PU-foams without chitosan coating. The addition of calcium carbonate to PU-foams/chitosan affected the cell structure, as shown in Fig. 4(c). The cells were starting to close together, probably

due to the increased dispersion of calcium carbonate on the entire surface of PU-foams/chitosan.

The addition of calcium carbonate in PU-foams/chitosan was analyzed (Fig. 5). The various concentrations of calcium carbonate aimed to optimize calcium carbonate concentrations that give the desired results. The SEM results of neat PU-foams, PU-foams/chitosan, and PU-foams/chitosan/calcium carbonate can be seen in Fig. 5. It was shown that the addition of calcium carbonate could reduce the size of the cell. The shape of the structure was also tidier and more uniform than PU-foams because the addition of inorganic material increased the bulk viscosity so that it could resist cell growth. This result was in accordance with the research conducted by Chuayjuljit et al. [21].

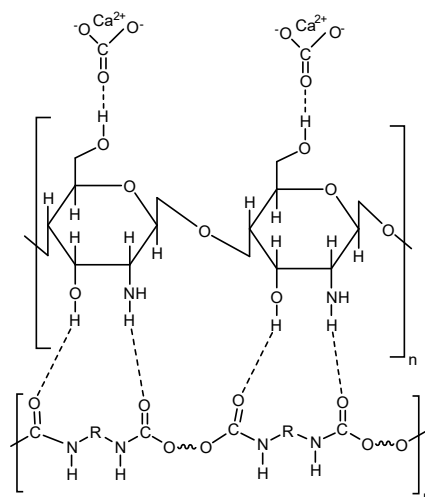


Fig 3. Proposed intermolecular hydrogen bond interactions between the PU-foam-chitosan and chitosan-calcium carbonate

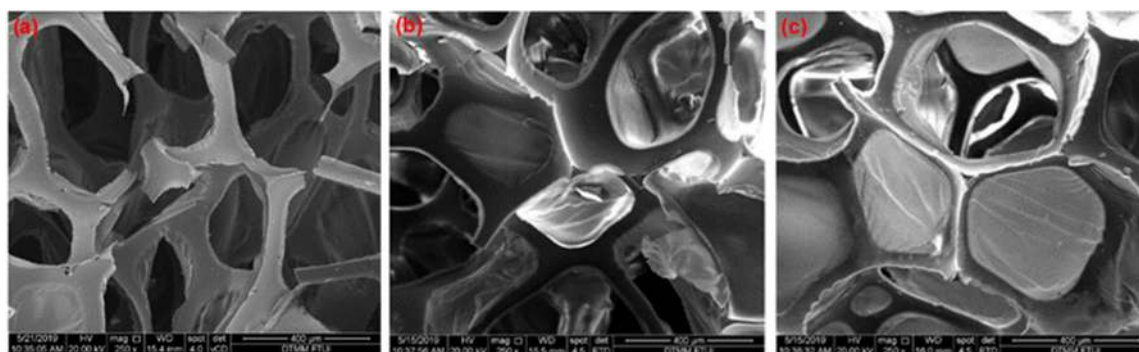


Fig 4. Comparison of morphology (a) PU-foams, (b) PU-foams/chitosan, and (c) 0.1% calcium carbonate in PU-foams/chitosan with a magnification of 250×

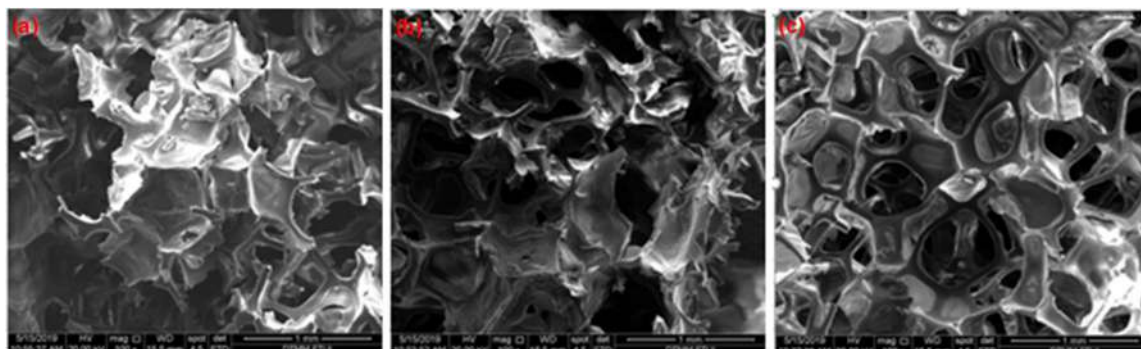


Fig 5. Morphological comparison of (a) 0.1%, (b) 0.2%, and (c) 0.3% calcium carbonate in PU-foams/chitosan with a magnification of 250×

Thermal Behavior of Coating

Thermogravimetric analysis (TGA) of coated PU samples was analyzed to observe the effect of coating on PU-foams' thermal stability in a nitrogen gas atmosphere at the heating rate of 10 °C/min. TGA and derivative thermogravimetric DTG curves obtained for PU-foams, PU-foams/chitosan, and PU-foams/chitosan/calcium carbonate were represented in Fig. 6. They corresponded to the sample's weight loss upon continuous heating to 500 °C. It was clarified from the TGA thermograms and data in the summarized table that the thermal stability of the PUs sample was slightly raised after being coated with calcium carbonate. This enhanced thermal stability was due to the homogenous calcium carbonate coating on the surface of PU, as shown in SEM images. This increase in

decomposition temperature indicated increased PU-foams/chitosan/calcium carbonate's thermal stability.

TGA results for PU-foams/chitosan and PU-foams/chitosan/calcium carbonate had an initial weight loss below 100 °C regardless of their water content. The initial change was ascribed to the vaporization of water because of the chitosan's hydrophilic character and the remaining solvent used to dilute chitosan and calcium carbonate. TGA results showed that all the PUs samples showed two-step degradation, with the initial step degradation appearing in the range of 200–340 °C and the subsequent step degradation occurring at 320–430 °C. The first degradation step was known as the initial degradation temperature (T^{d1}), where the degradation temperature of all samples occurred at temperatures of

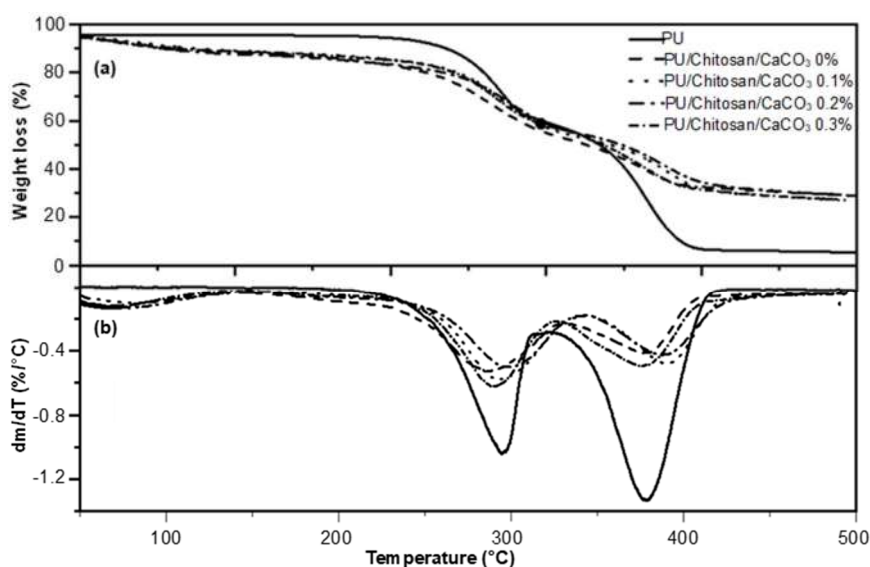


Fig 6. (a) TGA and (b) DTG curves of PU-foams, PU-foams/chitosan, and PU-foams/chitosan/calcium carbonate

200–340 °C. This was due to the decomposition temperature of urethane bonds to form CO₂, alcohols, aldehydes, amines, and solvent evaporation [22], the decomposition of diisocyanate as the hard segment of PU, and the decomposition of chitosan hydroxyl groups [23]. The second decomposition step (T^{d2}) was between 320–430 °C, representing the decomposition of the polyol molecules as the soft segment of PU. Meanwhile, the subsequent degradation was the degradation temperature of complex polyol molecules and other inorganic materials, including calcium carbonate [24].

The neat PU-foams have T^{d1} and T^{d2}, respectively, at around 294.7 °C and 376.1 °C, with a residual weight of 5.52%. As shown in Fig. 7, all the PUs samples with calcium carbonate showed thermal stability compared to samples without calcium carbonate at all stages. Therefore, it was concluded that the use of calcium carbonate and the incorporation of chitosan in the PU matrix enhanced the thermal stability and thermal degradation behavior of samples. This aspect was further reflected by the significant increase in the residual mass of neat PU-foams (5.52%) at 500 °C compared to PU-foams/chitosan (30.33%) and PU/chitosan/calcium carbonate (28.42–30.74%). As also reported in the research by Barikani et al. [25], compared with neat PU-foams and PU-foams/chitosan, the sample coated with calcium carbonate showed considerably higher thermal stability, especially at higher temperatures.

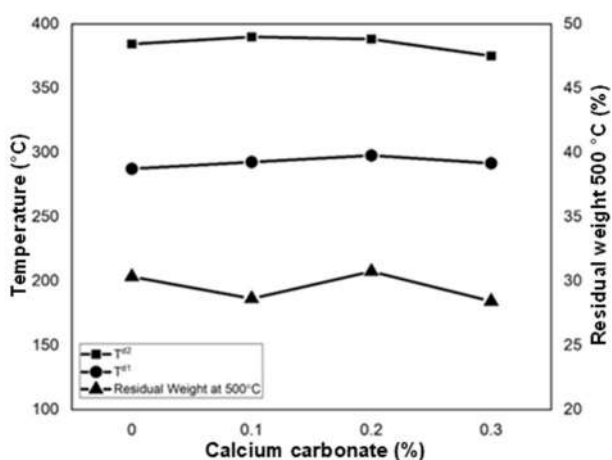


Fig 7. Degradation temperature and residual weight from PU-foams, PU-foams/chitosan, and PU-foams/chitosan/calcium carbonate

■ CONCLUSION

In a nutshell, we show a simple technique for preparing chitosan-calcium carbonate to improve the thermal and mechanical properties of PU-foams. From FTIR results, the possible hydrogen bond was between H from chitosan and O from PU-foams and O from carbonyl groups in calcium carbonate with H from hydroxyl groups in chitosan. Field Emission Scanning Electron Microscope (FE-SEM) shows that the shape of the structure was tidier and more uniform than PU-foams because the addition of inorganic material increased the bulk viscosity so that it could resist cell growth. It was clarified from the TGA thermograms that the thermal stability of the PU-foams sample was slightly raised after being coated with chitosan-calcium carbonate. The PU-foam coated with chitosan-added calcium carbonate can find potential applications requiring flame retardancy and good mechanical properties, such as automotive parts.

■ ACKNOWLEDGMENTS

The authors thank for the support from DRPM Universitas Indonesia through its program PUTI Grant scheme (grant number NKB-675/UN2.RST/HKP.05.00/2020), which made this research possible.

■ REFERENCES

- [1] Gama, N.V., Ferreira, A., and Barros-Timmons, A., 2018, Polyurethane foams: Past, present, and future, *Materials*, 11 (10), 1841.
- [2] Dolgopolsky, I., and Duley, J.A., 2000, Polyurethane foam as an integral “core” component of automotive headliner, *J. Ind. Text.*, 30 (1), 26–41.
- [3] Kustiyah, E., Putra, D.S., Gerry, D., Firdaus, D.F., and Chalid, M., 2020, Effect of lignin content as bio-chain extender in polyurethane foam, *Macromol. Symp.*, 391 (1), 1900153.
- [4] Cain, A.A., Plummer, M.G.B., Murray, S.E., Bolling, L., Regev, O., and Grunlan, J.C., 2014, Iron-containing, high aspect ratio clay as nanoarmor that imparts substantial thermal/flame protection to polyurethane with a single electrostatically-deposited bilayer, *J. Mater. Chem. A*, 2 (41), 17609–17617.

- [5] Kara, F., Aksoy, E.A., Yuksekdog, Z., Hasirci, N., and Aksoy, S., 2014, Synthesis and surface modification of polyurethanes with chitosan for antibacterial properties, *Carbohydr. Polym.*, 112, 39–47.
- [6] Javaid, M.A., Khera, R.A., Zia, K.M., Saito, K., Bhatti, I.A., and Asghar, M., 2018, Synthesis and characterization of chitosan modified polyurethane bio-nanocomposites with biomedical potential, *Int. J. Biol. Macromol.*, 115, 375–384.
- [7] Nik Pauzi, N.N.P., Majid, R.A., Dzulkifli, M.H., and Yahya, M.Y., 2014, Development of rigid bio-based polyurethane foam reinforced with nanoclay, *Composites, Part B*, 67, 521–526.
- [8] Dewi, R., Nasrun, Zulnazi, Riza, M., and Agusnar, H., 2019, Improved mechanical and thermal properties of modified thermoplastic starch (TPS) from sago by using chitosan, *Pertanika J. Sci. Technol.*, 27 (3), 1441–1450.
- [9] Centenaro, G.S.N.M., Facin, B.R., Valério, A., de Souza, A.A.U., da Silva, A., de Oliveira, J.V., and de Oliveira, D., 2017, Application of polyurethane foam chitosan-coated as a low-cost adsorbent in the effluent treatment, *J. Water Process Eng.*, 20, 201–206.
- [10] Carosio, F., Ghanadpour, M., Alongi, J., and Wågberg, L., 2018, Layer-by-layer-assembled chitosan/phosphorylated cellulose nanofibrils as a bio-based and flame protecting nano-exoskeleton on PU foams, *Carbohydr. Polym.*, 202, 479–487.
- [11] Bartczak, Z., Argon, A.S., Cohen, R.E., and Weinberg, M., 1999, Toughness mechanism in semi-crystalline polymer blends: II. High-density polyethylene toughened with calcium carbonate filler particles, *Polymer*, 40 (9), 2347–2365.
- [12] Ge, C., and Aldi, R., 2014, Effects of aragonite calcium carbonate on barrier and mechanical properties of a three-layer co-extruded blown low-density polyethylene film, *J. Plast. Film Sheeting*, 30 (1), 77–90.
- [13] Zhang, S., and Gonsalves, K.E., 1995, Synthesis of calcium carbonate–chitosan composites via biomimetic processing, *J. Appl. Polym. Sci.*, 56 (6), 687–695.
- [14] Zawadzki, J., and Kaczmarek, H., 2010, Thermal treatment of chitosan in various conditions, *Carbohydr. Polym.*, 80 (2), 394–400.
- [15] Yang, C., Wang, M., Xing, Z., Zhao, Q., Wang, M., and Wu, G., 2018, A new promising nucleating agent for polymer foaming: Effects of hollow molecular-sieve particles on polypropylene supercritical CO₂ microcellular foaming, *RSC Adv.*, 8 (36), 20061–20067.
- [16] Chalid, M., Heeres, H.J., and Broekhuis, A.A., 2015, Structure-mechanical and thermal properties relationship of novel γ -valerolactone-based polyurethanes, *Polym.-Plast. Technol. Eng.*, 54 (3), 234–245.
- [17] de Moura, A.P., da Silva, E.H.P., dos Santos, V.S., Galera, M.F., Sales, F.C.P., Elizario, S., de Moura, M.R., Rigo, V.A., and da Costa, R.R.C., 2021, Structural and mechanical characterization of polyurethane-CaCO₃ composites synthesized at high calcium carbonate loading: An experimental and theoretical study, *J. Compos. Mater.*, 55 (21), 2857–2866.
- [18] Reig, F.B., Adelantado, J.V.G., and Moya Moreno, M.C.M., 2002, FTIR quantitative analysis of calcium carbonate (calcite) and silica (quartz) mixtures using the constant ratio method. Application to geological samples, *Talanta*, 58 (4), 811–821.
- [19] Dinararum, R.R., Permana, D., and Atmaja, L., 2016, Effect of calcium carbonate as filler at the chitosan/calcium carbonate composite membrane, *IPTEK J. Proc. Ser.*, 1, 153–154.
- [20] Zuo, D.Y., Tao, Y.Z., Chen, Y.B., and Xu, W.L., 2009, Preparation and characterization of blend membranes of polyurethane and superfine chitosan powder, *Polym. Bull.*, 62 (5), 713–725.
- [21] Chuayjuljit, S., Maungchareon, A., and Saravari, O., 2010, Preparation and properties of palm oil-based rigid polyurethane nanocomposite foams, *J. Reinf. Plast. Compos.*, 29 (2), 218–225.
- [22] Stirna, U., Fridrihsone, A., Lazdina, B., Misāne, M., and Vilsons, D., 2013, Biobased polyurethanes from rapeseed oil polyols: Structure, mechanical and

- thermal properties, *J. Polym. Environ.*, 21 (4), 952–962.
- [23] Mazraeh-shahi, Z.T., Shoushtari, A.M., Bahramian, A.R., and Abdouss, M., 2015, Synthesis, pore structure and properties of polyurethane/silica hybrid aerogels dried at ambient pressure, *J. Ind. Eng. Chem.*, 21, 797–804.
- [24] Li, X.G., Lv, Y., Ma, B.G., Wang, W.Q., and Jian, S.W., 2013, Decomposition kinetic characteristics of calcium carbonate containing organic acids by TGA, *Arabian J. Chem.*, 10 (Suppl. 2), S2534–S2538.
- [25] Barikani, M., Honarkar, H., and Barikani, M., 2009, Synthesis and characterization of polyurethane elastomers based on chitosan and poly(ϵ -caprolactone), *J. Appl. Polym. Sci.*, 112 (5), 3157–3165.

CuO, MgO, and ZrO₂ Loading on HZSM5 by Deposition-precipitation: Study of Crystallinity, Specific Surface Area, and Morphology

Rizky Ibnufaatih Arvianto¹, Anatta Wahyu Budiman^{1*}, and Khoirina Dwi Nugrahaningtyas²

¹Department of Chemical Engineering, Faculty of Engineering, Universitas Sebelas Maret, Jl. Ir. Sutami 36A, Kentingan, Surakarta 57126, Indonesia

²Department of Chemistry, Faculty of Natural Sciences and Mathematics, Universitas Sebelas Maret, Jl. Ir. Sutami 36A, Kentingan, Surakarta 57126, Indonesia

* **Corresponding author:**

email: budiman@staff.uns.ac.id

Received: January 14, 2022

Accepted: March 23, 2022

DOI: 10.22146/ijc.72255

Abstract: Bifunctional catalysts are often used in multiple reactions to synthesize certain products. The catalytic activity of bifunctional catalysts is influenced by parameters such as crystallinity, specific surface area, metal distribution, and morphology. Bifunctional catalysts are manufactured by adding metal to the support. The metal loading to the support often affects these parameters. Therefore, this research was conducted to determine the effect of CuO, MgO, and ZrO₂ addition to HZSM5 on these parameters. The often-used loading method was deposition precipitation. The pH of the metal-support precursors' solution was increased to basic (pH of 8) to deposit the metal on the support. The loading effect was investigated by producing the following materials: CuO/HZSM5, CuO/ZrO₂/HZSM5, CuO/MgO/HZSM5, and CuO/MgO/ZrO₂/HZSM5. Each material was characterized using XRD, SAA, SEM, Mapping, EDS, and XRF. The results showed that all metal oxides could be embedded in the HZSM5. The loading of CuO, MgO, and ZrO₂ to HZSM5 did not affect the crystallinity (structure) and morphology, increased the specific surface area, and was evenly distributed inside the pore of HZSM5. Further research is needed to determine the effect of crystallinity, specific surface area, and morphology on other metals and support types.

Keywords: crystallinity; specific surface area; morphology; deposition-precipitation

■ INTRODUCTION

The application of catalysts in the industry is essential. Most of the chemical industry uses catalysts for certain product formations. Sustainable production requires suitable chemical processes and catalysts [1]. One of the uses of catalysts is in the DME manufacturing industry. Several industries use two reactors with the help of two catalysts, namely metal (for the CO/CO₂ hydrogenation reaction to methanol) and solid acid (for the methanol dehydration reaction to DME). However, this method requires a lot of costs [2]. Therefore, many studies have combined metals and solid acids to produce bifunctional catalysts so that reactions in two reactors can occur instantly in one reactor assisted by this catalyst. However, the metal addition to the support (solid acid) often affects the catalyst's crystallinity, specific surface

area, and morphology. Meanwhile, several studies showed an excellent catalyst gives a good performance related to the high crystallinity [3], high surface area [4], porous morphology [5,6], and metal distribution on support [5,7]. Therefore, it is crucial to study the effects of metal addition to support the bifunctional catalyst of direct DME synthesis.

CuO, MgO, and ZrO₂ have impressive abilities as metal catalysts to synthesize methanol. CuO is a catalyst for methanol synthesis from CO₂ [8-9] or CO [10]. Adding MgO or ZrO₂ can increase the formation of methanol [11-12]. One of the solid acids often used in the dehydration reaction of methanol to DME is HZSM5. The selection of HZSM5 is based on a high acidic site on the surface [13-14], high stability [11], large surface area, and pore diameter (5 to 7 Å) [15].

Deposition-precipitation involves a metal precursor precipitation onto a suspended support material by increasing the pH of the metal salt solution [16]. The addition of NH_4OH (as precipitant) at room temperature is one method to increase pH steadily [4]. The metal nucleation process is induced under primary conditions, so compounds with low solubility are formed [17].

Several studies on metal addition on the support have been published. CuO , ZnO , and MgO were loaded on $\gamma\text{-Al}_2\text{O}_3$ via the deposition-precipitation method at a pH of 7. The increase in specific surface area from $79 \text{ m}^2/\text{g}$ to $95.9 \text{ m}^2/\text{g}$ occurred with 20% Mg. Magnesium reduced Cu agglomeration so that the metal surface area was increased. However, the loading of 20% Mg decreased the crystallinity of the catalyst by 30%. The catalyst morphology showed degradation and distortion [12]. The MgO loading into the Cu-mordenite via deposition-precipitation method at pH of 8 showed a decrease in the specific surface area proportional to the Mg loading percentage from 0.1 to 0.4% [4]. The Mg loading did not affect the crystallinity of the catalyst because Mg was maximally dispersed. Analysis using FESEM showed that the catalyst morphology was not significantly affected by the loading of MgO [4]. The CuO , ZnO , ZrO_2 , and Al_2O_3 loading to $\gamma\text{-Al}_2\text{O}_3$ by the deposition-precipitation method at a pH of 7 was carried out by Ren et al. [11]. The ZrO_2 loading to the support caused a decrease in the specific surface area, from $128 \text{ m}^2/\text{g}$ to $109 \text{ m}^2/\text{g}$. In addition, the ZrO_2 loading increased the Cu dispersion from 16.3% to 18.9% [11].

In this research, CuO , MgO , and ZrO_2 were loaded on HZSM5 for bifunctional catalysts manufacture, namely $\text{CuO}/\text{HZSM5}$, $\text{CuO}/\text{ZrO}_2/\text{HZSM5}$, $\text{CuO}/\text{MgO}/\text{HZSM5}$, and $\text{CuO}/\text{MgO}/\text{ZrO}_2/\text{HZSM5}$. Each material was compared to determine the effect of adding CuO , MgO , and ZrO_2 . The impact of loading on crystallinity, specific surface area, and morphology was studied to obtain the high performance of bifunctional catalyst with high crystallinity, largest specific surface area, well-dispersed metals, and porous morphology.

■ EXPERIMENTAL SECTION

Materials

Zeolite type HZSM5 99% ($\text{Si}/\text{Al} = 26$) from ACS

material was used as catalyst support. $\text{Cu}(\text{NO}_3)_2 \cdot 3\text{H}_2\text{O}$ 99%, $\text{MgCl}_2 \cdot 6\text{H}_2\text{O}$ 99%, and $\text{ZrOCl}_2 \cdot 8\text{H}_2\text{O}$ 99% from Merck were used as the CuO , MgO , and ZrO_2 precursors.

Instrumentation

Materials were characterized by X-ray Diffractometer (XRD) Rigaku Miniflex 600 to investigate the effect of metal oxides loading on the crystallinity and X-ray Fluorescence (XRF) BRUKER S2 Ranger to determine the metal oxide content (wt.%). Crystallinity was determined using the XRD spectra of each material. Calculation of crystallinity was performed using Eq. (1):

$$\% \text{ Crystallinity} = \frac{\text{area of crystalline peaks}}{\text{Total area (crystalline and amorphous)}} \quad (1)$$

XRD analysis was conducted at a Bragg angle of $5\text{--}90^\circ$ (2θ) at room temperature. Refinement analysis was performed using Le Bail Methods with Rietica software to find the best fitting with the ICSD standard. The similarity between XRD Data and ICSD standard was represented as Rp and Rwp.

The nitrogen adsorption-desorption technique measured the material's surface area. The instrument used was Quantachrome NovaWin Version 11.04. The multi-point BET method was used to calculate the specific surface area using Eq. (2):

$$S_{\text{BET}} (\text{m}^2 / \text{g}) = \frac{4.355}{\text{intercept} + \text{gradient}} \quad (2)$$

The metal oxides loading effect on the morphology of materials was characterized by Scanning Electron Microscopy-Mapping-Energy Dispersive Spectroscopy (Phenom Desktop ProXL). The use of SEM images to determine porosity and particle diameter distribution. Surface porosity analysis was determined by the literature using SEM data [18-20]. Porosity can be calculated by Eq. (3).

$$\text{Porosity (\%)} = \frac{\text{Volume of pores}}{\text{Total volume}} \times 100 \quad (3)$$

The diameter of each particle depicted in the SEM image was measured by ImageJ software and processed by OriginPro 2021 software to determine the diameter distribution of particles [20].

Procedure

The mixture of metal and HZSM5 precursors was prepared according to Table 1. Firstly, each metal precursor was dissolved in the distilled water and placed in a 250 mL beaker glass over a hot plate heater with stirring. After the solution was dissolved entirely, HZSM5 was added to the solution. The solution pH was adjusted to 8 by adding NH_4OH 0.05 M. The solution was stirred at 400 rpm, 85–90 °C for 2 h. A slurry solution was cooled to room temperature and filtered by a Buchner filter. An evaporator dried the wet solid at 60 °C for 6 h. Then, the dry solid was calcinated at 550 °C for 4 h.

RESULTS AND DISCUSSION

The impregnation of CuO , MgO , and ZrO_2 on HZSM5 was performed using the deposition-precipitation technique. The loading scheme is explained in Fig. 1. The effect of these metal oxides loading was tested for crystallinity, specific surface area, and morphology.

XRD and XRF Analysis

Fig. 2 shows the XRD spectra of the support before and after loading. The peaks at 2θ (°) 7.95, 8.79, 23.01, 23.84, 24.54, and 45.18° support XRD spectra are identical to HZSM5 [21–23]. After metal oxides loading, there was no change in these peaks because metal oxides loading did not damage the structure of HZSM5.

Table 2 shows the effect of CuO , MgO , and ZrO_2 loading on crystallinity. The crystallinity did not significantly change after metal oxides loading compared with the support (HZSM5). It proves that the metal oxides loading did not damage the structure of HZSM5.

The characteristic peaks of CuO , MgO , and ZrO_2 are not visible in the XRD spectra (Fig. 2) because they were evenly dispersed over the HZSM5 surface [23–24]. The

same results were also obtained by Tursunov et al. [23], Din et al. [4], and Magomedova et al. [24].

Refinement analysis was shown by The Le Bail plot in Fig. 3. The similarity between the experimental XRD

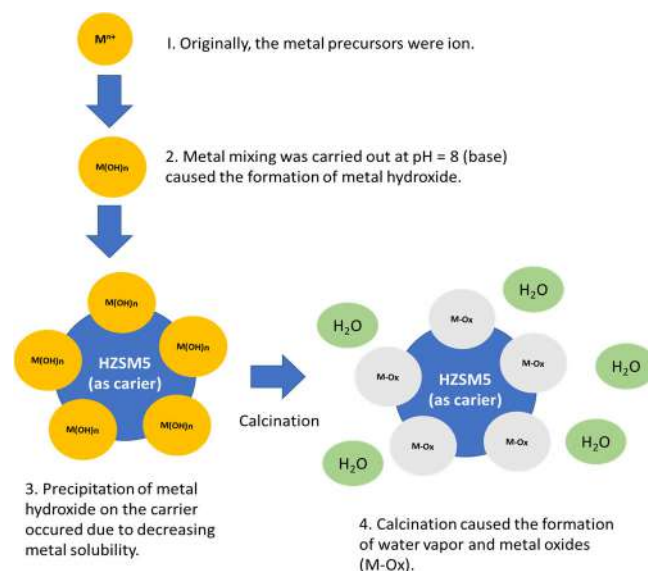


Fig 1. Scheme of CuO , MgO , and ZrO_2 formation

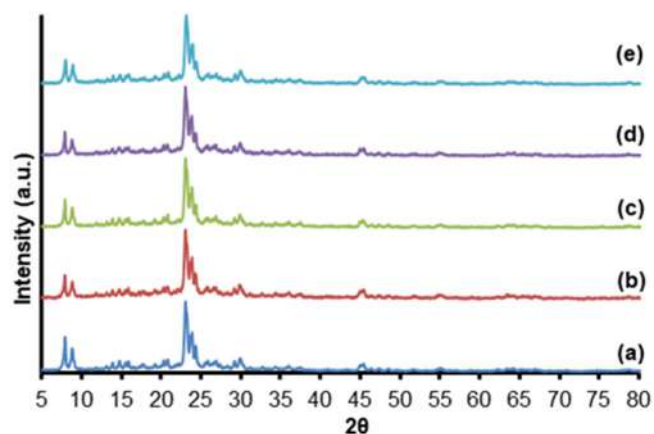


Fig 2. XRD spectra of materials: (a) HZSM5, (b) $\text{CuO}/\text{HZSM5}$, (c) $\text{CuO}/\text{MgO}/\text{HZSM5}$, (d) $\text{CuO}/\text{ZrO}_2/\text{HZSM5}$, (e) $\text{CuO}/\text{MgO}/\text{ZrO}_2/\text{HZSM5}$

Table 1. Composition of metal and HZSM5 precursors

Materials	Precursor			
	$\text{Cu}(\text{NO}_3)_2 \cdot 3\text{H}_2\text{O}$ (g)	$\text{MgCl}_2 \cdot 6\text{H}_2\text{O}$ (g)	$\text{ZrOCl}_2 \cdot 8\text{H}_2\text{O}$ (g)	HZSM5 (g)
$\text{CuO}/\text{HZSM5}$	1.9	-	-	10
$\text{CuO}/\text{MgO}/\text{HZSM5}$	1.9	0.8	-	10
$\text{CuO}/\text{ZrO}_2/\text{HZSM5}$	1.9	-	0.4	10
$\text{CuO}/\text{MgO}/\text{ZrO}_2/\text{HZSM5}$	1.9	0.8	0.4	10

Table 2. Crystallinity

Materials	Crystallinity (%)
HZSM5	79
CuO/HZSM5	79
CuO/ZrO ₂ /HZSM5	81
CuO/MgO/HZSM5	81
CuO/MgO/ZrO ₂ /HZSM5	81

pattern data and standard ICSD data were analyzed using the Le Bail method with Rietica software. The smaller value of Rp and Rwp represented that the standard tested is acceptable.

Each Le Bail plot in Fig. 3 shows a Rp and Rwp below 10. These results indicate a good fitting between the XRD

spectra and the tested ICSD standard [25-26]. Refinement analysis exhibited a good fitting between HZSM5 and ICSD 61010 (space group symmetry: Pn21a, orthorhombic crystal system, lattice parameters: $a = 20.09 \text{ \AA}$; $b = 19.97 \text{ \AA}$; $c = 13.36 \text{ \AA}$, angle between axes: $\alpha = \beta = \gamma = 90^\circ$ and $Z = 1$), CuO and ICSD 1381 (space group symmetry: I41, tetragonal crystal system, lattice parameters: $a = b = 5.817 \text{ \AA}$; $c = 9.893 \text{ \AA}$, angle between axes: $\alpha = \beta = \gamma = 90^\circ$ and $Z = 1$), MgO and ICSD 159376 (space group symmetry: Fm-3m, cubic crystal system, lattice parameters: $a = b = c = 4.212 \text{ \AA}$, angle between axes: $\alpha = \beta = \gamma = 90^\circ$ and $Z = 4$), ZrO₂ and ICSD 57451 (space group symmetry: C1, monoclinic crystal system, lattice parameters: $a = 5.1459 \text{ \AA}$; $b = 5.2115 \text{ \AA}$; $c = 5.3128 \text{ \AA}$, angle

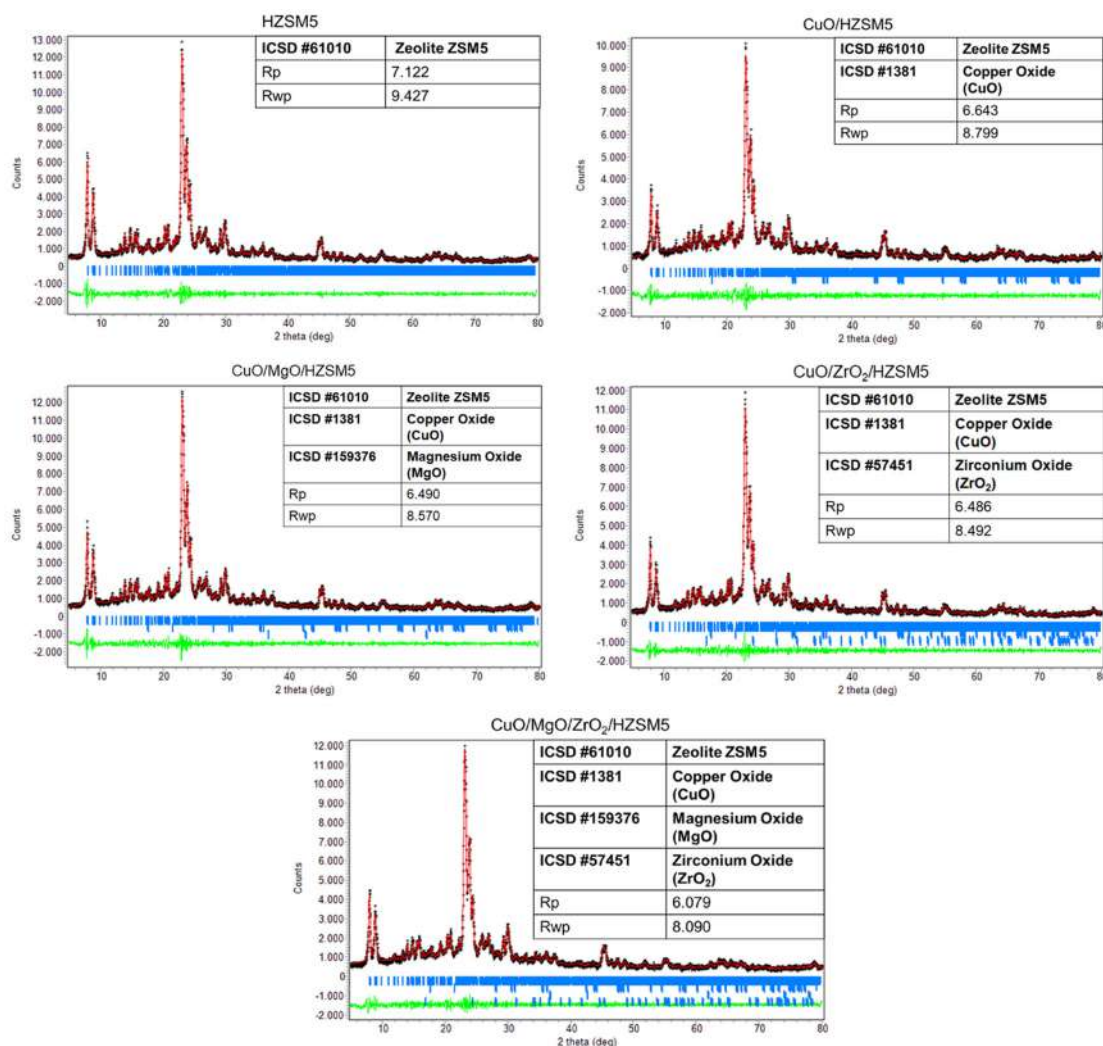


Fig 3. The Le Bails plot-supported XRD data with ICSD standard. XRD data (black); ICSD standard peaks (blue); calculation result (red); difference experiment data and calculation result (green)

Table 3. Lattice parameter and cell volume of HZSM5 before and after metal oxide addition

Materials	Lattice parameter (Å)			Cell volume (Å ³)
	a	b	c	
HZSM5	20.088	19.903	13.392	5340.515
CuO/HZSM5	20.098	19.891	13.387	5351.538
CuO/MgO/HZSM5	20.131	19.908	13.389	5365.801
CuO/ZrO ₂ /HZSM5	20.127	19.893	13.372	5353.833
CuO/MgO/ZrO ₂ /HZSM5	20.184	19.908	13.389	5370.292

between axes: $\alpha = 90^\circ$; $\beta = 99.222^\circ$; $\gamma = 90^\circ$ and $Z = 4$).

The CuO, MgO, and ZrO₂ addition caused a decrease in Rp and Rwp. Adding three metal oxides at once to HZSM5 showed the most reduction in Rp and Rwp. The reduction of residual factor value (Rp and Rwp) indicates the metal oxides' existence and the stability of the support (HZSM5) [25].

The metal oxides addition in HZSM-5 caused a stretching and contraction of the lattice parameters (Table 3). It indicates the presence of metal oxide insertion in HZSM5. The lattice parameter value of support before and after metal oxide loading was not significantly different, indicating the stability of the HZSM5 structure [25]. Meanwhile, the increase in cell volume also suggests the occurrence of metal oxide embedding in HZSM5 [25].

Table 4 represents a metal oxide content in HZSM5 and CuO/MgO/ZrO₂/HZSM5. SiO₂ and Al₂O₃ contents decreased because of the total mass increase after CuO, MgO, and ZrO₂ loading. Based on XRF analysis, CuO, MgO, and ZrO₂ were successfully added to HZSM5 in 10.62, 6.40, and 6.60%, respectively.

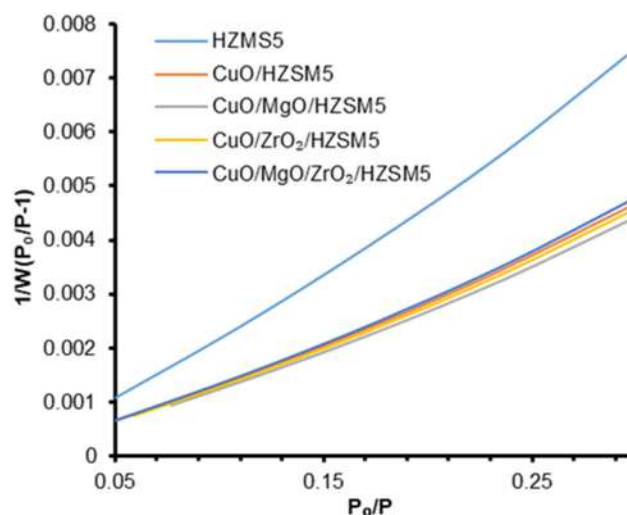
Surface Area Analysis

Fig. 4 shows the multi-point BET graph. Based on Fig 4, it can be seen that each material has a linear graph. Table 5 represents the support-specific surface area (HZSM5) before and after metal oxides loading. The CuO, ZrO₂, and MgO loading to the support caused an increase in the specific surface area. The S_{BET} value of the support (HZSM5) is lower than other materials. The increase in the specific surface area exhibits that metal oxides did not cover the support's pores [3,27], were evenly distributed on the support [3], and did not cause damage to the support [28-29].

The loading of MgO or ZrO₂ to CuO/HZSM5 produces in different specific surface areas. The specific the surface area of CuO/MgO/HZSM5 is larger than

Table 4. XRF data of HZSM5 and CuO/MgO/ZrO₂/HZSM5

Compounds	HZSM5 (wt.%)	CuO/MgO/ZrO ₂ /HZSM5 (wt.%)
SiO ₂	96.19%	74.4%
Al ₂ O ₃	2.81 %	0.98%
CuO	-	10.62%
MgO	-	6.40%
ZrO ₂	-	6.60%

**Fig 4.** Multi-point BET Graph**Table 5.** Surface area analysis

Material	S _{BET} (m ² /g)
HZSM5	171.457
CuO/HZSM5	275.633
CuO/ZrO ₂ /HZSM5	280.968
CuO/MgO/HZSM5	286.513
CuO/MgO/ZrO ₂ /HZSM5	270.497

CuO/ZrO₂/HZSM5 due to the different sizes of MgO and ZrO₂. MgO has a smaller size than ZrO₂, so MgO is more evenly distributed than ZrO₂ and does not excessively cover the pores of HZSM5. The CuO, MgO, and ZrO₂ loading at once to the HZSM5 causes a lower specific surface area than CuO/MgO/HZSM5 and CuO/ZrO₂/HZSM5 because more metal oxides were deposited on the support surface, resulting in some of them entering the pores.

Morphology Analysis

Fig. 5 shows SEM images of HZSM5 and CuO/MgO/ZrO₂/HZSM5. HZSM5 has a spherical morphology. The CuO, MgO, and ZrO₂ loading to HZSM5 did not affect its morphology because of the unchanged morphology of CuO/MgO/ZrO₂/HZSM5, as seen in Fig. 5(b) and 5(d). The same results were also obtained by the research of Din et al. and Ren et al., in which they have successfully loaded CuO, MgO, and ZrO₂ to the support without damaging or affecting the material morphology [4,11].

The CuO/MgO/ZrO₂/HZSM5 EDS spectra show the

appearance of new peaks from Cu, Mg, and Zr compared to the HZSM5 EDS spectra (Fig. 6). These results prove the success of loading CuO, MgO, and ZrO₂ on HZSM5 (presented as total metal). The decrease in Si, Al, and O content was caused by an increase in the total mass of the material after adding Cu, Mg, and Zr. Based on EDS analysis, Cu, Mg, and Zr were deposited at 48.56, 0.14, and 0.55%, respectively.

SEM images of HZSM5 and CuO/MgO/Zr/HZSM5 in Fig. 5 (with 10000× magnification) were used to calculate surface porosity. Table 6 shows the surface porosity of HZSM5 and CuO/MgO/Zr/HZSM5, i.e., 55 and 53%, respectively. There was no significant change in the material's surface porosity after CuO, MgO, and ZrO₂ loading. Therefore, it can be concluded that the loading of CuO, MgO, and ZrO₂ to HZSM5 did not change the morphology or excessively close up the pores. The result follows the description of the surface area analysis, which shows that the metal oxides did not enter the support pores. The insignificant change in surface porosity indicates the absence of volume and pore diameter expansion. Therefore, metal oxides loading does

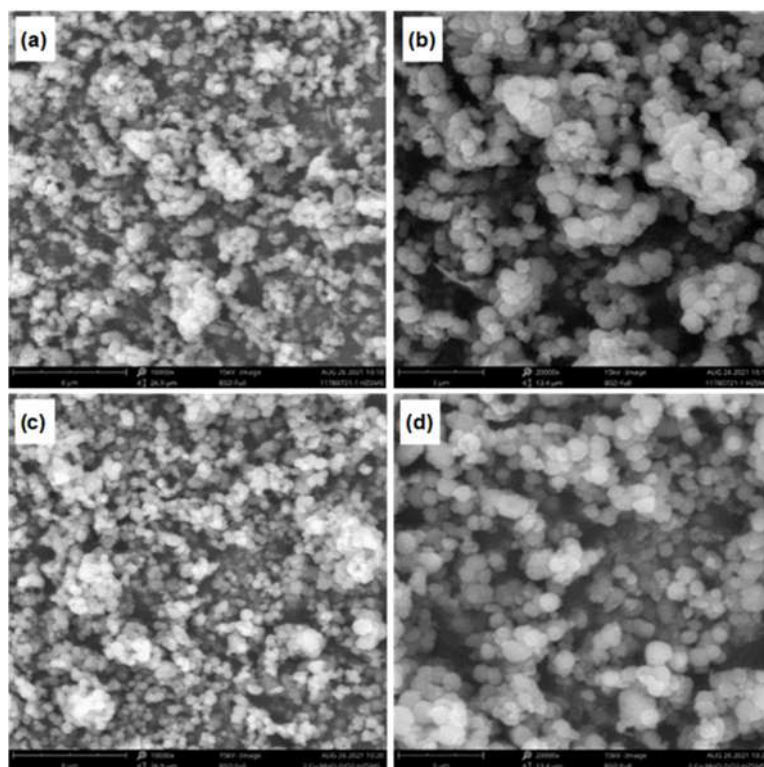


Fig 5. SEM Images of HZSM5 (a) 10000×, (b) 20000×; and CuO/MgO/ZrO₂/HZSM5 (c) 10000×, (d) 20000×

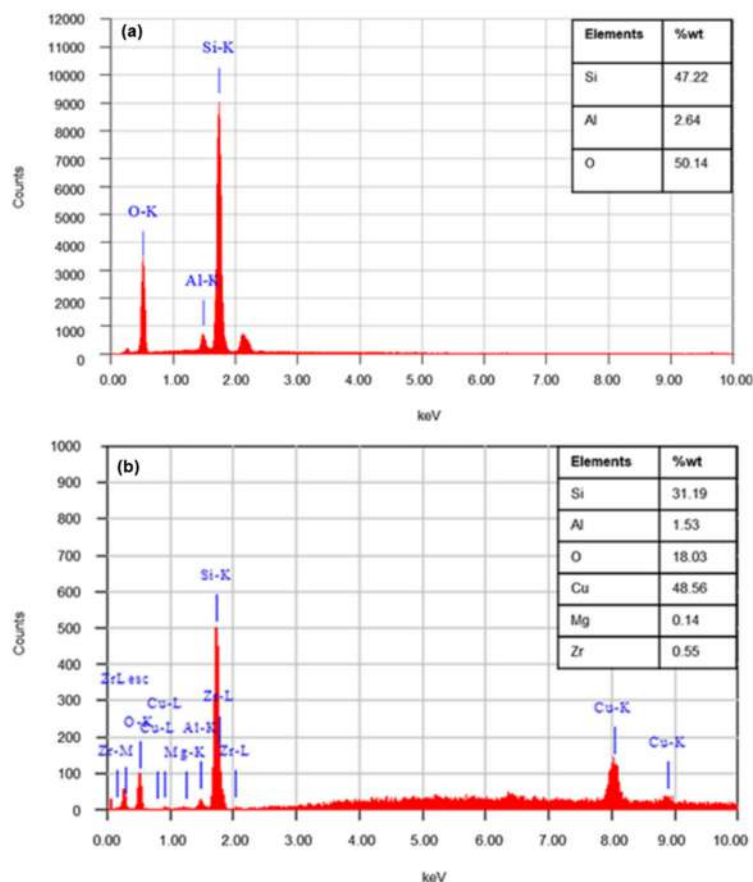


Fig 6. EDS Spectra: (a) HZSM5 and (b) CuO/MgO/ZrO₂/HZSM5

Table 6. Surface porosity analysis by SEM images

Materials	Porosity (%)
HZSM5	55
CuO/MgO/ZrO ₂ /HZSM5	53

not cause isomorphous substitution with Si⁴⁺ in the framework [30].

The measurement of particle diameter distribution

was done by ImageJ software using SEM images. Fig. 7 shows the diameter distribution for HZSM5 and CuO/MgO/ ZrO₂/HZSM5. Each image has a peak that shows the highest diameter value. The peak of HZSM5 ranged from 0.5–0.55 μm. The loading of CuO, MgO, and ZrO₂ to HZSM5 caused the peak to shift to 0.7–0.8 μm. The peak shifting shows an increase in HZSM5 size due to CuO, MgO, and ZrO₂ on its surface.

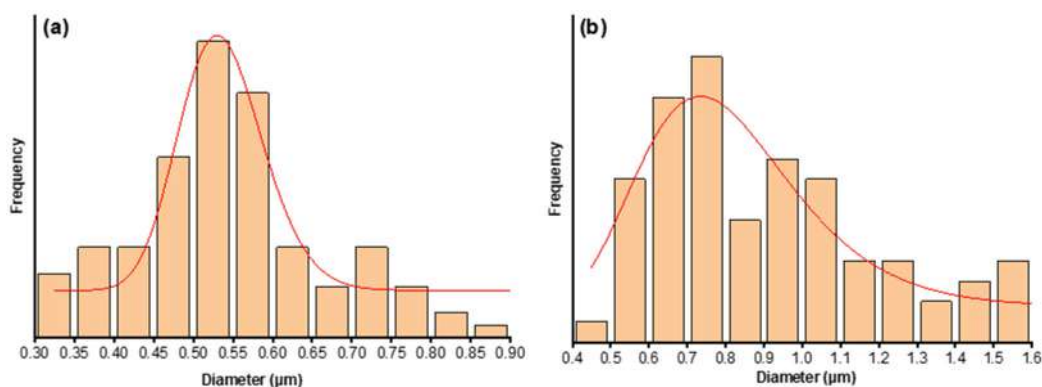


Fig 7. Diameter Distribution of (a) HZSM5 and (b) CuO/MgO/ZrO₂/HZSM5

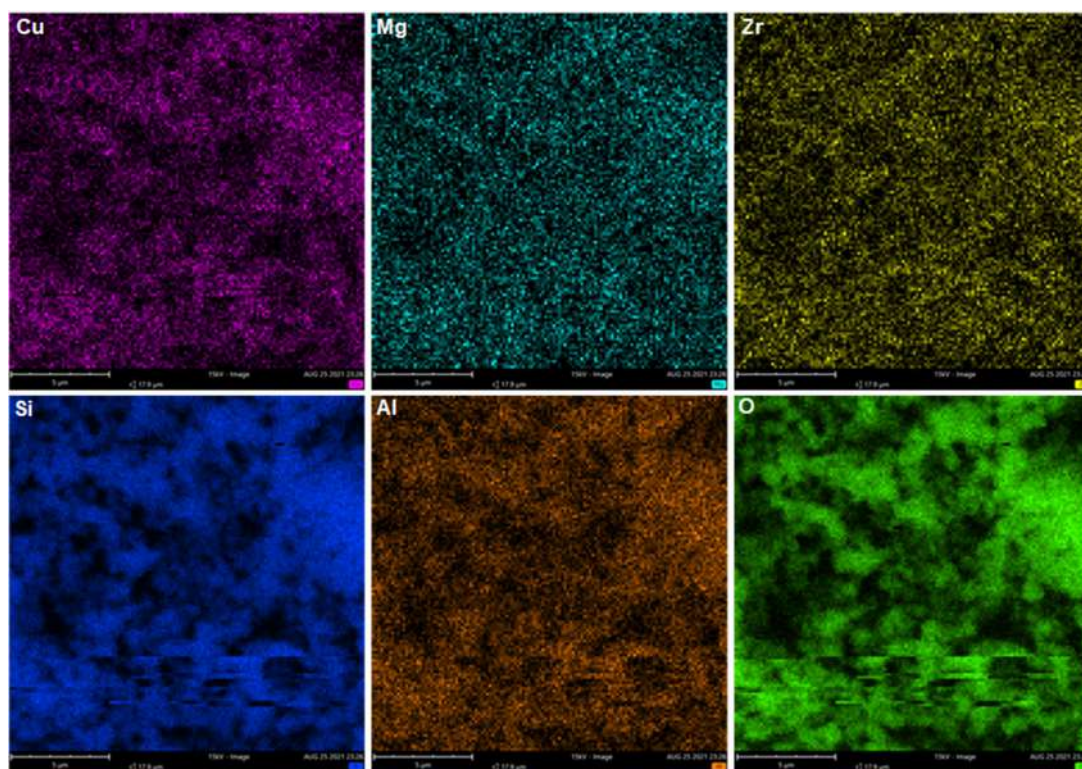


Fig 8. Elemental Mapping of CuO/MgO/ZrO₂/HZSM5

Fig. 8 shows the elemental mapping in the CuO/MgO/ZrO₂/HZSM5. According to Fig. 8, CuO, MgO, and ZrO₂ are evenly dispersed over HZSM5. In addition, these metal oxides did not form the clusters, indicating metal agglomeration on the carrier [31]. The metal oxides do not form agglomerates because they are dispersed on the support (HZSM5), thereby establishing metal oxides-support interactions and reducing metal oxides-metal oxides interactions. Therefore, the metal oxides will separate from their group (reduced agglomeration) [32].

■ CONCLUSION

CuO, MgO, and ZrO₂ have been successfully loaded to HZSM5, evidenced by the shifts of highest diameters particles, from 0.5–0.55 μm to 0.7–0.8 μm. XRF, XRD refinement, Mapping, and EDS analysis also exhibited the success of these metal oxides loading on the HZSM5. These metal oxides did not close the HZSM5's pores and were evenly distributed over the HZSM5 surface. Hence, the specific surface area increased, and HZSM5's porosity did not change drastically after the loading (the porous

material still exists). According to the XRD data, metal oxides loading did not affect the crystallinity of HZSM5. The similarity in the XRD pattern before and after loading proved that the metal oxide addition did not damage the HZSM5 structure. XRD refinement also confirmed the stability of the HZSM5 structure by the decrease in the Rp and Rwp value after metal oxide loading. Further research can be carried out with other support and types of metal.

■ ACKNOWLEDGMENTS

This research was supported by grants from The Ministry of Education, Culture, Research and Technology of Republic Indonesia under Excellence Basic Research of Universities (PDUPT) 2021 with contract number 11/E1/KP.PTNBH/2021 and 221.1/UN27.22/HK.07.00/2021.

■ AUTHOR CONTRIBUTIONS

All authors were involved in the preparation and design of the study. Rizky Ibnufaatih Arvianto was a research assistant who conducted experiments, analyzed

data, and wrote journals. Anatta Wahyu Budiman was the head of the research team. Khoirina Dwi Nugrahaningtyas was a member of the research team. All authors contributed to the improvement of the manuscript. All authors approve the final version of the manuscript and agree to be responsible for its content.

■ REFERENCES

- [1] Medford, A.J., Vojvodic, A., Hummelshøj, J.S., Voss, J., Abild-Pedersen, F., Studt, F., Bligaard, T., Nilsson, A., and Nørskov, J.K., 2015, From the Sabatier principle to a predictive theory of transition-metal heterogeneous catalysis, *J. Catal.*, 328, 36–42.
- [2] Kartohardjono, S., Adji, B.S., and Muharam, Y., 2020, CO₂ utilization process simulation for enhancing production of dimethyl ether (DME), *Int. J. Chem. Eng.*, 2020, 9716417.
- [3] Kristiani, A., Sudiyarmanto, S., Aulia, F., Nurul Hidayati, L., and Abimanyu, H., 2017, Metal supported on natural zeolite as catalysts for conversion of ethanol to gasoline, *MATEC Web Conf.*, 101, 01001.
- [4] Din, I.U., Alotaibi, M.A., and Alharthi, A.I., 2020, Green synthesis of methanol over zeolite based Cu nano-catalysts, effect of Mg promoter, *Sustainable Chem. Pharm.*, 16, 100264.
- [5] Frusteri, L., Bonura, G., Cannilla, C., Todaro, S., Giordano, G., Migliori, M., and Frusteri, F., 2020, Promoting direct CO₂ conversion to DME over zeolite-based hybrid catalysts, *Pet. Chem.*, 60 (4), 508–515.
- [6] Frusteri, F., Migliori, M., Cannilla, C., Frusteri, L., Catizzone, E., Aloise, A., Giordano, G., and Bonura, G., 2017, Direct CO₂-to-DME hydrogenation reaction: New evidences of a superior behaviour of FER-based hybrid systems to obtain high DME yield, *J. CO₂ Util.*, 18, 353–361.
- [7] Liu, Y., and Lu, H., 2020, Synthesis of ZSM-5 zeolite from fly ash and its adsorption of phenol, quinoline and indole in aqueous solution, *Mater. Res. Express*, 7 (5), 055506.
- [8] Jiang, Q., Liu, Y., Dintzer, T., Luo, J., Parkhomenko, K., and Roger, A.C., 2020, Tuning the highly dispersed metallic Cu species via manipulating Brønsted acid sites of mesoporous aluminosilicate support for CO₂ hydrogenation reactions, *Appl. Catal., B*, 269, 118804.
- [9] Chen, D., Mao, D., Wang, G., Guo, X., and Yu, J., 2019, CO₂ hydrogenation to methanol over CuO-ZnO-ZrO₂ catalyst prepared by polymeric precursor method, *J. Sol-Gel Sci. Technol.*, 89 (3), 686–699.
- [10] Yanti, F.M., Valentino, N., Juwita, A.R., Murti, S.D.S., Pertiwi, A., Rahmawati, N., Rini, T.P., Sholihah, A., Prasetyo, J., Saputra, H., Iguchi, S., and Noda, R., 2020, Methanol production from biomass syngas using Cu/ZnO/Al₂O₃ catalyst, *AIP Conf. Proc.*, 2223, 020006.
- [11] Ren, S., Fan, X., Shang, Z., Shoemaker, W.R., Ma, L., Wu, T., Li, S., Klinghoffer, N.B., Yu, M., and Liang, X., 2020, Enhanced catalytic performance of Zr modified CuO/ZnO/Al₂O₃ catalyst for methanol and DME synthesis via CO₂ hydrogenation, *J. CO₂ Util.*, 36, 82–95.
- [12] Asthana, S., Samanta, C., Bhaumik, A., Banerjee, B., Voolapalli, R.K., and Saha, B., 2016, Direct synthesis of dimethyl ether from syngas over Cu-based catalysts: Enhanced selectivity in the presence of MgO, *J. Catal.*, 334, 89–101.
- [13] Palomo, J., Rodríguez-Mirasol, J., and Cordero, T., 2019, Methanol dehydration to dimethyl ether on Zr-loaded P-containing mesoporous activated carbon catalysts, *Materials*, 12 (13), 2204.
- [14] Cheng, K., Zhou, W., Kang, J., He, S., Shi, S., Zhang, Q., Pan, Y., Wen, W., and Wang, Y., 2017, Bifunctional catalysts for one-step conversion of syngas into aromatics with excellent selectivity and stability, *Chem*, 3 (2), 334–347.
- [15] Widayat, W., and Annisa, A.N., 2017, Synthesis and characterization of ZSM-5 catalyst at different temperatures, *IOP Conf. Ser.: Mater. Sci. Eng.*, 214, 012032.
- [16] Barton, R.R., Carrier, M., Segura, C., Fierro, J.L.G., Escalona, N., and Peretti, S.W., 2017, Ni/HZSM-5 catalyst preparation by deposition-precipitation. Part 1. Effect of nickel loading and preparation conditions on catalyst properties, *Appl. Catal., A*, 540, 7–20.

- [17] Munnik, P., de Jongh, P.E., and de Jong, K.P., 2015, Recent developments in the synthesis of supported catalysts, *Chem. Rev.*, 115 (14), 6687–6718.
- [18] Abdullah, M., and Khairurrijal, K., 2009, A simple method for determining surface porosity based on SEM images using OriginPro software, *Indones. J. Phys.*, 20 (2), 37–40.
- [19] Hennemann, M., Gastl, M., and Becker, T., 2021, Optical method for porosity determination to prove the stamp effect in filter cakes, *J. Food Eng.*, 293, 110405.
- [20] Saraf, S., Singh, A., and Desai, B.G., 2019, Estimation of porosity and pore size distribution from scanning electron microscope image data of shale samples: A case study on Jhuran formation of Kachchh Basin, India, *ASEG Extended Abstracts*, 2019 (1), 1–3.
- [21] Xu, Y., Liu, J., Ma, G., Wang, J., Lin, J., Wang, H., Zhang, C., and Ding, M., 2018, Effect of iron loading on acidity and performance of Fe/HZSM-5 catalyst for direct synthesis of aromatics from syngas, *Fuel*, 228, 1–9.
- [22] Lin, B., Wang, J., Huang, Q., Ali, M., and Chi, Y., 2017, Aromatic recovery from distillate oil of oily sludge through catalytic pyrolysis over Zn modified HZSM-5 zeolites, *J. Anal. Appl. Pyrolysis*, 128, 291–303.
- [23] Tursunov, O., Kustov, L., and Tilyabaev, Z., 2019, Catalytic activity of H-ZSM-5 and Cu-HZSM-5 zeolites of medium SiO₂/Al₂O₃ ratio in conversion of *n*-hexane to aromatics, *J. Pet. Sci. Eng.*, 180, 773–778.
- [24] Magomedova, M., Galanova, E., Davidov, I., Afokin, M., and Maximov, A., 2019, Dimethyl ether to olefins over modified ZSM-5 based catalysts stabilized by hydrothermal treatment, *Catalysts*, 9 (5), 485.
- [25] Nugrahaningtyas, K.D., Putri, M.M., and Saraswati, T.E., 2020, Metal phase and electron density of transition metal/HZSM-5, *AIP Conf. Proc.*, 2237, 020003.
- [26] Ozaki, Y., Suzuki, Y., Hawai, T., Saito, K., Onishi, M., and Ono, K., 2020, Automated crystal structure analysis based on blackbox optimisation, *Npj Comput. Mater.*, 6 (1), 75.
- [27] Amin, M.H., Putla, S., Bee Abd Hamid, S., and Bhargava, S.K., 2015, Understanding the role of lanthanide promoters on the structure-activity of nanosized Ni/γ-Al₂O₃ catalysts in carbon dioxide reforming of methane, *Appl. Catal., A*, 492, 160–168.
- [28] Rodríguez-Martínez, C., García-Domínguez, Á.E., Guerrero-Robles, F., Saavedra-Díaz, R.O., Torres-Torres, G., Felipe, C., Ojeda-López, R., Silahua-Pavón, A., and Cervantes-Urbe, A., 2020, Synthesis of supported metal nanoparticles (Au/TiO₂) by the suspension impregnation method, *J. Compos. Sci.*, 4 (3), 89.
- [29] Liu, N., Chen, G., Dong, W., Liu, C., and Xu, C., 2017, Preparation of Au nanoparticles with high dispersion and thermal stability by a controlled impregnation method for alcohol oxidation, *Gold Bull.*, 50 (2), 163–175.
- [30] Brazovskaya, E.Y., and Golubeva, O.Y., 2017, Study of the effect of isomorphic substitutions in the framework of zeolites with a Beta structure on their porosity and sorption characteristics, *Glass Phys. Chem.*, 43 (4), 357–362.
- [31] Fakrudin, A., Ramli, A., and Abdul Mutalib, M.I., 2018, Effect of preparation method on physicochemical properties of Fe/zeolite catalyst, *J. Phys.: Conf. Ser.*, 1123, 012061.
- [32] Błaszczak, P., Mizera, A., Bochentyn, B., Wang, S.F., and Jasiński, P., 2022, Preparation of methanation catalysts for high temperature SOEC by β-cyclodextrin-assisted impregnation of nano-CeO₂ with transition metal oxides, *Int. J. Hydrogen Energy*, 47 (3), 1901–1916.

Synthesis of 2-Hydroxyethyl Esters from Castor Oil as Lubrication Bio-Additive Candidates for Low-Sulfur Fossil Diesel

Arizal Firmansyah^{1,2}, Yulfi Zetra¹, Rafwan Year Perry Burhan^{1,3*},
Didik Prasetyoko¹, and Novesar Jamarun⁴

¹Department of Chemistry, Faculty of Science and Data Analytics, Institut Teknologi Sepuluh Nopember, Kampus ITS Keputih, Surabaya 60111, Indonesia

²Department of Chemistry Education, Faculty of Science and Technology, Universitas Islam Negeri Walisongo Semarang, Kampus 3, Ngaliyan, Semarang 50185, Indonesia

³Polytechnic of Energy and Mineral Akamigas, Jl. Gajah Mada No. 38, Cepu 58315, Indonesia

⁴Department of Chemistry, University of Andalas, Limau Manis, Padang 25163, West Sumatera, Indonesia

* **Corresponding author:**

email: pburhan@chem.its.ac.id

Received: February 14, 2022

Accepted: April 1, 2022

DOI: 10.22146/ijc.73038

Abstract: The present work aims to study the synthesis of 2-hydroxyethyl esters from castor oil and its lubrication properties, promising as a lubrication bio-additive in low sulfur diesel fuel. This compound has been successfully synthesized from castor oil and ethylene glycol. The oil to ethylene glycol molar ratio was adjusted to 1:10, and the catalyst loading was used at 9% mole oil. Then, the mixture was refluxed for 5 h. The product components were characterized using GC-MS. The standard ASTM method was used to study the kinematic viscosity and lubrication. The product was dominated by 2-hydroxyethyl esters (94.16%), di-ester (1.12%), and cyclic ester (1.92%). The analysis of friction coefficient and wear scar diameter (WSD) using High-Frequency Reciprocating Rig (HFRR) shows the coefficient of friction and WSD of the product better than reference diesel fuel. From the results of this study, the 2-hydroxyethyl ester of castor oil, especially 2-hydroxyethyl ricinoleate, is the main responsible for the lubricating properties. Thus, 2-hydroxyethyl esters of castor oil can be proposed as an alternative bio-additive to improve the lubrication of low-sulfur fossil diesel fuels.

Keywords: 2-hydroxyethyl ester; castor oil; lubrication; bio-additive; diesel

■ INTRODUCTION

Fossil diesel still becomes a consumer choice because diesel engines have a higher efficiency than gasoline engines [1-2]. It was estimated that the demand for diesel from fossils has continued to increase [3-4]. However, fossil diesel's sulfur content causes air pollution and acid rain [5-6]. Therefore, a policy has been made to regulate allowed sulfur content in 10 to 500 ppm [7-8]. One strategy to meet this regulation is by applying the hydrodesulfurization method. Nevertheless, this method causes the compounds as natural lubricants to disappear [9-11], decreasing the lubricating properties of fossil diesel. Thus, lubrication enhancing additives are essential.

The fatty acids methyl ester (FAME) or fatty acids ethyl ester (FAEE) or biodiesel have been considered bio-additive with good lubricating properties. Adding biodiesel with a small concentration (less than 1%) into fossil diesel could improve its lubricity. Adding 1% methyl ester from rapeseed oil reduced 13% of diesel's wear scar diameter (WSD) [12]. The addition of 0.2 and 0.5 wt.% methyl ester of used oil caused the WSD values to decrease to 432 and 368 μm , respectively [13]. Addition of methyl ester in diesel was 0.1, 0.5, 1, 2, 5, and 10 wt.% from castor oil reduced the WSD from 581 to 299 μm [14]. Prasad et al. [15] reported that a mixture of 0.2 and 0.4% v of ethyl ester from castor oil into diesel decreased the WSD value to 320 and 186 μm , respectively.

Methyl or ethyl ester is generally prepared via transesterification of triglyceride or fatty acids using monohydroxy alcohol. Similar to this reaction principle, another ester can also be prepared by applying polyalcohols, such as ethylene glycol, to form the 2-hydroxyethyl esters [16-17]. Another study reported that low monoglycerides in FAME significantly contribute to FAME lubrication properties. It is due to hydroxy groups at head moiety [18-19]. However, it is challenging to synthesize FAME with a particular monoglyceride concentration [19]. Monoglyceride synthesis takes a long time, and special reactors [20-22] cannot be applied industrially [23]. Therefore, we synthesized esters whose structure is similar to monoglycerides by a simple reflux method, which did not require a long time, and tested their lubricity properties. The compound has a hydroxyl group at the head moiety (2-hydroxyethyl ester), which can be a bio-additive to improve the lubrication of low sulfur diesel. The 2-hydroxyethyl ester is vital as a starting point for other researchers in developing lubricity enhancer bio-additives for diesel in the future. So far, other researchers have not reported the lubricating properties of the 2-hydroxyethyl ester from non-edible oils.

Not many researchers have reported the synthesis of 2-hydroxyethyl esters from renewable feedstocks throughout our search. Rezende et al. [17] have reported the synthesis of 2-hydroxyethyl esters from cottonseed and sunflower oil. Nosal et al. [24] studied that fatty acids were esterified to 2-hydroxyethyl esters. Like other renewable raw materials, castor oil has the potential to be modified into 2-hydroxyethyl esters. Ricinoleic acid's high content (80–90% w/w) and its uniqueness in castor oil inspired researchers to develop bio-additives for lubrication of low sulfur diesel. The hydroxy group in ricinoleic acid improved the lubricating properties of low-sulfur diesel after adding methyl ricinoleate. Hence, the viscosity of methyl ricinoleate is higher than methyl esters of other fatty acids such as methyl stearate and methyl oleate. This increase in viscosity provides an advantage in lubricity behavior [25].

The basic principle in synthesizing the 2-hydroxyethyl ester is similar to the synthesis of FAME

or FAEE [26]. The vegetable oil can be transesterified with the desired alcohol, and the base or fatty acid esterified with the desired alcohol and acid catalyst. However, the alcohol used in this work is ethylene glycol. This alcohol provides one hydroxy group in the resulting 2-hydroxyethyl ester structure or a structure similar to FAEE with the addition of one hydroxy group. The structure is analogous to monoglycerides which have two hydroxy groups. Adding one hydroxy group to the 2-hydroxyethyl ester is expected to strengthen the interaction with the metal surface, similar to the function of the two hydroxy groups on the monoglyceride [27]. As a result, this produces a protective film that minimizes direct contact between metal surfaces. The strength of this protective layer is also supported by the fatty acids contained in vegetable oil [28].

Therefore, this paper aims to discuss the synthesis of 2-hydroxyethyl esters from castor oil and its lubricity properties. Interestingly, the product in this work demonstrated good lubrication properties. It can be proposed as a potential bio-additive for improving the lubricity of low-sulfur fossil diesel.

■ EXPERIMENTAL SECTION

Materials

The castor oil in this study is commercial refined castor oil in Indonesia. The utilized fossil diesel was the leading diesel commercialized in Indonesia, containing 300 ppm sulfur. Meanwhile, sulfuric acid (H_2SO_4) was obtained from SMART Lab Indonesia, and other chemicals were obtained from Sigma-Aldrich (EMSURE for analysis grade): ethylene glycol, potassium carbonate (K_2CO_3) that was heated before being used, ethyl acetate, potassium hydroxide (KOH), and sodium sulfate anhydrous (Na_2SO_4). All those chemicals were used without any purification.

Instrumentation

The instruments used in this work were GC-MS QP 2010 Shimadzu with the RTX5-MS column. The lubricity properties analyzed by HFRR with test ball specifications: SAE-AMS 6440 steel, diameter 6.00 mm, Rockwell "C" (HRC) scale hardness rating 58–66 (Class

28 per ISO 3290). Test disc specifications: SAE-AMS steel 10 mm disc 6440, which machined from annealed rods, Vickers solidity HV 30, in line with E92, scale number 10-210, rotated, stacked, and polished to obtain a surface of less than 0.02.

Procedure

Determination of fatty acids derived from castor oil

Methanol was used in this work because it is more reactive than ethylene glycol. The methoxide ion is more easily formed than the ethylene glycoxide ion. In addition, the methoxide ion is smaller than the ethylene glycoxide ion. Hence the methoxide ion more easily attacks the carbonyl carbon of the triglyceride [29]. The castor oil and methanolic KOH as base catalysts were preheated. The molar ratio of oil to methanol is 1:6, castor oil, 20 g and methanol, 4.1556 g and the base catalyst loading was used 1 wt.% of oil. Then, the oil and catalyst were mixed under reflux at 60 °C for 2 h. The mixture was left in a separation funnel overnight. The glycerol, methanol, and water occupied the lower layer. In the next step, this layer was discarded. The methyl ester in the upper layer was evaporated to eliminate the solvent and dried using Na₂SO₄ [30].

The purified methyl ester of refined castor oil was characterized using GC-MS with a capillary column comprised of 5% diphenyl and 95% dimethyl polysiloxane with a thickness of 0.25 mm, column length of 30.0 m, and an inner diameter of 0.25 μm. The injection temperature was adjusted to 250 °C. The split ratio mode was 138.7, with the flow rate of Helium gas being 1.16/min. The oven was programmed at 100 °C as the initial temperature for 4 min. Then, this temperature was raised to 240 °C at 3°C/min for 15 min. This temperature was raised to 250 °C again with 10 °C/min and maintained for 4 min.

Quantitative data from the characterized methyl esters were then used to calculate the molecular weight of castor oil according to Eq. (1) [31]. The obtained molecular weight of the castor oil was to synthesize 2-hydroxyethyl ester.

$$P_c = \sum (P_i \cdot Y_i) \quad (1)$$

P_c is the molecular weight of castor oil, P_i is the molecular weight of FAME in castor oil, and Y_i is the percentage of

FAME in castor oil.

Synthesis of 2-hydroxyethyl esters

The 2-hydroxyethyl esters compound from castor oil was synthesized without optimizing the reactant molar ratio, reaction time, reaction temperature, and catalyst loading parameters. The synthesis of the 2-hydroxyethyl ester procedure refers to Jiang et al. [16] with a slight modification in reaction time, temperature, and loading catalyst until form a product based on thin-layer chromatography (TLC) spots. The molar ratio of oil to ethylene glycol was adjusted to 1:10: castor oil, 20 g, and ethylene glycol, 13.4176 g. The castor oil was heated at 150 °C by reflux in this study. Then, ethylene glycol and K₂CO₃ as catalysts were added to that system. This condition was maintained for 5 h. Next, the mixture was neutralized until pH 7, transferred to a separating funnel, and left overnight until two layers were formed. As a result, esters were in the top layer, and glycerol at the bottom was discarded. Furthermore, the top layer was washed with hot water until the water layer was clear. The Na₂SO₄ was used to eliminate water in the mixture. Finally, the excess solvent was removed by a rotary evaporator [16].

Characterization of 2-hydroxyethyl esters

Transesterified products were checked through the TLC. The eluent used in this study was *n*-hexane and ethyl acetate (2:1). Spot of product observed in iodine chamber. Furthermore, the profile of the transesterified product was analyzed by GC-MS. The oven was programmed at 70 °C and ramped to 200 °C at 10 °C/min (hold time was 5 min). The temperature was ramped again to 305 °C at 4 °C/min (hold time was 15 min).

Kinematic viscosity and lubrication properties measurement of the product

The kinematic viscosity or fluidity property was measured by kinematic viscometer followed ASTM D445 procedure at 40 °C. This apparatus was chosen to measure based on the time for a volume to flow under gravity. The lubrication testing of the transesterified product was performed using the HFRR apparatus referring to ASTM D6079. The measurement condition was maintained at 2 mL of sample volume, 200 g of loading mass, the testing

duration of 75 min, and the temperature at 60 °C.

■ RESULTS AND DISCUSSION

Fatty Acids Profile Derived from Castor Oil

The fatty acids in castor oil are determined using a methanolysis reaction. The profile of fatty acids as their methyl esters and other published research can be seen in Table 1. Each of these methyl esters was identified by comparing each mass spectrum with the Wiley 9 database and analyzing the fragmentation pattern of each spectrum. Table 1 shows that the fatty acids of castor oil in this study are similar to other published reports. The castor oil is dominated by unsaturated fatty acids, especially methyl ricinoleate. It potentially has a good effect on the lubricity to low sulfur diesel [32]. The obtained methyl ester of castor oil was used to calculate the molecular weight of castor oil and synthesis of 2-hydroxyethyl ester, as shown in Table 2.

The fatty acid composition in castor oil was determined based on the optimum reaction conditions suggested by Rashid et al. [30]. This investigation provides a brief description of the types of fatty acids in the feedstock. However, compared with previous studies, the

fatty acid composition in this study did not differ much (Table 1). The percentage of fatty acids in the feedstock helps estimate the molecular weight of castor oil. This information is helpful in stoichiometric calculations for the preparation of 2-hydroxyethyl esters (Table 2).

Characterization of 2-Hydroxyethyl Esters

TLC was carried out to know whether 2-hydroxyethyl ester formed. Fig. 1 also demonstrated that the triglycerides had reduced and formed the product. Furthermore, detailed chemicals of the product were analyzed by GC-MS.

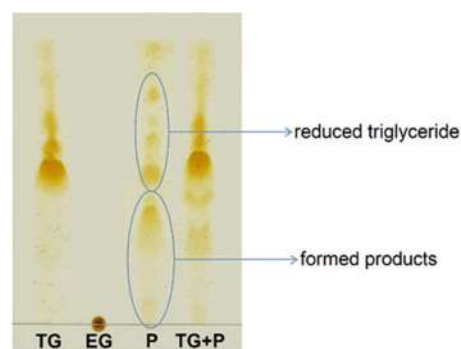


Fig 1. TLC spots of product synthesis. TG = triglyceride; EG = ethylene glycol; P = product

Table 1. Yield methyl ester of this study compared to another published research (%)

Yield GC-MS (%) of fatty acids methyl ester										Ref.
Palmitate (C16:0)	Palmitoleate (C16:1)	Stearate (C18:0)	Oleate (C18:1)	Linoleate (C18:2)	Linolenate (C18:3)	Ricinoleate (C18:1 OH)	Σ saturated methyl ester	Σ unsaturated methyl ester	Others	
1.30	-	1.31	3.57	4.52	0.41	88.89	2.61	97.39	2.61	This study
1.10	-	1.30	3.60	4.40	0.7	88.80	2.4	97.5	2.5	[34]
1.09	-	0.94	3.70	4.44	-	89.93	2.03	98.07	1.93	[35]
1.96	-	2.06	5.46	6.15	-	84.26	4.02	95.87	4.13	[36]
-	0.72	0.64	2.82	3.74	-	90.85	0.64	98.13	1.87	[37]
-	1.08	0.91	2.93	3.48	0.32	91.06	0.91	98.87	1.13	[38]

Table 2. Percentage of methyl ester and molecular weight of castor oil

FAME in castor oil	P_i (g/mol)	Y_i (%)	$P_c = \sum (P_i \cdot Y_i)$
Palmitate	807.29	1.30	10.49
Stearate	891.45	1.31	11.68
Oleate	885.45	3.57	31.61
Linoleate	879.45	4.52	39.75
Linolenate	873.45	0.41	3.58
Ricinoleate	902.45	88.89	802.19
			899.31

The obtained compounds are summarized in Table 3. This result was obtained from the percentage of the peak chromatogram. Similar to the FAME of castor oil (Table 2), 2-hydroxyethyl ricinoleate dominates 2-hydroxyethyl esters. The reaction mechanism for forming the proposed 2-hydroxyethyl ester shown in Fig. 2 is analogous to the transesterification of triglycerides with alcohols using a base catalyst [26]. In the first step, carbonate anions attack ethylene glycol protons to form ethylene glycolate anions as the nucleophile. Second step, carbonyl carbon of triglyceride is attacked by ethylene

glycol nucleophile to form 2-hydroxyethyl ester and diglyceride. The third and fourth step is similar to the second step. The ethylene glycol anion attacks the carbonyl carbon of di- and mono-glyceride to form mono-glyceride and glycerol, respectively, beside 2-hydroxyethyl ester.

According to Table 3, obtained product is also containing a di-ester. It may be due to the proton of the hydroxy group on the 2-hydroxyethyl ester allowing is attacked by the carbonate anion. In the next step, the anion of 2-hydroxyethyl ester attacks 2-hydroxyethyl

Table 3. The obtained product profile of castor oil

tR* (min)	Molecular ion (m/z)	Base peak (m/z)	Transesterified product	Yield GC-MS (%)
16.32	280	98	Cyclic ester	1.92
20.29	300	104	2-HE* palmitate	1.94
24.44	324	67	2-HE linoleate	6.33
24.53	326	55	2-HE oleate	5.93
25.02	328	104	2-HE stearate	2.21
29.41	342	55	2-HE ricinoleate	77.75
48.88	560	55	di-ester	1.12

*tR = retention time; *HE = hydroxyethyl

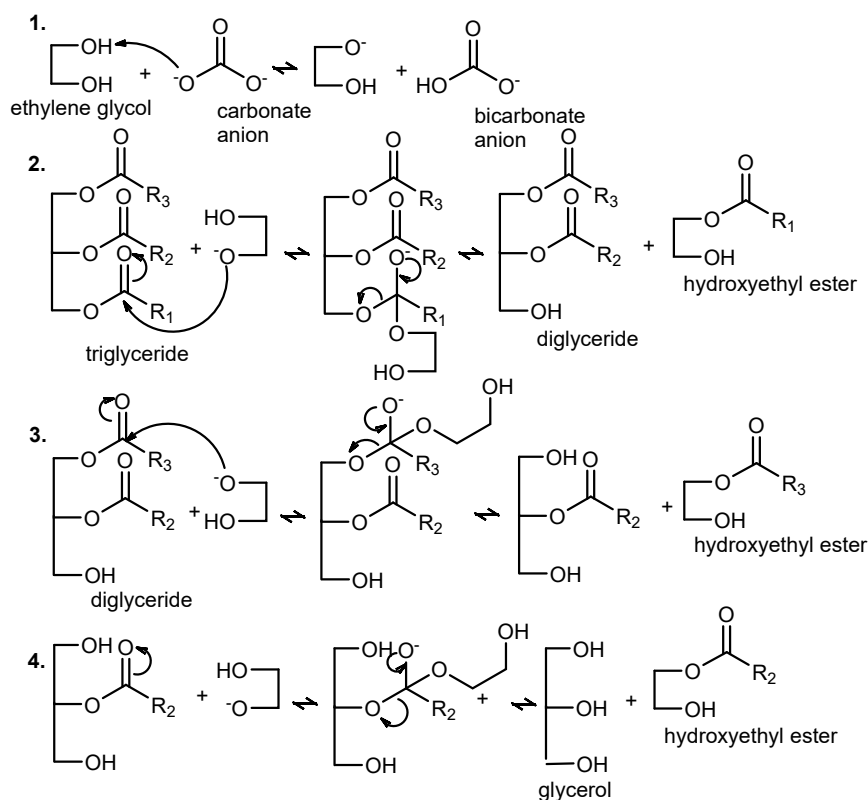


Fig 2. Proposed reaction mechanism of 2-hydroxyethyl esters formation

ester's carbonyl carbon. As a result, di-ester and ethylene glycol are produced, as shown in Fig. 3. The reaction mechanism for the formation of the di-ester, as in Fig. 3, is analogous to the di-esterification of ethylene glycol [38-39].

In this study, a cyclic ester was also identified. It may be derived from the intramolecular esterification of ricinoleic acid (Fig. 4). The reaction mechanism is generally a nucleophilic addition reaction to the carbonyl group [40]. The carbonate anion reacts with ethylene glycol to produce carbonic acid. Furthermore, ricinoleic acid in castor oil captures protons from carbonic acid. The carbon on the ricinoleic acid carbonyl becomes

electrophilic. It causes cyclization to form cyclic ester.

Kinematic Viscosity and Lubrication Properties of the Product

Kinematic viscosity and lubricity are vital properties of low-sulfur fossil diesel lubrication additives. The kinematic viscosity of the product in this study and low-sulfur fossil diesel can be seen in Table 4. The synthesized product is much more viscous (51.86 mm²/s) than the reference diesel fuel (3.39 mm²/s). Based on this information, the lubricating properties of the product are better than reference diesel fuel. Generally, better kinematic viscosity can lead to better lubrication [15,41].

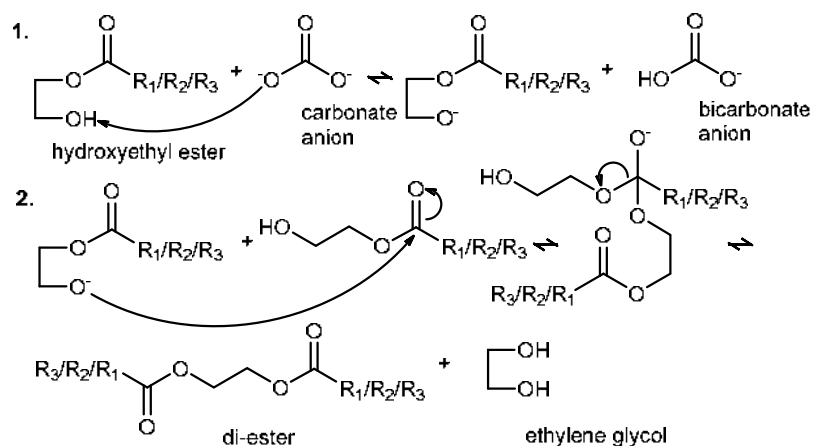


Fig 3. Proposed reaction mechanism of di-ester formation

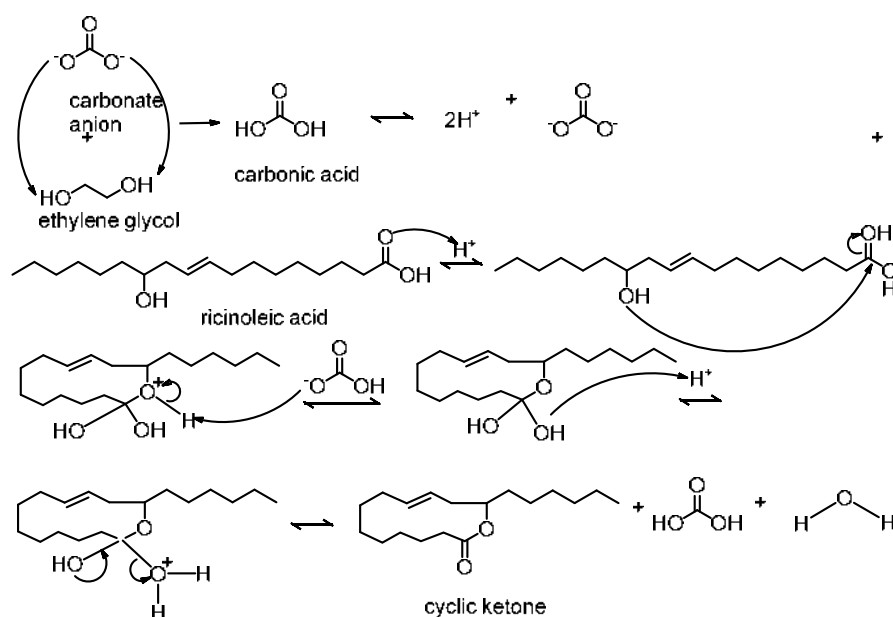


Fig 4. Proposed intramolecular esterification of ricinoleic acid

Table 4. Kinematic viscosity and lubrication properties of the transesterified product and low-sulfur fossil diesel

Properties	Unit	Testing method	Product of this study	Low-sulfur fossil diesel
Kinematic viscosity at 40 °C	mm ² /s	ASTM D445	51.86	3.39
Lubricity		ASTM D6079		
- WSD average	μm		198.5	279
- Coefficient of friction average	-		0.083	0.163
- Film thickness	%		75	77

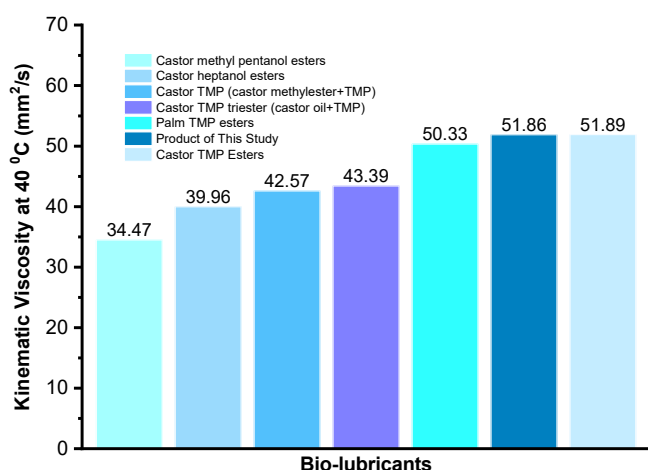


Fig 5. Comparison of kinematic viscosity between the product of this study and bio-lubricants. A–E (meet ISO viscosity grade 46); F–G (meet ISO viscosity grade 32). Reference of B [42]; C [43]; D [43]; E [42]; F [44]; G [44]. TMP = trimethyl propane

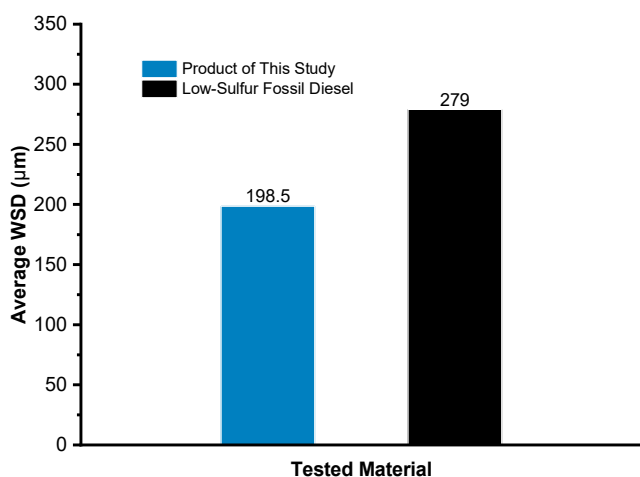


Fig 6. WSD value of product of this study (blue) and low-sulfur fossil diesel (black)

The kinematic viscosity in this work is similar to bio-lubricants 34–51 mm²/s, as reported by Heikal et al. [42] McNutt et al. [43], and Encinar et al. [44] (Fig. 5). The

kinematic viscosity of the product of this work met ISO Viscosity Grade 46.

From Fig. 6, it is known that the WSD value of the product in this study is below EN 590 (460 μm) and ASTM D975 (520 μm) limit. It is lower than the fossil diesel reference. This circumstance is caused by the ester and cyclic ester content in the product (Table 3), although the cyclic ester has a minor contribution to lubrication [45].

Based on obtained WSD value, the 2-hydroxyethyl esters are suspected to be the main contributors to lubrication, especially 2-hydroxyethyl ricinoleate (as shown in Table 3, 77.75%). This data is supported by film thickness data displayed in Fig. 7. The black line demonstrates that the lubrication film fluctuates in the fossil fuel during the test. Lubrication film is created and destroyed repeatedly. The destruction of the lubrication film is more severe in fossil diesel than in the product of this study (blue line). As a result, the WSD value of the product of this study is lower than fossil diesel. Based on this evidence, the head and tail polarity of 2-hydroxyethyl ricinoleate are responsible for the product's lubrication.

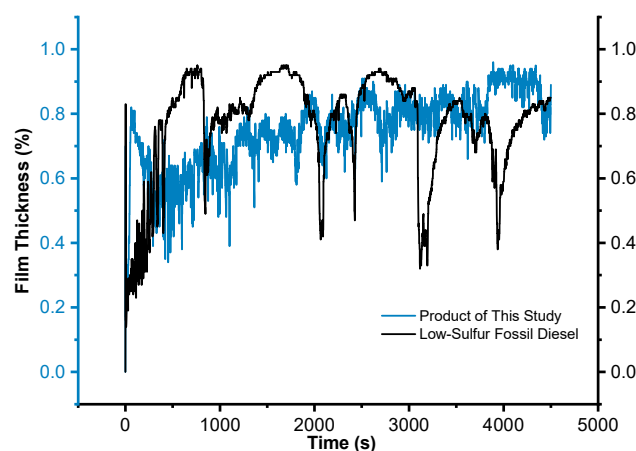


Fig 7. Graphic of film thickness: product in this study (blue) and low-sulfur fossil diesel (black)

It was similar to Canoira et al. [46] and Prasad et al. [15] that lubrication film formation related directly to methyl ricinoleate as the major component. Fig. 8 indicates that the friction coefficient of low-sulfur fossil diesel high-fluctuates at the beginning of the measurement (black). It means more friction occurred for low-sulfur fossil diesel than for the product in this study (blue). As a result, the friction coefficient value of low-sulfur diesel is higher than the product of this work.

We observe that the product's lubrication film and friction coefficient during testing are relatively more stable than fossil diesel. This phenomenon shows that utilizing ethylene glycol has successfully enhanced the polarity of ester. It also indicates that besides FAME or FAEE, the 2-hydroxyethyl ester can be a potential alternative bio-additive for lubricity enhancement of low-sulfur fossil diesel. This fact is supported by Sukjit et al. [45]. Knothe and Steidley [18] reported that the functional group polarity impacted the lubrication properties. The increasing functional group polarity causes lubrication properties enhancement significantly.

Analysis of the WSD value of this study compared to castor oil ethyl ester from the published article can be seen in Fig. 9. Although our product has a hydroxyl group on the alkyl ester, we notice a difference between the WSD value in this research and the ethyl ester of castor oil reported by Prasad et al. [15] and Yusoff et al. [29]. Some reasons may explain this phenomenon. First, the FFA content in our raw material was not decreased. The presence of FFA may react with part of carbonate ions to form soap. Consequently, it reduces hydroxyethyl esters yield (including 2-hydroxyethyl ricinoleate). It is analogous to the influence of FFA in the FAME synthesis [47]. The second reason is due to applying wet catalysts in this research. The presence of water content in K_2CO_3 may encourage hydrolysis and saponification reactions. It also decreased hydroxyethyl ester yield, and it is similar to the water content effect on the FAME synthesis [48]. Besides that, monoglyceride content significantly affects lubrication improvement. In this study, monoglyceride was not detected in the product. Hence, it diminishes lubrication [18-19,49].

For the reasons mentioned above, our product quality

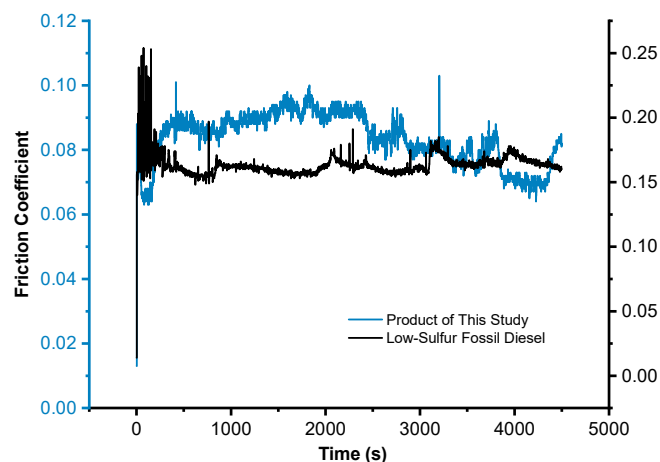


Fig 8. Graphic friction coefficient: product in this study (blue) and low-sulfur fossil diesel (black)

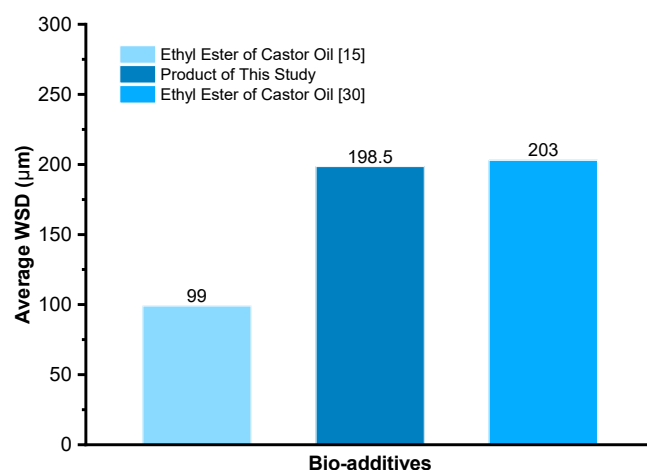


Fig 9. Comparison of WSD value between bio-additive this study and others. WSD value of other ethyl ester = 99 µm [15], 203 µm [29]

allows being boosted. The product can be a candidate bio-additive to improve low-sulfur fossil diesel lubrication.

Possibility of Lubrication Mechanism of 2-Hydroxyethyl Ester from Castor Oil

The lubrication mechanism of the product may be explained by the compound majority contained in the mixture, similar to Loehlè et al. [50-51]. As shown in Fig. 10, among fatty acid chains, 2-hydroxyethyl ricinoleate occurred Van der Waals forces, hydrogen bonding, and physisorption on the metal surface. Oxygen moieties of hydroxyl group or carbonyl group bound to iron or iron oxide of a metal surface (chemisorption). The presence of

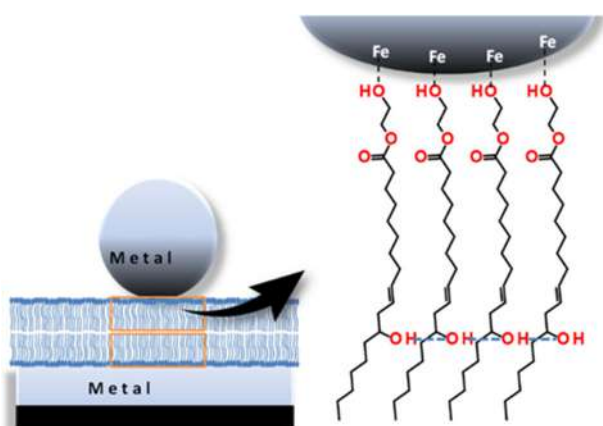


Fig 10. Possibility proposed lubrication mechanism of 2-hydroxyethyl ricinoleate

these sorptions generated and kept the boundary lubrication film. It prevents direct contact with metal surfaces, thereby dwindling friction and wear. The hydroxyl group at the alkyl chain played a vital role in the lubrication of the product of this study. This hypothesis agrees with the findings reported previously [18, 45].

■ CONCLUSION

The castor oil was successfully transesterified by ethylene glycol, and the fossil diesel fuel used as a reference in the lubrication comparison is low-sulfur commercial diesel fuel. Based on the measurement results, ethylene glycolysis products' kinematic viscosity and lubricity properties are better than low-sulfur fossil diesel. Although the film thickness of fossil diesel is slightly larger than that of the synthetic product, the stability of the protective layer of fossil diesel is worse than the product of this study. Good tribological behavior of the product of ethylene glycolysis due to the chemical contained in it, the compounds were 2-hydroxyethyl esters (94.16%), lactone (1.92%), and di-ester (1.12%). The central lubrication contributor was 2-hydroxyethyl ricinoleate. The kinematic viscosity and lubricity of the product were 51.86 mm²/s and 198.5 μm, respectively. It met ISO viscosity grade 46 and lubricity below EN 590 or ASTM D975 limit. It has proven that the product in this study deserves to be proposed as a bio-additive to enhance low-sulfur diesel lubrication derived from the desulfurization process at the refinery. However, it is necessary to carry out further research on this subject,

such as strategies to obtain the maximum 2-hydroxyethyl ester yield. The tribological effect of adding bio-additive to fossil diesel also needs to be attempted. Other studies can also be performed by comparing the tribological properties of 2-hydroxyethyl ester and ethyl ester of the same castor oil. Thus, the results of this study encourage other researchers to develop alternative bio-additives for fossil diesel lubricity enhancers.

■ ACKNOWLEDGMENTS

A.F would like to thank the financial support from Program 5000 Doktor Dalam Negeri Scholarship, Ministry of Religious Affairs, The Republic of Indonesia for the doctoral scholarship (KPPK Direktorat Pendidikan Tinggi Keagamaan Islam, Direktorat Jenderal Pendidikan Islam, Kementerian Agama No. 4021), the research and analytical support from Institut Teknologi Sepuluh Nopember (ITS) and PEM Akamigas. Also, express our deepest gratitude to Prof. Michelle Jakeline Cunha Rezende from the Institute of Chemistry, Federal University of Rio de Janeiro for her best advice in this research. Thanks also to Muhammad Salman Al Kahfi, who helped improve the figures.

■ AUTHOR CONTRIBUTIONS

Arizal Firmansyah: conceptualization, writing-original draft, and writing-review & editing. R. Y. Perry Burhan: conceptualization, methodology, supervision, writing-review & editing. Yulfi Zetra: validation, methodology, supervision, writing-review & editing. Didik Prasetyoko: validation, methodology, supervision, writing-review & editing. Novesar Jamarun: proofreading. All authors agreed to the final version of this manuscript.

■ REFERENCES

- [1] Sahin, Z., Kurt, M., and Durgun, O., 2018, Heat release analysis of gasoline fumigation in a diesel engine, *Energy Procedia*, 147, 322–328.
- [2] Hoseinpour, M., Sadrnia, H., Tabasizadeh, M., and Ghobadian, B., 2017, Energy and exergy analyses of a diesel engine fueled with diesel, biodiesel-diesel blend and gasoline fumigation, *Energy*, 141, 2408–2420.

- [3] Aklilu, A.Z., 2020, Gasoline and diesel demand in the EU: Implications for the 2030 emission goal, *Renewable Sustainable Energy Rev.*, 118, 109530.
- [4] Liddle, B., and Huntington, H., 2020, 'On the Road Again': A 118 country panel analysis of gasoline and diesel demand, *Transp. Res. A: Policy Pract.*, 142, 151–167.
- [5] Zhang, Y., Cao, Y., Tang, Y., Ying, Q., Hopke, P.K., Zeng, Y., Xu, X., Xia, Z., and Qiao, X., 2020, Wet deposition of sulfur and nitrogen at Mt. Emei in the West China Rain Zone, southwestern China: Status, inter-annual changes, and sources, *Sci. Total Environ.*, 713, 136676.
- [6] Qiao, X., Shu, X., Tang, Y., Duan, L., Seyler, B.C., Guo, H., Xiao, Y., Ying, Q., and Zhang, H., 2021, Atmospheric deposition of sulfur and nitrogen in the West China rain zone: Fluxes, concentrations, ecological risks, and source apportionment, *Atmos. Res.*, 256, 105569.
- [7] Zhang, W., Li, X., Wang, H., Song, Y., Zhang, S., and Li, C., 2017, Deep desulfurization of model oil by photocatalytic air oxidation and adsorption using $Ti_{(1-x)}M_xO_2$ ($M=Zr, Ce$), *Korean J. Chem. Eng.*, 34 (12), 3132–3141.
- [8] de León, J.N.D., Kumar, C.R., Antúnez-García, J., and Fuentes-Moyado, S., 2019, Recent insights in transition metal sulfide hydrodesulfurization catalysts for the production of ultra low sulfur diesel: A short review, *Catalysts*, 9 (1), 87.
- [9] Matzke, M., Jess, A., and Litzow, U., 2015, Polar nitrogen-containing aromatic compounds as carriers of natural diesel lubricity, *Fuel*, 140, 770–777.
- [10] Hsieh, P.Y., and Bruno, T.J., 2015, A perspective on the origin of lubricity in petroleum distillate motor fuels, *Fuel Process. Technol.*, 129, 52–60.
- [11] Hsieh, P.Y., Widegren, J.A., Slifka, A.J., Hagen, A.J., and Rorrer, R.A.L., 2015, Direct measurement of trace polycyclic aromatic hydrocarbons in diesel fuel with 1H and ^{13}C NMR spectroscopy: Effect of PAH content on fuel lubricity, *Energy Fuels*, 29 (7), 4289–4297.
- [12] Sukjit, E., and Dearn, K.D., 2011, Enhancing the lubricity of an environmentally friendly Swedish diesel fuel MK1, *Wear*, 271 (9-10), 1772–1777.
- [13] Sun, L., Li, M., Ma, C., Li, P., and Li, J., 2016, Preparation and evaluation of lubricity additives for low sulfur diesel fuel, *Energy Fuels*, 30 (7), 5672–5676.
- [14] Sun, L., Li, M., Ma, C., and Li, P., 2017, Preparation and evaluation of *Jatropha curcas* based catalyst and functionalized blend components for low sulfur diesel fuel, *Fuel*, 206, 27–33.
- [15] Prasad, L., Das, L.M., and Naik, S.N., 2012, Effect of castor oil, methyl and ethyl esters as lubricity enhancer for low lubricity diesel fuel (LLDF), *Energy Fuels*, 26 (8), 5307–5315.
- [16] Jiang, J., Zhang, Y., Zheng, Y., and Jiang, P., 2013, Transesterification of soybean oil with ethylene glycol, catalyzed by modified Li-Al layered double hydroxides, *Chem. Eng. Technol.*, 36 (8), 1371–1377.
- [17] Rezende, M.J.C., Perruso, C.R., Azevedo, D.A., and Pinto, A.C., 2005, Characterization of lubricity improver additive in diesel by gas chromatography-mass spectrometry, *J. Chromatogr. A*, 1063 (1-2), 211–215.
- [18] Knothe, G., and Steidley, K.R., 2005, Lubricity of components of biodiesel and petrodiesel. The origin of biodiesel lubricity, *Energy Fuels*, 19 (3), 1192–1200.
- [19] Hu, J., Du, Z., Li, C., and Min, E., 2005, Study on the lubrication properties of biodiesel as fuel lubricity enhancers, *Fuel*, 84 (12-13), 1601–1606.
- [20] Yang, T., Rebsdorf, M., Engelrud, U., and Xu, X., 2005, Monoacylglycerol synthesis via enzymatic glycerolysis using a simple and efficient reaction system, *J. Food Lipids*, 12 (4), 299–312.
- [21] Hobuss, C.B., da Silva, F.A., dos Santos, M.A.Z., de Pereira, C.M.P., Schulz, G.A.S., and Bianchini, D., 2020, Synthesis and characterization of monoacylglycerols through glycerolysis of ethyl esters derived from linseed oil by green processes, *RSC Adv.*, 10 (4), 2327–2336.
- [22] Pyo, Y.G., Hong, S.I., Kim, Y., Kim, B.H., and Kim, I.H., 2012, Synthesis of monoacylglycerol containing pinolenic acid via stepwise esterification using a cold active lipase, *Biotechnol. Prog.*, 28 (5), 1218–1224.

- [23] Luo, H., Zhai, Z., Fan, W., Cui, W., Nan, G., and Li, Z., 2015, Monoacylglycerol synthesis by glycerolysis of soybean oil using alkaline ionic liquid, *Ind. Eng. Chem. Res.*, 54 (18), 4923–4928.
- [24] Nosal, H., Moser, K., Warzała, M., Holzer, A., Stańczyk, D., and Sabura, E., 2020, Selected fatty acids esters as potential PHB-V bioplasticizers: Effect on mechanical properties of the polymer, *J. Polym. Environ.*, 29 (1), 38–53.
- [25] Rios, Í.C., Cordeiro, J.P., Arruda, T.B.M.G., Rodrigues, F.E.A., Uchoa, A.F.J., Luna, F.M.T., Cavalcante, C.L., and Ricardo, N.M.P.S., 2020, Chemical modification of castor oil fatty acids (*Ricinus communis*) for biolubricant applications: An alternative for Brazil's green market, *Ind. Crops Prod.*, 145, 112000.
- [26] Changmai, B., Vanlalveni, C., Ingle, A.P., Bhagat, R., and Rokhum, L., 2020, Widely used catalysts in biodiesel production: A review, *RSC Adv.*, 10 (68), 41625–41679.
- [27] Wang, W., Shen, B., Li, Y., Ni, Q., Zhou, L., and Du, F., 2021, Friction reduction mechanism of glycerol monooleate-containing lubricants at elevated temperature - transition from physisorption to chemisorption, *Sci. Prog.*, 104 (1), 1–15.
- [28] Shen, W., Hirayama, T., Yamashita, N., Adachi, M., Oshio, T., Tsuneoka, H., Tagawa, K., Yagishita, K., and Yamada, N.L., 2022, Relationship between interfacial adsorption of additive molecules and reduction of friction coefficient in the organic friction modifiers-ZDDP combinations, *Tribol. Int.*, 167, 107365.
- [29] Yusoff, M.F.M., Xu, X., and Guo, Z., 2014, Comparison of fatty acid methyl and ethyl esters as biodiesel base stock: A review on processing and production requirements, *J. Am. Oil Chem. Soc.*, 91 (4), 525–531.
- [30] Rashid, U., Anwar, F., Moser, B.R., and Ashraf, S., 2008, Production of sunflower oil methyl esters by optimized alkali-catalyzed methanolysis, *Biomass Bioenergy*, 32 (12), 1202–1205.
- [31] Sánchez, A., Maceiras, R., Cancela, A., and Rodríguez, M., 2012, Influence of *n*-hexane on *in Situ* transesterification of marine macroalgae, *Energies*, 5 (2), 243–257.
- [32] Geller, D.P., and Goodrum, J.W., 2004, Effects of specific fatty acid methyl esters on diesel fuel lubricity, *Fuel*, 83 (17-18), 2351–2356.
- [33] Sáez-Bastante, J., Pinzi, S., Jiménez-Romero, F.J., Luque de Castro, M.D., Priego-Capote, F., and Dorado, M.P., 2015, Synthesis of biodiesel from castor oil: Silent *versus* sonicated methylation and energy studies, *Energy Convers. Manage.*, 96, 561–567.
- [34] Dias, J.M., Araújo, J.M., Costa, J.F., Alvim-Ferraz, M.C.M., and Almeida, M.F., 2013, Biodiesel production from raw castor oil, *Energy*, 53, 58–66.
- [35] Thakkar, K., Kachhwaha, S.S., and Kodgire, P., 2022, Multi-response optimization of transesterification reaction for biodiesel production from castor oil assisted by hydrodynamic cavitation, *Fuel*, 308, 121907.
- [36] Guo, S., Li, C., Zhang, Y., Yang, M., Jia, D., Zhang, X., Liu, G., Li, R., Bing, Z., and Ji, H., 2018, Analysis of volume ratio of castor/soybean oil mixture on minimum quantity lubrication grinding performance and microstructure evaluation by fractal dimension, *Ind. Crops Prod.*, 111, 494–505.
- [37] Bekele, B.A., Ourgessa, A.W., Terefe, A.A., and Hailu, S.S., 2018, Studies on Ethiopian castor seed (*Ricinus communis* L.): Extraction and characterization of seed oil, *J. Nat. Prod. Resour.*, 4 (2), 188–190.
- [38] Pečar, D., and Goršek, A., 2015, Kinetic modeling of ethylene glycol monoesterification, *Int. J. Chem. Kinet.*, 47 (10), 658–663.
- [39] Hiware, S.B., and Gaikar, V.G., 2020, Solvent-free esterification of stearic acid and ethylene glycol with heterogeneous catalysis in a stirred batch microwave reactor, *SN Appl. Sci.*, 2 (4), 712.
- [40] Clayden, J., Greeves, N., Warren, S., and Wothers, P., 2001, Organic Chemistry, Oxford University Press, Oxford, UK.
- [41] Long, Y., Galipaud, J., Weihnacht, V., Makowski, S., Martin, J.M., and De Barros Bouchet, M.I., 2022, Achieving superlubricity using selected tribo-pairs

- lubricated by castor oil and unsaturated fatty acids, *Tribol. Int.*, 169, 107462.
- [42] Heikal, E.K., Elmelawy, M.S., Khalil, S.A., and Elbasuny, N.M., 2017, Manufacturing of environment friendly biolubricants from vegetable oils, *Egypt. J. Pet.*, 26 (1), 53–59.
- [43] McNutt, J., and He, Q.S., 2016, Development of biolubricants from vegetable oils via chemical modification, *J. Ind. Eng. Chem.*, 36, 1–12.
- [44] Encinar, J.M., Nogales-Delgado, S., Sánchez, N., and González, J.F., 2020, Biolubricants from rapeseed and castor oil transesterification by using titanium isopropoxide as a catalyst: Production and characterization, *Catalysts*, 10 (4), 366.
- [45] Sukjit, E., Poapongsakorn, P., Dearn, K.D., Lapuerta, M., and Sánchez-Valdepeñas, J., 2017, Investigation of the lubrication properties and tribological mechanisms of oxygenated compounds, *Wear*, 376-377, 836–842.
- [46] Canoira, L., García Galeán, J., Alcántara, R., Lapuerta, M., and García-Contreras, R., 2010, Fatty acid methyl esters (FAMES) from castor oil: Production process assessment and synergistic effects in its properties, *Renewable Energy*, 35 (1), 208–217.
- [47] Bouaid, A., Vázquez, R., Martinez, M., and Aracil, J., 2016, Effect of free fatty acids contents on biodiesel quality. Pilot plant studies, *Fuel*, 174, 54–62.
- [48] Anantapinitwatna, A., Ngaosuwan, K., Kiatkittipong, W., Wongsawaeng, D., Anantpinijwatna, A., Quitain, A.T., and Assabumrungrat, S., 2021, Water influence on the kinetics of transesterification using CaO catalyst to produce biodiesel, *Fuel*, 296, 120653.
- [49] Sundus, F., Masjuki, H.H., and Fazal, M.A., 2017, Analysis of tribological properties of palm biodiesel and oxidized biodiesel blends, *Tribol. Trans.*, 60 (3), 530–536.
- [50] Loehlé, S., Matta, C., Minfray, C., Mogne, T.L., Iovine, R., Obara, Y., Miyamoto, A., and Martin, J.M., 2015, Mixed lubrication of steel by C18 fatty acids revisited. Part I: Toward the formation of carboxylate, *Tribol. Int.*, 82, 218–227.
- [51] Loehlé, S., Matta, C., Minfray, C., Mogne, T.L., Iovine, R., Obara, Y., Miyamoto, A., and Martin, J.M., 2016, Mixed lubrication of steel by C18 fatty acids revisited. Part II: Influence of some key parameters, *Tribol. Int.*, 94, 207–216.

Effect of Ascorbic Acid Concentration on the Stability of Tartrate-Capped Silver Nanoparticles

Indah Miftakhul Janah, Roto Roto, and Dwi Siswanta*

Department of Chemistry, Faculty of Mathematics and Natural Sciences, Universitas Gadjah Mada, Sekip Utara, Yogyakarta 55281, Indonesia

* **Corresponding author:**

email: dsiswanta@ugm.ac.id

Received: February 22, 2022

Accepted: April 1, 2022

DOI: 10.22146/ijc.73196

Abstract: In this work, tartrate-capped silver nanoparticles (AgNPs) by reducing Ag^+ ions into Ag^0 using L-ascorbic acid and capping disodium tartrate have been prepared. The reaction was carried out at room temperature in an alkaline medium of pH 11 to obtain a rapid and one-step green synthesis method. The effect of L-ascorbic acid concentration on the synthesis preparation was studied to investigate their impact on the particle size, morphology, and stability of the AgNPs. The obtained tartrate capped AgNPs have SPR absorbance in 390–410 nm. They have a spherical shape, as confirmed by TEM. Increasing L-ascorbic acid concentrations from 25 mM to 100 and 200 mM leads to the 27, 17, and 11 nm particle size distributions. They give the zeta potential of -33.5 , -20.8 , and -21.3 , respectively. After a week, the decreasing absorbance peaks were 0.151, 0.0105, and 0.336 a.u. The optimum L-ascorbic acid concentration was obtained at 100 mM, indicated by the smallest FWHM point. Thus, we may conclude that lower or higher levels of reducing agents resulted in low stability. Therefore, controlling L-ascorbic acid concentration is an important parameter. A sufficient concentration and an appropriate capping agent can produce good nanoparticle stability essential for further application.

Keywords: silver nanoparticles; L-ascorbic acid; disodium tartrate; green synthesis; stability

■ INTRODUCTION

Metal nanoparticles display unique physicochemical properties different from bulk metal, including large surface area, high-volume ratio, powerful optical, conductivity, catalytic, and magnetic properties [1]. Their properties are promising for various purposes, such as biological [2-3], chemical [4-5], and environmental [6-7] applications. AgNPs showed better performance in many applications, especially for sensing, than AuNPs because of the higher extinction coefficient, the ratio of scattering to extinction, field enhancements, and extinction bands, which are powerful in many applications, especially for sensing [8]. However, the lower chemical stability of silver nanoparticles becomes weakness of their properties, but many studies have been conducted to improve their stability by using a capping agent [8]. As a consequence, silver nanoparticles are popular for many purposes. These physicochemical nanostructure properties could be

maintained by understanding that stability is an essential parameter for fundamental and applied studies explained as a function of composition, size, shape, and surface chemistry [9-10].

Recently, green chemistry topics have rapidly grown in various research fields. Green synthesis design related to green chemical reactants, processes, and products reduced the use of hazardous materials and has become a critical issue in the nanomaterial topics [1]. Various synthesis strategies, including chemical, physical, and biological methods, have been developed to produce AgNPs [11]. The chemical reduction method achieved by reducing a metal salt is the most frequently chosen among other methods because easy to control the reaction process and product [12]. Factors that affect the reduction process include the solvent medium, reducing, and capping agent [1]. Previous research reported using organic solvents and environmentally hazardous reducing

agents in the wet chemical reduction methods (i.e., hydrazine, sodium borohydride, dimethyl-formamide, formaldehyde, sodium hypophosphite, or hydroxylamine hydrochloride) [1]. L-ascorbic acid has been applied previously for green nanoparticles synthesized [11,13-14]. It is a green chemical that is a highly water-soluble compound, biodegradable, and environmentally friendly. It is an effective reducing agent to mediate the formation of spherical silver nanoparticles than other reducing agents [15]. Besides these advantages, the low stability of silver nanoparticles using L-ascorbic acid as a reducing agent has seldom been reported. The zeta potential is one of the parameters that indicate the stability of metal nanoparticles. The stable metal nanoparticles have a zeta potential value $> +25$ mV or < -25 mV [13]. Previous research synthesized PVA capped AgNPs using L-ascorbic acid as a reducing agent, resulting in the zeta potential of -10.40 mV [16] and L-ascorbic acid capped AuNPs zeta potential of -4 mV [17]. The weakness related to the properties of L-ascorbic acid is that it is easy to degrade. It decomposes into biologically inactive species in the air and oxygen, at high temperatures and in moist conditions [14]. The shortcomings of L-ascorbic acid can be overcome by adding several capping agents to reaction media to maintain the stability of metal nanoparticles. We used disodium tartrate as the capping agent that acts as stabilizing agents and ligands in an aqueous solution. Tartrate ligand is biocompatible, highly soluble in water, and environmentally benign. Meanwhile, it shows optical properties such as intrinsic fluorescence and enhanced photocatalytic activities [18]. The tartrate ion consists of the carboxyl group, tetrahedral carbon, and hydroxyl oxygen atom. In addition, some tartrate molecules are hydrated, i.e., they contain one, two, three, or four molecules of water [19].

The size and morphology of synthesized metal nanoparticles are essential to study because they determine the application's performance. The synthesis and catalytic properties of spherical Cu NPs were reported using L-ascorbic acid as a reducing and capping agent. The result indicates that the size of Cu NPs decreases (28 nm to 12 nm), and the catalytic activity increases along with the concentration of L-ascorbic acid [20]. An

increasing concentration of L-ascorbic acid is produced in sharp Au NPs called Au-sea urchin-like architecture. The particle size distribution was 600–800 nm which is made up of some nanopricks with an average length of 100–200 nm. SERS studies show that its performance is superior [21]. Synthesized Au NPs were done using sodium tartrate as a mild reducing agent. The result AuNPs showed that the increasing sodium tartrate concentration decreased particle size [22]. The study about the influence of tartaric acid concentration on structural and optical properties of Cu Se nanoparticles revealed that the particle size decreases with an increase in tartaric acid concentration, and the hexagonal structure was seen. The prepared Cu Se NPs' bandgap increased [23]. Ascorbic acid capped AgNPs [24], and tartrate capped AgNPs [25] were also chosen as capping for selective and sensitive Cr ion detection using the hydroxyl group as the conjugating site.

This study aimed to investigate the effect of L-ascorbic acid concentrations on the stability and properties of tartrate capped silver nanoparticles during storage. For this purpose, we prepared the tartrate capped silver nanoparticles using various concentrations of L-ascorbic acid as a reducing agent and capping with disodium tartrate. Then, we characterized the produced tartrate capped AgNPs in terms of particle size, morphology, and stability, important for further applications.

■ EXPERIMENTAL SECTION

Materials

Silver nitrate (AgNO_3) MERCK 1.01512, L-ascorbic acid ($\text{C}_6\text{H}_8\text{O}_6$) MERCK 1.00468, disodium tartrate dihydrate ($\text{C}_4\text{H}_8\text{Na}_2\text{O}_8 \cdot x\text{H}_2\text{O}$) MERCK 1.06663, and sodium hydroxide (NaOH) MERCK 1.06498 in the analytical grade were used without further purification.

Instrumentation

UV-Visible spectra were collected on a SPECORD 200 PLUS Analytic Jena UV-Visible spectrophotometer. TEM images were taken on a JEOL JEM-1400 electron microscope operated at an accelerating voltage of 120 kV, in which the colloid was dropped onto the

copper grid. The distribution of AgNPs particle size was calculated by using ImageJ software. Zeta potential was obtained on HORIBA Scientific SZ-100.

Procedure

Silver nanoparticles were prepared with a reducing agent of L-ascorbic acid and a capping agent of disodium tartrate. Typically, a 1 mL L-ascorbic acid solution with various concentrations (25, 50, 75, 100, 150, and 200 mM) was added to 16.0 mL disodium tartrate 4 mM. It was adjusted to pH 11.0 by adding 0.6 mol L⁻¹ NaOH solution. The 200 μ L of the aqueous solution of AgNO₃ 0.01 M was added under a stirring speed of 600 rpm at room temperature for 60 min. The effects of L-ascorbic acid concentrations on the synthesis preparation of silver nanoparticles were studied. In addition, the influence of storage time on the nanoparticle size and properties was investigated to know the stability of the produced nanoparticles.

RESULTS AND DISCUSSION

UV-Visible Study of the Effect of Ascorbic Acid on the Synthesized Tartrate Capped AgNPs

The increasing concentration of L-ascorbic acid on the UV-Vis spectra data of produced tartrate capped AgNPs was presented in Fig. 1(a). The peak absorbances are seen at 390, 400, 394, 391, 398, and 393, with the full width at half-maximum (FWHM) of 182.94, 147.01,

121.22, 108.65, 152.36, and 167.58 nm, respectively. The SPR absorbance of AgNPs appears at 350–450 nm [26]. The full width at half maxima (FWHM) of the SPR peaks describes the homogeneity of the nanoparticle size distribution. Increasing the FWHM values is proportional to increased particle size or polydispersity [27]. The UV-Vis spectra data concluded that the optimum L-ascorbic acid concentration was obtained at 100 mM, with the narrowest peak shape indicated by the smallest FWHM point. This result was confirmed by TEM in Fig. 2.

The resulted UV-Vis spectra of time evolution are shown in Fig. 1(b). The reducing and capping reaction was finished after 30 min as the UV-Vis absorption curves of 30–120 min overlapped. The L-ascorbic acid acts as the catalyst of the reaction. Therefore, a rapid synthesis can be carried out at room temperature without specific conditions. Insufficient or excess L-ascorbic acid concentration results in the broadening absorbance peak of the produce tartrate capped AgNPs.

On the other hand, low L-ascorbic acid concentration caused the silver salt to remain unchanged because of the insufficient reducing ability and generated the bigger size and irregular shape of NPs [28], as confirmed by TEM in Fig. 2(a). Meanwhile, the excess concentration resulted in explosive nucleation. This finding is related to the previous study that excessive concentration of caffeic acid [28] and ascorbic acid [21]

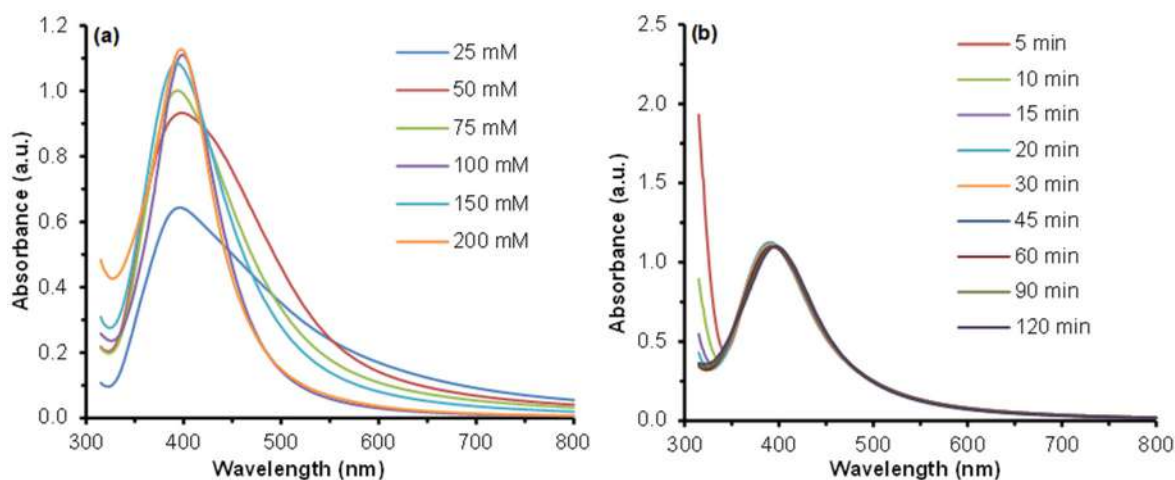


Fig 1. The UV-Visible spectrum of tartrate capped AgNPs (a) with various L-ascorbic acid concentrations, and (b) The synthesis time evolution

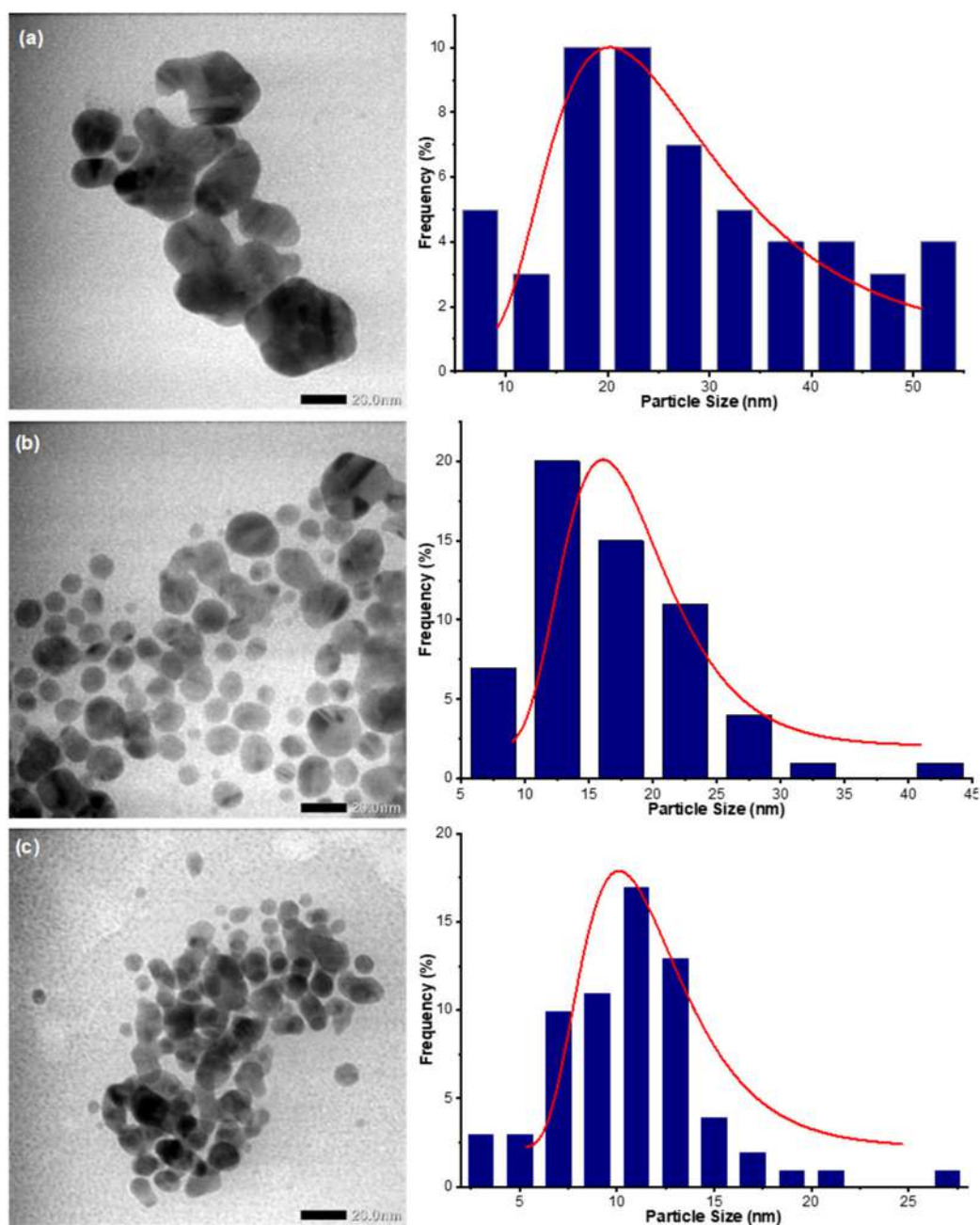


Fig 2. TEM images and particle size distribution histogram of the produced tartrate capped AgNPs with increasing concentration of L-ascorbic acid (a) 25, (b) 100, and (c) 200 mM with average particle sizes were 27, 17, and 11 nm

as reducing agents on the AuNPs synthesis generated sea-urchin architecture Au particle because of the rapid nucleation.

Metal nanoparticles are very sensitive to the environment, including pH conditions, ionic strength effect, and the addition of analytes producing an aggregation phenomenon [29]. Therefore, tartrate acted

as a stabilizing agent and played a critical role in the capping formation of the monodispersed nanoparticles after the reducing process. The capping agent gives a negative surface charge, resulting in electrostatic repulsion and increasing nanoparticles' stability [8]. Surface chemistry stability depends on the surrounding nanoparticles' composition (molecule content, pH). A

complex environment can cause exchange phenomena during storage [9].

Size and Morphology Analysis of the Effect of Ascorbic Acid on the Synthesized Tartrate Capped AgNPs

TEM analysis aims to confirm the morphology of the produced nanoparticles. TEM images and the histogram of the produced tartrate capped AgNPs were presented in Fig. 2. The measurement of the particle size distributions along with the increasing concentration of L-ascorbic acid (25, 100, and 200 mM) were 27, 17, and 11 nm, respectively. A previous study stated increasing L-ascorbic acid concentration decreased particle size [20].

A small concentration of L-ascorbic acid as a reducing agent resulted in a partially remaining unchanged silver ion and produced the bigger particle size of nanoparticles as represented by the TEM image in Fig. 2(a). The higher concentration of L-ascorbic acid, the smaller particle size was achieved in the reducing process of Ag^+ into Ag^0 because the surface of produced AgNPs is adsorbed by oxidation products and inhibits nanoparticles from growing further resulting in ultrafine AgNPs. Therefore, as the concentration of L-ascorbic acid increased, the encapsulated Ag^+ decreased, resulting in smaller AgNPs (Fig. 2(b)).

While an excess concentration of L-ascorbic acid caused explosive nucleation, a complex compound was formed from the lone pair electrons of L-ascorbic acid's polar groups that occupy two sp orbitals of the silver ion. Then Ag^+ is reduced to Ag^0 inside the nanoscopic templates. In nanoscopic templates, large random nuclei will be formed by homogeneous nucleation, and small silver nanoparticles are easily assembled. The silver core will grow into primary nanoparticles and be aggregated into microspheres to reduce the total energy system. The formed nanoparticles produce defects in their structure to become sites for further deposition of silver. Crystal growth was affected by the oxidation byproduct of L-ascorbic acid on the AgNPs after the reduction process was finished. L-ascorbic acid is oxidized into its byproduct dehydroascorbic acid during this process. The structure of dehydroascorbic acid shows three carbonyl

groups (1,2,3-tricarbonyl) which are very electrophilic. The interaction between 3-carbonyl and 6-OH groups rapidly forms the hemiacetal species. Dehydroascorbic acid resulted in pricks on the microsphere's surface and finally evolved into rough surface structures [21]. Therefore, the influence of excess L-ascorbic acid concentration produced explosive nucleation with a rough surface, as confirmed by the TEM image in Fig. 2(c).

Proposed Mechanism

The results show that tartrate-capped AgNPs can be achieved by reducing Ag^+ by L-ascorbic acid and capping using disodium tartrate. L-ascorbic acid is easily soluble in water that acts as a vinylous carboxylic acid. A conjugated system is formed by the lactone ring carbonyl double bond, the hydroxyl group lone pair, and the electrons in the double bond [1]. L-ascorbic acid acts as a stable (electron+proton) donor in the redox system. It changed into the radical ion species called semidehydro[ascorbic acid] and was further converted into dehydroascorbic acid's final product. Dehydroascorbic acid and L-ascorbic acid constitute the redox system sufficient to reduce Ag^+ to Ag^0 (Fig. 3).

Reduction of Ag^+ into Ag^0 by L-ascorbic acid and capped with tartrate gives stable colloidal AgNPs. The oxidation of L-ascorbic acid is a typical spontaneous redox system [1]. The nucleation rate goes up due to the increased reactivity of the L-ascorbic acid in an alkaline solution. Interaction of tartrate with Ag^0 is critical to control nanoparticle formation and prevent further aggregation and agglomeration. The proposed mechanism of tartrate capped AgNPs formation is displayed in Fig. 4.

The Stability Study of the Effect of Ascorbic Acid on the Synthesized Tartrate Capped AgNPs

The stability of nanoparticles is one of the critical parameters to further applications [9]. The use of a capping agent can prevent the agglomeration of particles. The prepared tartrate capped AgNPs with the high L-ascorbic acid concentration of 25, 100, and 200 mM gave lower stability as indicated by decreasing

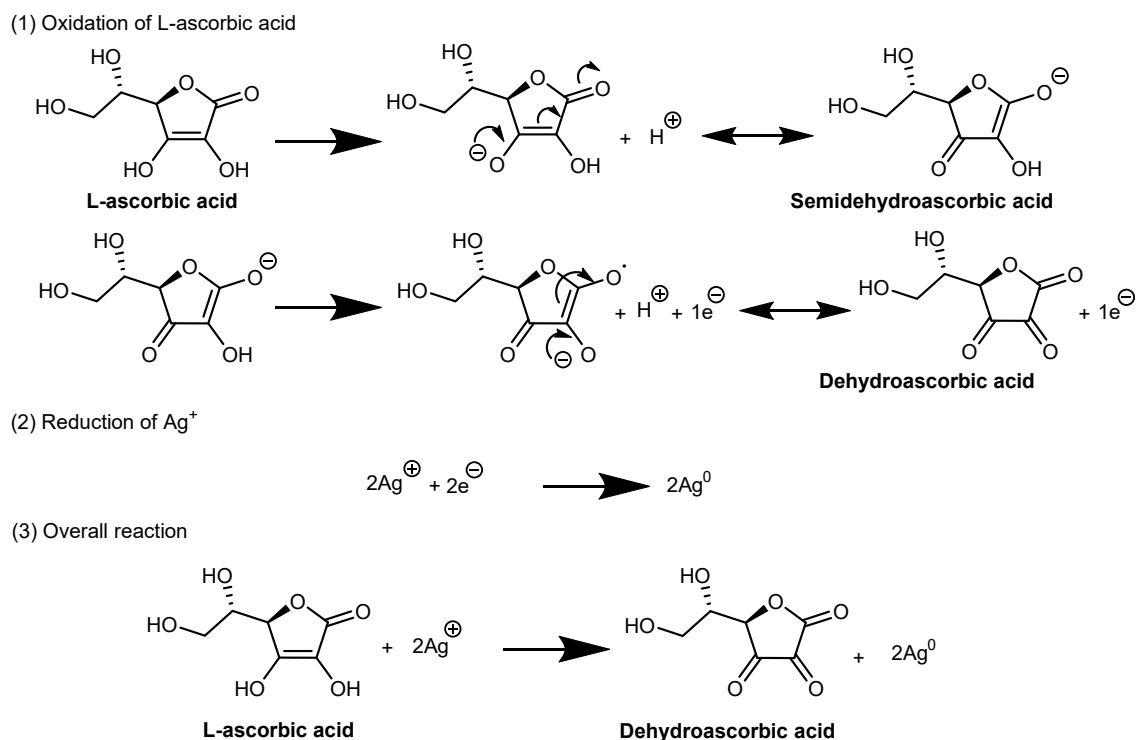


Fig 3. The reduction reaction for the formation of silver nanoparticles

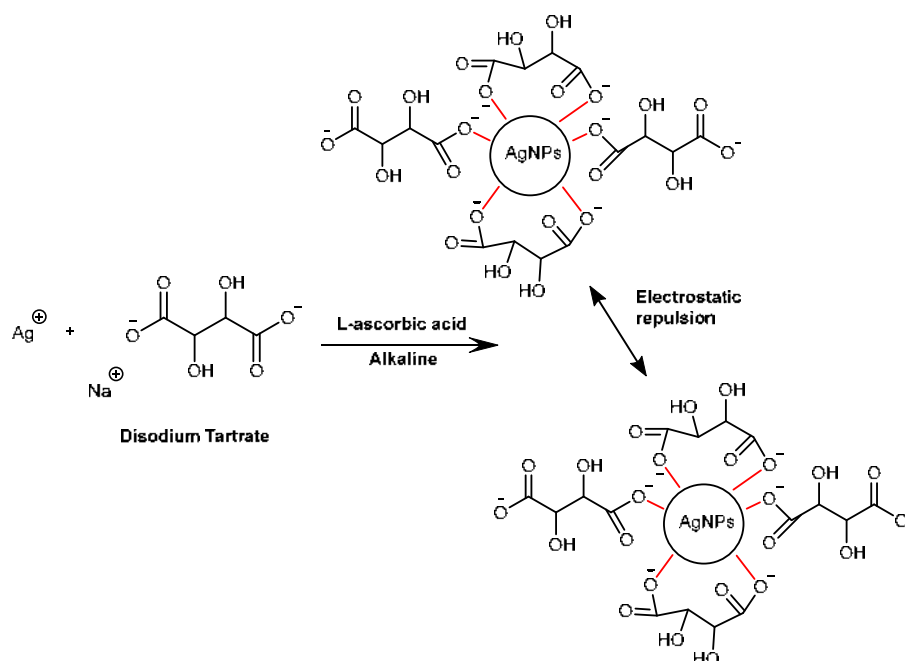


Fig 4. Proposed mechanism of tartrate capped AgNPs formation and stabilization

the zeta potential point of -33.5 , -20.8 , and -21.3 , respectively (Fig. 5). The stability of the product upon storage is shown in Fig. 6. The absorbance of the colloids decreased after one week with the order of L-ascorbic acid

concentrations of 25, 100, and 200 mM, which are 0.151, 0.0105, and 0.336.

The results suggest that a low concentration of L-ascorbic acid (25 mM) has the highest zeta potential

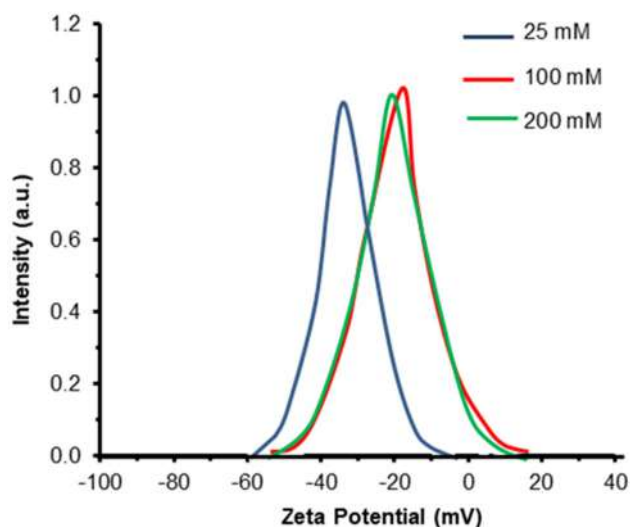


Fig 5. Zeta potential of tartrate capped AgNPs prepared in 25, 100, and 200 mM L-ascorbic acid

value, but it caused a faster decrease in absorbance than 100 mM. Meanwhile, the high concentration of L-ascorbic acid of 200 mM resulted in the most significant

reduction instability compared to the others. The zeta potential was similar for 100 mM. Thus, we may conclude that low or high levels of reducing agents resulted in low stability. Therefore, we should control the use of L-ascorbic acid concentration. The appropriate capping agent concentration can improve the produced nanoparticle stability.

UV-Visible spectra evaluated the stability of the produced colloidal AgNPs extended measurement during storage for AA 100 mM. Fig. 7 displays the UV-Vis spectra of the colloid measured from freshly prepared to 16 weeks. On day one, the peak absorbance was 1.1137, decreased to 0.9232 after 12 weeks, and decreased to 0.3411 after 16 weeks of storage. It means that the colloid is stable for up to 12 weeks. The lower the intensity, the broader the peak with the longer storage time. It indicated the reduced homogeneity of the particle size caused by the formation of larger particle sizes due to the nanoparticle aggregation and agglomeration to yield the

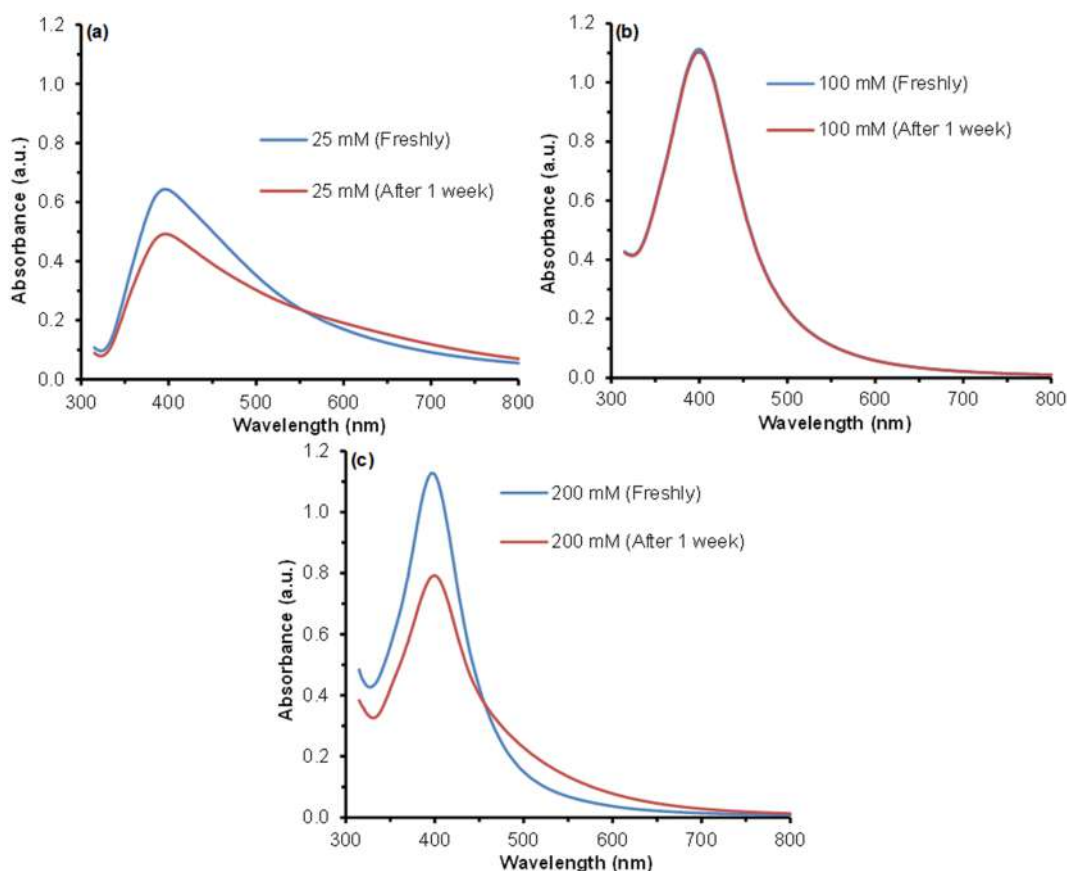


Fig 6. UV-Visible spectra of tartrate capped AgNPs by use of L-ascorbic acid (a) 25 mM, (b) 100 mM, and (c) 200 mM, freshly prepared and after one week

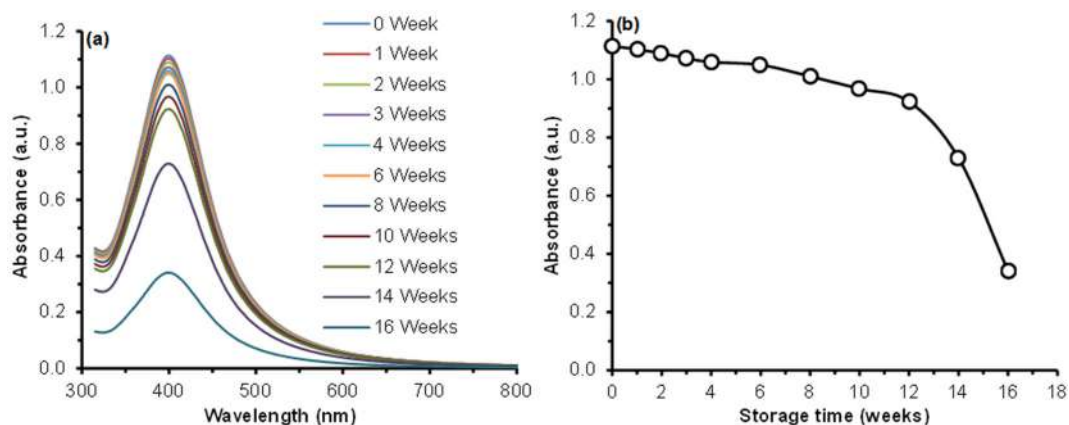


Fig 7. The absorbance change over the tartrate time capped AgNPs from week 1 to week 16

Table 1. Size distribution and zeta potential values of metal NPs in comparison with previous literature

Capping Agent	Reducing agent	Size distribution(nm)	Zeta potential (mV)	Reference
Chitosan capped AgNPs	ascorbic acid	200–700	+23.8 to +32.1	[30]
AA capped AuNPs	ascorbic acid	20–40	-4	[17]
PVA capped AgNPs	ascorbic acid	30	-10.40	[16]
Tartrate capped AgNPs	ascorbic acid	17	-20.8	This work

polydispersity of the colloid. The FWHM of the SPR absorbance peaks described the dispersity of nanoparticles, where a large FWHM value indicated the peak broadening due to increased polydispersity of nanoparticles [27].

The comparison between metal NPs size and stability reported earlier by L-ascorbic acid-reducing agents and this work is given in Table 1. The more positive or negative the zeta potential value, the better stability [13]. The produced tartrate capped colloidal AgNPs have relatively small particle sizes and good stability.

■ CONCLUSION

The concentration of ascorbic acid plays an important role in controlling the size, morphology, and stability of the produced tartrate capped AgNPs. Increasing L-ascorbic acid concentration from 25 mM to 100 mM and 200 mM decreased the particle size distributions from 27.29 to 16.87 and 10.72 nm, respectively. The zeta potential decreased from -33.5, -20.8, and -21.3 mV, lowering the absorbance peak after a week to 0.151, 0.0105, and 0.336, respectively. Reduction of silver nitrate by L-ascorbic acid is best performed at the concentration of 100 mM with a reaction time of around 30 min. The obtained colloids have good stability for the first 12 weeks. Based on our

result (1), the low concentration of L-ascorbic acid generated the bigger size and irregular shape of AgNPs. (2) As the concentration increases, the size of AgNPs were decreased with spherical shape and better uniformity due to the stabilizing effect. Meanwhile, the excess concentration resulted in explosive nucleation, generating the sea-urchin architecture. The less or excessive L-ascorbic acid concentration resulted in low stability. Therefore, the right concentration of L-ascorbic acid and appropriate capping agent can produce stable nanoparticles with homogeneous size and shape, essential for future applications.

■ ACKNOWLEDGMENTS

The authors thank Indonesia's Ministry of Research and Higher Education for providing the *Pendidikan Magister Menuju Doktor Untuk Sarjana Unggul* (PMDSU) scholarships for IMJ and research funding contract number 6/E1/KP.PTNBH/2021 and 2333/UN1/DITLIT/DIT-LIT/PT/2021.

■ REFERENCES

- [1] Xiong, J., Wang, Y., Xue, Q., and Wu, X., 2011, Synthesis of highly stable dispersions of nanosized

- copper particles using L-ascorbic acid, *Green Chem.*, 13 (4), 900–904.
- [2] Martinez-Andrade, J.M., Avalos-Borja, M., Vilchis-Nestor, A.R., Sanchez-Vargas, L.O., and Castro-Longoria, E., 2018, Dual function of EDTA with silver nanoparticles for root canal treatment—A novel modification, *PLoS One*, 13 (1), 1–19.
- [3] Guimarães, M.L., da Silva, F.A.G., da Costa, M.M., and de Oliveira, H.P., 2020, Green synthesis of silver nanoparticles using Ziziphus joazeiro leaf extract for production of antibacterial agents, *Appl. Nanosci.*, 10 (4), 1073–1081.
- [4] Xia, Y., Zhu, C., Bian, J., Li, Y., Liu, X., and Liu, Y., 2019, Highly sensitive and selective colorimetric detection of creatinine based on synergistic effect of PEG/Hg²⁺-AuNPs, *Nanomaterials*, 9 (10), 1424.
- [5] Li, J., Hou, C., Huo, D., Shen, C., Luo, X., Fa, H., Yang, M., and Zhou, J., 2017, Detection of trace nickel ions with a colorimetric sensor based on indicator displacement mechanism, *Sens. Actuators, B*, 241, 1294–1302.
- [6] Yakoh, A., Rattanarat, P., Siangproh, W., and Chailapakul, O., 2018, Simple and selective paper-based colorimetric sensor for determination of chloride ion in environmental samples using label-free silver nanoprisms, *Talanta*, 178, 134–140.
- [7] Ma, Y., Pang, Y., Liu, F., Xu, H., and Shen, X., 2016, Microwave-assisted ultrafast synthesis of silver nanoparticles for detection of Hg²⁺, *Spectrochim. Acta, Part A*, 153, 206–211.
- [8] Caro, C., Castillo, P.M., Klippstein, R., Pozo, D., and Zaderenko, A.P., 2010, "Silver Nanoparticles: Sensing and Imaging Applications" in *Silver Nanoparticles*, Eds. Perez, D.P., IntechOpen, Rijeka, Croatia, 201–225.
- [9] Phan, H.T., and Haes, A.J., 2019, What does nanoparticle stability mean?, *J. Phys. Chem. C*, 123 (27), 16495–16507.
- [10] Riaz Ahmed, K.B., Nagy, A.M., Brown, R.P., Zhang, Q., Malghan, S.G., and Goering, P.L., 2017, Silver nanoparticles: Significance of physicochemical properties and assay interference on the interpretation of in vitro cytotoxicity studies, *Toxicol. in Vitro*, 38, 179–192.
- [11] Elahi, N., Kamali, M., and Baghersad, M.H., 2018, Recent biomedical applications of gold nanoparticles: A review, *Talanta*, 184, 537–556.
- [12] Beyene, H.D., Werkneh, A.A., Bezabh, H.K., and Ambaye, T.G., 2017, Synthesis paradigm and applications of silver nanoparticles (AgNPs), a review, *Sustainable Mater. Technol.*, 13, 18–23.
- [13] Shnoudeh, A.J., Hamad, I., Abdo, R.W., Qadumii, L., Jaber, A.Y., Salim, H., and Alkelany, S.Z., 2019, "Synthesis, Characterization, and Applications of Metal Nanoparticles" in *Biomaterials and Bionanotechnology*, Eds. Tekade, R.K., Academic Press, Cambridge, US, 527–612.
- [14] Jang, K.I., and Lee, H.G., 2008, Stability of stability of chitosan nanoparticles for L-ascorbic acid during heat treatment in aqueous solution, *J. Agric. Food Chem.*, 56 (6), 1936–1941.
- [15] Qin, Y., Ji, X., Jing, J., Liu, H., Wu, H., and Yang, W., 2010, Size control over spherical silver nanoparticles by ascorbic acid reduction, *Colloids Surf., A*, 372 (1-3), 172–176.
- [16] Roto, R., Rasydta, H.P., Suratman, A., and Aprilita, N.H., 2018, effect of reducing agents on physical and chemical properties of silver nanoparticles, *Indones. J. Chem.*, 18 (4), 614–620.
- [17] Annur, S., Santosa, S.J., and Aprilita, N.H., 2018, PH dependence of size control in gold nanoparticles synthesized at room temperature, *Orient. J. Chem.*, 34 (5), 2305–2312.
- [18] Chakraborty, I., Rakshit, R., and Mandal, K., 2017, Synthesis and functionalization of MnFe₂O₄ nano-hollow spheres for novel optical and catalytic properties, *Surf. Interfaces*, 7, 106–112.
- [19] Abdel-Kader, M.M., El-Kabbany, F., and Taha, S., 1990, Physical properties and phase transitions in sodium tartrate dihydrate, *J. Mater. Sci.: Mater. Electron.*, 1 (4), 201–203.
- [20] Jain, S., Jain, A., Kachhawah, P., and Devra, V., 2015, Synthesis and size control of copper nanoparticles and their catalytic application, *Trans. Nonferrous Met. Soc. China*, 25 (12), 3995–4000.
- [21] Wang, X., Yang, D.P., Huang, P., Li, M., Li, C., Chen, D., and Cui, D., 2012, Hierarchically

- assembled Au microspheres and sea urchin-like architectures: Formation mechanism and SERS study, *Nanoscale*, 4 (24), 7766–7772.
- [22] González-Mendoza, A.L., and Cabrera-Lara, L.I., 2015, Reaction parameters for controlled sonosynthesis of gold nanoparticles, *J. Mex. Chem. Soc.*, 59 (2), 119–129.
- [23] Shitu, I.G., Talib, Z.A., Chi, J.L.Y., Kechick, M.M.A., and Baqiah, H., 2020, influence of tartaric acid concentration on structural and optical properties of CuSe nanoparticles synthesized via microwave assisted method, *Results Phys.*, 17, 103041.
- [24] Wu, X., Xu, Y., Dong, Y., Jiang, X., and Zhu, N., 2013, Colorimetric determination of hexavalent chromium with ascorbic acid capped silver nanoparticles, *Anal. Methods*, 5 (2), 560–565.
- [25] Xu, Y., Dong, Y., Jiang, X., and Zhu, N., 2013, Colorimetric detection of trivalent chromium in aqueous solution using tartrate-capped silver nanoparticles as probe, *J. Nanosci. Nanotechnol.*, 13 (10), 6820–6825.
- [26] Rycenga, M., Cobley, C.M., Zeng, J., Li, W., Moran, C.H., Zhang, Q., Qin, D., and Xia, Y., 2011, Controlling the synthesis and assembly of silver nanostructures for plasmonic applications, *Chem. Rev.*, 111 (6), 3669–3712.
- [27] Sharma, R., Dhillon, A., and Kumar, D., 2018, Mentha-stabilized silver nanoparticles for high-performance colorimetric detection of Al(III) in aqueous system, *Sci. Rep.*, 8 (1), 5189.
- [28] Kim, H., Seo, Y.S., Kim, K., Han, J.W., Park, Y., and Seonho, C., 2016, Concentration effect of reducing agents on green synthesis of gold nanoparticles: Size, morphology, and growth mechanism, *Nanoscale Res. Lett.*, 11, 230.
- [29] Du, H., Chen, R., Du, J., Fan, J., and Peng, X., 2016, Gold nanoparticle-based colorimetric recognition of creatinine with good selectivity and sensitivity, *Ind. Eng. Chem. Res.*, 55 (48), 12334–12340.
- [30] Zain, N.M., Stapley, A.G.F., and Shama, G., 2014, Green synthesis of silver and copper nanoparticles using ascorbic acid and chitosan for antimicrobial applications, *Carbohydr. Polym.*, 112, 195–202.

Protein Markers Related to Non-halal Slaughtering Process of Rat as Mammal Animal's Model Detected Using Mass Spectrometry Proteome Analysis

Alvina Nur Aini¹, Claude Mona Airin², and Tri Joko Raharjo^{1,3*}

¹Department of Chemistry, Faculty of Mathematics and Natural Sciences, Universitas Gadjah Mada, Sekip Utara, Yogyakarta 55281, Indonesia

²Department of Physiology, Faculty of Veterinary Medicine, Universitas Gadjah Mada, Jl. Fauna No. 2 Karangmalang, Yogyakarta 55281, Indonesia

³Institute of Halal Industry and System (IHIS), Universitas Gadjah Mada, Yogyakarta 55281, Indonesia

* **Corresponding author:**

email: trijr_mipa@ugm.ac.id

Received: March 18, 2022

Accepted: May 24, 2022

DOI: 10.22146/ijc.73656

Abstract: Meat produced from non-halal slaughter is forbidden for Moslems. The slaughter methods contribute to the physiological response of animals expressed as different proteome profile. Proteome of two meat obtained from the halal and non-halal slaughter of Wistar rats (*Rattus norvegicus*) as an animal model was used to search for protein markers related to the slaughter method. The analysis employed Sodium Dodecyl Sulphate Polyacrylamide Gel Electrophoresis (SDS-PAGE), and High-Resolution Mass Spectrometer (HRMS) assisted with Label-Free Quantification (LFQ) Proteome Discoverer software. The non-halal slaughter contributed to the changes in protein expression in animal meat where thirteen proteins were up-regulated and three proteins were specifically identified in the non-halal slaughter, these three proteins are NSFL1 cofactor p47, transketolase, and Von Willebrand. There are three stable peptides identified of those three proteins including SYQDPSNAQFLESIR ($m/z = 1755$, $z = +1$) part of NSFL1 cofactor p47, LGQSDPAPLQHQVDVYQK ($m/z = 2023$, $z = +1$) part of transketolase, and VPLLCTNGSVVHHEVINAMQCR ($m/z = 2550$, $z = +1$) part of Von Willebrand. Two of peptides can be targeted as markers in MRM mode LC-MS/MS routine analysis to authentication-halal slaughtering meat. The proposed MRM pair ions are 1755 to 1376, 1262, 1164, and 963, 2033 to 1355, 1016, and 762.

Keywords: non-halal slaughter; stress response; biomarker; mass spectrometry; label-free proteomics

■ INTRODUCTION

The large Muslim population and the increasing need for meat lead the determining of halal properties of meat is very important. To date, halal analysis that has been studied is related to the counterfeiting of non-halal products. Adulteration of meat and meat products with non-halal components, such as pork meat, has been extensively studied, and several methods have been developed to detect such adulteration [1-3]. Furthermore, the halal status of the meat is not only determined based on the animal used but also on the producing process of the meat, including the slaughtering process. To become

halal meat, the meat must be obtained from the animal that is slaughtered according to the halal method. Therefore, the development of methods to determine whether the meat is halal or non-halal based on the slaughtering methods have become crucial.

In general, slaughter of an animal is performed by using stunning techniques before cutting the jugular vein and carotid artery on the neck near the head. Otherwise, halal slaughter is performed by severing the animal neck using a sharp knife and acting in the name of God. Islam does not allow any deliberate torture to injure the animal before or after slaughter. Halal slaughter requires gentle handling of the animal before

and during the slaughter process. Therefore, halal slaughter should omit the stunning process. Good handling of animals during pre-slaughter and slaughter contributes significantly to the good meat quality as a product. Harsh treatment in handling animals before slaughter causes stress and produces low meat quality [4]. An effective slaughter will cause 40–60% of blood volume lost from animal bodies [5]. One of the factors that affect meat quality, contamination, and deterioration is the amount of blood retained in the animal body [6]. Blood is an excellent medium for the growth of bacteria. Blood components, especially hemoglobin, promote the lipid oxidation and decrease the shelf-life of meat and fish products [7]. Long transit time before slaughter also influenced the stress response and protein expression of animals [8]. According to Huang et al., the difference in treatment in the slaughtering process caused a stress response related to the expression level of certain genes of the animal [9].

In line with the halal authentication efforts, several studies have been conducted to compare the meat characteristics of meat due to the different pre-slaughter methods, mainly between the stunning and the non-stunning methods [10-12]. The difference in meat quality of lamb meat was found between those methods [13]. The stunning treatment could affect the stress response of animals [14], through changing gene expressions leading to different proteome patterns of the meat compared to the untreated one [9]. A study using 2D-electrophoresis-MALDI TOF showed different proteins of chicken meat resulting from the electrical current pre-treatment slaughter compared to the non-stunning chicken meat protein [15]. The protein of Voltage-Dependent Anion Channel 2 (VDAC2) was identified as a protein marker of the chicken meat treated using electrical stunning before slaughter. Further study reported other biomarker proteins related to the same treatment, which were troponin I and actin, both known as alpha cardiac muscle [16]. The same technique successfully identified a different pattern of the proteome of sheep meat due to the electrical stunning before slaughter [17]. In the comparison of chicken treated with gas stunning against non-stunning, a proteome analysis using 2D electrophoresis-MALDI

TOF revealed an increased expression of β -enolase, pyruvate kinase, and creatine kinase from the chicken meat treated by gas stunning [18].

Most of the reported techniques to distinguish the meat resulted from stunning and non-stunning slaughter used the laborious 2-D electrophoresis coupled with MALDI-TOF mass spectrometry. More sophisticated liquid chromatography coupled with high-resolution mass spectrometry (LC-HRMS) instruments has been successfully used in proteomic studies due to their simplicity [19]. This method is interesting to use to replace the 2D-electrophoresis MALDI-TOF system in the identification of protein markers in meat related to the slaughter process. On the other hand, most studies on searching protein markers to differentiate meat resulting from halal and non-halal slaughter used poultry as the sample, which was not representative of all meat-producing animals. Mammals, such as cattle, could have different metabolism systems to the poultry leading to different protein markers. This study aimed to identify proteins marker of meat resulting from non-halal slaughter using LC-HRMS, with a rat (*Rattus norvegicus*) used as a mammal model. The protein markers are concluded not only to the protein that was specifically expressed related to the non-halal slaughter but also to that which was up-regulated due to the process.

■ EXPERIMENTAL SECTION

Materials

The male, three months old Wistar rat (*Rattus norvegicus*) with an average weight of 200 g was used as the subject of the research. The sequencing grade modified trypsin (Promega) together with ammonium bicarbonate (Merck, Germany), dithiothreitol (Promega, USA), and iodoacetamide (Merck, Germany) were used to digest the protein. Sodium dodecyl sulfonate (SDS) (Merck), acrylamide, bisacrylamide, and ammonium persulfate (APS) (Sigma, USA), Precision Plus Protein Dual Color protein (BioRad, USA), were used during the SDS-PAGE profiling. The LC-HRMS analysis used MS-grade acetonitrile (Merck, Germany) and double distilled water as mobile phase.

Instrumentation

The instrumentations used in this study were the Ultimate 3000 Rapid Separation Ultra-High-Performance Liquid Chromatography connected to the Q-Exactive Orbitrap Mass Spectrometer (LC-HRMS) (Thermo Scientific, USA) and SDS- electrophoresis PAGE Mini Protean® II Cell (Bio-Rad), shaker incubator (Thermo Scientific, USA), refrigerated centrifuge (High-Speed Sigma Sartorius 3-30K, Sigma, USA) electric scale (Denver AA-250), vortex (MX-S IKA), and shaker mixer (RATEK Instrument). The softwares used in this study included Xcalibur and Proteome Discoverer 2.2 (Thermo Scientific, USA), ImageJ 1.52a, and STRING v11 [20-21].

Procedure

Animal slaughter

The protocol was approved by the Ethical Committee of Integrated Research and Testing Laboratory of Universitas Gadjah Mada, Yogyakarta (Ethical Clearance No. 00058/04/LPPT/2018 dated 6th June 2018). Six rats (*Rattus norvegicus*) were divided into two treatment groups. The first group of 3 was slaughtered according to the halal slaughtering guideline, which basically, the animal should not be dead prior to slaughtering. The slaughtering was performed by cutting the jugular vein, artery carotid, trachea, and esophagus using a sharp knife. While the second group of 3 was slaughtered through the cervical dislocation without anesthesia, as the non-halal method. After being slaughtered, meat was pooled and chilled at -80 °C until the extraction of protein.

Protein extraction

Protein was extracted from 0.5 g of meat from each rat using 2.5 mL of 0.05 M Tris HCl buffer (pH 7–8). The meat was homogenized with the buffer at room temperature using a vortex. The suspension was then centrifuged using a refrigerated centrifuge at 10,000 rpm for 20 min. The protein concentration of the supernatant was estimated using Lowry's protocol. The protein supernatant was stored at -80 °C until the digestion.

SDS-PAGE profiling

Protein supernatant was mixed with loading buffer and heated at 95 °C for 5 min. As much as 25 µg protein

for each sample was loaded into the gel. Protein was separated on 10% separating gel at a constant voltage of 125 V, 70 mA for 90 min. After the electrophoresis, the gel was stained using 10% of acetic acid, 45% of methanol, and 0.3% of Coomassie blue (v/v), followed by destaining using 10% of acetic acid and 20% of methanol. The interpretation of each protein band was carried out using ImageJ 1.52a [20].

Protein tryptic digestion

Two hundred µL of protein supernatant was transferred into a microcentrifuge tube and precipitated with 1,000 µL of ice-cold acetone at -20 °C for 24 h. The protein pellet was separated through centrifugation at 10,000 rpm for 20 min. The protein pellet was then dissolved in 0.05 M of ammonium bicarbonate. The protein solution was reduced and alkylated with 2 mM of dithiothreitol and 5 mM of iodoacetamide, respectively. As much as 2 µg of sequencing grade modified trypsin was added to the sample, and the enzymatic reaction lasted at 37 °C for 24 h. The digestion was stopped by adding 100% of formic acid to pH < 3. The digested protein was diluted with ultrapure distilled water: acetonitrile (95:5) and filtered through a nylon syringe filter before LC-HRMS analysis [22].

Liquid chromatography-high resolution mass spectrometry (LC-HRMS) analysis

Peptides obtained from the trypsin digestion, were separated using LC-HRMS equipped with a C18 trap column. As much as 5 µL of protein hydrolysate was eluted from the trap column and separated using Acclaim PepMap RSLC C18 column (75 µm × 150 mm, Thermo Fisher Scientific). A gradient system was adapted to separate the peptides. Mobile phase A consisted of water, and mobile phase B consisted of water containing 0.1% of formic acid and acetonitrile containing 0.08% of formic acid, with a ratio of 1:4. The initial gradient was 96% A and 4% B from 0 to 3 min. The portion of solvent B was increased linearly to reach 95% at 50 min and maintained at the same ratio until the end of analysis at 90 min. The flow rate was fixed at 0.3 µL/min. The Q Exactive Orbitrap Mass Spectrometer equipped with nano spray ionization was employed to detect the peptides operated under positive ion mode.

The MS parameters were set to analyze the m/z range of 200–2000, using full-MS/dd-MS2 mode. The resolving power of MS1 and MS2 were set at 140,000 and 17,500 (FWHM), respectively.

Protein identification and data analysis

The software Proteome Discoverer (PD) 2.2 was used to identify the protein based on the Uniprot database of *Rattus norvegicus*. The label-free quantification (LFQ) quantification workflow was performed through MS/MS signal intensity of identified protein. Calculation of the statistical significance was carried out using Student's *t*-test at level of p -value < 0.05. The differentially changed proteins were identified by performing a *Quan-ratio distribution* analysis between non-halal and halal slaughter identified proteins. For protein pathways, identification over the Kyoto Encyclopedia of Genes and Genomes (KEGG) was selected [23].

RESULTS AND DISCUSSION

Protein SDS-PAGE Profile

Protein profiling using the SDS-PAGE technique was carried out as the initial checking whether any clear differences in protein expression were caused by the different slaughter methods. Since the protein was isolated from meat, it was assumed that most of the protein belonged to the muscle proteins. According to Fig. 1, most of the protein observed in both group samples have sizes ranging from 17 to 115 kDa. Doherty et al., and the protein database The Uniprot Consortium have published the number of muscle proteins and their size [24–25]. The thick band with the size of approximately 17 kDa was identified most probably as myoglobin, while the tiny band above 100 kDa was calculated to have 116.2 kDa size and presumably identified as 2-oxoglutarate dehydrogenase. Further identification using ImageJ 1.52a produced some protein bands with the size of approximately 55, 49, 46, 41, and 26 kDa. There is plenty of possible proteins within those ranges of sizes. However, some possible proteins involved in the metabolism process of animal cells are enolase, creatine kinase, pyruvate kinase, phosphorylase, and myoglobin which are the main sarcoplasmic proteins. Meanwhile, the possible proteins contained in the skeletal muscle are sarcoplasmic, myofibrillar, myosin binding,

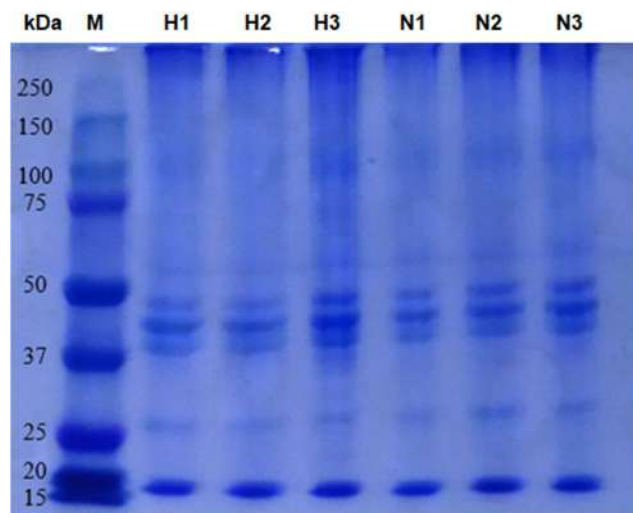


Fig 1. SDS-PAGE profile of the rat's muscle proteins for halal and non-halal slaughter. Each sample gave seven protein bands. M: protein marker; H1: halal method 1; H2: halal method 2; H3: halal method 3; N1: non-halal method 1; N2: non-halal method 2; N3: non-halal method 3

actin, and stromal proteins [26]. Some other possible proteins are dihydrolipoyl dehydrogenase, myosin-binding, calreticulin, and aspartate aminotransferase [24–25].

Comparison of the SDS-PAGE profile between proteins originating from halal and non-halal slaughter was proven to be difficult. The band with the size of 26 kDa shows a slight thicker for the non-halal slaughter protein. The lack of SDS-PAGE imaging comparison, such as an image analyzer for 2-D gel, hindered further investigation. At least, the SDS-PAGE data confirmed the success of protein isolation. Not only the main muscle proteins were successfully extracted, but also other proteins can be observed and interested to be further analyzed using mass spectrometry.

Up-Regulated Protein Abundance Due to Non-halal Slaughtering

A total of 253 proteins were identified from the LC-HRMS analysis from all samples, in which the abundance of several proteins was significantly different either in non-halal or halal slaughter. A *Quan-ratio* distribution was performed to determine the abundance ratio of the two slaughter groups. This comparison was

obtained through a ratio of non-halal/halal. Furthermore, the abundance of 13 proteins of non-halal slaughter was higher than the halal slaughter, as given in Table 1.

Most proteins (21.69% of the whole proteins) were associated with the metabolic process, while 29.97% of proteins acted as the protein binding. According to the KEGG database, some of these proteins were involved in the process of glucose metabolism in cells, such as β -enolase, dihydrolipoyl dehydrogenase, phosphoglucomutase 1, and malate dehydrogenase that present in glycolysis and gluconeogenesis process. Aspartate aminotransferase acted in the amino acid metabolism. Myc box-dependent-interacting protein, myosin-binding for fast-type C protein, tropomyosin alpha-1 chain, troponin I, and filamin were the proteins related to the structure and activity of muscle tissue. Calreticulin drove the calcium regulation in cells, while the superoxide dismutase and stress-70 protein used in the oxidative stress and stress response.

According to Astuti et al., the stress in the animal can lead to an increase in glycogen breakdown in muscle. Furthermore, glycogen would be converted into glucose to produce ATP as energy-saving [27-28]. Salwani et al. reported that stress could be in the form of high energy requirements [18]. The reduction of oxygen supply to the body during exsanguination increased the rate of glycolysis to produce ATP. This would cause some

enzymes associated with the glycolysis process to be highly expressed. In non-halal slaughter, the stress response was thought to be greater because animals experienced greater physiological discomfort. In this study, cervical dislocation caused brain and spinal injury before death. The process of cervical dislocation provided two traumatic effects, not only the hematoma, brain damage, spinal fractures, and spinal cord disorders, but also severe lacerations (rips injuries) in the medulla oblongata [29].

In this study, some of the proteins that were significantly changed included glycolysis proteins, such as β -enolase, dihydrolipoyl dehydrogenase, phosphoglucomutase 1, and malate dehydrogenase. Referring to Nakyinsige et al., aspartate aminotransferase was also found to be higher in the non-halal group [30]. This indicated that the stress response of non-halal slaughter increased the glucose and energy metabolism of an animal so that several proteins associated with the glycolysis were higher expressed. The high energy required for animal muscle activity was obtained from the metabolism of glucose (from glycogen) in the muscle [31]. It was also supposed that some proteins related to the muscle tissue activity increased, such as myc box-dependent-interacting 1, myosin-binding protein C fast-type, tropomyosin alpha-1 chain, troponin I, and filamin-C. Calcium regulation in

Table 1. Proteins abundance and the ratio of non-halal to halal slaughter

Protein	Abundance (a.u.)		Ratio (non-halal/halal)	<i>p</i> -value
	Non-halal	Halal		
Mitochondrial aspartate aminotransferase (Got2)	163.6	36.4	4.495	0.00023
Beta-enolase (Eno3)	118.9	81.1	1.467	0.03162
Calreticulin (Calr)	116.6	83.4	1.398	0.03450
Dihydrolipoyl dehydrogenase (Dld)	155.9	44.1	3.535	0.02769
Filamin-C (Flnc)	162.1	37.9	4.277	0.00127
Phosphoglucomutase 1 (Pgm1)	123.4	34.4	1.611	0.00015
Mitochondrial malate dehydrogenase (Mdh2)	165.6	76.6	4.814	0.01434
Myc box-dependent-interacting 1 (Bin1)	133.9	66.1	2.026	0.04250
Myosin binding protein C, fast-type (Mybpc2)	149.1	50.9	4.865	0.00294
Stress-70 protein (Hspa9)	174.3	25.7	6.782	0.03666
Superoxide dismutase [Cu-Zn] (Sod1)	152.5	47.5	3.210	0.01466
Tropomyosin alpha-1 chain (Tpm1)	122.5	77.5	1.580	0.00154
Troponin I (Tnni2)	188.8	11.2	16.86	0.01736

the body was useful to maintain homeostasis. Loss of energy causes the loss of cellular homeostasis and damages Ca^{2+} signaling, which directed the endoplasmic reticulum stress response activity [32]. This is supposed to increase the expression of calreticulin protein. Furthermore, the proteins that were up-regulated in the non-halal slaughter could be proposed as the candidates for markers for non-halal animal slaughtering.

Specifically Expressed Proteins Caused by Non-halal Slaughtering

Although the up-regulated protein related to the non-halal slaughter has been identified, it cannot easily be used as a marker since it must employ the comparison study of each analysis. A protein marker specifically expressed only in non-halal slaughter was the best candidate for the marker. There were three proteins, NSFL1 cofactor p47 (Nsf11c), transketolase (Tkt), and Von Willebrand factor (Vwf), consistently present only in the non-halal samples. Transketolase proteins were involved in the regulatory process, cell organization, biogenesis, and metabolism. Meanwhile, the Von Willebrand factor was a protein involved in the response to stimulus. This protein worked in the blood coagulation process caused by wounds or injuries on the blood vessels [33]. The process of cervical dislocation could be thought to stimulate the excretion of the Von Willebrand factor due to the occurrence of injuries in an animal body. The process of cervical dislocation-initiated hematoma, whereas the halal slaughter process created a large incision on the neck's blood vessels that caused the blood to quickly run out of the body [29]. Therefore, the blood clotting process might not occur. In contrast to cervical dislocation, wounds arise on the blood vessels of an animal body so that the blood clotting could occur as a response to stopping internal bleeding. Therefore, these proteins were proposed to be the potential candidates for markers for non-halal animal slaughtering.

Interactions of the up-regulated and specifically expressed proteins were analyzed using STRING v11. Fig. 2. shows the protein-protein interaction from 16 proteins. The network indicates 16 nodes and 55 edges with an average node degree of 6.88 and an average local clustering

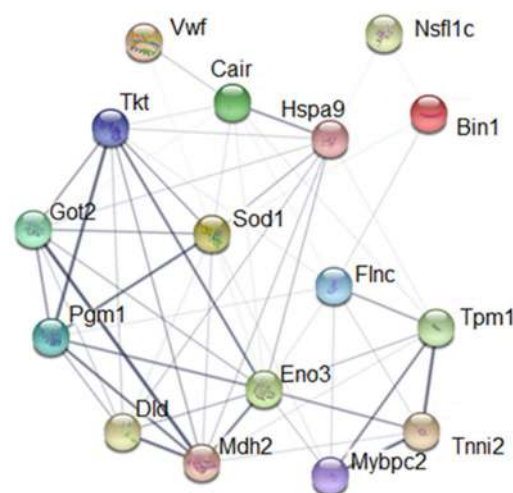


Fig 2. Protein-protein interaction from the up-regulated and specifically expressed protein in non-halal slaughter. The thickness of the line represents the confidence of the protein interaction

coefficient of 0.79. Proteins can interact and associate physically or functionally. From this result, it might be concluded that the identified proteins were related to each other. One protein expression would stimulate the expression of other proteins. Further studies were required to better understand the relationship between proteins and the slaughter process.

Peptide Target for Protein Marker Analysis of Non-halal Slaughtering

The common method to detect protein markers, in this case, the specific proteins present in non-halal slaughtering meat samples, is by detecting the specific peptide of the protein. Proteome discoverer analysis of HRMS data revealed several peptides specific to the proteins NSFL1 cofactor p47, transketolase, and Von Willebrand factor. The sequence of the peptides was confirmed by analysis of MS/MS data using the Proteome discoverer. Fig. 3(a) shows the MS/MS spectra of the NSFL1 cofactor p47 peptide obtained from the fragmentation of a peptide with the molecular mass (MH^+) = 1754.83213. However, the most stable ion of the peptide was detected as an ion with $m/z = 877.92064$ ($z = +2$). Fig. 3(b) confirmed the match of the fragment mass and the difference mass between the fragments to the mass database to possibly construct the peptide sequence.

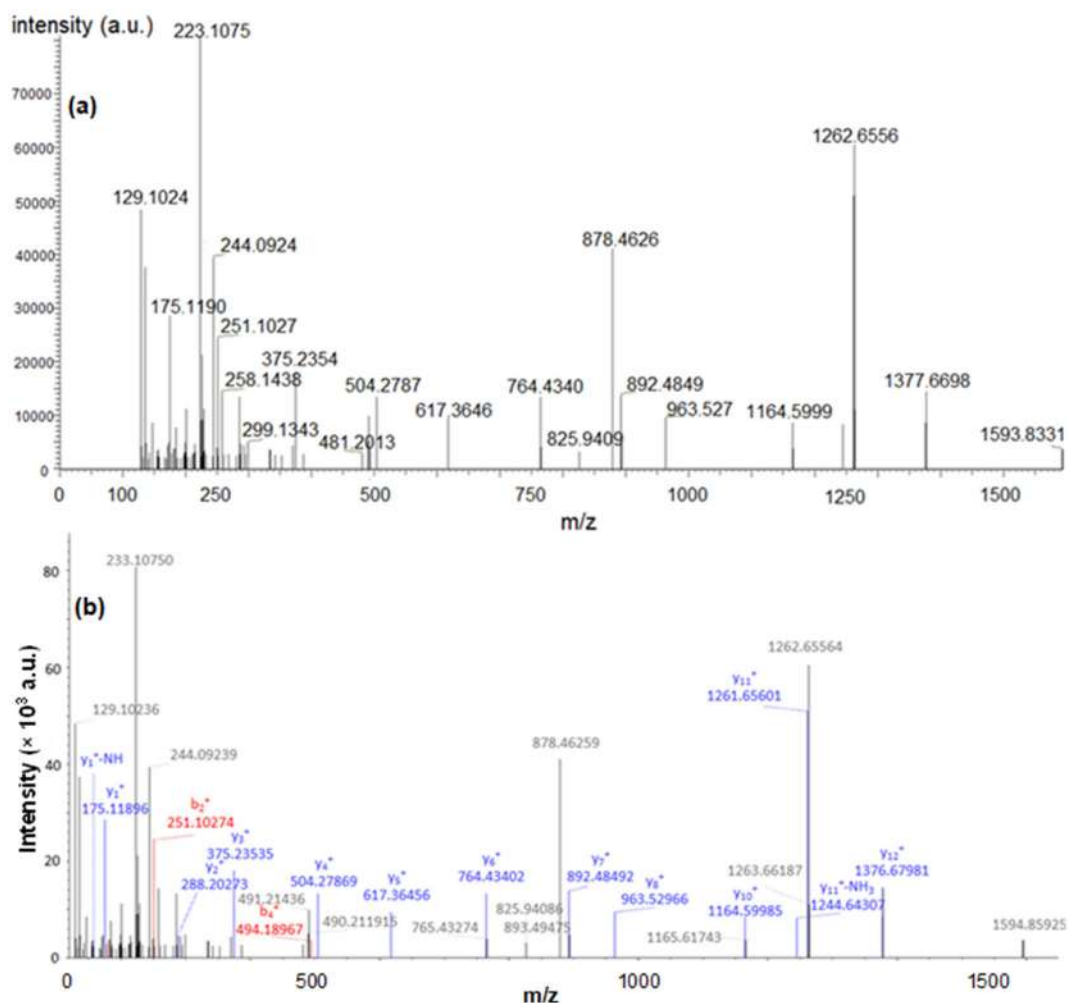


Fig 3. The Mass spectra of peptide-specific to NSFL1 cofactor p47 protein. (a) The raw MS/MS fragmentation of the peptide. (b) Proteome discoverer identification of the fragment b^+ and y^+ from raw MS/MS leading to a sequence of the peptide

The dominant ions were y^+ ions. To be mentioned, a few of the fragmentation analyses were the difference between the y_{12}^+ fragment (1376.67981) and the y_{11}^+ (1261.65601) was confirmed as amino acid D (115.03), the difference between y_{11}^+ with y_{10}^+ (1164.59985) was confirmed as P (97.05). By using the same calculation, DPSNAQFLESIR was obtained. After comparing the sequence to the whole sequence of NSFL1 cofactor p47 protein and possible trypsin digestion product of the protein, it was concluded that the peptide sequence is SYQDPSNAQFLESIR.

Fig. 4(a) shows the MS/MS spectra of the transketolase protein-peptide as the result of peptide fragmentation with molecular mass (MH^+) of 2023.02262, which present as molecular ion with m/z of 675.01275 (z

= +3). Interpretation of Fig. 4(b) using Proteome discoverer revealed several match ions with possible ion fragment peptides that were part of transketolase protein. Analysis of the difference among several detected y^+ fragments led to a sequence of the peptides. The difference between the y_8^+ ion (1016.52655) to the y_6^+ ion (751.39722) was equal to the mass of QH, then the difference of the y_6^+ to the y_5^+ ion (652.32953) led to V, followed by the mass difference of the y_5^+ ion to the y_4^+ ion (537.30408) was equal to the mass of D. Furthermore, the different of the y_4^+ ion to the y_3^+ ion (438.23602) could be read as V, while the difference between the y_3^+ ion to the $y_2^+-NH_3$ (258.14426) was equal to Y, and the $y_2^+-NH_3$ to the y_1^+ (147.11281) was equal to Q. The analysis of the y^+

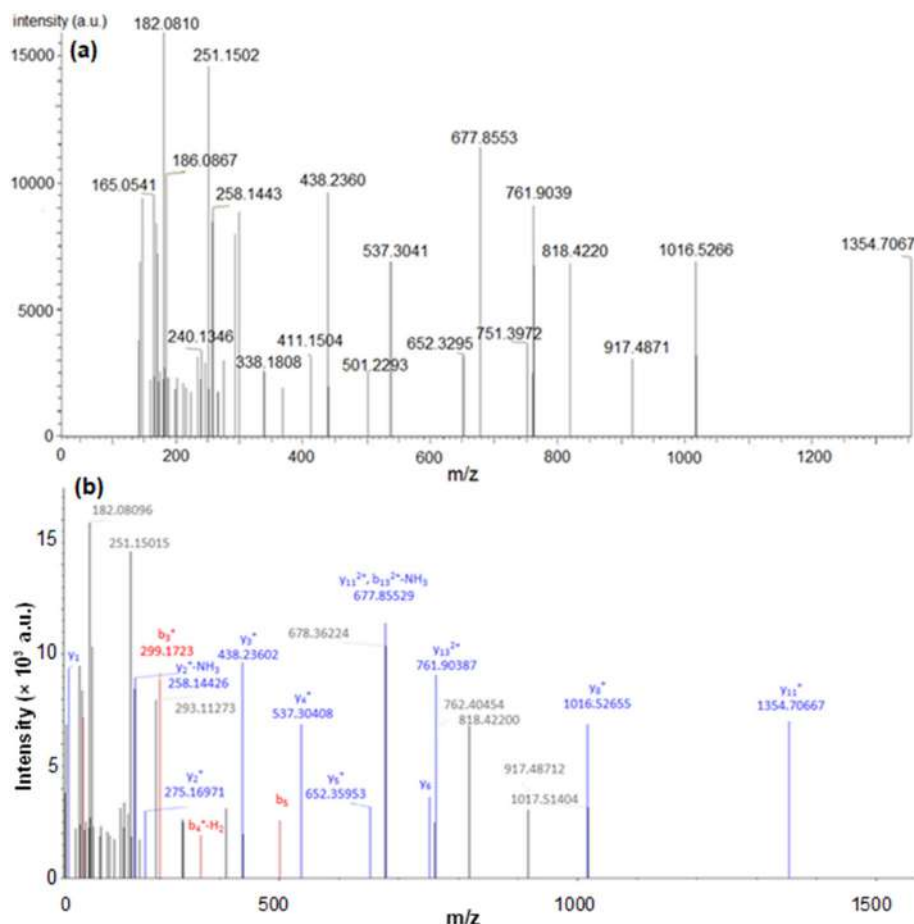


Fig 4. The Mass spectra of peptides specific to transketolase protein (a) The raw MS/MS fragmentation of the peptide (b) Proteome discoverer identification of the fragment b^+ and y^+ from raw MS/MS leading to a sequence of the peptide

ions fragment mass concluded the sequence QHQVDVYQK as part of the peptide sequence. The same approach to analyze the b^+ ions including b_5^+ (501.22931), $b_4^+ - H_2O$ (368.19409) b_3^+ (299.17123), and b_2^+ (171.11282) concluded the sequence QSD as part of the peptide. Based on this information and the protein database, the proteome discoverer confirmed the sequence of the peptide is LGQSDPAPLQHQVDVYQK.

The sequence of the specific peptide of Von Willebrand factor was revealed mainly based on the protein database and the high-resolution MS of the molecular ion of peptide, with MH^+ of 2550.23739 and m/z of 510.85397 ($z = +5$). Only a few of the fragmentation of MS2 was identified as the b_3^+ ion (195.11179) and the y_1^+ 175.11818. The proteome discoverer concluded the sequence as VPLLCTNGSVVHHEVINAMQCR.

These three peptides were suggested to be used as a

target for routine analysis. The targeted analysis usually employed standard LC-MS/MS using an MRM (Multiple Reaction Monitoring) which was known as the best mode to perform both qualitative and quantitative analysis using LC-MS/MS. This approach required information regarding the mass of the selected peptide as the precursor peptide ion targets and the production of the MS2 fragmentation [34]. Based on the MS spectra in Fig. 3(b) and 4(b), several MRM pairs were proposed to identify each protein that was specifically expressed in the non-halal slaughter process. Those pairs of MRMs are presented in Table 2 selected based on certain criteria. According to You et al., the precursor ion must be the predominant specific peptide with a size of approximately 600–2000 [35]. Among the three protein-specific peptides, only the first two peptides met those criteria (peptide number one and two). Meanwhile, the

Table 2. The proposed MRM pairs to detect specifically expressed protein related to non-halal slaughter using LC-MS/MS

No	Specific peptides	MRM pair	
		Precursor ion mass	Fragment ion mass
1	SYQDPSNAQFLESIR	1755	1376
			1262
			1164
			963
2	LGQSDPAPLQHQVDVYQK	2023	1355
			1016
			762

production ions should be the predominant single charged ions generated from the fragmentation, which were preferable for the ions with m/z higher than m/z of the precursor ion. The first peptide had $m/z = 877.92064$ ($z = 2$), meaning that the production higher than 877, which were 1376, 1262, 1164, and 963 will be the good options. The production of 892 was also shown predominant signal, but both were selected because they had an m/z value close to the precursor ion. The second peptide had m/z of 675.01275 ($z = 3$), making the production of 1355, 1016, and 762 met the criteria as MRM productions.

■ CONCLUSION

The study demonstrated that the different slaughter methods altered the proteome expression of animal meat. Thirteen proteins were identified to be up-regulated on non-halal slaughter. Proteome analysis also revealed that three proteins were specifically expressed on non-halal slaughter, which were NSFL1 cofactor p47, transketolase, and Von Willebrand factor, and proposed as the biomarker protein related to non-halal slaughter. The up-regulated and the specifically expressed proteins suggested that non-halal slaughter could contribute to stress response in the animal. The two stable peptides of SYQDPSNAQFLESIR ($m/z = 1755$, $z = +1$) part of NSFL cofactor p47, and LGQSDPAPLQHQVDVYQK ($m/z = 2023$, $z = +1$) part of transketolase can be targeted as markers in MRM mode LC-MS/MS routine analysis to distinguish non-halal slaughtering meat from halal slaughtering originated meat. The proposed MRM pair ions were 1755 to 1376, 1262, 1164, 963, and 2033 to 1355, 1016, 762.

■ ACKNOWLEDGMENTS

This research was financially supported by Institute Halal for Industry and System, Universitas Gadjah Mada. The author would like to thank the Integrated Research and Testing Laboratory (LPPT) of Universitas Gadjah Mada, Yogyakarta for providing the necessary facilities.

■ AUTHOR CONTRIBUTIONS

The first author conducted the experiment of protein extraction and protein digestion as well SDS-PAGE and some data analysis, the second author conducted the animal experiments including ethical clearance admission, the third author did the HRMS analysis. The third author conducted the data analysis, wrote and revised the manuscript together with the first author. All authors agreed to the final version of this manuscript.

■ REFERENCES

- [1] Raharjo, T.J., Cahyaningtyas, W., Surajiman, S., Istini, I., and Pranowo, D., 2012, Validation of PCR-RFLP testing method to detect porcine contamination in chicken nugget, *Indones. J. Chem.*, 12 (3), 302–307.
- [2] Rohman, A., Erwanto Y., Hossain, M.A.M., Rizou, M., Aldawoud, T.M.S., and Galanakis, C.M., 2021, “The Application of DNAZ-based methods for authentication analysis: Examples in halal and kosher food products” in *Food Authentication and Traceability*, Eds. Galanakis, C.M., Academic Press, Cambridge, US, 195–213.

- [3] Nalazek-Rudnicka, K., Kłosowska-Chomiczewska, I., Wasik, A., and Macierzanka, A., 2019, MRM–MS of marker peptides and their abundance as a tool for authentication of meat species and meat cuts in single-cut meat products, *Food Chem.*, 283, 367–374.
- [4] Grandin, T., 2001, "Antemortem handling and welfare" in *Meat Science and Applications*, Eds. Hui, Y.H., Nip, W.K., Rogers, R.W., and Young, O.A., Marcel Dekker, New York, 221–254.
- [5] Bakhsh, A., Ismail, I., Hwang, Y.H., Lee, J.G., and Joo, S.T., 2018, Comparison of blood loss and meat quality characteristics in Korean black goat subjected to head-only electrical stunning or without stunning, *Korean J. Food Sci. Anim. Resour.*, 38 (6), 1286–1293.
- [6] Ali, S.A.M., Abdalla, H.O., and Mahgoub, I.M., 2011, Effect of slaughtering method on the keeping quality of broiler chicken meat, *Egypt Poult. Sci.*, 31 (4), 727–736.
- [7] Maqsood, S., and Benjakul, S., 2011, Effect of bleeding on lipid oxidation and quality changes of Asian seabass (*Lates calcarifer*) muscle during iced storage, *Food Chem.*, 124 (2), 459–467.
- [8] Mouzo, D., Rodríguez-Vázquez, R., Lorenzo, J.M., Franco, D., Zapata, C., and López-Pedrouso, M., 2020, Proteomic application in predicting food quality relating to animal welfare. A review, *Trends Food Sci. Technol.*, 99, 520–530.
- [9] Huang, J.C., Huang, M., Yang, J., Wang, P., Xu, X.L., and Zhou, G.H., 2014, The effects of electrical stunning methods on broiler meat quality: Effect on stress, glycolysis, water distribution, and myofibrillar ultra-structures, *Poult. Sci.*, 93 (8), 2087–2095.
- [10] Addeen, A., Benjakul, S., Wattanachant, S., and Maqsood, S., 2014, Effect of Islamic slaughtering on chemical compositions and post-mortem quality changes of broiler chicken meat, *Int. Food Res. J.*, 21 (3), 897–907.
- [11] Nielsen, S.S., Alvarez, J., Bicout, D.J., Calistri, P., Depner, K., Drewe J.A., Garin-Bastuji, B., Rojas, J.L.G., Schmidt, C.G., Herskin, M., Michel, V., Chueca, M.A.M., Roberts, H.C., Sihvonen, C.G., Spooler, H., Stahl, K., Velarde, A., Viltrop, A., Candani, D., Van der Stede, Y., and Winckler, C., 2020, Welfare of cattle during killing for purposes other than slaughter, *EFSA J.*, 18 (11), e06312.
- [12] Żurek, J., Rudy, M., Kachel, M. and Rudy, S., 2021, Conventional versus ritual slaughter—ethical aspects and meat quality, *Processes*, 9 (8), 1381.
- [13] Velarde, A., Gispert, M., Diestre, A., and Manteca, X., 2013, Effect of electrical stunning on meat and carcass quality in lambs, *Meat Sci.*, 63 (1), 35–38.
- [14] Yardimci, M., 2019, Comparison of the stunning and non-stunning slaughtering methods in the light of the current knowledge, *J. Vet. Anim. Res.*, 2 (3), 1–5.
- [15] Samah, N.A., Amid, A., and Yusof, F., 2011, Overexpression of voltage-dependent anion channel 2 (VDAC2) in muscles of electrically stunned chickens, *IIUM Eng. J.*, 12 (4), 213–222.
- [16] Amid, A., Samah, N.A., and Yusof, F., 2012, Identification of troponin I and actin, alpha cardiac muscle 1 as potential biomarkers for hearts of electrically stimulated chickens, *Proteome Sci.*, 10 (1), 1.
- [17] Kiran, M., Naveena, B.M., Smrutirekha, M., Baswa Reddy, P., Banerjee, R., Praveen, K.Y., Venkatesh, C., and Rapole, S., 2019, Traditional halal slaughter without stunning versus slaughter with electrical stunning of sheep (*Ovis aries*), *Meat Sci.*, 148, 127–136.
- [18] Salwani, M.S., Adeyemi, K.D., Sarah, S.A., Vejayan, J., Zulkifli, I., and Sazili, A.Q., 2015, Skeletal muscle proteome and meat quality of broiler chickens subjected to gas stunning prior slaughter or slaughtered without stunning, *CyTA-J. Food*, 14 (3), 375–381.
- [19] Yates, J.R., 2013, The revolution and evolution of shotgun proteomics for large-scale proteome analysis, *J. Am. Chem. Soc.*, 135 (5), 1629–1640.
- [20] Aini, A.N., 2019, Identifikasi Protein Penanda Spesifik Metode Penyembelihan Hewan Menggunakan Spektrometri Massa Resolusi Tinggi, *Thesis*, Universitas Gadjah Mada, Indonesia.
- [21] Szklarczyk, D., Gable A.L., Lyon, D., Junge, A., Wyder, S., Huerta-Cepas, J., Simonovic, M., Doncheva, N.T., Morris, J.H., Bork, P., Jensen, L.J.,

- and von Mering, C., 2019, STRING v11: protein-protein association networks with increased coverage, supporting functional discovery in genome-wide experimental datasets, *Nucleic Acids Res.*, 47 (D1), D607–613.
- [22] Orduna, A.R., Husby, E., Yang, C.T., Ghosh, D., and Beaudry, F., 2017, Detection of meat species adulteration using high-resolution mass spectrometry and a proteogenomics strategy, *Food Addit. Contam., Part A*, 34 (7), 1110–1120.
- [23] Kanehisa, M., and Goto, S., 2000, KEGG: Kyoto encyclopedia of genes and genomes, *Nucleic Acids Res.*, 28 (1), 27–30.
- [24] Doherty, M.K., McLean, L., Hayter, J.R., Pratt, J.M., Duncan, H.L., Robertson, D.H., El-Shafei, A., Gaskell, S.J., and Beynon, R.J., 2004, The proteome of chicken skeletal muscle: Changes in soluble protein expression during growth in a layer strain, *Proteomics*, 4 (7), 2082–2093.
- [25] The UniProt Consortium, 2019, UniProt: A worldwide hub of protein knowledge, *Nucleic Acid Res.*, 47 (D1), D506–515.
- [26] Feng, Y.H., Zhang, S.S., Sun, B.Z., Xie, P., Wen, K.X., and Xu, C.C., 2020, Changes in physical meat traits, protein solubility, and the microstructure of different beef muscles during post-mortem aging, *Foods*, 9 (6), 806.
- [27] Astuti, P., Putro, C.P.C., Airin, C.M., Sjahfirdi, L., Widiyanto, S., and Maheshwari, H., 2014, Comparison of process slaughtered on beef cattle based on level of cortisol and Fourier Transform Infrared Spectroscopy (FTIR), *Int. J. Anim. Vet. Sci.*, 8 (12), 876–879.
- [28] Adeva-Andany, M.M., González-Lucán, M., Donapetry-García, C., Fernández-Fernández, C., and Ameneiros-Rodríguez, E., 2016, Glycogen metabolism in humans, *BBA Clin.*, 5, 85–100.
- [29] Bader, S., Meyer-Kühling, B., Günther, R., Breithaupt, A., Rautenschlein, S., and Gruber, A.D., 2014, Anatomical and histological pathology induced by cervical dislocation following blunt head trauma for on-farm euthanasia of poultry, *J. Appl. Poult. Res.*, 23 (3), 546–556.
- [30] Nakyinsige, K., Fatimah, A., Aghwan, Z.A., Zulkifli, I., Goh, Y.M., and Sazili, A.Q., 2014, Bleeding efficiency and meat oxidative stability and microbiological quality of New Zealand white rabbits subjected to halal slaughter without stunning and gas stun killing, *Asian-Australas. J. Anim. Sci.*, 27 (3), 406–413.
- [31] Abdela, N., Jilo, K., Siraj, S., Adem, J., and Mohammed, A., 2016, Impact of stress on health and productivity of animal: A review, *J. Nat. Sci. Res.*, 6 (9), 45–51.
- [32] Krebs, J., Agellon, L.B., and Michalak, M., 2015, Ca²⁺ homeostasis and endoplasmic reticulum (ER) stress: An integrated view of calcium signaling, *Biochem. Biophys. Res. Commun.*, 460 (1), 114–121.
- [33] Zeng, J., Shu, Z., Liang, Q., Zhang, J., Wu, W., Wang, X., and Zhou, A., 2022, Structural basis of von Willebrand factor multimerization and tubular storage, *Blood*, 139 (22), 3314–3324.
- [34] Rauh, M., 2012, LC-MS/MS for protein and peptide quantification in clinical chemistry, *J. Chromatogr. B*, 883–884, 58–67.
- [35] You, J., Willcox, M.D., Madigan, M.C., Wasinger, V., Schiller, B., Walsh, B.J., Graham, P.H., Kearsley, J.H., and Li, Y., 2013, Tear fluid protein biomarkers, *Adv. Clin. Chem.*, 62, 151–196.